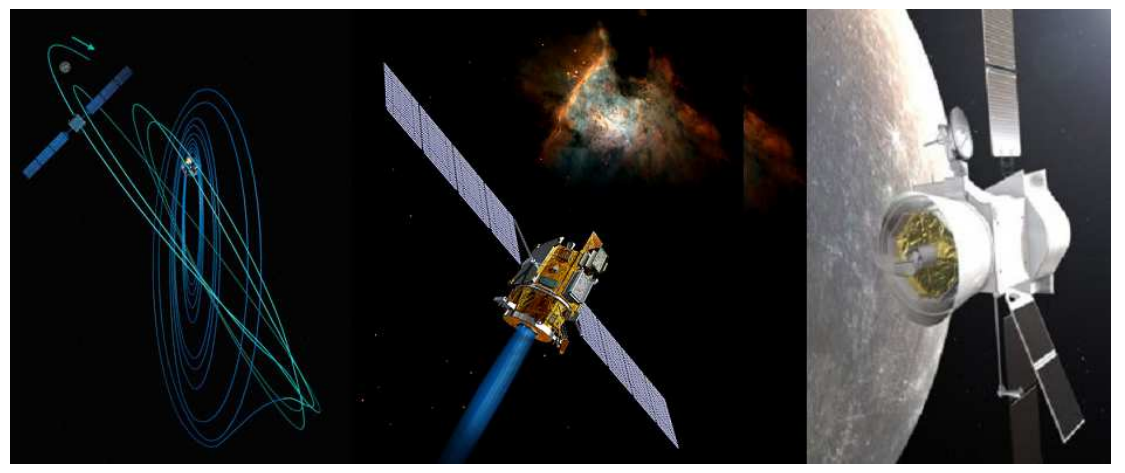
Analytical Representations of Low-Thrust Trajectories

Master Thesis Report



Tatiana Paulino

Delft University of Technology December, 8th 2008



1

Analytical	Representations of Lo	ow-Thrust Trajector
11110007111000		The section of the se

Acknowledgments

This master thesis would not be possible without the help of many people.

First, I would like to thank Ir. Ron Noomen for giving me the chance to work in such interesting topic for my master thesis as interplanetary low-thrust. His guidance and patience were very important for the outcome of my work.

I would like also to express my gratitude to Prof. Ir. B.A.C. Ambrosius and to Dr. Guillermo Ortega, the Head of the Dynamics and Mathematical Analysis Unit (TEC-ECM) of ESTEC (ESA) for giving me the opportunity to do my internship at ESA, in the development of the Interplanetary Low-Thrust module in STA. The experience that I gained during my internship was also very important for outcome of this thesis.

I would like to thank Stefano Corradini for providing me with the results of the exponential sinusoid implemented in Galomusit.

My special thanks to Dr. Dario Izzo for being available to answer to all my questions and for lending me his integrator routines. Also, I would like to thank Ir. Robin Biesbroek for giving me access to SBC 8 and Ir. Jeroen Melman for sharing helpful information for this project.

Of course, this thesis will not be possible without my friends' support: Fred for listening patiently to all my complains, Nuno for being the most reasonable person I know, Inês for giving me 'positive energies', Lascas and Zé for all the nice weekends, Christina for the nice conversations, Luísa for being just like me and eng. Tixa (a.k.a. Paulo) for the nice time we all spent together. I would also like to thank to all the people in the 9th floor of the Aerospace faculty for the good and bad moments we spent together, in particular to Ir. Jeannette Heiligers for helping me to overcome the difficulties in my master thesis.

Finally, I would like to thank my family, specially my parents for always supporting me in every decision I made regarding my stay here in the Netherlands.

Contents

Ack	nowledgn	nents	iii
Sum	mary		ix
List	of Figures	S	xi
List	of Tables		xxiii
Non	nenclature		xxvii
Intro	oduction		1
1.	Orbital M	Techanics	3
1.1.	Refe	erence Frames	3
1.2.	Orb	ital elements	5
1.3.	Two	o-body problem	6
	1.3.1.	Elliptic orbits	9
	1.3.2.	Parabolic orbits	10
	1.3.3.	Hyperbolic orbits	11
1.4.	4. Perturbing Forces		
1.5.	Coo	rdinate Systems	14
2.	Numerica	al Integration Methods	17
2.1.	Run	ge-Kutta Methods	18
2.2.	Ana	lysis	22
2.3.	Disc	cussion	23
3.	Spacecra	ft Propulsion	25
3.1.	Prin	ciples of Propulsion	25
3.2.	Che	mical Propulsion System	26
	3.2.1.	Types of Chemical Propellants	27
3.3.	Elec	etric Spacecraft Propulsion	29
	3.3.1.	Basic Principles	30
	3.3.2.	Methods	32
	3.3.3.	Examples of Missions using Electric Propulsion	
4.	Non-perturbed Transfer Orbits		
4.1.	Heli	ocentric Phase	38
4.2.		netocentric Phases	
5.	Low-Thr	ust Trajectories	45
5.1.	Basi	ic Equations of Motion for Low-Thrust Trajectories	46

5.2.	Exp	onential Sinusoid – Geometry and Dynamics	47
5.3.	. Exponential Sinusoid using Tangential Thrust		
5.4.	Pro	cedure done by Petropoulos and Longuski	54
	5.4.1.	In-Plane Motion	55
	5.4.2.	Out-of-Plane Motion	57
5.5.	Pro	cedure done by Izzo	59
6.	Candida	te Shapes for Low-Thrust Trajectories	65
6.1.	Rac	lius Equations and Geometric Parameters	65
6.2.	Imp	lementation	71
6.3.	Cor	nstraint Equation – Tangential Thrust	77
	6.3.1.	Archimedean Spiral	77
	6.3.2.	Logarithmic Spiral	79
	6.3.3.	Poinsot's Spiral (hyperbolic sine)	80
	6.3.4.	Poinsot's Spiral (hyperbolic cosine)	82
	6.3.5.	Sinusoidal Spiral	83
6.4.	Cor	astraint Equations and Computation Problems - Acceleration	Inversely
Squa	are and C	onstant Acceleration Cases of the Thrust Profile	84
6.5.	Sun	nmary	86
7.	Sensitivi	ty Study of the Shapes' Performance	87
7.1.	Arc	himedean Spiral	88
7.2.	Log	garithmic spiral	103
7.3.	Poi	nsot's spiral (hyperbolic sine)	117
7.4.	Poi	nsot's spiral (hyperbolic cosine)	130
7.5.	Sin	usoidal spiral	145
7.6.	Exp	onential Sinusoid	158
7.7.	Cor	iclusions	174
8.	Optimisa	ation	179
8.1.	Opt	imisation Methods	179
	8.1.1.	Calculus-Based Methods	180
	8.1.2.	Enumerative Methods	181
	8.1.3.	Random Methods	182
8.2.		lti-Objective Optimisation	
8.3.	Opt	imisation Procedure	185
	8.3.1.	Description of the Optimisation Problem	185

	8.3.2.	Computation of the Total Fuel Mass Consumption	187
	8.3.3.	Fuel Mass Consumption (Low-Thrust Phase)	189
	8.3.4.	Thrust Acceleration Constraint	191
9.	Verificat	ion	195
10.	Results		201
10.1	. Eart	th - Mars Flight: Tangential Thrust	201
	10.1.1.	Analysis of the Pareto Fronts	204
	10.1.2.	Thrust Acceleration Constraint	208
10.2	. Eart	th - Mercury Flight: Tangential Thrust	211
	10.2.1.	Thrust Acceleration Constraint	213
10.3	. Eart	th-Mars Flight: Acceleration Inversely Square Case	217
	10.3.1.	Thrust Acceleration Constraint	219
10.4	. Eart	th - Mercury Flight: Acceleration Inversely Square Case	221
	10.4.1.	Thrust Acceleration Constraint	222
10.5	. Con	nclusions	226
11.	Final cor	nclusions	231
12.	Recomm	endations	235
Bibl	iography.		239
App	endices		Ai

Summary

Low-thrust electric propulsion is one of the most promising technologies in interplanetary missions, due to its large savings in propellant cost. It has already been tested in missions, like SMART-1 (ESA) and Deep Space 1 (NASA).

Since the beginning of space exploration, methods using analytical representations to describe spacecraft's trajectory have been used in order to serve as "fast mission" generators. In 1999, Petropoulos introduced an analytical representation capable of representing low-thrust trajectories: the exponential sinusoid [Petropoulos et al, 1999]. However, only one particular steering program was studied: trajectories with tangential and continuous thrust, modulated by the distance to the Sun.

The aim of this master thesis is to analyse several analytical representations (shapes) and steering programs, in addition to the one considered in [Petropoulos et al, 1999] and compare their performance with the exponential sinusoid using continuous tangential thrust. The shapes that are considered in this project, already mentioned and pre-selected in the literature survey [Paulino, 2007], were: the Archimedean spiral, the logarithmic spiral, the Poinsot's spiral (hyperbolic cosine), the sinusoidal spiral and the exponential sinusoid. Also, three different thrust profiles were analysed: (1) "acceleration inversely square", where the magnitude of the thrust acceleration monotonically decreases with the square of the distance to the Sun - $a = a_0 \mu/r^2$ and a_0 is the thrust acceleration normalised by the local gravitational acceleration (i.e. it is non-dimensional), which is considered constant; (2) "constant acceleration", where the magnitude of the thrust acceleration is constant: $a = a_0 \mu/r_1^2$; (3) "tangential" thrust profile where continuous tangential thrust is considered (studied in [Petropoulos and Longuski, 2004] and [Izzo, 2006]).

A technique related to the one developed by Dario Izzo [Izzo, 2006] to find feasible trajectories using low-thrust propulsion for a 2D problem was implemented. In this master thesis, given the shape, the initial and final points of the trajectory, the angle between them and the number of complete revolutions, the excess velocities, the TOF and the fuel mass consumption during the low-thrust transfer can be computed.

Multi-objective optimization using a Monte Carlo method was implemented for the 6 shapes and the acceleration inversely square and the tangential cases of the thrust profile. The total excess velocity and the fuel mass consumption during the interplanetary low-thrust phase were the two objective functions that were minimized. Pareto fronts were built for all 6 shapes, two thrust profiles and three different test missions: an Earth-to-Mars flight, an Earth-to-Jupiter flight and an Earth-to-Mercury flight.

The sinusoidal spiral using continuous tangential thrust had the best Pareto front for all three missions. Compared with the exponential sinusoid using the tangential thrust profile, the computation time is smaller, the minimum total excess velocity value achieved is lower and the number of individuals that respect the maximum thrust acceleration constraint is higher. The other combinations of shapes and thrust profiles performed worse than the exponential sinusoid using the tangential thrust profile in at least one of these three criteria. Unfortunately, it was proven not be worthwhile to use the acceleration inversely square case of the thrust profile in a fast mission generator, since the computation time was significantly higher (approximately 46 times the computation time of the tangential case, for an Earth-Mars flight, using the sinusoidal spiral).

List of Figures

Figure 1.1: The non-rotating heliocentric ecliptic reference frame using Cartesian and spherical coordinates 4
Figure 1.2: Representation of the orbital elements [Montenbruck et al., 2005]
Figure 1.3: The three types of conic sections: the ellipse, the parabola and the hyperbola, based on [Montenbruck et al., 2005]
Figure 1.4: Distance versus velocity for three hyperbolic trajectories [Melman, 2007]
Figure 2.1: Approximate solution of the differential equation $\dot{y} = f(t, y)$ [Montenbruck et al., 2005]18
Figure 2.2: The Butcher tableau [Montenbruck et al., 2005]
Figure 2.3: The number of function calls in function of accuracy for Runge-Kutta methods: DOPRI5 (5 th order), RKF7 (7 th order) and DOPRI8 (8 th order) [Montenbruck et al., 2005]
Figure 4.1: Heliocentric transfer orbit [Cornelisse et al., 1979]
Figure 4.2: Hohmann Transfer Orbit [Wertz, 2001]41
Figure 5.1: Shapes that can be represented by an exponential sinusoid [Petropoulos et al., 1999]48
Figure 5.2: Example of exponential sinusoid shapes from pericentre to apocentre using $k_1 = 0.5$ and (a)
$k_2 = 2/3$ and (b) $k_2 = 2/11$ [Petropoulos and Longuski, 2004]49
Figure 5.3: Representation of the low-thrust reference plane and the out-of-plane additional force \overline{a}_{out} 55
Figure 5.4: (a) Position of the spacecraft in the out-of plane motion, (b) velocity vector in the XY-plane58
Figure 5.5: Representation of the transfer plane
Figure 5.6: (a) the TOF versus the initial flight path angle γ_1 for the class $S_{1/12}(1,1.5,\pi/2,N)$ and (b)
feasible exponential sinusoids for the class $S_{1/12}(1,1.5,\pi/2,0)$ [Izzo, 2006]63
Figure 5.7: TOF as function of γ_1 for the exponential sinusoid $S_{0.4}\left(r_{\text{Earth}}, r_{\text{Mars}}, \pi/2, 3\right)$, in an Earth-to-Mars
flight64
Figure 6.1: The Archimedes's spiral (green), the Fermat's spiral (blue), the hyperbolic spiral (orange) and the lituus (red) [Weisstein, 2007]66
Figure 6.2: Logarithmic spiral [Weisstein, 2007]67
Figure 6.3: (a) The Poinsot's spiral (hyperbolic sine) and the (b) Poinsot's spiral (hyperbolic cosine) [Weisstein, 2007]69
Figure 6.4: The Cayley's sextet (n=1/3), the cardioid (n=1/2) and the lemniscate of Bernoulli (n=2)

Figure 6.5: The sinusoidal spiral
Figure 6.6: Representation of the celestial longitude, the radial and tangential velocities at the target planet.76
Figure 7.1: TOF for θ_i values of (0°, 120°, 240°, 360°) from left to right in the figure, α_0 values of (-60°, -
50°, -40°, -30°, -20°), $\Delta\theta$ values of (90°, 150°, 210°, 270°, 340°) (N=0), m =0.05, a_0 =0.1, acceleration
inversely square case of the thrust profile (Archimedean spiral), Earth-Mars flight89
Figure 7.2: $V_{\infty,T}$ for θ_i values of (0°, 120°, 240°, 360°) from left to right in the figure, α_0 values of (-60°, -
50°, -40°, -30°, -20°), $\Delta\theta$ values of (90°, 150°, 210°, 270°, 340°) (N=0), m =0.05, $a_{_0}$ =0.1, acceleration
inversely square case of the thrust profile (Archimedean spiral), Earth-Mars flight89
Figure 7.3: TOF for θ_i values of (0°, 120°, 240°, 360°) from left to right in the figure, α_0 values of (-60°, -
50°, -40°, -30°, -20°), $\Delta\theta$ values of (90°, 150°, 210°, 270°, 340°), m =0.05, acceleration inversely square
case of the thrust profile (Archimedean spiral), Earth-Mars flight, N=1 (a_0 =0.03) and N=2 (a_0 =0.02)91
Figure 7.4: $V_{\infty,T}$ for θ_i values of (0°, 120°, 240°, 360°) from left to right in the figure, α_0 values of (-60°, -
50°, -40°, -30°, -20°), $\Delta\theta$ values of (90°, 150°, 210°, 270°, 340°), m =0.05, acceleration inversely square
case of the thrust profile (Archimedean spiral), Earth-Mars flight, N=1 ($a_0 = 0.03$) and N=2 ($a_0 = 0.02$)91
Figure 7.5: Polar plot for N=1 (a_0 =0.04) and N=2 (a_0 =0.03), θ_i =0°, $\Delta\theta$ =90°, α_0 =-20°, m values of
(0.02;0.64;1.26;1.88;2.5), acceleration inversely square case (Archimedean spiral), Earth-Mars flight94
Figure 7.6: <i>a</i> plot for N=1 (a_0 =0.04) and N=2 (a_0 =0.03), θ_i =0°, $\Delta\theta$ =90°, α_0 =-20°, <i>m</i> values of
(0.02;0.64;1.26;1.88;2.5), acceleration inversely square case (Archimedean spiral), Earth-Mars flight94
Figure 7.7: α plot for N=1 (a_0 =0.04) and N=2 (a_0 =0.03), θ_i =0°, $\Delta\theta$ =90°, α_0 =-20°, m values of
(0.02;0.64;1.26;1.88;2.5), acceleration inversely square case (Archimedean spiral), Earth-Mars flight95
Figure 7.8: $\dot{\theta}$ plot for N=1 (a_0 =0.04) and N=2 (a_0 =0.03), θ_i =0°, $\Delta\theta$ =90°, α_0 =-20°, m values of
(0.02;0.64;1.26;1.88;2.5), acceleration inversely square case (Archimedean spiral), Earth-Mars flight95
Figure 7.9: γ plot for N=1 (a_0 =0.04) and N=2 (a_0 =0.03), θ_i =0°, $\Delta\theta$ =90°, α_0 =-20°, m values of
(0.02;0.64;1.26;1.88;2.5), acceleration inversely square case (Archimedean spiral), Earth-Mars flight96
Figure 7.10: TOF for θ_i values of (0°, 120°, 240°, 360°) from left to right in the figure, m values of
$(0.02; 0.64; 1.26; 1.88; 2.5), \ \Delta\theta \ \ \text{values of } (90^\circ, 150^\circ, 210^\circ, 270^\circ, 340^\circ) \ (N=0), \ \text{tangential thrust profile}$
(Archimedean spiral), Earth-Mars flight97
Figure 7.11: $V_{\infty,T}$ for θ_i values of (0°, 120°, 240°, 360°) from left to right in the figure, m values of
$(0.02; 0.64; 1.26; 1.88; 2.5), \ \Delta\theta$ values of $(90^{\circ}, 150^{\circ}, 210^{\circ}, 270^{\circ}, 340^{\circ})$ (N=0), tangential thrust profile
(Archimedean spiral) Farth-Mars flight

Figure 7.12: TOF for θ_i values of (0°, 120°, 240°, 360°) from left to right in the figure, m values of
$(0.02;0.64;1.26;1.88;2.5)$, $\Delta\theta$ values of $(90^\circ, 150^\circ, 210^\circ, 270^\circ, 340^\circ)$, tangential thrust profile (Archimedean spiral), Earth-Mars flight, for N=1 and N=298
Figure 7.13: $V_{\infty,T}$ for θ_i values of (0°, 120°, 240°, 360°) from left to right in the figure, m values of
$(0.02; 0.64; 1.26; 1.88; 2.5), \Delta\theta$ values of $(90^{\circ}, 150^{\circ}, 210^{\circ}, 270^{\circ}, 340^{\circ})$, tangential thrust profile
(Archimedean spiral), Earth-Mars flight, for N=1 and N=2
Figure 7.14: Polar plot for N=1 and N=2, θ_i =0°, $\Delta\theta$ =90°, m values of (0.02;0.64;1.26;1.88;2.5), tangential thrust profile (Archimedean spiral), Earth-Mars flight
Figure 7.15: <i>a</i> plot for N=1 and N=2, θ_i =0°, $\Delta\theta$ =90°, <i>m</i> values of (0.02;0.64;1.26;1.88;2.5), tangential thrust
profile (Archimedean spiral), Earth-Mars flight
Figure 7.16: α plot for N=1 and N=2, $\theta_i = 0^\circ$, $\Delta \theta = 90^\circ$, m values of (0.02;0.64;1.26;1.88;2.5), tangential
thrust profile (Archimedean spiral), Earth-Mars flight
Figure 7.17: $\dot{\theta}$ plot for N=1 and N=2, $\theta_i = 0^{\circ}$, $\Delta \theta = 90^{\circ}$, m values of (0.02;0.64;1.26;1.88;2.5), tangential
thrust profile (Archimedean spiral), Earth-Mars flight
Figure 7.18: TOF for θ_i values of (0°, 120°, 240°, 360°) from left to right in the figure, α_0 values of (-60°, -
50°, -40°, -30°, -20°), $\Delta\theta$ values of (90°, 150°, 210°, 270°, 340°) (N=0), m =0.05, $a_{_0}$ =0.11, acceleration
inversely square case of the thrust profile (logarithmic spiral), Earth-Mars flight103
Figure 7.19: $V_{\infty,T}$ for θ_i values of (0°, 120°, 240°, 360°) from left to right in the figure, α_0 values of (-60°, -
50°, -40°, -30°, -20°), $\Delta\theta$ values of (90°, 150°, 210°, 270°, 340°) (N=0), m =0.05, $a_{_0}$ =0.11, acceleration
inversely square case of the thrust profile (logarithmic spiral), Earth-Mars flight104
Figure 7.20: TOF for θ_i values of (0°, 120°, 240°, 360°) from left to right in the figure, α_0 values of (-60°, -
50°, -40°, -30°, -20°), $\Delta\theta$ values of (90°, 150°, 210°, 270°, 340°), m =0.05, acceleration inversely square
case of the thrust profile (logarithmic spiral), Earth-Mars flight, N=1 (a_0 =0.03), N=2 (a_0 =0.02)105
Figure 7.21: $V_{\infty,T}$ for θ_i values of (0°, 120°, 240°, 360°) from left to right in the figure, α_0 values of (-60°, -
50°, -40°, -30°, -20°), $\Delta\theta$ values of (90°, 150°, 210°, 270°, 340°), m =0.05, acceleration inversely square
case of the thrust profile (logarithmic spiral), Earth-Mars flight, N=1 (a_0 =0.03), N=2 (a_0 =0.02)105
Figure 7.22: Polar plot for N=1 and N=2, $\theta_i = 0^\circ$, $\Delta \theta = 90^\circ$, $\alpha_0 = -20^\circ$, $\alpha_0 = 0.05$, m values of (0.05; 0.15; 0.25;
0.35; 0.45), acceleration inversely square case of the thrust profile (logarithmic spiral), Earth-Mars flight
108

Figure 7.23: a plot for N=1 and N=2, θ_i =0°, $\Delta\theta$ =90°, α_0 =-20°, a_0 =0.05, m values of (0.05; 0.15; 0.25;
0.35; 0.45), acceleration inversely square case of the thrust profile (logarithmic spiral), Earth-Mars flight
Figure 7.24: α plot for N=1 and N=2, θ_i =0°, $\Delta\theta$ =90°, α_0 =-20°, a_0 =0.05, m values of (0.05; 0.15; 0.25; 0.35; 0.45), acceleration inversely square case of the thrust profile (logarithmic spiral), Earth-Mars flight
Figure 7.25: $\dot{\theta}$ plot for N=1 and N=2, θ_i =0°, $\Delta\theta$ =90°, α_0 =-20°, a_0 =0.05, m values of (0.05; 0.15; 0.25; 0.35; 0.45), acceleration inversely square case of the thrust profile (logarithmic spiral), Earth-Mars flight
Figure 7.26: γ plot for N=1 and N=2, θ_i =0°, $\Delta\theta$ =90°, α_0 =-20°, a_0 =0.05, m values of (0.05; 0.15; 0.25; 0.35; 0.45), acceleration inversely square case of the thrust profile (logarithmic spiral), Earth-Mars flight
Figure 7.27: TOF for θ_i values of (0°, 120°, 240°, 360°) from left to right in the figure, m values of (0.05; 0.15; 0.25; 0.35; 0.45), $\Delta\theta$ values of (90°, 150°, 210°, 270°, 340°) (N=0), tangential thrust profile (logarithmic spiral), Earth-Mars flight
Figure 7.28: $V_{\infty,T}$ for θ_i values of (0°, 120°, 240°, 360°) from left to right in the figure, m values of (0.05; 0.15; 0.25; 0.35; 0.45), $\Delta\theta$ values of (90°, 150°, 210°, 270°, 340°) (N=0), tangential thrust profile (logarithmic spiral), Earth-Mars flight
Figure 7.29: TOF for θ_i values of (0°, 120°, 240°, 360°) from left to right in the figure, m values of (0.05; 0.15; 0.25; 0.35; 0.45), $\Delta\theta$ values of (90°, 150°, 210°, 270°, 340°), tangential thrust profile (logarithmic spiral), Earth-Mars flight for N=1 and N=2
Figure 7.30: $V_{\infty,T}$ for θ_i values of (0°, 120°, 240°, 360°) from left to right in the figure, m values of (0.05; 0.15; 0.25; 0.35; 0.45), $\Delta\theta$ values of (90°, 150°, 210°, 270°, 340°), tangential thrust profile (logarithmic spiral), Earth-Mars flight for N=1 and N=2
Figure 7.31: Polar plot for N=1 and N=2, θ_i =0°, $\Delta\theta$ =90°, m values of (0.05; 0.15; 0.25; 0.35; 0.45), tangential thrust profile (logarithmic spiral), Earth-Mars flight
Figure 7.32: a plot for N=1 and N=2, θ_i =0°, $\Delta\theta$ =90°, m values of (0.05; 0.15; 0.25; 0.35; 0.45), tangential thrust profile (logarithmic spiral), Earth-Mars flight
Figure 7.33: α plot for N=1 and N=2, θ_i =0°, $\Delta\theta$ =90°, m values of (0.05; 0.15; 0.25; 0.35; 0.45), tangential thrust profile (logarithmic spiral), Earth-Mars flight
Figure 7.34: $\dot{\theta}$ plot for N=1 and N=2, θ_i =0°, $\Delta\theta$ =90°, m values of (0.05; 0.15; 0.25; 0.35; 0.45), tangential thrust profile (logarithmic spiral), Earth-Mars flight11

Figure 7.35: TOF for $\theta_i + \phi$ values of (120°, 200°, 280°, 360°) from left to right in the figure, α_0 values of (-
60°, -50°, -40°, -30°, -20°), $\Delta\theta$ values of (90°, 150°, 210°, 270°, 340°) (N=0), m =0.6, $a_{_0}$ =0.11, acceleration
inversely square case (Poinsot's spiral (hyperbolic sine)), Earth-Mars flight
Figure 7.36: $V_{\infty,T}$ for $\theta_i + \phi$ values of (120°, 200°, 280°, 360°) from left to right in the figure, α_0 values of (-
60°, -50°, -40°, -30°, -20°), $\Delta\theta$ values of (90°, 150°, 210°, 270°, 340°) (N=0), m =0.6, $a_{_0}$ =0.11, acceleration
inversely square case (Poinsot's spiral (hyperbolic sine)), Earth-Mars flight
Figure 7.37: TOF for $\theta_i + \phi$ values of (120°, 200°, 280°, 360°) from left to right in the figure, α_0 values of (-
60°, -50°, -40°, -30°, -20°), $\Delta\theta$ values of (90°, 150°, 210°, 270°, 340°), m =0.6, acceleration inversely square
case (Poinsot's spiral (hyperbolic sine), Earth-Mars flight, N=1 ($a_0 = 0.03$) and N=2 ($a_0 = 0.02$)119
Figure 7.38: $V_{\infty,T}$ for $\theta_i + \phi$ values of (120°, 200°, 280°, 360°) from left to right in the figure, α_0 values of (-
60°, -50°, -40°, -30°, -20°), $\Delta\theta$ values of (90°, 150°, 210°, 270°, 340°), m =0.6, acceleration inversely square
case (Poinsot's spiral (hyperbolic sine), Earth-Mars flight, N=1 ($a_0 = 0.03$) and N=2 ($a_0 = 0.02$)119
Figure 7.39: Polar plot for N=1 ($a_0 = 0.05$) and N=2 ($a_0 = 0.04$), $\theta_i + \phi = 120^\circ$, $\Delta \theta = 90^\circ$, m values of (0.01;
0.11; 0.21; 0.31; 0.41), α_0 =-20°, acceleration inversely square case (Poinsot's spiral (hyperbolic sine)),
Earth-Mars flight
Figure 7.40: a plot for N=1 (a_0 =0.05) and N=2 (a_0 =0.04), θ_i + ϕ =120°, $\Delta\theta$ =90°, m values of (0.01; 0.11;
0.21; 0.31; 0.41), α_0 =-20°, acceleration inversely square case (Poinsot's spiral (hyperbolic sine)), Earth-
Mars flight
Figure 7.41: α plot for N=1 (a_0 =0.05) and N=2 (a_0 =0.04), θ_i + ϕ =120°, $\Delta\theta$ =90°, m values of (0.01; 0.11;
0.21; 0.31; 0.41), α_0 =-20°, acceleration inversely square case (Poinsot's spiral (hyperbolic sine)), Earth-
Mars flight
Figure 7.42: $\dot{\theta}$ plot for N=1 (a_0 =0.05) and N=2 (a_0 =0.04), θ_i + ϕ =120°, $\Delta\theta$ =90°, m values of (0.01; 0.11;
0.21; 0.31; 0.41), α_0 =-20°, acceleration inversely square case (Poinsot's spiral (hyperbolic sine)), Earth-
Mars flight
Figure 7.43: γ plot for N=1 (a_0 =0.05) and N=2 (a_0 =0.04), θ_i + ϕ =120°, $\Delta\theta$ =90°, m values of (0.01; 0.11;
0.21; 0.31; 0.41), α_0 =-20°, acceleration inversely square case (Poinsot's spiral (hyperbolic sine)), Earth-
Mars flight
Figure 7.44: TOF for $\theta_i + \phi$ values of (120°, 200°, 280°, 360°) from left to right in the figure, m values of
$(0.01; 0.11; 0.21; 0.31; 0.41), \Delta\theta$ values of $(90^{\circ}, 150^{\circ}, 210^{\circ}, 270^{\circ}, 340^{\circ}), (N=0)$, tangential thrust profile
(Poinsot's spiral (hyperbolic sine)), Earth-Mars flight

Figure 7.45: $V_{\infty,T}$ for $\theta_i + \phi$ values of (120°, 200°, 280°, 360°) from left to right in the figure, m values of	
$(0.01; 0.11; 0.21; 0.31; 0.41)$, $\Delta\theta$ values of $(90^\circ, 150^\circ, 210^\circ, 270^\circ, 340^\circ)$, $(N=0)$, tangential thrust profile (Poinsot's spiral (hyperbolic sine)), Earth-Mars flight	25
Figure 7.46: TOF for $\theta_i + \phi$ values of (120°, 200°, 280°, 360°) from left to right in the figure, m values of (0.01; 0.11; 0.21; 0.31; 0.41), $\Delta\theta$ values of (90°, 150°, 210°, 270°, 340°), tangential thrust profile (Poinsot's spiral (hyperbolic sine)), Earth-Mars flight, N=1 and N=2	
Figure 7.47: $V_{\infty,T}$ for $\theta_i + \phi$ values of (120°, 200°, 280°, 360°) from left to right in the figure, m values of	
$(0.01; 0.11; 0.21; 0.31; 0.41)$, $\Delta\theta$ values of $(90^\circ, 150^\circ, 210^\circ, 270^\circ, 340^\circ)$, tangential thrust profile (Poinsot's spiral (hyperbolic sine)), Earth-Mars flight N=1 and N=2	26
Figure 7.48: Polar plot for N=1 and N=2, $\theta_i + \phi = 120^\circ$, $\Delta\theta = 90^\circ$, m values of (0.01; 0.11; 0.21; 0.31; 0.41), tangential thrust profile (Poinsot's spiral (hyperbolic sine)), Earth-Mars flight	
Figure 7.49: a plot for N=1 and N=2, $\theta_i + \phi = 120^\circ$, $\Delta\theta = 90^\circ$, m values of (0.01; 0.11; 0.21; 0.31; 0.41), tangential thrust profile (Poinsot's spiral (hyperbolic sine)), Earth-Mars flight	29
Figure 7.50: α plot for N=1 and N=2, $\theta_i + \phi = 120^\circ$, $\Delta\theta = 90^\circ$, m values of (0.01; 0.11; 0.21; 0.31; 0.41), tangential thrust profile (Poinsot's spiral (hyperbolic sine)), Earth-Mars flight	30
Figure 7.51: $\dot{\theta}$ plot for N=1 and N=2, $\theta_i + \phi = 120^\circ$, $\Delta \theta = 90^\circ$, m values of (0.01; 0.11; 0.21; 0.31; 0.41), tangential thrust profile (Poinsot's spiral (hyperbolic sine)), Earth-Mars flight	30
Figure 7.52: TOF for θ_i values of (30°, 140°, 250°, 340°) from left to right in the figure, α_0 values of (-60°, 50°, -40°, -30°, -20°), $\Delta\theta$ values of (90°,150°,210°,270°,340°) (N=0), m =0.05, a_0 =0.09, acceleration inversely square case (Poinsot's spiral (hyperbolic cosine)), Earth-Mars flight	
Figure 7.53: $V_{\infty,T}$ for θ_i values of (30°, 140°, 250°, 340°) from left to right in the figure, α_0 values of (-60°, 50°, -40°, -30°, -20°), $\Delta\theta$ values of (90°,150°,210°,270°,340°) (N=0), m =0.05, a_0 =0.09, acceleration inversely square case (Poinsot's spiral (hyperbolic cosine)), Earth-Mars flight	
Figure 7.54: TOF for θ_i values of (30°, 140°, 250°, 340°) from left to right in the figure, α_0 values of (-60°, 50°, -40°, -30°, -20°), $\Delta\theta$ values of (90°, 150°, 210°, 270°, 340°), m =0.05, acceleration inversely square case (Poinsot's spiral (hyperbolic cosine), Earth-Mars flight, N=1 (a_0 =0.04) and N=2 (a_0 =0.03)	
Figure 7.55: $V_{\infty,T}$ for θ_i values of (30°, 140°, 250°, 340°) from left to right in the figure, α_0 values of (-60°, 50°, -40°, -30°, -20°), $\Delta\theta$ values of (90°, 150°, 210°, 270°, 340°), m =0.05, acceleration inversely square case (Poinsot's spiral (hyperbolic cosine), Earth-Mars flight, N=1 (α_0 =0.04) and N=2 (α_0 =0.03)	

Figure 7.56: Polar plot for N=1 (a_0 =0.04) and N=2 (a_0 =0.03), θ_i =30°, $\Delta\theta$ =90°, α_0 =-20°, m values of
(0.01; 0.11; 0.21; 0.31; 0.41), acceleration inversely square case (Poinsot's spiral (hyperbolic cosine), Earth-Mars flight
Figure 7.57: a plot for N=1 (a_0 =0.04) and N=2 (a_0 =0.03), θ_i =30°, $\Delta\theta$ =90°, α_0 =-20°, m values of (0.01; 0.11; 0.21; 0.31; 0.41), acceleration inversely square case (Poinsot's spiral (hyperbolic cosine), Earth-Mars flight
Figure 7.58: α plot for N=1 (a_0 =0.04) and N=2 (a_0 =0.03), θ_i =30°, $\Delta\theta$ =90°, α_0 =-20°, m values of (0.01; 0.11; 0.21; 0.31; 0.41), acceleration inversely square case (Poinsot's spiral (hyperbolic cosine), Earth-Mars flight
Figure 7.59: $\dot{\theta}$ plot for N=1 (a_0 =0.04) and N=2 (a_0 =0.03), θ_i =30°, $\Delta\theta$ =90°, α_0 =-20°, m values of (0.01; 0.11; 0.21; 0.31; 0.41), acceleration inversely square case (Poinsot's spiral (hyperbolic cosine), Earth-Mars flight
Figure 7.60: γ plot for N=1 (a_0 =0.04) and N=2 (a_0 =0.03), θ_i =30°, $\Delta\theta$ =90°, α_0 =-20°, m values of (0.01; 0.11; 0.21; 0.31; 0.41), acceleration inversely square case (Poinsot's spiral (hyperbolic cosine), Earth-Mars flight
Figure 7.61: TOF for θ_i values of (30°, 140°, 250°, 360°) from left to right in the figure, m values of (0.01; 0.11; 0.21; 0.31; 0.41), $\Delta\theta$ values of (90°, 150°, 210°, 270°, 340°) (N=0), tangential thrust profile (Poinsot's spiral (hyperbolic cosine)), Earth-Mars flight
Figure 7.62: $V_{\infty,T}$ for θ_i values of (30°, 140°, 250°, 360°) from left to right in the figure, m values of (0.01; 0.11; 0.21; 0.31; 0.41), $\Delta\theta$ values of (90°, 150°, 210°, 270°, 340°) (N=0), tangential thrust profile (Poinsot's spiral (hyperbolic cosine)), Earth-Mars flight
Figure 7.63: TOF for θ_i values of (30°, 140°, 250°, 360°) from left to right in the figure, m values of (0.01; 0.11; 0.21; 0.31; 0.41), $\Delta\theta$ values of (90°, 150°, 210°, 270°, 340°), tangential thrust profile (Poinsot's spira (hyperbolic cosine)), Earth-Mars flight, N=1 and N=2
Figure 7.64: $V_{\infty,T}$ for θ_i values of (30°, 140°, 250°, 360°) from left to right in the figure, m values of (0.01; 0.11; 0.21; 0.31; 0.41), $\Delta\theta$ values of (90°, 150°, 210°, 270°, 340°), tangential thrust profile (Poinsot's spira (hyperbolic cosine)), Earth-Mars flight, N=1 and N=2
Figure 7.65: Polar plot for N=1 and N=2, θ_i =30°, $\Delta\theta$ =90°, m values of (0.01; 0.11; 0.21; 0.31; 0.41), tangential thrust profile (Poinsot's spiral (hyperbolic cosine)), Earth-Mars flight
Figure 7.66: a plot for N=1 and N=2, θ_i =30°, $\Delta\theta$ =90°, m values of (0.01; 0.11; 0.21; 0.31; 0.41), tangential thrust profile (Poinsot's spiral (hyperbolic cosine)), Earth-Mars flight

Figure 7.67: α plot for N=1 and N=2, $\theta_i = 30^\circ$, $\Delta \theta = 90^\circ$, m values of (0.01; 0.11; 0.21; 0.31; 0.41),
tangential thrust profile (Poinsot's spiral (hyperbolic cosine)), Earth-Mars flight144
Figure 7.68: $\dot{\theta}$ plot for N=1 and N=2, θ_i =30°, $\Delta\theta$ =90°, m values of (0.01; 0.11; 0.21; 0.31; 0.41), tangential
thrust profile (Poinsot's spiral (hyperbolic cosine)), Earth-Mars flight
Figure 7.69: TOF for θ_i values of (120°, 200°, 280°, 360°) from left to right in the figure, α_0 values of (-60°,
-50°, -40°, -30°, -20°), $\Delta\theta$ values of (90°, 150°, 210°, 270°, 340°) (N=0), m =0.05, $a_{_0}$ =0.09, acceleration
inversely square case of the thrust profile (sinusoidal spiral), Earth-Mars flight
Figure 7.70: $V_{\omega,T}$ for θ_i values of (120°, 200°, 280°, 360°) from left to right in the figure, α_0 values of (-60°,
-50°, -40°, -30°, -20°), $\Delta\theta$ values of (90°, 150°, 210°, 270°, 340°) (N=0), m =0.05, $a_{_0}$ =0.09, acceleration
inversely square case of the thrust profile (sinusoidal spiral), Earth-Mars flight
Figure 7.71: TOF for θ_i values of (120°, 200°, 280°, 360°) from left to right in the figure, α_0 values of (-60°,
-50° , -40° , -30° , -20°), $\Delta\theta$ values of (90°, 150°, 210°, 270°, 340°), m =0.05, acceleration inversely square
case of the thrust profile (sinusoidal spiral), Earth-Mars flight, N=1 (a_0 =0.04), N=2 (a_0 =0.03)147
Figure 7.72: $V_{\infty,T}$ for θ_i values of (120°, 200°, 280°, 360°) from left to right in the figure, α_0 values of (-60°,
-50°, -40°, -30°, -20°), $\Delta\theta$ values of (90°, 150°, 210°, 270°, 340°), m =0.05, acceleration inversely square
case of the thrust profile (sinusoidal spiral), Earth-Mars flight, N=1 ($a_0 = 0.04$), N=2 ($a_0 = 0.03$)147
Figure 7.73: Polar plot for N=1 ($a_0 = 0.04$) and N=2 ($a_0 = 0.03$), $\theta_i = 120^\circ$, $\Delta \theta = 90^\circ$, $\alpha_0 = -20^\circ$, m values of
(0.01; 0.055; 0.1; 0.145; 0.19), acceleration inversely square case (sinusoidal spiral), Earth-Mars flight150
Figure 7.74: a plot for N=1 (a_0 =0.04) and N=2 (a_0 =0.03), θ_i =120°, $\Delta\theta$ =90°, α_0 =-20°, m values of (0.01;
0.055; 0.1; 0.145; 0.19), acceleration inversely square case (sinusoidal spiral), Earth-Mars flight150
Figure 7.75: α plot for N=1 (a_0 =0.04) and N=2 (a_0 =0.03), θ_i =120°, $\Delta\theta$ =90°, α_0 =-20°, m values of (0.01;
0.055; 0.1; 0.145; 0.19), acceleration inversely square case (sinusoidal spiral), Earth-Mars flight151
Figure 7.76: $\dot{\theta}$ plot for N=1 (a_0 =0.04) and N=2 (a_0 =0.03), θ_i =120°, $\Delta\theta$ =90°, α_0 =-20°, m values of (0.01;
0.055; 0.1; 0.145; 0.19), acceleration inversely square case (sinusoidal spiral), Earth-Mars flight151
Figure 7.77: γ plot for N=1 (a_0 =0.04) and N=2 (a_0 =0.03), θ_i =120°, $\Delta\theta$ =90°, α_0 =-20°, m values of (0.01;
0.055; 0.1; 0.145; 0.19), acceleration inversely square case (sinusoidal spiral), Earth-Mars flight152
Figure 7.78: TOF for θ_i values of (120, 200°, 280°, 360°) from left to right in the figure, m values of (0.01;
$0.055; 0.1; 0.145; 0.19), \Delta\theta$ values of (90°, 150°, 210°, 270°, 340°) (N=0), tangential thrust profile
(sinusoidal spiral), Earth-Mars flight

Figure 7.79: $V_{\infty,T}$ for θ_i values of (120, 200°, 280°, 360°) from left to right in the figure, m values of (0.01;
$0.055; 0.1; 0.145; 0.19), \Delta\theta$ values of (90°, 150°, 210°, 270°, 340°) (N=0), tangential thrust profile (sinusoidal spiral), Earth-Mars flight
Figure 7.80: TOF for θ_i values of (120, 200°, 280°, 360°) from left to right in the figure, m values of (0.01; 0.055; 0.1; 0.145; 0.19), $\Delta\theta$ values of (90°, 150°, 210°, 270°, 340°), tangential thrust profile (sinusoidal spiral), Earth-Mars flight for N=1 and N=2
Figure 7.81: $V_{\infty,T}$ for θ_i values of (120, 200°, 280°, 360°) from left to right in the figure, m values of (0.01; 0.055; 0.1; 0.145; 0.19), $\Delta\theta$ values of (90°, 150°, 210°, 270°, 340°), tangential thrust profile (sinusoidal spiral), Earth-Mars flight for N=1 and N=2
Figure 7.82: Polar plot for N=1 and N=2, θ_i =120°, $\Delta\theta$ =90°, m values of (0.01; 0.055; 0.1; 0.145; 0.19), tangential thrust profile (sinusoidal spiral) Earth-Mars flight
Figure 7.83: a plot for N=1 and N=2, θ_i =120°, $\Delta\theta$ =90°, m values of (0.01; 0.055; 0.1; 0.145; 0.19), tangential thrust profile (sinusoidal spiral) Earth-Mars flight
Figure 7.84: α plot for N=1 and N=2, θ_i =120°, $\Delta\theta$ =90°, m values of (0.01; 0.055; 0.1; 0.145; 0.19), tangential thrust profile (sinusoidal spiral) Earth-Mars flight
Figure 7.85: $\dot{\theta}$ plot for N=1 and N=2, θ_i =120°, $\Delta\theta$ =90°, m values of (0.01; 0.055; 0.1; 0.145; 0.19), tangential thrust profile (sinusoidal spiral) Earth-Mars flight
Figure 7.86: TOF for k_2 values of (0.1; 0.15; 0.2; 0.25) from left to right in the figure, α_0 values of (20°, 30° 40°, 50°, 60°), $\Delta\theta$ values of (90°, 150°, 210°, 270°, 340°) (N=0), θ_i =0°, γ_1 =0°, α_0 =0.07, acceleration inversely square case of the thrust profile (exponential sinusoid), Earth-Mars flight
Figure 7.87: $V_{\infty,T}$ for k_2 values of (0.1; 0.15; 0.2; 0.25) from left to right in the figure, α_0 values of (20°, 30° 40°, 50°, 60°), $\Delta\theta$ values of (90°, 150°, 210°, 270°, 340°) (N=0), θ_i =0°, γ_1 =0°, a_0 =0.07, acceleration inversely square case of the thrust profile (exponential sinusoid), Earth-Mars flight
Figure 7.88: TOF for k_2 values of (0.1; 0.15; 0.2; 0.25) from left to right in the figure, α_0 values of (20°, 30° 40°, 50°, 60°), $\Delta\theta$ values of (90°, 150°, 210°, 270°, 340°), γ_1 =0°, θ_i =0°, acceleration inversely square case of the thrust profile (exponential sinusoid), Earth-Mars flight, N=1 (a_0 =0.04) and N=2 (a_0 =0.05)16
Figure 7.89: $V_{\infty,T}$ for k_2 values of (0.1; 0.15; 0.2; 0.25) from left to right in the figure, α_0 values of (20°, 30° 40°, 50°, 60°), $\Delta\theta$ values of (90°, 150°, 210°, 270°, 340°), γ_1 =0°, θ_i =0°, acceleration inversely square case of the thrust profile (exponential sinusoid), Earth-Mars flight, N=1 (a_0 =0.04) and N=2 (a_0 =0.05)162

Figure 7.90: Polar plot for N=1 and N=2, $a_0 = 0.04$, $k_2 = 0.01$, $\Delta \theta = 90^{\circ}$, $\alpha_0 = 20^{\circ}$, γ_1 values of (0°; 0.75°; 1.5°;
2.25°; 3°), θ_i =0°, acceleration inversely square case (exponential sinusoid), Earth-Mars flight164
Figure 7.91: <i>a</i> plot for N=1 and N=2, $a_0 = 0.04$, $k_2 = 0.01$, $\Delta \theta = 90^{\circ}$, $\alpha_0 = 20^{\circ}$, γ_1 values of (0°; 0.75°; 1.5°;
2.25°; 3°), θ_i =0°, acceleration inversely square case (exponential sinusoid), Earth-Mars flight165
Figure 7.92: α plot for N=1 and N=2, a_0 =0.04, k_2 =0.01, $\Delta\theta$ =90°, α_0 =20°, γ_1 values of (0°; 0.75°; 1.5°;
2.25°; 3°), $\theta_i = 0^\circ$, acceleration inversely square case (exponential sinusoid), Earth-Mars flight165
Figure 7.93: $\dot{\theta}$ plot for N=1 and N=2, a_0 =0.04, k_2 =0.01, $\Delta\theta$ =90°, α_0 =20°, γ_1 values of (0°; 0.75°; 1.5°;
2.25°; 3°), $\theta_i = 0$ °, acceleration inversely square case (exponential sinusoid), Earth-Mars flight166
Figure 7.94: γ plot for N=1 and N=2, a_0 =0.04, k_2 =0.01, $\Delta\theta$ =90°, α_0 =20°, γ_1 values of (0°; 0.75°; 1.5°;
2.25°; 3°), $\theta_i = 0$ °, acceleration inversely square case (exponential sinusoid), Earth-Mars flight166
Figure 7.95: TOF for k_2 values of (0.1; 0.15; 0.2; 0.25) from left to right in the figure, γ_1 values of (0°;
0.75° ; 1.5° ; 2.25° ; 3°), $\theta_i = 0^{\circ}$, $\Delta\theta$ values of (90°, 150°, 210°, 270°, 340°) (N=0), tangential thrust profile
(exponential sinusoid), Earth-Mars flight
Figure 7.96: $V_{\infty,T}$ for k_2 values of (0.1; 0.15; 0.2; 0.25) from left to right in the figure, γ_1 values of (0°; 0.75°;
1.5°; 2.25°; 3°), $\theta_i = 0^\circ$, $\Delta \theta$ values of (90°, 150°, 210°, 270°, 340°) (N=0), tangential thrust profile
(exponential sinusoid), Earth-Mars flight
Figure 7.97: TOF for k_2 values of (0.1; 0.15; 0.2; 0.25) from left to right in the figure, γ_1 values of (0°;
0.75° ; 1.5° ; 2.25° ; 3°), $\theta_i = 0^{\circ}$, $\Delta\theta$ values of (90°, 150°, 210°, 270°, 340°), tangential thrust profile
(exponential sinusoid), Earth-Mars flight, N=1 and N=2169
Figure 7.98: $V_{\infty,T}$ for k_2 values of (0.1; 0.15; 0.2; 0.25) from left to right in the figure, γ_1 values of (0°; 0.75°;
1.5°; 2.25°; 3°), θ_i =0°, $\Delta\theta$ values of (90°, 150°, 210°, 270°, 340°), tangential thrust profile (exponential
sinusoid), Earth-Mars flight, N=1 and N=2
Figure 7.99: Polar plot for N=1 and N=2, $k_2 = 0.01$, $\Delta \theta = 90^{\circ}$, γ_1 values of $(0^{\circ}; 0.75^{\circ}; 1.5^{\circ}; 2.25^{\circ}; 3^{\circ})$, $\theta_i = 0^{\circ}$,
tangential thrust profile (exponential sinusoid), Earth-Mars flight
Figure 7.100: <i>a</i> plot for N=1 and N=2, k_2 =0.01, $\Delta\theta$ =90°, γ_1 values of (0°; 0.75°; 1.5°; 2.25°; 3°), θ_i =0°,
tangential thrust profile (exponential sinusoid), Earth-Mars flight
Figure 7.101: α plot for N=1 and N=2, k_2 =0.01, $\Delta\theta$ =90°, γ_1 values of (0°; 0.75°; 1.5°; 2.25°; 3°), θ_i =0°,
tangential thrust profile (exponential sinusoid). Farth-Mars flight

Figure 7.102: $\dot{\theta}$ plot for N=1 and N=2, k_2 =0.01, $\Delta\theta$ =90°, γ_1 values of (0°; 0.75°; 1.5°; 2.25°; 3°), θ_i =0°,
tangential thrust profile (exponential sinusoid), Earth-Mars flight
Figure 7.103: Representation of the dynamic parameters: thrust acceleration (\overline{a}), the velocity of the
spacecraft (\overline{V}), the thrust angle ($\pmb{\alpha}$) and the flight path angle ($\pmb{\gamma}$)178
Figure 8.1: A multimodal function: $f(x, y) = 3(1 - x^2)e^{-x^2 - (y+1)^2} - 10(x/5 - x^3 - y^5)e^{-x^2 - y^2} - 1/3e^{-(x+1)^2 - y^2}$
[Melman, 2007]
Figure 8.2: Scheme illustrating the steps to take in a GA method
Figure 8.3: Example of a Pareto front (individuals in red)
Figure 10.1: Pareto fronts for the Archimedean spiral, logarithmic spiral, Poinsot's spiral (hyperbolic sine), Poinsot's spiral (hyperbolic cosine), sinusoidal spiral and exponential sinusoid, tangential thrust profile, Earth-Mars flight
Figure 10.2: Pareto fronts for the Archimedean spiral, logarithmic spiral, Poinsot's spiral (hyperbolic sine), Poinsot's spiral (hyperbolic cosine), sinusoidal spiral and exponential sinusoid, tangential thrust profile, Earth-Mars flight. On the right, only individuals with values of total excess velocity lower than 3 km/s and values of fuel mass consumption between 80 and 100 kg are present
Figure 10.3: Pareto front for the sinusoidal spiral, Earth-Mars flight
Figure 10.4: Polar plot for the sinusoidal spiral, Earth-to-Mars flight (m = -0.9996, $\Delta\theta$ = 175.8° with N=1 and θ_i = 194.7°)
Figure 10.5: k_2 of the Pareto front individuals versus the fuel mass consumption during the low-thrust phase, exponential sinusoid, Earth-to-Mars flight
Figure 10.6: Pareto front of the sinusoidal spiral, using $m=[-0.7;0.7]$ (blue) and $m=(-1;1)$ (red)207
Figure 10.7: Pareto fronts for the sinusoidal spiral, for the entire population (on the right) and only for individuals in the population that respect the condition (8.7) (the 3 cases of available thrust acceleration), tangential thrust profile, Earth-Mars flight
Figure 10.8: Pareto fronts for the exponential sinusoid, for the entire population (on bottom right) and only for individuals in the population that respect the condition (8.7) (the 3 cases of available thrust acceleration), tangential thrust profile, Earth-Mars flight
Figure 10.9: Pareto fronts for the Archimedean spiral, logarithmic spiral, Poinsot's spiral (hyperbolic sine), Poinsot's spiral (hyperbolic cosine), sinusoidal spiral and exponential sinusoid, tangential thrust profile, Earth-Mercury flight
Figure 10.10: Pareto fronts for the Archimedean spiral, logarithmic spiral, Poinsot's spiral (hyperbolic sine), Poinsot's spiral (hyperbolic cosine), sinusoidal spiral and exponential sinusoid, tangential thrust profile, Earth-Mercury flight

Figure 10.11: Pareto fronts for the sinusoidal spiral, for the entire population (on the right) and only for individuals in the population that respect the condition (8.7) (the 3 cases of the available thrust	
acceleration), tangential thrust profile, Earth-Mercury flight	.215
Figure 10.12: Pareto fronts for the exponential sinusoid, for the entire population (on the right) and only f individuals in the population that respect the condition (8.7) (the 3 cases of the available thrust acceleration), tangential thrust profile, Earth-Mercury flight	
Figure 10.13: Pareto fronts for the sinusoidal spiral and the exponential sinusoid, acceleration inversely square case, Earth-Mars flight	.217
Figure 10.14: Pareto fronts for the sinusoidal spiral and the exponential sinusoid – acceleration inversely square case of the thrust profile, Earth-Mars flight	.218
Figure 10.15: Pareto fronts for the sinusoidal spiral, for the entire population (on the bottom right) and on for individuals in the population that respect the condition (8.7) (the 3 cases of the available thrust acceleration), acceleration inversely square case, Earth-Mars flight	
Figure 10.16: Pareto fronts for the exponential sinusoid, for the entire population (on the right) and only f individuals in the population that respect the condition (8.7) (the 3 cases of the available thrust acceleration), acceleration inversely square case, Earth-Mars flight	
Figure 10.17: Pareto fronts for the sinusoidal spiral and the exponential sinusoid, acceleration inversely square case, Earth-Mercury flight	.221
Figure 10.18: Pareto fronts for the sinusoidal spiral and for the exponential sinusoid, acceleration inversel square case, Earth-Mercury flight	•
Figure 10.19: Pareto fronts for the sinusoidal spiral, for the entire population (on the right) and only for individuals in the population that respect the condition (8.7) (the 3 cases of the available thrust acceleration), acceleration inversely square case, Earth-Mercury flight	224
Figure 10.20: Pareto fronts for the exponential sinusoid, for the entire population (on the right) and only f individuals in the population that respect the condition (8.7) (the 3 cases of the available thrust acceleration), acceleration inversely square case, Earth-Mercury flight	
Figure 10.21: Pareto fronts for the sinusoidal spiral and the exponential sinusoid, acceleration inversely square case, tangential thrust, Earth-Mars flight	.227
Figure 10.22: Pareto fronts for the sinusoidal spiral and the exponential sinusoid for the acceleration inversely square case of the thrust profile and the tangential thrust for an Earth-Mercury flight	228
Figure 10.23: Pareto fronts for the Archimedean spiral, logarithmic spiral, Poinsot's spiral (hyperbolic sin Poinsot's spiral (hyperbolic cosine), sinusoidal spiral and exponential sinusoid, tangential thrust, Earth-Mars flight, for different values of N	

List of Tables

Table 3.1: Examples of bi-propellant liquid engines [Zandbergen, 2004] and [Cornelisse et al, 1979]29
Table 3.2: Propulsion system characteristics of SMART-1 [ESA/SMART-1, 2007I], MUSES-C [Komuraki, 2003] and Deep Space 1 [NASA/JPL, 2002] [Rayman et al, 1999]
Table 4.1: The TOF and the total impulse velocities at the departure planet and at the target planet with the Earth as departure planet (1.1 radius distance from the planet). * the velocity of the Earth is considered circular and equal to 29.79 km/s [Cornelisse et al., 1979]
Table 5.1: Four different types of transfer orbits [Wertz, 2001]
Table 6.1: Conditions required for the Archimedean spiral, the logarithmic spiral, the Poinsot's spiral (hyperbolic sine), the Poinsot's spiral (hyperbolic cosine) and the sinusoidal spiral to obtain feasible trajectories for a low-thrust problem
Table 7.1: The excess velocities and the TOF values for N=1, θ_i =0°, $\Delta\theta$ =90°, α_0 =-20°, a_0 =0.04, m values of (0.02;0.64;1.26;1.88;2.5), acceleration inversely square case of the thrust profile (Archimedean spiral), Earth-Mars flight
Table 7.2: The excess velocities and the TOF values for N=2, θ_i =0°, $\Delta\theta$ =90°, α_0 =-20°, a_0 =0.03, m values of (0.02;0.64;1.26;1.88;2.5), acceleration inversely square case of the thrust profile (Archimedean spiral), Earth-Mars flight
Table 7.3: The excess velocities and the TOF values for N=1, θ_i =0°, $\Delta\theta$ =90°, m values of (0.02;0.64;1.26;1.88;2.5), tangential thrust profile (Archimedean spiral), Earth-Mars flight
Table 7.4: The excess velocities and the TOF values for N=2, θ_i =0°, $\Delta\theta$ =90°, m values of (0.02;0.64;1.26;1.88;2.5), tangential thrust profile (Archimedean spiral), Earth-Mars flight
Table 7.5: The excess velocities and the TOF values for N=1, θ_i =0°, $\Delta\theta$ =90°, α_0 =-20°, a_0 =0.05, m values of (0.05; 0.15; 0.25; 0.35; 0.45), acceleration inversely square case of the thrust profile (logarithmic spiral), Earth-Mars flight
Table 7.6: The excess velocities and the TOF values for N=2, θ_i =0°, $\Delta\theta$ =90°, α_0 =-20°, a_0 =0.05, m values of (0.05; 0.15; 0.25; 0.35; 0.45), acceleration inversely square case of the thrust profile (logarithmic spiral), Earth-Mars flight
Table 7.7: Excess velocities and TOF values for N=1, θ_i =0°, $\Delta\theta$ =90°, m values of (0.05; 0.15; 0.25; 0.35; 0.45), tangential thrust profile (logarithmic spiral), Earth-Mars flight
Table 7.8: Excess velocities and TOF values for N=2, θ_i =0°, $\Delta\theta$ =90°, m values of (0.05; 0.15; 0.25; 0.35; 0.45), tangential thrust profile (logarithmic spiral), Earth-Mars flight

Table 7.9: The excess velocities and the TOF values for N=1, $\theta_i + \phi = 120^\circ$, $\Delta\theta = 90^\circ$, m values of (0.01;
0.11; 0.21; 0.31; 0.41), $\alpha_0 = -20^\circ$, $a_0 = 0.05$, acceleration inversely square case (Poinsot's spiral (hyperbolic
sine)), Earth-Mars flight
Table 7.10: The excess velocities and the TOF values for N=2, $\theta_i + \phi = 120^\circ$, $\Delta\theta = 90^\circ$, m values of (0.01;
0.11; 0.21; 0.31; 0.41), $\alpha_{_0}$ =-20°, $a_{_0}$ =0.04, acceleration inversely square case (Poinsot's spiral (hyperbolic
sine)), Earth-Mars flight
Table 7.11: Excess velocities and TOF values for N=1, $\theta_i + \phi = 120^\circ$, $\Delta\theta = 90^\circ$, m values of (0.01; 0.11; 0.21;
0.31; 0.41), tangential thrust profile (Poinsot's spiral (hyperbolic sine)), Earth-Mars flight127
Table 7.12: Excess velocities and TOF values for N=2, $\theta_i + \phi = 120^\circ$, $\Delta\theta = 90^\circ$, m values of (0.01; 0.11; 0.21;
0.31; 0.41), tangential thrust profile (Poinsot's spiral (hyperbolic sine)), Earth-Mars flight128
Table 7.13: The excess velocities and the TOF values for N=1, θ_i =30°, $\Delta\theta$ =90°, α_0 =-20°, m values of
$(0.01; 0.11; 0.21; 0.31; 0.41), a_0 = 0.04$, acceleration inversely square case (Poinsot's spiral (hyperbolic
cosine), Earth-Mars flight
Table 7.14: The excess velocities and the TOF values for N=2, θ_i =30°, $\Delta\theta$ =90°, α_0 =-20°, m values of
$(0.01; 0.11; 0.21; 0.31; 0.41)$, $a_0 = 0.03$, acceleration inversely square case (Poinsot's spiral (hyperbolic
cosine), Earth-Mars flight
Table 7.15: Excess velocities and TOF values for N=1, θ_i =30°, $\Delta\theta$ =90°, m values of (0.01; 0.11; 0.21; 0.31;
0.41), tangential thrust profile (Poinsot's spiral (hyperbolic cosine)), Earth-Mars flight141
Table 7.16: Excess velocities and TOF values for N=2, θ_i =30°, $\Delta\theta$ =90°, m values of (0.01; 0.11; 0.21; 0.31;
0.41), tangential thrust profile (Poinsot's spiral (hyperbolic cosine)), Earth-Mars flight142
Table 7.17: The excess velocities and the TOF values for N=1, θ_i =120°, $\Delta\theta$ =90°, α_0 =-20°, m values of
$(0.01; 0.055; 0.1; 0.145; 0.19)$, $a_0 = 0.04$, acceleration inversely square case (sinusoidal spiral), Earth-Mars
flight
Table 7.18: The excess velocities and the TOF values for N=2, θ_i =120°, $\Delta\theta$ =90°, α_0 =-20°, m values of
$(0.01; 0.055; 0.1; 0.145; 0.19), a_0 = 0.03$, acceleration inversely square case (sinusoidal spiral), Earth-Mars
flight
Table 7.19: Excess velocities and TOF values for N=1, θ_i =120°, $\Delta\theta$ =90°, m values of (0.01; 0.055; 0.1;
0.145; 0.19), tangential thrust profile (sinusoidal spiral) Earth-Mars flight
Table 7.20: Excess velocities and TOF values for N=2, θ_i =120°, $\Delta\theta$ =90°, m values of (0.01; 0.055; 0.1;
0.145; 0.19), tangential thrust profile (sinusoidal spiral) Earth-Mars flight

Table 7.21: The excess velocities and the TOF values for N=1, $k_2 = 0.01$, $\Delta\theta = 90^\circ$, $\alpha_0 = 20^\circ$, γ_1 values of (0°;
0.75°; 1.5°; 2.25°; 3°), a_0 =0.04, θ_i =0°, acceleration inversely square case (exponential sinusoid), Earth-Mars flight
Wais fight
Table 7.22: The excess velocities and the TOF values for N=2, k_2 =0.01, $\Delta\theta$ =90°, α_0 =20°, γ_1 values of (0°;
0.75° ; 1.5° ; 2.25° ; 3°), $a_{0} = 0.04$, $\theta_{i} = 0^{\circ}$, acceleration inversely square case (exponential sinusoid), Earth-
Mars flight
Table 7.23: Excess velocities and TOF values for N=1, k_2 =0.01, $\Delta\theta$ =90°, γ_1 values of (0°; 0.75°; 1.5°;
2.25°; 3°), $\theta_i = 0$ °, tangential thrust profile (exponential sinusoid), Earth-Mars flight
Table 7.24: Excess velocities and TOF values for N=2, k_2 =0.01, $\Delta\theta$ =90°, γ_1 values of (0°; 0.75°; 1.5°;
2.25°; 3°), $\theta_i = 0$ °, tangential thrust profile (exponential sinusoid), Earth-Mars flight
Table 7.25: Minimum values for the total excess velocity and the range of values for the thrust acceleration, for the acceleration inversely square and tangential cases of the thrust profile
Table 7.26: Minimum values for the total excess velocity and for the normalised thrust acceleration, for the acceleration inversely square and constant acceleration cases of the thrust profile
Table 8.1: Deep Space 1 characteristics [Rayman, 1999] [NASA/JPL, 2002]
Table 9.1: Test scenario (Earth-Mars mission) for verification of the excess velocities, TOF and fuel mass consumption computed in low2D
Table 9.2: Results from Galomusit and low2D for the 3 individuals, Earth-Mars flight
Table 9.3: Errors between the results given by Galomusit and low2D
Table 9.4: TOF given by Galomusit, low2D and Izzo's integrator routines and the errors between the results given by Izzo and low2D
Table 9.5: Results from STA and low2D for the 3 individuals, for Earth to Mars
Table 10.1: Minimum values for the fuel mass consumption during the low-thrust phase and for the total excess velocity for the individuals in the Pareto fronts for all 6 shapes, tangential case, Earth-Mars flight
Table 10.2: Computation time, number of individuals in the Pareto front ($N_{_{Pf}}$) and the percentage of
individuals in the Pareto front G_{p_f} and in the population $G_{p_{op}}$ that respect the maximum value for the ratio
between the required thrust acceleration of the spacecraft and the available one for the 6 shapes and for the
3 cases of $a_{\text{max}} = a_{\text{max}} (1;1.5;2)$, Earth-Mars flight (tangential case)

Table 10.3: Minimum values for the fuel mass consumption during the low-thrust phase and for the total
excess velocity for the individuals in the Pareto fronts for all 6 shapes, tangential case, Earth-Mercury flight
213
Table 10.4: Computation time, number of individuals in the Pareto front ($N_{_{\mathrm{Pf}}}$) and the percentage of
individuals in the Pareto front G_{p_f} and in the population $G_{p_{op}}$ that respect the maximum value for the ratio
between the required thrust acceleration of the spacecraft and the available one for the 6 shapes and for the
3 cases of $a_{0,available} = a_{0,DS1} (1.5;2.25;3)$, Earth-Mercury flight (tangential case)
Table 10.5: Computation time, number of individuals in the Pareto front ($N_{_{Pf}}$) and the percentage of
individuals in the Pareto front G_{p_f} and in the population $G_{p_{op}}$ that respect the maximum value for the ratio
between the required thrust acceleration of the spacecraft and the available one, for the sinusoidal spiral and
the exponential sinusoid, 3 cases of $a_{0,available} = a_{0,DS1}(1;1.5;2)$, Earth-Mars flight (acceleration inversely
square case)
Table 10.6: Computation time, number of individuals in the Pareto front ($N_{\mbox{\tiny Pf}}$) and the percentage of
individuals in the Pareto front G_{p_f} and in the population $G_{p_{op}}$ that respect the maximum value for the ratio
between the required thrust acceleration of the spacecraft and the available one, for the sinusoidal spiral and
the exponential sinusoid, 3 cases of $a_{0,available} = a_{0,DS1} (1.5; 2.25; 3)$, Earth-Mercury flight (acceleration
inversely square case)

Nomenclature

Parameters

- a Semi-major axis [m]
- a Thrust acceleration $\lceil m/s^2 \rceil$
- a_0 Thrust acceleration normalised by local gravitational acceleration
- c Speed of light, $2.9979 \times 10^8 \, m/s$
- e Eccentricity
- e Local truncation error
- E Eccentric anomaly [rad]
- f Force [N]
- g_0 Gravitational acceleration at sea level,
- $9.81 \, m/s^2$
- G Universal gravity constant,

$$6.673 \times 10^{-20} \, km^3 / (kg \cdot s^2)$$

- h Step-size
- *H* Angular momentum vector per unit of mass $\lceil m^2/(kg \cdot s) \rceil$
- i Inclination [°]
- I Impulse $[N \cdot s]$
- I_{sp} Specific impulse [s]
- k_0 Scaling factor
- k_1 Dynamic range parameter

- k_2 Winding parameter
- J_2 Dynamic form factor
- m Mass rate [kg/s]
- *m* Geometric parameter
- M Mean anomaly [rad]
- M Instantaneous mass of a spacecraft or satellite [kg]
- *n* Mean angular motion $[s^{-1}]$
- N Number of complete revolutions
- p Semi-latus rectum [m]
- p Order of the polynomial
- P Power [W]
- P_i Power jet [W]
- r Radius [m]
- r_B Current radius [m]
- R Reflection coefficient
- s Number of function evaluations
- S Surface area $[m^2]$
- S Cross-sectional area $\lceil m^2 \rceil$
- t Time [s]
- TOF Time of flight [s]

V_z Velocity normal to the orbital plane	θ True anomaly [rad]
[m/s]	$\dot{\theta}$ Polar angle rate [rad/s]
V Velocity of the spacecraft $[m/s]$	ρ Atmospheric density $\left[kg/m^3\right]$
V_{θ} Tangential velocity $[m/s]$	τ Time of pericentre $[s]$
V_r Radial velocity $[m/s]$	ω Argument of perigee [rad]
V_{∞} Hyperbolic excess velocity $[m/s]$	
U Gravitational potential $[N \cdot m]$	Δ Variation
w Exhaust velocity $[m/s]$	Υ First Point of Aries or vernal equinox direction
W Power density $\left[W/m^2\right]$	Ω Right ascension of the ascending node [rad]
$1/\alpha_w$ Specific power $[W/kg]$	$\Delta\theta$ Transfer angle [rad]
α Thrust angle [rad]	Sub and a
α Thrust angle [rad] ϵ Total energy per unit of mass $[W/kg]$	Subscripts 0 Initial
	-
ϵ Total energy per unit of mass $[W/kg]$	0 Initial
ϵ Total energy per unit of mass $[W/kg]$ ϵ Tolerance	0 Initial 1 Initial orbit
ϵ Total energy per unit of mass $[W/kg]$ ϵ Tolerance ϵ Power conversion efficiency	0 Initial 1 Initial orbit 2 Final orbit
ϵ Total energy per unit of mass $[W/kg]$ ϵ Tolerance ϵ Power conversion efficiency ϵ Specific mass of the energy source	 0 Initial 1 Initial orbit 2 Final orbit c Circular
ϵ Total energy per unit of mass $[W/kg]$ ϵ Tolerance ϵ Power conversion efficiency ϵ Specific mass of the energy source ϕ Increment function	 0 Initial 1 Initial orbit 2 Final orbit c Circular d Departure planet
ϵ Total energy per unit of mass $[W/kg]$ ϵ Tolerance ϵ Power conversion efficiency ϵ Specific mass of the energy source ϕ Increment function ϕ Phase angle [rad]	 0 Initial 1 Initial orbit 2 Final orbit c Circular d Departure planet e End of thrusting phase
ϵ Total energy per unit of mass $[W/kg]$ ϵ Tolerance ϵ Power conversion efficiency ϵ Specific mass of the energy source ϕ Increment function ϕ Phase angle [rad] ϕ Heliocentric latitude [rad]	 0 Initial 1 Initial orbit 2 Final orbit c Circular d Departure planet e End of thrusting phase eng Engine

 μ Gravitational parameter [m^3/s^2]

m Main body

p Propellant

ps Propulsion system

s Satellite or spacecraft

st Storage tanks

S Sun

t Target planet

tp Projected target

T Total

w Power source

wc Power controller

∞ Infinity

Acronyms

DP Dynamic Programming

DS1 Deep Space 1

EP Evolution Programming

FEED Field Effect Electrostatic

Propulsion

GA Genetic Algorithm

MPD Magnetoplasmadynamic

MMH Monomethylhydrazine

MON Mixed Oxides of Nytrogen

 N_2H_4 Hydrazine

NTO Nitrogen tetroxide

RK Runge-Kutta

SA Simulated Annealing

SBC Swing-By Calculator

STA Space Trajectory Analysis

Introduction

Centuries ago, the motion of planets was studied to find which shape would better characterize the trajectories of celestial bodies. The conical sections (elliptic, parabolic and hyperbolic orbits) were found to be the best analytical representations for this problem and they are known as Keplerian orbits. Nowadays, the same sort of mathematical studies are made in order to determine shapes that best represent the motion of spacecraft with certain steering profiles, using low-thrust propulsion. Analytical representations for low-thrust trajectories have been developed [Petropoulos et al., 1999], but only for one particular steering program: trajectories with tangential and continuous thrust, modulated by the distance to the Sun. Considering the wide range of possibilities, it will be important to analyze other steering programs and find other analytical representations for these trajectories. In this way, the main purpose of this master thesis is to analyse possible steering programs and mathematical functions that can represent low-thrust trajectories and compare their performance with the performance of the exponential sinusoid already found [Petropoulos et al., 1999]. Moreover, this trajectories' study will not be focused on a particular mission, but on a general one, i.e., with arbitrary initial and final conditions.

More recently a master student of T.U. Delft finished his master thesis project on the study of a new method to find a good initial guess for short (one third or half a revolution) low-thrust trajectories between two celestial bodies [De Vogeleer, 2008]. This master thesis, like De Vogeleer's thesis, will try to find an analytical representation for low-thrust trajectories that can surpass the exponential sinusoid in terms of computation time, velocity increments at departure and arrival and thrust acceleration values during the low-thrust interplanetary phase.

Some principles of celestial mechanics and the conclusions made about the influence of perturbations on the spacecraft's motion in the literature survey [Paulino, 2007] will be discussed in chapter 1. In chapter 2, the numerical integration method that will be used to compute the time of flight (TOF) for the low-thrust trajectories described by the analytical representations will be presented. Important data about and the theoretical principles of low-thrust propulsion are addressed in chapter 3. In chapter 4, interplanetary missions are

described, assuming that no thrust and no perturbing forces are acting on the spacecraft. The analysis already done for low-thrust trajectories using the exponential sinusoid with tangential thrust ([Petropoulos and Longuski, 2004] and [Izzo, 2006]) will be presented in chapter 5, while the study and some mission example results using other steering programs and other shapes will be discussed in chapter 6 and 7, respectively. In chapter 8, an introduction and a description of the optimisation procedure done for the chosen analytical representations will be given. The verification of the program developed in this master thesis will be given in chapter 9. The results from the optimisation procedure will be shown in chapter 10. Finally, the conclusions of the master thesis work and some recommendations are given in chapters 11 and 12, respectively.

1. Orbital Mechanics

In this initial chapter, basic principles of astrodynamics will be described. These principles are important to understand the motion and the position of celestial bodies in space. Only by making use of reference frames (section 1.1) and coordinate systems (section 1.5), it is possible to know the exact location of a spacecraft. Through orbit elements (section 1.2), laws of motion (section 1.3) and knowing the influence of perturbations (section 1.4) on the spacecraft's motion, it is possible to understand its trajectory in space.

1.1. Reference Frames

Before describing the motion of celestial bodies and spacecraft, reference frames have to be defined, since it is not possible to discuss trajectories in space without defining the reference with respect to which this motion is expressed. A special reference frame is the inertial reference frame that is defined from [Wakker, 20051]: "An inertial reference frame is a reference frame with respect to which a particle remains at rest or in uniform rectilinear motion if no resultant force acts upon that particle". In practice it is not possible to use this reference frame, so pseudo-inertial reference frames are applied instead [Wakker, 20051]. For instance, in the motion of Solar System planets around the Sun, the origin of the reference frame should be chosen at the centre of the Solar System and not at the centre of the universe. Therefore, the motion of the Sun with respect to the true inertial reference frame, that is located at the centre of the universe, is neglected. Reference frames can be described for Earth orbit missions and interplanetary missions. Since this master thesis will only focus on the heliocentric phase of interplanetary missions, planetary centred reference frames will not be described here.

The origin of a non-rotating reference frame in an interplanetary flight is the Sun. Typically, the XY-plane is the ecliptic plane. The Z-axis is chosen to be perpendicular to this plane. The angle between the ecliptic plane and the equatorial plane (Earth) is about 23°27' and it is called the obliquity of the ecliptic [Wakker, 20051]. The (+) X-axis of this reference frame is pointed at the First Point of Aries or vernal equinox direction (Υ) . The

(+) Y-axis is chosen so that the reference frame is right-handed. This reference frame is called the non-rotating heliocentric ecliptic reference frame. Due to precession (change in the Earth's rotation axis), the ecliptic will change during time. Therefore, a reference epoch should be always specified. Usually epoch J2000 (January, 1st 2000, noon terrestrial time) is taken.

This reference frame can also be described using other sets of coordinates besides the Cartesian ones, like the spherical coordinates. An arbitrary point P in the heliocentric nonrotating ecliptic frame can be described by a heliocentric radius r, a heliocentric longitude λ and a heliocentric latitude φ , as illustrated in figure 1.1. The heliocentric longitude is described by the angular distance along the ecliptic from the direction Υ to the projection of the object's position in the ecliptic. This angular distance is measured from 0° to 360°, eastward along the ecliptic. The heliocentric latitude is the angular distance along the circle of heliocentric longitude passing through the vehicle, from the ecliptic to the spacecraft. It is measured from -90° to 90° and it is taken positive when the spacecraft is north of the ecliptic and negative when the spacecraft is south of the ecliptic.

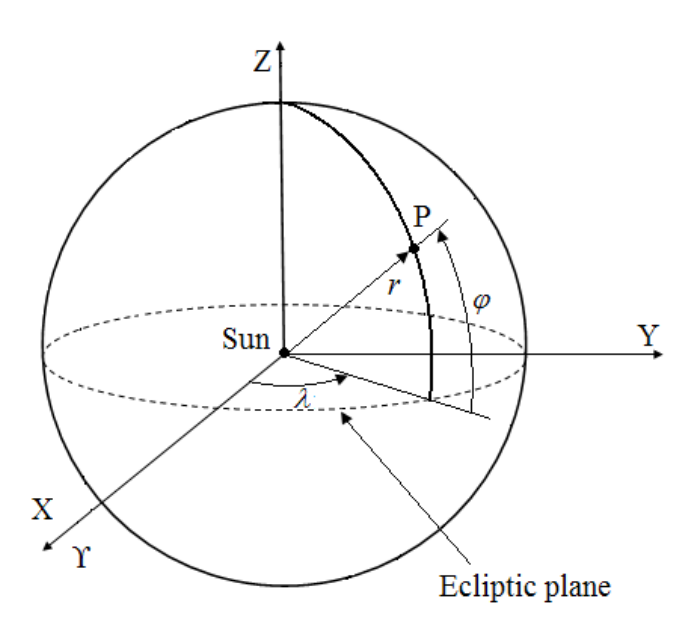


Figure 1.1: The non-rotating heliocentric ecliptic reference frame using Cartesian and spherical coordinates

1.2. Orbital elements

Planets, artificial satellites and other celestial bodies describe a path that revolves around other bodies, mainly under the influence of a centrifugal force (the gravity force). In other words, they orbit other celestial bodies. To describe this motion, the position and the velocity of a body which is orbiting must be known (three position components and three velocity components) at every instant, since they change constantly. However, an orbit can also be described by six independent parameters that are constant in a Keplerian orbit (section 1.3). They are called the classical orbital parameters: a, e, ω , τ , Ω and i. These parameters are represented in figure 1.2.

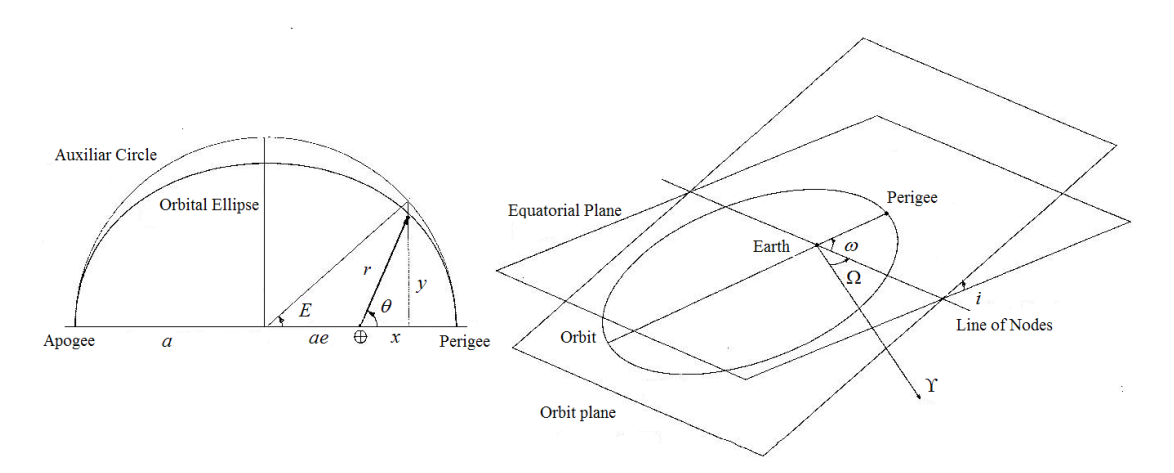


Figure 1.2: Representation of the orbital elements [Montenbruck et al., 2005]

Parameter a is the semi-major axis and parameter e is the eccentricity. They determine the size and the shape of an orbit, respectively. Parameter Ω is the longitude of the ascending node in an ecliptic frame and it represents the angle between a reference direction (vernal equinox is normally used) and the point where the satellite crosses the equator from south to north (ascending node). It is measured eastward from 0° to 360° . Parameter ω is the argument of perigee and it represents the angle between the direction of the ascending node and the direction of the perigee. This parameter determines the orientation of the conic section in the orbital plane. The integration constant τ is the time of pericentre passage and it associates time with position in the orbit. Parameter i is the inclination and it represents the angle measured from the reference plane to the orbital

plane. When looking from the ascending node to the origin of the reference frame, this angle should be measured counter-clockwise from the reference frame and its range is from 0° to 180° . Satellites that travel in a direction opposite to the rotation of the Earth along its axis, have inclination values between $(90^{\circ},180^{\circ})$ and they are said to move in a retrograde orbit. On the other hand, satellites travelling in the same direction as the Earth rotates about its axis have an inclination in the interval $[0^{\circ},90^{\circ})$ and they are said to move in a prograde orbit. Parameters Ω and i determine the orientation of the orbital plane relative to the reference plane.

1.3. Two-body problem

In a realistic situation, to describe the motion of a body i with respect to a non-rotating reference frame, with body k as origin, all gravitational forces between bodies i, k and other bodies j presented in the system must be taken into account. However, as a first approximation, the gravitational attraction between bodies i and j can be neglected with respect to the effect of the main gravitational attraction between bodies i and k [Wakker, 2005I]. In this way, a two-body problem can be considered and the following assumptions are made [Bate et al., 1971]:

- Bodies are perfect spheres, which mean that the mass of celestial bodies is concentrated at their centres and, therefore the celestial bodies are represented by points in space;
- There are no external or internal forces acting on a two-body system, other than gravitational forces.

The equation of motion of body i with respect to body k is given by [Wakker, 2005I]:

$$\ddot{\overline{r}} = -\frac{\mu}{r^3}\overline{r} \tag{1.1}$$

Parameter μ from equation (1.1) is the gravitational parameter that is given by: $\mu = G(m_i + m_k)$ and \overline{r} is the position vector from body k to body i. Parameter G is the universal gravity constant, m_i and m_k are the masses of bodies i and k, respectively. Before attempting to solve equation (1.1), two important conservation laws in the motion of body i with respect to body k must be described [Wakker, 2005I]:

$$\begin{cases} \frac{1}{2}V^2 - \frac{\mu}{r} = -\frac{\mu}{2a} = \varepsilon = \text{const} \\ \overline{r} \times \overline{V} = \overline{H} = \text{const} \end{cases}$$
 (1.2)

In equation (1.2), parameter ε indicates the total energy per unit of mass of body i. The first term of the first equation indicates the kinetic energy per unit of mass of body i, while the second term of this equation is the potential energy per unit of mass of body i. The total energy remains constant during the motion of body i, i.e., there is an exchange of energy between kinetic and potential. In this way, a vehicle will slow down as it gains altitude and it will speed up as it decreases in altitude. Parameter \overline{H} is the angular momentum vector per unit of mass of the motion of body i which is constant, implying that body i moves in one fixed plane perpendicular to \overline{H} . Using the first conservation law of the total energy, the velocity can be expressed in the so-called vis-viva equation as [Wakker, 2005I]:

$$V = \sqrt{\mu \left(\frac{2}{r} - \frac{1}{a}\right)} \tag{1.3}$$

From equation (1.1), the position of a body i with respect to a body k is given by [Wakker, 20051]:

$$r = \frac{H^2/\mu}{1 + c\cos(\varphi - \omega)} \tag{1.4}$$

This orbital equation describes the relation between r and φ . Equation (1.4) is equal to the shape of a conic section. Substituting H^2/μ for p, $\varphi-\omega$ for θ and c for e, r is expressed by:

$$r = \frac{p}{1 + e\cos\theta} \tag{1.5}$$

Equation (1.5) is given in polar coordinates and it defines the shape of the trajectory of body i with body k at a focal point. This equation only represents possible paths for a two-body problem. Parameter p is called the semi-latus rectum and θ is the true anomaly. The three types of conic sections are: ellipses (circles are ellipses with zero eccentricity), parabolas and hyperbolas, represented in figure 1.3. First-order, celestial bodies move in conical paths: planets, artificial and natural satellites move in elliptical (near-circular) orbits; parabolic and hyperbolic orbits are used by comets and spacecraft in interplanetary missions. These conical sections are known as Keplerian orbits.

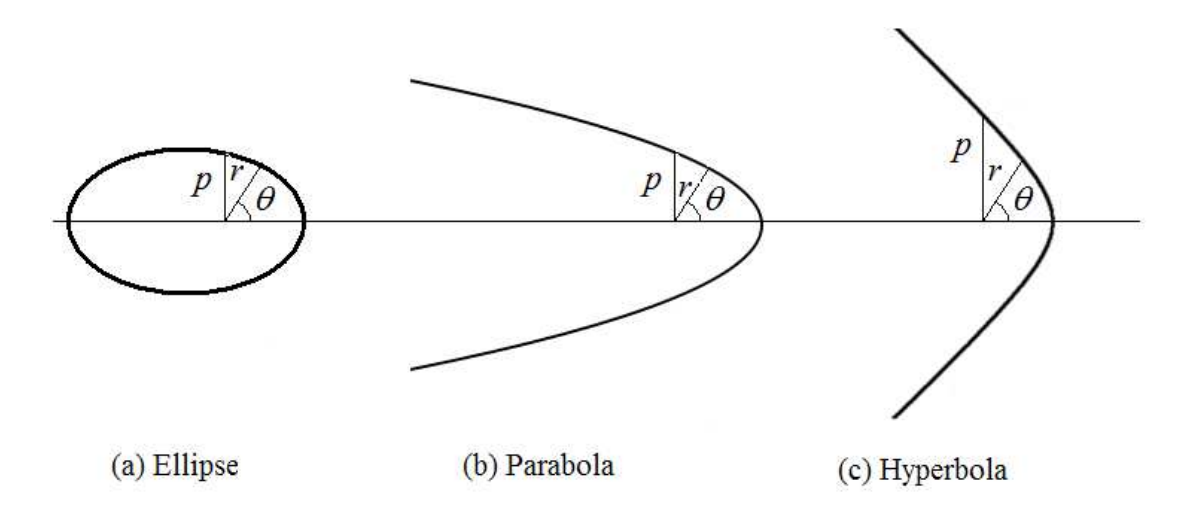


Figure 1.3: The three types of conic sections: the ellipse, the parabola and the hyperbola, based on [Montenbruck et al., 2005]

In the following sections, the three different types of Keplerian orbits will be briefly described.

1.3.1. Elliptic orbits

In the Solar System, the orbits of all planets and the orbits of Earth satellites are approximated by ellipses (see figure 1.3(a)). An ellipse is a closed and periodic curve therefore a body in an elliptic path travels the same trajectory over and over. This conic section is characterized by e < 1 and its major axis 2a is expressed by:

$$2a = r_a + r_p = \frac{p}{1 - e} + \frac{p}{1 + e} = \frac{2p}{1 - e^2}$$
, so that $p = a(1 - e^2)$ (1.6)

Parameters r_a and r_p are the apocentre and the pericentre radius, respectively.

From equation (1.3), the velocity reaches its maximum value at the pericentre:

$$V_{p} = \sqrt{\mu \left(\frac{2}{a(1-e)} - \frac{1}{a}\right)} = \sqrt{\frac{\mu}{a} \left(\frac{1+e}{1-e}\right)} = V_{c_{p}} \sqrt{1+e}$$
(1.7)

The velocity reaches its minimum value at the apocentre:

$$V_{a} = \sqrt{\mu \left(\frac{2}{a(1+e)} - \frac{1}{a}\right)} = \sqrt{\frac{\mu}{a} \left(\frac{1-e}{1+e}\right)} = V_{c_{a}} \sqrt{1-e}$$
(1.8)

Circular velocities at the pericentre and the apocentre are represented by V_{c_p} and V_{c_a} , respectively.

The period of an elliptic orbit is given by [Wakker, 2005I]:

$$T = 2\pi \sqrt{\frac{a^3}{\mu}} = \frac{2\pi}{n} \tag{1.9}$$

Parameter n in equation (1.9) is called the mean angular motion.

1.3.2. Parabolic orbits

Parabolic orbits are conic sections rarely found in celestial bodies' trajectories (see figure 1.3(b)). A body travelling in a parabolic orbit will have a one-way trip to infinity. A parabolic orbit is characterized by e=1, which simplifies the equation of motion: $r=p/(1+\cos\theta)$. Using this result, the spacecraft's pericentre ($\theta=0^{\circ}$) distance is:

$$r_p = \frac{p}{2} \tag{1.10}$$

Only a finite amount of kinetic energy is needed to overcome the effects of gravity and launch a spacecraft into infinity, since the strength of a gravity field decreases rapidly with distance from the main body. A spacecraft in a parking orbit around a planet can be "pulled" into a parabolic orbit by accelerating to a velocity that is $\sqrt{2}$ times the velocity in the local circular orbit. This means that, using equation (1.3) and the fact that the semi-major axis $a = \infty$, the velocity is given by [Wakker, 20051]:

$$V_{\text{escape}} = \sqrt{\frac{2\mu}{r}} = \sqrt{2}V_c \tag{1.11}$$

Parameter V_c in equation (1.11) is the instantaneous circular velocity of the spacecraft. The spacecraft will always describe a parabolic path with $V_{\rm escape}$, independently of the velocity's direction. Using this velocity value in the total energy equation, it yields $\varepsilon=0$. From equation (1.11), it can be concluded that at infinity, $r=\infty$, the velocity is minimal and equal to zero and at pericentre, the velocity is maximal and equal to $\sqrt{2\mu/r_p}$.

It must be said that highly eccentric elliptic orbits or low eccentric hyperbolic orbits are often approximated by parabolic orbits, since computations are faster when using parabolic equations [Wakker, 2005I].

1.3.3. Hyperbolic orbits

A hyperbolic orbit is important to be studied when a spacecraft is required to move with a certain velocity after escaping the departure planet, i.e., these orbits are important in interplanetary missions. A hyperbola has two branches and they represent each other's mirror-image with respect to a line perpendicular to the major axis. The right branch has no physical meaning for celestial mechanics, but the left branch, illustrated in figure 1.3(c), represents a hyperbolic motion in a gravity field. Since e > 1, from equation (1.5), it can be concluded that the true anomaly is limited by: $\cos \theta > -1/e$. The major axis of the hyperbola 2a is the distance between the tops of its two branches and due to simplicity in computations, it is considered negative, while r and p are positive [Wakker, 20051].

As usual, the distance to pericentre is: $r_p = a(1-e)$, where the velocity reaches its maximum value:

$$V_p^2 = \mu \left(\frac{2}{a(1-e)} - \frac{1}{a} \right) = \frac{\mu}{-a} \left(\frac{e+1}{e-1} \right) = V_{cp}^2 \left(e+1 \right)$$
 (1.12)

The minimum velocity value occurs for $r = \infty$ and it is given by:

$$V_{\infty}^2 = -\frac{\mu}{a} \tag{1.13}$$

This means that for an infinite distance from body k, body i still has a finite velocity with respect to body k. At every point in a hyperbolic orbit, the instantaneous velocity can be determined by the local escape velocity (equation (1.11)) and by the velocity at infinity (equation (1.13)) [Wakker, 20051]:

$$V^2 = V_{\text{escape}}^2 + V_{\infty}^2 \tag{1.14}$$

Consider a case where a spacecraft has only enough velocity to escape the gravitational field of the departing planet. This means that the velocity will tend towards zero as the

distance from the gravity field approximates infinity. However, the velocity given to the vehicle in equation (1.14) can be more than the escape velocity. This finite residual velocity at infinity, V_{∞} is called the hyperbolic excess velocity. Figure 1.4 illustrates the distance versus the velocity for a hyperbolic orbit around the Earth, using three values of the eccentricity (e=1.1, e=1.5 and e=3). The local escape velocity curve is also shown in figure 1.4. The perigee altitude from the Earth's surface used was 500km. Note that for significantly small velocity increments above the escape velocity at 500km, V_{∞} values are significantly large. Also, for higher distances the differences between the hyperbolic velocity and V_{∞} become smaller.

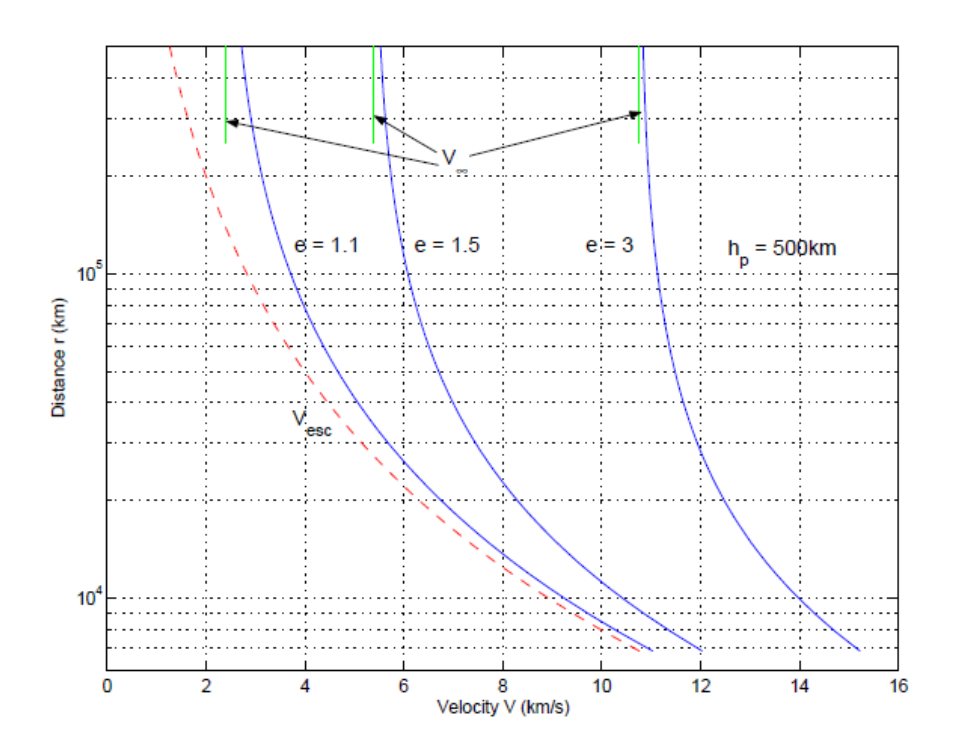


Figure 1.4: Distance versus velocity for three hyperbolic trajectories [Melman, 2007]

When hyperbolic orbits are discussed, the sphere of influence of the planet in question must be defined. The meaning of "escaping from the gravity field of a planet" is connected with the distance from the planet where the spacecraft is no longer under the influence of the gravity field of that planet – sphere of influence. So, when the spacecraft crosses the edge of this sphere of influence, it is assumed to have escaped from the gravitational body.

1.4. Perturbing Forces

Assuming an interplanetary mission from one planet to another, simplifications to this problem can be made such that no perturbation forces are taken into account (section 1.3). In this case, only gravitational forces from the main bodies are present, which are considered to be radially symmetrical. Therefore, in this situation, the spacecraft moves always in Keplerian orbits. However, in reality, other external forces interfere with the spacecraft's trajectory, slightly deviating the vehicle from the Keplerian orbit. In this way, perturbed Keplerian orbits must be mentioned. In the literature survey [Paulino, 2007], the following perturbing forces were studied: gravity field perturbations, third-body perturbations, solar radiation pressure, atmospheric drag, electromagnetic forces and relativistic effects. Theoretical information and mission examples were given in the literature survey in order to analyse typical values of the perturbing acceleration. After assessing their magnitudes, a comparison between these values and the magnitude values of the main acceleration from the Sun was made.

From all perturbations mentioned in the literature survey [Paulino, 2007], radiation pressure had the highest effect in the spacecraft trajectory, with a maximal order of magnitude acceleration of $10^{-6} \, m/s^2$ (at Mercury). This value can be neglected with respect to the main acceleration of the Sun (at Mercury, the order of magnitude of the main acceleration is $10^{-2} \, m/s^2$). In this way, due to this significantly small value and also as a matter of simplicity for the analysis of the low-thrust problem, perturbations will be neglected in this master thesis.

Note that, although all the perturbation forces were neglected, there is one force that cannot be rejected: the low-thrust force that will define the spacecraft's trajectory. Typical order of magnitude of low-thrust acceleration values is between $10^{-5} m/s^2$ and $10^{-2} m/s^2$ (chapter 7). Therefore, this force cannot be considered a "perturbing" force.

1.5. Coordinate Systems

As already mentioned in the previous sections 1.1 and 1.2, the position and velocity of body i can be expressed in at least three different ways:

- 1. Cartesian coordinates: $x, y, z, \dot{x}, \dot{y}, \dot{z}$
- 2. Spherical coordinates: $r, \lambda, \varphi, V, \gamma, \psi$
- 3. Keplerian coordinates: $a, e, i, \Omega, \omega, \tau$

In this master thesis, coordinate transformations are only required between spherical and Cartesian coordinate systems.

The coordinates of a point P in Cartesian (x, y, z) and in spherical (r, λ, φ) coordinates are represented in figure 1.1. In order to obtain the Cartesian coordinates from the spherical ones, the following equations should be used [Wertz, 2001]:

$$x = r \cos \varphi \cos \lambda$$

$$y = r \cos \varphi \sin \lambda$$

$$z = r \sin \varphi$$
(1.15)

The spacecraft position in spherical coordinates can also be obtained from Cartesian coordinates, using the following equations [Wertz, 2001]:

$$r = \sqrt{x^2 + y^2 + z^2}$$

$$\lambda = \arctan 2\left(\frac{y}{x}\right)$$

$$\phi = \arctan\left(\frac{z}{r_{xy}}\right)$$
(1.16)

In equations (1.16), the distance r_{xy} is computed through $r_{xy} = \sqrt{x^2 + y^2}$. The function arctan 2 is a four-quadrant inverse tangent function. This function differs from the normal

inverse tangent function \arctan , whose results are limited to solutions in the interval $[-\pi/2;\pi/2]$, i.e., to the first and fourth quadrants. The function $\arctan 2$ gives the angle in the correct quadrant immediately.

2. Numerical Integration Methods

Assumptions and simplifications are often done to solve equations of motion analytically. In these cases, equations of motion are solved for specific situations. However, a general approach to a solution is more desirable. Therefore, numerical integration techniques are required. In this master thesis, numerical integration is needed in order to compute the time of flight (TOF) of the spacecraft for a certain mission. Also, numerical integration of the equations of motion was necessary to verify the results in this master thesis (chapter 9 and appendix F).

In this chapter, a certain nomenclature will be used in the numerical integration methods. To represent the position and the velocity of the spacecraft, vector \overline{y} and vector \overline{f} are defined, respectively by [Montenbruck et al., 2005]:

$$\overline{y} = \begin{pmatrix} \overline{r} \\ \dot{\overline{r}} \end{pmatrix} \Leftrightarrow \dot{\overline{y}} = \overline{f}(t, y) = \begin{pmatrix} \dot{\overline{r}} \\ a(t, \overline{r}, \dot{\overline{r}}) \end{pmatrix}$$
(2.1)

Parameter \overline{y} is a six-dimensional state-vector that combines the position and the velocity of the spacecraft and $\overline{f}(t,y)$ is also a six-dimensional vector and it combines the velocity and the acceleration $(\overline{a}(t,\overline{r},\dot{r})=\ddot{r})$ of the vehicle, hence it is the time-derivative of \overline{y} . As a matter of simplicity, vector signs will not be included in equations from chapter 2. All the variables presented in this chapter are vectors or matrix quantities.

The most important numerical integration methods are the Runge-Kutta methods, the multistep methods and the extrapolation methods [Montenbruck et al., 2005]. Runge-Kutta methods are single-step methods that can be applied in a significant wide range of problems and they are easy to use compared with other numerical methods. Multistep methods provide a high accuracy in the results; however storage of previous data points is needed. Finally, extrapolation methods are known by their high accuracy in the results.

In the literature survey [Paulino, 2007], the Runge-Kutta methods were found to be the most suitable ones to be implemented in the master thesis. For this reason, in this chapter, multistep methods and extrapolation methods will not be discussed. In section 2.1, theoretical information about the Runge-Kutta methods will be given and in section 2.2 and 2.3 the reasons behind this choice will be presented.

2.1. Runge-Kutta Methods

To calculate an approximation for a certain function y(t), given an initial value of y at time t_0 ($y_0 = y(t_0)$), the approximation function at some later time ($t = t_0 + h$) is expressed by [Montenbruck et al., 2005]:

$$y(t_0 + h) \approx y_0 + h \dot{y}_0 \Leftrightarrow y(t_0 + h) \approx y_0 + h \phi = \eta(t_0 + h)$$
(2.2)

Parameter h is the time step-size and ϕ is the increment function that should be closely approximate to the tangent of y(t) between steps. Equation (2.2) is known as the Euler step and it is derived from a first-order Taylor expansion.

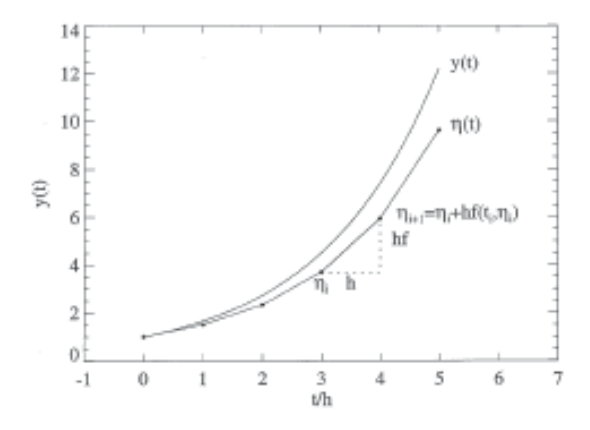


Figure 2.1: Approximate solution of the differential equation $\dot{y} = f(t, y)$ [Montenbruck et al., 2005]

As illustrated in figure 2.1, since the increment function ϕ deviates significantly from the secant, the Euler step is not considered a very accurate method. For this reason, a different increment function is used [Montenbruck et al., 2005]:

$$\phi = \sum_{i=1}^{s} b_i k_i \tag{2.3}$$

Parameter s is the number of function evaluations in a general explicit Runge-Kutta formula and parameters k_i are defined by [Montenbruck et al., 2005]:

$$k_{i} = f\left(t_{0} + c_{i} \cdot h, y_{0} + h \sum_{j=1}^{i-1} a_{ij} k_{j}\right) \quad (i = 2...s)$$
(2.4)

Note that only the explicit Runge-Kutta methods are described here, since the implicit ones are complex, requiring the solution of a non-linear system of equations to find the state of a system at later time. The coefficients of equation (2.4) are determined so that they obey to the following relations [Montenbruck et al., 2005]:

$$\sum_{i=1}^{s} b_i = 1, c_1 = 0, c_i = \sum_{i=1}^{i-1} a_{ij} (i > 1) (2.5)$$

For each stage a_{ij} , b_i and c_i coefficients can be found in a Butcher tableau, represented in figure 2.2. After this process, an approximate solution can be obtained through the same equation used in the Euler step, the second equation in (2.2).

Figure 2.2: The Butcher tableau [Montenbruck et al., 2005]

As an example, the 4^{th} -order Runge-Kutta method (RK4) is presented. The number of evaluations s used is four and the increment function is given by [Montenbruck et al., 2005]:

$$\phi_{RK4} = \frac{1}{6} (k_1 + 2k_2 + 2k_3 + k_4) \tag{2.6}$$

Parameters k_i with i = 1...4 are given by:

$$k_{1} = f(t_{0}, y_{0})$$

$$k_{2} = f(t_{0} + h/2, y_{0} + h k_{1}/2)$$

$$k_{3} = f(t_{0} + h/2, y_{0} + h k_{2}/2)$$

$$k_{4} = f(t_{0} + h, y_{0} + h k_{3})$$
(2.7)

In the case of RK4, the number of evaluations s is the same as the order p of the local truncation error, which is given by [Montenbruck et al., 2005]:

$$e_{RK4} = \left| y(t_0 + h) - \eta(t_0 + h) \right| \le const \cdot h^{p+1} = const \cdot h^5$$

$$(2.8)$$

However, generally s is not the same as p. Results from Runge-Kutta methods with the same number of stages, i.e., the same set of function evaluations, but with different order of Taylor polynomial can be compared (order p and p+1). This allows an easy estimation of the local truncation error. Given two independent approximation functions [Montenbruck et al., 2005]:

$$\eta(t_0 + h) = y_0 + h \sum_{i=1}^{s} b_i k_i
\hat{\eta}(t_0 + h) = y_0 + h \sum_{i=1}^{s} \hat{b}_i k_i$$
(2.9)

The truncation errors for these two approximations are given by [Montenbruck et al., 2005]:

$$e = |y(t_0 + h) - \eta(t_0 + h)| \le ch^{p+1}$$

$$\hat{e} = |y(t_0 + h) - \hat{\eta}(t_0 + h)| \le \hat{c}h^{p+2}$$
(2.10)

Assuming that the truncation error \hat{e} is smaller than e by the order of h, the local truncation error of the p^{th} -order can be estimated from the difference between the two solutions [Montenbruck et al., 2005]:

$$e = |y - \eta| \approx |\hat{\eta} - \eta| \tag{2.11}$$

Methods of neighbouring order that are based on the same set of function evaluations and that allow this easy estimation of the local truncation error are called embedded Runge-Kutta methods.

The step-size h is an important issue in numerical integration methods. The step-size should not be too large, due to truncation errors, but it cannot be also too short, because round-off errors and computation effort increase in these conditions [Montenbruck et al., 2005]. A technique can be applied to help choosing suitable values for the step-size. Given a step-size h, a local truncation error given by equation (2.11) is calculated and it might have a value higher than the tolerance ε . So, a smaller step-size has to be chosen. After some mathematic manipulations, the maximum allowed step-size to be used in the next step can be derived [Montenbruck et al., 2005]:

$$h^* = p+1 \sqrt{\frac{\mathcal{E}}{e(h)}} \cdot h \approx p+1 \sqrt{\frac{\mathcal{E}}{|\hat{\eta} - \eta|}} \cdot h \tag{2.12}$$

Parameter h^* can be used in the next step, if this step was successful. It should be noticed that the value of h should not be changed more than a factor of two to five from one step to the next one [Montenbruck et al., 2005].

A variable step-size may be needed when the function behaves inconstantly and rapidly in some intervals of times. The easiest way to implement variable step-size with Runge-Kutta

methods is to stop the integration and start again with new starting values for another stepsize. This approach is feasible when the number of these intervals is low and the integration is done mostly with a constant integration step.

Figure 2.3 illustrates the performance of three Runge-Kutta methods. The three methods are: DOPRI5 – 7th stage method of order 5 with an embedded method of order 4 developed by Dormand & Prince (1980); RKF7 – 7th order method for integration, while 8th order method for error estimation, developed by Fehlberg (1968); and DOPRI8 – 13 function evaluations for a 8th order approximation, developed by Dormand & Prince (1981). For higher orders, methods can achieve higher accuracies at the same time computation effort increases. The order of a Runge-Kutta method must be chosen, depending on the kind of accuracy required.

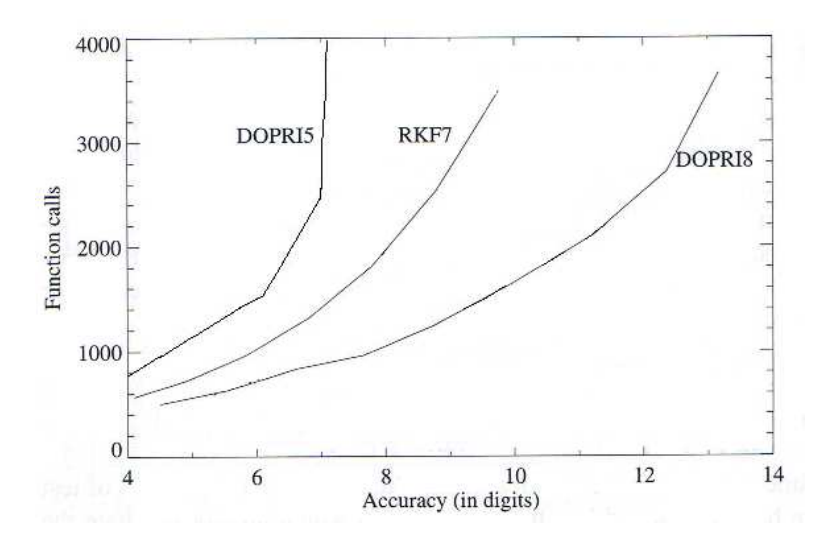


Figure 2.3: The number of function calls in function of accuracy for Runge-Kutta methods: DOPRI5 (5th order), RKF7 (7th order) and DOPRI8 (8th order) [Montenbruck et al., 2005]

2.2. Analysis

In this section, an analysis will be made about the importance of some factors for the choice of the numerical integration method that will be used in this thesis project. The factors that are responsible for the selection of the most suitable numerical integration method are: speed, accuracy, storage and complexity. However, all these factors and their

weight depend on the problem that needs to be solved. In this way, some questions [Bate et al, 1979] and answers will be provided:

1. How many independent variables are required (large number of integrations steps)?

In order to compute the TOF of the spacecraft during its interplanetary mission, certain dynamic parameters need to be computed using numerical integration (chapters 5 and 6): two at maximum. During the integration procedure, only one independent variable is necessary: the time t or the polar angle θ . Since there is only one independent variable and the dynamic parameters that will be computed change slowly with time, there is no reason to require a large number of integration steps.

2. Are the results of the problem susceptible to small errors?

Low-thrust mathematical representations have a spiral shape that slowly moves from the departure planet to the target planet. Small errors can become a problem for this kind of trajectory, since the spacecraft will take a long time to accomplish its mission (long integration time).

3. Is a constant step-size satisfactory?

Although dynamic parameters of low-thrust trajectories change slowly with time, a variable step-size might be necessary in order to obtain accurate results.

2.3. Discussion

As already said in this chapter, low-thrust trajectories change slowly with time and therefore large integration steps can be used. The computation time is still a very important issue in this problem, since low-thrust missions have a long TOF and consequently the time to integrate the trajectories will also be long. In this way, the computation effort should be reduced as far as possible, making the extrapolation methods not a reasonable option. Multistep methods obtain the same accuracy using a lower number of function calls than the Runge-Kutta methods. However, at not significantly high accuracy values, the difference between the numbers of function calls used in these two types of methods is not

considerably large. In this way, there is no need, in this case, to store values from previous steps to reduce the number of function calls (multistep methods). Since in this master thesis, a variable step is preferable, the easiest and simplest way to implemented it is using the Runge-Kutta method.

Therefore, a Runge-Kutta method with a variable step-size is suitable to integrate low-thrust trajectories in this thesis project. To choose the order (p) and the number of function evaluations (s) of the Runge-Kutta method, it should be analysed for a certain accuracy required if the method chosen is stable with the parameters s and p selected. An embedded Runge-Kutta method allows an easier estimation of the errors and consequently allows an efficient step-size control. In this way, a reasonable option for the low-thrust problem will be, for instance, a Runge-Kutta method of order 5 with an embedded method of order 4. The application of this method in the master thesis will be better explained in chapter 6.

Note that a large number of numerical methods could have been analysed in the literature survey [Paulino, 2007] and although their performance is better than the standard Runge-Kutta method, there is no time available to study all of them and their improvements would not have been significant.

3. Spacecraft Propulsion

In a general perspective, space propulsion systems are important in three situations [Wertz et al., 1999]: (1) the lift of the launch vehicle and its payload from the ground into a low-Earth orbit; (2) the transfer of the payload from parking orbits into higher orbits that can encounter planets (the most important for this master thesis); (3) in-orbit corrections and attitude control.

The aim of a propulsion system is to allow changes in magnitude and direction of the spacecraft position and velocity. In section 3.1, some basic notions of propulsion will be given. Finally, in this chapter, two propulsion system categories will be discussed: the chemical propulsion system (section 3.2) and the electric propulsion system (section 3.3).

3.1. Principles of Propulsion

Before describing the two main types of propulsion systems, it is important to describe the basic principles that are common to both chemical and electric propulsion. Spacecraft's acceleration in space occurs from propellant's discharge. The equation of motion of a rocket-propelled spacecraft, neglecting gravitational and drag is given by [ESA/SMART-1, 20071]:

$$M\frac{dV}{dt} = \frac{dM}{dt}w\tag{3.1}$$

In equation (3.1), parameter M is the instantaneous mass of the vehicle, dV/dt is the vehicle's acceleration, dM/dt is the rate of mass change due to propellant expulsion and w is the exhaust velocity of the stream.

From equation (3.1), the thrust generated by the propulsion system is given by:

$$T = m \cdot w \tag{3.2}$$

Using a single integration in equation (3.2), the impulse or change of momentum yields [ESA/SMART-1, 2007I]:

$$I = \int_0^{t_a} Tdt \tag{3.3}$$

Variable t_a in equation (3.3) is the action time, i.e., the time for which the thrust is applied. The specific impulse is the measure of how much impulse is produced over the propellant weight that the spacecraft spends. For constant mass flow and exhaust velocity, the specific impulse, expressed in seconds, is given by [Zandbergen, 2004]:

$$I_{sp} = \frac{\int_{0}^{t_{a}} T dt}{g_{0} \int_{0}^{t_{a}} m dt} = \frac{w}{g_{0}}$$
(3.4)

Parameter g_0 in equation (3.4) is the gravitational acceleration at sea level.

Finally, the ideal velocity rate of a spacecraft can be computed through Tsiolkowski's law, where gravity losses or perturbations are not taken into account and the exhaust velocity *w* is constant [Wertz et al, 1999]:

$$\Delta V = w \cdot \ln \left(\frac{M_0}{M_e} \right) \tag{3.5}$$

Parameter M_0 is the initial mass of the spacecraft and M_e is the spacecraft's mass at the end of the thrusting period.

3.2. Chemical Propulsion System

In a chemical spacecraft propulsion system, the propellant gas is thermodynamically expanded through a nozzle to create thrust. In this way, this system stores its energy in the propellants, without making use of any other mechanism to obtain energy. Therefore, it is

said that chemical propulsion is "energy limited", since the propellant has a fixed amount of energy per mass, which limits the maximum exhaust velocity and the specific impulse [ESA/SMART-1, 2007I]. Chemical propulsion systems are known by their relatively large thrust-to-mass ratio and, therefore, by a significantly short thrusting time, with low specific impulse. Due to limited available reaction energy and thermal transfer restrictions, chemical propulsion exhaust velocities are limited to a few thousand meters per second. Chemical propulsion systems are important in high energy transfer orbits and in Hohmann transfer orbits, where impulsive shots are used to obtain large variations of velocity, enough to directly escape a planet. In interplanetary flights, chemical propulsion is required at the departure planet (the spacecraft escapes) and possibly at the target planet (the spacecraft is captured). The variation of velocity and thrust values can be computed using the equations described in section 3.1.

Chemical burns are still required in low-thrust interplanetary missions at the departure and arrival planets. In order to compute the ΔV required, a value for the specific impulse will have to be assumed. Therefore, different types of chemical propellants will be discussed in section 3.3.1.

3.2.1. Types of Chemical Propellants

Chemical propellants use an association between fuel and oxidizer to create, in certain conditions, a chemical energy that will be needed to obtain exhaust velocity. The chemical propellants that are described in this section are: liquid, solid and hybrid. Cold gas is not mentioned since it does not have any utility in interplanetary transfers.

Liquid propellants are known by storing fuel and oxidizer in the liquid state. An important type of liquid propellants is the monopropellants. These liquid propellants combine the oxidizer and the fuel in one molecule or in a mixture. Monopropellant systems are reliable in orbit maintenance and attitude control. However they do not have the performance to produce large ΔV with high efficiency, needed for interplanetary orbits. Their range of specific impulse in vacuum is 150-225 seconds [Wertz et al., 1999]. A more important group is the bipropellants. They use fuel and oxidizer in separate tanks, since they have a

violent reaction when mixed. Bipropellant engines provide the highest performance system of all chemical engines, but they are also the most complex ones with a large number of systems. Another disadvantage is that most of them use toxic and dangerous propellants. The range of vacuum specific impulse values for bipropellant engines is 300-430 seconds [Wertz et al, 1999].

Solid propellants are known by storing fuel and oxidizer in a condensed solid state. Solid propellant motors have the advantage of: using harmless propellants in contrast with many liquid ones; having a simple structure with a small number of components and systems (cooling and feed system are not needed), which makes them reliable; and having a long storage time [Cornelisse et al, 1979]. However, solid motors have a relatively low specific impulse compared with rockets using other types of chemical propellant. Due to their simplicity, attention to the nozzle construction design is required, since no cooling system is active. Also, it is more difficult to modulate and control the thrust vector with a solid motor. It is important to remember that once ignited, generally the solid propellant motors burn until the end, since there is no physical way to stop the burning within the motor volume. In this way, the restart of a solid motor is not possible [Cornelisse et al, 1979]. Their typical range of vacuum specific impulse is 280-300 seconds [Wertz et al, 1999].

Hybrid propellants consist of a solid fuel and a liquid (or gaseous) oxidizer. Hybrid rockets have the advantage of: storing the fuel like the solid motors; restarting unlike the solid motors that cannot stop the burning once ignited; providing a cleaner environment than the solid motors; being safe, since explosions are not possible during the mixture of fuel and oxidizer; and finally throttling, i.e., it is possible to throttle the engine by modulating the oxidizer flow rate. The typical values of the specific impulse range are 250-340 seconds [Wertz et al, 1999].

In chemical propulsion systems, the most important parameter for the selection of the propellant is the specific impulse [Zandbergen, 2004]. In this way, the best choice for the high-thrust propulsion system is the bi-propellant liquid system. In table 3.1, some examples of bi-propellant liquid engines are given.

Engine	Developer	Vacuum Thrust (N)	$I_{sp}(s)$	Propellants	Engine mass (kg)
R-4D	Marquardt	490	309	NTO / MMH	3.76
RS-45	Rocketdyne	4.5	300	NTO / MMH	0.73
S400/1	DASA	400	303	MON / MMH	2.8
MMBPS	TRW	445	302	NTO / MMH	5.22
ADLAE	TRW	445	330	NTO/N_2H_4	4.5
RS-41	Rocketdyne	11100	312	NTO / MMH	68.95
S3K	DASA	3500	352	MON / MMH	14.5
R-42	Marquardt	890	303	MON / MMH	4.54

Table 3.1: Examples of bi-propellant liquid engines [Zandbergen, 2004] and [Cornelisse et al, 1979]

3.3. Electric Spacecraft Propulsion

Rocket engines using electric propulsion obtain thrust by making use of electric, magnetic and thermal energy to accelerate the propellant. Therefore, vehicles with electric propulsion systems do not use propellant as a power source. Instead, they use a separate source of energy. Until now, solar panels have been used for all electrically propelled spacecrafts to obtain energy. However, other alternatives have to be developed for missions far from the Sun. An example of an alternative is the use of nuclear electric power system.

The magnitude of acceleration provided by an electric propulsion system is significantly smaller than the gravitational acceleration of the planets within the sphere of influence of the planet. For this reason, spacecraft with this kind of propulsion system cannot leave a planet's surface. A chemical system (high thrust-to-mass ratio) has to be used to achieve a parking orbit about the planet and only from the parking orbit electric propulsion can be used in the vehicle.

It is important to notice that electric propulsion systems are not "energy limited", which allows the exhaust velocity to be much larger than the one available for the chemical system. Electric propulsion is limited by the maximum power provided by the power plant to the propellant. In this way, electric propulsion systems are called "power limited" systems. Subsequently, thrust is limited for a given spacecraft mass. Thus, electric propulsion vehicles tend to be low thrust-to-mass ratio, i.e., they tend to have low accelerations [ESA/SMART-1, 20071]. The advantage in electric propulsion systems is their large total amount of impulse. Therefore, though electric systems have low thrust-to-mass ratio, thrust operates for long periods, from hours to years.

3.3.1. Basic Principles

A propulsion system mass depends on the specific impulse (exhaust velocity), on the thrust level and on the total impulse. The total mass of a chemical propulsion system is given by the sum of the propellant(s) mass (M_p) , the storage tanks (M_{st}) , the engine (M_{eng}) and the control system $(M_{control})$. In an electric propulsion system two other masses have to be added: the mass of the power source (M_w) and the mass of the power controller (M_{wc}) , which are exclusive for the electric propulsion system. All these masses together, except the propellant mass, are called the dry mass of the propulsion system, M_{ps} . So, the total mass of an electric propulsion system is [ESA/SMART-1, 2007I]:

$$M_{Total} = M_p + M_{st} + M_{eng} + M_{control} + M_w + M_{wc} = M_p + M_{ps}$$
 (3.6)

This mass excess (compared to chemical engines) is compensated by reducing the propellant mass used by this propulsion system. This means that while the mass of the power source increases with the increase of specific impulse, the propellant mass decreases.

In electric propulsion systems, power sources provide power to ionize propellant and accelerate particles, so that the power source energy is converted into kinetic energy [Zandbergen, 2004]:

$$P_{j} = \varepsilon P = \frac{1}{2} m \cdot w^{2} \tag{3.7}$$

Parameter P_j is the power of exhaust jet, P is the power that is obtained through solar panels or another kind of power plant and ε is the power conversion efficiency.

In electric propulsion there is no limit for the exhaust velocity other than the speed of light, however the power required may increase to a point where there is no economic feasibility in obtaining more acceleration. In this way, it is important to find the optimum exhaust velocity and, consequently the optimum specific impulse of the system, I_{ssp} [Wertz et al, 1999]. In case where the solar energy is used to obtain power, the dry mass of the propulsion system is dominated by the mass of the power source and can be approximated by [Zandbergen, 2004]:

$$M_{ps} \approx M_{w} = \alpha_{w} P \tag{3.8}$$

Parameter $1/\alpha_w$ is the specific power [W/kg]. The specific impulse can also be given by [Zandbergen, 2004]:

$$I_{ssp} = \frac{w \cdot g_0}{1 + \varepsilon \cdot w^2} \tag{3.9}$$

Parameter $\varepsilon = \alpha_w/(2\eta t)$ is called the specific mass of the energy source. From equation (3.9), the optimum exhaust velocity is derived:

$$\frac{dI_{ssp}}{dw} = 0 \Leftrightarrow w_{op} = \sqrt{\frac{1}{\varepsilon}}$$
(3.10)

It should be mentioned that economically it is preferable to work slightly below the optimum value, because propellant is normally cheaper than using more power supply [Wertz et al., 1999].

3.3.2. Methods

There are three basic types of electric propulsion systems: electrothermal, electrostatic and electromagnetic. These methods are categorized by the way the propellant in the vehicle is accelerated.

a) Electrothermal Propulsion

This system is characterized by using heat to accelerate the propellant. There are three subtypes: resistojets, arcjets and inductively or radiatively heated systems (there are no application examples of this technique yet) [ESA/SMART-1, 2007I].

Resistojets use an electric heater to heat gaseous propellant that afterwards is expanded in a conventional nozzle to generate thrust. Usually, this type of propulsion is used to improve the performance of high-thrust propulsion systems (chemical systems), where the electric heater is used to further accelerate the propellant. An application of this type of electrothermal propulsion is done with hydrazine. Exhaust velocities of $3500 \, m/s$ and specific impulses of 350 seconds are achieved [ESA/SMART-1, 20071]. The specific impulse of resistojets is limited, since the molecular mass of the gases used is significantly high and the maximum surface temperature sustainable is limited.

Arcjets use an electric arc to heat the propellant before it expands in the nozzle. This type of propulsion can achieve core arc temperatures of 10000 to 20000 K and exhaust velocities of 5000 to $6000 \, m/s$ (I_{sp} from 500 to $600 \, {\rm seconds}$) at efficiencies of 40% with catalytically decomposed hydrazine [ESA/SMART-1, 2007I]. Portions of the propellant mass flow at these high temperatures cannot be in contact with the engine component walls.

b) Electromagnetic Propulsion

This system uses orthogonal electric and magnetic fields to ionize propellant particles, accelerating them. There are some developed and underdeveloped techniques like pulsed

plasma thrusters and magnetoplasmadynamic thrusters (MPD thrusters) [ESA/SMART-1, 20071].

Pulsed plasma thrusters with solid propellant are used for low power propulsion systems. They have a self-induced magnetic field that after moving in an electric field, a Lorentz body force is created, accelerating the plasma. This kind of thrusters does not produce enough thrust to be a primary propulsion system in the near future.

MPD thrusters work at high power levels (kilowatts to megawatts) and generate high thrust with reasonable specific impulse. Because they consume much power and they are still in development phase, MPD thrusters are not considered a primary propulsion system in the near future.

c) Electrostatic Propulsion

In this system, the ionised propellant is accelerated by an electric field. The main techniques are field effect electrostatic propulsion (FEEP), colloidal thrusters and gridded ion accelerators (ion engine) [ESA/SMART-1, 2007I].

FEEP applies a strong electric field ($\sim 10^{20} \, V/m$) to extract ions from an ionisable metal. Using an extraction voltage of 10kV, exhaust velocities of $100000 \, m/s$ (specific impulse of 10000 seconds) are achievable [ESA/SMART-1, 2007I]. FEEP thrusters using caesium as propellant have very low thrust levels and thrust per unit power: $1\mu N$ to 5mN on earth and $\sim 15 \, \mu N/W$, respectively. Nowadays, FEEP is not operational due to the low thrust-to-power ratio and contamination due to caesium. They provide insufficient thrust to be considered using in a primary propulsion system.

Colloidal thrusters achieve exhaust velocities of $10000\,\text{m/s}$ (I_{sp} of 1000 seconds) on earth [ESA/SMART-1, 20071]. Some problems, like the requirement of high acceleration voltages and high beam divergence, reflect the insufficient maturity of this kind of propulsion system.

Ion thrusters can achieve exhaust velocities of $30000 \, m/s$ (I_{sp} of 3000 seconds) and they are being used since the mid nineteen-nineties for station keeping of geostationary satellites [ESA/SMART-1, 2007I]. NASA's Deep Space 1 (DS1) and MUSES-C already demonstrated this technology for interplanetary missions.

3.3.3. Examples of Missions using Electric Propulsion

Electric propulsion systems have proven its worthiness in missions like DS1 launched in 1998 by NASA, SMART-1 launched in 2003 by ESA and MUSES-C launched in 2003 by JAXA. Before these missions, electric propulsion systems were mainly used for attitude control and orbit correction of space vehicles. In table 3.2, values for parameters like specific impulse, power and thrust are presented for DS1, SMART-1 and for MUSES-C propulsion system.

Characteristics	SMART-1	MUSES-C	Deep Space 1
Propellant	Xenon	Xenon	Xenon
Thrust (N)	6.8×10^{-2}	$5.12 \times 10^{-3} - 23.6 \times 10^{-3}$	9.2×10 ⁻²
Specific Impulse (s)	1640	2687-3011	1900-3200
Propellant consumed (kg)	82	61.9	74
Power source (W)	462-1190	310-1158	2300

Table 3.2: Propulsion system characteristics of SMART-1 [ESA/SMART-1, 20071], MUSES-C [Komuraki, 2003] and Deep Space 1 [NASA/JPL, 2002] [Rayman et al, 1999]

DS1 [Rayman et al, 1999] tested twelve advanced, high-risk technologies in space and at the end of its mission, it encountered the comet Borrely, presenting images and data from this comet. This satellite was the first one to use an (electrostatic) ion propulsion system as the primary propulsion system.

SMART-1 [ESA/SMART-1, 2007I] was used to test its electric propulsion system and other deep-space technologies, while observing the Moon. Hall Effect thrusters, which are both electrostatic and electromagnetic propulsion systems, were implemented in this spacecraft.

MUSES-C [Kuninaka et al, 2007] did a successful rendezvous with the asteroid Itokawa, using ion engines in its two year heliocentric flight.

Most recently, BepiColombo [ESA/BepiColombo, 2008] will be launched in 2013 and it will take approximately six years to arrive at Mercury. BepiColombo will perform a lunar flyby to reach the interplanetary trajectory. A cruise trajectory by ion propulsion stage - the Solar Electric Propulsion Module (SEPM), up to 0.25 N thrust, with five gravity assists: Earth, Venus (2×) and Mercury (2×) - will be accomplished. This mission will be an ESA mission in cooperation with Japan. The mission will consist of two separate spacecraft that will orbit the planet. ESA is building one of the main spacecraft, the Mercury Planetary Orbiter (MPO), and the Japanese space agency ISAS/JAXA will contribute the other, the Mercury Magnetospheric Orbiter (MMO) [ESA/BepiColombo, 2008].

4. Non-perturbed Transfer Orbits

In this chapter, simple analytical concepts of spacecraft trajectories that leave the gravitational attraction of a body to be captured by the gravitational field of another body will be studied. This chapter is an introduction to a more complex study of interplanetary missions that will be described in chapter 5, where in addition to the gravitational force there is a thrust force from an electric propulsion system. However, in this chapter, only gravitational forces from the main bodies will be considered.

Interplanetary missions are considered when a spacecraft escapes from a planet's gravity attraction, like the Earth's, and it moves in a hyperbolic trajectory with respect to the planet. The vehicle will enter in a heliocentric orbit and it will approximate the target planet also with a hyperbolic trajectory with respect to this planet. Different missions can be categorized, depending on the approach to the target planet [Cornelisse et al., 1979]:

- Flyby mission the spacecraft will pass the target planet at a relatively small distance;
- Orbiter mission the spacecraft will need a propulsion engine to decelerate and enter an orbit around the planet;
- Lander mission the final velocity of the spacecraft with respect to the planet's surface will have to be reduced to a very small value.

These interplanetary missions are divided in three phases of two-body Keplerian orbits, around different gravity fields in each phase. First, the spacecraft will be under the influence of the departure or initial planet's gravity field (section 4.2), from where it is going to escape after the first impulsive shot. Second, after escaping, it will move in a heliocentric motion, i.e., under the influence of Sun's gravity field (section 4.1). Finally, the spacecraft will perform a planetocentric orbit at destination, so it will be under the influence of the target planet's gravity field (section 4.2). The transition between phases is done using the concept of sphere of influence, already explained in section 1.3. When the spacecraft is out of the sphere of influence of the departure or target planet, the Sun is the

main gravitational body, therefore the gravitational influence from other planets is not considered [Cornelisse et al., 1979].

The patched-conic approximation will be used to calculate analytically the heliocentric departure and arrival velocities in terms of direction and magnitude. The three phases will be discussed in detail in the following sections.

4.1. Heliocentric Phase

Figure 4.1 illustrates a general heliocentric transfer orbit. The initial and final orbits of the starting and arriving planets are assumed to be circular. This is a realistic assumption since most of the celestial bodies orbiting the Sun, with exception of Mercury and Pluto, have nearly circular orbits around it. This heliocentric transfer orbit takes the vehicle from the sphere of influence of the departure planet to the sphere of influence of the arriving planet.

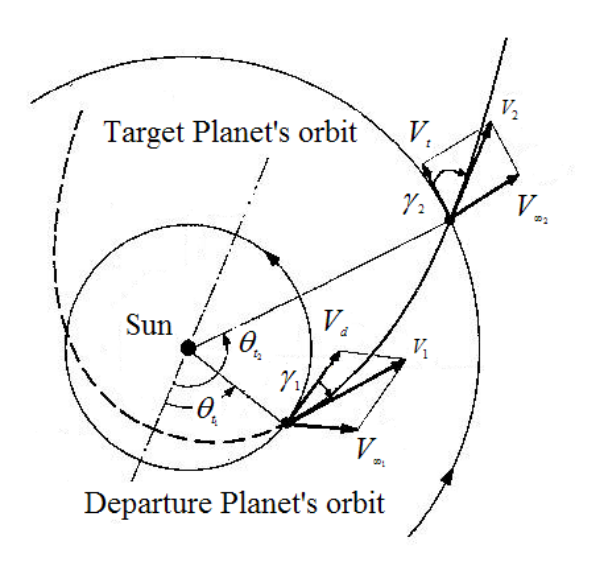


Figure 4.1: Heliocentric transfer orbit [Cornelisse et al., 1979]

From figure 4.1, the initial and the final orbit radius can be computed through:

$$r_1 = \frac{a(1-e^2)}{1+e\cos\theta_{t_1}} \text{ and } r_2 = \frac{a(1-e^2)}{1+e\cos\theta_{t_2}}$$
 (4.1)

Parameters θ_{t_1} and θ_{t_2} are the true anomaly at the point where the transfer orbit intersects the initial and the final orbit, respectively (figure 4.1). The flight path angle γ is the angle between the local horizon and the velocity vector. The parameters a and e are the semi-major axis and the eccentricity of the transfer orbit, respectively, and both can be determined through the equations (4.1), knowing θ_{t_1} , θ_{t_2} and the departure and the target planets (r_1 and r_2 , respectively).

The angles γ_1 and γ_2 are the flight path angles for the initial and final epochs, respectively (figure 4.1). These two angles are computed using equations $H^2 = p/\mu$, (1.6) and the equation of the angular momentum with a certain flight path angle: $H = rV \cos \gamma$, [Wakker, 2005II]:

$$\cos \gamma_1 = \sqrt{\frac{a(1 - e^2)}{\mu r_1^2 V_1^2}} \text{ and } \cos \gamma_2 = \sqrt{\frac{a(1 - e^2)}{\mu r_2^2 V_2^2}}$$
 (4.2)

The velocities V_1 and V_2 are the heliocentric departure and arrival velocities respectively that can be calculated through equation (1.3). The gravitational parameter μ considered in equation (4.2) is that of the Sun.

The travel time of the heliocentric transfer orbit can be determined through:

$$TOF = t_{f_2} - t_{f_1}$$
 (4.3)

The variables t_{f_2} and t_{f_1} are the time since the pericentre passage of the transfer orbit at the departure point (with radius r_1) and at the arrival point (with radius r_2), respectively. These two times can be determined using the equation of Kepler [Montenbruck et al., 2005]:

$$E - e \sin E = M = n(t - \tau) \tag{4.4}$$

Parameter M is called the mean anomaly and parameter E is the eccentric anomaly, and this last parameter is related to the true anomaly using the equation [Wakker, 2005I]:

$$\tan\frac{\theta}{2} = \sqrt{\frac{1+e}{1-e}} \tan\frac{E}{2} \tag{4.5}$$

In this way, assuming $\tau = 0$, t_{f_2} and t_{f_1} are calculated through:

$$t_{f_1} = \sqrt{\frac{a^3}{\mu}} \left(E_{t_1} - e \sin E_{t_1} \right) \text{ and } t_{f_2} = \sqrt{\frac{a^3}{\mu}} \left(E_{t_2} - e \sin E_{t_2} \right)$$
 (4.6)

Parameters E_{t_1} and E_{t_2} are given by equation (4.5).

From figure 4.1, it is possible to calculate the hyperbolic excess velocities at the departure and arrival planets [Cornelisse et al., 1979]:

$$V_{\infty_1} = \sqrt{V_1^2 + V_d^2 - 2V_1 V_d \cos \gamma_1}$$

$$V_{\infty_2} = \sqrt{V_2^2 + V_t^2 - 2V_2 V_t \cos \gamma_2}$$
(4.7)

Parameter V_d is the heliocentric departure planet's velocity and V_t is the heliocentric target planet's velocity.

Hohmann transfer orbits are transfer trajectories where the propellant consumption is minimal. As already derived from Tsiolkowski's law in chapter 3, the minimal propellant consumption requires that the value for the ΔV has to be minimal. These transfer orbits are defined by an elliptical orbit (figure 4.2) that touches the initial circular orbit at pericentre and touches the final circular orbit at apocentre. It is assumed that both circular orbits are coplanar. A coplanar problem assumption is a realistic assumption, because the

difference between inclinations of the Solar System planets is significantly small, with the exception of Mercury and Pluto (7° and 17.14°, respectively). Both impulse velocity vectors, $\Delta \overline{V}_1$ and $\Delta \overline{V}_2$, are tangential to the initial and final orbit, respectively. It is important to mention that these impulsive shots change the velocity of the spacecraft instantaneously, leaving the position of the spacecraft at that instant unchanged. The circular velocities of the initial and final orbits, V_{c1} and V_{c2} , are given by $\sqrt{\mu/r}$ where r parameter is substituted by r_1 and r_2 , respectively.

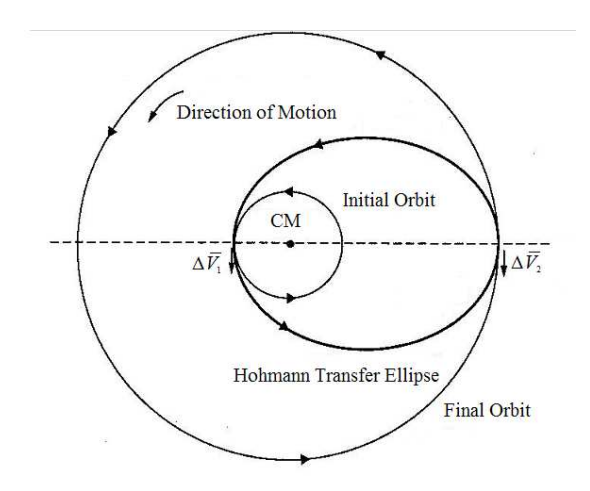


Figure 4.2: Hohmann Transfer Orbit [Wertz, 2001]

The Hohmann transfer orbit is considered when parameters γ_1 and γ_2 are zero. In this situation, the TOF can be computed through [Wakker, 2005II]:

$$TOF_{_{_{\mathit{H}}}} = \pi \sqrt{\frac{a^3}{\mu}} \tag{4.8}$$

4.2. Planetocentric Phases

Consider a spacecraft moving in a circular parking orbit around a certain planet. An impulsive shot, using chemical propulsion will be performed and the spacecraft will escape the gravity field of this planet and continue to move in a hyperbolic orbit. This impulsive shot is most efficient if it is implemented tangentially to the parking orbit and where the

orbital velocity is maximum [Cornelisse et al., 1979]. The velocity change is given by [Cornelisse et al., 1979]:

$$\Delta V_{1} = V_{1_{hyperbolic}} - V_{1_{circular}} = \sqrt{\frac{2\mu_{d}}{r_{c_{1}}} + V_{\infty_{1}}^{2}} - \sqrt{\frac{\mu_{d}}{r_{c_{1}}}}$$
(4.9)

In the same way, the impulsive shot needed to decrease the spacecraft's hyperbolic velocity to the target circular velocity is given by [Cornelisse et al., 1979]:

$$\Delta V_2 = V_{2_{hyperbolic}} - V_{2_{circular}} = \sqrt{\frac{2\mu_t}{r_{c_2}} + V_{\infty_2}^2} - \sqrt{\frac{\mu_t}{r_{c_2}}}$$
(4.10)

The excess hyperbolic velocities are computed using equations (4.7). Finally, the total impulsive shot ΔV_T can be computed by adding ΔV_1 and ΔV_2 :

$$\Delta V_T = \Delta V_1 + \Delta V_2 \tag{4.11}$$

In table 4.1, values for the time of flight (TOF), the hyperbolic velocities V_1 and V_2 as well as the hyperbolic excess velocities V_{∞_1} and V_{∞_2} are presented for the Hohmann transfer orbit. The impulse velocities ΔV_1 and ΔV_2 are also represented and they were computed at 1.1 radius distance from the planet (i.e., the vehicle starts and ends up in a circular parking orbit at an altitude of $0.1 \cdot r_{planet}$). These values are listed for the Earth as the departure planet.

Target	V_1	$V_{\scriptscriptstyle{\infty_{_{\!\scriptscriptstyle{1}}}}}*$	V_{t}	V_2	$V_{_{\infty_2}}$	ΔV_1	ΔV_2	$\Delta V_{\scriptscriptstyle T}$	TOF
Body	[km/s]	[km/s]	[km/s]	[km/s]	[km/s]	[km/s]	[km/s]	[km/s]	[years]
Mercury	22.25	-7.53	47.87	57.49	9.61	5.52	7.57	13.08	0.289
Venus	27.29	-2.50	35.02	37.73	2.71	3.41	3.26	6.67	0.400
Mars	32.73	2.95	24.13	21.48	-2.65	3.52	2.09	5.61	0.709
Jupiter	38.58	8.79	13.06	7.41	-5.64	6.28	16.91	23.19	2.733
Saturn	40.07	10.29	9.65	4.20	-5.44	7.28	10.34	17.62	6.051
Uranus	41.07	11.28	6.80	2.14	-4.66	7.98	6.48	14.46	16.050
Neptune	41.44	11.65	5.43	1.38	-4.05	8.26	6.93	15.18	30.635
Pluto	41.60	11.81	4.74	1.05	-3.69	8.38	3.05	11.42	45.563
Escape from the Solar System	42.12	12.34	-	0	-	8.77	0	8.75	-

Table 4.1: The TOF and the total impulse velocities at the departure planet and at the target planet with the Earth as departure planet (1.1 radius distance from the planet). * the velocity of the Earth is considered circular and equal to 29.79 km/s [Cornelisse et al., 1979]

From table 4.1, the values of the TOF are large, so other transfer orbits may be considered. Nevertheless, the Hohmann transfer orbit offers the yardstick for the minimum total impulsive velocity required in a transfer trajectory.

5. Low-Thrust Trajectories

In chapter 4, interplanetary missions were analysed using a coasting phase in the heliocentric phase characterized by a Keplerian orbit. In this chapter a more complicated trajectory will be studied, involving low-thrust propulsion during the heliocentric phase. High-thrust propulsion is still needed to escape the departure planet, because otherwise, the mission would take too long just to leave the sphere of influence of the planet. In this way, as already mentioned in chapter 4, the spacecraft will be launched into a circular parking orbit and it will escape from the departure planet using high-thrust propulsion. In table 5.1, four different types of transfer orbits are shown.

Transfer Type	Orbit Type	Typical Acceleration	ΔV	Typical transfer time
High Energy	Elliptical or hyperbolic	10g	Higher than Hohmann's	lower than the Hohmann's transfer period
Hohmann - minimum energy, high thrust	Hohmann transfer	1 to 5g	Equations 4.9 4.10	Equation 4.8
Low Thrust Chemical	Hohmann transfer segments	0.02 to 0.5g	Same as Hohmann	6 to 8 times the Hohmann's period
Electric propulsion	Spiral transfer	0.0001 to 0.001g	Difference between velocities at the final orbit and at the initial orbit	

Table 5.1: Four different types of transfer orbits [Wertz, 2001]

In a mission from one celestial body to another, the spacecraft is unlikely to thrust the entire period of time. In interplanetary flights, coasting periods are usually switched with thrusting periods. However, only low-thrust trajectories using continuous thrust will be discussed in this chapter.

In the past, the conical sections were considered to be the most suitable analytical representation for the motion of spacecraft. More recently, a shape-based study was made in order to find the best analytical representation for low-thrust trajectories. The exponential sinusoid was introduced as a shape capable of representing these trajectories in [Petropoulos et al., 1999]. This shape was further studied by Izzo [Izzo, 2006] who used a different approach in order to obtain an exponential sinusoid that respects the initial and final positions and time of flight (TOF) specified by the user. In order to implement this kind of shape-based method, the mathematical function that describes the trajectory of the spacecraft – e.g. exponential sinusoid used by Petropoulos and Izzo - will have to be defined. From this mathematical expression, the equations for the thrust acceleration, the thrust angle, the radial and tangential velocities can be derived using the equations of motion of a spacecraft. For a certain exponential sinusoid and giving the TOF and initial and final positions of the thrust arc as input, the values for the total excess velocity and the fuel mass consumption during the heliocentric phase can be computed.

In section 5.1, basic notions of low-thrust trajectories are addressed. In section 5.2 and 5.3, the geometric and the dynamic properties regarding a low-thrust problem using the exponential sinusoid shape will be given for a general case and for the tangential case, respectively. Also in this chapter, two approaches, one done by [Petropoulos and Longuski, 2004] and another done by [Izzo, 2006] to compute the position, the velocity and the acceleration of the spacecraft with time will be discussed in sections 5.4 and 5.5, respectively.

5.1. Basic Equations of Motion for Low-Thrust Trajectories

Equation (1.1) describes the motion of a spacecraft under the influence of the gravity field of the main body. In low-thrust trajectories another force has to be taken into account [Wakker, 2005II]:

$$\frac{\ddot{r}}{r} = -\frac{\mu}{r^3} \overline{r} + \overline{a} \tag{5.1}$$

Parameter \bar{a} is the thrust acceleration vector. The instantaneous rate of change of the specific total energy can be computed by multiplying equation (5.1) by the velocity of the spacecraft \bar{V} [Wakker, 2005II]:

$$\frac{d\varepsilon}{dt} = \overline{V} \cdot \overline{a} \tag{5.2}$$

The rate of change of the total orbital energy in equation (5.2) reaches a maximum value if the thrust vector is tangential to the trajectory – tangential steering. However, from equation (5.2), it should not be concluded that the tangential thrust profile is the optimum one since the minimal total propellant consumption is not necessarily associated with constant instantaneous maximal rate of change of the total orbital energy [Wakker, 2005II]. In fact, the computation of the optimal thrust profile is a difficult topic. The optimal thrust profile will depend on the planets that are being considered for the flight, the mass of the spacecraft, the thrust magnitude, among others. However, from all steering programs that can be considered, the radial thrusting case cannot be considered an attractive thrust profile. Compared with the tangential thrust profile, it yields longer flight times and higher propellant consumption in an interplanetary mission [Wakker, 2005II].

5.2. Exponential Sinusoid – Geometry and Dynamics

In this section, the geometric and dynamic properties of the exponential sinusoid in terms of representation for low-thrust trajectories already made in [Petropoulos and Longuski, 2004] will be presented. The radius equation of the exponential sinusoid is given by:

$$r = k_0 e^{q\theta + k_1 \sin(k_2\theta + \phi)} \tag{5.3}$$

Using this representation, a large variety of shapes can be drawn and some examples are represented in figure 5.1.

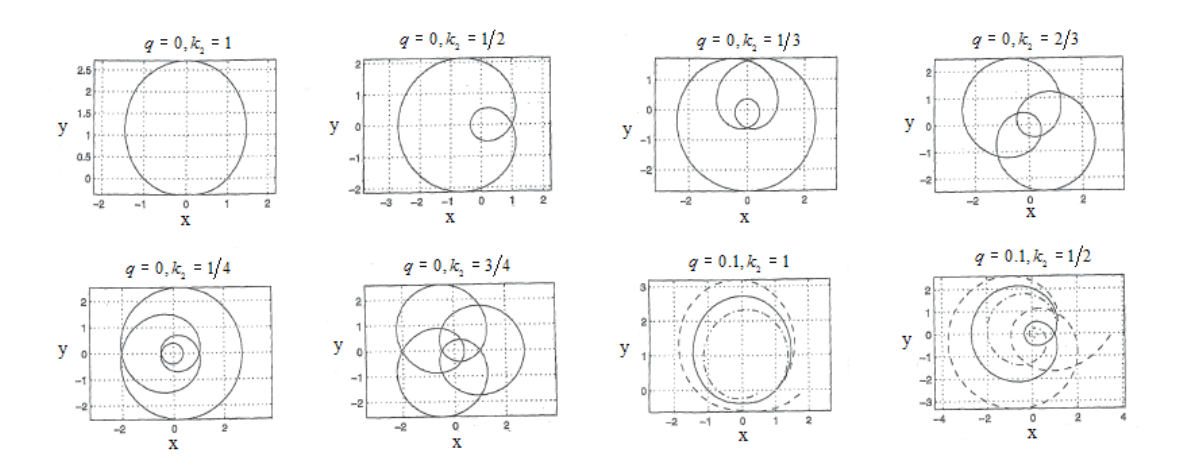


Figure 5.1: Shapes that can be represented by an exponential sinusoid [Petropoulos et al., 1999]

The use of five constant parameters $(k_0, k_1, k_2, q \text{ and } \phi)$ allows a considerably flexibility in the geometry described by equation (5.3). Each parameter has a different impact on the shape of the exponential sinusoid. Parameter q denotes the difference between a pure exponential sinusoid (q=0) and a more flexible one $(q \neq 0)$. Parameter ϕ is called the phase angle and it controls the orientation of the exponential sinusoid in the plane. The quantity k_0 is the scaling factor and it controls the absolute range of the pericentre and the apocentre. Parameter k_1 is called the dynamic range and it controls the ratio between the apocentre and the pericentre distance. Assuming q=0, this ratio can be deduced through equation (5.3) and it is given by: $r_a/r_p = e^{2k_1}$. Finally, the quantity k_2 is the winding parameter and it is associated with the number of revolutions of the spiral: the smaller k_2 , the more revolutions the spacecraft will perform from the pericentre to the apocentre and vice-versa. The number of revolutions (it can also be a fraction of a revolution) from the pericentre to the apocentre can be deduced from equation (5.3) and it is given by:

$$N_{n2a} = 1/(2k_2) \tag{5.4}$$

Two examples of the effect of the winding parameter k_2 are represented in figure 5.2. Note that when k_1 is large, i.e., when the ratio between the apocentre and the pericentre is large, the parameter k_2 is usually small, because many revolutions are necessary to reach the

apocentre. On the other hand, when k_2 is large (few or none complete revolutions), parameter k_1 must be small, since the dynamic range is also small.

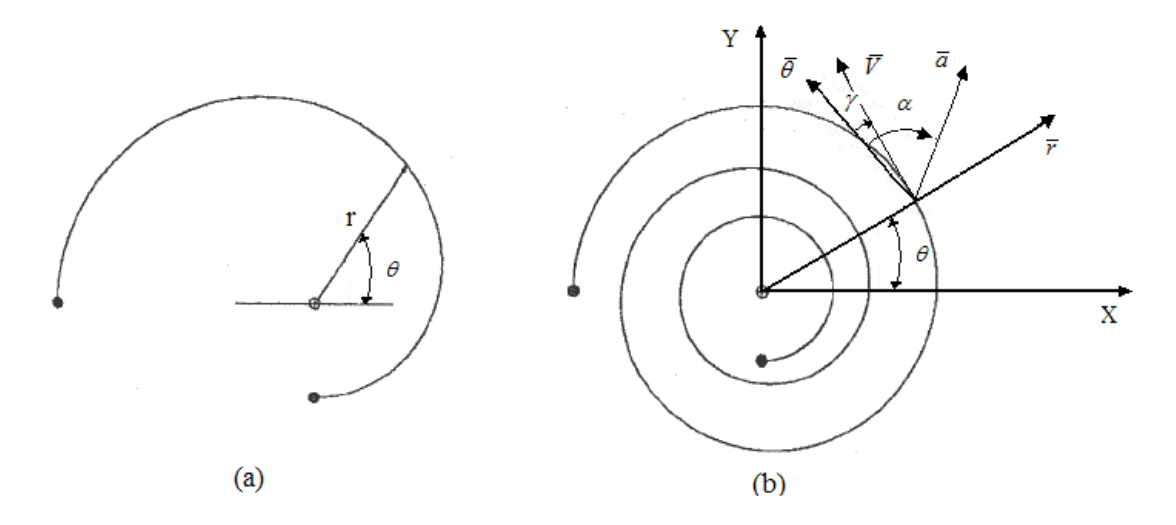


Figure 5.2: Example of exponential sinusoid shapes from pericentre to apocentre using $k_1 = 0.5$ and (a) $k_2 = 2/3$ and (b) $k_2 = 2/11$ [Petropoulos and Longuski, 2004]

Now, this shape will be applied to the equations of motion of a spacecraft that are expressed in the radial and tangential direction, respectively by [Petropoulos et al, 1999]:

$$\begin{cases} \ddot{r} - r\dot{\theta}^2 + \frac{\mu}{r^2} = a\sin\alpha \\ \frac{1}{r}\frac{d}{dt}(r^2\dot{\theta}) = a\cos\alpha \Leftrightarrow 2\dot{r}\dot{\theta} + r\ddot{\theta} = a\cos\alpha \end{cases}$$
 (5.5)

The first and second time-derivatives of r, \dot{r} and \ddot{r} , are given by:

$$\dot{r} = \dot{\theta} (q + k_1 k_2 c) r
\ddot{r} = (\ddot{\theta} (q + k_1 k_2 c) + \dot{\theta}^2 (q + k_1 k_2 c)^2 - \dot{\theta}^2 k_1 k_2^2 s) r$$
(5.6)

Variables s and c stand for $\sin(k_2\theta + \phi)$ and $\cos(k_2\theta + \phi)$, respectively. In equation (5.5), the magnitude of the thrust acceleration a was already introduced in section 5.1 in equation (5.1), while α is the thrust angle. These two parameters are represented in figure

5.2b. The flight path angle γ is also represented in figure 5.2(b) and it is defined using the first equation in (5.6), by:

$$\tan \gamma = \frac{dr/dt}{rd\theta/dt} = q + k_1 k_2 c \tag{5.7}$$

At this point five equations ((5.3), (5.5) and (5.6)) with seven unknowns $(r, \dot{r}, \ddot{r}, \dot{\theta}, \ddot{\theta}, a, \alpha)$ are presented, with θ or t as independent variables. So, two more equations are needed to make the system determinable. Using the four equations in (5.5) and (5.6) already described, the equation for the rate of the polar angle $\dot{\theta}$ can be calculated through [Petropoulos et al., 1999]:

$$\dot{\theta}^2 = \left(\frac{\mu}{r^3}\right) \frac{a_0 \cos \alpha \tan \gamma - a_0 \sin \alpha + 1}{\tan^2 \gamma + k_1 k_2^2 s + 1} \tag{5.8}$$

All the derivation steps used in this expression are done in appendix A. Note that equation (5.8) allows retrograde motion by taking the negative square root of the right-hand side to obtain $\dot{\theta} < 0$. However, for purposes of convenience in discussion, only the prograde motion will be examined here. Parameter a_0 is the thrust acceleration normalised by the local gravitational acceleration:

$$a_0 = a \frac{r^2}{\mu} \tag{5.9}$$

Assuming a constant value for a_0 , the magnitude of the thrust acceleration a will decrease monotonically with $1/r^2$. This is a good approximation for significant parts of the trajectory when solar-powered propulsion systems are used [Petropoulos et al., 2004].

Knowing $\dot{\theta}$ through equation (5.8), the expressions for the radial velocity and the tangential velocity can be derived:

$$V_{r} = \dot{r} = \dot{\theta} \left(q + k_{1} k_{2} c \right) r$$

$$V_{\theta} = r \dot{\theta} = r \sqrt{\left(\frac{\mu}{r^{3}} \right) \frac{a_{0} \cos \alpha \tan \gamma - a_{0} \sin \alpha + 1}{\tan^{2} \gamma + k_{1} k_{2}^{2} s + 1}}$$
(5.10)

Note that it is only possible to calculate $\dot{\theta}$ if parameters α , a_0 and r are known. The thrust angle α can be computed by integrating the following equation for $\dot{\alpha}$ [Petropoulos et al., 1999]:

$$\dot{\alpha} = \left\{ \left(\tan \gamma \dot{\theta}^2 r^3 / \mu - 2a_0 \cos \alpha \right) \left(\tan^2 \gamma + k_1 k_2^2 s + 1 \right)^2 - \right. \\
\left. - \left(a_0 \cos \alpha \tan \gamma - a_0 \sin \alpha + 1 \right) \left(k_1 k_2^3 c - 2 \tan \gamma k_1 k_2^2 s \right) \\
\left. - a_0 k_1 k_2^2 s \cos \alpha \left(\tan^2 \gamma + k_1 k_2^2 s + 1 \right) \right\} \dot{\theta} / \left(\left(a_0 \sin \alpha \tan \gamma + a_0 \cos \alpha \right) \left(\tan^2 \gamma + k_1 k_2^2 s + 1 \right) \right)$$
(5.11)

Equation (5.11) is derived in appendix A. Note that the expressions for $\dot{\theta}$ and $\dot{\alpha}$ are coupled, intractable, first-order differential equations. For this reason, numerical integration is necessary to find values for θ and α , and consequently to determine the position and the velocity of the spacecraft. Finally, the TOF can be computed by integrating equation (5.8):

$$TOF = \int_{\theta_i}^{\theta_f} \frac{1}{\dot{\theta}} d\theta = \int_{\theta_i}^{\theta_f} \left(\left(\frac{\mu}{r^3} \right) \frac{a_0 \cos \alpha \tan \gamma - a_0 \sin \alpha + 1}{\tan^2 \gamma + k_1 k_2^2 s + 1} \right)^{-\frac{1}{2}} d\theta$$
 (5.12)

In equation (5.12), parameter θ_i is the initial polar angle and parameter θ_f is the final polar angle for the thrust arc.

5.3. Exponential Sinusoid using Tangential Thrust

In order to avoid numerical integration that is required to find θ and α (as mentioned in the end of section 5.2), a special case of thrusting is assumed: the tangential thrust profile, allowing simplifications in equation (5.8). The thrust vector can be along or against the velocity vector ($\alpha = \gamma + n\pi$, with n = 0,1, respectively). In this special case, due to

simplifications in equation (5.8), the dynamic parameter a_0 can be analytically computed. Parameters a_0 and $\dot{\theta}^2$ are given by [Petropoulos and Longuski, 2004]:

$$\dot{\theta}^2 = \left(\frac{\mu}{r^3}\right) \frac{1}{\tan^2 \gamma + k_1 k_2^2 s + 1} \tag{5.13}$$

$$a_0 = \frac{\left(-1\right)^n \tan \gamma}{2 \cos \gamma} \left[\frac{1}{\tan^2 \gamma + k_1 k_2^2 s + 1} - \frac{k_2^2 \left(1 - 2k_1 s\right)}{\left(\tan^2 \gamma + k_1 k_2^2 s + 1\right)^2} \right]$$
 (5.14)

Finally, the expression for the TOF can be simplified and it is given by:

$$TOF = \int_{\theta_i}^{\theta_f} \sqrt{r^3 \left(\tan^2 \gamma + k_1 k_2^2 s + 1\right) / \mu} \ d\theta$$
 (5.15)

As for the equations in section 5.2, both equations (5.13) and (5.14) are derived in appendix A. From these equations, the rate of the polar angle $\dot{\theta}$, the normalised thrust acceleration a_0 and consequently the radial and tangential velocities are calculated as a function of the polar angle θ only (the geometric parameters are constant, the flight path angle and r depend only on the geometric parameters and on θ (equations (5.7) and (5.3))). As equation (5.8), equation (5.13) allows a retrograde motion by taking the negative square root of the right hand-side, obtaining $\dot{\theta} < 0$.

Note that $\dot{\theta}^2$ can become negative when the denominator $\tan^2 \gamma + k_1 k_2^2 s + 1 < 0$ (equation (5.13)). Also, equation (5.13) for $\dot{\theta}^2$ and equation (5.14) for the normalised thrust acceleration a_0 can present singularities when the denominator $\tan^2 \gamma + k_1 k_2^2 s + 1$ becomes zero. Considering parameters k_1 and k_2 positive, this situation will happen when $k_1 k_2^2$ approaches unity from below, at the pericentre where s=-1 (considering $k_2\theta + \phi = -\pi/2$ and q=0). From equation (5.13), it should be noticed that $\dot{\theta}^2$ can be less than zero for $k_1 k_2^2 > 1$ in regions near the pericentre of the trajectory. In these situations, it is not possible to represent low-thrust trajectories using the exponential sinusoid with a tangential thrust profile [Petropoulos and Longuski, 2004], i.e. the physical problem cannot be satisfied

using this specific shape and this thrust profile combined. In this way, in order to avoid singularities around the pericentre and situations where $\dot{\theta}^2$ is negative, the following condition shall be respected [Petropoulos and Longuski, 2004]:

$$1 - k_1 k_2^2 > 0 ag{5.16}$$

The condition described in equation (5.16) ensures that the denominator of equation (5.13) is always positive. For practical purposes, upper limits of 2 and 1 were chosen for the geometric parameters k_1 and k_2 , respectively, since the thrust levels become unreasonably high when $1-k_1k_2^2$ approaches zero [Petropoulos and Longuski, 2004]. Note that the condition in equation (5.16) should always be respected: when k_1 is large (the apocentre is much greater than the pericentre – large dynamic range), k_2 must be small, i.e., many revolutions around the central body are required between the pericentre and the apocentre. In opposition, when k_1 is small (apocentre is not much greater than the pericentre), k_2 must be large (not many revolutions are required). Considering $k_2 = 0.01$, the spacecraft is allowed to spiral up to 50 revolutions around the Sun between the pericentre and the apocentre (equation (5.4)). This number of revolutions is untenably high to be considered in a real mission (due to TOF), therefore there is no reason to choose values of k_2 lower than 0.01. By changing parameter k_2 , a velocity analysis through a comparison between the exponential sinusoid velocity and the local circular velocity can be made. For a many revolution case (small k_2), the exponential sinusoid velocity is not much different from the local circular velocity, specially in the apocentre and in the pericentre. In this case, a launch from, or a rendezvous at, will be most efficient in these regions. On the other hand, the exponential sinusoid velocity is significantly non-circular for large values of k_2 , a situation that favours gravity-assist.

From the analysis done in this section, although condition (5.16) is required, the exponential sinusoid (tangential thrust profile) can be used as an analytical representation for low-thrust trajectories. Given the TOF and the initial and final conditions at the departure and target planets, respectively, there should be an exponential sinusoid,

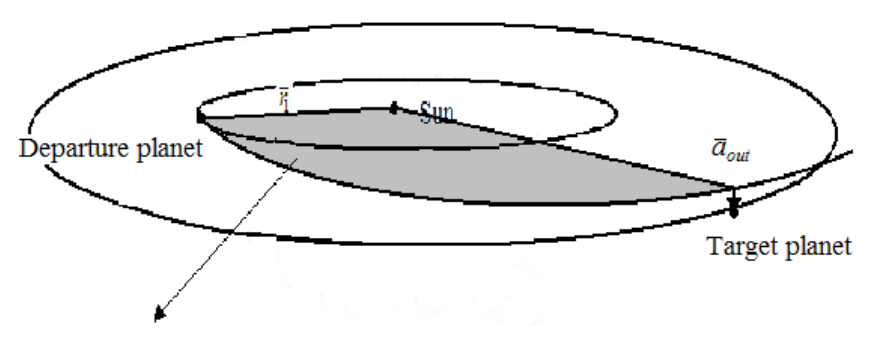
characterized by the geometric parameters k_0 , k_1 , k_2 , q and ϕ that respect these initial inputs. In the following two sections 5.4 and 5.5, two different studies in how to find feasible exponential sinusoids will be discussed. The first procedure that will be described (section 5.4) is the one used in [Petropoulos and Longuski, 2004], while the second is the one used in [Izzo, 2006] (section 5.5).

5.4. Procedure done by Petropoulos¹ and Longuski²

Consider the situation where the spacecraft's trajectory follows an exponential sinusoid shape with a tangential thrust. The reference plane in which the motion of the spacecraft occurs is called the low-thrust reference plane and it is normal to the spacecraft's initial angular momentum vector. In a two-dimensional problem, this plane is the same as the orbital plane of the initial and final planets. However, in a three-dimensional problem, since the angular momentum direction at the initial planet is different from the one at the arrival planet (i.e., the target orbital plane does not lie exactly in the same plane as the initial planet) and exponential sinusoids are pure planar shapes, the trajectory of the spacecraft will only be able to intersect the projection of the target's orbit onto the low-thrust reference plane (figure 5.3). The motion of the spacecraft in the low-thrust reference plane that is assumed to follow the exponential sinusoid is called the in-plane motion and it will be discussed in section 5.4.1. In addition, the spacecraft will need an additional force acting along or against the spacecraft's angular momentum \overline{a}_{out} in order to meet the target's orbit (section 5.4.2) (see figure 5.3).

¹Senior member of the Engineering Staff, Navigation and Mission Design section, Jet Propulsion Laboratory

² Professor, Purdue University, associate fellow AAIA



Low-thrust reference plane

Figure 5.3: Representation of the low-thrust reference plane and the out-of-plane additional force \overline{a}_{out}

5.4.1. In-Plane Motion

In this section, the two-dimensional motion of the spacecraft that follows the exponential sinusoid will be analysed. The equations for parameters $\dot{\theta}^2$, a_0 and the TOF were already presented in section 5.3 in equations (5.13), (5.14) and (5.15), respectively. The condition in equation (5.16) should be respected to avoid singularities around the pericentre and to avoid $\dot{\theta}^2 < 0$. After a brief analysis of the geometric parameters k_1 and k_2 in the end of section 5.3, the interval of available values for k_2 can be determined. In cases where the outbound targets are considered, the minimum projected radius r_{\min} is higher than the current radius r_B (q = 0), the range of k_2 values is limited to [Petropoulos and Longuski, 2004]:

$$k_2^2 \le \frac{\tan^2 \gamma - 2k_{12s} \ln \left(r_{\min}/r_B\right)}{\left(\ln \left(r_{\min}/r_B\right)\right)^2} \tag{5.17}$$

In cases of inbound targets, where the maximum projected radius r_{max} is less than the current radius, the condition for k_2 is [Petropoulos and Longuski, 2004]:

$$k_2^2 \le \frac{\tan^2 \gamma + 2k_{12s} \ln (r_B/r_{\text{max}})}{\left(\ln (r_B/r_{\text{max}})\right)^2}$$
(5.18)

These two equations are derived in appendix A. It may happen that the right-hand side of equations (5.17) and (5.18) is negative and in these cases, the target cannot be reached using the exponential sinusoid. Note that the parameter k_2 continues to depend on the limits for k_1 and on condition (5.16). For specific initial and final conditions, there is only one k_2 value that corresponds to the TOF that was given as an input. An analytic process to find this specific value for k_2 is not available and the only way is to step through the range of k_2 values and at each step compute the intersection point with the target projected orbit. The TOF is calculated through equation (5.15).

In [Petropoulos and Longuski, 2004], the intersection points were found using a numerical root-finding technique. A step-size and step-direction-controlled Newton method was applied, with the goal of putting to zero the following expression:

$$d_i(\theta) = 1/r_i(\theta_{t=TOF}) - 1/r(\theta_{t=TOF})$$
(5.19)

The target's orbit is assumed to be conic and it has to be projected onto the low-thrust reference plane. The parameter r_i is the projected radius for the target planet and r and θ are the position of the spacecraft and the polar angle, respectively in the low-thrust reference plane. It should be noticed that the inverse radius is applied to simplify the equation for the derivative required by the Newton method. The advantage is having faster computations.

Now knowing the geometric parameters of the exponential sinusoid that yield the necessary TOF, it is possible to compute the amount of propellant used during the low-thrust flight and also the amount of propellant necessary for the initial and the final chemical impulsive shots at the departure and arrival planets, respectively. The computation of fuel consumptions will be explained later in chapter 8.

5.4.2. Out-of-Plane Motion

As already mentioned before in chapter 4, celestial bodies in the Solar System orbit around the Sun with different inclinations with respect to the ecliptic plane. In this section, a method will be discussed to match the final position of the spacecraft with the target's orbit. To reach the out-of-plane position of a target (see figure 5.3) with respect to an inplane encounter at the same instant, an additional force is necessary [Petropoulos and Longuski, 2000]:

$$a_{out} = a_{0,out} \frac{\mu}{r^2} \tag{5.20}$$

As for the thrust acceleration a, a_{out} also varies with $1/r^2$, meaning that it decreases according to the amount of solar energy available at a certain distance from the Sun. The in-plane components of the angular momentum, h_x and h_y act according to [Petropoulos and Longuski, 2000]:

$$\frac{dh_x}{d\theta} \approx \frac{ra_{out}\sin\theta}{\dot{\theta}}$$

$$\frac{dh_y}{d\theta} \approx -\frac{ra_{out}\cos\theta}{\dot{\theta}}$$
(5.21)

The expressions (5.21) were derived under the assumption that the out-of-plane thrust acceleration is considerably smaller than the gravitational acceleration from the main body, which is the Sun. In equations (5.21), the X-direction is considered to be along the line $\theta = 0$. Because the angular momentum components remain significantly small, the total angular momentum is assumed to be equal to the out-of-plane component $r^2\dot{\theta}$, as if a_{out} was equal to zero. This means that the position vector of the spacecraft and the angular momentum and also the velocity vector and the angular momentum are assumed to be perpendicular, respectively:

$$\overline{r} \cdot \overline{h} \approx 0 \text{ and } \overline{V} \cdot \overline{h} \approx 0$$
 (5.22)

Figure 5.4(a) illustrates the position of a spacecraft in an out-of-plane case. Using figure 5.4(a) and the relations described in equation (5.22), the out-of-plane angle ϕ_{out} and the velocity V_z that is normal to the plane are respectively given by:

$$\tan \phi_{out} \approx \frac{r_z}{r} = -\frac{r_x h_x + r_y h_y}{r \cdot h_z} \Leftrightarrow \tan \phi_{out} \approx -\frac{\cos \theta h_x + \sin \theta h_y}{r^2 \dot{\theta}}$$
 (5.23)

$$V_z \approx \frac{-\left(V_x h_x + V_y h_y\right)}{h_z} \approx \frac{h_x \left(\sin \theta - \tan \gamma \cos \theta\right) - h_y \left(\cos \theta + \tan \gamma \sin \theta\right)}{r}$$
(5.24)

The velocities in X- and Y-direction are derived from figure 5.4(b):

$$V_{x} = -r\dot{\theta}\sin\theta + \dot{r}\cos\theta = (-\sin\theta + \tan\gamma\cos\theta)r\dot{\theta}$$

$$V_{y} = r\dot{\theta}\cos\theta + \dot{r}\sin\theta = (\cos\theta + \tan\gamma\sin\theta)r\dot{\theta}$$
(5.25)

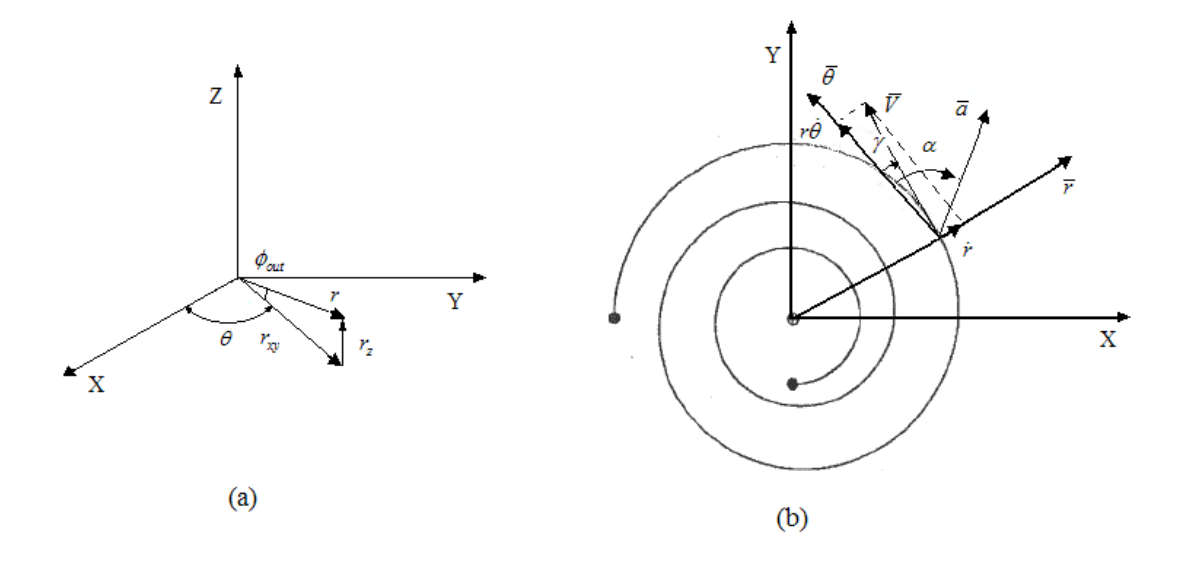


Figure 5.4: (a) Position of the spacecraft in the out-of plane motion, (b) velocity vector in the XY-plane

The out-of-plane angle ϕ_{out} and the velocity V_z at the end of an out-of-plane thrust motion from θ_i to θ_f , are defined by [Petropoulos and Longuski, 2000]:

$$\tan \phi_{out} \approx \frac{a_{0,out} \mu}{r_f^2 \dot{\theta}_f} \left(I_y \sin \theta_f - I_x \cos \theta_f \right)$$
 (5.26)

$$V_z \approx \frac{a_{0,out}\mu}{r_f} \left(I_x \left(\sin \theta_f - \tan \gamma \cos \theta_f \right) + I_y \left(\cos \theta_f + \tan \gamma \sin \theta_f \right) \right)$$
 (5.27)

The quantities I_x and I_y in equations (5.26) and (5.27) are defined as:

$$I_{x} = \int_{\theta_{0}}^{\theta_{f}} \frac{\sin \theta}{r\dot{\theta}} d\theta$$

$$I_{y} = \int_{\theta_{0}}^{\theta_{f}} \frac{\cos \theta}{r\dot{\theta}} d\theta$$
(5.28)

These integrals described in equations (5.28) can be determined numerically. Through equation (5.26) and knowing the out-of-plane angle ϕ_{out} , $a_{0,out}$ can be computed at each integration step. Afterwards, the out-of-plane velocity V_z can be calculated through equation (5.27).

It should be noticed that the effect of the out-of-plane motion on the TOF was neglected. The method described does not take into account the use of the most satisfactory thrust profile. Therefore, little consideration should be given to the out-of-plane thrust and associated propellant value. According to [Petropoulos and Longuski, 2000], this method allows fast computations and it is increasingly accurate for smaller out-of-plane excursions. Note that these analytical solutions only provide a starting point for full numerical optimisations.

5.5. Procedure done by Izzo³

Although quite successful from a numerical point of view, Petropoulos and Logunski's work lacks of a generic discussion on the possibility of using the exponential sinusoid to travel from a generic point P_1 to another point P_2 , given a certain TOF as an input [Izzo,

³ Research Fellow, Advanced Concepts Team, European Space Research and Technology centre, The Netherlands

2006]. Izzo uses the same equations for the parameters $\dot{\theta}$ and a_0 (equations (5.13) and (5.14)). However, instead of using a numerical root-finding technique to find intersection points, followed by a step-size- and step-direction-controlled to match the target's orbit with the spacecraft's trajectory (exponential sinusoid), a multi-revolution Lambert's problem for exponential sinusoids using tangential thrusting is introduced. This new procedure will be discussed below.

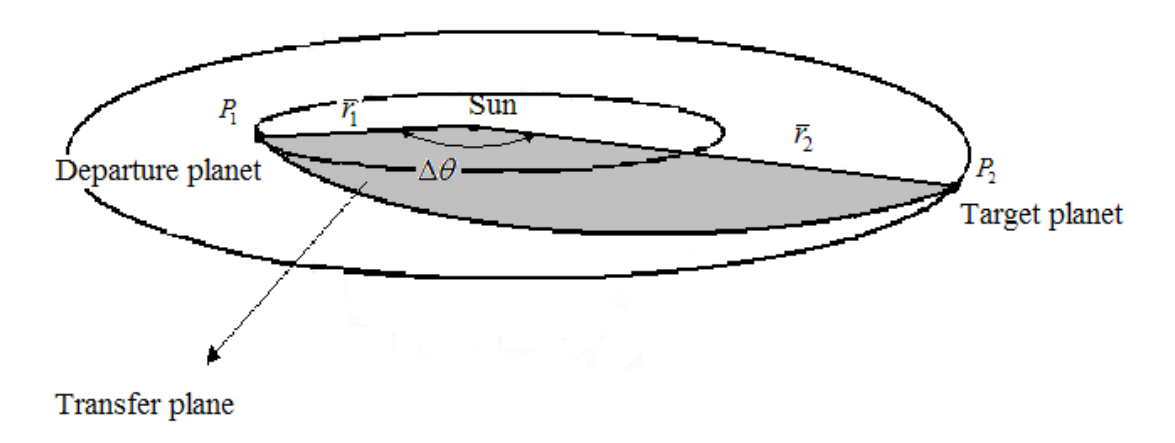


Figure 5.5: Representation of the transfer plane

Given the initial and final radii r_1 and r_2 , i.e., the distances of the departure and arrival planets from the Sun, respectively, and the transfer angle $\Delta\theta$ (see figure 5.5), it is possible to find all the exponential sinusoids, defined by equation (5.3) that link the two positions for a given TOF, allowing multiple complete revolutions. In order to force the exponential sinusoid to pass by point P_1 and point P_2 , the following geometric equations have to be satisfied:

$$r_1 = r(\theta_i) = k_0 \exp(k_1 \sin(k_2 \theta_i + \phi))$$

$$r_2 = r(\theta_f) = k_0 \exp(k_1 \sin(k_2 \theta_f + \phi))$$
(5.29)

Parameter θ_i is the initial polar angle and the final polar angle is given by: $\theta_f = \theta_i + \Delta\theta + 2\pi N$, where N is the number of complete revolutions performed before the

spacecraft arrives at point P_2 . Since the number of geometric parameters is always higher than two, these two equations are not enough to determine the position of the spacecraft.

Note that the transfer plane where the spacecraft moves (figure 5.5) is defined by two vectors: $\overline{r_1}$ and $\overline{r_2}$ (from the Sun to the departure and arrival planets, respectively) and it differs from the low-thrust reference plane (section 5.4).

As already mentioned in section 5.2, the geometric parameters considered in the exponential sinusoid are k_0 , k_1 , k_2 , q and ϕ . In order to simplify the mathematical expression of the exponential sinusoid, a zero value was assumed for q. So, instead of five unknown geometric parameters, there are four. The search space can be further reduced by assuming the parameter k_2 fixed and given as an input. Therefore, all exponential sinusoids will be studied for a fixed value of k_2 and three free parameters k_0 , k_1 and ϕ . Finally, considering θ_i zero degrees, the geometric parameter k_1 can be computed through [Izzo,2006]:

$$k_1^2 = \left(\frac{\ln(r_1/r_2) + (\tan\gamma_1/k_2)\sin(k_2\theta_f)}{1 - \cos(k_2\theta_f)}\right)^2 + \frac{\tan^2\gamma_1}{k_2^2}$$
 (5.30)

The parameter γ_1 is the flight path angle at the starting point of the thrust arc. Equation (5.30) is derived in appendix A. The sign of k_1 is known from the following expression [Izzo,2006]:

$$\operatorname{sign}(k_{1}) = \operatorname{sign}\left(|k_{1}| \frac{\ln(r_{1}/r_{2}) + (\tan\gamma_{1}/k_{2})\sin(k_{2}\theta_{f})}{1 - \cos(k_{2}\theta_{f})} \left(k_{1}^{2} - \frac{\tan^{2}\gamma_{1}}{k_{2}^{2}}\right)^{-0.5}\right)$$
(5.31)

Since the assumption $\theta_i = 0^{\circ}$ was made, the phase angle ϕ (using equation (5.7)) is given by:

$$\tan \gamma_1 = k_1 k_2 \cos \phi \Leftrightarrow \phi = \arccos\left(\frac{\tan \gamma_1}{k_1 k_2}\right)$$
 (5.32)

Finally, the geometric parameter k_0 will be calculated through one of the following geometric equations:

$$r_{1} = k_{0} \exp(k_{1} \sin \phi) \Leftrightarrow k_{0} = r_{1} / \exp(k_{1} \sin \phi)$$

$$r_{2} = k_{0} \exp(k_{1} \sin(k_{2}\theta_{f} + \phi)) \Leftrightarrow k_{0} = r_{1} / \exp(k_{1} \sin(k_{2}\theta_{f} + \phi))$$
(5.33)

Note that from equation (5.32), the angle ϕ is always considered in the first two quadrants, since considering the other two quadrants, it will only return the same exponential sinusoid. The assumption regarding the initial polar angle θ_i was necessary in order to find analytical expressions for k_1 and ϕ that were not correlated.

In order to compute the exponential sinusoid, parameters γ_1 and k_2 are required. As already said before, the geometric parameter k_2 is fixed, but the initial flight path angle γ_1 is considered a free parameter and the interval of values available can be calculated using the constraint equation (section 5.3) already discussed in [Petropoulos and Longuski, 2004], when tangential thrust is assumed:

$$k_1 k_2^2 < 1$$

This condition can be rewritten in terms of $\tan \gamma_1$ [Izzo, 2006]:

$$\tan \gamma_1 \in \left(\tan \gamma_{1,m}, \tan \gamma_{1,M}\right) \tag{5.34}$$

$$\tan \gamma_{l_{m,M}} = \frac{k_2}{2} \left[-\ln \left(\frac{r_1}{r_2} \right) \cot \frac{k_2 \theta_f}{2} \pm \sqrt{\Delta} \right], \text{ where } \Delta = \frac{2\left(1 - \cos k_2 \theta_f \right)}{k_2^4} - \ln^2 \left(\frac{r_1}{r_2} \right)$$
 (5.35)

Note that if Δ is negative, there is no shape that can represent the spacecraft's trajectory for the initial and final conditions that are being selected and for the parameter k_2 that was

picked. The interval in equation (5.34) limits the search space for the free parameter γ_1 . The derivation of equation (5.35) is done in appendix A.

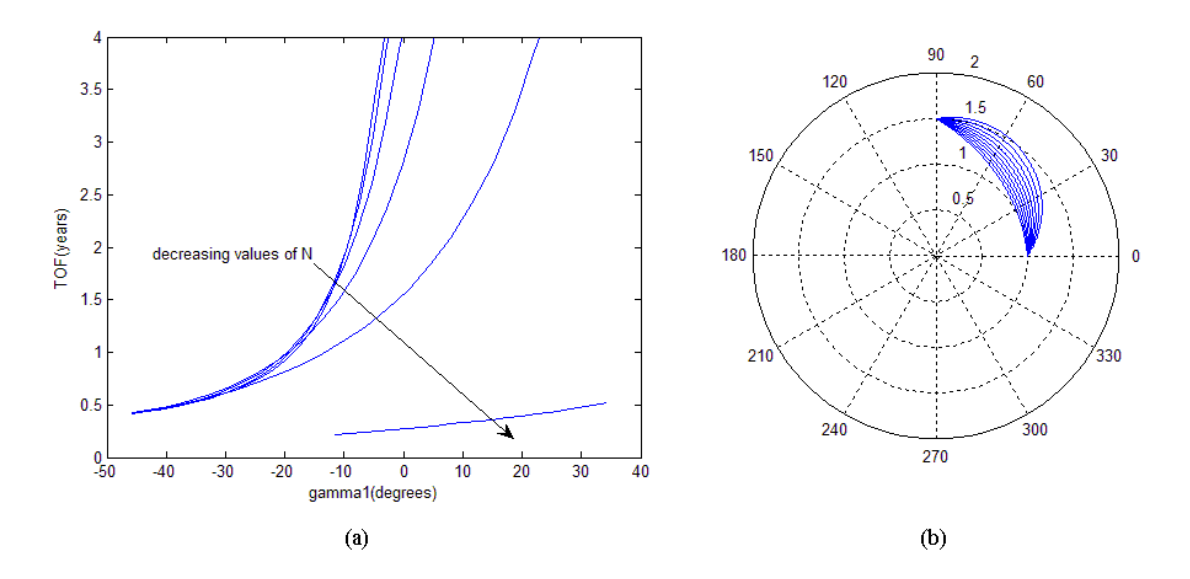


Figure 5.6: (a) the TOF versus the initial flight path angle γ_1 for the class $S_{1/12}\left(1,1.5,\pi/2,\mathrm{N}\right)$ and (b) feasible exponential sinusoids for the class $S_{1/12}\left(1,1.5,\pi/2,0\right)$ [Izzo, 2006]

Given the geometry of a problem, i.e., r_1 , r_2 , $\Delta\theta$ and the number of complete revolutions N, for $\forall k_2$, there is a class of feasible exponential sinusoids passing through the points P_1 and P_2 , using the free parameter γ_1 represented by $S_{k_2}(r_1,r_2,\Delta\theta,N)$. As an example, figure 5.6(a) illustrates the TOF versus the initial flight path angle at the starting point of the thrust arc γ_1 for a family of exponential sinusoids characterized by $S_{1/12}(1,1.5,\pi/2,N)$, where N = 0,1,...5. The TOF in figure 5.6(a) was computed by integrating numerically the expression (5.13), in section 5.3. Also, in figure 5.6(b), some of the feasible exponential sinusoids characterized by $S_{1/12}(1,1.5,\pi/2,0)$ are illustrated.

For a given TOF, a simple numerical method can be used to find a solution for this Lambert's problem for low-thrust trajectories. This solution can be found for a particular class of exponential sinusoids S_{k_2} by locating the intersection between the TOF curve and a horizontal line (figure 5.6 (a)). Using this method, the values for γ_1 can be found and

consequently the geometric parameters (k_0, k_1, ϕ) that yield the desired TOF can be obtained. Note that from figure 5.6(a), an asymptotic behaviour in the TOF curve can be observed, which leads to a conclusion: the low-thrust problem using a pseudo-Lambert method with the exponential sinusoid might not have a solution. Also, although the curve illustrated in figure 5.6(a) is monotonous, according to [Corradini, 2007], this situation not always happens. This means that two exponential sinusoids that have different γ_1 but the same S_{k_2} yield the equal TOF (see figure 5.7).

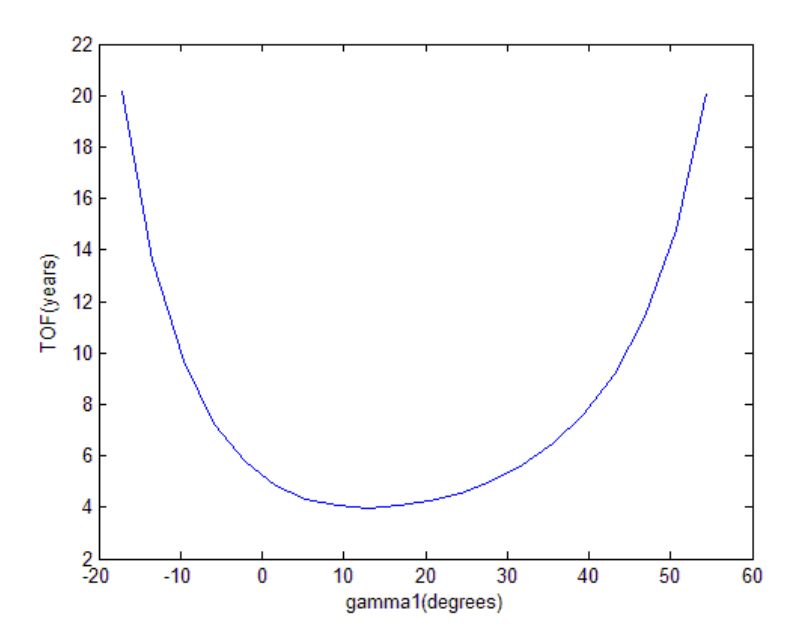


Figure 5.7: TOF as function of γ_1 for the exponential sinusoid $S_{0.4}\left(r_{\rm Earth},r_{\rm Mars},\pi/2,3\right)$, in an Earth-to-Mars flight

Izzo's procedure [Izzo, 2006] is more generic and easier to use than the one done by Petropoulos and Longuski [Petropoulos and Longuski, 2004]. For this reason, a technique related to the one developed by Izzo will be applied for the other analytical representations for low-thrust trajectories proposed in this master thesis.

6. Candidate Shapes for Low-Thrust Trajectories

As already mentioned in chapters 3 and 5, electric propulsion has proven to be a very interesting option for future interplanetary missions. In chapter 5, expressions for the thrust acceleration a, the thrust angle α , the radial and tangential velocities and the TOF were derived for the exponential sinusoid. Also, the influence of the geometric parameters of this shape $(k_1 \text{ and } k_2)$ on the trajectory of the spacecraft and the choice of geometric parameters in order to obtain feasible exponential sinusoids (equation (5.34)) was discussed.

In this chapter, a similar study will be done for five other shapes that were considered feasible to represent low-thrust trajectories in the literature survey [Paulino, 2007]. The five shapes are: the Archimedean spiral, the logarithmic spiral, the Poinsot's spiral (hyperbolic sine), Poinsot's spiral (hyperbolic cosine) and the sinusoidal spiral. A similar study to the one done with the exponential sinusoid in [Izzo, 2006] will be made for each of the five shapes. Other shapes were addressed in the literature survey [Paulino, 2007]. However, since these shapes cannot spiral using multiple revolutions, they were discarded and they are not going to be mentioned in this master thesis.

In section 6.1, a brief introduction about the shapes chosen in the literature survey [Paulino, 2007] will be given. In section 6.2, the reasoning used to compute the time of flight (TOF), the excess velocities and the thrust acceleration vector for different thrust profiles will be shown. An analysis regarding singularities and constraint conditions will be done in sections 6.3 and 6.4. This analysis is important in order to obtain feasible results and save computation time during the sensitivity analysis of the shapes' performance in chapter 7 and during the optimisation procedure in chapter 8. Finally, a summary of the constraint conditions will be given in section 6.5.

6.1. Radius Equations and Geometric Parameters

In this section, geometric properties of the five shapes besides the exponential sinusoid chosen in the literature survey will be discussed: the Archimedean spiral, the logarithmic spiral, the Poinsot's spiral (hyperbolic sine), Poinsot's spiral (hyperbolic cosine) and the sinusoidal spiral.

a) Archimedean spiral

The Archimedean spirals are defined by the equation [Lawrence, 1972]:

$$r^m = a^m \theta \tag{6.1}$$

Parameter a is a scaling factor and parameter m defines the spiral shape. These two parameters are called geometric parameters. Special cases of Archimedean spirals are: the Archimedes' spiral (m=1), the Fermat's spiral (m=2), the hyperbolic spiral (m=-1) and the lituus (m=-2). These spirals are represented in figure 6.1.

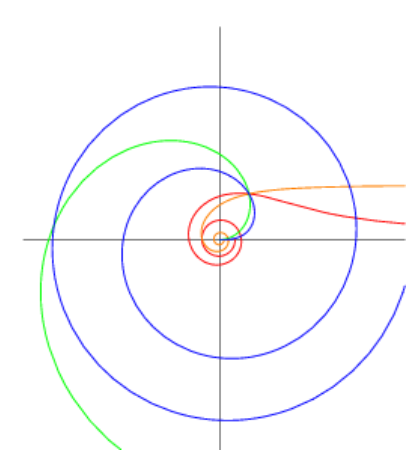


Figure 6.1: The Archimedes's spiral (green), the Fermat's spiral (blue), the hyperbolic spiral (orange) and the lituus (red) [Weisstein, 2007]

Equation (6.1) only has two geometric parameters and these two parameters can easily be computed if the initial and final radii are known. In order to obtain more than one shape for certain initial and final conditions, equation (6.1) will be changed in order to have three geometric parameters instead of two. In this way, another constant can be added to equation (6.1) as a quantity that translates the spiral in the radial direction, but also changes the ratio between the apocentre and pericentre radii. In this way, one of the shape equations that will be analysed in order to describe a low-thrust trajectory in this master thesis is:

$$r^m = k_0 \theta + k_1 \tag{6.2}$$

The shape represented by equation (6.2) is not the same as presented in [Lawrence, 1972]. The reader should take this into account during the remainder of the thesis, since from this point on equation (6.2) will be referred to the radius equation of the Archimedean spiral.

b) Logarithmic spiral

The logarithmic spiral is also known as the equiangular spiral. The equation that represents the logarithmic spiral shape is [Lawrence, 1972]:

$$r = ae^{m\theta} ag{6.3}$$

Parameter *m* is a winding quantity, associated with the number of revolutions that the shape can perform before reaching the target and *a* is a scaling factor. Figure 6.2 illustrates a logarithmic spiral. Initially, this shape was studied in *[Petropoulos et al., 1999]* in order to evaluate if it could represent a feasible option for the representation of low-thrust trajectories. According to *[Petropoulos et al., 1999]*, the TOF and the excess velocity performance given by the logarithmic spiral should be improved. For this reason, since the exponential sinusoid was also analysed and it showed better results *[Petropoulos et al., 1999]*, the logarithmic spiral was discarded.

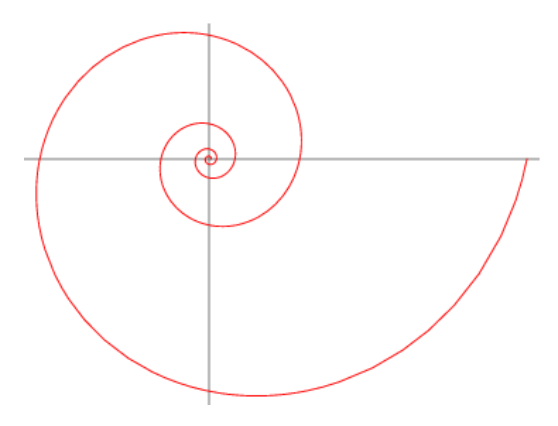


Figure 6.2: Logarithmic spiral [Weisstein, 2007]

Because only two geometric parameters were considered in equation (6.3), in the literature survey [Paulino, 2007] this equation was modified by introducing a new constant. In this way, another parameter was added to equation (6.3): a constant k_1 that, like for the Archimedean spiral, translates the shape in the radial direction, but also changes the ratio between the pericentre and the apocentre. In this way, a new radius equation can be given as:

$$r = k_0 e^{m\theta} + k_1 \tag{6.4}$$

From this point on, equation (6.4) will be referred to the radius equation of the logarithmic spiral.

c) Poinsot's spirals

There are two Poinsot's spirals and their polar equations are defined as [Lawrence, 1972]:

$$r_1 \cosh(m\theta) = a$$

$$r_2 \sinh(m\theta) = a$$
(6.5)

Parameter a is a scaling factor and parameter m defines the shape of the spiral. Figure 6.3(a) shows the Poinsot's spiral (hyperbolic sine), while figure 6.3(b) shows the Poinsot's spiral (hyperbolic cosine). The Poinsot's spiral described in equation (6.5) with the hyperbolic sine has a singularity in $\theta = 0^{\circ}$. To avoid the singularity and using the fact that only positive values of θ are considered, this expression can be changed to:

$$r_2 \sinh\left(m(\theta + \varphi)\right) = a \tag{6.6}$$

The variable φ is a phase angle that is considered positive. Equation (6.6) and the first equation in (6.5) can also be changed by adding a new constant k_1 that translates the shape in the radial direction, but also changes the ratio between the pericentre and the apocentre radii. The equations that will be used in this master thesis are:

$$r = k_0 \left(\sinh \left(m \left(\theta + \varphi \right) \right) \right)^{-k_1} \tag{6.7}$$

$$r = k_0 \left(\cosh\left(m\theta\right)\right)^{-k_1} \tag{6.8}$$

From this point on, equation (6.7) and (6.8) will be referred to as the radius equation of the Poinsot's spiral (hyperbolic sine) and the Poinsot's spiral (hyperbolic cosine), respectively.

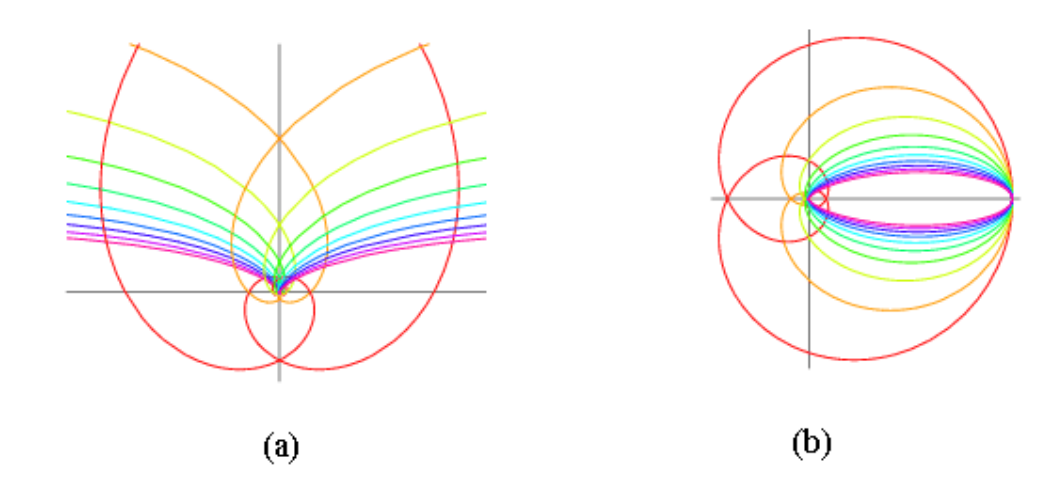


Figure 6.3: (a) The Poinsot's spiral (hyperbolic sine) and the (b) Poinsot's spiral (hyperbolic cosine) [Weisstein, 2007]

d) Sinusoidal spiral

The sinusoidal spiral shape is expressed by equation [Lawrence, 1972]:

$$r^m = a^m \cos(m\theta) \tag{6.9}$$

Parameter a is a scaling factor and parameter m defines the shape of the spiral. Equation (6.9) can represent many shapes: the Cayley's sextet (m = 1/3), the cardioid (m = 1/2), the lemniscate of Bernoulli (m = 2), among others. Figure 6.4 shows these three shapes that are all closed curves.

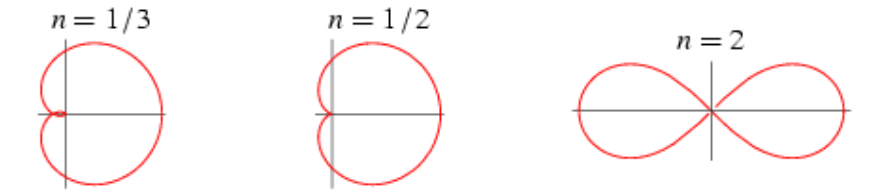


Figure 6.4: The Cayley's sextet (n=1/3), the cardioid (n=1/2) and the lemniscate of Bernoulli (n=2) [Weisstein, 2007]

Equation (6.9) can be slightly modified to increase its flexibility by adding a new constant k_1 :

$$r = \left(k_0 \cos\left(m\theta\right) + k_1\right)^{1/m} \tag{6.10}$$

Parameter m is a winding parameter that controls the number of revolutions, parameter k_0 controls the ratio between the apocentre and the pericentre radii, while parameter k_1 controls the shape. Figure 6.5 illustrates one of the shapes described by equation (6.10). The sinusoidal spiral is a closed curve that spirals outwards and after a certain number of revolutions, it spirals inwards until it reaches the same initial position. This shape could represent the trajectory of a spacecraft that encounters a certain planet and then returns to its departure planet. Although it is a closed shape, the sinusoidal spiral is a valid option to represent low-thrust trajectories in this thesis, since it can easily spiral many times, it is practically tangential to the initial and final orbits and it does not present significant shape variations during a revolution. Of course, only the outwards spiral part of the shape will be considered for outward planets and only the inward spiral part will be considered for missions to inner planets.

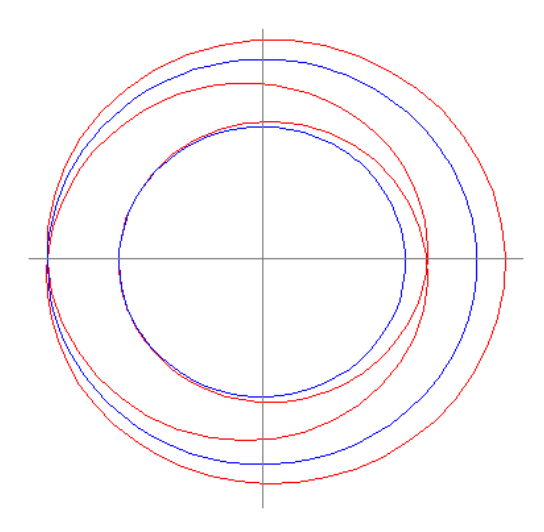


Figure 6.5: The sinusoidal spiral

6.2. Implementation

In this section, a description of the procedure that was used in this master thesis in the sensitivity analysis of the performance of the 5 candidate shapes to represent low-thrust trajectories (chapter 7) will be made. The aim of this sensitivity analysis (chapter 7) is to understand the influence of the geometric parameters of each shape in the outputs of the TOF, the excess velocities and the thrust acceleration.

In this analysis, a two-dimensional problem was considered, i.e., the spacecraft, the departure and target planets orbit are in the same plane (coplanar). This assumption and the assumption that the planets move in circular orbits were made in order to simplify the problem (without jeopardizing conclusions about each shape's performance) and consequently gain in computation time. Therefore, the ephemeris of the planets as in a three-dimensional case was not taken into account.

Consider figure 5.5 in chapter 5 to illustrate $\overline{r_1}$ and $\overline{r_2}$ (the initial and the final positions of the spacecraft, respectively) in a two-dimensional case. In the analysis done in chapter 7, the two-dimensional vector $\overline{r_1}$ will be considered fixed and the transfer angle $\Delta\theta$ will be given as an input. Knowing the transfer angle, the two-dimensional vector $\overline{r_2}$ can be computed.

 $K = (k_0, k_1, m)$

The radius expressions for these shapes were already introduced in section 6.1 and they are summarized below:

Archimedean spiral:
$$r = (k_0 \theta + k_1)^{1/m}$$
 $K = (k_0, k_1, m)$ Logarithmic spiral: $r = k_0 e^{m\theta} + k_1$ $K = (k_0, k_1, m)$ Poinsot's spiral (hyperbolic sine): $r = k_0 \left(\sinh\left(m(\theta + \varphi)\right)\right)^{-k_1}$ $K = (k_0, k_1, m, \varphi)$ Poinsot's spiral (hyperbolic cosine): $r = k_0 \left(\cosh\left(m\theta\right)\right)^{-k_1}$ $K = (k_0, k_1, m)$

Sinusoidal spiral: $r = (k_0 \cos(m\theta) + k_1)^{1/m}$

Vector K represents the geometric parameters for each shape; the radius r is the distance of the spacecraft with respect to the Sun and θ is the polar angle, measured with respect to an arbitrary reference line. As already said in section 6.1, φ is a parameter that was added in the Poinsot's spiral (hyperbolic sine) radius equation (equation (6.7)) in order to prevent the term inside the sinh () from becoming zero, otherwise r becomes ∞ . From all five radius equations, vector K contains four parameters for the Poinsot's spiral (hyperbolic sine), while for the other four shapes only three parameters are required to compute r.

The objective of this master thesis was not only to attempt to find other analytical representations, besides the exponential sinusoid using continuous tangential thrust that could have a better performance in low-thrust trajectories. This master thesis purpose is also to analyse different thrust profiles and verify if the tangential one assumed in [Petropoulos and Longuski, 2004] and in [Izzo, 2006] is the one that should be considered as a first guess for a low-thrust mission generator. Due to a time constraint, only three cases of thrust profiles were analysed for the five shapes presented in section 6.1 and the exponential sinusoid: (1) "acceleration inversely square", a thrust profile where the magnitude of the thrust acceleration monotonically decreases with the square of the distance to the Sun - $a = a_0 \mu/r^2$, where a_0 is the thrust acceleration normalised by the local gravitational acceleration (it is non-dimensional and constant); (2) "constant acceleration", a thrust profile where the magnitude of the thrust acceleration is constant:

 $a = a_0 \mu/r_1^2$ (r_1 is the heliocentric radius at the starting point of the thrust arc); (3) "tangential" thrust profile that was already studied in [Petropoulos and Longuski, 2004] and in [Izzo, 2006] and addressed in chapter 5. Note that in the first two cases of the thrust profile presented, an assumption is made for the thrust acceleration, but the thrust direction, i.e., the thrust angle is free; while in the tangential case an assumption is made for the thrust angle (which is equal to the flight path angle) and the thrust acceleration is given as an output.

The method necessary to compute the TOF, the position and the velocity with time of the spacecraft is similar for the first and second cases of the thrust profile. For these two cases, given the normalised magnitude of the thrust acceleration a_0 as an input, the following variables need to be determined:

- $\dot{\theta}$: the first derivative of θ computed in the transfer plane. This variable depends on: K, θ, α and a_0 ;
- θ : the polar angle that is computed by integrating $\dot{\theta}$ from θ_i to θ_f ;
- \dot{r} : the radial velocity that can be obtained by differentiating the equation for r. This equation depends on: K, θ, α and a_0 ;
- α : the thrust angle was already represented in figure 5.2(b) and it is obtained by integrating the equation for $\dot{\alpha}$: K, θ, α and a_0 .

As already concluded in section 5.2, the expressions for the derivatives $\dot{\theta}$ and $\dot{\alpha}$ are coupled, intractable, first-order differential equations. For this reason, numerical integration is necessary to find the values for θ and α , and consequently to determine the position and velocity of the spacecraft. All equations for the dynamic parameters of all shapes and for the three thrust profiles mentioned above are given in appendix B.

When considering the tangential thrust profile, the $\dot{\theta}^2$ equations for all five shapes no longer depend on the magnitude of the normalised thrust acceleration a_0 . Therefore, parameter a_0 does not have to be given as an input; it can be computed through an

analytical expression (see equations in appendix B). For this thrust profile case, the following variables need to be determined:

- $\dot{\theta}$: the first derivative of θ computed in the transfer plane. This variable depends on: K and θ ;
- θ : the polar angle that is computed by integrating $\dot{\theta}$ from θ_i to θ_f , just like for the first case of thrust profile presented above;
- \dot{r} : the radial velocity computed in the transfer plane, that can be obtained by differentiating the equation for r. This equation depends on: K and θ ;
- a: the thrust acceleration and it depends on: K and θ .

For the tangential case, numerical integration is necessary to find values for θ and consequently to determine the position, the velocity and the TOF of the spacecraft. Note that computation time in the tangential case is significantly smaller than the time necessary to compute a trajectory using the acceleration inversely square and the constant acceleration cases of the thrust profile. This is because the thrust angle α needs to be calculated through numerical integration for these two cases. The advantage of the methods developed by Izzo [Izzo, 2006] and Petropoulos and Longuski [Petropoulos and Longuski, 2004], using the tangential profile, is that all the dynamic parameters, except the TOF, can be computed through analytical expressions. However, although numerical integration is required to compute the thrust angle α in the acceleration inversely square and the constant acceleration cases of the thrust profile, the computation time is still significantly small compared with the computation time required to integrate the entire trajectory (at least fifteen times more, depending on the type of mission, i.e., for longer missions, the differences in computation time increases). For this reason, it is still meaningful to analyse the acceleration inversely square and the constant acceleration cases of the thrust profile for all shapes.

The integrator that was chosen in all three cases of the thrust profile was the Runge-Kutta 4(5), as already mentioned in chapter 2. Since the programming code done in this master thesis was implemented in MATLAB, a Runge-Kutta 4(5) integrator function that is part of the MATLAB software was used. During the integration procedure, for increasing values

of t (time), θ and α vectors for the acceleration inversely square and the constant acceleration cases of the thrust profile and only θ vector for the tangential thrust profile were built. The TOF was known by stopping the integration procedure at $\theta = \theta_f$ and verifying at which instant of time that happens.

After the integration procedure, the position and the velocity of the spacecraft can be computed and, consequently, the excess velocities, which are given by the following equations:

$$\overline{V}_{\infty,1} = \overline{V}_{\text{shape,initial}} - \overline{V}_d \tag{6.11}$$

$$\overline{V}_{\infty,2} = \overline{V}_{\text{shape,final}} - \overline{V}_{t} \tag{6.12}$$

The variable \overline{V}_d is the velocity vector of the departure planet at the departure instant and the variable \overline{V}_t is the target planet velocity vector at the arrival instant. The variables $\overline{V}_{\text{shape,initial}}$ and $\overline{V}_{\text{shape,final}}$ are the shape velocity vectors at θ_i and θ_f , respectively. The velocity of the shape is computed using the following equation:

$$\overline{V}_{\text{shape}} = \overline{V}_r + \overline{V}_{\theta} \tag{6.13}$$

The radial and tangential velocities can be computed in Cartesian coordinates for a twodimensional case:

$$\begin{cases} V_r(x) = \dot{r}\cos\lambda \\ V_r(y) = \dot{r}\sin\lambda \\ V_r(z) = 0 \end{cases}$$
(6.14)

$$\overline{V}_{\theta} = r\dot{\theta} \frac{\overline{r}_{1} \times \overline{r}_{2}}{r_{1}.r_{2}} \times \frac{\overline{r}}{r}$$
(6.15)

The velocity vectors $\overline{V}_{\text{shape,initial}}$ and $\overline{V}_{\text{shape,final}}$ can be computed in Cartesian coordinates, since λ (heliocentric longitude) is known for the initial and final positions. In figure 6.6, the radial and tangential velocities are represented at the target planet.

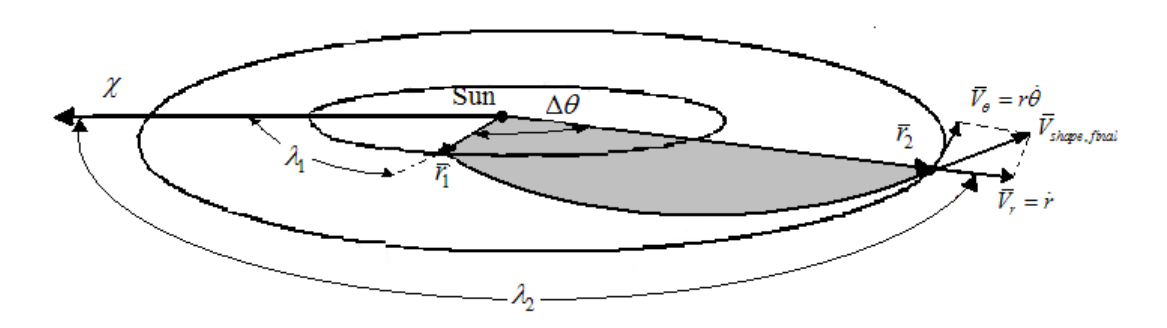


Figure 6.6: Representation of the celestial longitude, the radial and tangential velocities at the target planet

At this moment, in order to do the sensitivity analysis, the class of variables that are required as an input for a low-thrust problem, for the acceleration inversely square and the constant acceleration cases of the thrust profile is:

$$S = [r_1, r_2, \theta_i, \theta_f, K, \alpha_0, a_0]$$

While the class of variables required for the tangential thrust case is:

$$S = \left[r_1, r_2, \theta_i, \theta_f, K \right]$$

Knowing these classes of variables, numerical integration can be used to compute the TOF for the acceleration inversely square, the constant acceleration and the tangential cases of the thrust profile, followed by an evaluation of the excess velocities and of the thrust acceleration. If the mathematical expression for $\dot{\theta}^2$ presents singularities or restrictions, the shape parameters K (free variables) will be characterized by an interval of values that satisfies the constraint equation for $\dot{\theta}^2$. This reasoning was implemented in [Izzo, 2006] and it was applied for the shapes presented in this master thesis in section 6.3.

6.3. Constraint Equation – Tangential Thrust

In this section, a brief discussion about constraint equations that can be derived from the expression for $\dot{\theta}^2$ that each shape may have will be done for the tangential thrust profile. For the other two thrust profiles, this discussion will be made in section 6.4.

6.3.1. Archimedean Spiral

The radius equation for the Archimedean spiral (equation (6.2)) and the equation for the dynamic parameter $\dot{\theta}^2$ (equation (B.4), appendix B) are given by:

$$r = (k_0 \theta + k_1)^{1/m}$$

$$\dot{\theta}^2 = \frac{\mu}{r^3} \frac{a_0 \cos \alpha \tan \gamma - a_0 \sin \alpha + 1}{(m+1) \tan^2 \gamma + 1} \Rightarrow \dot{\theta}^2 = \frac{\mu}{r^3} \frac{1}{(m+1) \tan^2 \gamma + 1} \text{ for the tangential case}$$

The geometric variable m was chosen to be an input parameter – free geometric parameter. The other two geometric parameters k_0 and k_1 are computed through the radius equations at the departure and target planets:

$$r_{1} = \left(k_{0}\theta_{i} + k_{1}\right)^{1/m} \iff k_{1} = r_{1}^{m} - k_{0}\theta_{i}$$

$$r_{2} = \left(k_{0}\theta_{f} + k_{1}\right)^{1/m} \iff k_{0} = \left(r_{2}^{m} - r_{1}^{m}\right) / \left(\theta_{f} - \theta_{i}\right)$$

$$(6.16)$$

For the tangential case, the Archimedean spiral does not present a constraint equation when considering $r_2 > r_1$ (the orbit of the departure planet is inner with respect to the orbit of the target planet). However, there is a situation that should be detected during the analysis of the shapes' performance (chapter 7) or the optimisation procedure (chapter 8), since they can lead to wrong results or errors. In a mission where $r_2 > r_1$, the values for m have to be always positive (m>0). For increasing values of m, k_0 also increases. Analytical expressions for certain dynamic parameters have the parameter k_0^3 and after a certain values of m, this parameter is considered infinite by MATLAB and other mathematical

software. This happens because values for k_0 can be of order 10^{21} and when used in these analytical expressions, the MATLAB tolerances for the maximum allowed value are met.

Consider now a mission using the tangential thrust profile where $r_2 < r_1$, for instance from Earth to Mercury. In this case, $\dot{\theta}^2$ (equation B.4 in appendix B) can become negative, due to the fact that for flights to inner planets m has to be always negative.

To avoid negative values for $\dot{\theta}^2$, the following condition should be respected:

$$(m+1)\tan^2\gamma > -1 \Leftrightarrow m > -1/\tan^2\gamma - 1 \tag{6.17}$$

In order to obtain a feasible Archimedean spiral, the geometric parameter m should be:

$$m > -\frac{1}{\tan^2 \gamma}\Big|_{\min} -1 \Leftrightarrow m > -\frac{1}{\tan^2 \gamma}\Big|_{\max} -1 \Leftrightarrow m > -\frac{1}{\tan^2 \gamma}\Big|_{\theta}$$
 (6.18)

The flight path angle γ can be computed through the equation (B.2) in appendix B:

$$\tan \gamma = (1/m)k_0(k_0\theta + k_1)^{-1}$$

Since k_0 is always positive for any value of m (see equation (6.16)), the maximum value for $\tan^2 \gamma$ occurs when $\theta = \theta_i$. The condition presented in equation (6.18) should be always verified after selecting m. If the geometric parameter m does not respect the condition (6.18), then it is discarded before the numerical integration procedure begins. The case presented for $r_2 > r_1$ where the MATLAB tolerances are met for the variable k_0 does not occur for $r_2 < r_1$. Therefore, when the orbit of the target planet is inner with respect to the orbit of the departure planet, computation problems ($\dot{\theta}^2 < 0$) occur only if the condition (6.18) is not respected.

6.3.2. Logarithmic Spiral

The radius equation for the logarithmic spiral (equation (6.4)) and the equation for $\dot{\theta}^2$ (equation (B.13), appendix B) are given by:

$$r = k_0 e^{m\theta} + k_1$$

$$\dot{\theta}^2 = \frac{\mu}{r^3} \frac{a_0 \cos \alpha \tan \gamma - a_0 \sin \alpha + 1}{2 \tan^2 \gamma - m \tan \gamma + 1} \Rightarrow \dot{\theta}^2 = \frac{\mu}{r^3} \frac{1}{2 \tan^2 \gamma - m \tan \gamma + 1} \text{ for the tangential case}$$

The geometric variable m was chosen to be an input parameter – free geometric parameter. Note that this parameter cannot be zero, otherwise the spacecraft will perform a circular orbit around the Sun, instead of spiralling towards the target planet. As before, the other two geometric parameters k_0 and k_1 are computed through the radius equations at the departure and target planets:

$$r_{1} = k_{0}e^{m\theta_{i}} + k_{1} \iff k_{1} = r_{1} - k_{0}e^{m\theta_{i}}$$

$$r_{2} = k_{0}e^{m\theta_{f}} + k_{1} \iff k_{0} = (r_{2} - r_{1}) / (e^{m\theta_{f}} - e^{m\theta_{i}})$$
(6.19)

The equation for $\dot{\theta}^2$ will never become negative for negative values of m and for $r_2 > r_1$, since $\tan \gamma$ is always positive and consequently $2\tan^2 \gamma - m\tan \gamma + 1$ is also always positive. The equation for $\tan \gamma$ is given by equation B.11 in appendix B:

$$\tan \gamma = \frac{\dot{r}}{r\dot{\theta}} = \frac{k_0 m e^{m\theta}}{k_0 e^{m\theta} + k_1}$$

For increasing positive values of the geometric parameter m, $\dot{\theta}^2$ will decrease and at certain point, it will become less than zero. For $r_2 < r_1$, the inverse situation occurs: the variable $\dot{\theta}^2$ is always positive for positive values of m, while for negative values of m, $\dot{\theta}^2$ can become negative. In cases where $\dot{\theta}^2$ can become negative, the following condition should be respected:

$$2\tan^2\gamma + 1 > |m\tan\gamma| \tag{6.20}$$

The condition (6.20) is always respected for |m| < 1. For |m| > 1, the total excess velocity and the thrust acceleration values become unrealistically high (chapter 7). For this reason, only values |m| < 1 with $m \ne 0$ will be given as an input for the computation of the logarithmic spiral.

6.3.3. Poinsot's Spiral (hyperbolic sine)

The radius equation for the Poinsot's spiral (hyperbolic sine) (equation (6.7)) and the equation for $\dot{\theta}^2$ (equation (B.21), appendix B) are given by:

$$r = k_0 \left(\sinh \left(m(\theta + \varphi) \right) \right)^{-k_1}$$

$$\dot{\theta}^2 = \frac{\mu}{r^3} \frac{a_0 \cos (\alpha) \tan \gamma - a_0 \sin (\alpha) + 1}{\tan^2 \gamma - k_1 m^2 \sinh \left(m(\theta + \varphi) \right)^{-2} + 1} \Leftrightarrow$$

$$\Rightarrow \dot{\theta}^2 = \frac{\mu}{r^3} \frac{1}{\tan^2 \gamma - k_1 m^2 \sinh \left(m(\theta + \varphi) \right)^{-2} + 1} \text{ for the tangential case}$$

The geometric variable m was chosen as a free parameter. For any case of the thrust profile or any departure-target bodies' combination, m should always be considered positive in order to respect the two following equations:

$$r_{1} = k_{0} \left(\sinh \left(m(\theta_{i} + \varphi) \right) \right)^{-k_{1}} \Leftrightarrow k_{0} = r_{1} / \left(\sinh \left(m(\theta_{i} + \varphi) \right) \right)^{-k_{1}}$$

$$r_{2} = k_{0} \left(\sinh \left(m(\theta_{f} + \varphi) \right) \right)^{-k_{1}} \Leftrightarrow$$

$$\Leftrightarrow k_{1} = -\log \left(r_{2} / r_{1} \right) / \log \left(\sinh \left(m(\theta_{f} + \varphi) \right) / \sinh \left(m(\theta_{i} + \varphi) \right) \right)$$

$$(6.21)$$

A maximum value for m has to be defined in order to avoid exceeding MATLAB tolerances for the highest value permitted by the software. When passing this limit, the

spacecraft is unable to move in a spiral trajectory from the departure to the target planet, because k_1 becomes zero. Instead, it performs a circular orbit around the Sun.

Instead of considering four different geometric variables, only three will be taken into account, since θ and φ always appear in the form $\theta + \varphi$ in all mathematical expressions. Note that $\theta_i + \varphi$ has to be different from zero, otherwise $r = \infty$.

Like the Archimedean spiral, the Poinsot's spiral (hyperbolic sine expression) does not have a constraint equation in $\dot{\theta}^2$, when considering the tangential thrust profile and $r_2 > r_1$ (the orbit of the departure planet is inner with respect to the orbit of the target planet), since the geometric parameter k_1 is always negative (second equation in (6.21)).

However, when considering $r_2 < r_1$, the geometric parameter k_1 will always be positive and for this reason, $\dot{\theta}^2$ can become negative for certain combinations of m and θ_i . In this case, the following condition will have to be respected:

$$\tan^2 \gamma - k_1 m^2 \sinh^{-2} \left(m \left(\theta + \varphi \right) \right) + 1 > 0 \Leftrightarrow 1 + \tan^2 \gamma > \frac{k_1 m^2}{\sinh^2 \left(m \left(\theta + \varphi \right) \right)}$$
 (6.22)

The right-hand side of the condition (6.22) has its highest value when $\theta + \varphi$ is minimum, i.e., for $\theta = \theta_i$, while the left-hand side has its lowest value when $\tan^2 \gamma$ is minimum and this happens for $\theta = \theta_f$. The minimum value that the left-hand side of equation (6.22) can have is: $1 + k_1^2 m^2$, since the equation for the flight path angle is given by (equation B.19 in appendix B):

$$\tan \gamma = \frac{\dot{r}}{r\dot{\theta}} = -mk_1 \coth(m(\theta + \varphi))$$

In this way, the condition (6.22) cannot be tested before the integration procedure begins like it was done for the Archimedean spiral. Shapes with $\dot{\theta}^2 < 0$ problems will have to be identified and discarded during the integration procedure.

6.3.4. Poinsot's Spiral (hyperbolic cosine)

The radius equation for the Poinsot's spiral (hyperbolic cosine) (equation (6.8)) and the equation for $\dot{\theta}^2$ (equation (B.29), appendix B) are given by:

$$r = k_0 \left(\cosh\left(m\theta\right)\right)^{-k_1}$$

$$\dot{\theta}^2 = \frac{\mu}{r^3} \frac{a_0 \cos\left(\alpha\right) \tan \gamma - a_0 \sin\left(\alpha\right) + 1}{\tan^2 \gamma + k_1 m^2 \cosh^{-2}\left(m\theta\right) + 1} \iff$$

$$\Rightarrow \dot{\theta}^2 = \frac{\mu}{r^3} \frac{1}{\tan^2 \gamma + k_1 m^2 \cosh^{-2}\left(m\theta\right) + 1} \text{ for the tangential case}$$

The geometric variable m was chosen to be an input parameter. Like for the Poinsot's spiral (hyperbolic sine), the spacecraft is unable to move in a spiral trajectory from the departure to the target planet for higher values of the geometric parameter m. For any case of the thrust profile or any departure-target bodies' combination, m should always be considered positive in order to respect the two following equations:

$$r_{1} = k_{0} \left(\cosh\left(m\theta_{i}\right) \right)^{-k_{1}} \iff k_{0} = r_{1} / \left(\cosh\left(m\theta_{i}\right) \right)^{-k_{1}}$$

$$r_{2} = k_{0} \left(\cosh\left(m\theta_{f}\right) \right)^{-k_{1}} \iff k_{1} = -\log\left(r_{2} / r_{1}\right) / \log\left(\cosh\left(m\theta_{f}\right) / \cosh\left(m\theta_{i}\right) \right)$$
(6.23)

Unlike the Archimedean spiral and the Poinsot's spiral (hyperbolic sine), this shape has a constraint equation in $\dot{\theta}^2$ when $r_2 > r_1$, when considering the tangential thrust profile. The geometric parameter k_1 is negative, so in order to respect $\dot{\theta}^2 > 0$:

$$1 + \tan^2 \gamma > |k_1 m^2 \cosh^{-2} (m\theta)| \tag{6.24}$$

The left-hand side and the right-hand side of condition (6.24) have their lowest and highest values, respectively when $\theta = \theta_i$. The equation for the flight path angle is given by (equation (B.27), in appendix B):

$$\tan \gamma = \frac{\dot{r}}{r\dot{\theta}} = -mk_1 \tanh(m\theta)$$

In this way, like for the Archimedean spiral, the condition (6.24) can be tested before the integration procedure begins and shapes with $\dot{\theta}^2 < 0$ will be picked up and discarded.

Note that when $r_2 < r_1$, the geometric parameter k_1 will always be positive and $\dot{\theta}^2$ will never be negative.

6.3.5. Sinusoidal Spiral

The radius equation for the sinusoidal spiral (equation (6.10)) and the equation for $\dot{\theta}^2$ (equation (B.37), in appendix B) are given by:

$$r = \left(k_0 \cos\left(m\theta\right) + k_1\right)^{1/m}$$

$$\dot{\theta}^2 = \frac{\mu}{r^3} \frac{a_0 \cos\alpha \tan\gamma - a_0 \sin\alpha + 1}{\tan^2 \gamma (1+m) + k_0 C \cdot m \cos\left(m\theta\right) + 1} \iff$$

$$\Rightarrow \dot{\theta}^2 = \frac{\mu}{r^3} \frac{1}{\tan^2 \gamma (1+m) + k_0 C \cdot m \cos\left(m\theta\right) + 1} \text{ for the tangential case}$$

The parameter C is given by:

$$C = \left(k_0 \cos(m\theta) + k_1\right)^{-1}$$

The geometric variable m was chosen to be an input parameter. This variable can vary from (-1,1). Note that m cannot have a zero value, otherwise equation (6.10) cannot be used. The other two geometric parameters k_0 and k_1 are computed through the radius equations at the departure and target planets:

$$r_{1} = \left(k_{0}\cos\left(m\theta_{i}\right) + k_{1}\right)^{1/m} \iff k_{1} = r_{1}^{m} - k_{0}\cos\left(m\theta_{i}\right)$$

$$r_{2} = \left(k_{0}\cos\left(m\theta_{f}\right) + k_{1}\right)^{1/m} \iff k_{0} = \left(r_{2}^{m} - r_{1}^{m}\right) / \left(\cos\left(m\theta_{f}\right) - \cos\left(m\theta_{i}\right)\right)$$
(6.25)

Unlike the other shapes, the behaviour of the sinusoidal spiral in terms of $\dot{\theta}^2$ being negative is unpredictable. In order to have $\dot{\theta}^2 > 0$, the following condition should be respected:

$$\tan^{2} \gamma (1+m) + k_{0} C \cdot m \cos(m\theta) + 1 > 0 \tag{6.26}$$

The expression $\tan^2 \gamma(1+m)+1$ is always positive, however the sign of $k_0C \cdot m\cos(m\theta)$ can vary. The sign of the $\cos()$ depends on the input parameters θ_i and $\Delta\theta$ that are picked. Also, C can be negative, depending on the sign of $\cos()$ and the geometric parameters k_0 and k_1 . If $k_0C \cdot m\cos(m\theta)$ is negative, then the condition (6.26) should be written as:

$$\tan^2 \gamma (1+m) + 1 > \left| k_0^m C \cdot m \cos(m\theta) \right| \tag{6.27}$$

The allowable region for the geometric parameters cannot be defined through a constraint equation that can be applied for any combination of parameters of this shape. For this reason, the only alternative is to stop the integration procedure once $\dot{\theta}^2$ becomes zero.

6.4. Constraint Equations and Computation Problems – Acceleration Inversely Square and Constant Acceleration Cases of the Thrust Profile

Until this moment, when dealing with constraint equations, only the situation using the tangential thrust profile was mentioned. For the acceleration inversely square and the constant acceleration cases of the thrust profile, the reasoning to find constraint equations is not as straightforward as for the tangential case. For each shape that was discussed before, the difference between the equations for $\dot{\theta}^2$ for different thrust profiles lies in the

numerator: $a_0 \tan \gamma \cos \alpha - a_0 \sin \alpha + 1$ (for the acceleration inversely square case), $(1/r) \left(a_0 \, \mu/r_1^2 \tan \gamma \cos \alpha - a_0 \, \mu/r_1^2 \sin \alpha + \mu/r^2\right)$ (for the constant acceleration case) and 1 (for the tangential case). In the case of the Archimedean spiral, for example, the denominator for $\dot{\theta}^2$ is always positive. Therefore in order to have $\dot{\theta}^2 > 0$, $a_0 \tan \gamma \cos \alpha - a_0 \sin \alpha + 1$ for the acceleration inversely square case of the thrust profile and $\left(a_0 \, \mu/r_1^2 \tan \gamma \cos \alpha - a_0 \, \mu/r_1^2 \sin \alpha + \mu/r^2\right)$ for the constant thrust one have to be always positive. The constraint equations that were already defined for the tangential case will be also used for the acceleration inversely square and the constant acceleration cases of the thrust profile, together with the constraint equations: $a_0 \tan \gamma \cos \alpha - a_0 \sin \alpha + 1 > 0$ and $a_0 \, \mu/r_1^2 \tan \gamma \cos \alpha - a_0 \, \mu/r_1^2 \sin \alpha + \mu/r^2 > 0$, respectively.

Besides the computation problems presented in section 6.3, another computation problem may occur when considering the acceleration inversely square and the constant acceleration cases of the thrust profile. During the integration procedure to obtain the TOF, the integrator can throw an error. This error states that the program is unable to meet integration tolerances at a certain instant of time (that is smaller than the time required for the spacecraft to meet the target planet) without reducing the step-size below the smallest value allowed. In order words, a singularity was found. This problem happens because at a certain point in the trajectory, the denominator of $\dot{\alpha}$ will be zero and the integration procedure cannot be completed. According to [Petropoulos et al, 1999], when past this point, there is no thrust direction which can maintain the selected shape and continuity of velocity, using the current thrust profile. This means that the spacecraft cannot follow the prescribed shape. There is no way to predict this situation. However, the integration should be stopped once the denominator of $\dot{\alpha}$ becomes zero. A numerical example of this problem is given in appendix C.

6.5. Summary

In table 6.1, the constraint conditions for the five shapes addressed in this chapter will be summarized for the tangential case of the thrust profile.

Shapes	Condition for feasibility (tangential case)
Archimedean spiral	$m > -1/\tan^2 \gamma \Big _{\theta_i} -1 \ (r_2 < r_1)$
	None $(r_2 > r_1)$
Logarithmic spiral	m < 1
Poinsot's spiral (hyperbolic sine)	$1 + \tan^2 \gamma > \frac{k_1 m^2}{\sinh^2 \left(m(\theta + \varphi) \right)} (r_2 < r_1)$
	None $(r_2 > r_1)$
Poinsot's spiral (hyperbolic cosine)	$1 + \tan^2 \gamma \Big _{\theta = \theta_i} > \left k_1 m^2 \cosh^{-2} \left(m \theta_i \right) \right \left(r_2 > r_1 \right)$
	None $(r_2 < r_1)$
Sinusoidal spiral	$\tan^2 \gamma (1+m) + 1 > \left k_0^m C \cdot m \cos(m\theta) \right $

Table 6.1: Conditions required for the Archimedean spiral, the logarithmic spiral, the Poinsot's spiral (hyperbolic sine), the Poinsot's spiral (hyperbolic cosine) and the sinusoidal spiral to obtain feasible trajectories for a low-thrust problem

For the remainder two cases of the thrust profile, the equations presented in table 6.1 will still have to be taken into account. Since the numerator for the acceleration inversely square and for the constant acceleration cases of the thrust profile can be negative, $a_0 \tan \gamma \cos \alpha - a_0 \sin \alpha + 1 > 0$ and $a_0 \mu/r_1^2 \tan \gamma \cos \alpha - a_0 \mu/r_1^2 \sin \alpha + \mu/r^2 > 0$ will have to be respected.

7. Sensitivity Study of the Shapes' Performance

In this chapter, an analysis of the Archimedean spiral (section 7.1), the logarithmic spiral (section 7.2), the Poinsot's spirals (hyperbolic sine and cosine) (section 7.3 and 7.4, respectively), the sinusoidal spiral (section 7.5) and the exponential sinusoid (section 7.6)⁴ will be done in terms of time of flight (TOF), excess velocities and thrust acceleration. In this master thesis, results for 3 mission examples – an Earth-Mars flight, an Earth-Jupiter flight and an Earth-Mercury flight – will be shown and the shapes' performance will be compared between different missions and between different cases of the thrust profile. Note that, as mentioned in chapter 6, a two-dimensional problem and a circular motion for the planets' orbit was assumed. In this way, the real ephemeris was not applied to this problem to obtain the position and the velocity of the planets with time. Instead, a constant distance between the Sun and the planets was used ($r_{\text{Mercury}} = 0.3871$ AU, $r_{\text{Earth}} = 0.9997$ AU, $r_{\text{Mars}} = 1.5238$ AU and $r_{\text{Jupiter}} = 5.2032$ AU).

Only the results and conclusions for the Earth-Mars mission using the acceleration inversely square and the tangential cases of the thrust profile will be given in this chapter. The results for the constant acceleration case for an Earth-Mars flight will be presented in appendix D. Results for the other two missions using the exponential sinusoid and the acceleration inversely square and tangential cases will be presented in the appendix E (for the other 5 shapes the results and remarks are similar). The reason why the constant acceleration case analysis was excluded from this chapter is because the results from this sensitivity analysis were not promising (appendix D and section 7.7).

⁴ The mathematical expressions for the 5 shapes introduced in this master thesis is different from the ones given in literature (chapter 6)

7.1. Archimedean Spiral

In this section 7.1, results for the TOF, the excess velocities and the thrust acceleration will be shown and discussed for the Archimedean spiral and for an Earth-Mars mission. The thrust profiles used in this analysis are: "acceleration inversely square", where the magnitude of the thrust acceleration monotonically decreases with the square of the distance to the Sun - $a = a_0 \mu/r^2$ (a) and the tangential case (b).

a) Acceleration Inversely Square Case of the Thrust Profile

Figures 7.1 and 7.2 show the TOF and the total excess velocity when varying parameter θ_i and the transfer angle $\Delta\theta$, when the number of revolutions N is 0. Note that the polar angle at the target planet is given by: $\theta_f = \theta_i + \Delta\theta + 2\pi N$. The values used in figures 7.1 and 7.2 for the geometric parameter m was 0.05, for the initial value of α (α_0) were (-60°, -50°, -40°, -30°, -20°), for the initial polar angle θ_i were (0°, 120°, 240°, 360°) and the transfer angle $\Delta\theta$ were (90°, 150°, 210°, 270°, 340°).

The initial polar angle θ_i is considered an input variable, since by starting in different segments of the shape, different results for the total excess velocity, the thrust acceleration and the TOF might be obtained. Note that this angle θ_i is the polar angle for the shape and it is different from the initial polar angle of the spacecraft in its interplanetary trajectory in the non-rotating heliocentric ecliptic reference frame. The normalised thrust acceleration a_0 value used in figures 7.1 and 7.2 was 0.1.

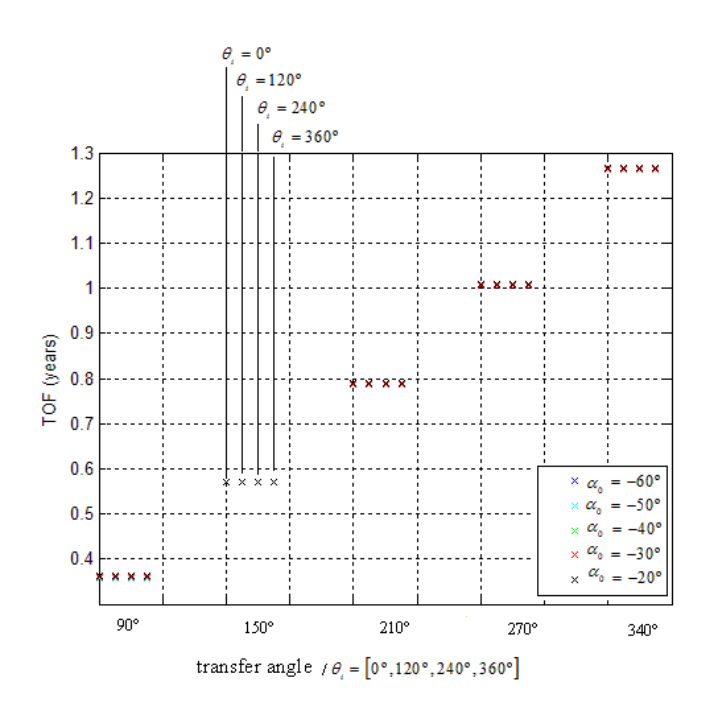


Figure 7.1: TOF for θ_i values of (0°, 120°, 240°, 360°) from left to right in the figure, α_0 values of (-60°, -50°, -40°, -30°, -20°), $\Delta\theta$ values of (90°, 150°, 210°, 270°, 340°) (N=0), m=0.05, a_0 =0.1, acceleration inversely square case of the thrust profile (Archimedean spiral), Earth-Mars flight

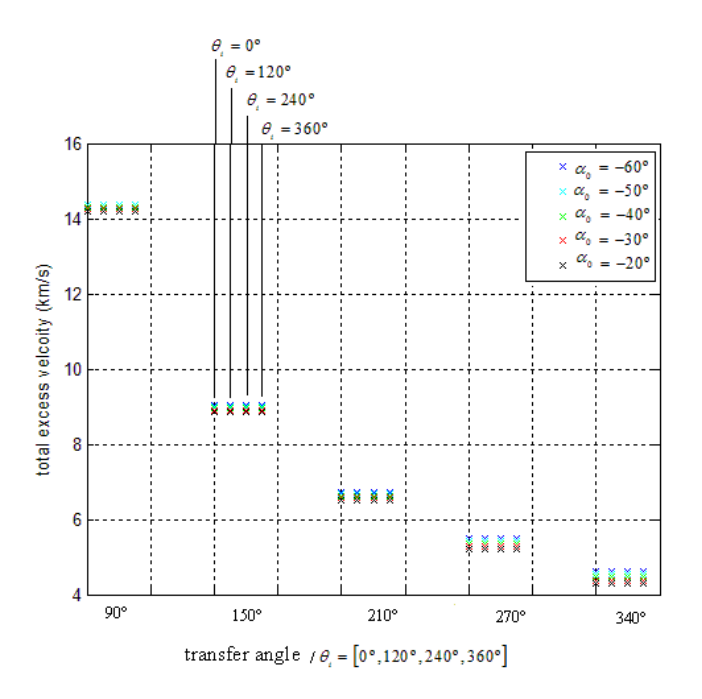


Figure 7.2: $V_{a,T}$ for θ_i values of (0°, 120°, 240°, 360°) from left to right in the figure, α_0 values of (-60°, -50°, -40°, -30°, -20°), $\Delta\theta$ values of (90°, 150°, 210°, 270°, 340°) (N=0), m=0.05, a_0 =0.1, acceleration inversely square case of the thrust profile (Archimedean spiral), Earth-Mars flight

Some remarks can be drawn from figures 7.1 and 7.2. As expected, the TOF increases when increasing the transfer angle, while the total excess velocity ($V_{\infty,\text{departure}} + V_{\infty,\text{arrival}}$) decreases. By changing the initial polar angle θ_i , the differences between values for the TOF and for the total excess velocity are significantly small. The order of magnitude of the highest difference in TOF between different θ_i for the same transfer angle and α_0 is 10^{-4} seconds, while the order of magnitude of the highest difference in total excess velocity is $10^{-8} \, m/s$. By changing the initial value of α_0 , the order of magnitude of the differences in TOF is 10^{-3} years, which is less than a day. The TOF increases when increasing values of α_0 . On the other hand, the total excess velocity decreases when increasing α_0 (see figure 7.2).

Similar figures can be shown for 1 and 2 revolutions, using the same values for the geometric parameter m, for the transfer angle $\Delta\theta$ and for the initial values of α and θ . The values for the normalised thrust acceleration a_0 used in figures 7.3 and 7.4 were 0.03 and 0.02 for N=1 and N=2, respectively. Note that the values assumed for a_0 for N=1 and N=2 are the minimum values that can be used in both cases for this shape without facing integration problems for the interval of input parameters considered (explained in section 6.4). These values were chosen because, for higher values of a_0 , the total excess velocity values will also be higher. Note that for N=2, the minimum value allowed is smaller than for N=1.

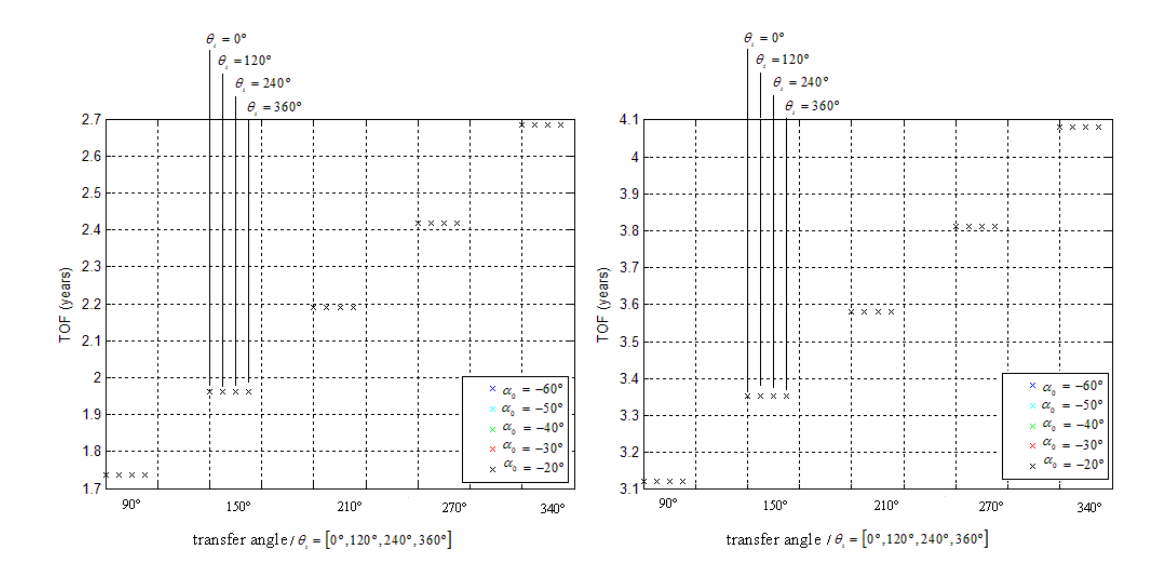


Figure 7.3: TOF for θ_i values of (0°, 120°, 240°, 360°) from left to right in the figure, α_0 values of (-60°, -50°, -40°, -30°, -20°), $\Delta\theta$ values of (90°, 150°, 210°, 270°, 340°), m=0.05, acceleration inversely square case of the thrust profile (Archimedean spiral), Earth-Mars flight, N=1 (α_0 =0.03) and N=2 (α_0 =0.02)

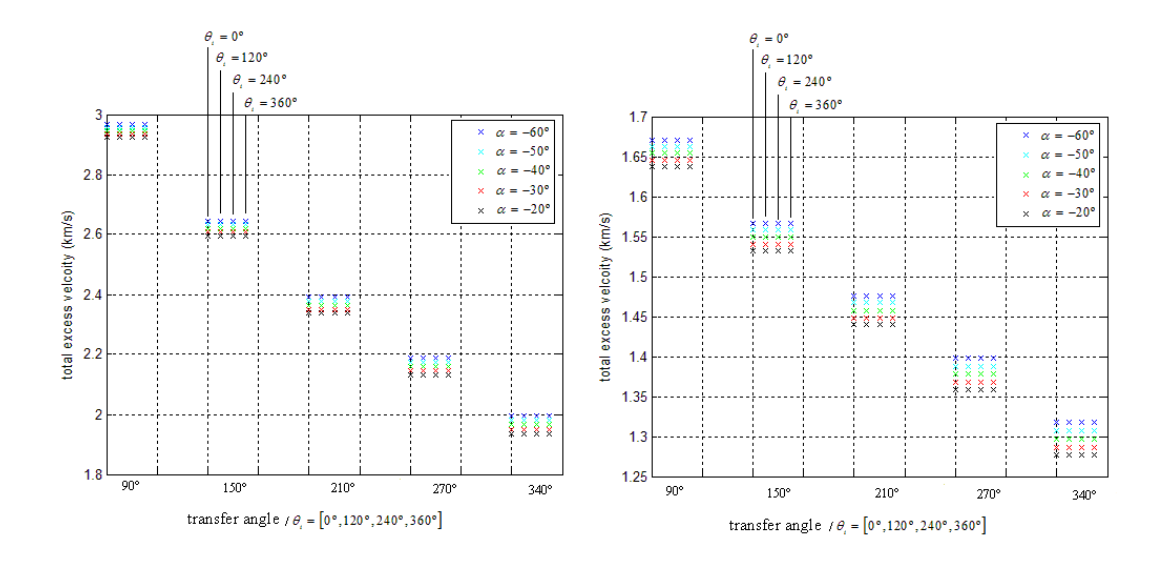


Figure 7.4: $V_{_{\odot,T}}$ for $\theta_{_i}$ values of (0°, 120°, 240°, 360°) from left to right in the figure, $\alpha_{_0}$ values of (-60°, -50°, -40°, -30°, -20°), $\Delta\theta$ values of (90°, 150°, 210°, 270°, 340°), m=0.05, acceleration inversely square case of the thrust profile (Archimedean spiral), Earth-Mars flight, N=1 ($a_{_0}$ =0.03) and N=2 ($a_{_0}$ =0.02)

From figures 7.3 and 7.4, as expected, when N increases, the TOF increases and the total excess velocity decreases. As for the N=0 case, the order of magnitude of the differences in TOF and total excess velocity between different θ_i values and for the same transfer angle and α_0 can be neglected for the cases N=1 and N=2. In this way, due to the significantly

small influence that the parameter θ_i has on the TOF, on the total excess velocity and also, although not shown in the previous figures, on the acceleration, this parameter will not be considered a variable in the optimisation procedure for an Earth-Mars flight in chapter 8.

The TOF range for this Earth-Mars flight is from 0.3577 years to 4.0801 years. The total excess velocity has a minimum value of $1.2767 \, km/s$ and a maximum value of $14.3812 \, km/s$. The maximum differences in TOF between 2 consecutive values of the transfer angle $\Delta\theta$ are about 0.27 years. For a certain number of revolutions, these differences increase when increasing the transfer angle. The differences in terms of total excess velocity between 2 consecutive transfer angles is always highest between $\Delta\theta = 90^{\circ}$ and $\Delta\theta = 150^{\circ}$. The maximum value for these differences is $5.3535 \, km/s$ for N=0 and the minimum value is about $80 \, m/s$ for N=2.

Tables 7.1 and 7.2 show the TOF and the excess velocity values, for an Earth-Mars flight. Parameter θ_i was assumed 0°, parameter α_0 was assumed -20°, the transfer angle $\Delta\theta$ was assumed 90° and N was taken 1 for the first table and 2 for the second one. In table 7.1, the normalised thrust acceleration a_0 assumed was 0.04 and in table 7.2, it was 0.03.

N=1	m = 0.02	m = 0.64	m = 1.26	m = 1.88	m = 2.5
$V_{\infty,total}\left(km/s\right)$	2.9742	3.0516	3.1977	3.4182	3.7228
$V_{\infty,1}(km/s)$	1.6263	1.8492	2.1155	2.4351	2.8216
$V_{\infty,2}(km/s)$	1.3480	1.2024	1.0822	0.9830	0.9012
TOF (years)	1.7219	1.7470	1.7725	1.7985	1.8260

Table 7.1: The excess velocities and the TOF values for N=1, θ_i =0°, $\Delta\theta$ =90°, $\alpha_{_0}$ =-20°, $a_{_0}$ =0.04, m values of (0.02;0.64;1.26;1.88;2.5), acceleration inversely square case of the thrust profile (Archimedean spiral), Earth-Mars flight

N=2	m = 0.02	m = 0.64	m = 1.26	m = 1.88	m = 2.5
$V_{\scriptscriptstyle{\infty,total}}\left(km/s ight)$	1.6955	1.7439	1.8308	1.9591	2.1336
$V_{\infty,1}(km/s)$	0.9089	1.0332	1.1820	1.3607	1.5761
$V_{\infty,2}(km/s)$	0.7865	0.7106	0.6488	0.5984	0.5575
TOF (years)	3.1018	3.1451	3.1884	3.2316	3.2745

Table 7.2: The excess velocities and the TOF values for N=2, θ_i =0°, $\Delta\theta$ =90°, α_0 =-20°, a_0 =0.03, m values of (0.02;0.64;1.26;1.88;2.5), acceleration inversely square case of the thrust profile (Archimedean spiral), Earth-Mars flight

From tables 7.1 and 7.2, the order of magnitude of the total excess velocity values is $10^0 \ km/s$. For increasing values of m, the total excess velocity and the TOF increase. The values for the total excess velocity are higher when N=1 than when N=2, i.e., although the TOF is higher, there is an advantage in terms of fuel consumption (total excess velocity is lower) when using N=2. Note that the excess velocity $V_{\infty,1}$ increases faster than the excess velocity $V_{\infty,2}$ decreases and the value of $V_{\infty,2}$ when m=2.5 is about 3 times smaller than the value of $V_{\infty,1}$ for both cases of N.

In figures 7.5 to 7.9, the polar plot, the thrust acceleration a, the thrust angle α , the polar angle rate $\dot{\theta}$ and the flight path angle as function of time are illustrated for N=1 and N=2 cases that were presented in tables 7.1 and 7.2.

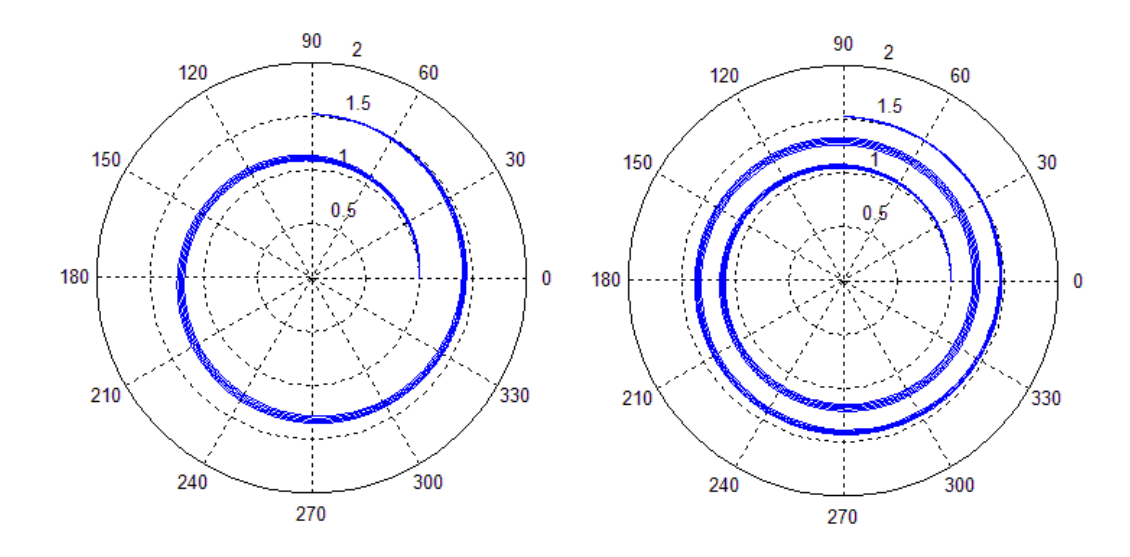


Figure 7.5: Polar plot for N=1 (a_0 =0.04) and N=2 (a_0 =0.03), θ_i =0°, $\Delta\theta$ =90°, α_0 =-20°, m values of (0.02;0.64;1.26;1.88;2.5), acceleration inversely square case (Archimedean spiral), Earth-Mars flight

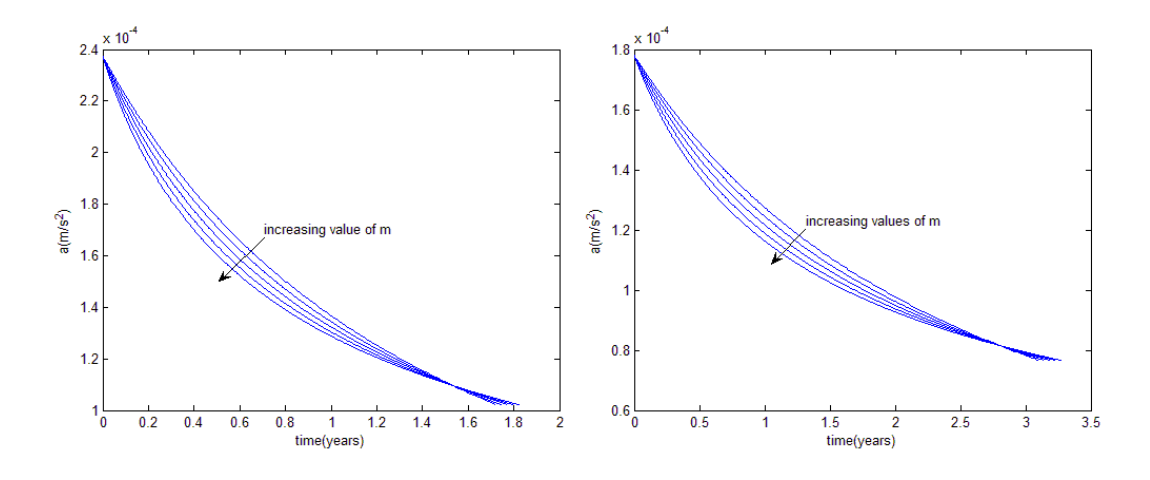


Figure 7.6: *a* plot for N=1 (a_0 =0.04) and N=2 (a_0 =0.03), θ_i =0°, $\Delta\theta$ =90°, α_0 =-20°, *m* values of (0.02;0.64;1.26;1.88;2.5), acceleration inversely square case (Archimedean spiral), Earth-Mars flight

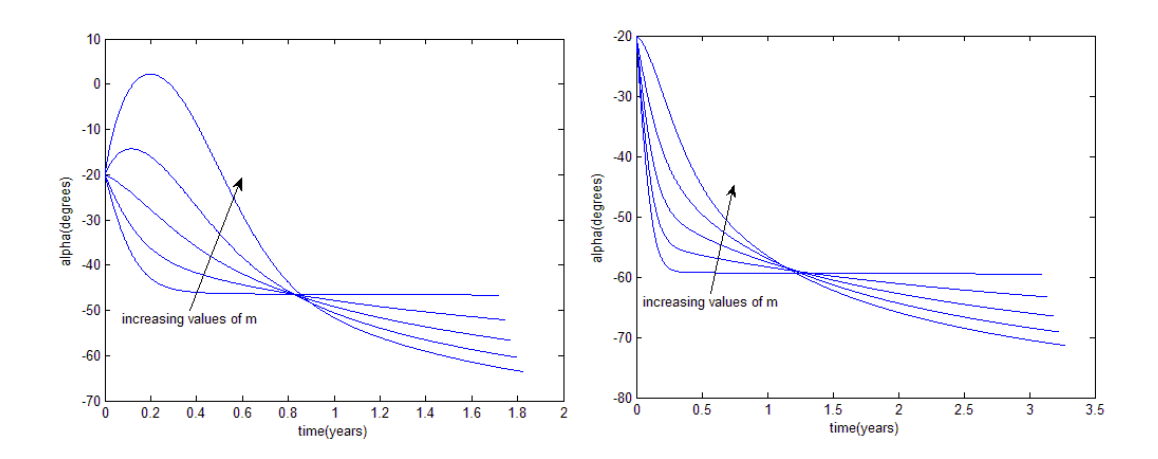


Figure 7.7: α plot for N=1 (a_0 =0.04) and N=2 (a_0 =0.03), θ_i =0°, $\Delta\theta$ =90°, α_0 =-20°, m values of (0.02;0.64;1.26;1.88;2.5), acceleration inversely square case (Archimedean spiral), Earth-Mars flight

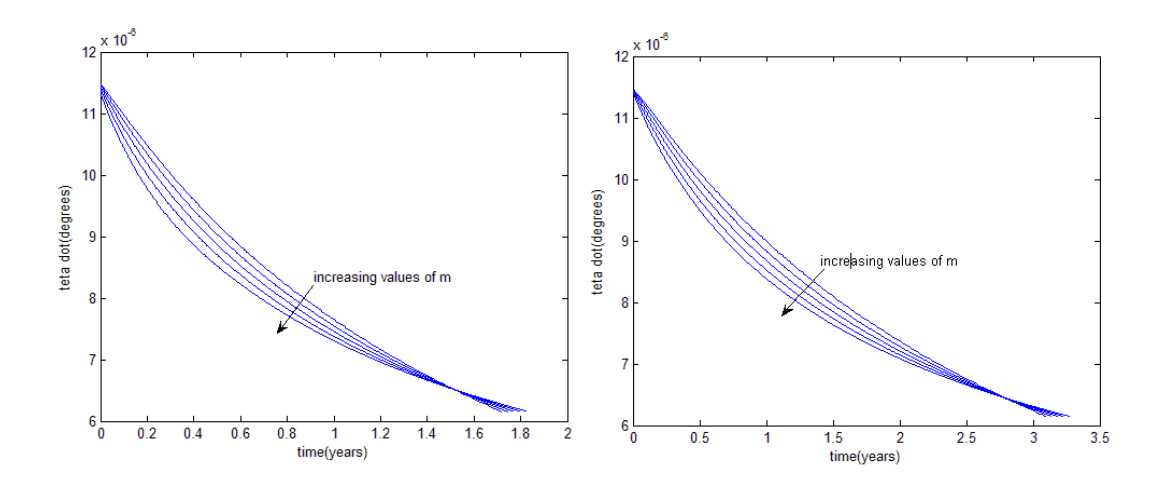


Figure 7.8: $\dot{\theta}$ plot for N=1 (a_0 =0.04) and N=2 (a_0 =0.03), θ_i =0°, $\Delta\theta$ =90°, α_0 =-20°, m values of (0.02;0.64;1.26;1.88;2.5), acceleration inversely square case (Archimedean spiral), Earth-Mars flight

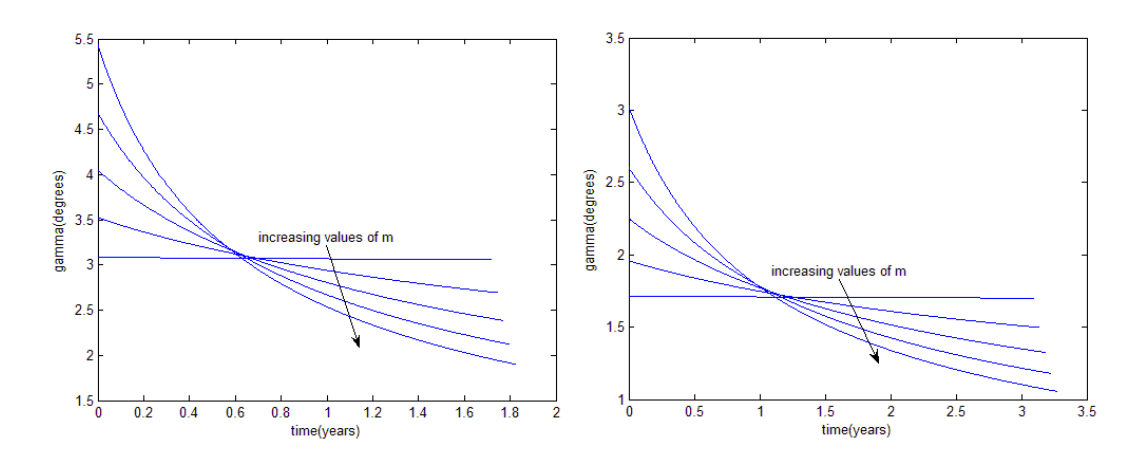


Figure 7.9: γ plot for N=1 (a_0 =0.04) and N=2 (a_0 =0.03), θ_i =0°, $\Delta\theta$ =90°, α_0 =-20°, m values of (0.02;0.64;1.26;1.88;2.5), acceleration inversely square case (Archimedean spiral), Earth-Mars flight

From figure 7.6, the magnitude of the thrust acceleration is higher for N=1 than for N=2 because the assumed normalised thrust acceleration a_0 is also higher for N=1 than for N=2. Since these are the minimum values of a_0 for N=1 and N=2, the magnitude of the instantaneous thrust required for a longer flight is smaller. Note also that the thrust acceleration trend is similar to the $\dot{\theta}$ trend, since for the acceleration inversely square case a varies with $1/r^2$ and $\dot{\theta}$ varies with $1/r^2 \cdot f(\theta)$ ($1/r^2$ term in $\dot{\theta}$ has higher influence than $f(\theta)$). The values of the thrust angle α are higher for N=1 than for N=2. During the interplanetary flight for both cases in figure 7.7, the spacecraft is thrusting inwards in the radial direction, while in the tangential direction it thrusts in the positive direction (α is negative, higher than -90° - see figure 5.2b). This means that the vehicle is thrusting in the same direction of the gravitational acceleration. This situation will be further analysed in section 7.7. The magnitude values of the flight path angle γ are smaller for N=2 than for N=1.

b) Tangential Case of the Thrust Profile

Figures 7.10 and 7.11 show the TOF and the total excess velocity when varying the parameter θ_i and the transfer angle $\Delta\theta$ (N=0). The values used in figures 7.10 and 7.11 for m were (0.02; 0.64; 1.26; 1.88; 2.5), for the initial polar angle θ_i were (0°, 120°, 240°, 360°) and for the transfer angle $\Delta\theta$ were (90°, 150°, 210°, 270°, 340°).

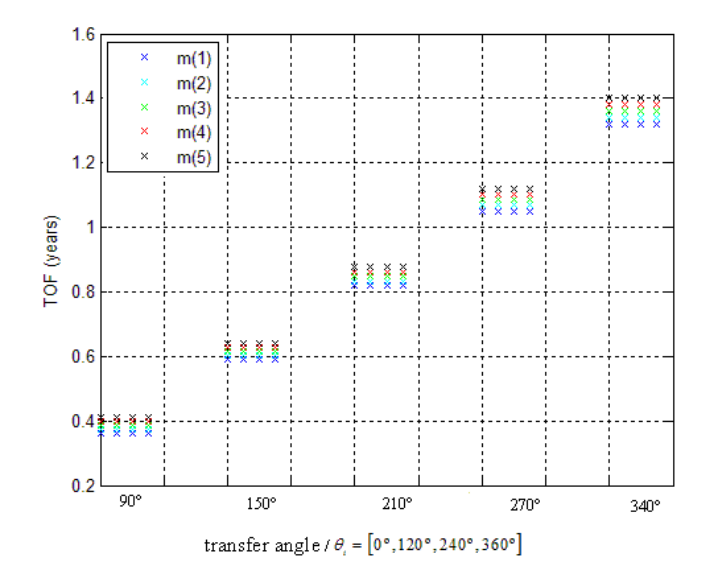


Figure 7.10: TOF for θ_i values of (0°, 120°, 240°, 360°) from left to right in the figure, m values of (0.02;0.64;1.26;1.88;2.5), $\Delta\theta$ values of (90°, 150°, 210°, 270°, 340°) (N=0), tangential thrust profile (Archimedean spiral), Earth-Mars flight

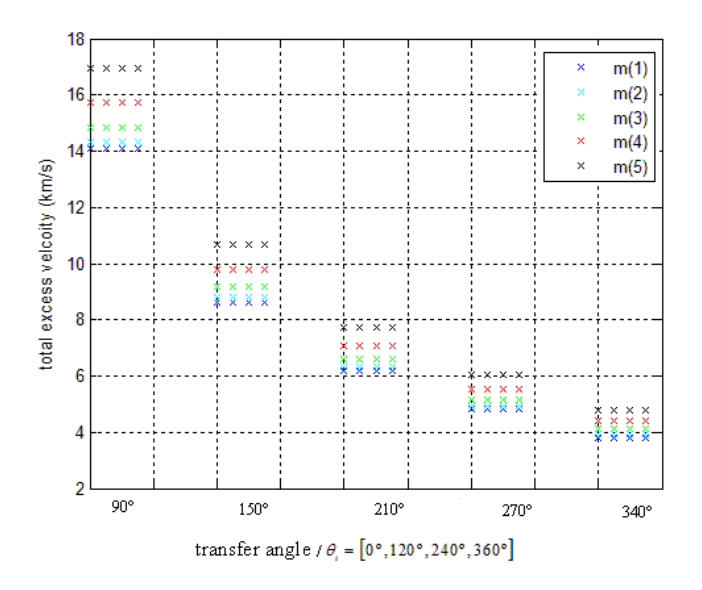


Figure 7.11: $V_{_{\circ,T}}$ for $\theta_{_i}$ values of (0°, 120°, 240°, 360°) from left to right in the figure, m values of (0.02;0.64;1.26;1.88;2.5), $\Delta\theta$ values of (90°, 150°, 210°, 270°, 340°) (N=0), tangential thrust profile (Archimedean spiral), Earth-Mars flight

Some remarks can be drawn from figures 7.10 and 7.11. By changing the initial polar angle θ_i , the differences between values for the TOF and for the total excess velocity are negligibly small, just like for the acceleration inversely square case of the thrust profile.

The order of magnitude of the highest difference in TOF between different θ_i for the same transfer angle and m is 10^{-1} seconds, while the order of magnitude of the highest difference in total excess velocity is $10^{-11} m/s$. The differences for the total excess velocity between different values of m increase when increasing this geometric parameter. For higher values of m, the total excess velocity and the TOF increase.

Similar figures can be shown for 1 and 2 revolutions, using the same values for the geometric parameter m, for the transfer angle $\Delta\theta$ and for the initial value of θ (θ_i) as the ones used for N=0.

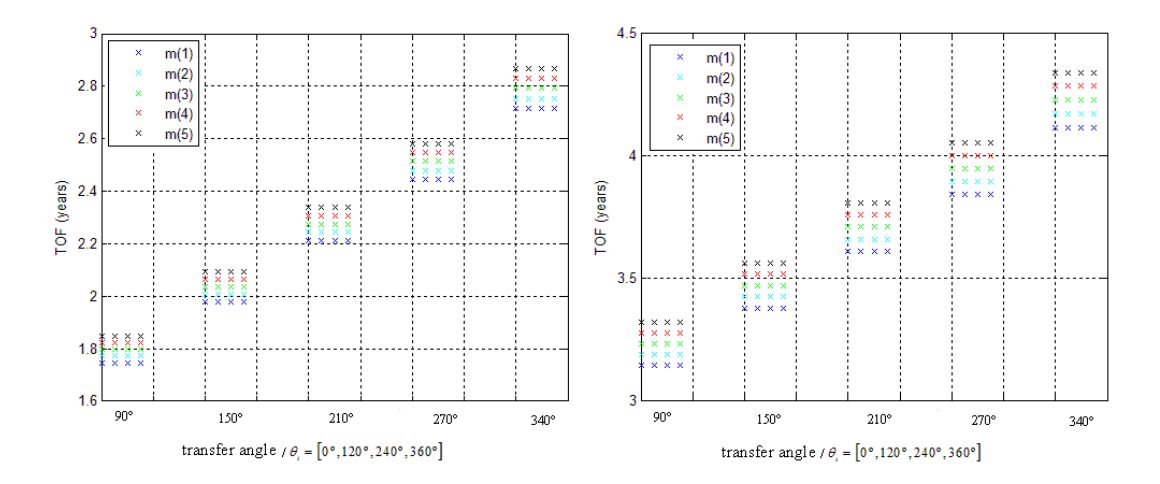


Figure 7.12: TOF for θ_i values of (0°, 120°, 240°, 360°) from left to right in the figure, m values of (0.02;0.64;1.26;1.88;2.5), $\Delta\theta$ values of (90°, 150°, 210°, 270°, 340°), tangential thrust profile (Archimedean spiral), Earth-Mars flight, for N=1 and N=2

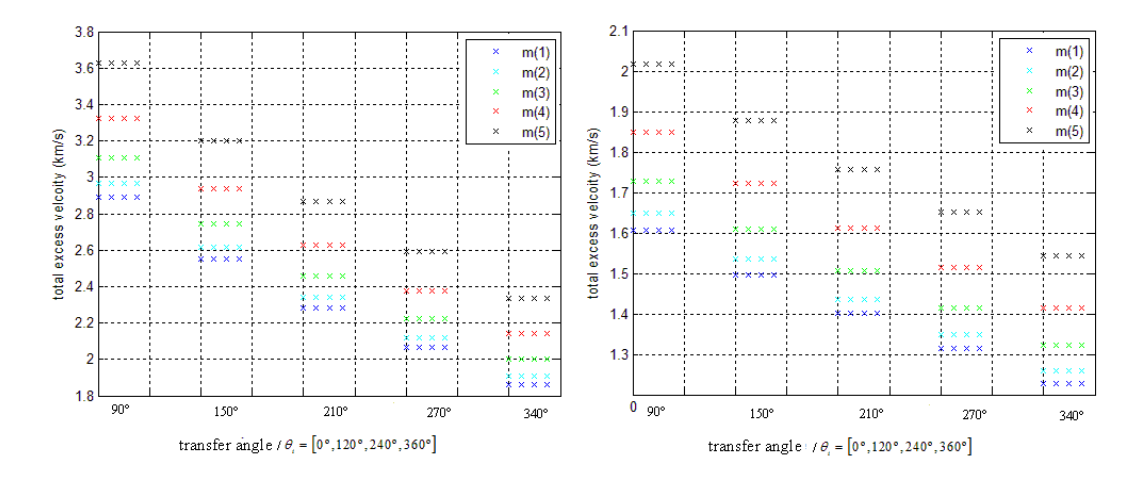


Figure 7.13: $V_{_{\infty,T}}$ for $\theta_{_i}$ values of (0°, 120°, 240°, 360°) from left to right in the figure, m values of (0.02;0.64;1.26;1.88;2.5), $\Delta\theta$ values of (90°, 150°, 210°, 270°, 340°), tangential thrust profile (Archimedean spiral), Earth-Mars flight, for N=1 and N=2

Similar remarks to the ones given for N=0 can be drawn for figures 7.12 and 7.13, when in this case for N=1 and N=2, the highest difference in the TOF between different θ_i and for the same transfer angle and m is about 0.2 seconds, while the order of magnitude of the highest difference in the total excess velocity is $10^{-12} m/s$. As already verified for the acceleration inversely square case of the thrust profile, due to the significantly small influence that the parameter θ_i has on the TOF, total excess velocity variation and thrust acceleration (although it is not shown in previous figures), this parameter will not be considered a variable in the optimisation procedure for an Earth-Mars flight in chapter 8.

The TOF range for this Earth-Mars flight is from 0.3615 years to 4.3365 years. The total excess velocity has a minimum value of $1.2285\,km/s$ and a maximum value of $16.9655\,km/s$. The maximum differences in TOF between two consecutive values of the transfer angle $\Delta\theta$ are about 0.29 years. For a certain number of revolutions, these differences increase when increasing the transfer angle. The differences in terms of total excess velocity between two consecutive transfer angles is always highest between $\Delta\theta = 90^\circ$ and $\Delta\theta = 150^\circ$. The maximum value for these differences is $6.2897\,km/s$ for N=0 and in the minimum value is $84.82\,m/s$ for 2 revolutions.

Tables 7.3 and 7.4 show the values of the TOF and the excess velocity for an Earth-Mars flight. Parameter θ_i assumed was 0°, the transfer angle $\Delta\theta$ assumed was 90° and the number of revolutions was taken 1 for the first table and 2 for the second one.

N=1	m = 0.02	m = 0.64	m = 1.26	m = 1.88	m = 2.5
$V_{\infty,total}\left(km/s\right)$	2.8912	2.9649	3.1074	3.3250	3.6279
$V_{\infty,1}(km/s)$	1.6034	1.8313	2.1038	2.4313	2.8277
$V_{\infty,2}\left(km/s\right)$	1.2879	1.1336	1.0037	0.8937	0.8001
TOF (years)	1.7472	1.7726	1.7980	1.8233	1.8484

Table 7.3: The excess velocities and the TOF values for N=1, θ_i =0°, $\Delta\theta$ =90°, m values of (0.02;0.64;1.26;1.88;2.5), tangential thrust profile (Archimedean spiral), Earth-Mars flight

N=2	m = 0.02	m = 0.64	m = 1.26	m = 1.88	m = 2.5
$V_{\infty,total}\left(km/s\right)$	1.6074	1.6489	1.7287	1.8499	2.0179
$V_{\infty,1}(km/s)$	0.8914	1.0187	1.1708	1.3533	1.5733
$V_{\infty,2}(km/s)$	0.7160	0.6302	0.5579	0.4967	0.4446
TOF (years)	3.1418	3.1856	3.2294	3.2729	3.3159

Table 7.4: The excess velocities and the TOF values for N=2, θ_i =0°, $\Delta\theta$ =90°, m values of (0.02;0.64;1.26;1.88;2.5), tangential thrust profile (Archimedean spiral), Earth-Mars flight

From tables 7.3 and 7.4, the order of magnitude of the total excess velocity values is $10^0 \ km/s$. For increasing values of m, the total excess velocity and the TOF increase. The values for the total excess velocity are higher when N=1 than when N=2, and the values for $V_{\infty,2}$ are at least 3 times smaller than the values for $V_{\infty,1}$, like for the acceleration inversely square case. Compared with this case of the thrust profile (tables 7.1 and 7.2), the TOF is higher and the total excess velocity is smaller for the tangential case.

In figures 7.14 to 7.17, the polar plot, the thrust acceleration a, the thrust angle α and the polar angle rate $\dot{\theta}$ as function of time are illustrated for N=1 and N=2 cases that were presented in tables 7.3 and 7.4.

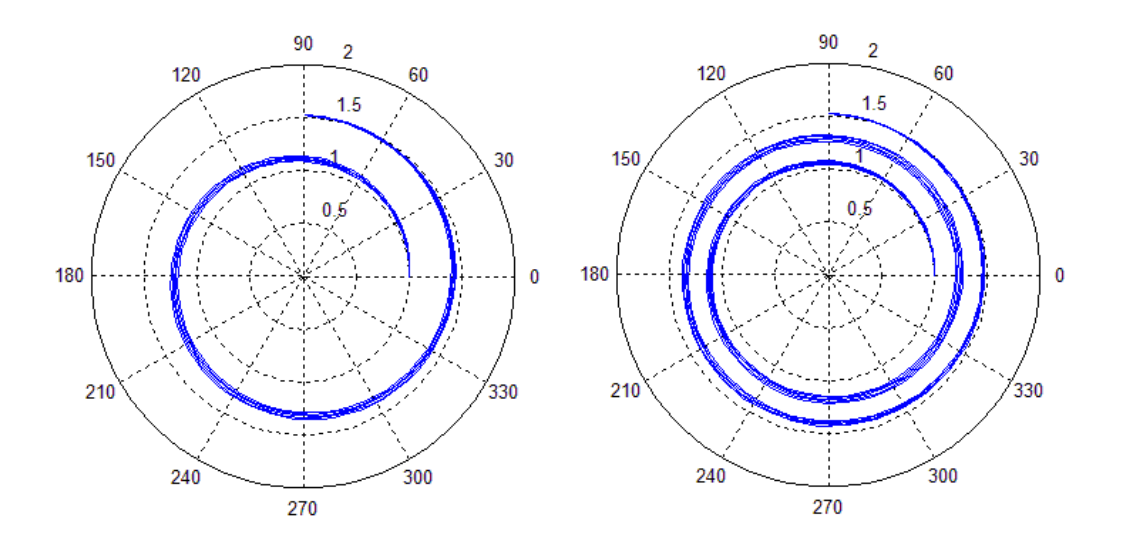


Figure 7.14: Polar plot for N=1 and N=2, θ_i =0°, $\Delta\theta$ =90°, m values of (0.02;0.64;1.26;1.88;2.5), tangential thrust profile (Archimedean spiral), Earth-Mars flight

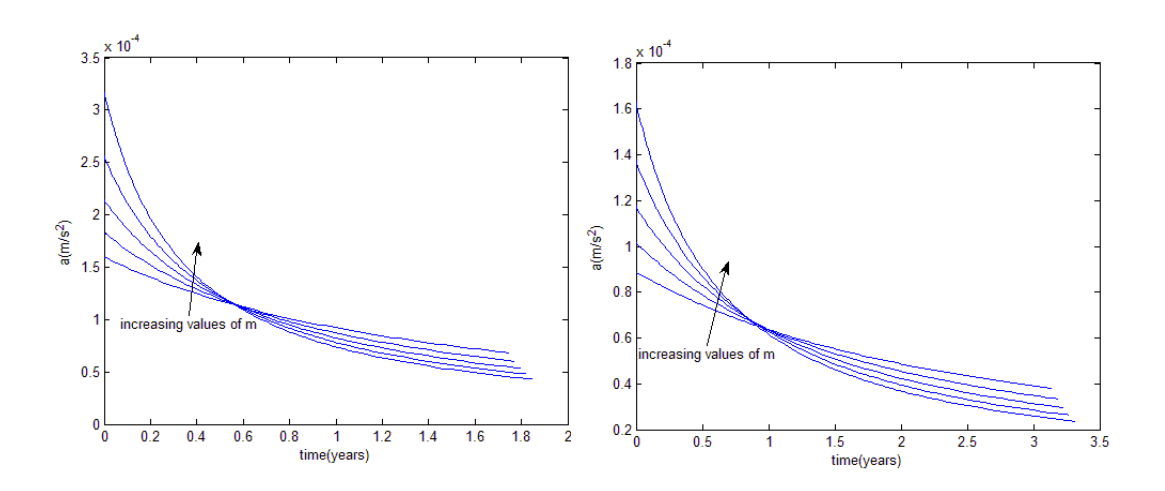


Figure 7.15: a plot for N=1 and N=2, θ_i =0°, $\Delta\theta$ =90°, m values of (0.02;0.64;1.26;1.88;2.5), tangential thrust profile (Archimedean spiral), Earth-Mars flight

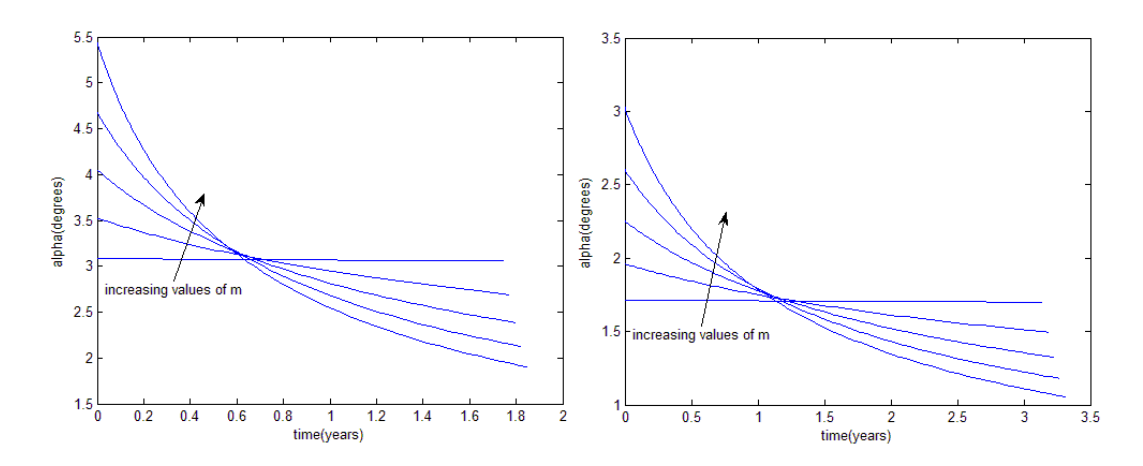


Figure 7.16: α plot for N=1 and N=2, θ_i =0°, $\Delta\theta$ =90°, m values of (0.02;0.64;1.26;1.88;2.5), tangential thrust profile (Archimedean spiral), Earth-Mars flight

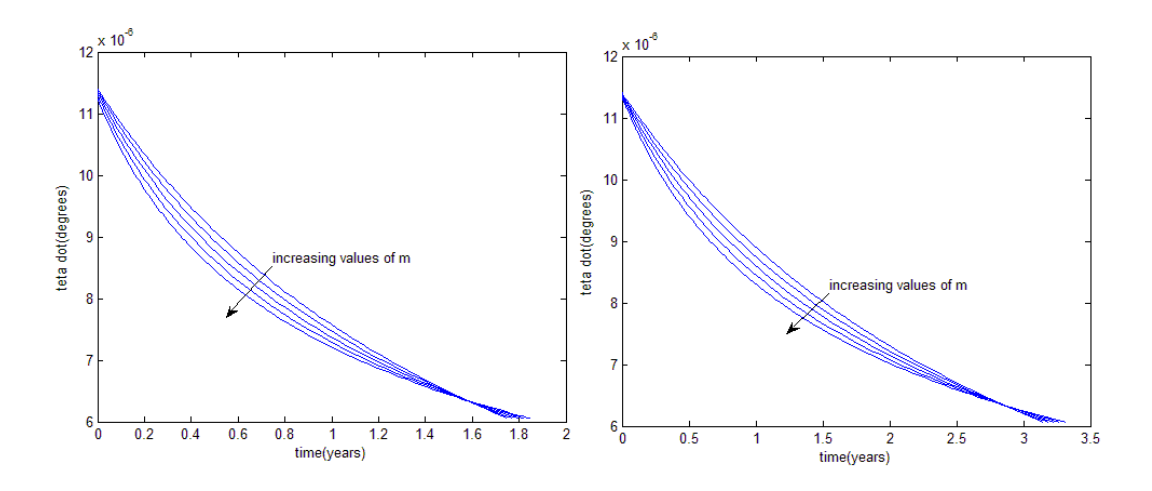


Figure 7.17: $\dot{\theta}$ plot for N=1 and N=2, θ_i =0°, $\Delta\theta$ =90°, m values of (0.02;0.64;1.26;1.88;2.5), tangential thrust profile (Archimedean spiral), Earth-Mars flight

The magnitude of the thrust acceleration is higher for N=1 than for N=2 which means that the magnitude of the instantaneous thrust required for a longer flight is smaller (figure 7.15). The values of the thrust angle α are higher in magnitude for N=1 than for N=2. Note that, compared with the acceleration inversely square case (figure 7.7), the thrust angle in figure 7.16 presents a more stable behaviour and the values are always positive for the entire mission. The plot of the flight path angle γ in function of time is not shown, since in the tangential case $\alpha = \gamma$. The differences in magnitude of the polar angle rate $\dot{\theta}$ between N=1 and N=2 are significantly small (figure 7.17).

7.2. Logarithmic spiral

In this section 7.2, results for the TOF, the excess velocities and the thrust acceleration will be shown and discussed for the logarithmic spiral and for an Earth-Mars mission. The thrust profiles used in this analysis are the same used for the Archimedean spiral.

a) Acceleration Inversely Square Case of the Thrust Profile

Figures 7.18 and 7.19 show the TOF and the total excess velocity when varying parameter θ_i and the transfer angle $\Delta\theta$, when the number of revolutions N is 0. The value for the geometric parameter m used in figure 7.18 and 7.19 was 0.05, the values for the initial value of α were (-60°, -50°, -40°, -30°, -20°), for the initial polar angle θ_i were (0°, 120°, 240°, 360°) and for the transfer angle $\Delta\theta$ were (90°, 150°, 210°, 270°, 340°). The normalised thrust acceleration a_0 value used in figures 7.18 and 7.19 was 0.11.

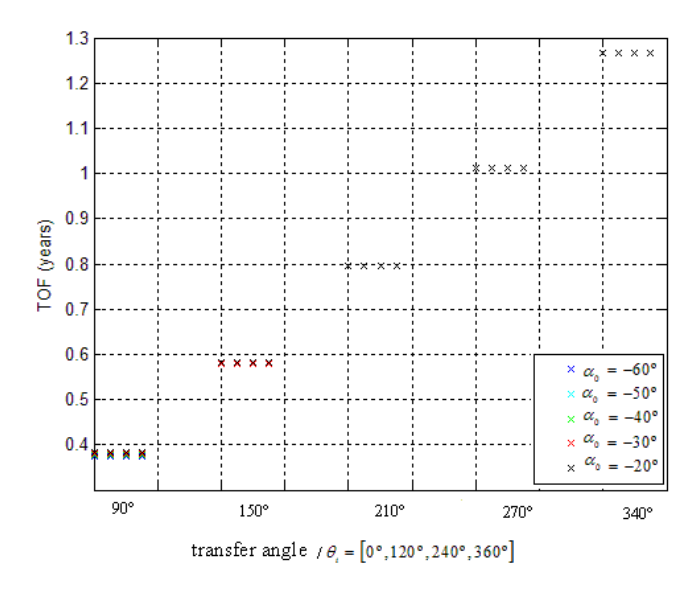


Figure 7.18: TOF for θ_i values of (0°, 120°, 240°, 360°) from left to right in the figure, α_0 values of (-60°, -50°, -40°, -30°, -20°), $\Delta\theta$ values of (90°, 150°, 210°, 270°, 340°) (N=0), m=0.05, a_0 =0.11, acceleration inversely square case of the thrust profile (logarithmic spiral), Earth-Mars flight

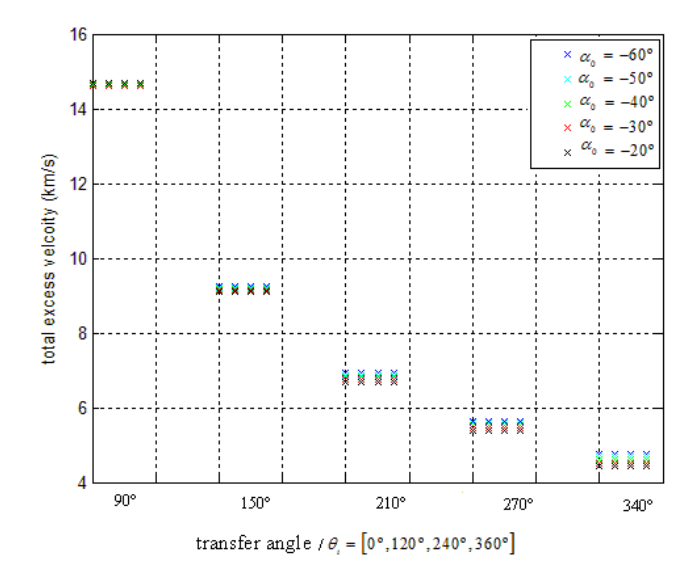


Figure 7.19: $V_{-,T}$ for θ_i values of (0°, 120°, 240°, 360°) from left to right in the figure, α_0 values of (-60°, -50°, -40°, -30°, -20°), $\Delta\theta$ values of (90°, 150°, 210°, 270°, 340°) (N=0), m=0.05, a_0 =0.11, acceleration inversely square case of the thrust profile (logarithmic spiral), Earth-Mars flight

By changing the initial polar angle θ_i (same transfer angle and α_0), the differences between values for the TOF and for the total excess velocity are significantly small. For increasing values of α_0 , the total excess velocity decreases, while the TOF increases. The total excess velocity differences between different values of α_0 increase when increasing the transfer angle $\Delta\theta$.

Similar figures can be shown for 1 and 2 revolutions, using the same values for the geometric parameter m, for the transfer angle $\Delta\theta$ and the initial values of α and θ . The normalised thrust acceleration a_0 values used in figures 7.20 and 7.21 were 0.03 and 0.02 for N=1 and N=2, respectively. Like for the Archimedean spiral, the values assumed for a_0 are the minimum values that can be used in both cases for this shape without facing integration problems for the interval of input parameters considered. The minimum values for a_0 were chosen because the total excess velocity increases when increasing the values of a_0 .

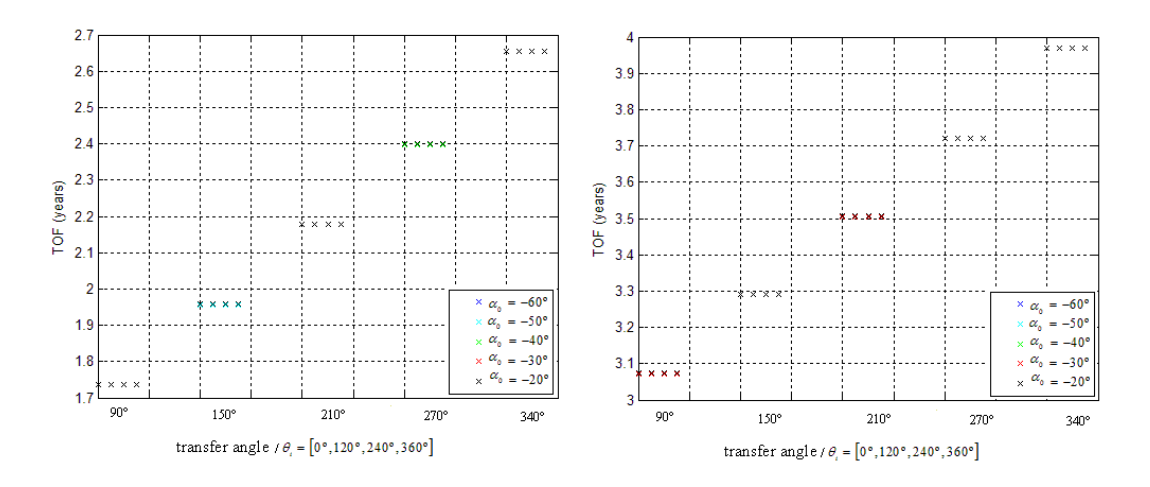


Figure 7.20: TOF for θ_i values of $(0^\circ, 120^\circ, 240^\circ, 360^\circ)$ from left to right in the figure, α_0 values of $(-60^\circ, -50^\circ, -40^\circ, -30^\circ, -20^\circ)$, $\Delta\theta$ values of $(90^\circ, 150^\circ, 210^\circ, 270^\circ, 340^\circ)$, m=0.05, acceleration inversely square case of the thrust profile (logarithmic spiral), Earth-Mars flight, N=1 (a_0 =0.03), N=2 (a_0 =0.02)

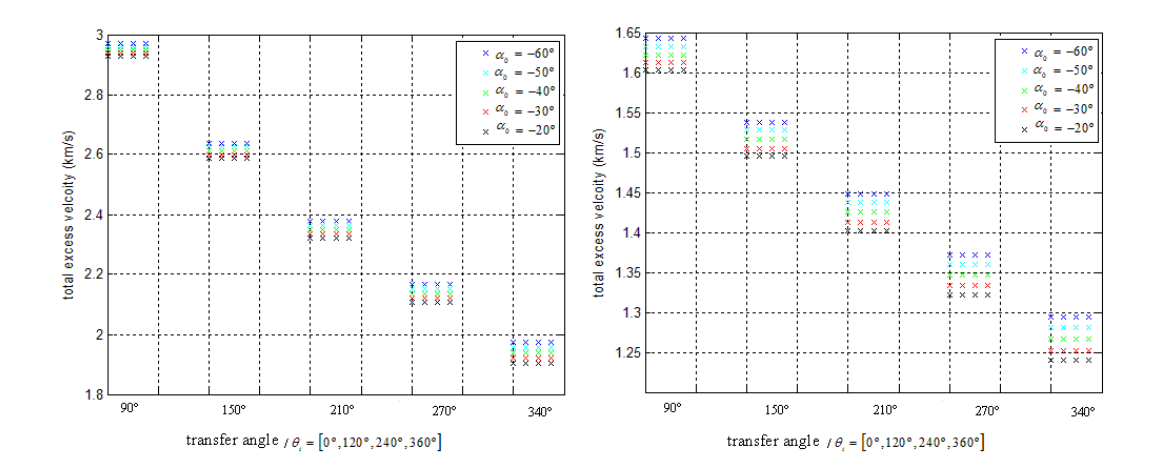


Figure 7.21: $V_{\omega,T}$ for θ_i values of $(0^\circ, 120^\circ, 240^\circ, 360^\circ)$ from left to right in the figure, α_0 values of $(-60^\circ, -50^\circ, -40^\circ, -30^\circ, -20^\circ)$, $\Delta\theta$ values of $(90^\circ, 150^\circ, 210^\circ, 270^\circ, 340^\circ)$, m=0.05, acceleration inversely square case of the thrust profile (logarithmic spiral), Earth-Mars flight, N=1 (a_0 =0.03), N=2 (a_0 =0.02)

Similar remarks to the ones given for N=0 can be drawn for figures 7.20 and 7.21. As for the Archimedean spiral, due to the very small influence that the parameter θ_i has on the TOF, total excess velocity variation and thrust acceleration (although not shown in previous figures), this parameter will not be considered a variable in the optimisation procedure for an Earth-Mars flight in chapter 8.

The TOF range for this Earth-Mars flight is from 0.3758 years to 3.9702 years. The total excess velocity has a minimum value of $1.2397 \, km/s$ and a maximum value of $14.6815 \, km/s$. As expected, the minimum value for the TOF and the maximum value for the total excess velocity occur for the smallest transfer angle -90° (N=0); while the maximum value for the TOF and the minimum value for the total excess velocity occur for the highest transfer angle presented -340° (N=2).

The maximum differences in TOF between two consecutive values of the transfer angle $\Delta\theta$ are about 0.25 years. The differences in terms of total excess velocity between two consecutive transfer angles is always highest between $\Delta\theta = 90^{\circ}$ and $\Delta\theta = 150^{\circ}$. The maximum value for these differences is $5.5853 \, km/s$ for zero value of N and the minimum value is about $77.25 \, m/s$ for 2 revolutions.

Tables 7.5 and 7.6 show the values for the TOF and the excess velocities for an Earth-Mars flight. Parameter θ_i was assumed 0°, parameter α_0 was assumed -20°, the transfer angle $\Delta\theta$ was assumed 90° and the number of revolutions taken was one for the first table and two for the second one. In tables 7.5 and 7.6, the normalised thrust acceleration a_0 considered was 0.05.

N=1	m = 0.05	m = 0.15	m = 0.25	m = 0.35	m = 0.45
$V_{\infty,total}\left(km/s\right)$	3.0424	2.9825	3.2022	3.6382	4.2179
$V_{\infty,1}(km/s)$	1.6543	1.1005	0.7265	0.4975	0.3723
$V_{\infty,2}(km/s)$	1.3881	1.8820	2.4757	3.1407	3.8457
TOF (years)	1.7136	1.6421	1.5782	1.5235	1.4784

Table 7.5: The excess velocities and the TOF values for N=1, θ_i =0°, $\Delta\theta$ =90°, α_0 =-20°, a_0 =0.05, m values of (0.05; 0.15; 0.25; 0.35; 0.45), acceleration inversely square case of the thrust profile (logarithmic spiral), Earth-Mars flight

N=2	m = 0.05	m = 0.15	m = 0.25	m = 0.35	m = 0.45
$V_{\infty,total}\left(km/s\right)$	1.8191	1.9659	2.5192	3.2448	4.0104
$V_{\infty,1}(km/s)$	0.8131	0.4281	0.2955	0.2643	0.2570
$V_{\infty,2}(km/s)$	1.0060	1.5378	2.2238	2.9805	3.7534
TOF (years)	3.0225	2.8173	2.6613	2.5531	2.4800

Table 7.6: The excess velocities and the TOF values for N=2, θ_i =0°, $\Delta\theta$ =90°, α_0 =-20°, a_0 =0.05, m values of (0.05; 0.15; 0.25; 0.35; 0.45), acceleration inversely square case of the thrust profile (logarithmic spiral), Earth-Mars flight

From tables 7.5 and 7.6, for increasing values of m, the total excess velocity increases for N=2, while the TOF decreases. For N=1, the total excess velocity decreases between m=0.05 and m=0.15, while for higher values of m, it increases. Note that, the excess velocity $V_{\infty,1}$ decreases slower than the excess velocity $V_{\infty,2}$ increases, except for N=1 between m=0.05 and m=0.15. The value of $V_{\infty,2}$ when m=0.45 is more than 10 times higher than the value of $V_{\infty,1}$ for N=1 and more than 14 times higher for N=2. This situation is attractive for a mission where swing-bys are used instead of orbit insertion (section 7.7).

In figures 7.22 to 7.26, the polar plot, the thrust acceleration a, the thrust angle α , the polar angle rate $\dot{\theta}$ and the flight path angle as function of time are illustrated for N=1 and N=2 cases that were presented in tables 7.5 and 7.6.

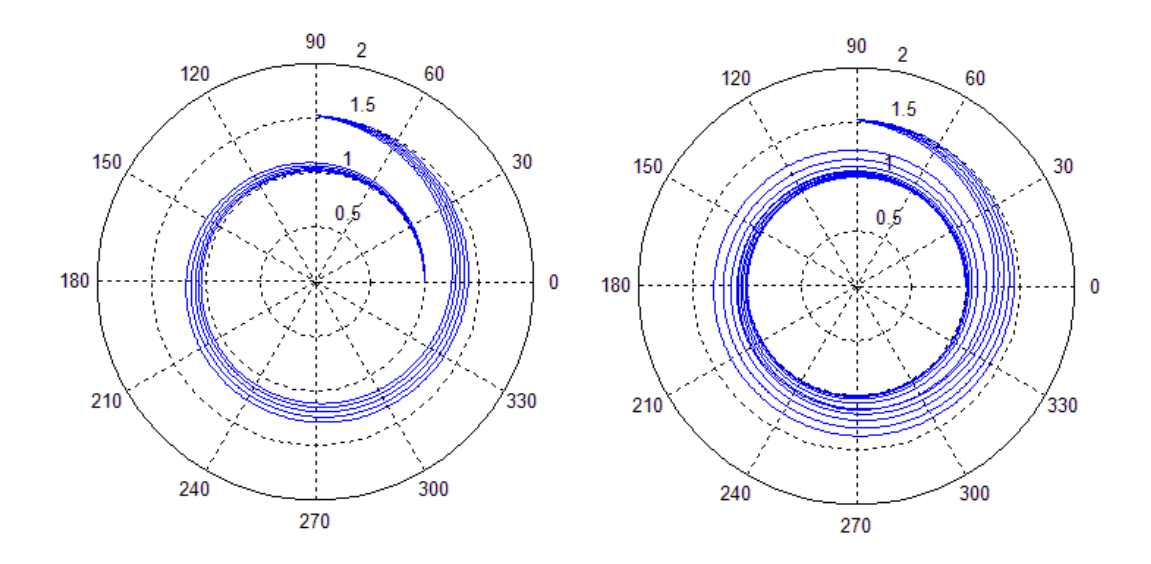


Figure 7.22: Polar plot for N=1 and N=2, θ_i =0°, $\Delta\theta$ =90°, α_0 =-20°, a_0 =0.05, m values of (0.05; 0.15; 0.25; 0.35; 0.45), acceleration inversely square case of the thrust profile (logarithmic spiral), Earth-Mars flight

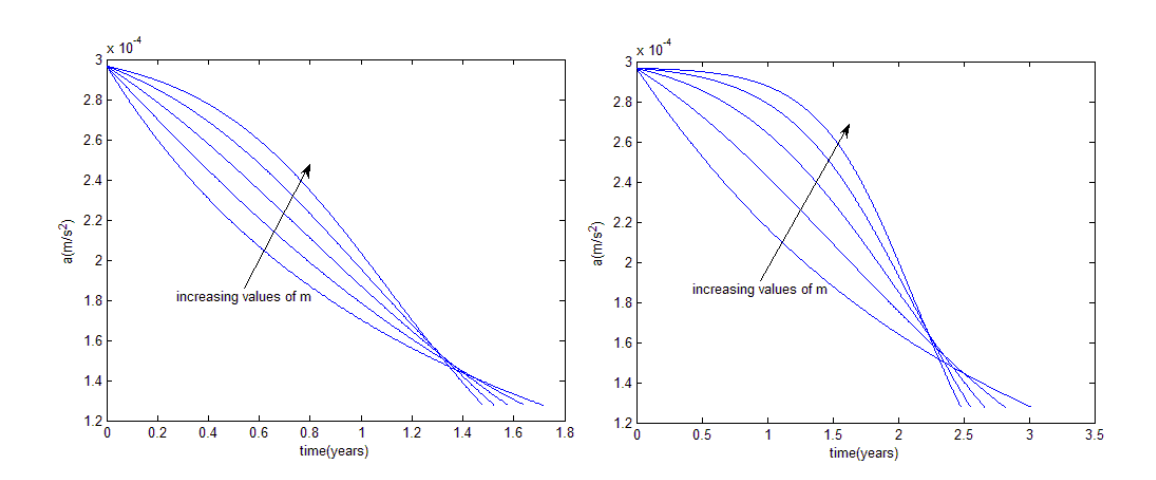


Figure 7.23: a plot for N=1 and N=2, θ_i =0°, $\Delta\theta$ =90°, α_0 =-20°, a_0 =0.05, m values of (0.05; 0.15; 0.25; 0.35; 0.45), acceleration inversely square case of the thrust profile (logarithmic spiral), Earth-Mars flight

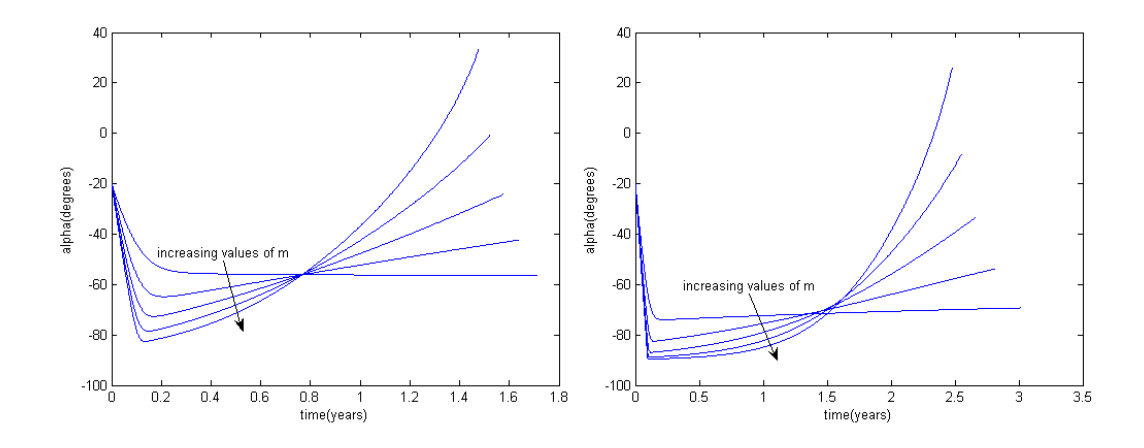


Figure 7.24: α plot for N=1 and N=2, θ_i =0°, $\Delta\theta$ =90°, α_0 =-20°, a_0 =0.05, m values of (0.05; 0.15; 0.25; 0.35; 0.45), acceleration inversely square case of the thrust profile (logarithmic spiral), Earth-Mars flight

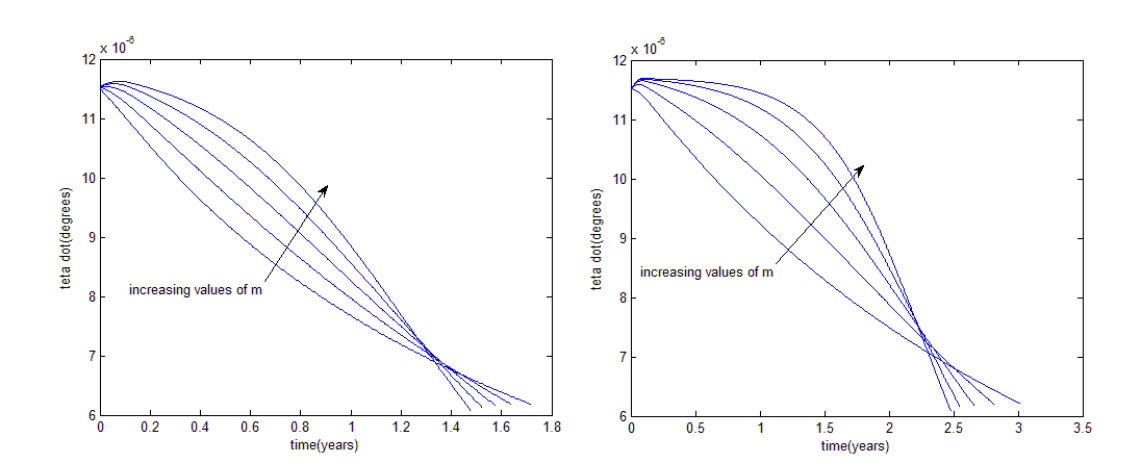


Figure 7.25: $\dot{\theta}$ plot for N=1 and N=2, θ_i =0°, $\Delta\theta$ =90°, α_0 =-20°, a_0 =0.05, m values of (0.05; 0.15; 0.25; 0.35; 0.45), acceleration inversely square case of the thrust profile (logarithmic spiral), Earth-Mars flight

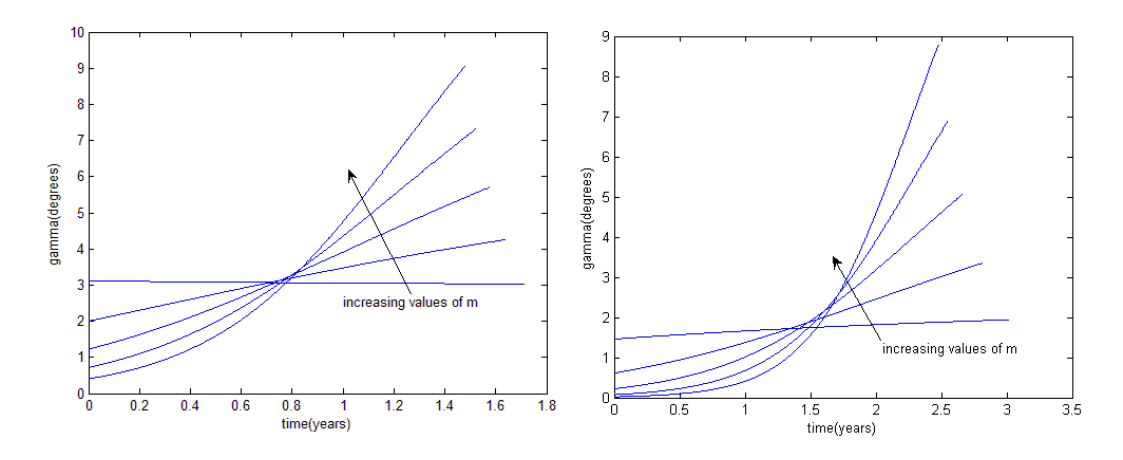


Figure 7.26: γ plot for N=1 and N=2, θ_i =0°, $\Delta\theta$ =90°, α_0 =-20°, a_0 =0.05, m values of (0.05; 0.15; 0.25; 0.35; 0.45), acceleration inversely square case of the thrust profile (logarithmic spiral), Earth-Mars flight

Note that, although the assumed normalised thrust acceleration a_0 is the same for N=1 and for N=2, differences in the instantaneous thrust acceleration values between the two cases can be seen in figure 7.23. During the interplanetary flight for both cases in figure 7.24, the spacecraft is thrusting inwards in the radial direction, while in the tangential direction it thrusts in the positive direction (α is negative, higher than -90°), like for the Archimedean spiral.

b) Tangential Case of the Thrust Profile

Figures 7.27 and 7.28 show the TOF and the total excess velocity when changing parameter θ_i and the transfer angle $\Delta\theta$, when the number of revolutions N is 0. Values of (0.05; 0.15; 0.25; 0.35; 0.45), (0°, 120°, 240°, 360°) and (90°, 150°, 210°, 270°, 340°) were used in these figures for the geometric parameter m, for the initial polar angle θ_i and for the transfer angle $\Delta\theta$, respectively.

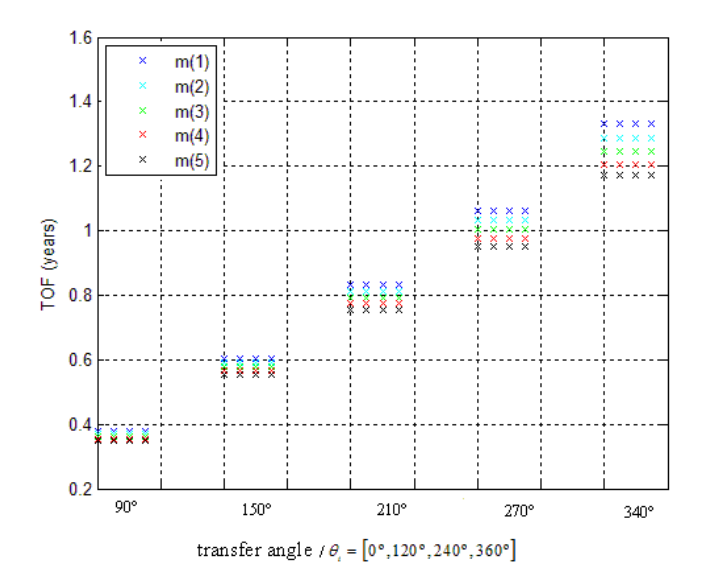


Figure 7.27: TOF for θ_i values of $(0^\circ, 120^\circ, 240^\circ, 360^\circ)$ from left to right in the figure, m values of (0.05; 0.15; 0.25; 0.35; 0.45), $\Delta\theta$ values of $(90^\circ, 150^\circ, 210^\circ, 270^\circ, 340^\circ)$ (N=0), tangential thrust profile (logarithmic spiral), Earth-Mars flight

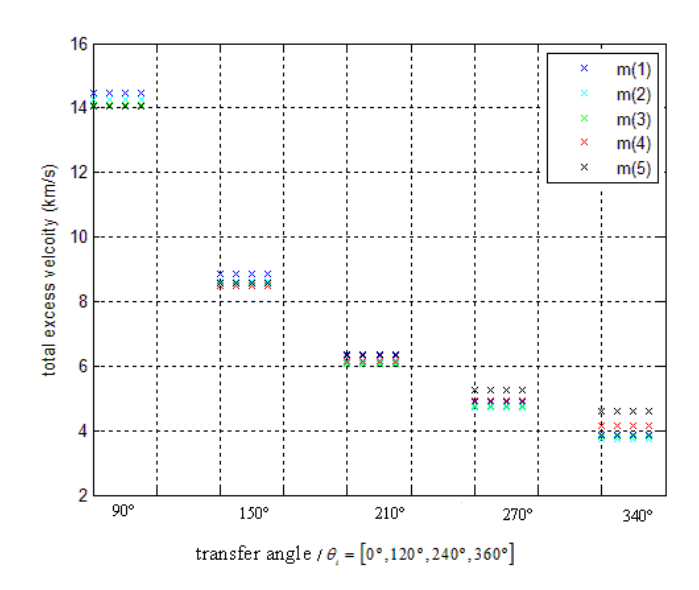


Figure 7.28: $V_{\omega,T}$ for θ_i values of (0°, 120°, 240°, 360°) from left to right in the figure, m values of (0.05; 0.15; 0.25; 0.35; 0.45), $\Delta\theta$ values of (90°, 150°, 210°, 270°, 340°) (N=0), tangential thrust profile (logarithmic spiral), Earth-Mars flight

Some remarks can be drawn from figures 7.27 and 7.28. By changing the initial polar angle θ_i , the differences between values for the TOF and for the total excess velocity are again very small, like for the acceleration inversely square case. For increasing values of m, the

TOF decreases while the total excess velocity increases for transfer angles higher than 210° (inclusive) and it decreases for transfer angles smaller than 210°.

Similar figures can be shown for 1 and 2 revolutions, using the same values for the geometric parameter m, for the transfer angle $\Delta\theta$ and for the initial value of θ (θ_i) as the ones used for N=0.

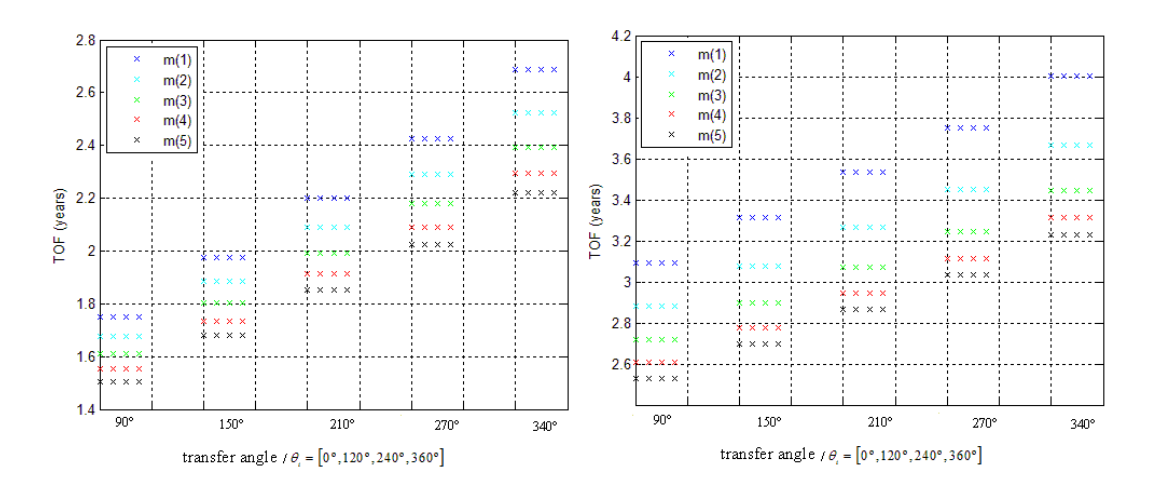


Figure 7.29: TOF for θ_i values of (0°, 120°, 240°, 360°) from left to right in the figure, m values of (0.05; 0.15; 0.25; 0.35; 0.45), $\Delta\theta$ values of (90°, 150°, 210°, 270°, 340°), tangential thrust profile (logarithmic spiral), Earth-Mars flight for N=1 and N=2

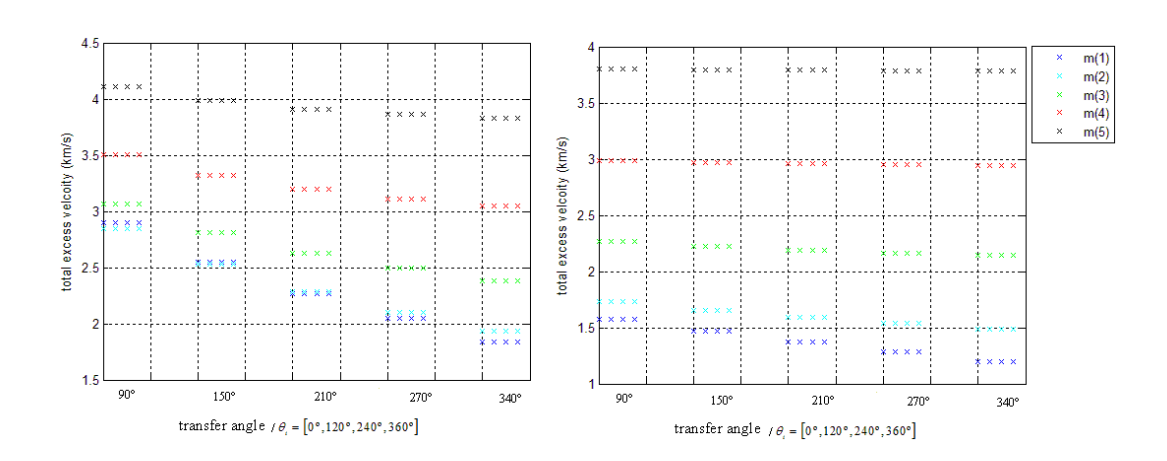


Figure 7.30: $V_{_{\infty,T}}$ for $\theta_{_i}$ values of (0°, 120°, 240°, 360°) from left to right in the figure, m values of (0.05; 0.15; 0.25; 0.35; 0.45), $\Delta\theta$ values of (90°, 150°, 210°, 270°, 340°), tangential thrust profile (logarithmic spiral), Earth-Mars flight for N=1 and N=2

Similar remarks to the ones given for N=0 can be drawn for figures 7.29 and 7.30. For higher values of N, the differences in total excess velocity and in TOF, between the minimum and the maximum values of m, increase.

The TOF range from Earth-Mars is from 0.3482 years to 4.0022 years. The total excess velocity has a minimum value of $1.2004\,km/s$ and a maximum value of $14.4610\,km/s$. The maximum differences in TOF between two consecutive values of the transfer angle $\Delta\theta$ are about 0.27 years. The differences in terms of total excess velocity between two consecutive transfer angles is always highest between $\Delta\theta=90^\circ$ and $\Delta\theta=150^\circ$. The maximum value for these differences is $5.6372\,km/s$ for N=0 and the minimum value is of $1.9360\,m/s$ for 2 revolutions.

Tables 7.7 and 7.8 show the values for the TOF and the excess velocity for an Earth-Mars flight. Parameter θ_i was consider 0°, the transfer angle $\Delta\theta$ was consider 90° and the number of revolutions was taken 1 for the first table and 2 for the second one.

N=1	m = 0.05	m = 0.15	m = 0.25	m = 0.35	m = 0.45
$V_{\infty,total}(km/s)$	2.8972	2.8423	3.0621	3.5041	4.1119
$V_{\infty,1}(km/s)$	1.6212	1.0440	0.6422	0.3793	0.2165
$V_{\infty,2}(km/s)$	1.2761	1.7983	2.4199	3.1248	3.8955
TOF (years)	1.7492	1.6758	1.6093	1.5517	1.5033

Table 7.7: Excess velocities and TOF values for N=1, θ_i =0°, $\Delta\theta$ =90°, m values of (0.05; 0.15; 0.25; 0.35; 0.45), tangential thrust profile (logarithmic spiral), Earth-Mars flight

N=2	m = 0.05	m = 0.15	m = 0.25	m = 0.35	m = 0.45
$V_{\infty,total}(km/s)$	1.5781	1.7360	2.2633	2.9881	3.8035
$V_{\infty,1}(km/s)$	0.7597	0.3201	0.1182	0.0397	0.0125
$V_{\infty,2}(km/s)$	0.8184	1.4159	2.1451	2.9485	3.7970
TOF (years)	3.0934	2.8823	2.7209	2.6079	2.5304

Table 7.8: Excess velocities and TOF values for N=2, θ_i =0°, $\Delta\theta$ =90°, m values of (0.05; 0.15; 0.25; 0.35; 0.45), tangential thrust profile (logarithmic spiral), Earth-Mars flight

For increasing values of m, the total excess velocity increases for N=2, while the TOF decreases. For N=1, the total excess velocity decreases between m = 0.05 and m = 0.15, while it increases for higher values of m. Normally for longer missions (higher TOF), the total excess velocity decreases. This does not happen between m = 0.05 and m = 0.15 for N=1. As for the previous situations, the values for the total excess velocity are higher when N=1 than when N=2. Note that, like for the acceleration inversely square case, the excess velocity $V_{\infty,2}$ increases faster than the excess velocity $V_{\infty,1}$ decreases, except for N=1 between m = 0.05 and m = 0.15. The value of $V_{\infty,2}$ when m = 0.45 is more than 17 times higher than the value of $V_{\infty,1}$ for N=1 and more than 300 times higher for N=2. Compared with the acceleration inversely square case, the TOF and the total excess velocity values from tables 7.7 and 7.8 are higher and smaller, respectively for the tangential case. For values of m higher than 0.45, the total excess velocity increases. For m=1 and N=2, the total excess velocity is $8.8950 \, km/s$ and for m = 1.5, the total excess velocity is 14.7330 km/s. These values are too high to be considered in a mission from Earth-Mars, when doing orbit insertion, but they still can be used for flybys. Note that for higher values of m, the order of magnitude of $V_{\infty,1}$ is $10^{-2} \, km/s$ or less and $V_{\infty,2}$ is approximately $V_{\infty,T}$. Unfortunately, for values of m higher than 1, the thrust acceleration starts to increase significantly to orders of magnitude of $10^{-2} m/s^2$. These values of thrust acceleration correspond to the upper limit that can be used in a low-thrust mission. In this way and since feasible shapes can always be computed if |m| < 1 (see section 6.3.2), values of m

higher than 1 in the optimisation procedure for an Earth-Mars flight (chapter 8) will not be considered.

In figures 7.31 to 7.34, the polar plot, the thrust acceleration a, the thrust angle α and the polar angle rate $\dot{\theta}$ as function of time are illustrated for the cases N=1 and N=2 that were presented in tables 7.7 and 7.8.

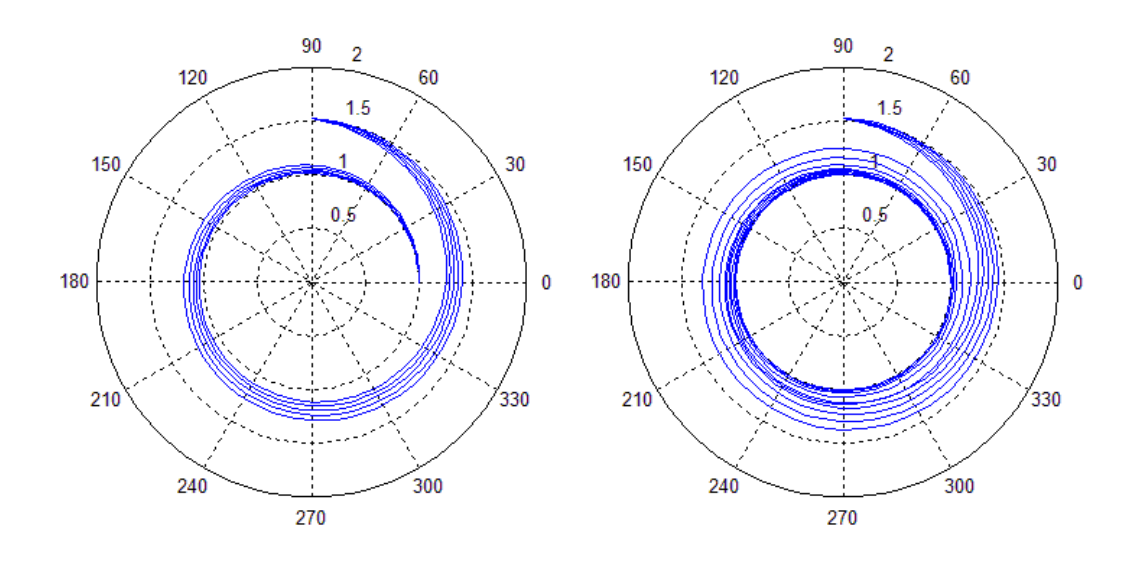


Figure 7.31: Polar plot for N=1 and N=2, θ_i =0°, $\Delta\theta$ =90°, m values of (0.05; 0.15; 0.25; 0.35; 0.45), tangential thrust profile (logarithmic spiral), Earth-Mars flight

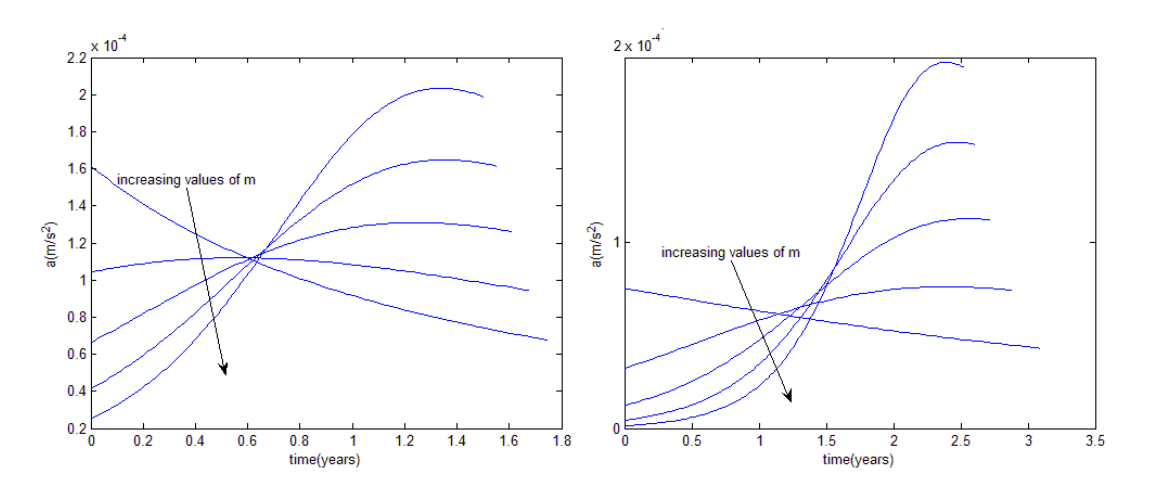


Figure 7.32: a plot for N=1 and N=2, θ_i =0°, $\Delta\theta$ =90°, m values of (0.05; 0.15; 0.25; 0.35; 0.45), tangential thrust profile (logarithmic spiral), Earth-Mars flight

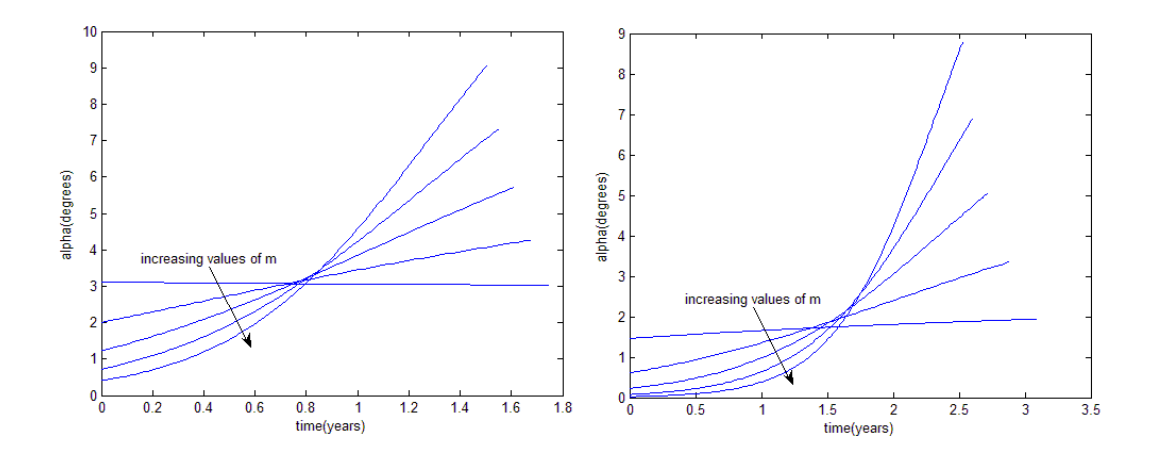


Figure 7.33: α plot for N=1 and N=2, θ_i =0°, $\Delta\theta$ =90°, m values of (0.05; 0.15; 0.25; 0.35; 0.45), tangential thrust profile (logarithmic spiral), Earth-Mars flight

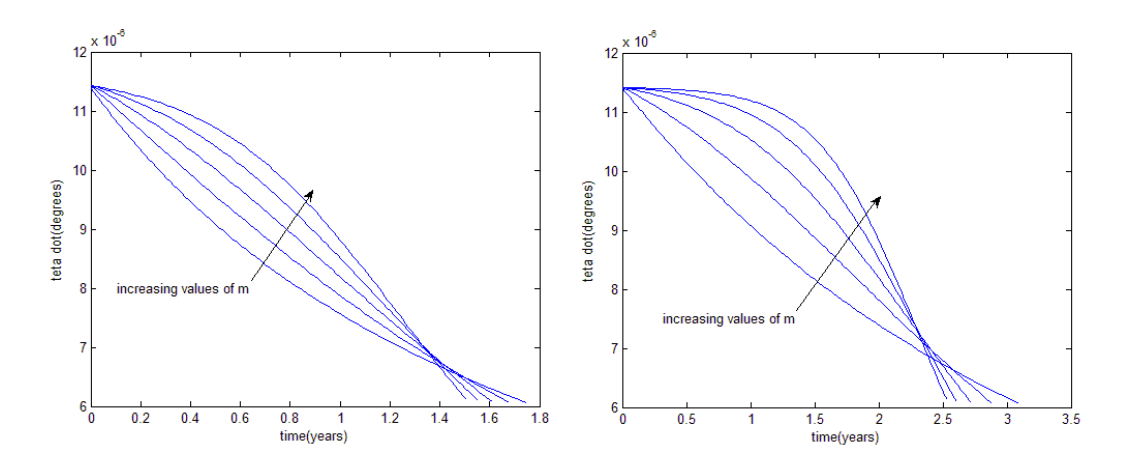


Figure 7.34: $\dot{\theta}$ plot for N=1 and N=2, θ_i =0°, $\Delta\theta$ =90°, m values of (0.05; 0.15; 0.25; 0.35; 0.45), tangential thrust profile (logarithmic spiral), Earth-Mars flight

From figure 7.32, the magnitude of the thrust acceleration is higher for N=1 than for N=2 for most of the interplanetary flights which means that the magnitude of the instantaneous thrust required for a longer flight is smaller. Except for m = 0.05, the thrust acceleration will increase during time until it reaches its maximum value almost in the end of the flight. Note that the differences between the maximum values of a for N=1 and N=2 are negligibly small. Although there are no significant differences between the maximum values for the thrust angle α for N=1 and for N=2, during most of the interplanetary flight, the values for this angle are smaller for N=2 than for N=1.

7.3. Poinsot's spiral (hyperbolic sine)

Results for the TOF, the excess velocities and the thrust acceleration will be shown and discussed for the Poinsot's spiral (hyperbolic sine) and for an Earth-Mars mission in this section. The thrust profiles used in this analysis are the same as the ones used for the shapes previously presented.

a) Acceleration Inversely Square Case of the Thrust Profile

The TOF and the total excess velocity when changing parameter $\theta_i + \phi$ and the transfer angle $\Delta\theta$ (N=0) are shown in figures 7.35 and 7.36. The value used for m in figures 7.35 and 7.36 was 0.6, the values used for the initial polar angle combined with the phase angle $\theta_i + \phi$ were (120°, 200°, 280°, 360°) and the values for α_0 and $\Delta\theta$ were the same as for the previous shapes. Note that $\theta_i + \phi$ cannot be zero, otherwise $r = \infty$. The value for the normalised thrust acceleration a_0 value used in figures 7.35 and 7.36 was 0.11.

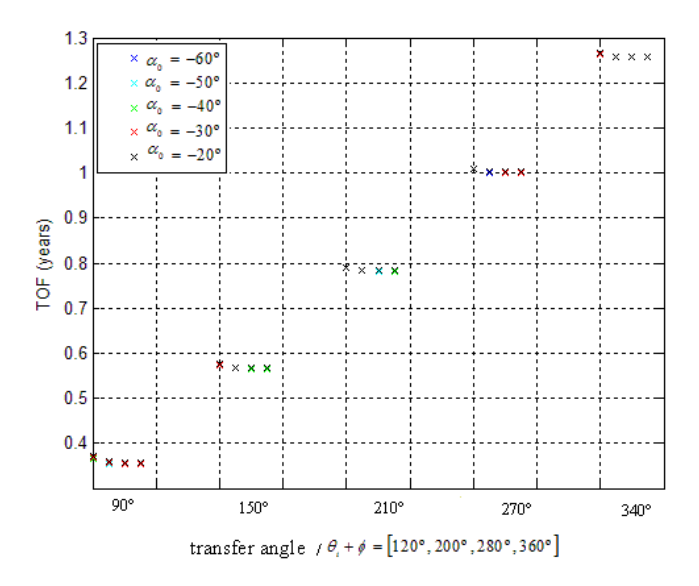


Figure 7.35: TOF for $\theta_{_{i}}+\phi$ values of (120°, 200°, 280°, 360°) from left to right in the figure, $\alpha_{_{0}}$ values of (-60°, -50°, -40°, -30°, -20°), $\Delta\theta$ values of (90°, 150°, 210°, 270°, 340°) (N=0), m=0.6, $a_{_{0}}$ =0.11, acceleration inversely square case (Poinsot's spiral (hyperbolic sine)), Earth-Mars flight

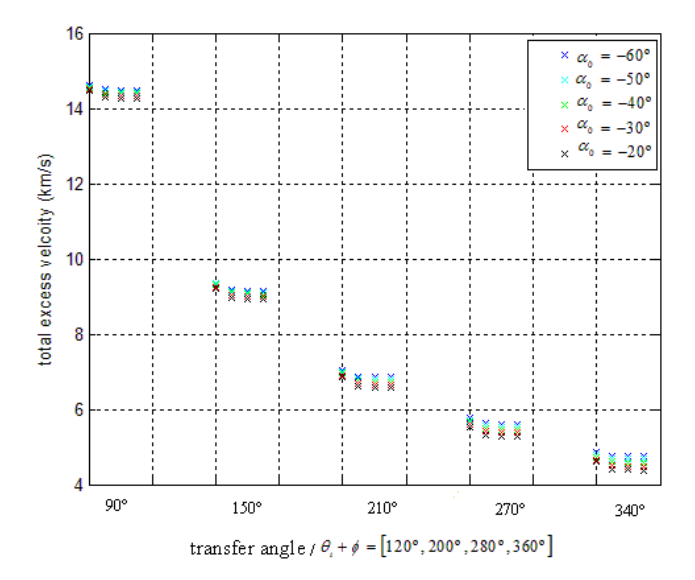


Figure 7.36: $V_{\omega,T}$ for $\theta_+ + \phi$ values of (120°, 200°, 280°, 360°) from left to right in the figure, α_0 values of (-60°, -50°, -40°, -30°, -20°), $\Delta\theta$ values of (90°, 150°, 210°, 270°, 340°) (N=0), m=0.6, a_0 =0.11, acceleration inversely square case (Poinsot's spiral (hyperbolic sine)), Earth-Mars flight

From figures 7.35 and 7.36, by increasing the combination of angles $\theta_i + \phi$, the TOF and the total excess velocity decrease. The highest difference in TOF and in total excess velocity between different $\theta_i + \phi$ occurs between $\theta_i + \phi = 120^\circ$ and $\theta_i + \phi = 200^\circ$. For higher values of $\theta_i + \phi$, the variations in TOF and in total excess velocity are very small. The highest difference in TOF between different $\theta_i + \phi$ for the same transfer angle and α_0 is about 0.014 years, while the highest difference in total excess velocity is about 0.2941km/s. For increasing values of the initial thrust angle α_0 , the total excess velocity decreases, while the TOF increases.

Similar figures can be shown for 1 and 2 revolutions, using the same values for m, for $\Delta\theta$ and for the initial values of α and $\theta+\phi$. The normalised thrust acceleration a_0 values used in figures 7.37 and 7.38 were 0.03 and 0.02 for N=1 and N=2, respectively. Similar remarks as the ones given for N=0 can be drawn for figures 7.37 and 7.38.

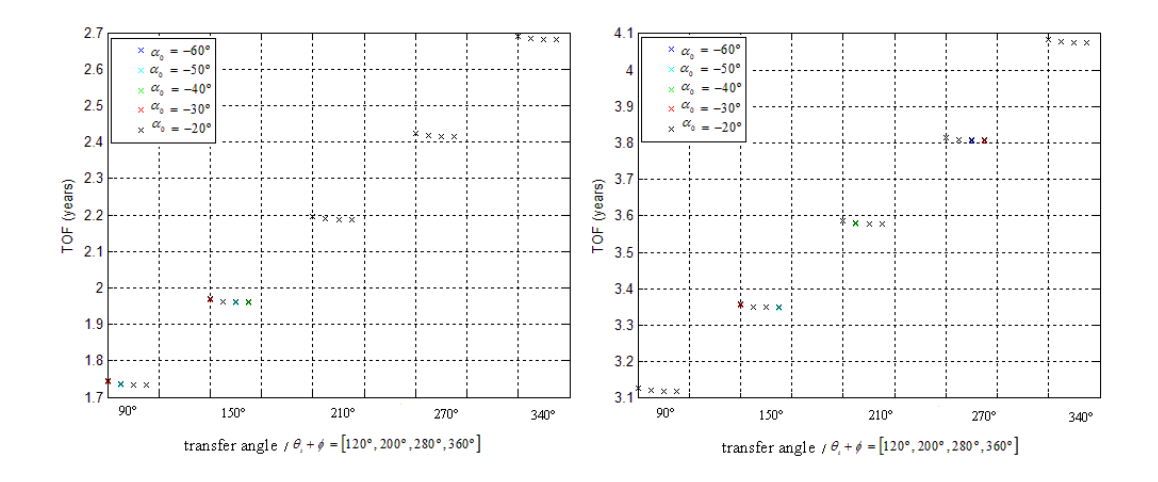


Figure 7.37: TOF for $\theta_i + \phi$ values of (120°, 200°, 280°, 360°) from left to right in the figure, α_0 values of (-60°, -50°, -40°, -30°, -20°), $\Delta\theta$ values of (90°, 150°, 210°, 270°, 340°), m=0.6, acceleration inversely square case (Poinsot's spiral (hyperbolic sine), Earth-Mars flight, N=1 (α_0 =0.03) and N=2 (α_0 =0.02)

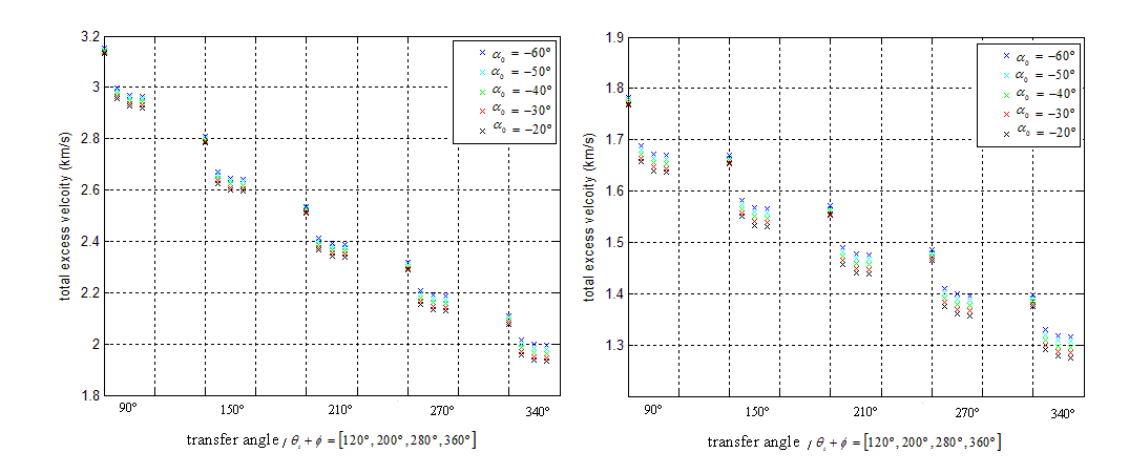


Figure 7.38: $V_{\omega,T}$ for $\theta_1 + \phi$ values of (120°, 200°, 280°, 360°) from left to right in the figure, α_0 values of (-60°, -50°, -40°, -30°, -20°), $\Delta\theta$ values of (90°, 150°, 210°, 270°, 340°), m=0.6, acceleration inversely square case (Poinsot's spiral (hyperbolic sine), Earth-Mars flight, N=1 (a_0 =0.03) and N=2 (a_0 =0.02)

The TOF range for an Earth-Mars flight is from 0.3531 years to 4.0842 years. The total excess velocity has a minimum value of $1.2754\,km/s$ and a maximum value of $14.5992\,km/s$. The maximum differences in TOF between two consecutive values of the transfer angle $\Delta\theta$ are about 0.27 years and for a certain number of revolutions, these differences increase when increasing the transfer angle. The differences in terms of total excess velocity between two consecutive transfer angles is always highest between $\Delta\theta = 90^\circ$ and $\Delta\theta = 150^\circ$, as for the previous situations. The maximum value for these

differences is $5.3522 \, km/s$ for N=0 and the minimum value is about $79 \, m/s$ for 2 revolutions.

Tables 7.9 and 7.10 show the values for the TOF and the excess velocities for an Earth-Mars flight. Parameter $\theta_i + \phi$ was consider 120°, parameter α_0 was consider -20°, the transfer angle $\Delta\theta$ was consider 90° and the number of revolutions taken was 1 for the first table and 2 for the second one. In table 7.9, the normalised thrust acceleration a_0 was 0.05, while in table 7.10, this parameter was 0.04.

N=1	m = 0.01	m = 0.11	m = 0.21	m = 0.31	m = 0.41
$V_{\infty,total}\left(km/s\right)$	4.6793	4.4645	4.0855	3.7452	3.4989
$V_{\infty,1}(km/s)$	3.8225	3.4865	2.9270	2.4680	2.1601
$V_{\infty,2}(km/s)$	0.8568	0.9780	1.1584	1.2772	1.3388
TOF (years)	1.8760	1.8354	1.7868	1.7536	1.7347

Table 7.9: The excess velocities and the TOF values for N=1, $\theta_i + \phi = 120^\circ$, $\Delta\theta = 90^\circ$, m values of (0.01; 0.11; 0.21; 0.31; 0.41), $\alpha_0 = -20^\circ$, $a_0 = 0.05$, acceleration inversely square case (Poinsot's spiral (hyperbolic sine)), Earth-Mars flight

N=2	m = 0.01	m = 0.11	m = 0.21	m = 0.31	m = 0.41
$V_{\infty,total}\left(km/s\right)$	3.4777	3.0791	2.5845	2.2606	2.0680
$V_{\infty,1}(km/s)$	2.9203	2.4177	1.8182	1.4476	1.2351
$V_{\infty,2}(km/s)$	0.5574	0.6613	0.7663	0.8130	0.8329
TOF (years)	3.4155	3.3009	3.1894	3.1353	3.1103

Table 7.10: The excess velocities and the TOF values for N=2, $\theta_i + \phi$ =120°, $\Delta\theta$ =90°, m values of (0.01; 0.11; 0.21; 0.31; 0.41), α_0 =-20°, a_0 =0.04, acceleration inversely square case (Poinsot's spiral (hyperbolic sine)), Earth-Mars flight

For increasing values of m, the total excess velocity and the TOF decrease. Note that the excess velocity $V_{\infty,1}$ decreases faster than the excess velocity $V_{\infty,2}$ increases, as for the Archimedean spiral.

In figures 7.39 to 7.43, the polar plot, the thrust acceleration a, the thrust angle α , the polar angle rate $\dot{\theta}$ and the flight path angle as function of time are illustrated for N=1 and N=2 cases that were presented in tables 7.9 and 7.10.

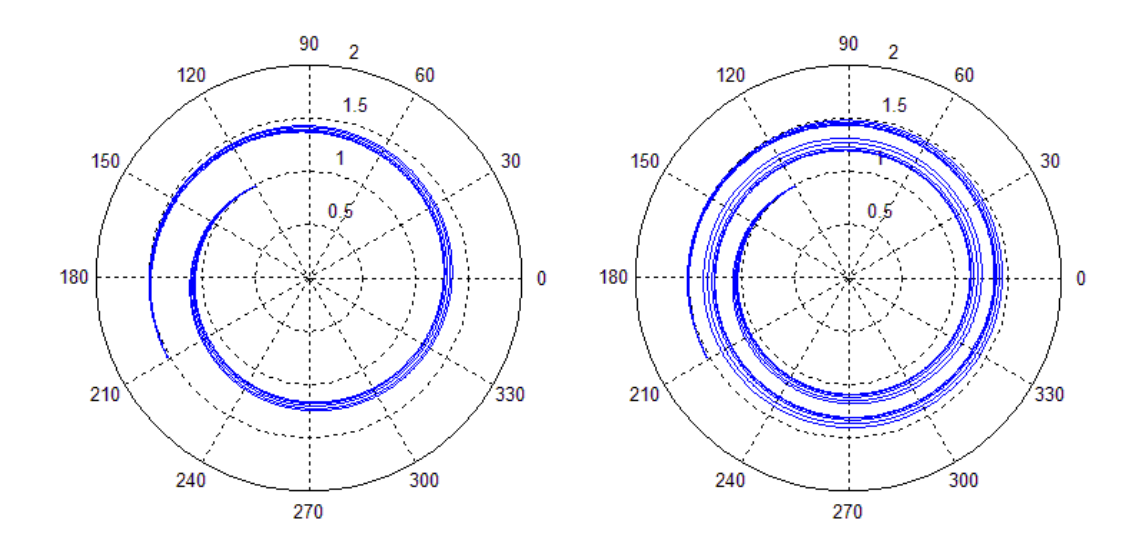


Figure 7.39: Polar plot for N=1 (a_0 =0.05) and N=2 (a_0 =0.04), θ_i + ϕ =120°, $\Delta\theta$ =90°, m values of (0.01; 0.11; 0.21; 0.31; 0.41), α_0 =-20°, acceleration inversely square case (Poinsot's spiral (hyperbolic sine)), Earth-Mars flight

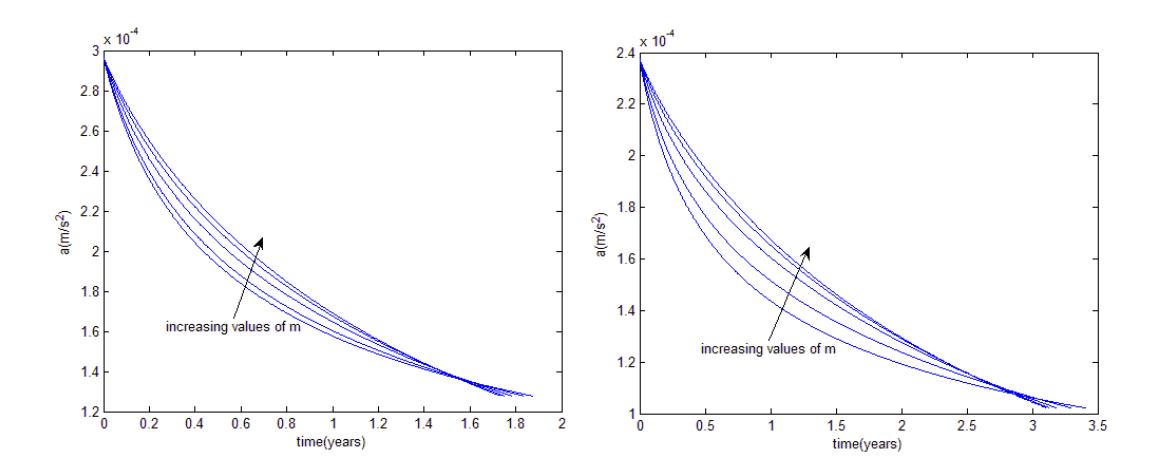


Figure 7.40: a plot for N=1 (a_0 =0.05) and N=2 (a_0 =0.04), θ_i + ϕ =120°, $\Delta\theta$ =90°, m values of (0.01; 0.11; 0.21; 0.31; 0.41), α_0 =-20°, acceleration inversely square case (Poinsot's spiral (hyperbolic sine)), Earth-Mars flight

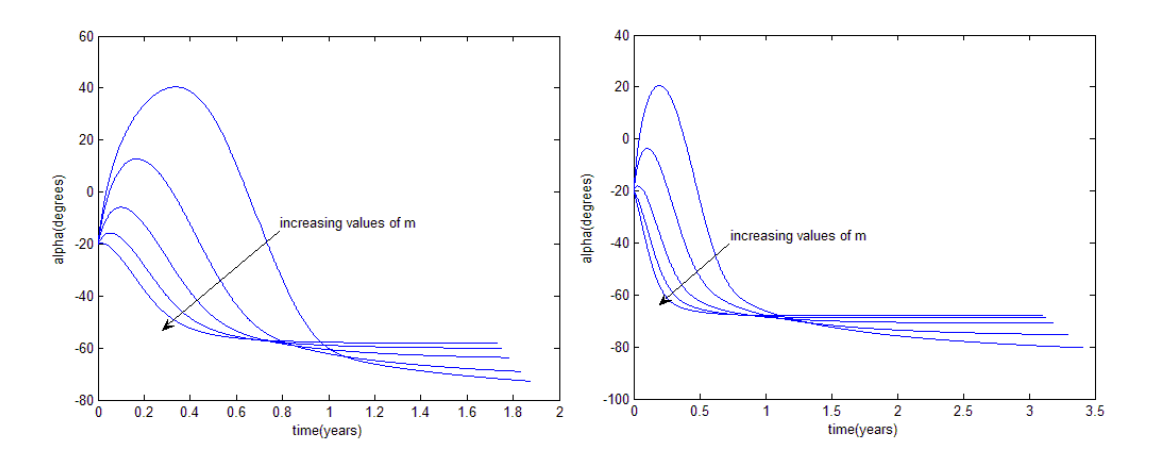


Figure 7.41: α plot for N=1 (a_0 =0.05) and N=2 (a_0 =0.04), θ_i + ϕ =120°, $\Delta\theta$ =90°, m values of (0.01; 0.11; 0.21; 0.31; 0.41), α_0 =-20°, acceleration inversely square case (Poinsot's spiral (hyperbolic sine)), Earth-Mars flight

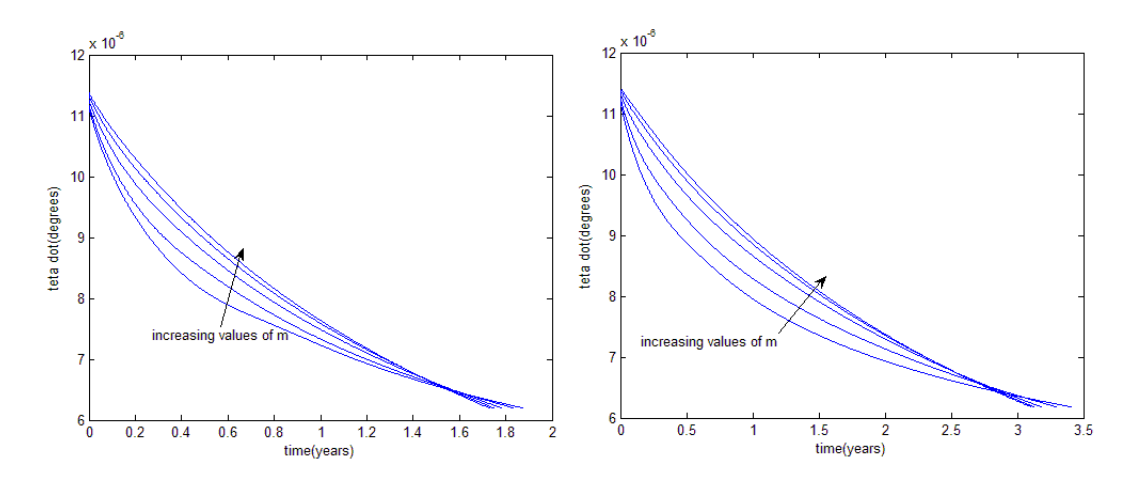


Figure 7.42: $\dot{\theta}$ plot for N=1 (a_0 =0.05) and N=2 (a_0 =0.04), θ_i + ϕ =120°, $\Delta\theta$ =90°, m values of (0.01; 0.11; 0.21; 0.31; 0.41), α_0 =-20°, acceleration inversely square case (Poinsot's spiral (hyperbolic sine)), Earth-Mars flight

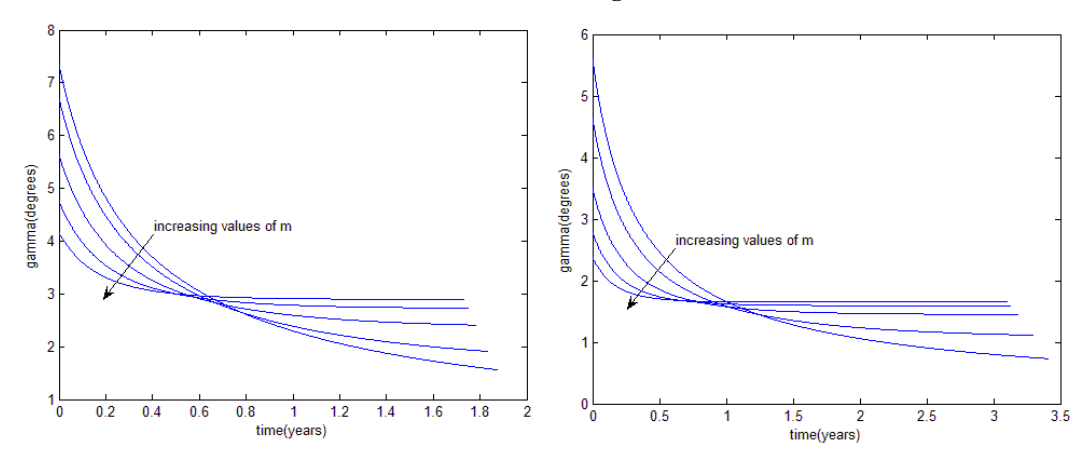


Figure 7.43: γ plot for N=1 (a_0 =0.05) and N=2 (a_0 =0.04), θ_i + ϕ =120°, $\Delta\theta$ =90°, m values of (0.01; 0.11; 0.21; 0.31; 0.41), α_0 =-20°, acceleration inversely square case (Poinsot's spiral (hyperbolic sine)), Earth-Mars flight

From figure 7.40, the magnitude of the thrust acceleration is higher for N=1 than for N=2 because the assumed normalised thrust acceleration a_0 is also higher for N=1 than for N=2. Note that the thrust acceleration trend is similar to the $\dot{\theta}$ trend, as already seen for the previous shapes and explained for the Archimedean spiral. The values of the thrust angle α are higher for N=1 than for N=2. For most of the interplanetary flight, for both cases in figure 7.41, the spacecraft is thrusting inwards in the radial direction, while in the tangential direction it thrusts in the positive direction (α is negative, higher than -90°),

like for the previous shapes. This situation will be further analysed in section 7.7. The magnitude values of the flight path angle γ are smaller for N=2 than for N=1.

b) Tangential Case of the Thrust Profile

Figures 7.44 and 7.45 show the TOF and the total excess velocity when varying parameter $\theta_i + \phi$ and the transfer angle $\Delta\theta$ (N=0). The values used in these figures for m, for the initial angle $\theta_i + \phi$ and the transfer angle $\Delta\theta$ were the same as the ones used for the acceleration inversely square case.

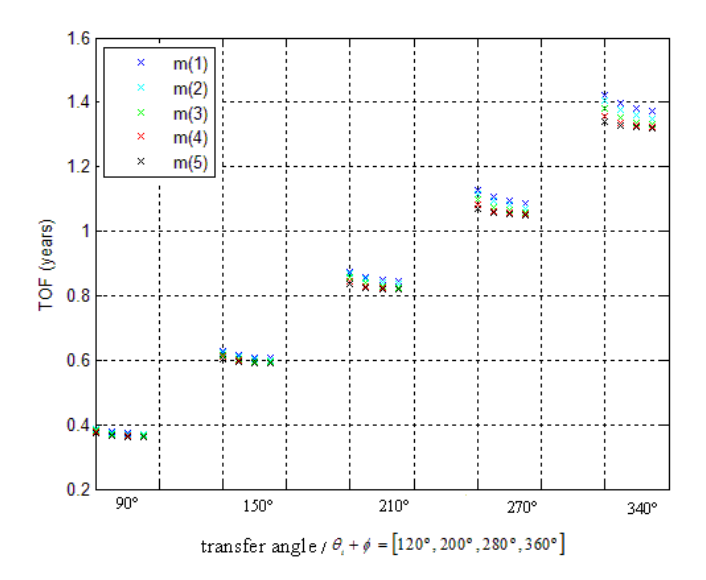


Figure 7.44: TOF for $\theta_i + \phi$ values of (120°, 200°, 280°, 360°) from left to right in the figure, m values of (0.01; 0.11; 0.21; 0.31; 0.41), $\Delta\theta$ values of (90°, 150°, 210°, 270°, 340°), (N=0), tangential thrust profile (Poinsot's spiral (hyperbolic sine)), Earth-Mars flight

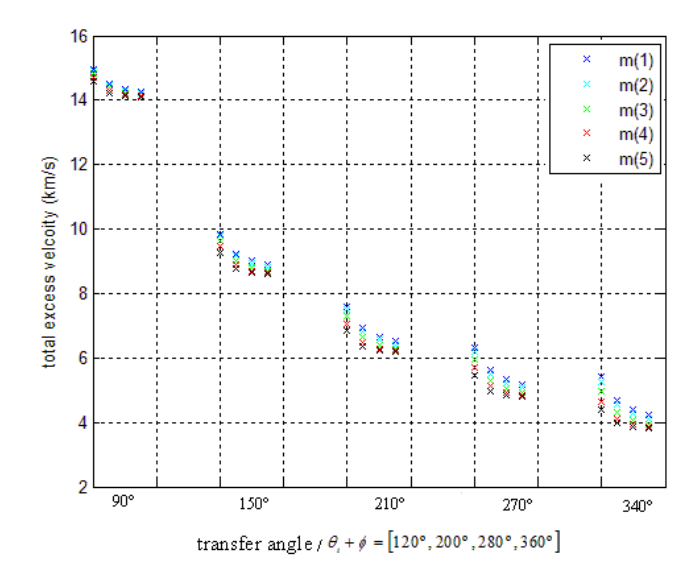


Figure 7.45: $V_{_{\infty,T}}$ for $\theta_{_i}+\phi$ values of (120°, 200°, 280°, 360°) from left to right in the figure, m values of (0.01; 0.11; 0.21; 0.31; 0.41), $\Delta\theta$ values of (90°, 150°, 210°, 270°, 340°), (N=0), tangential thrust profile (Poinsot's spiral (hyperbolic sine)), Earth-Mars flight

From figures 7.44 and 7.45, by increasing the initial angle $\theta_i + \phi$, the TOF and the total excess velocity decrease as for the acceleration inversely square case. The differences in TOF and in total excess velocity between different values of m decrease when increasing $\theta_i + \phi$. The highest difference in TOF between different $\theta_i + \phi$ for the same transfer angle and m is 0.0567 years, while the highest difference in total excess velocity is $1.1630 \, km/s$, which are higher compared with the acceleration inversely square case. The differences in TOF and in total excess velocity between different values of m increase when increasing the transfer angle $\Delta\theta$.

Similar figures can be shown for 1 and 2 revolutions, using the same values for the geometric parameter m, for the transfer angle $\Delta\theta$ and for $(\theta_i + \phi)$ as the ones used for N=0.

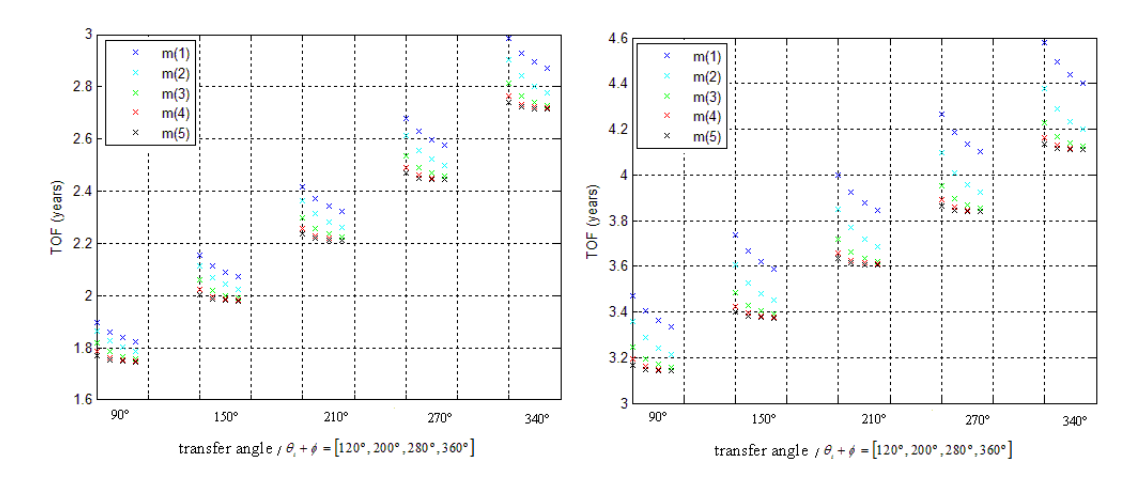


Figure 7.46: TOF for $\theta_i + \phi$ values of (120°, 200°, 280°, 360°) from left to right in the figure, m values of (0.01; 0.11; 0.21; 0.31; 0.41), $\Delta\theta$ values of (90°, 150°, 210°, 270°, 340°), tangential thrust profile (Poinsot's spiral (hyperbolic sine)), Earth-Mars flight, N=1 and N=2

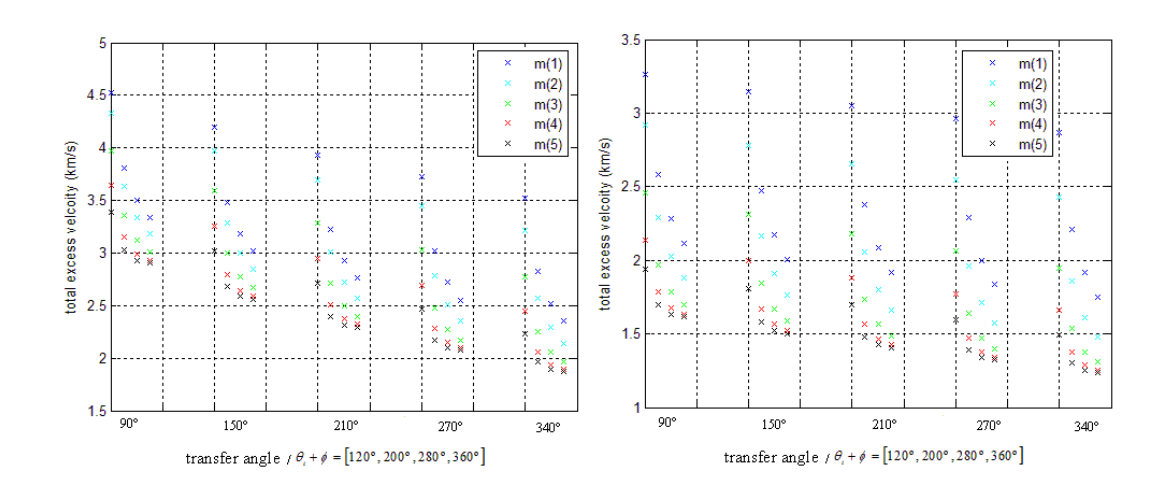


Figure 7.47: $V_{_{\infty,T}}$ for $\theta_{_i}+\phi$ values of (120°, 200°, 280°, 360°) from left to right in the figure, m values of (0.01; 0.11; 0.21; 0.31; 0.41), $\Delta\theta$ values of (90°, 150°, 210°, 270°, 340°), tangential thrust profile (Poinsot's spiral (hyperbolic sine)), Earth-Mars flight N=1 and N=2

Similar remarks to the ones given for N=0 can be drawn for figures 7.46 and 7.47, when in this case for N=1, the highest difference in TOF between different $\theta_i + \phi$ and for the same transfer angle is about 0.1229 years, while the highest difference in total excess velocity is 1.1776 km/s. For N=2, the highest difference in the TOF between different $\theta_i + \phi$ and for the same transfer angle and m is about 0.1763 years, while the highest difference in the total excess velocity is 1.1487 km/s. Compared with the acceleration inversely square case, these differences are much higher. So, in the tangential case, the results for the TOF and

the total excess velocity are more sensitive to the $\theta_i + \phi$ variation. Note that the differences between the total excess velocity and the TOF values for different values of m increase between N=1 and N=2.

The TOF range for an Earth-Mars flight is from 0.3615 years to 4.5782 years. The total excess velocity has a minimum value of $1.2349 \, km/s$ and a maximum value of $14.9404 \, km/s$. The maximum differences in TOF between two consecutive values of the transfer angle $\Delta\theta$ are about 0.31 years and for a certain number of revolutions, these differences increase when increasing the transfer angle. The differences in terms of total excess velocity between two consecutive transfer angles is always highest between $\Delta\theta = 90^{\circ}$ and $\Delta\theta = 150^{\circ}$, like for the previous shapes. The maximum value for these differences is $5.4909 \, km/s$ for N=0 and the minimum value is $81.22 \, m/s$ for N=2.

Tables 7.11 and 7.12 show the values for the TOF and the excess velocity for an Earth-Mars flight. Parameter $\theta_i + \phi$ was assumed 120°, the transfer angle $\Delta\theta$ was assumed 90° and the number of revolutions was taken 1 for the first table and 2 for the second one.

N=1	m = 0.01	m = 0.11	m = 0.21	m = 0.31	m = 0.41
$V_{\infty,total}(km/s)$	4.5194	4.3276	3.9723	3.6403	3.3924
$V_{\infty,1}(km/s)$	3.8617	3.5236	2.9584	2.4908	2.1731
$V_{\infty,2}(km/s)$	0.6577	0.8040	1.0139	1.1495	1.2194
TOF (years)	1.8957	1.8658	1.8204	1.7882	1.7697

Table 7.11: Excess velocities and TOF values for N=1, $\theta_i + \phi = 120^\circ$, $\Delta \theta = 90^\circ$, m values of (0.01; 0.11; 0.21; 0.31; 0.41), tangential thrust profile (Poinsot's spiral (hyperbolic sine)), Earth-Mars flight

N=2	m = 0.01	m = 0.11	m = 0.21	m = 0.31	m = 0.41
$V_{\infty,total}(km/s)$	3.2626	2.9186	2.4547	2.1354	1.9391
$V_{\infty,1}(km/s)$	2.9545	2.4497	1.8440	1.4651	1.2437
$V_{\infty,2}(km/s)$	0.3080	0.4689	0.6106	0.6704	0.6953
TOF (years)	3.4695	3.3579	3.2465	3.1920	3.1668

Table 7.12: Excess velocities and TOF values for N=2, $\theta_i + \phi = 120^\circ$, $\Delta \theta = 90^\circ$, m values of (0.01; 0.11; 0.21; 0.31; 0.41), tangential thrust profile (Poinsot's spiral (hyperbolic sine)), Earth-Mars flight

For increasing values of m, the total excess velocity and the TOF decrease. Note that, like for the acceleration inversely square case, the excess velocity $V_{\infty,1}$ decreases faster than the excess velocity $V_{\infty,2}$ increases. Compared with this previous case of the thrust profile, the values for the TOF and the total excess velocity given in tables 7.11 and 7.12 are higher and smaller, respectively, as for the previous shapes.

In figures 7.48 to 7.51, the polar plot, the thrust acceleration a, the thrust angle α and the polar angle rate $\dot{\theta}$ as function of time are illustrated for N=1 and N=2 cases that were presented in tables 7.11 and 7.12.

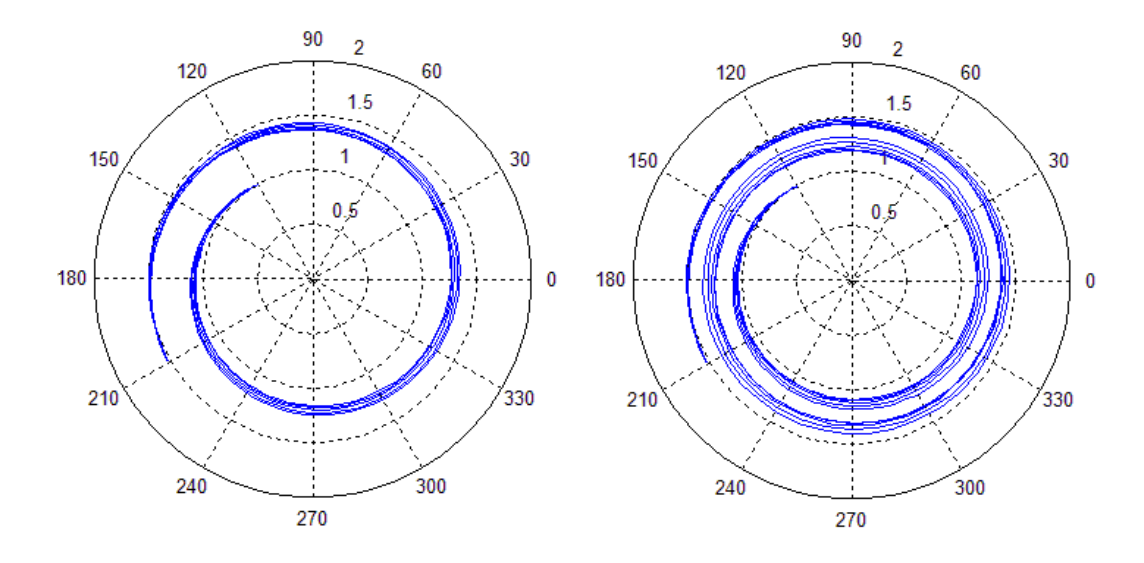


Figure 7.48: Polar plot for N=1 and N=2, $\theta_i + \phi = 120^\circ$, $\Delta \theta = 90^\circ$, m values of (0.01; 0.11; 0.21; 0.31; 0.41), tangential thrust profile (Poinsot's spiral (hyperbolic sine)), Earth-Mars flight

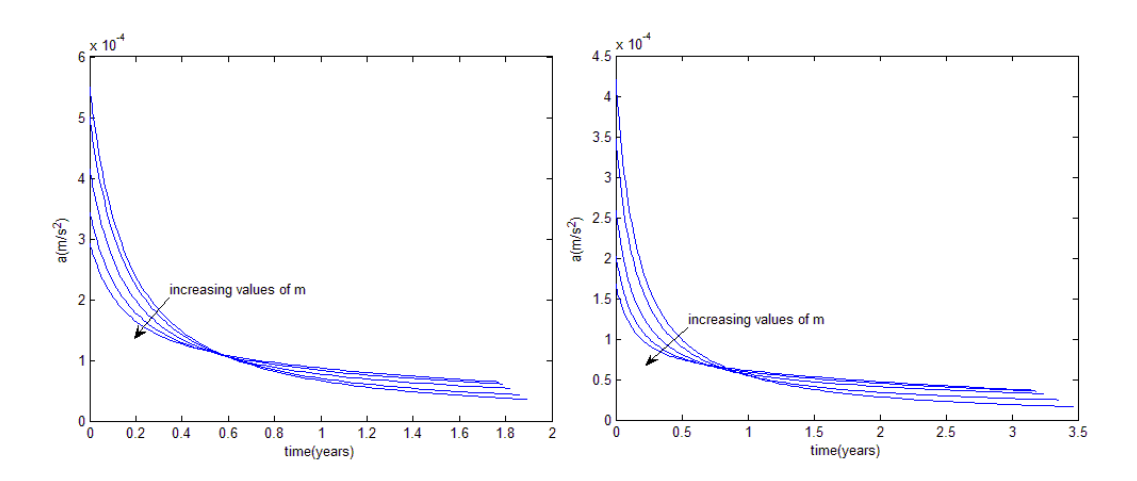


Figure 7.49: a plot for N=1 and N=2, $\theta_i + \phi = 120^\circ$, $\Delta\theta = 90^\circ$, m values of (0.01; 0.11; 0.21; 0.31; 0.41), tangential thrust profile (Poinsot's spiral (hyperbolic sine)), Earth-Mars flight

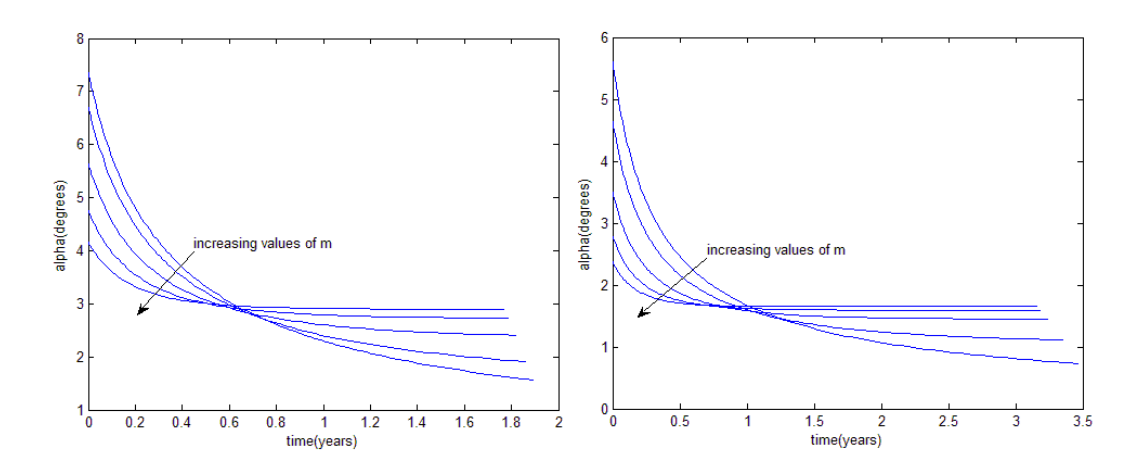


Figure 7.50: α plot for N=1 and N=2, $\theta_i + \phi = 120^\circ$, $\Delta \theta = 90^\circ$, m values of (0.01; 0.11; 0.21; 0.31; 0.41), tangential thrust profile (Poinsot's spiral (hyperbolic sine)), Earth-Mars flight

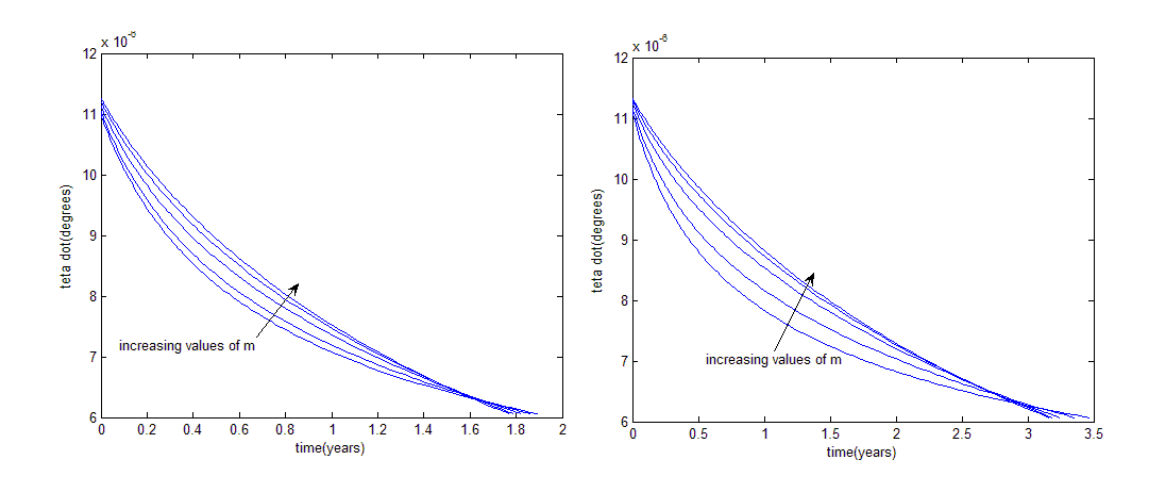


Figure 7.51: $\dot{\theta}$ plot for N=1 and N=2, $\theta_i + \phi = 120^\circ$, $\Delta \theta = 90^\circ$, m values of (0.01; 0.11; 0.21; 0.31; 0.41), tangential thrust profile (Poinsot's spiral (hyperbolic sine)), Earth-Mars flight

The magnitude of the thrust acceleration is higher for N=1 than for N=2 which means that the magnitude of the instantaneous thrust required for a longer flight is smaller. Also, the values for the thrust angle α are smaller for N=2 than for N=1.

7.4. Poinsot's spiral (hyperbolic cosine)

In this section 7.4, results for the TOF, the excess velocities and the thrust acceleration will be shown and discussed for the Poinsot's spiral (hyperbolic cosine) and for an Earth-Mars

mission. The thrust profiles used in this analysis are the same as the ones used for the shapes previously presented.

a) Acceleration Inversely Square Case of the Thrust Profile

Figures 7.52 and 7.53 show the TOF and the total excess velocity when varying parameter θ_i and the transfer angle $\Delta\theta$, when the number of revolutions N is 0. The value used in figures 7.52 and 7.53 for m was 0.05, for a_0 was 0.09, the values for α_0 were (-60°, -50°, -40°, -30°, -20°), for the initial polar angle θ_i were (30°, 140°, 250°, 340°) and for the transfer angle $\Delta\theta$ were (90°, 150°, 210°, 270°, 340°).

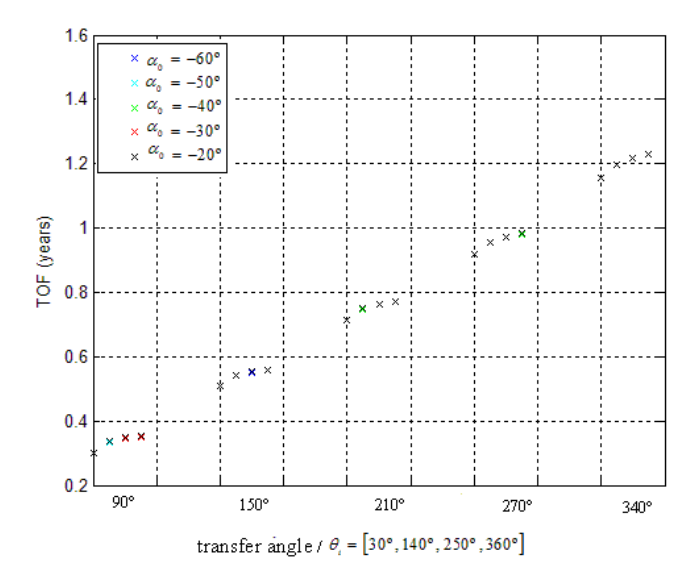


Figure 7.52: TOF for θ_i values of (30°, 140°, 250°, 340°) from left to right in the figure, α_0 values of (-60°, -50°, -40°, -30°, -20°), $\Delta\theta$ values of (90°,150°,210°,270°,340°) (N=0), m=0.05, a_0 =0.09, acceleration inversely square case (Poinsot's spiral (hyperbolic cosine)), Earth-Mars flight

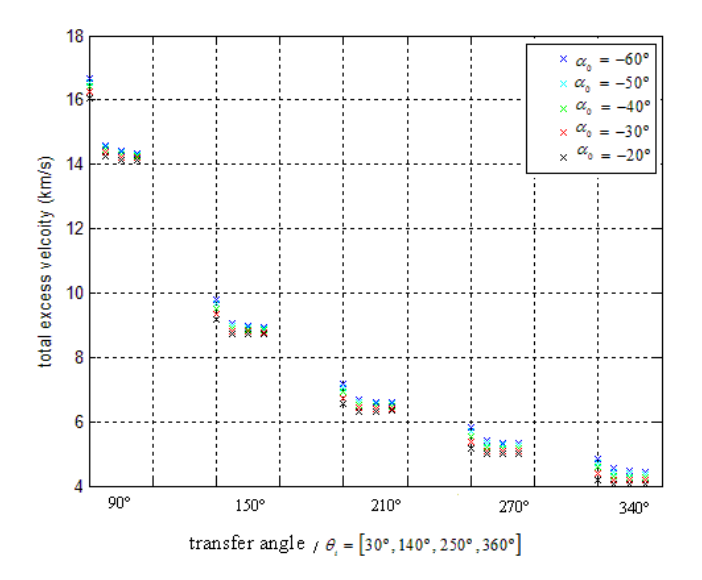


Figure 7.53: $V_{\circ,T}$ for θ_i values of (30°, 140°, 250°, 340°) from left to right in the figure, α_0 values of (-60°, -50°, -40°, -30°, -20°), $\Delta\theta$ values of (90°,150°,210°,270°,340°) (N=0), m=0.05, a_0 =0.09, acceleration inversely square case (Poinsot's spiral (hyperbolic cosine)), Earth-Mars flight

Some remarks can be drawn from figures 7.52 and 7.53. As expected, the TOF increases when increasing the transfer angle, while the total excess velocity decreases. By increasing the initial polar angle θ_i , the TOF increases while the total excess velocities decreases. The highest variation in TOF and in total excess velocity when changing θ_i is between $\theta_i = 30^\circ$ and $\theta_i = 140^\circ$, as for the Poinsot's spiral (hyperbolic sine). This variation becomes smaller for higher values of the transfer angle $\Delta\theta$. The highest difference in TOF between different θ_i for the same transfer angle and α_0 is 0.0747 years, while the highest difference in total excess velocity is 2.3111 km/s. For increasing values of α_0 , the total excess velocity decreases and the TOF increases.

Figures 7.54 and 7.55 show the TOF and the total excess velocity for 1 and 2 revolutions, using the same values for m, for $\Delta\theta$, for α_0 and θ_i as for the situation where N=0. The normalised thrust acceleration a_0 values used in these figures were 0.04 and 0.03 for N=1 and N=2, respectively.

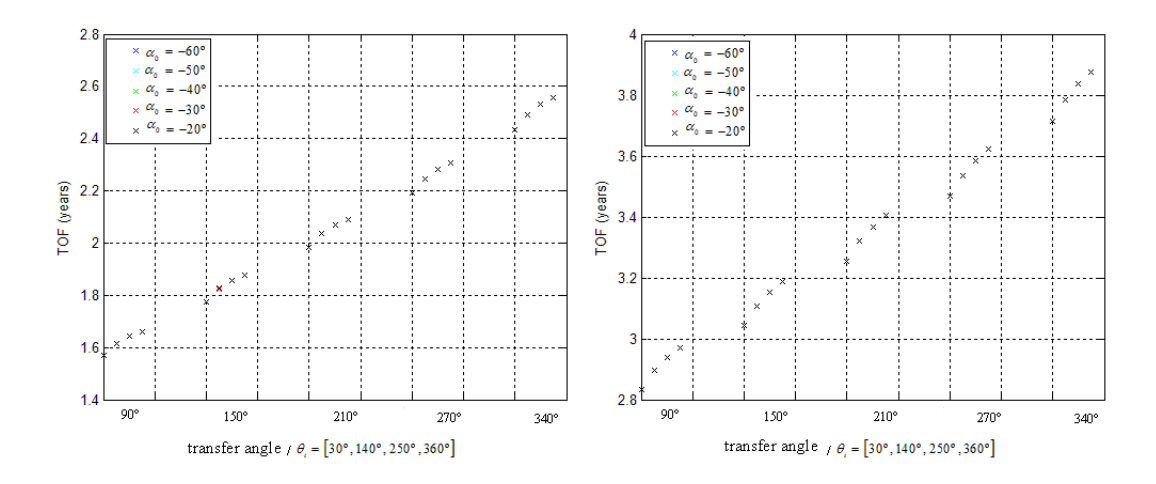


Figure 7.54: TOF for θ_i values of (30°, 140°, 250°, 340°) from left to right in the figure, α_0 values of (-60°, -50°, -40°, -30°, -20°), $\Delta\theta$ values of (90°, 150°, 210°, 270°, 340°), m=0.05, acceleration inversely square case (Poinsot's spiral (hyperbolic cosine), Earth-Mars flight, N=1 (α_0 =0.04) and N=2 (α_0 =0.03)

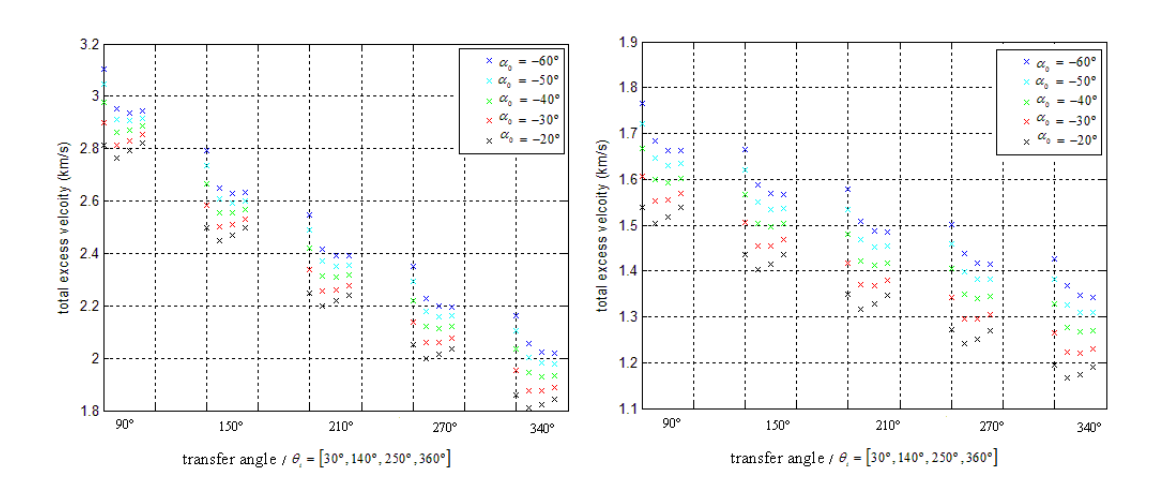


Figure 7.55: $V_{\circ,T}$ for θ_i values of (30°, 140°, 250°, 340°) from left to right in the figure, α_0 values of (-60°, -50°, -40°, -30°, -20°), $\Delta\theta$ values of (90°, 150°, 210°, 270°, 340°), m=0.05, acceleration inversely square case (Poinsot's spiral (hyperbolic cosine), Earth-Mars flight, N=1 (a_0 =0.04) and N=2 (a_0 =0.03)

Similar remarks as the ones given for N=0 can be drawn for figures 7.54 and 7.55. In figure 7.55, when increasing θ_i , for highest value of α_0 the total excess velocity trend is not monotonous. For N=1, the highest difference in TOF between different θ_i and for the same transfer angle and α_0 is about 0.1238 years, while the highest difference in the total excess velocity is $0.1662 \, km/s$. For N=2, the highest difference in TOF between different θ_i and for the same transfer angle and α_0 is about 0.1609 years, while the highest

difference in total excess velocity is $0.1026 \, km/s$. In this way, for increasing values of N, the TOF becomes more sensitive to θ_i changes, while the total excess velocity becomes less sensitive to these changes.

The TOF range for this Earth-Mars flight is from 0.2986 years to 3.8762 years. The total excess velocity has a minimum value of $1.1663 \, km/s$ and a maximum value of $16.6570 \, km/s$. The maximum differences in TOF between two consecutive values of the transfer angle $\Delta \theta$ are about 0.25 years. For a certain number of revolutions, these differences increase when increasing the transfer angle. The differences in terms of total excess velocity between two consecutive transfer angles is always highest between $\Delta \theta = 90^{\circ}$ and $\Delta \theta = 150^{\circ}$. The maximum value for these differences is $6.8886 \, km/s$ for N=0 and the minimum value is about $70 \, m/s$ for 2 revolutions.

Tables 7.13 and 7.14 show the values for the TOF and the excess velocity for an Earth-Mars flight. Parameter θ_i was chosen 30°, parameter α_0 was chosen -20°, the transfer angle $\Delta\theta$ was chosen 90° and the number of revolutions was taken 1 for the first table and 2 for the second one. In table 7.13, the normalised thrust acceleration a_0 considered was 0.04, while in table 7.14, this parameter was 0.03.

N=1	m = 0.01	m = 0.11	m = 0.21	m = 0.31	m = 0.41
$V_{\infty,total}\left(km/s\right)$	2.8684	2.6493	2.4036	2.2976	2.2838
$V_{\infty,1}(km/s)$	0.4329	0.4653	0.5354	0.6228	0.7157
$V_{\infty,2}(km/s)$	2.4355	2.1841	1.8682	1.6748	1.5681
TOF (years)	1.5654	1.5830	1.6124	1.6379	1.6566

Table 7.13: The excess velocities and the TOF values for N=1, θ_i =30°, $\Delta\theta$ =90°, α_0 =-20°, m values of (0.01; 0.11; 0.21; 0.31; 0.41), a_0 =0.04, acceleration inversely square case (Poinsot's spiral (hyperbolic cosine), Earth-Mars flight

N=2	m = 0.01	m = 0.11	m = 0.21	m = 0.31	m = 0.41
$V_{\scriptscriptstyle{\infty,total}}\left(km/s ight)$	1.6262	1.3633	1.2393	1.2290	1.2540
$V_{\infty,1}(km/s)$	0.2212	0.2479	0.2964	0.3505	0.4052
$V_{\infty,2}(km/s)$	1.4050	1.1154	0.9430	0.8785	0.8488
TOF (years)	2.8141	2.8866	2.9606	3.0042	3.0302

Table 7.14: The excess velocities and the TOF values for N=2, θ_i =30°, $\Delta\theta$ =90°, α_0 =-20°, m values of (0.01; 0.11; 0.21; 0.31; 0.41), a_0 =0.03, acceleration inversely square case (Poinsot's spiral (hyperbolic cosine), Earth-Mars flight

From tables 7.13 and 7.14, the order of magnitude of the total excess velocity values is $10^0 \ km/s$. For increasing values of m, the total excess velocity decreases, while the TOF increases for N=1. For N=2, the total excess velocity decreases until m=0.31 and it increases between m=0.31 and m=0.41, while the TOF increases like for N=1. Note that the excess velocity $V_{\infty,2}$ decreases faster than the excess velocity $V_{\infty,1}$ increases, except for N=2 between m=0.31 and m=0.41.

In figures 7.56 to 7.60, the polar plot, the thrust acceleration a, the thrust angle α , the polar angle rate $\dot{\theta}$ and the flight path angle as function of time are illustrated for N=1 and N=2 cases that were presented in tables 7.13 and 7.14.

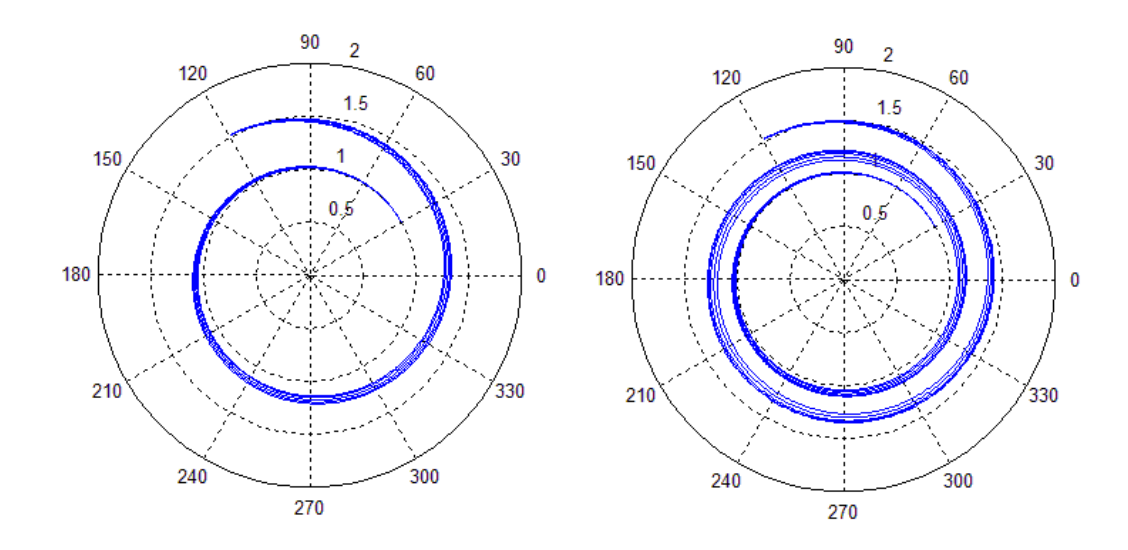


Figure 7.56: Polar plot for N=1 (a_0 =0.04) and N=2 (a_0 =0.03), θ_i =30°, $\Delta\theta$ =90°, α_0 =-20°, m values of (0.01; 0.11; 0.21; 0.31; 0.41), acceleration inversely square case (Poinsot's spiral (hyperbolic cosine), Earth-Mars flight

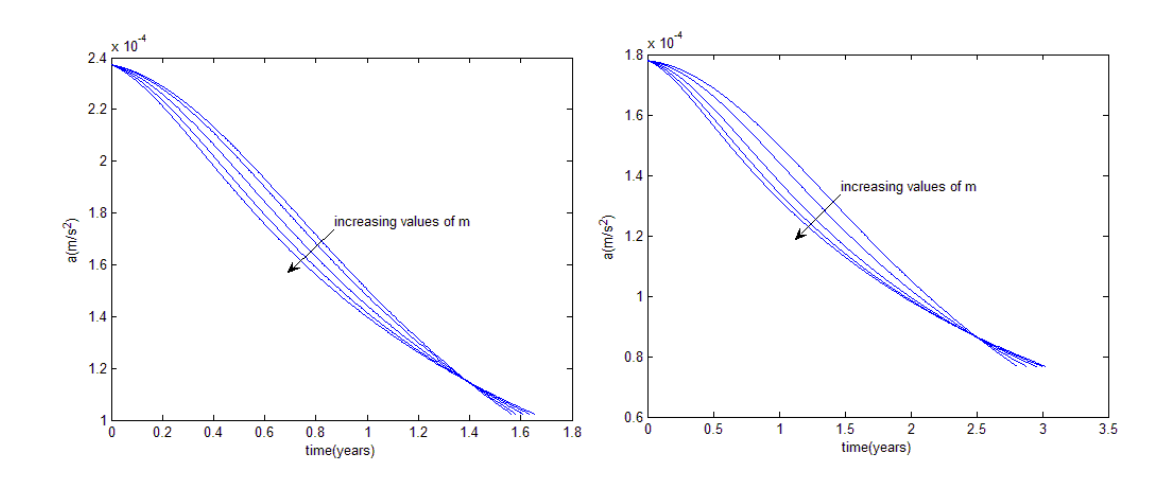


Figure 7.57: a plot for N=1 (a_0 =0.04) and N=2 (a_0 =0.03), θ_i =30°, $\Delta\theta$ =90°, α_0 =-20°, m values of (0.01; 0.11; 0.21; 0.31; 0.41), acceleration inversely square case (Poinsot's spiral (hyperbolic cosine), Earth-Mars flight

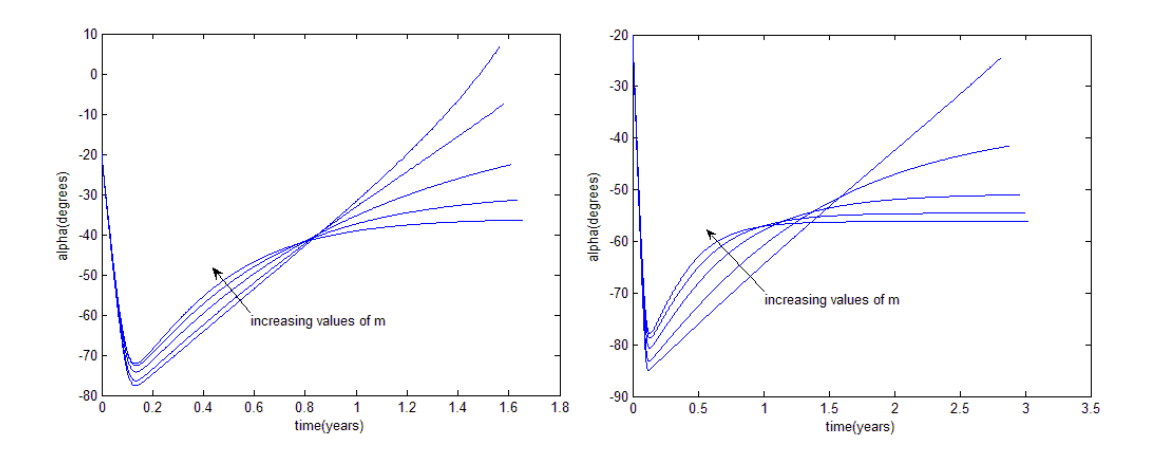


Figure 7.58: α plot for N=1 (a_0 =0.04) and N=2 (a_0 =0.03), θ_i =30°, $\Delta\theta$ =90°, α_0 =-20°, m values of (0.01; 0.11; 0.21; 0.31; 0.41), acceleration inversely square case (Poinsot's spiral (hyperbolic cosine), Earth-Mars flight

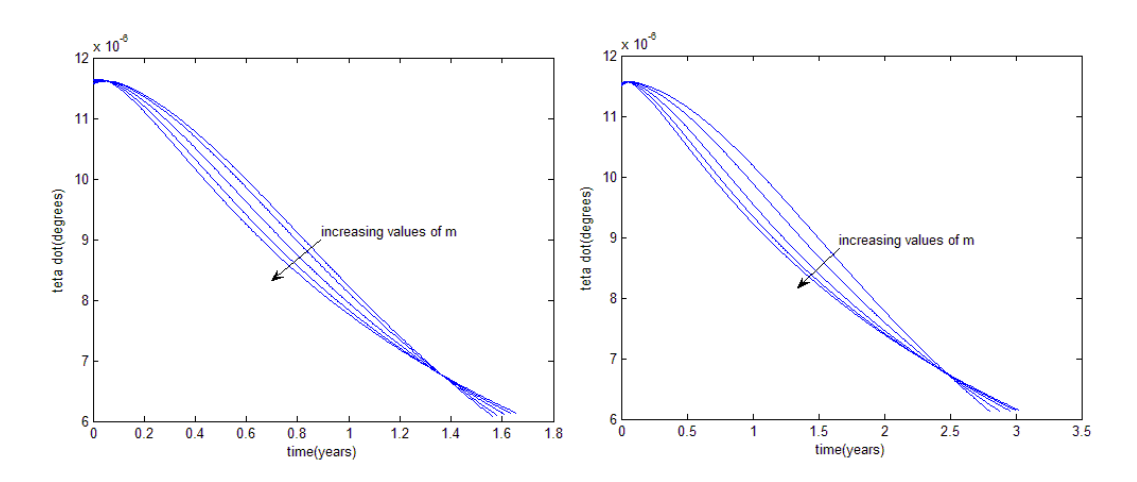


Figure 7.59: $\dot{\theta}$ plot for N=1 (a_0 =0.04) and N=2 (a_0 =0.03), θ_i =30°, $\Delta\theta$ =90°, α_0 =-20°, m values of (0.01; 0.11; 0.21; 0.31; 0.41), acceleration inversely square case (Poinsot's spiral (hyperbolic cosine), Earth-Mars flight

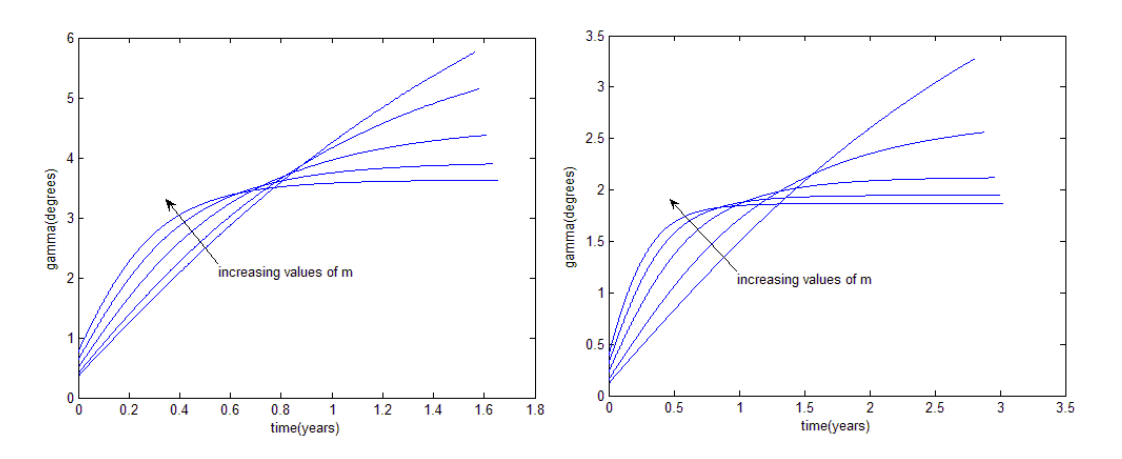


Figure 7.60: γ plot for N=1 (a_0 =0.04) and N=2 (a_0 =0.03), θ_i =30°, $\Delta\theta$ =90°, α_0 =-20°, m values of (0.01; 0.11; 0.21; 0.31; 0.41), acceleration inversely square case (Poinsot's spiral (hyperbolic cosine), Earth-Mars flight

From figure 7.57, the magnitude of the thrust acceleration is higher for N=1 than for N=2 because the assumed normalised thrust acceleration a_0 is also higher for N=1 than for N=2. Note that the thrust acceleration trend is similar to the $\dot{\theta}$ trend. The values for the thrust angle α are higher for N=1 than for N=2. For most of the interplanetary flight for both cases in figure 7.58, as for the other shapes, the spacecraft is thrusting inwards in the radial direction, while in the tangential direction it thrusts in the positive direction. The magnitude values of the flight path angle γ are smaller for N=2 than for N=1.

b) Tangential Case of the Thrust Profile

Figures 7.61 and 7.62 show the TOF and the total excess velocity for (30°, 140°, 250°, 360°) values of parameter θ_i and (90°, 150°, 210°, 270°, 340°) values of the transfer angle $\Delta\theta$ (N=0). The values used in these figures for the geometric parameter m were (0.01; 0.11; 0.21; 0.31; 0.41).

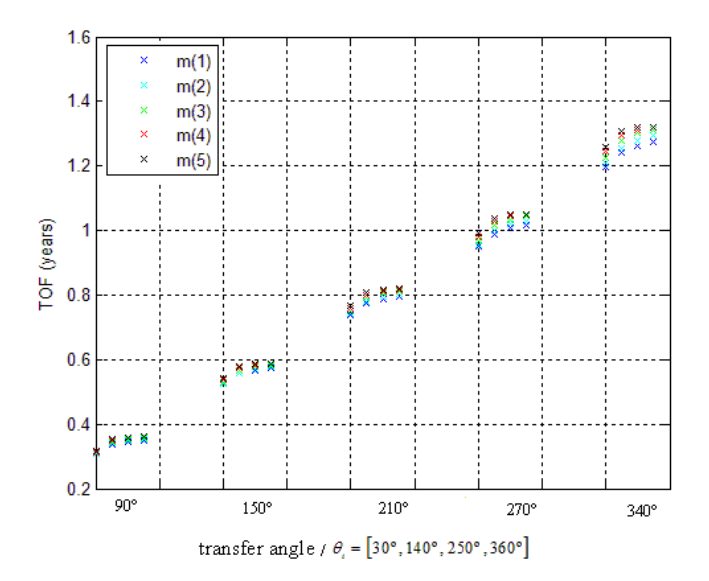


Figure 7.61: TOF for θ_i values of (30°, 140°, 250°, 360°) from left to right in the figure, m values of (0.01; 0.11; 0.21; 0.31; 0.41), $\Delta\theta$ values of (90°, 150°, 210°, 270°, 340°) (N=0), tangential thrust profile (Poinsot's spiral (hyperbolic cosine)), Earth-Mars flight

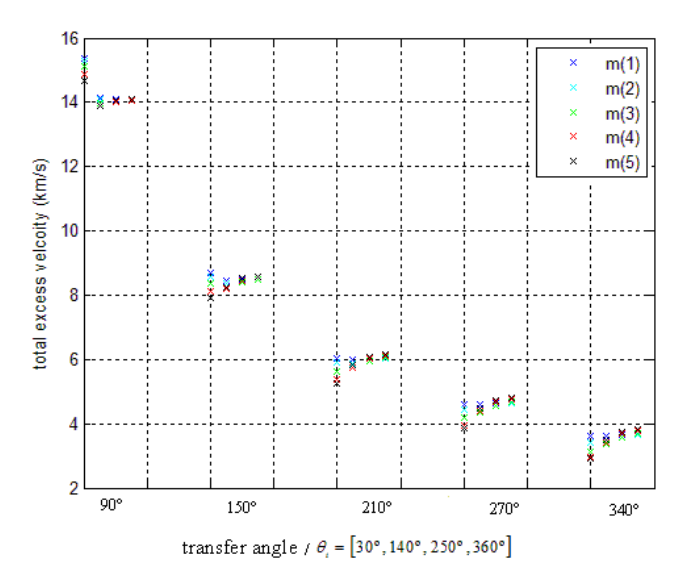


Figure 7.62: $V_{_{\circ,T}}$ for $\theta_{_i}$ values of (30°, 140°, 250°, 360°) from left to right in the figure, m values of (0.01; 0.11; 0.21; 0.31; 0.41), $\Delta\theta$ values of (90°, 150°, 210°, 270°, 340°) (N=0), tangential thrust profile (Poinsot's spiral (hyperbolic cosine)), Earth-Mars flight

From figures 7.61 and 7.62, by increasing the angle θ_i , the TOF increases and the differences in total excess velocity between different values of m decrease. The highest difference in TOF between different θ_i for the same transfer angle and m is 0.0836 years, while the highest difference in total excess velocity is $1.2939 \, km/s$. For higher values of

m, the TOF increases, while the total excess velocity decreases for $\theta_i = 30^{\circ}$ and $\theta_i = 140^{\circ}$, and it increases for $\theta_i = 250^{\circ}$ and $\theta_i = 360^{\circ}$.

Similar figures can be shown for 1 and 2 revolutions, using the same values for the geometric parameter m, for the transfer angle $\Delta\theta$ and for the initial value of θ_i as the ones used for N=0.

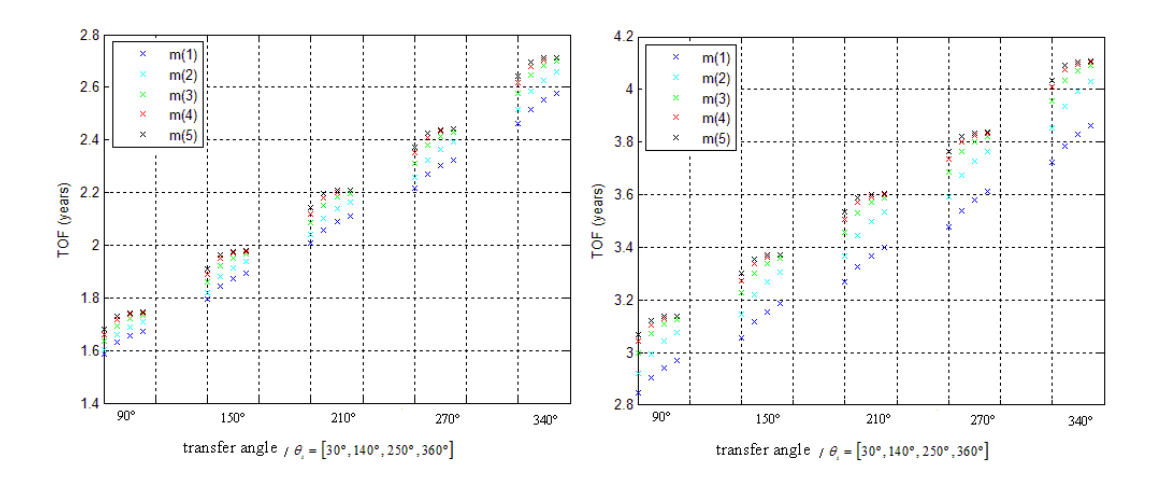


Figure 7.63: TOF for θ_i values of (30°, 140°, 250°, 360°) from left to right in the figure, m values of (0.01; 0.11; 0.21; 0.31; 0.41), $\Delta\theta$ values of (90°, 150°, 210°, 270°, 340°), tangential thrust profile (Poinsot's spiral (hyperbolic cosine)), Earth-Mars flight, N=1 and N=2

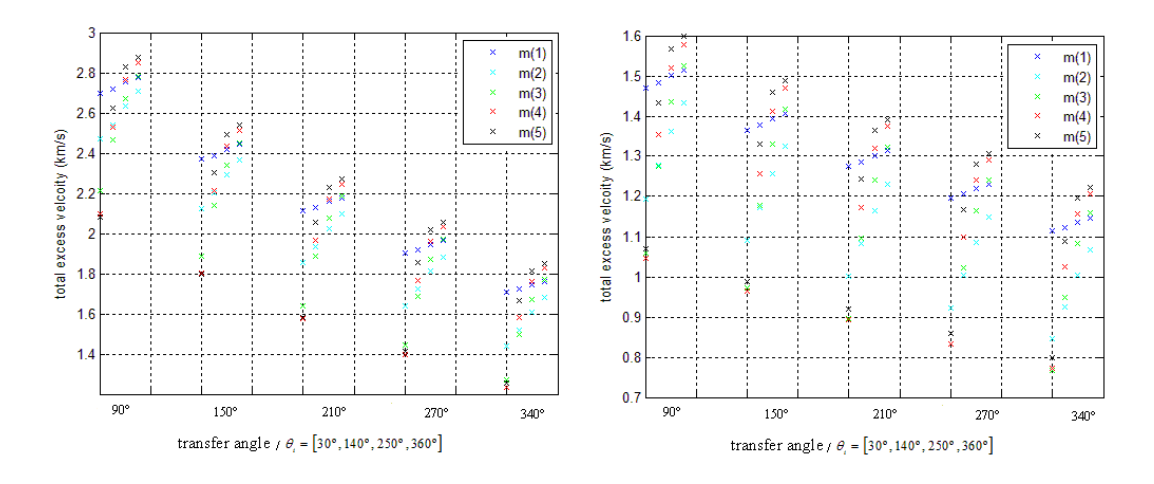


Figure 7.64: $V_{_{\infty,T}}$ for $\theta_{_i}$ values of (30°, 140°, 250°, 360°) from left to right in the figure, m values of (0.01; 0.11; 0.21; 0.31; 0.41), $\Delta\theta$ values of (90°, 150°, 210°, 270°, 340°), tangential thrust profile (Poinsot's spiral (hyperbolic cosine)), Earth-Mars flight, N=1 and N=2

For N=1, the highest difference in TOF between different θ_i for the same transfer angle and m is about 0.1371 years, while the highest difference in total excess velocity is 0.7976 km/s. For N=2, the highest difference in TOF between different θ_i for the same transfer angle is about 0.1696 years, while the highest difference in total excess velocity is 0.5334 km/s. Therefore, when increasing N the TOF becomes more sensitive to θ_i changes, while the total excess velocity becomes less sensitive to θ_i changes.

The TOF range for this Earth-Mars flight is from 0.3082 years to 4.1081 years. The total excess velocity has a minimum value of $0.7682\,km/s$ and a maximum value of $15.3776\,km/s$. The maximum differences in TOF between two consecutive values of the transfer angle $\Delta\theta$ are about 0.27 years and for a certain number of revolutions, these differences increase when increasing the transfer angle. The difference in terms of total excess velocity between two consecutive transfer angles is highest between $\Delta\theta = 90^{\circ}$ and $\Delta\theta = 150^{\circ}$ for N=0. The maximum value for these differences is $6.7795\,km/s$ for N=0 and the minimum value is $60.03\,m/s$ for N=2.

Tables 7.15 and 7.16 show the values for the TOF and the excess velocity in an Earth-Mars flight. Parameter θ_i was chosen 30°, the transfer angle $\Delta\theta$ was chosen 90° and N was taken 1 for the first table and 2 for the second one.

N=1	m = 0.01	m = 0.11	m = 0.21	m = 0.31	m = 0.41
$V_{\infty,total}(km/s)$	2.6984	2.4687	2.2125	2.0987	2.0794
$V_{\infty,1}(km/s)$	0.2619	0.2956	0.3681	0.4574	0.5520
$V_{\infty,2}(km/s)$	2.4365	2.1731	1.8444	1.6413	1.5274
TOF (years)	1.5854	1.6042	1.6350	1.6615	1.6810

Table 7.15: Excess velocities and TOF values for N=1, θ_i =30°, $\Delta\theta$ =90°, m values of (0.01; 0.11; 0.21; 0.31; 0.41), tangential thrust profile (Poinsot's spiral (hyperbolic cosine)), Earth-Mars flight

N=2	m = 0.01	m = 0.11	m = 0.21	m = 0.31	m = 0.41
$V_{\infty,total}\left(km/s\right)$	1.4696	1.1940	1.0600	1.0454	1.0689
$V_{\infty,1}(km/s)$	0.0851	0.1150	0.1676	0.2248	0.2819
$V_{\infty,2}(km/s)$	1.3844	1.0791	0.8924	0.8206	0.7871
TOF (years)	2.8476	2.9222	2.9981	3.0426	3.0692

Table 7.16: Excess velocities and TOF values for N=2, θ_i =30°, $\Delta\theta$ =90°, m values of (0.01; 0.11; 0.21; 0.31; 0.41), tangential thrust profile (Poinsot's spiral (hyperbolic cosine)), Earth-Mars flight

For increasing values of m the TOF increases and the total excess velocity decreases for N=1. For N=2, the total excess velocity decreases until m=0.31 and increases for m between 0.31 and 0.41, as for the acceleration inversely square case. The values for the total excess velocity are higher when N=1 than when N=2. Note that the excess velocity $V_{\infty,2}$ decreases faster than the excess velocity $V_{\infty,1}$ increases, except for N=2, for m between 0.31 and 0.41. As for the other shapes, the total excess velocity and the TOF are smaller and higher, respectively, compared with the acceleration inversely square case of the thrust profile.

In figures 7.65 to 7.68, the polar plot, the thrust acceleration a, the thrust angle α and the polar angle rate $\dot{\theta}$ as function of time are illustrated for N=1 and N=2 cases that were presented in tables 7.15 and 7.16.

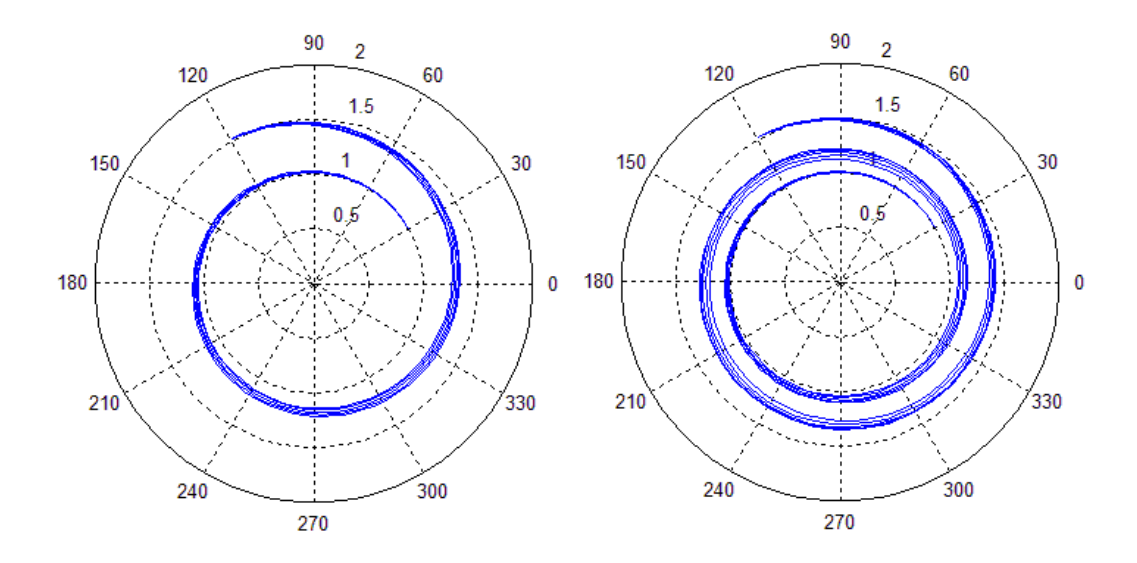


Figure 7.65: Polar plot for N=1 and N=2, θ_i =30°, $\Delta\theta$ =90°, m values of (0.01; 0.11; 0.21; 0.31; 0.41), tangential thrust profile (Poinsot's spiral (hyperbolic cosine)), Earth-Mars flight

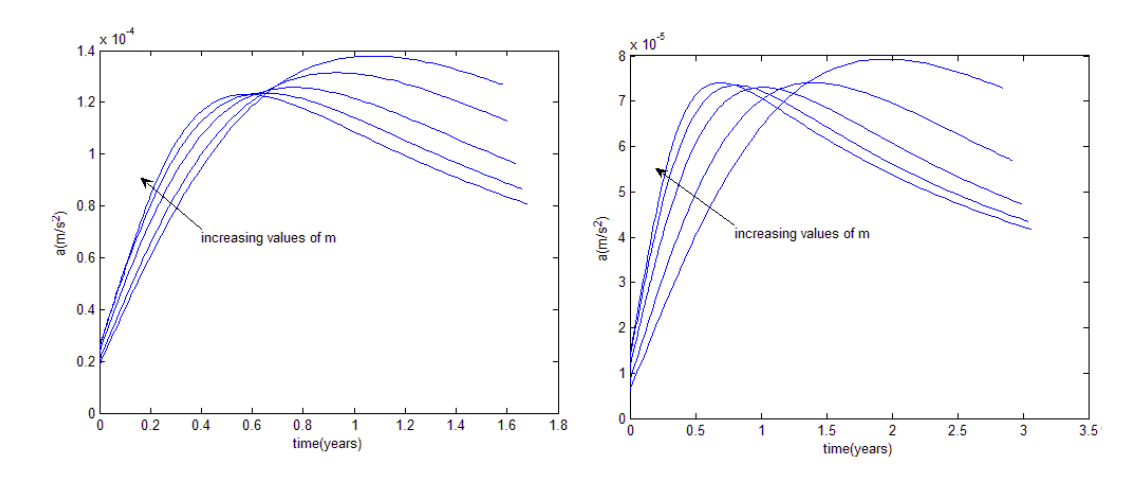


Figure 7.66: *a* plot for N=1 and N=2, θ_i =30°, $\Delta\theta$ =90°, *m* values of (0.01; 0.11; 0.21; 0.31; 0.41), tangential thrust profile (Poinsot's spiral (hyperbolic cosine)), Earth-Mars flight

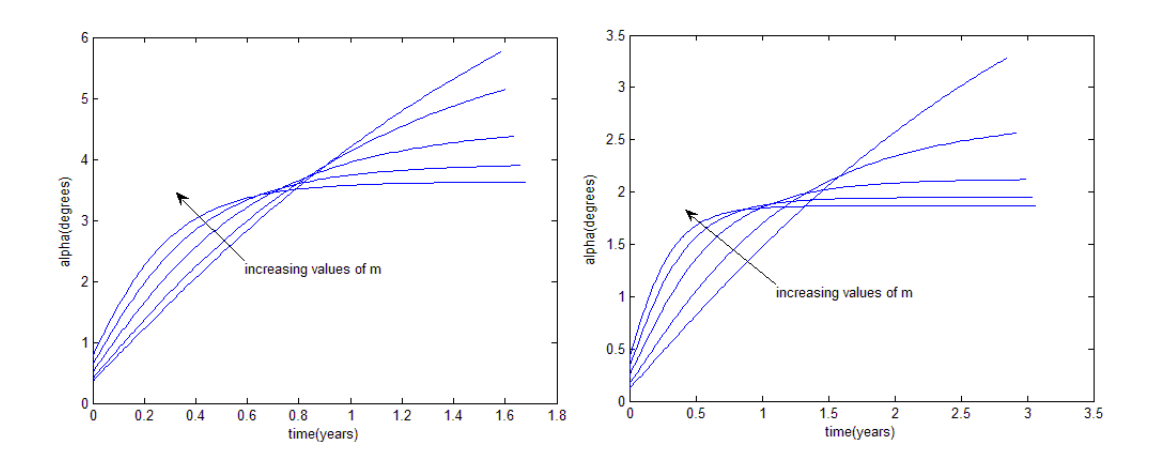


Figure 7.67: α plot for N=1 and N=2, θ_i =30°, $\Delta\theta$ =90°, m values of (0.01; 0.11; 0.21; 0.31; 0.41), tangential thrust profile (Poinsot's spiral (hyperbolic cosine)), Earth-Mars flight

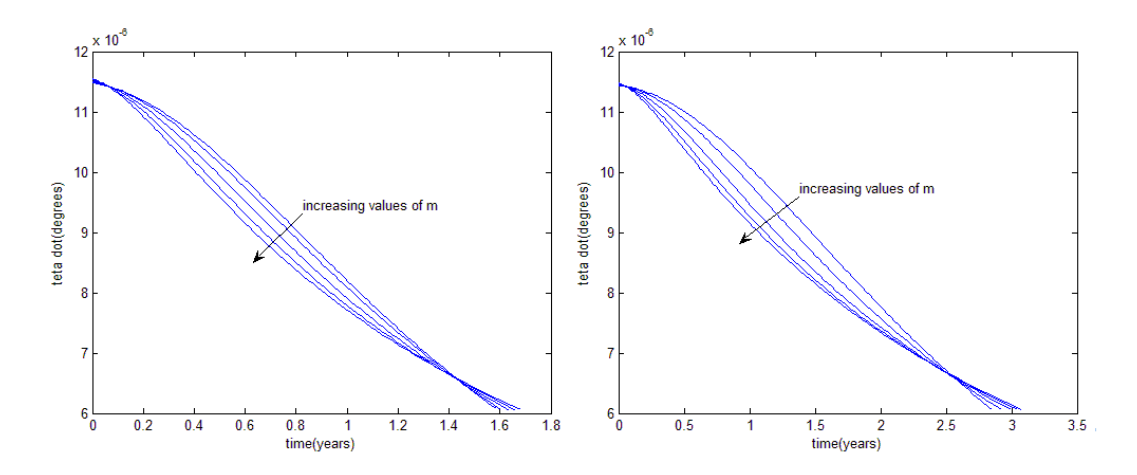


Figure 7.68: $\dot{\theta}$ plot for N=1 and N=2, θ_i =30°, $\Delta\theta$ =90°, m values of (0.01; 0.11; 0.21; 0.31; 0.41), tangential thrust profile (Poinsot's spiral (hyperbolic cosine)), Earth-Mars flight

The magnitude of the thrust acceleration is higher for N=1 than for N=2 which means that the magnitude of the instantaneous thrust required for a longer flight is smaller. Also, the values for the thrust angle α are smaller in magnitude for N=2 than for N=1.

7.5. Sinusoidal spiral

Results for the TOF, the excess velocities and the thrust acceleration will be shown and discussed for the sinusoidal spiral and for an Earth-Mars mission in this section. The thrust profiles used in this analysis are similar to the ones used for the shapes previously presented.

a) Acceleration Inversely Square Case of the Thrust Profile

Figures 7.69 and 7.70 show the TOF and the total excess velocity when varying parameter θ_i and the transfer angle $\Delta\theta$, when the number of revolutions N is 0. In these figures, the value used for m was 0.05, for a_0 was 0.09, the values for α_0 were (-60°, -50°, -40°, -30°, -20°), for the initial polar angle θ_i were (120°, 200°, 280°, 360°) and for the transfer angle $\Delta\theta$ were (90°, 150°, 210°, 270°, 340°).

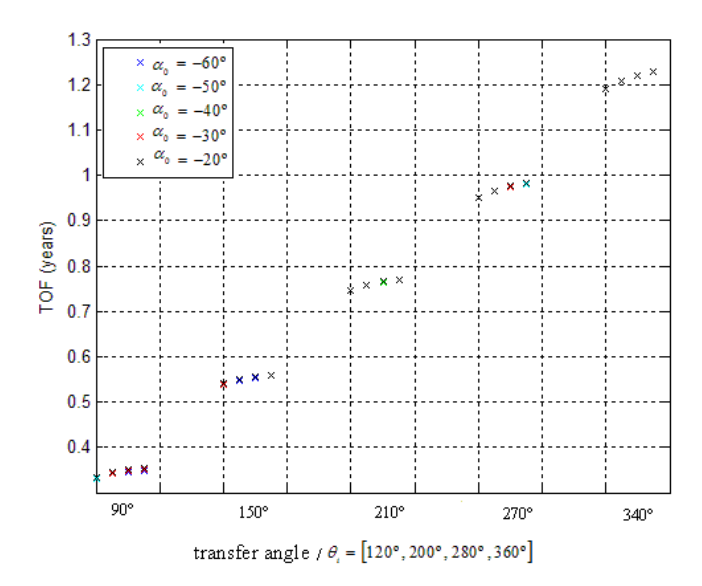


Figure 7.69: TOF for θ_i values of (120°, 200°, 280°, 360°) from left to right in the figure, α_0 values of (-60°, -50°, -40°, -30°, -20°), $\Delta\theta$ values of (90°, 150°, 210°, 270°, 340°) (N=0), m=0.05, a_0 =0.09, acceleration inversely square case of the thrust profile (sinusoidal spiral), Earth-Mars flight

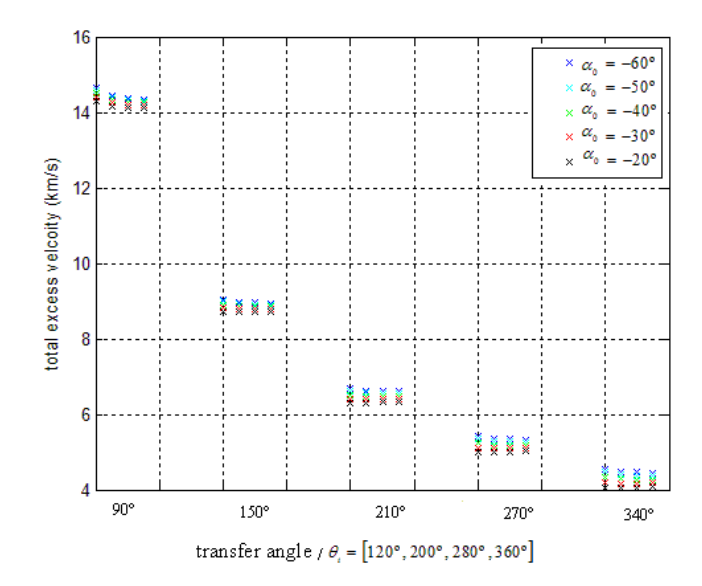


Figure 7.70: $V_{-,T}$ for θ_i values of (120°, 200°, 280°, 360°) from left to right in the figure, α_0 values of (-60°, -50°, -40°, -30°, -20°), $\Delta\theta$ values of (90°, 150°, 210°, 270°, 340°) (N=0), m=0.05, a_0 =0.09, acceleration inversely square case of the thrust profile (sinusoidal spiral), Earth-Mars flight

From figures 7.69 and 7.70, the TOF increases while the total excess velocities decreases, when increasing θ_i . The differences in TOF and in total excess velocity between different values of θ_i , decrease for higher values of the initial polar angle. The highest difference in TOF between different θ_i for the same transfer angle and α_0 is 0.0369 years, while the highest difference in total excess velocity is 0.3027 km/s, which are higher than the ones for the Poinsot's spiral (hyperbolic sine). For higher values of α_0 , the total excess velocity decreases, while the TOF increases.

Figures for 1 and 2 revolutions, using the same values for the geometric parameter m, for the transfer angle $\Delta\theta$ and for the initial values of α and θ can be shown. The normalised thrust acceleration a_0 values used in figures 7.71 and 7.72 were 0.04 and 0.03 for N=1 and N=2, respectively.

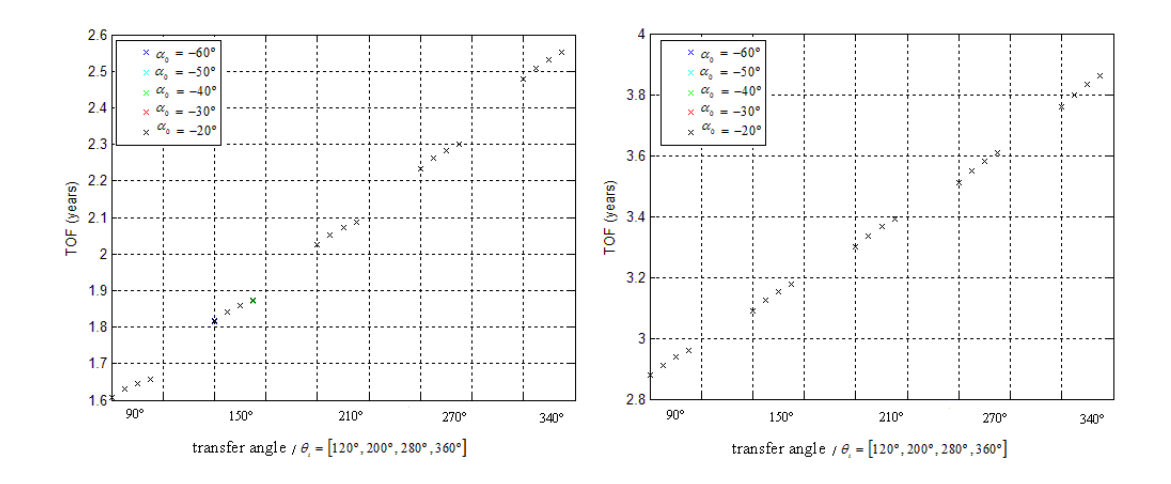


Figure 7.71: TOF for θ_i values of (120°, 200°, 280°, 360°) from left to right in the figure, α_0 values of (-60°, -50°, -40°, -30°, -20°), $\Delta\theta$ values of (90°, 150°, 210°, 270°, 340°), m=0.05, acceleration inversely square case of the thrust profile (sinusoidal spiral), Earth-Mars flight, N=1 (a_0 =0.04), N=2 (a_0 =0.03)

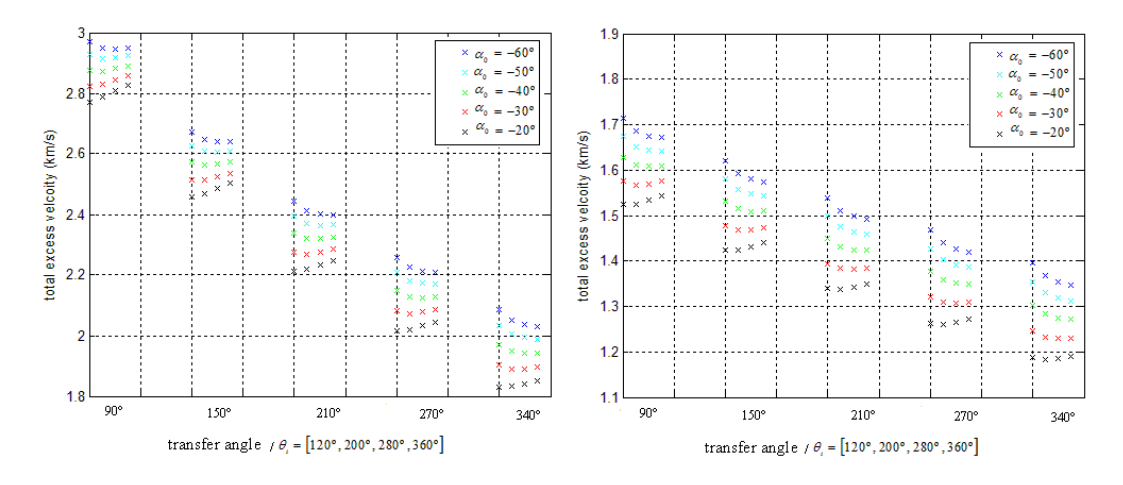


Figure 7.72: $V_{\omega,T}$ for θ_i values of (120°, 200°, 280°, 360°) from left to right in the figure, α_0 values of (-60°, -50°, -40°, -30°, -20°), $\Delta\theta$ values of (90°, 150°, 210°, 270°, 340°), m=0.05, acceleration inversely square case of the thrust profile (sinusoidal spiral), Earth-Mars flight, N=1 (a_0 =0.04), N=2 (a_0 =0.03)

In figures 7.71 and 7.72, for N=1, the highest difference in TOF between different θ_i for the same transfer angle and α_0 is about 0.0707 years, while the highest difference in total excess velocity is 57.7082 m/s. For N=2, the highest difference in TOF between different θ_i for the same transfer angle and α_0 is about 0.0995 years, while the highest difference in total excess velocity is 48.7113 m/s. Therefore, for higher values of N, θ_i increases and decreases its influence in the TOF and in the total excess velocity, respectively.

The TOF range for this Earth-Mars flight is from 0.3316 years to 3.8613 years. The total excess velocity has a minimum value of $1.1820\,km/s$ and a maximum value of $14.6387\,km/s$. The maximum differences in TOF between two consecutive values of the transfer angle $\Delta\theta$ are about 0.25 years and for a certain number of revolutions, these differences increase when increasing the transfer angle. The differences in terms of total excess velocity between two consecutive transfer angles is always highest between $\Delta\theta = 90^{\circ}$ and $\Delta\theta = 150^{\circ}$, as for the other shapes. The maximum value for these differences is $5.6043\,km/s$ for N=0 and the minimum value is about $70.73\,m/s$ for N=2.

Tables 7.17 and 7.18 show the values for the TOF and the excess velocity for an Earth-Mars flight. Parameters θ_i , α_0 , $\Delta\theta$ were assumed 120°, -20° and 90°, respectively. The number of revolutions was taken 1 for the first table and 2 for the second one. In table 7.17, the normalised thrust acceleration a_0 was 0.04, while in table 7.18, this parameter was 0.03. Note that the values assumed for a_0 for N=1 and N=2 are the minimum values that can be used in both cases for this shape without facing integration problems for the interval of input parameters considered.

N=1	m = 0.01	m = 0.055	m = 0.1	m = 0.145	m = 0.19
$V_{\infty,total}\left(km/s\right)$	2.8108	2.7616	2.6656	2.5239	2.3377
$V_{\infty,1}(km/s)$	0.6601	0.6781	0.7160	0.7791	0.8772
$V_{\infty,2}\left(km/s\right)$	2.1507	2.0835	1.9496	1.7448	1.4605
TOF (years)	1.6039	1.6093	1.6204	1.6384	1.6653

Table 7.17: The excess velocities and the TOF values for N=1, $\theta_{_{|}}$ =120°, $\Delta\theta$ =90°, $\alpha_{_{0}}$ =-20°, m values of (0.01; 0.055; 0.1; 0.145; 0.19), $a_{_{0}}$ =0.04, acceleration inversely square case (sinusoidal spiral), Earth-Mars flight

N=2	m = 0.01	m = 0.055	m = 0.1	m = 0.145	m = 0.19
$V_{\infty,total}\left(km/s\right)$	1.5861	1.5105	1.3054	1.0891	0.8450
$V_{\infty,1}(km/s)$	0.2891	0.3028	0.3386	0.4135	0.5727
$V_{\infty,2}(km/s)$	1.2970	1.2083	1.0068	0.6757	0.2723
TOF (years)	2.8608	2.8815	2.9325	3.0302	3.2189

Table 7.18: The excess velocities and the TOF values for N=2, $\theta_{_{|}}$ =120°, $\Delta\theta$ =90°, $\alpha_{_{0}}$ =-20°, m values of (0.01; 0.055; 0.1; 0.145; 0.19), $a_{_{0}}$ =0.03, acceleration inversely square case (sinusoidal spiral), Earth-Mars flight

From tables 7.17 and 7.18, the order of magnitude of the total excess velocity values is $10^0 \, km/s$ and $10^{-1} \, km/s$. For increasing values of m, the total excess velocity decreases, while the TOF increases. The values for the total excess velocity are higher for N=1 than for N=2. Note that the excess velocity $V_{\infty,2}$ decreases faster than the excess velocity $V_{\infty,1}$ increases, for both cases N=1 and N=2. For all values of m, except for m=0.19, $V_{\infty,2}$ is higher than $V_{\infty,1}$, a situation that is attractive for the use of swing-bys.

In figures 7.73 to 7.77, the polar plot, the thrust acceleration a, the thrust angle α , the polar angle rate $\dot{\theta}$ and the flight path angle as function of time are illustrated for N=1 and N=2 cases that were presented in tables 7.17 and 7.18.

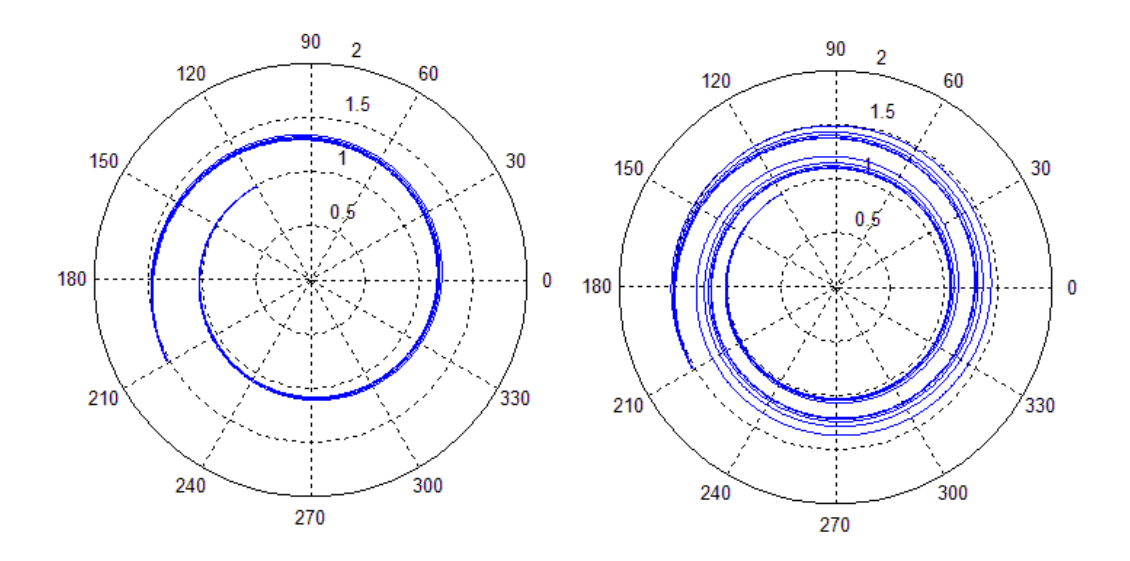


Figure 7.73: Polar plot for N=1 (a_0 =0.04) and N=2 (a_0 =0.03), θ_i =120°, $\Delta\theta$ =90°, α_0 =-20°, m values of (0.01; 0.055; 0.1; 0.145; 0.19), acceleration inversely square case (sinusoidal spiral), Earth-Mars flight

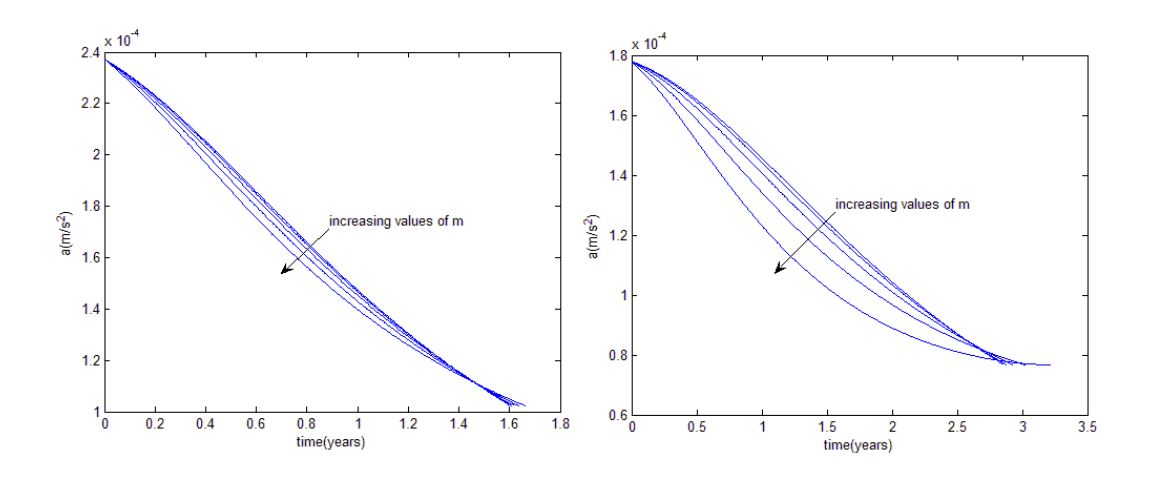


Figure 7.74: *a* plot for N=1 (a_0 =0.04) and N=2 (a_0 =0.03), θ_i =120°, $\Delta\theta$ =90°, α_0 =-20°, *m* values of (0.01; 0.055; 0.1; 0.145; 0.19), acceleration inversely square case (sinusoidal spiral), Earth-Mars flight

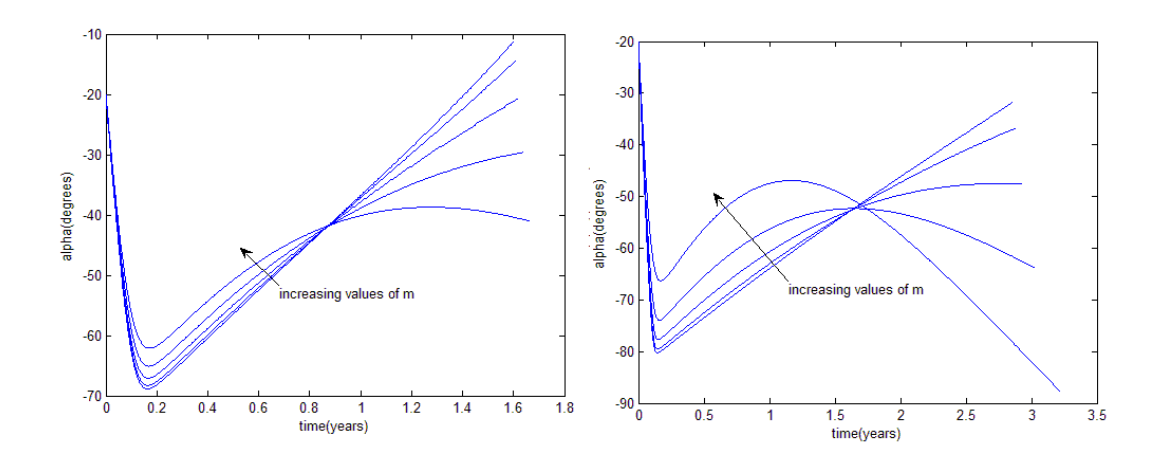


Figure 7.75: α plot for N=1 (a_0 =0.04) and N=2 (a_0 =0.03), θ_i =120°, $\Delta\theta$ =90°, α_0 =-20°, m values of (0.01; 0.055; 0.1; 0.145; 0.19), acceleration inversely square case (sinusoidal spiral), Earth-Mars flight

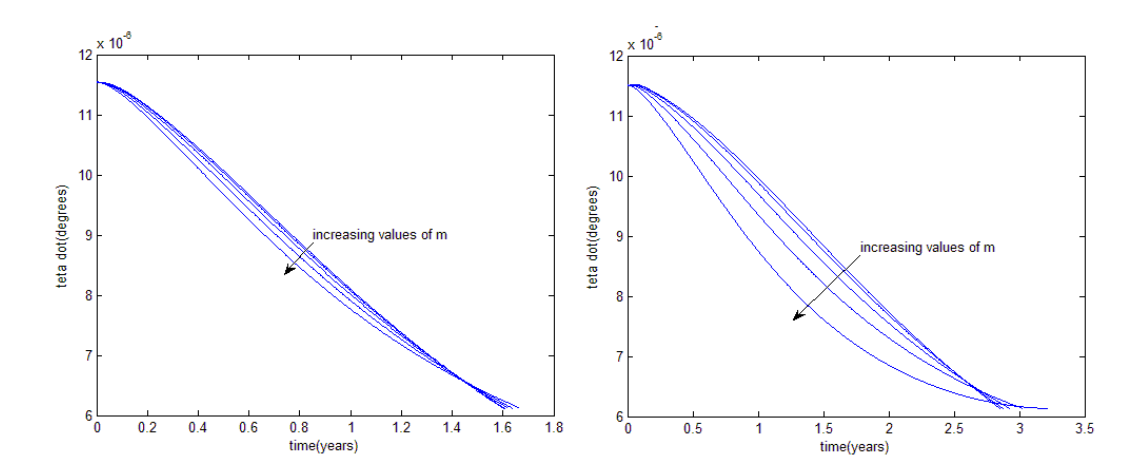


Figure 7.76: $\dot{\theta}$ plot for N=1 (a_0 =0.04) and N=2 (a_0 =0.03), θ_i =120°, $\Delta\theta$ =90°, α_0 =-20°, m values of (0.01; 0.055; 0.1; 0.145; 0.19), acceleration inversely square case (sinusoidal spiral), Earth-Mars flight

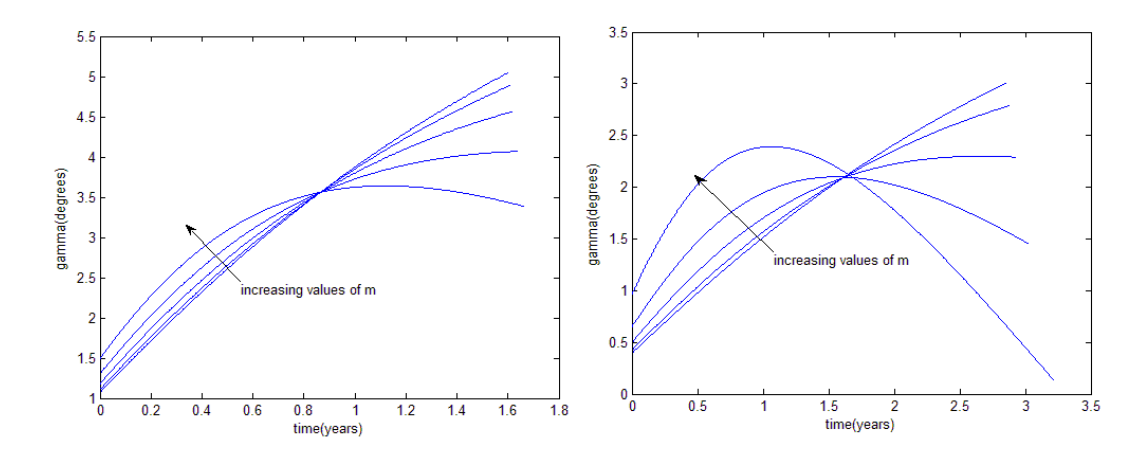


Figure 7.77: γ plot for N=1 (a_0 =0.04) and N=2 (a_0 =0.03), θ_i =120°, $\Delta\theta$ =90°, α_0 =-20°, m values of (0.01; 0.055; 0.1; 0.145; 0.19), acceleration inversely square case (sinusoidal spiral), Earth-Mars flight

The magnitude of the thrust acceleration is higher for N=1 than for N=2 because the assumed normalised thrust acceleration a_0 is also higher for N=1 than for N=2. Note that the thrust acceleration trend is similar to the $\dot{\theta}$ trend, since the acceleration inversely square case of the thrust profile is being considered. The values of the thrust angle α are higher for N=1 than for N=2. For most of the interplanetary flight for both cases in figure 7.75, the spacecraft is thrusting inwards in the radial direction, while in the tangential direction it thrusts in the positive direction (α is negative, higher than -90°), like for the other shapes.

b) Tangential Case of the Thrust Profile

In figures 7.78 and 7.79, the TOF and the total excess velocity are illustrated for different values of parameter θ_i and of the transfer angle $\Delta\theta$ (N=0). The values used in these figures for m were (0.01; 0.055; 0.1; 0.145; 0.19), for θ_i and for $\Delta\theta$ were the same as the ones used for the acceleration inversely square case.

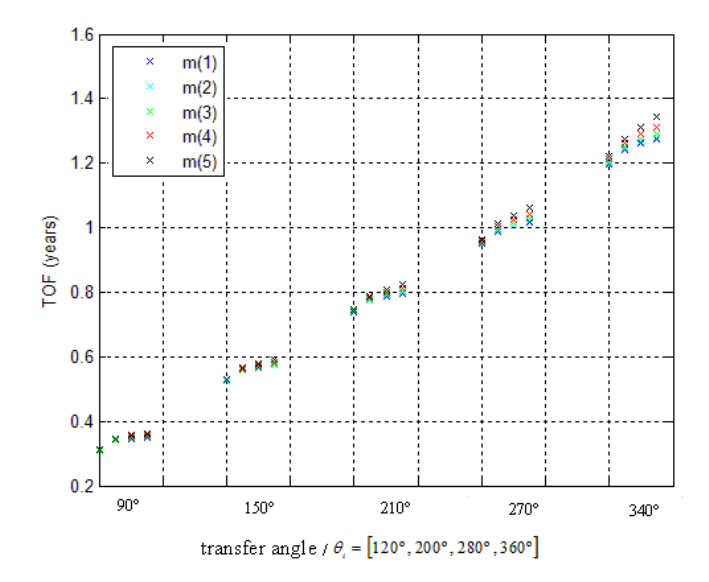


Figure 7.78: TOF for θ_i values of (120, 200°, 280°, 360°) from left to right in the figure, m values of (0.01; 0.055; 0.1; 0.145; 0.19), $\Delta\theta$ values of (90°, 150°, 210°, 270°, 340°) (N=0), tangential thrust profile (sinusoidal spiral), Earth-Mars flight

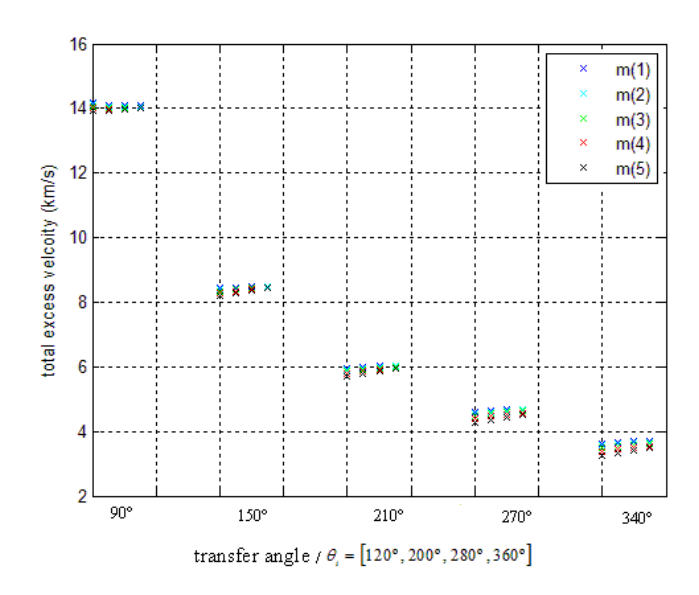


Figure 7.79: $V_{_{\infty,T}}$ for $\theta_{_{i}}$ values of (120, 200°, 280°, 360°) from left to right in the figure, m values of (0.01; 0.055; 0.1; 0.145; 0.19), $\Delta\theta$ values of (90°, 150°, 210°, 270°, 340°) (N=0), tangential thrust profile (sinusoidal spiral), Earth-Mars flight

Some remarks can be drawn from figures 7.78 and 7.79. By increasing the initial polar angle θ_i , the TOF increases, as for the acceleration inversely square case. The highest difference in TOF and in total excess velocity between different values of θ_i occurs between $\theta_i = 120^{\circ}$ and $\theta_i = 200^{\circ}$. The highest difference in TOF between different θ_i for

the same transfer angle and m is 0.07458 years, while the highest difference in total excess velocity is $0.2598 \, km/s$. For higher values of m, the total excess velocity decreases, while the TOF increases.

Similar figures can be shown for 1 and 2 revolutions, using the same values for the geometric parameter m, for the transfer angle $\Delta\theta$ and for the initial value of θ_i as the ones used for N=0.

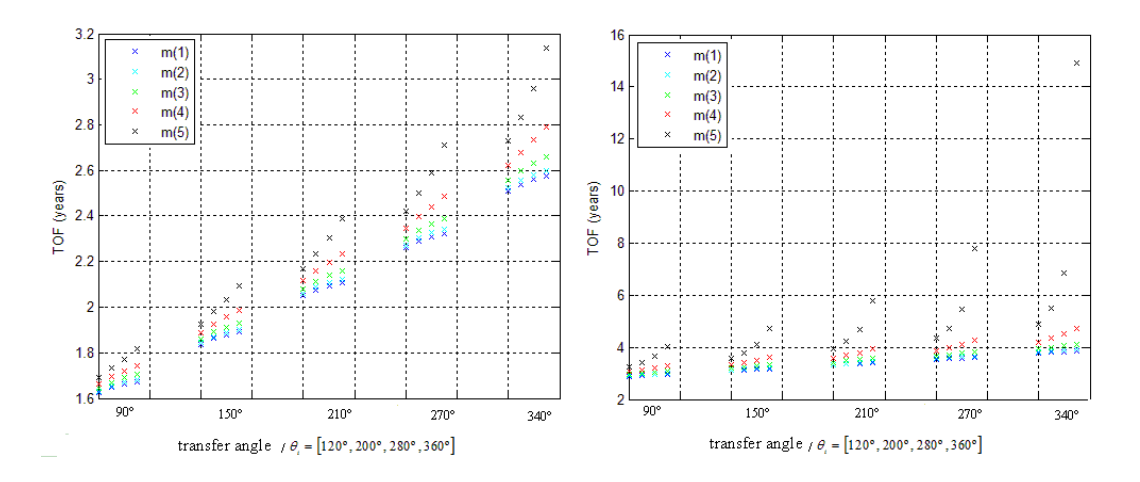


Figure 7.80: TOF for θ_i values of (120, 200°, 280°, 360°) from left to right in the figure, m values of (0.01; 0.055; 0.1; 0.145; 0.19), $\Delta\theta$ values of (90°, 150°, 210°, 270°, 340°), tangential thrust profile (sinusoidal spiral), Earth-Mars flight for N=1 and N=2

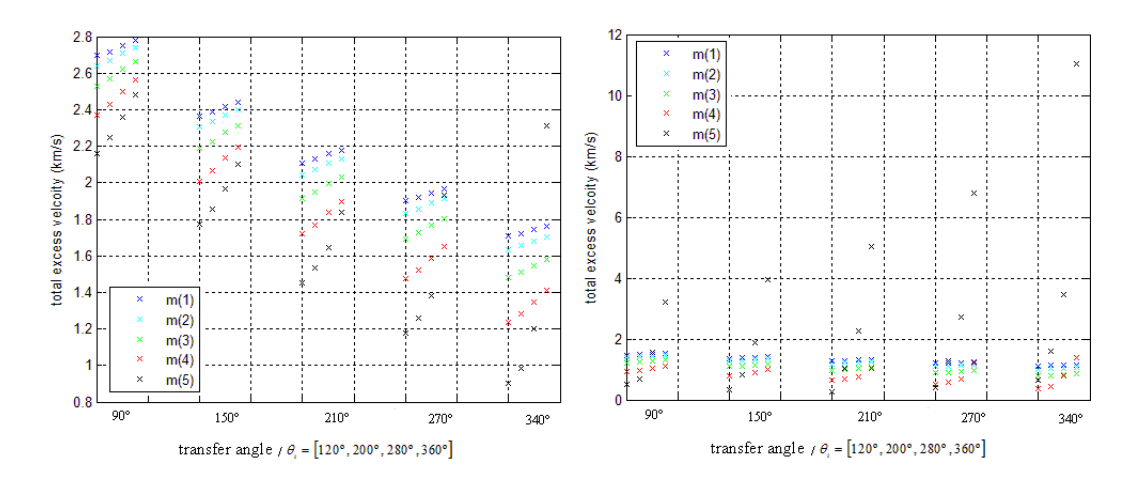


Figure 7.81: $V_{\omega,T}$ for θ_i values of (120, 200°, 280°, 360°) from left to right in the figure, m values of (0.01; 0.055; 0.1; 0.145; 0.19), $\Delta\theta$ values of (90°, 150°, 210°, 270°, 340°), tangential thrust profile (sinusoidal spiral), Earth-Mars flight for N=1 and N=2

Similar remarks to the ones given for N=0 can be drawn for figures 7.80 and 7.81. The differences between the minimum and the maximum values of α_0 in total excess velocity and in TOF increase with the number of revolutions and also with the transfer angle $\Delta\theta$. Note that the TOF and the total excess velocity, for N=1 and N=2, become more sensitive to θ_i change than for N=0 and for the acceleration inversely square case. For N=1, the highest difference in TOF between different θ_i for the same transfer angle and m is about 0.3946 years, while the highest difference in total excess velocity is $1.3503 \, km/s$. For N=2, the highest difference in TOF between different θ_i for the same transfer angle and m is about 9.7278 years, while the highest difference in total excess velocity is $9.6402 \, km/s$.

The TOF range for this Earth-Mars flight is from 0.3366 years to 14.9125 years. The total excess velocity has a minimum value of $0.4223 \, km/s$ and a maximum value of $14.1791 \, km/s$. The maximum differences in TOF between two values of the transfer angle $\Delta \theta$ are about 7.1279 years, which much higher than for the other shapes. The difference in terms of total excess velocity between two consecutive transfer angles is highest between $\Delta \theta = 90^\circ$ and $\Delta \theta = 150^\circ$ for N=0. The maximum value for these differences is $5.7521 \, km/s$ for zero value of N and the minimum value is $4.3180 \, m/s$ for 2 revolutions.

Tables 7.19 and 7.20 show the values for the TOF and the excess velocity for an Earth-Mars flight. Parameter θ_i was assumed 120°, the transfer angle $\Delta\theta$ was assumed 90° and the number of revolutions was taken 1 for the first table and 2 for the second one.

N=1	m = 0.01	m = 0.055	m = 0.1	m = 0.145	m = 0.19
$V_{\infty,total}(km/s)$	2.7085	2.6572	2.5579	2.4126	2.2241
$V_{\infty,1}(km/s)$	0.5746	0.5935	0.6332	0.6989	0.8002
$V_{\infty,2}(km/s)$	2.1339	2.0638	1.9247	1.7137	1.4239
TOF (years)	1.6259	1.6315	1.6432	1.6620	1.6899

Table 7.19: Excess velocities and TOF values for N=1, θ_i =120°, $\Delta\theta$ =90°, m values of (0.01; 0.055; 0.1; 0.145; 0.19), tangential thrust profile (sinusoidal spiral) Earth-Mars flight

N=2	m = 0.01	m = 0.055	m = 0.1	m = 0.145	m = 0.19
$V_{\infty,total}(km/s)$	1.4787	1.4015	1.2303	0.9596	0.6214
$V_{\infty,1}(km/s)$	0.2098	0.2256	0.2660	0.3476	0.5146
$V_{\infty,2}(km/s)$	1.2690	1.1759	0.9643	0.6120	0.1068
TOF (years)	2.8957	2.9170	2.9693	3.0690	3.2602

Table 7.20: Excess velocities and TOF values for N=2, θ_i =120°, $\Delta\theta$ =90°, m values of (0.01; 0.055; 0.1; 0.145; 0.19), tangential thrust profile (sinusoidal spiral) Earth-Mars flight

From tables 7.19 and 7.20, the order of magnitude of the total excess velocity values is $10^0 \, km/s$ and $10^{-1} \, km/s$. For increasing values of m, the total excess velocity decreases, while the TOF increases. The values for the total excess velocity are higher when N=1 than when N=2. Note that the excess velocity $V_{\infty,2}$ decreases faster than the excess velocity $V_{\infty,1}$ increases. As for the other shapes, compared with the acceleration inversely square case, the TOF and the total excess velocity are higher and smaller for the tangential case, respectively.

In figures 7.82 to 7.85, the polar plot, the thrust acceleration a, the thrust angle α and the polar angle rate $\dot{\theta}$ as function of time are illustrated for N=1 and N=2 cases that were presented in tables 7.19 and 7.20.

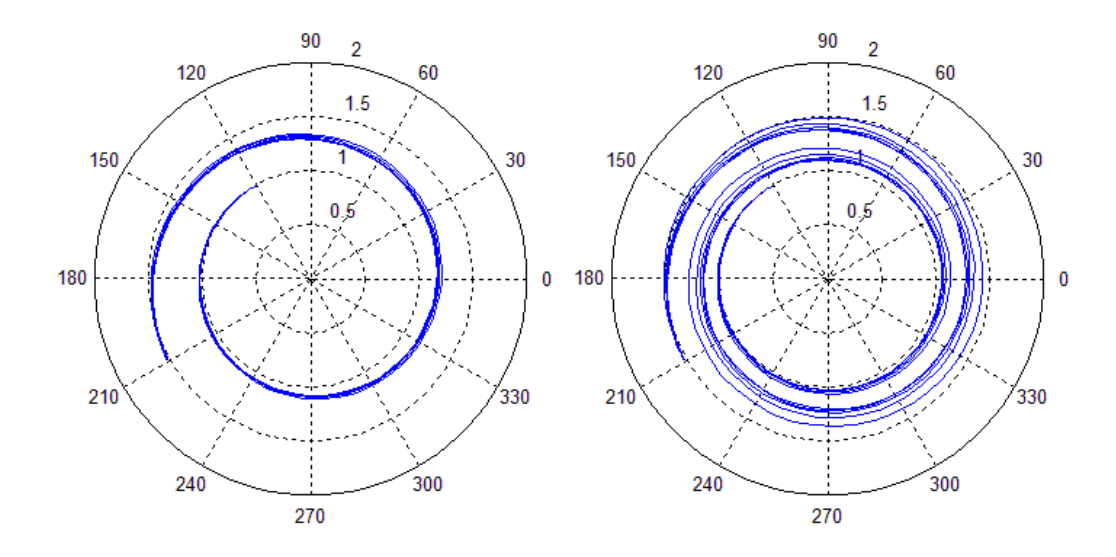


Figure 7.82: Polar plot for N=1 and N=2, θ_i =120°, $\Delta\theta$ =90°, m values of (0.01; 0.055; 0.1; 0.145; 0.19), tangential thrust profile (sinusoidal spiral) Earth-Mars flight

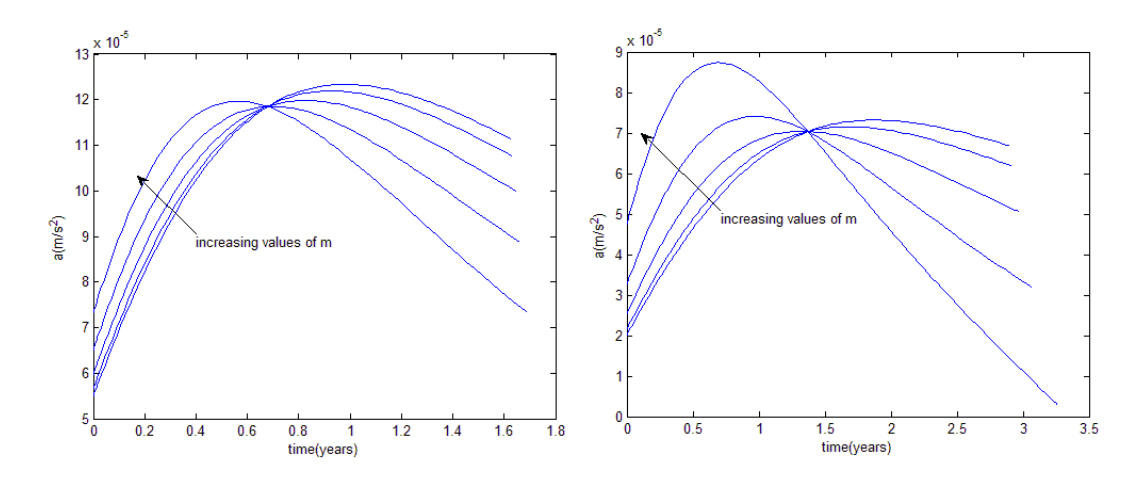


Figure 7.83: a plot for N=1 and N=2, θ_i =120°, $\Delta\theta$ =90°, m values of (0.01; 0.055; 0.1; 0.145; 0.19), tangential thrust profile (sinusoidal spiral) Earth-Mars flight

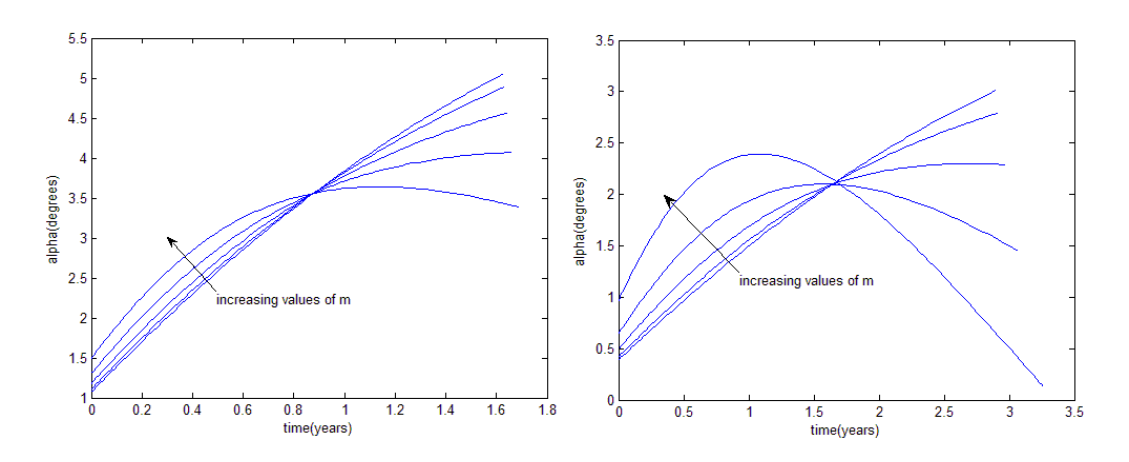


Figure 7.84: α plot for N=1 and N=2, θ_i =120°, $\Delta\theta$ =90°, m values of (0.01; 0.055; 0.1; 0.145; 0.19), tangential thrust profile (sinusoidal spiral) Earth-Mars flight

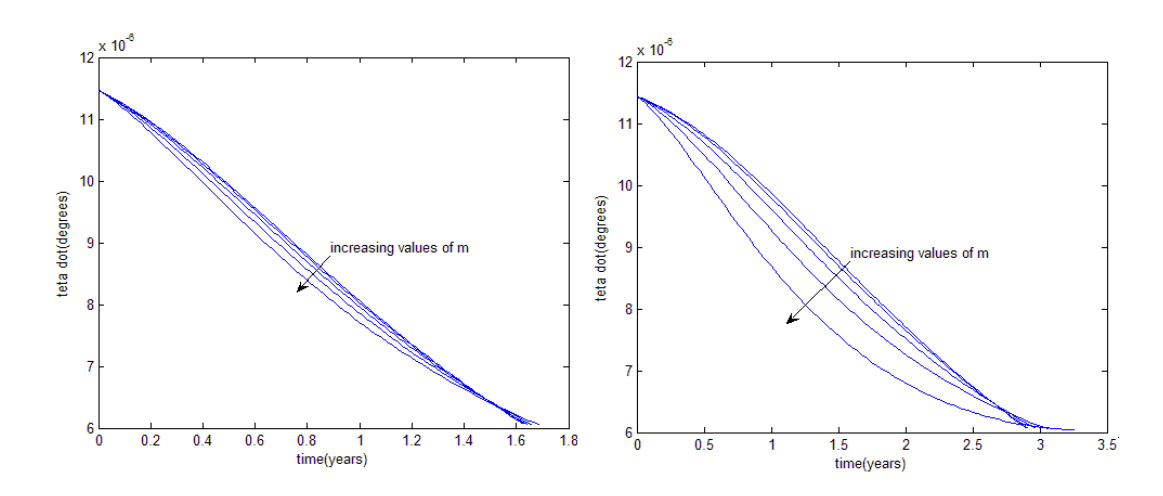


Figure 7.85: $\dot{\theta}$ plot for N=1 and N=2, θ_i =120°, $\Delta\theta$ =90°, m values of (0.01; 0.055; 0.1; 0.145; 0.19), tangential thrust profile (sinusoidal spiral) Earth-Mars flight

From figure 7.83, the magnitude of the thrust acceleration is higher for N=1 than for N=2 which means that the magnitude of the instantaneous thrust required for a longer flight is smaller. Also, the values for the thrust angle α are smaller for N=2 than for N=1.

7.6. Exponential Sinusoid

In this section 7.6, results for the TOF, the excess velocities and the thrust acceleration will be shown and discussed for the exponential sinusoid and for an Earth-Mars mission. The

thrust profiles used in this analysis are the same as the ones used for the shapes previously presented.

a) Acceleration Inversely Square Case of the Thrust Profile

Figures 7.86 and 7.87 show the TOF and the total excess velocity when changing parameter k_2 and the transfer angle $\Delta\theta$, when N=0. Note that the initial polar angle θ_i is zero degrees. The values used in these figures for the geometric parameter k_2 were (0.1; 0.15; 0.2; 0.25), for the initial value of α were (20°, 30°, 40°, 50°, 60°), for the initial flight path angle γ_1 was 0° and for the transfer angle $\Delta\theta$ were (90°, 150°, 210°, 270°, 340°). The normalised thrust acceleration a_0 value used in figures 7.86 and 7.87 was 0.07.

Note that values used for the geometric parameter k_2 were not chosen according to equation (5.4) presented in chapter 5: $N_{p2a} = 1/(2k_2)$. Instead, the interval of values for k_2 was selected because it could be used for N = 0,1,2 and for different values of transfer angles $\Delta\theta$ without causing integration errors (chapter 6), while using the acceleration inversely square case. Through equation (5.4), the minimum value for the geometric parameter k_2 can be computed for a trajectory that has its minimum radius (pericentre) at the initial point of the thrust arc and its maximum radius (apocentre) when the spacecraft reach the final point of thrust arc. In this master thesis, this equation was not used as a constraint, i.e., smaller values of k_2 than the ones given by equation (5.4) can still be picked. In this way, feasible solutions with these values of k_2 are still taken into account. In order to better compare the results between the acceleration inversely square case and the tangential case, the same values of k_2 (0.1; 0.15; 0.2; 0.25) were used for this last case of the thrust profile (section 7.6b).

Note also that the values chosen for the initial thrust angle α_0 were positive, unlike the values chosen for the other five shapes. For the other shapes, integration errors occur if the positive values are used, however for the exponential sinusoid if the negative values of α_0

are assumed, the total excess velocity values will be higher compared with the situation where positive ones are picked.

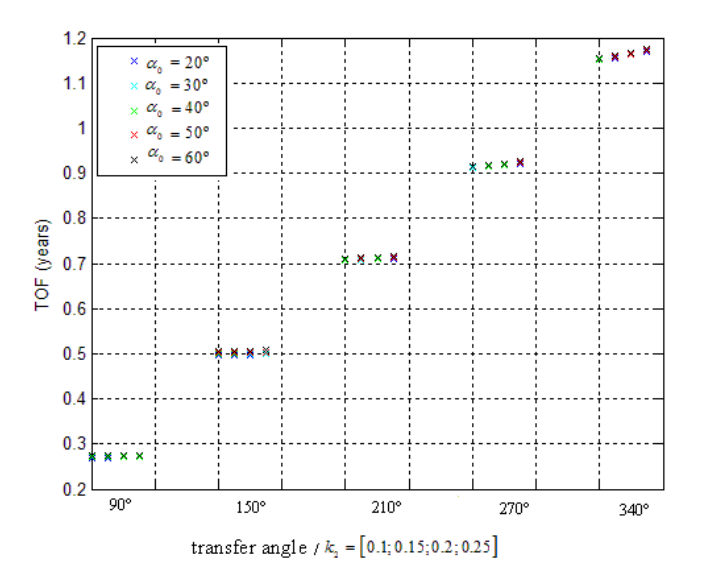


Figure 7.86: TOF for k_2 values of (0.1; 0.15; 0.2; 0.25) from left to right in the figure, α_0 values of (20°, 30°, 40°, 50°, 60°), $\Delta\theta$ values of (90°, 150°, 210°, 270°, 340°) (N=0), θ_i =0°, γ_1 =0°, a_0 =0.07, acceleration inversely square case of the thrust profile (exponential sinusoid), Earth-Mars flight

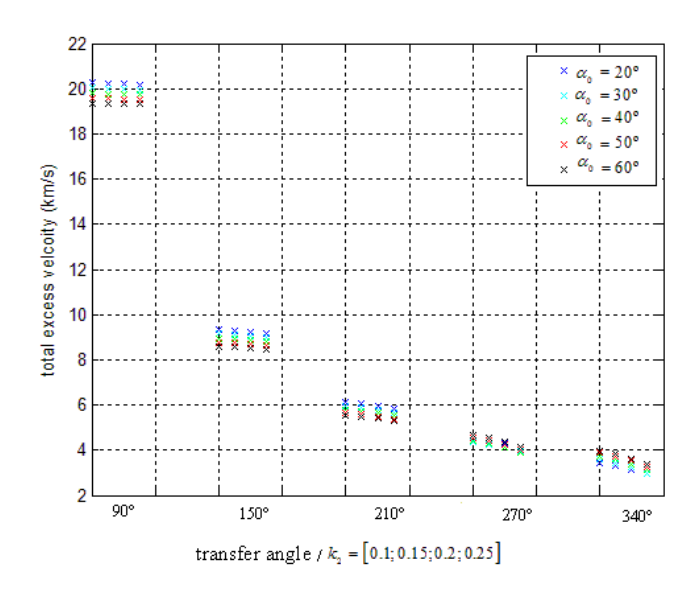


Figure 7.87: $V_{\infty,T}$ for k_2 values of (0.1; 0.15; 0.2; 0.25) from left to right in the figure, α_0 values of (20°, 30°, 40°, 50°, 60°), $\Delta\theta$ values of (90°, 150°, 210°, 270°, 340°) (N=0), θ_i =0°, γ_i =0°, a_0 =0.07, acceleration inversely square case of the thrust profile (exponential sinusoid), Earth-Mars flight

Some remarks can be drawn from figures 7.86 and 7.87. By increasing the geometric parameter k_2 , the TOF increases, while the total excess velocity decreases. The differences in TOF and in total excess velocity between different values of k_2 increase for higher values of the transfer angle $\Delta\theta$. The highest difference in TOF between different values of k_2 for the same transfer angle and α_0 is 0.0187 years, while the highest difference in total excess velocity is $0.6295 \, km/s$. For increasing values of α_0 , the TOF increases while the total excess velocity decreases for transfer angles smaller than 210° (inclusive) and it decreases for transfer angles higher than 210°.

Similar figures can be shown for 1 and 2 revolutions, using the same values for the geometric parameter k_2 , for $\Delta\theta$, α_1 and γ_1 . The normalised thrust acceleration a_0 values used in figures 7.88 and 7.89 were 0.04 and 0.05 for N=1 and N=2, respectively. Unlike for the other shapes, the normalised thrust acceleration is higher for N=2 than for N=1. This is due to integration errors that occur for the geometric parameter k_2 and for the initial flight path angle γ_1 chosen.

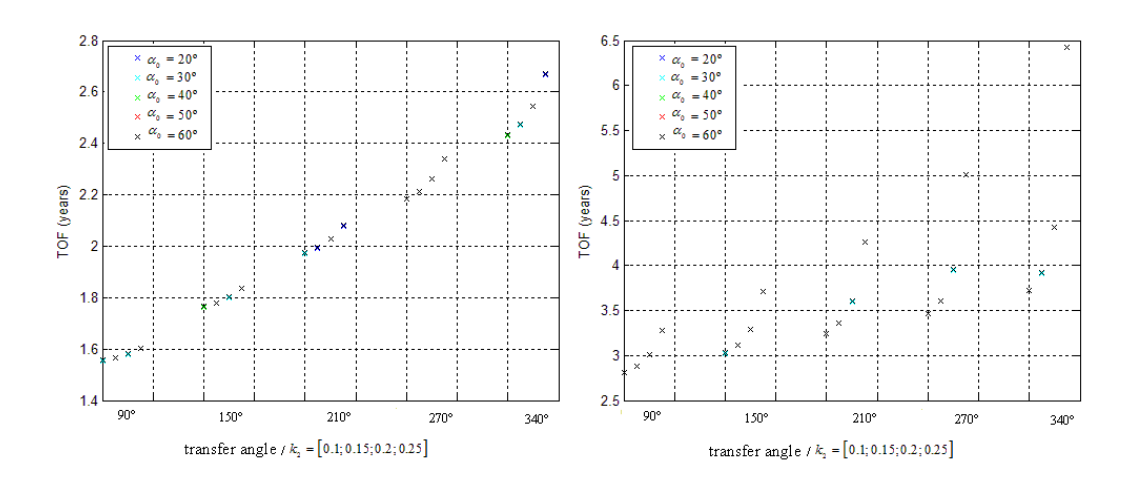


Figure 7.88: TOF for k_2 values of (0.1; 0.15; 0.2; 0.25) from left to right in the figure, α_0 values of (20°, 30°, 40°, 50°, 60°), $\Delta\theta$ values of (90°, 150°, 210°, 270°, 340°), $\gamma_1 = 0^\circ$, $\theta_i = 0^\circ$, acceleration inversely square case of the thrust profile (exponential sinusoid), Earth-Mars flight, N=1 ($\alpha_0 = 0.04$) and N=2 ($\alpha_0 = 0.05$)

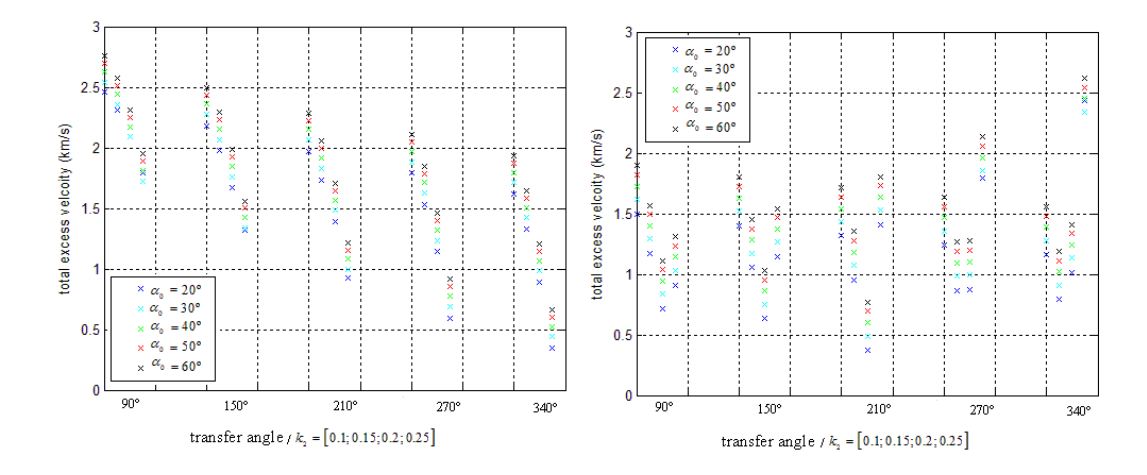


Figure 7.89: $V_{\infty,T}$ for k_2 values of (0.1; 0.15; 0.2; 0.25) from left to right in the figure, α_0 values of (20°, 30°, 40°, 50°, 60°), $\Delta\theta$ values of (90°, 150°, 210°, 270°, 340°), $\gamma_1 = 0^\circ$, $\theta_2 = 0^\circ$, acceleration inversely square case of the thrust profile (exponential sinusoid), Earth-Mars flight, N=1 ($\alpha_0 = 0.04$) and N=2 ($\alpha_0 = 0.05$)

Similar remarks as the ones given for N=0 can be drawn for figures 7.88 and 7.89. Note that, unlike for N=0 and N=1, for N=2 and between $k_2 = 0.2$ and $k_2 = 0.25$, the total excess velocity increases. For N=1, the highest difference in TOF between different k_2 and for the same transfer angle and α_0 is about 0.2311 years, while the highest difference in total excess velocity is $1.2725 \, km/s$. These differences are considerably high compared with the ones for the sinusoidal spiral, for the same thrust profile. For N=2, the highest difference in TOF between different k_2 and for the same transfer angle and α_0 is about 2.6208 years, while the highest difference in total excess velocity is about $1.3 \, km/s$.

The TOF range for this Earth-Mars flight is from 0.2701 years to 6.4256 years. The total excess velocity has a minimum value of $0.3715 \, km/s$ and a maximum value of $20.2533 \, km/s$. As expected, the minimum value for the TOF and the maximum value for the total excess velocity occur for the smallest transfer angle -90° (N=0). The maximum value for the TOF occurs for the highest transfer angle presented -340° (N=2), while the minimum value for the total excess velocity occurs for the transfer angle 210° (N=2), unlike for the other shapes.

The maximum difference in TOF between two consecutive values of the transfer angle $\Delta\theta$ is about 1.41 years. The maximum value for these differences is 10.9661 km/s for N=0 and the minimum value is about 76.26 m/s for 2 revolutions.

Tables 7.21 and 7.22 show the values for the TOF and the excess velocity for an Earth-Mars flight. Parameter k_2 was chosen 0.01, α_0 was chosen 20°, $\Delta\theta$ was chosen 90° and N was taken 1 for the first table and 2 for the second one. In these tables, the normalised thrust acceleration a_0 was 0.04. Note that the values assumed for a_0 for N=1 and N=2 are the minimum values that can be used in both cases for this shape without facing integration problems for the interval of the geometric parameter γ_1 and for the other input parameters considered.

N=1	$\gamma_1 = 0^{\circ}$	$\gamma_1 = 0.75^{\circ}$	$\gamma_1 = 1.5^{\circ}$	$\gamma_1 = 2.25^{\circ}$	$\gamma_1 = 3^{\circ}$
$V_{\infty,total}\left(km/s\right)$	2.5808	2.6746	2.7666	2.8564	2.9449
$V_{\infty,1}\left(km/s\right)$	1.5×10 ⁻⁴	0.3920	0.7834	1.1742	1.5644
$V_{\infty,2}(km/s)$	2.5806	2.2826	1.9832	1.6822	1.3805
TOF (years)	1.5476	1.5874	1.6293	1.6731	1.7192

Table 7.21: The excess velocities and the TOF values for N=1, k_2 =0.01, $\Delta\theta$ =90°, α_0 =20°, γ_1 values of (0°; 0.75°; 1.5°; 2.25°; 3°), a_0 =0.04, θ_i =0°, acceleration inversely square case (exponential sinusoid), Earth-Mars flight

N=2	$\gamma_1 = 0^{\circ}$	$\gamma_1 = 0.75^{\circ}$	$\gamma_1 = 1.5^{\circ}$	$\gamma_1 = 2.25^{\circ}$	$\gamma_1 = 3^{\circ}$
$V_{\infty,total}\left(km/s\right)$	1.6411	1.6292	1.7236	1.8480	2.0391
$V_{\infty,1}(km/s)$	0.1418	0.4212	0.7985	1.1831	1.5695
$V_{\infty,2}(km/s)$	1.4994	1.2080	0.9252	0.6649	0.4696
TOF (years)	2.7789	2.9085	3.0464	3.1933	3.3498

Table 7.22: The excess velocities and the TOF values for N=2, k_2 =0.01, $\Delta\theta$ =90°, α_0 =20°, γ_1 values of (0°; 0.75°; 1.5°; 2.25°; 3°), a_0 =0.04, θ_i =0°, acceleration inversely square case (exponential sinusoid), Earth-Mars flight

For increasing values of m, the total excess velocity and the TOF increase. The values for the total excess velocity are higher for N=1 than for N=2. Note that the excess velocity $V_{\infty,1}$ increases faster than the excess velocity $V_{\infty,2}$ decreases, for both cases N=1 and N=2.

In figures 7.90 to 7.94, the polar plot, the thrust acceleration a, the thrust angle α , the polar angle rate $\dot{\theta}$ and the flight path angle as function of time are illustrated for N=1 and N=2 cases that were presented in tables 7.21 and 7.22.

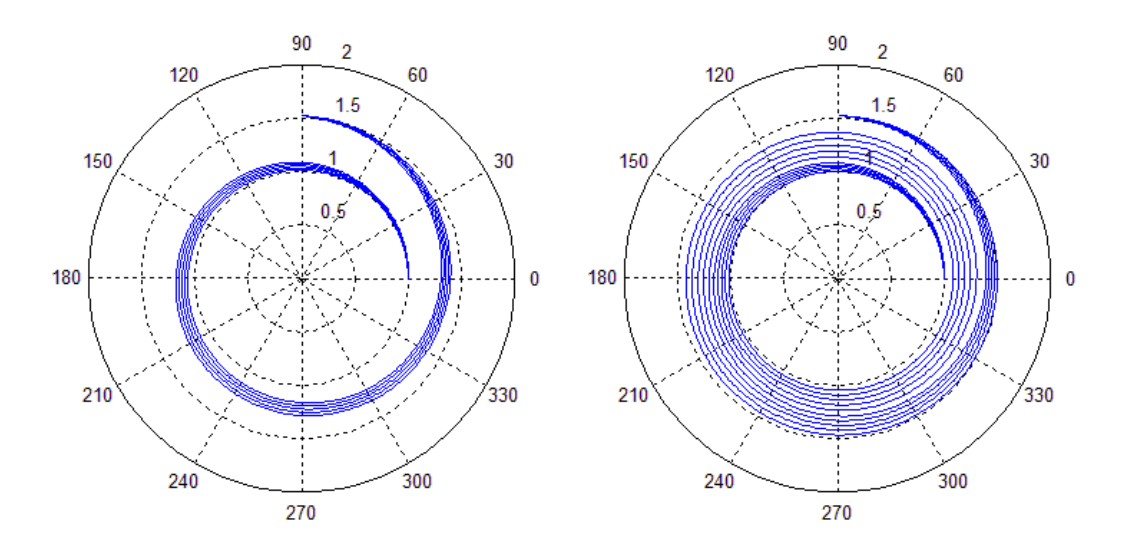


Figure 7.90: Polar plot for N=1 and N=2, a_0 =0.04, k_2 =0.01, $\Delta\theta$ =90°, α_0 =20°, γ_1 values of (0°; 0.75°; 1.5°; 2.25°; 3°), θ_i =0°, acceleration inversely square case (exponential sinusoid), Earth-Mars flight

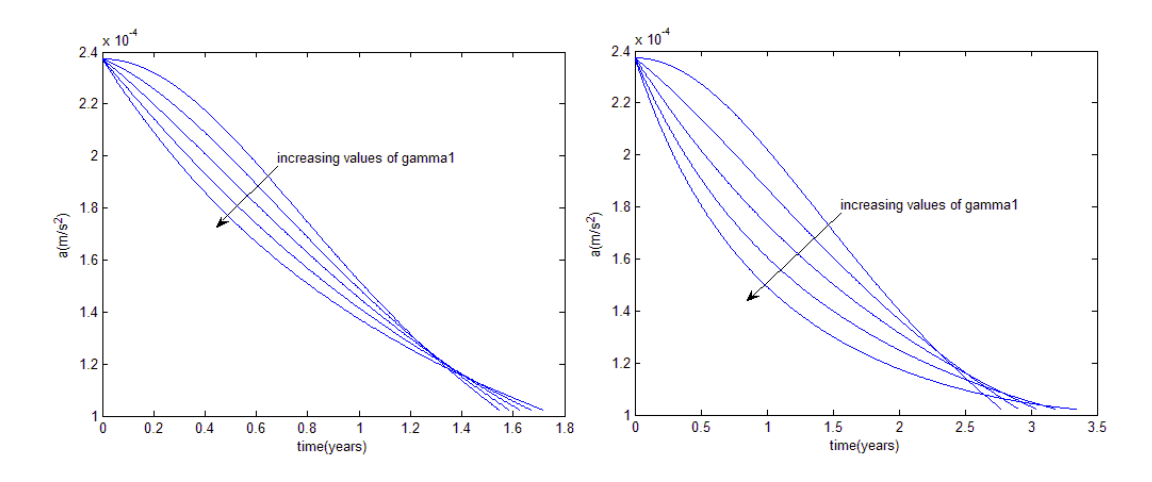


Figure 7.91: a plot for N=1 and N=2, a_0 =0.04, k_2 =0.01, $\Delta\theta$ =90°, α_0 =20°, γ_1 values of (0°; 0.75°; 1.5°; 2.25°; 3°), θ_1 =0°, acceleration inversely square case (exponential sinusoid), Earth-Mars flight

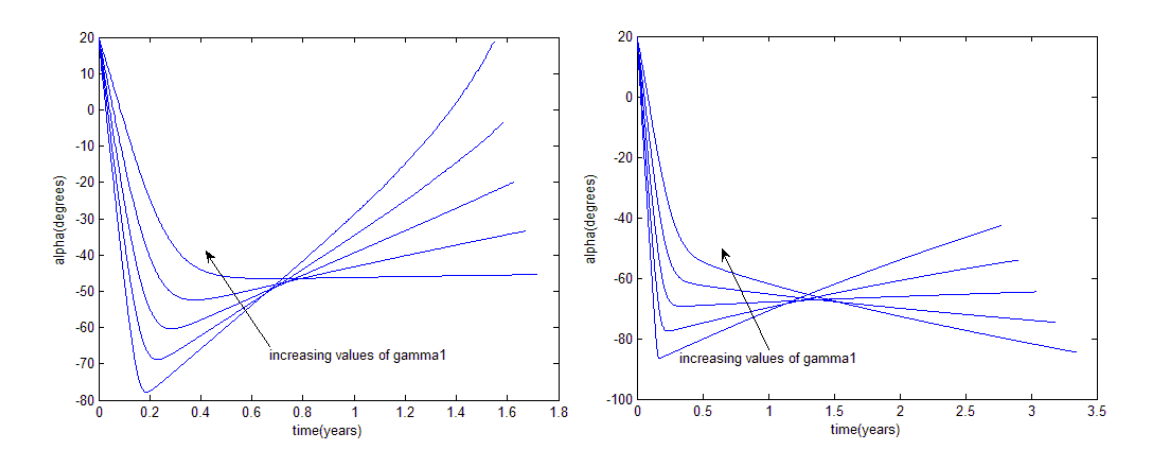


Figure 7.92: α plot for N=1 and N=2, a_0 =0.04, k_2 =0.01, $\Delta\theta$ =90°, α_0 =20°, γ_1 values of (0°; 0.75°; 1.5°; 2.25°; 3°), θ_i =0°, acceleration inversely square case (exponential sinusoid), Earth-Mars flight

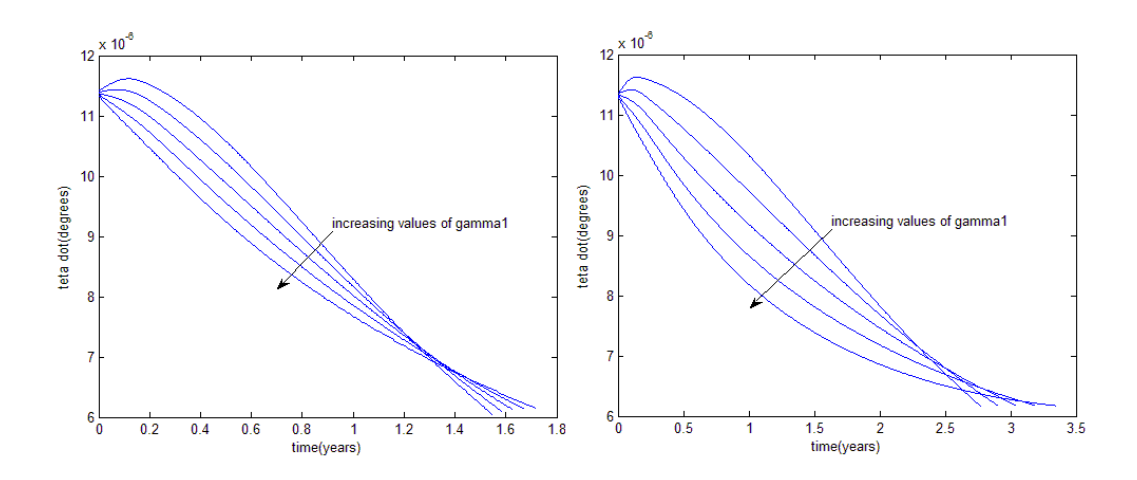


Figure 7.93: $\dot{\theta}$ plot for N=1 and N=2, a_0 =0.04, k_2 =0.01, $\Delta\theta$ =90°, α_0 =20°, γ_1 values of (0°; 0.75°; 1.5°; 2.25°; 3°), θ_1 =0°, acceleration inversely square case (exponential sinusoid), Earth-Mars flight

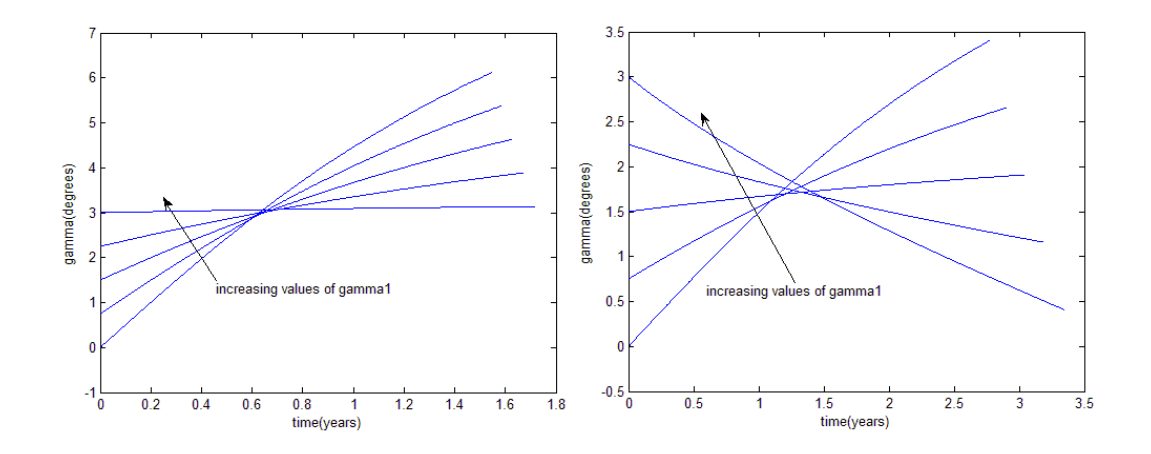


Figure 7.94: γ plot for N=1 and N=2, a_0 =0.04, k_2 =0.01, $\Delta\theta$ =90°, α_0 =20°, γ_1 values of (0°; 0.75°; 1.5°; 2.25°; 3°), θ_i =0°, acceleration inversely square case (exponential sinusoid), Earth-Mars flight

From figure 7.91, although the assumed normalised thrust acceleration a_0 is the same for N=1 and for N=2, differences in values of the instantaneous thrust acceleration between the two cases of N. Note that the thrust acceleration trend is similar to the $\dot{\theta}$ trend. The values of the thrust angle α are higher for N=1 than for N=2. For most of the interplanetary flight for the case N=1 in figure 7.92, the spacecraft is thrusting inwards in the radial direction, while in the tangential direction it thrusts in the positive direction (α is negative, higher than -90°), as for the other shapes.

b) Tangential Case of the Thrust Profile

Figures 7.95 and 7.96 show the TOF and the total excess velocity when changing parameter k_2 and the transfer angle $\Delta\theta$ (N=0). The values used in these figures for the geometric parameter k_2 were (0.1; 0.15; 0.2; 0.25), for the initial flight path angle γ_1 were (0°; 0.75°; 1.5°; 2.25°; 3°) and for the transfer angle $\Delta\theta$ were (90°, 150°, 210°, 270°, 340°).

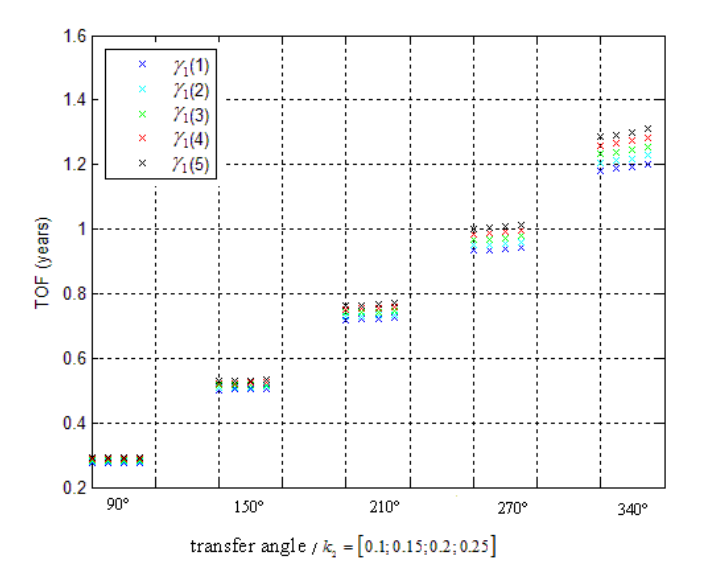


Figure 7.95: TOF for k_2 values of (0.1; 0.15; 0.2; 0.25) from left to right in the figure, γ_1 values of (0°; 0.75°; 1.5°; 2.25°; 3°), θ_i =0°, $\Delta\theta$ values of (90°, 150°, 210°, 270°, 340°) (N=0), tangential thrust profile (exponential sinusoid), Earth-Mars flight

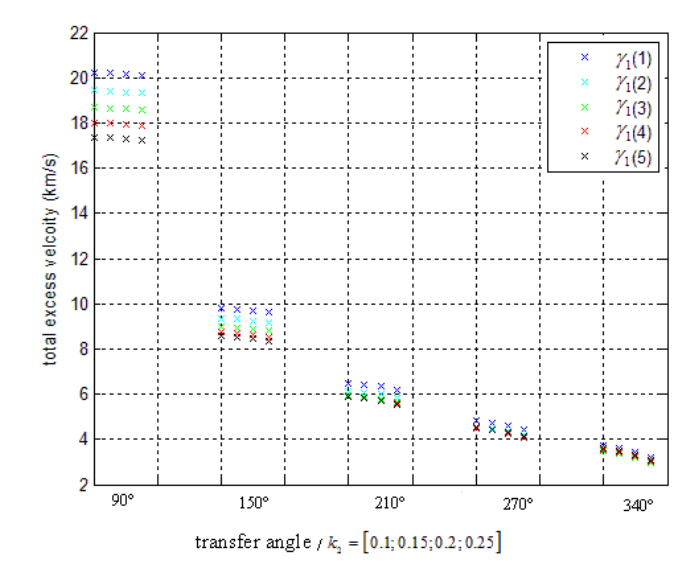


Figure 7.96: $V_{\omega,T}$ for k_2 values of (0.1; 0.15; 0.2; 0.25) from left to right in the figure, γ_1 values of (0°; 0.75°; 1.5°; 2.25°; 3°), θ_i =0°, $\Delta\theta$ values of (90°, 150°, 210°, 270°, 340°) (N=0), tangential thrust profile (exponential sinusoid), Earth-Mars flight

From figures 7.95 and 7.96, by increasing the geometric parameter k_2 , the TOF increases, while the total excess velocity decreases, as for the acceleration inversely square case. For increasing values of γ_1 , the TOF increases, while the total excess velocity decreases. The highest difference in TOF between different k_2 for the same transfer angle and m is 0.02547 years, while the highest difference in total excess velocity is 0.5343 km/s. The differences in TOF and in total excess velocity between different values of γ_1 increase and decrease, respectively for higher values of the transfer angle $\Delta\theta$.

Similar figures can be shown for 1 and 2 revolutions, using the same values for the geometric parameter k_2 , for the transfer angle $\Delta\theta$ and for the initial flight path angle γ_1 as the ones used for N=0.

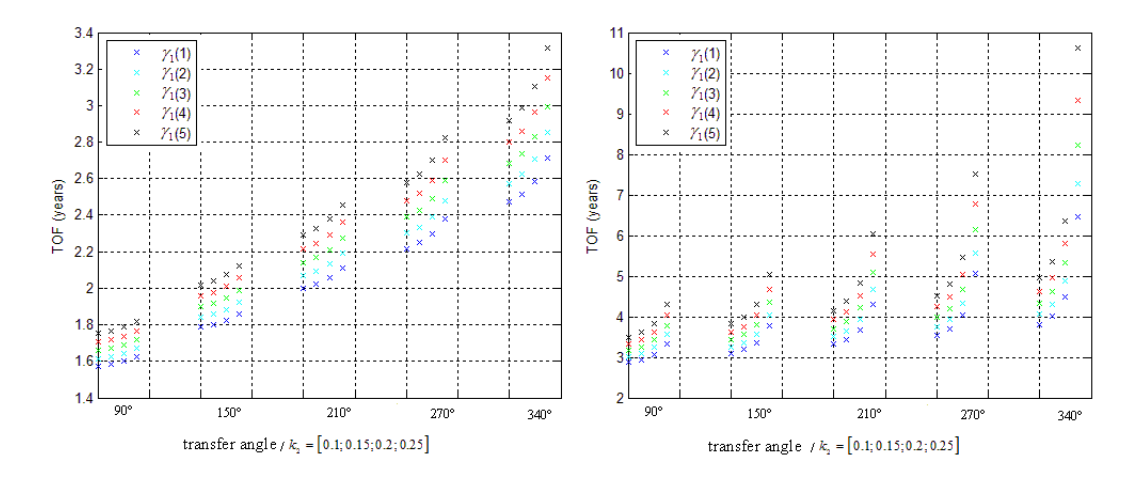


Figure 7.97: TOF for k_2 values of (0.1; 0.15; 0.2; 0.25) from left to right in the figure, γ_1 values of (0°; 0.75°; 1.5°; 2.25°; 3°), θ_i =0°, $\Delta\theta$ values of (90°, 150°, 210°, 270°, 340°), tangential thrust profile (exponential sinusoid), Earth-Mars flight, N=1 and N=2

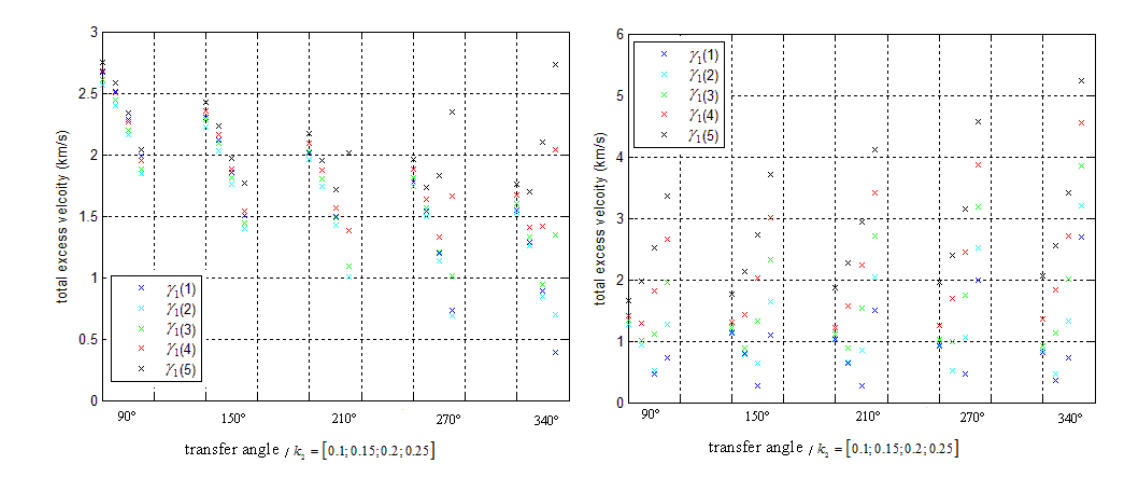


Figure 7.98: $V_{_{\infty,T}}$ for $k_{_2}$ values of (0.1; 0.15; 0.2; 0.25) from left to right in the figure, $\gamma_{_1}$ values of (0°; 0.75°; 1.5°; 2.25°; 3°), $\theta_{_i}$ =0°, $\Delta\theta$ values of (90°, 150°, 210°, 270°, 340°), tangential thrust profile (exponential sinusoid), Earth-Mars flight, N=1 and N=2

Similar remarks to the ones given for N=0 can be drawn for figures 7.97 and 7.98. For N=1, the total excess velocity decreases with the increasing of k_2 for transfer angles smaller or equal to 150°. For higher values of $\Delta\theta$, the total excess velocity increases for values of k_2 higher than 0.15 (for the highest values of γ_1). For N=1, the highest difference in TOF between different k_2 for the same transfer angle and α_0 is about 0.3825 years, while the highest difference in total excess velocity is 1.1566 km/s. For N=2, the highest difference in TOF between different k_2 for the same transfer angle and α_0 is about

5.5085 years, while the highest difference in total excess velocity is $3.1882 \, km/s$. So, for higher values of N, the TOF and the total excess velocity become more sensitive to k_2 variation.

The TOF range for this Earth-Mars flight is from 0.2759 years to 10.6231 years. The total excess velocity has a minimum value of $0.2732 \, km/s$ and a maximum value of $20.2235 \, km/s$. As expected, the minimum value for the TOF and the maximum value for the total excess velocity occur for the smallest transfer angle -90° (N=0); while the minimum value for the total excess velocity occurs for the transfer angle 210° (N=2), unlike for the other shapes.

The maximum difference in TOF between two consecutive values of the transfer angle $\Delta\theta$ is about 3.1011 years. For a certain number of revolutions, these differences increase when increasing the transfer angle. The difference in terms of total excess velocity between two consecutive transfer angles is highest between $\Delta\theta = 90^{\circ}$ and $\Delta\theta = 150^{\circ}$ for N=0. The maximum value for these differences is 10.4851 km/s for N=0 and the order of magnitude of the minimum value is $10^{-11} m/s$ for 2 revolutions.

Tables 7.23 and 7.24 show the values for the TOF and the excess velocity for an Earth-Mars flight. Parameter k_2 was assumed 0.01, the transfer angle $\Delta\theta$ was assumed 90° and the number of revolutions was taken 1 for the first table and 2 for the second one.

N=1	$\gamma_1 = 0^{\circ}$	$\gamma_1 = 0.75^{\circ}$	$\gamma_1 = 1.5^{\circ}$	$\gamma_1 = 2.25^{\circ}$	$\gamma_1 = 3^{\circ}$
$V_{\infty,total}(km/s)$	2.7967	2.6945	2.7448	2.8113	2.8818
$V_{\infty,1}(km/s)$	0.2057	0.4206	0.7882	1.1721	1.5597
$V_{\infty,2}(km/s)$	2.5909	2.2739	1.9566	1.6393	1.3221
TOF (years)	1.5652	1.6072	1.6506	1.6955	1.7420

Table 7.23: Excess velocities and TOF values for N=1, k_2 =0.01, $\Delta\theta$ =90°, γ_1 values of (0°; 0.75°; 1.5°; 2.25°; 3°), θ_1 =0°, tangential thrust profile (exponential sinusoid), Earth-Mars flight

N=2	$\gamma_1 = 0^{\circ}$	$\gamma_1 = 0.75^{\circ}$	$\gamma_1 = 1.5^{\circ}$	$\gamma_1 = 2.25^{\circ}$	$\gamma_1 = 3^{\circ}$
$V_{\infty,total}(km/s)$	1.4997	1.5122	1.5841	1.6577	1.7348
$V_{\infty,1}(km/s)$	0.0631	0.3918	0.7800	1.1695	1.5590
$V_{\infty,2}(km/s)$	1.4366	1.1204	0.8041	0.4882	0.1758
TOF (years)	2.8267	2.9597	3.1006	3.2498	3.4081

Table 7.24: Excess velocities and TOF values for N=2, k_2 =0.01, $\Delta\theta$ =90°, γ_1 values of (0°; 0.75°; 1.5°; 2.25°; 3°), θ_i =0°, tangential thrust profile (exponential sinusoid), Earth-Mars flight

For increasing values of γ_1 , the TOF and the total excess velocity increase for N=2. For N=1, the total excess velocity decreases between $\gamma_1 = 0^{\circ}$ and $\gamma_1 = 0.75^{\circ}$, while it increases for values of γ_1 between 0.75° and 3°. The opposite situation occurred for the acceleration inversely square case.

In figures 7.99 to 7.102, the polar plot, the thrust acceleration a, the thrust angle α and $\dot{\theta}$ as function of time are shown for N=1 and N=2 cases presented in tables 7.23 and 7.24.

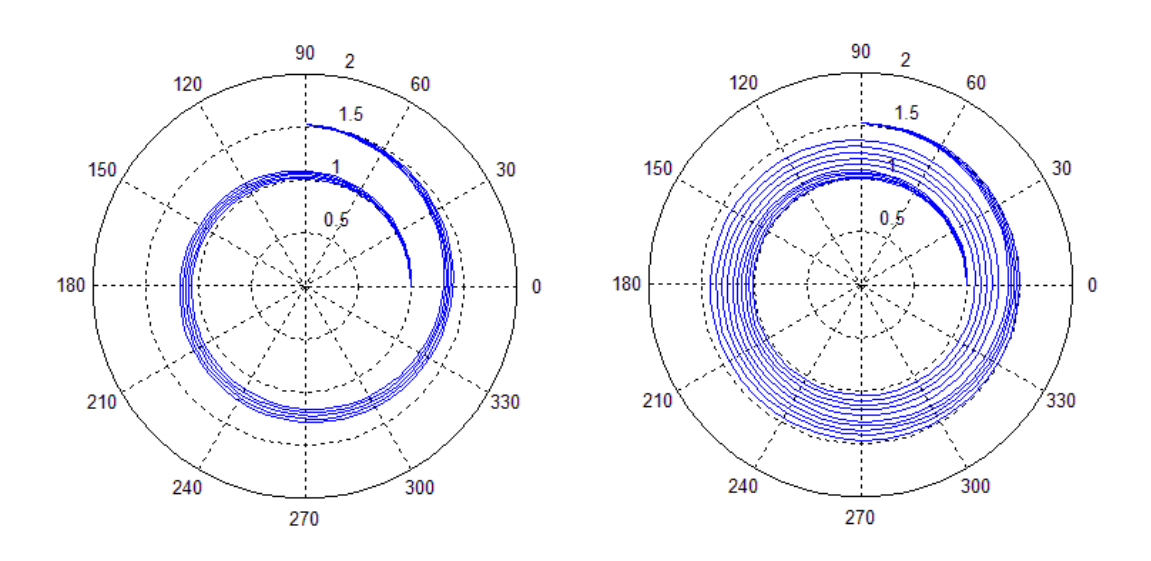


Figure 7.99: Polar plot for N=1 and N=2, k_2 =0.01, $\Delta\theta$ =90°, γ_1 values of (0°; 0.75°; 1.5°; 2.25°; 3°), θ_1 =0°, tangential thrust profile (exponential sinusoid), Earth-Mars flight

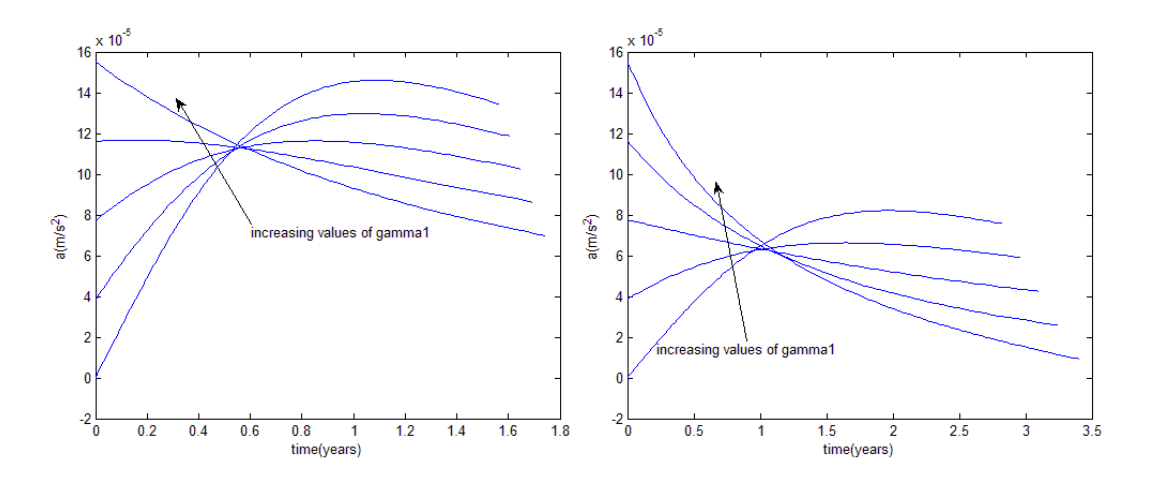


Figure 7.100: a plot for N=1 and N=2, k_z =0.01, $\Delta\theta$ =90°, γ_1 values of (0°; 0.75°; 1.5°; 2.25°; 3°), θ_i =0°, tangential thrust profile (exponential sinusoid), Earth-Mars flight

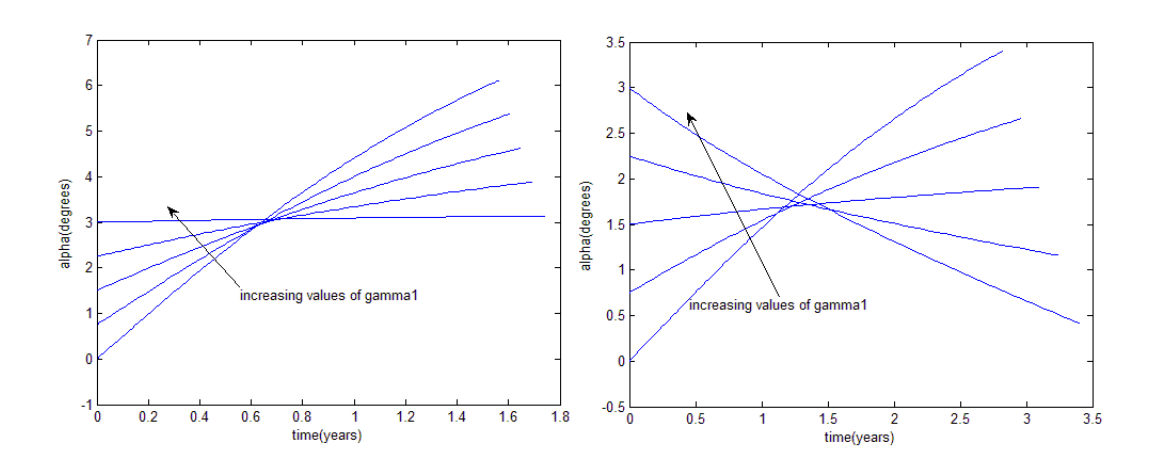


Figure 7.101: α plot for N=1 and N=2, k_2 =0.01, $\Delta\theta$ =90°, γ_1 values of (0°; 0.75°; 1.5°; 2.25°; 3°), θ_i =0°, tangential thrust profile (exponential sinusoid), Earth-Mars flight

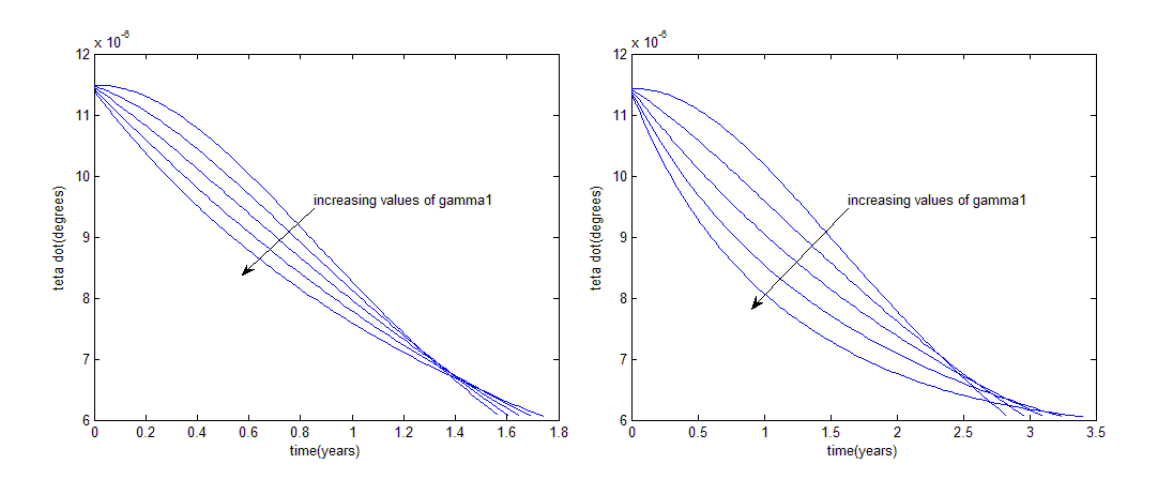


Figure 7.102: $\dot{\theta}$ plot for N=1 and N=2, k_2 =0.01, $\Delta\theta$ =90°, γ_1 values of (0°; 0.75°; 1.5°; 2.25°; 3°), θ_i =0°, tangential thrust profile (exponential sinusoid), Earth-Mars flight

The values for the thrust angle α are smaller for N=2 than for N=1. The magnitude of the thrust acceleration is higher for N=1 than for N=2 which means that the magnitude of the instantaneous thrust required for a longer flight is smaller.

7.7. Conclusions

Some conclusions can be drawn from the analyse done in the previous sections.

The variation of the parameter θ_i does not have any influence on the performance of the spacecraft in terms of TOF, thrust acceleration and excess velocities for the Archimedean spiral and for the logarithmic spiral, for both thrust profiles analysed in this chapter and for the constant acceleration case of the thrust profile presented in appendix D. In this way, for these two shapes, θ_i is not part of the class of variables S (chapter 6) that are required as an input for a low-thrust problem.

As already mentioned in this chapter, due to integration problems (chapter 6), feasible shapes can only be found for certain combination of parameters. For the lowest value of the normalised thrust acceleration in the acceleration inversely square case of the thrust profile (to obtain a feasible shape), the available interval of values for the geometric parameter is always narrower than the interval for the tangential case. However, in order to have a better comparison between different thrust profiles, the same values for the input variables (transfer angle, geometric parameters and initial polar angle) were used. Therefore, a narrower interval of values for the geometric parameters was used for the tangential case compared with the available interval that could have been chosen for this thrust profile.

Note that for the logarithmic spiral and for the Poinsot's spiral (hyperbolic cosine), for the examples given in this chapter, the excess velocity at the target planet $(V_{\infty,2})$ is significantly higher than the excess velocity at the departure planet $(V_{\infty,1})$. This situation is attractive for a mission where swing-bys are used. In this case, there is no need to slow down the spacecraft, therefore high values of the excess velocity $V_{\infty,2}$ are preferable if the purpose is to use gravity assist at that planet and not orbit insertion.

Table 7.25 shows the range for the thrust acceleration and the minimum values for the total excess velocity for the cases presented in this chapter and for the acceleration inversely square and tangential cases of the thrust profile.

Shapes	Minimum $V_{_{\infty,T}}$ (acceleration inversely square case) (km/s)	Range for <i>a</i> (acceleration inversely square case) (m/s^2)	Minimum $V_{\omega,T}$ (tangential case) (km/s)	Range for a (tangential case) (m/s^2)
Archimedean spiral	1.2767	$\sim 0.8 - 2.4 \times 10^{-4}$	1.2285	$\sim 0.2 - 3.2 \times 10^{-4}$
Logarithmic spiral	1.2397	$\sim 1.2 - 3 \times 10^{-4}$	1.2004	~1 - 20×10 ⁻⁵
Poinsot's spiral (hyperbolic sine)	1.2754	$\sim 1 - 3 \times 10^{-4}$	1.2349	$\sim 0.2 - 5.5 \times 10^{-4}$
Poinsot's spiral (hyperbolic cosine)	1.1663	$\sim 0.8 - 2.4 \times 10^{-4}$	0.7682	~0.8 – 14×10 ⁻⁵
Sinusoidal spiral	1.1820	~0.8 - 2.4×10 ⁻⁴	0.4223	$\sim 10^{-6} - 1.4 \times 10^{-4}$
Exponential sinusoid	0.3715	~1 - 2.4×10 ⁻⁴	0.2732	~10 ⁻⁶ - 1.6×10 ⁻⁴

Table 7.25: Minimum values for the total excess velocity and the range of values for the thrust acceleration, for the acceleration inversely square and tangential cases of the thrust profile

In the tangential thrust case, for the examples given, the sinusoidal spiral and the exponential sinusoid have the lower values of thrust acceleration, while the Poinsot's spiral (hyperbolic sine) and the Archimedean spiral have the highest. In terms of total excess velocity, the sinusoidal spiral and the exponential sinusoid show the lowest values, while the Poinsot's spiral (hyperbolic sine) has the highest. Note that this does not mean that this last shape performs worse that the other shapes. This only means that for the input parameters chosen, this shape showed the worst results. During this sensitivity analysis, it was not possible to understand completely the influence of the input parameters $(\theta_i, \Delta\theta, K)$ on the shapes' performance (TOF, excess velocities and thrust acceleration). For instance, the excess velocity variation trend with the geometric parameter might not be monotonous (the logarithmic spiral (table 7.7) and the exponential sinusoid (table 7.23)) for a certain value of the transfer angle $\Delta\theta$, but it can be for other values of $\Delta\theta$.

In the acceleration inversely square thrust profile case, for the examples given (table 7.25), the exponential sinusoid has the lowest value of the total excess velocity, while the Archimedean spiral has the highest one. The shapes' performance in terms of TOF, thrust acceleration and excess velocities depends on the minimum allowed value for the

parameter a_0 for certain combination of input parameters. For higher values of the transfer angle $\Delta\theta$ and complete number of revolutions N, the minimum value for a_0 that can be selected without having integration errors (chapter 6) generally decreases. However, this value not only depends on $\Delta\theta$ and N, but also on the geometric parameter and on the initial values for θ and α that are being picked. Often during this sensitivity analysis, when changing the available interval of values for one input parameter, the interval of available values for the other input parameters is affected. In this way, it is not possible to limit the search space in order to avoid integration problems, since the available interval of values for each input variable constantly varies. In chapter 8 and 9, an optimisation procedure will be done in order to compare the shapes' performance. Due to the fact that there will be no reduction on the search space of the input variables, computation time of this optimisation procedure will be significantly larger compared with the tangential case, since there are two more input variables and there will be integration problems that will slow down the program.

Comparing the performance between the acceleration inversely square case of the thrust profile and the tangential case, the instantaneous thrust acceleration values are generally higher for the first case than for the tangential one. Also, the total excess velocity values are generally smaller for the tangential case than for the acceleration inversely square case of the thrust profile. Note that although in these examples the acceleration inversely square case performed worse than the tangential case, it does not mean that this thrust profile should be discarded. An optimisation procedure is still required for both cases in order to compare them and to find which one yields the best results.

Table 7.26 shows the minimum values for the total excess velocity and for the normalised thrust acceleration for the example cases presented in this chapter and in appendix D, for the acceleration inversely square and constant acceleration cases of the thrust profile.

Shapes	Minimum $V_{\infty,T}$ (acceleration inversely square case) (km/s)	Minimum a_0 (acceleration inversely square case)	Minimum $V_{_{\infty,T}}$ (constant acceleration case) (km/s)	Minimum a_0 (constant acceleration case)
Archimedean spiral	1.2767	0.02	1.4630	0.02
Logarithmic spiral	1.2397	0.02	1.4021	0.02
Poinsot's spiral (hyperbolic sine)	1.2754	0.02	2.5842	0.04
Poinsot's spiral (hyperbolic cosine)	1.1663	0.03	1.3095	0.02
Sinusoidal spiral	1.1820	0.03	1.3107	0.02
Exponential sinusoid	0.3715	0.04	0.3772	0.03

Table 7.26: Minimum values for the total excess velocity and for the normalised thrust acceleration, for the acceleration inversely square and constant acceleration cases of the thrust profile

Regarding the constant acceleration case of the thrust profile, the minimum total excess velocity values are always higher than for the acceleration inversely square case of the thrust profile. Note that the values for the input variables in both cases were the same in this chapter and in appendix D, except for the normalised thrust acceleration ones. For all shapes, except for the Poinsot's spiral (hyperbolic sine), the minimum values for the normalised thrust acceleration used without causing integration errors are higher or equal for the acceleration inversely square case of the thrust profile than for the constant thrust one. Generally, for increasing values of the transfer angle $\Delta\theta$ and of the complete number of revolutions N, the difference of values for the minimum normalised thrust acceleration between these two cases of the thrust profile decreases. For the Archimedean spiral and for the logarithmic spiral, the values used for a_0 are the same for both cases of the thrust profile, for N=2. Note that the thrust acceleration required for the constant acceleration case is significantly higher since the differences in a_0 between this case and the acceleration inversely square one are not significantly high and $a = a_0 \mu/r_1^2 = \text{const}$ (for the constant acceleration case), while for the acceleration inversely square case, the thrust acceleration decreases with $1/r^2$. Also, the total excess velocity is, generally, higher than for the acceleration inversely square case. For these reasons, the analysis for the constant acceleration case of the thrust profile will not carry on and an optimisation procedure will not be done in chapter 8.

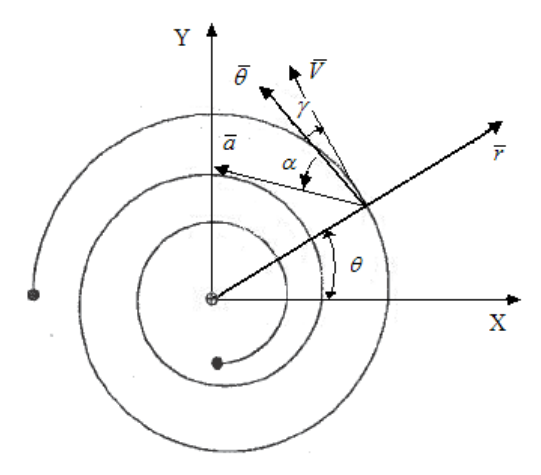


Figure 7.103: Representation of the dynamic parameters: thrust acceleration (\overline{a}) , the velocity of the spacecraft (\overline{V}) , the thrust angle (α) and the flight path angle (γ)

One important remark was present in all sections of this chapter and in appendix D for the acceleration inversely square and constant acceleration cases of the thrust profile: the negative values of the thrust angle α . Figure 7.103 illustrates the situation that will be discussed in this paragraph. In all shapes, the thrust angle α is negative and it can reach values of -70°; this means that the spacecraft is almost thrusting inwards in the radial direction, in the same direction as the gravitational acceleration, while in the tangential direction it thrusts in the positive direction. These results are valid since they were benchmarked by a test program. The only explanation for these negative values of the thrust angle is that in order to satisfy the initial and final conditions imposed by the lowthrust problem (Earth-Mars flight), the spacecraft will have to thrust inwards in the radial direction. Note that all the initial values for the thrust angle, α_0 were negative, except for the exponential sinusoid. Negative values were chosen, because otherwise the trajectory would not be computed, due to integration problems. Note that for the tangential case, the magnitude of the thrust angle is not higher than 17° for all shapes. On the other hand, values for the thrust angle will have to reach at least -70°, in order for the spacecraft to thrust according to $a = a_0 \mu/r^2$ or $a = a_0 \mu/r_1^2 = \text{const}$.

8. Optimisation

Optimisation refers to a study of a problem, where "the best" out of many solutions is sought. In an interplanetary mission where a spacecraft trajectory is being designed, "the best" means the trajectory that can perform "better" than any other possible trajectory. Performing "better" means that the trajectory chosen maximizes or minimizes a certain objective function. Often, for a trajectory design problem, the fuel mass consumption and the time of flight (TOF) functions are the ones that need to be minimized. Note that the optimized trajectory is chosen among possible trajectories, i.e., among trajectories that respect constraints that the user imposes for the problem. For instance, constraints can be given for the maximum TOF, the maximum total excess velocity or interval of time for the launch date.

In sections 8.1 and 8.2, an overview of some optimisation methods and a brief description about multi-objective optimisation will be presented, respectively. An explanation about the optimisation procedure implemented in this master thesis will be given in section 8.3.

8.1. Optimisation Methods

Optimisation methods are divided in two categories [Noomen, 2007]: the analytical methods that have a direct solving and the numerical methods that need an iteration procedure to be solved. Among the numerical methods, there are three main types [Melman, 2007]:

- Calculus-based
- Enumerative
- Random search

These three methods will be discussed in detail in the following sections.

8.1.1. Calculus-Based Methods

Calculus- or gradient-based techniques are optimisation methods that use the derivatives of the objective function. Calculus-based methods are divided in two main classes: the direct methods and the indirect methods [Melman, 2007]. The indirect methods find the maximum or the minimum of a certain objective function by setting its gradient equal to zero, while the direct methods find the optimal solution by moving in the direction of the largest gradient [Melman, 2007]. Unfortunately, these methods are only efficient if the objective function is unimodal, i.e., it has only one local maximum or minimum. To better explain this situation, figure 8.1 illustrates a function that is multimodal, i.e., that has multiple minima and maxima. For instance, if the search for the global minimum starts near one of the local minima, the procedure will not find overall the optimal one. This means that frequently the use of calculus-based methods in this kind of functions results in the determination of a local optimum. Note that the fact that derivatives are required represents a drawback in these methods. In many problems, the expressions for the derivatives are quite complex and also present singularities.

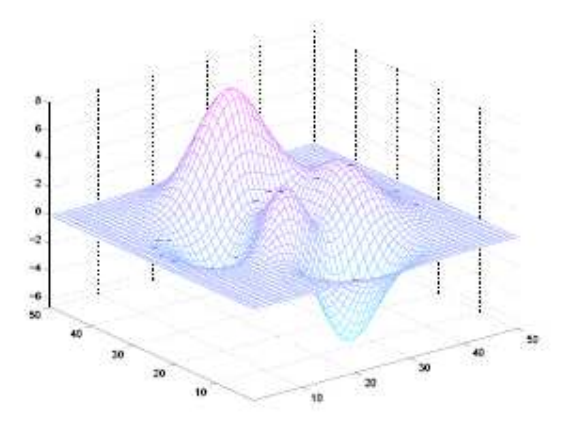


Figure 8.1: A multimodal function: $f(x, y) = 3(1-x^2)e^{-x^2-(y+1)^2} - 10(x/5-x^3-y^5)e^{-x^2-y^2} - 1/3e^{-(x+1)^2-y^2}$ [Melman, 2007]

The problem presented in this master thesis is a complex and multimodal problem, with several undefined derivatives. For this reason, the calculus-based method was not chosen in this master thesis.

8.1.2. Enumerative Methods

Enumerative methods are quite straightforward methods. Within a search space, these methods find the optimal solution by looking at all objective function values, one at the time. They are mostly rejected due to their lack of efficiency, i.e., the search space, for most problems, is too large to search for all objective function values one at the time. A more advanced form for the enumerative techniques is Dynamic Programming (DP). The DP technique divides a complex problem into many sub-problems that are more likely to be solved [Melman, 2007]. Knowing the sub-solutions of the simpler problems, the solution of the original problem can be found by combining these sub-solutions. DP has the disadvantage of becoming very slow when the problem in question increases in size and complexity.

The Simulated Annealing (SA) can be also considered part of the enumerative methods [Noomen, 2007]. This technique imitates the annealing of metal, where the objective function corresponds to the energy state of the metal that has to be minimized [Melman, 2007]. This method makes use of a search procedure that uses random choice as a tool to guide a highly exploitative search through a coding parameter space. This kind of search does not necessarily mean directionless, unlike for the random methods (see section 8.1.3).

According to [Noomen, 2007], the Genetic Algorithm (GA) method (or Evolution Programming (EP)) can be inserted in the category of the enumerative methods. GA is a relatively new area of research that applies the 'survival-of-the fitness' principle. It tries to find the optimal solution through a certain population of solutions that have the opportunity to evolve and create new solutions (individuals). The fittest individuals have higher probability to be chosen to produce offspring, and after a certain number of generations, only fitter individuals are most likely to survive and become close to the optimal solution. Figure 8.2 illustrates how GA works.

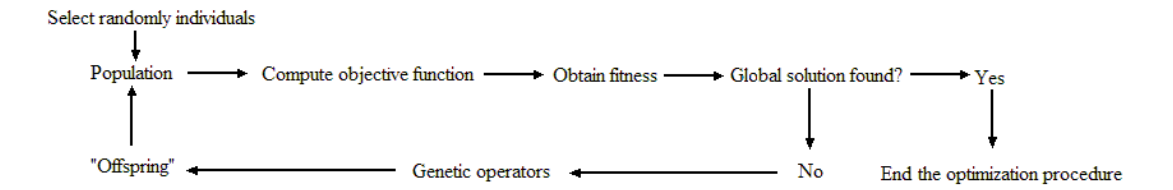


Figure 8.2: Scheme illustrating the steps to take in a GA method

An initial population is created randomly. This means that a good starting point is not necessary. Afterwards, the objective function is evaluated for each individual in the population, yielding the fitness of each individual. Next, the test is made to check if the global solution was found. If the optimal was found, the program will stop; otherwise, some genetic operators (crossover, mutation, immigration, among others) are applied to the population creating offspring. The offspring will take the place of their parents and form a new population. In this way, the cycle will be repeated over and over until the optimum is found.

GA has already proven to be useful in large and complex problems [Melman, 2007]. Although very efficient, GA is not going to be used in this master thesis. The problem does not have many independent variables and, mainly due to programming time, it will have to be rejected.

8.1.3. Random Methods

In random methods, individuals are randomly picked out of a certain search space, their objective function is computed and the best one is saved. They are not expected to perform better that the standard enumerative methods. The Monte Carlo technique (random method) has the advantage of being a straightforward method (quite simple to implement). Since the problem in this master thesis does not involve many input variables (at maximum five), there is no need to use a more complex method, like the GA method. The time required to implement a Monte Carlo algorithm is significantly less than the one required for the GA, the SA or the DP.

8.2. Multi-Objective Optimisation

Often when designing an interplanetary mission, more than one objective is required to be optimized. The mass of the spacecraft is normally the primary measure of performance, i.e., the objective is usually to maximize the mass of the spacecraft (minimize fuel mass consumption). However, the minimization of the TOF, for instance, can also be considered an important optimisation objective. Depending on the mission purpose, other objectives might be chosen. The combination of these objectives yields a multi-objective optimisation problem.

In multi-objective optimisation, a common method used is to combine the multiple objectives into a scalar objective F. This is obtained by weighting the influence of each sub-objective f_i and summing them [Melman, 2007]:

$$F(a) = \sum_{j=1}^{k} \omega_j f_j(a)$$
(8.1)

The parameter ω_j in equation (8.1) is a weighting factor. This is a quite simple method, but it introduces new parameters: weighting factors. In order to use this method, the user should be familiar with the proper value that should be attributed to the weighting factors. Note that a single-objective optimisation will generally have a single optimal solution. This means that using this method, it is not possible to see and analyse trades between different objectives. An optimal solution will depend on the relationship between the sub-objectives (weighting factors). The determination of the weighting factors itself can be considered an optimisation procedure. Due to the lack of experience in choosing values for the weighting factors, this method was not used in this master thesis. Instead, a Pareto optimisation was implemented.

Pareto optimisation uses the principle of optimizing multiple objectives. The Pareto-optimum is a group of optimal individuals and they are optimal in the sense that no improvements can be obtained in one objective without degradation in the others [Melman, 2007]:

$$f_i(a) \le f_i(b) \quad \forall \quad 1 \le i \le k; \quad f_i(a) < f_i(b) \quad \exists \quad 1 \le i \le k$$
 (8.2)

In the case of minimization, individual b is dominated by individual a if the conditions in (8.2) are satisfied. This means that individual b performs worse or equal to individual a. In the case where individual a is not dominated by any other individual in the population, this individual is called Pareto-optimal and it belongs to the Pareto front. The Pareto front corresponds to a family of individuals that are Pareto-optimal. In figure 8.3, the individuals selected for the Pareto front are represented with a red colour, while the rest of the individuals of the population that were not selected are with black colour. Note that although individual a performs better in terms of the objective a0 with respect to individual a1, it performs worse in terms of the objective a1 with respect to individual a2.

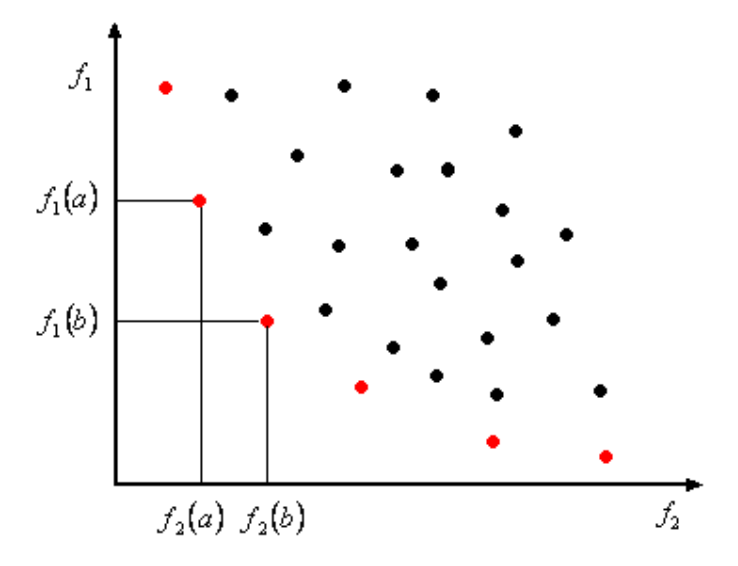


Figure 8.3: Example of a Pareto front (individuals in red)

In this master thesis, after using a Monte Carlo optimisation method, a Pareto front will be built using two objectives: the fuel mass consumption (during the low-thrust flight) and the total excess velocity (chemical burn). Both objectives should be minimized.

8.3. Optimisation Procedure

The first step before using optimisation is to choose the cases that are the most interesting to be analysed. For instance, there is no time to analyse all shapes for all combinations possible of departure and target planets and thrust profiles. Instead, 3 representative missions are selected – Earth-to-Mars, Earth-to-Jupiter and Earth-to-Mercury, for the 2 thrust profiles presented before and for the 6 shapes named in chapter 6. Therefore, 36 cases will be analysed.

8.3.1. Description of the Optimisation Problem

In this master thesis, a Monte Carlo optimisation method (section 8.1.3) was used to obtain Pareto fronts (section 8.2) for the 6 shapes described in chapter 6, for 3 missions: Earth-to-Mars, Earth-to-Jupiter and Earth-to-Mercury and for 2 thrust profiles: "acceleration inversely square", where the magnitude of the thrust acceleration monotonically decreases with the square distance to the Sun and the tangential one. The number of individuals of the population used in the program was 75 000 for the tangential and for the acceleration inversely square cases of the thrust profile. 75 000 was the number chosen for both thrust profiles after some tests with different numbers for the population (see appendix G).

In order to implement a Monte Carlo method, random values were picked for each input variables. For the acceleration inversely square case, these values are:

input =
$$\left[K^*, \theta_i, \Delta\theta + 2\pi N, \alpha_0, a_0\right]$$

For the tangential thrust profile case, the input variables are:

input =
$$\left[K^*, \theta_i, \Delta\theta + 2\pi N\right]$$

Note that K^* represents all the geometric variables that have to be given as input in order to compute the radius r. For all shapes, except for the exponential sinusoid, K^*

corresponds to only one variable. In the case of the exponential sinusoid shape, there are 2 geometric variables that have to be given as an input and θ_i is no longer an input variable (see section 5.5). Also, for the Archimedean spiral and for the logarithmic spiral, θ_i is no longer an input variable, therefore the number of variables is two for the tangential case and four for the acceleration inversely square case of the thrust profile. Note that $\Delta\theta$ is the angle between $\overline{r_1}$ and $\overline{r_2}$, without taking into account the number of revolutions ($\theta_f = \theta_i + \Delta\theta + 2\pi N$). Notice that the terms $\Delta\theta + 2\pi N$ are considered only one parameter in the optimization procedure. This optimisation procedure will be done for at maximum 3 complete revolutions in the Earth-Mars case, 4 revolutions in the Earth-Jupiter case and 2 revolutions in the Earth-Mercury case.

Due to lack of time, a two-dimensional problem optimisation was used, instead of a three-dimensional one. So, the real three-dimensional ephemeris of the planets was not taken into account. Note that vectors $\overline{r_1}$ and $\overline{r_2}$ are not part of the input parameters, only $\Delta\theta + 2\pi N$ is, since r_1 and r_2 are considered to be constants for a particular mission from one planet to another, as for the sensitivity analysis in chapter 7. In the optimisation procedure, the TOF for each individual was computed by integrating $\dot{\theta}$, as explained in section 6.2. This means that the technique used to find the free geometric parameter (the intersection between the TOF curve and a horizontal line in the plot TOF versus free geometric parameter (figure 5.6a)) by knowing the TOF required through the position of the departure and target planets for the departure and arrival dates was not applied in this master thesis (see section 5.5).

The values of the geometric parameters and the thrust acceleration during time, as well as the excess velocities and the TOF, are stored, in order to obtain the Pareto front in the end. The theory behind a Pareto front conception was given in section 8.2. The two objectives chosen were the total excess velocity and the total fuel mass that was consumed during the low-thrust phase. Note that instead of optimizing the total excess velocity, the total impulsive shot ΔV_T could have been one of the objective functions. This variable ΔV_T can be computed through equation (4.11) in chapter 4. The fuel mass consumption for the electric part and the chemical part could have been computed and added, using a single

objective optimisation instead of a multiple objective optimisation. However, this was not done. This decision will be explained in following section.

8.3.2. Computation of the Total Fuel Mass Consumption⁵

Assuming a value for the initial mass of the spacecraft M_0 , the mass of the vehicle M_0^* after the first impulsive shot can be computed through the initial impulsive shot ΔV_1 expression calculated through equation (4.9). Knowing ΔV_1 , the spacecraft's mass after the first impulsive shot can be computed through Tsiolkowski's law (equation (3.5)):

$$\boldsymbol{M}_{0}^{*} = \boldsymbol{M}_{0} \exp \left(\frac{-\Delta V_{1}}{I_{sp_{c}} g_{0}} \right)$$

The variable I_{sp_c} is the specific impulse for the chemical burn. In order to compute the total fuel mass consumption during the two burns, Tsiolkowski's law is again used:

$$M_e = M_{e,\text{low-thrust}} \exp\left(\frac{-\Delta V_2}{I_{sp_c} g_0}\right)$$

The variable $M_{e,\text{low-thrust}}$ is the initial mass of the spacecraft before the second impulsive shot (or after the low-thrust transfer) and it can be computed by knowing the fuel mass consumption during the low-thrust transfer. The variable M_e is the spacecraft's mass at the end of its mission. The final impulsive shot ΔV_2 can be calculated through equation (4.10). The total chemical mass can be computed by adding the fuel mass consumption during the first and the second burns (equation (4.11)). In the end, the fuel consumption from the chemical burns could have been added to the fuel mass consumption from the low-thrust phase. In this way, a single optimisation could have been used. However, note that in this case three assumptions would have to be made for I_{sp_e} , for the altitudes of the parking orbits at departure and target planets h_{c_1} and h_{c_2} , respectively (from equations (4.9) and

187

⁵ This was not implemented in the master thesis

(4.10)). These variables influence the computation of the fuel mass consumption for the chemical burns. A study would be necessary to find the most suitable values. Since the objective is not to design a mission, but to study the performance of the shapes already mentioned, a multiple-objective optimisation procedure was chosen instead of a single one, separating the electric part from the chemical one. Also, the total excess velocity was used instead of the impulsive shots in order to avoid assumptions for I_{sp_c} , h_{c_1} and h_{c_2} .

As an example, consider a spacecraft using a low-thrust engine and moving with continuous thrust from Earth-Mars. An individual in the Pareto front of the sinusoidal spiral that has excess velocity values of $V_{\infty,1}=0.2809\,km/s$ and $V_{\infty,2}=0.1959\,km/s$ was picked. Assuming values for the heights of the circular orbits of the spacecraft around the departure and target planets: $h_{c_1}=185\,$ km and $h_{c_2}=300\,$ km, respectively, the impulse velocities ΔV_1 and ΔV_2 can be computed through equations (4.9) and (4.10), respectively:

$$\Delta V_1 = 3.2334 \, km/s$$

 $\Delta V_2 = 1.4152 \, km/s$

Considering $M_0 = 1200 \text{ kg}$, through equation (3.5), the mass of spacecraft after the first burn M_0^* would have to be:

$$M_0^* = M_0 \exp(-\Delta V_1/(I_{sp_c}g_0)) = 1200 \cdot \exp(-3233.4/(350 \times 9.81)) = 467.95 \text{ kg}$$

Note that the value taken for the specific impulse during both chemical burns at the departure and target planets was 350 seconds. For this individual, 91.48 kg were spent during the low-thrust transfer (see further equation (8.5)). The mass of the spacecraft in the end of this mission can be computed using again equation (3.5):

$$M_e = M_{e,\text{low-thrust}} \exp(-\Delta V_2/(I_{sp_e}g_0)) = 376.47 \cdot \exp(-1415.2/(350 \times 9.81)) = 249.30 \text{ kg}$$

In this mission, 859.22 kg was spent in total during the two chemical burns, which is more than 9 times the value spent during the low-thrust transfer. If all the fuel is spent in this mission, the dry mass is about 20.78% of the initial mass that was initially assumed. It is more important to choose individuals with lower values of the total excess velocity than with lower values of fuel mass consumption during the low-thrust transfer. However, normally these individuals require also a higher TOF, which is the drawback of the electric propulsion technology.

8.3.3. Fuel Mass Consumption (Low-Thrust Phase)

In order to obtain the fuel mass consumption during the interplanetary phase (low-thrust engine), some assumptions have to be made and some variables have to be given. The values used for the Deep Space 1 (DS1) mission will be taken as a reference for the Earth-Mars flight:

Characteristics	Deep Space-1
Propellant	Xenon
Thrust (N)	9.2×10 ⁻²
Specific Impulse (s)	1900-3200
Initial mass (kg)	486.3

Table 8.1: Deep Space 1 characteristics [Rayman, 1999] [NASA/JPL, 2002]

The thrust generated by the propulsion system is given by equation (3.2):

$$T = M \cdot a = m \cdot w \tag{8.3}$$

The variable M is the instantaneous mass of the vehicle, a is the vehicle's acceleration, m is the rate of mass change due to propellant expulsion that is negative and w is the exhaust velocity of the stream. As a matter of simplicity, the specific impulse will be considered constant and equal to 2550s, which is the average value of the interval presented in table 8.1. In this way, using equation (3.4), equation (8.3) can be rewritten:

$$\frac{dM}{M(t)} = -\frac{a(t)}{I_{sp}g_0}dt \Leftrightarrow \int dM = -\int \frac{|a(t)|M(t)}{I_{sp}g_0}dt \tag{8.4}$$

Since the thrust acceleration and the instantaneous mass do not vary rapidly during time, the total fuel mass consumed until the instant t_{i+1} will be:

$$M_{fuel}(t_{i+1}) = M_{fuel}(t_i) + \frac{|a(t_i)|M(t_i)}{I_{sp}g_0}(t_{i+1} - t_i)$$
(8.5)

Note that the second term on the right hand side of equation (8.5) has to be always positive, independently if the spacecraft is thrusting in opposite direction to its velocity. The instantaneous mass for each instant of time is given by:

$$M(t_{i+1}) = M_0^* - M_{fuel}(t_{i+1})$$
(8.6)

In this way, in order to compute the fuel mass consumption during the interplanetary flight, the mass of the spacecraft before the low-thrust engine starts will have to be assumed. The mass M_0^* considered in the Earth-Mars case was 486.3kg (the same as for DS1), in the Earth-Jupiter case it was 2223kg (the same as the Galileo spacecraft) and in the Earth-Mercury case it was 1093kg (the same as the Messenger spacecraft). Note that the missions done by these spacecraft (DS1, the Galileo and the Messenger) are very different from the type of mission that is being tested. Galileo and Messenger did not use low-thrust propulsion as primary source, only high-thrust propulsion. DS1 used low-thrust propulsion, but the thrust was not continuous and this spacecraft did not meet Mars, it encountered two comets and one asteroid (at ~1.3 AU, while Mars is at ~1.5 AU). Since no low-thrust missions were planned for Mercury, Mars or nor Jupiter using continuous thrust, these values for M_0^* were chosen and they should only be considered as initial guesses. BepiColombo, as already mentioned in chapter 3, will be launched in 2013 to Mercury with a launch mass of 2300 kg (MPO mass is 520 kg and MMO mass is 250 kg) [ESA/BepiColombo, 2008]. The data of BepiColombo were not used in this master thesis

since it was considered to be preferable to use a higher initial mass for these simulations. Note that the fuel mass spent during the first burn was not taken into account in these values.

The values for the specific impulse for Earth-to-Jupiter and for Earth-to-Mercury missions were considered the same as the one used for the Earth-to-Mars flight.

8.3.4. Thrust Acceleration Constraint

Note that the total fuel mass spent during the flight is not sufficient to evaluate the performance of an individual during the transfer orbit. The energy source of most low-thrust engines comes from the Sun. So, for far away distances, the available energy and consequently the thrust acceleration that the spacecraft is allowed to achieve, decreases. For this reason, it is important that the maximum ratio between the thrust acceleration that is given as an output from a certain shape and the available thrust acceleration of each individual in the Pareto front is less or equal to one:

$$\frac{a_{shape}}{a_{available}} \le 1, \text{ for } \forall t$$
(8.7)

Again, the DS1 mission was taken as reference for the Earth-Mars flight. For this mission, the nominal thrust (T_N) is considered 9.2×10^{-2} N (table 8.1). Knowing the initial mass for the DS1 ($M_0 = 486.3$ kg), the trend of the thrust acceleration can be given by:

$$a_{available} = a_0 \, \mu/r^2 \approx 0.032 \, \mu/r^2$$

This is the available thrust acceleration, $a_{available}$. The available thrust acceleration is important in order to test if the values of acceleration computed using the 6 analytical representations can be achieved in a real mission. In this master thesis, the thrust acceleration values given by the 6 shapes will be tested with three different trends of the available thrust acceleration: (1) $a_{available} = 0.032 \,\mu/r^2$ (the same as DS1), (2)

 $a_{available} = 0.048 \, \mu/r^2$ (1.5 times $a_{available}$ in DS1) and (3) $a_{available} = 0.064 \, \mu/r^2$ (twice $a_{available}$ in DS1). Tests were performed for different values of $a_{available}$. After these tests, the values of available thrust acceleration (2) and (3) were chosen to show the trend of the number of individuals in the Pareto front that respect the $a_{available}$ constraint.

For the other missions, Earth-Jupiter and Earth-Mercury, the values for the available thrust acceleration will not be the same as for the Earth-to-Mars flight. During the sensitivity study in chapter 7 and in appendix E, for the acceleration inversely square case of the thrust profile using the exponential sinusoid, the minimum values for the magnitude of the given by $a_M = 0.04 \,\mu/r^2$, $a_I = 0.07 \,\mu/r^2$ acceleration thrust were $a_{\rm \textit{Mer}} = -0.06\,\mu/r^2$, for an Earth-to-Mars mission, for an Earth-to-Jupiter mission and an Earth-to-Mercury mission, respectively. Since a_J is approximately twice a_M for the same values of heliocentric distance, the three different trends of the available thrust acceleration considered for an Earth-Jupiter flight will be also twice the ones assumed for an Earth-Mars mission. These three trends will be: (1) $a_{available} = 0.064 \,\mu/r^2$ (twice $a_{available}$ in DS1), (2) $a_{available} = 0.096 \,\mu/r^2$ (3 times $a_{available}$ in DS1) and (3) $a_{available} = 0.128 \,\mu/r^2$ (4 times $a_{available}$ in DS1). For an Earth-Mercury flight, since $\left|a_{\mathit{Mer}}\right|$ is 1.5 times a_{M} , the three different trends of the available thrust acceleration considered for this mission will be also 1.5 times the ones assumed for an Earth-Mars mission. The available thrust acceleration will be given by: (1) $a_{available} = 0.048 \mu/r^2$ (1.5 times $a_{available}$ in DS1), (2) $a_{available} = 0.072 \,\mu/r^2$ (2.25 times $a_{available}$ in DS1) and (3) $a_{available} = 0.096 \,\mu/r^2$ (3 times $a_{available}$ in DS1). Note that for an Earth-Mercury flight, the available thrust is increasing by r^2 when the spacecraft is moving from Earth towards Mercury. This means that the vehicle will be able to achieve higher levels of thrust acceleration for distances nearer the Sun. However, in reality, the maximum thrust that the spacecraft can obtain depends on the maximum power that the solar arrays can provide. This means that for missions to inner planets, at certain point, the maximum thrust that the power system can provide will be achieved. From this point on, the thrust acceleration can no longer increase with r^2 . Instead, it will depend only on the instantaneous mass drop. In this master thesis, this

situation was not considered. In this way, the available thrust acceleration for an Earth-Mercury flight will have the same trend as for the other two missions to outer planets.

9. Verification

This master thesis deals with many mathematical expressions (appendix B), so mistakes can be made easily when writing the equations in MATLAB code. A MATLAB program was developed in this thesis in order to compute the thrust acceleration, the thrust angle, the TOF, the excess velocities and the fuel consumption during the heliocentric phase, giving the geometric parameters as input for a certain mission with a certain profile. This MATLAB program can be called *low2D*. In order to verify the results achieved in low2D for each shape (TOF, excess velocities, thrust acceleration and thrust angle), another program in MATLAB was developed: Test2D. This program uses the values of the thrust acceleration, thrust angle, the TOF and the initial position and velocity of the spacecraft in the heliocentric phase as inputs. Through a Runge-Kutta 4(5) integrator, it computes the trajectory of the spacecraft in the transfer plane. In the end, if low2D is correct, the values for the final position and velocity should match the ones given by Test2D (appendix F). For the examples given in appendix F, the differences in position at the final point of the thrust arc between low2D and Test2D are less than 60 km. Considering that the position of the targets are always given in astronomical units (150×10⁶ km), these differences are negligibly small. In terms of velocity at the end point of the thrust arc, maximum difference values of $\sim 29 \, cm/s$ are achieved. The order of magnitude of the hyperbolic velocities at the target planet is $10^2 \, km/s$, therefore these differences are negligibly small also.

The verification will only be complete if the results given by low2D are compared with other results given by independent software. Unfortunately, the only performance results available in literature are for the exponential sinusoid (tangential thrust) and they can be found in [Izzo, 2006], in Galomusit [Melman, 2007], in STA [Paulino, 2008] and in the Swing-By Calculator (SBC) [JAQAR, 2007], among other software.

Galomusit is a software tool that was built by students from the Faculty of Aerospace Engineering in Delft and it handles interplanetary trajectories using high-thrust and, more recently, low-thrust trajectories using the exponential sinusoid [Corradini, 2008].

STA stands for Space Trajectory Analysis and, like Galomusit, it can compute interplanetary trajectories, using multiple flybys and high- and low-thrust propulsion. STA software is developed by ESA in cooperation with several European universities.

As the name suggests, the "Swing-By calculator", is a software to compute interplanetary missions using multiple flybys. The version 8 of the SBC gives the opportunity to use optimisation in low-thrust trajectories described by the exponential sinusoids. This software was used to verify STA.

Since STA was developed by me during my internship in ESTEC, it cannot be used for verification in this master thesis. Unfortunately, SBC cannot also be used for the verification. The output results given by this software, which are the excess velocities and the total fuel mass consumption (chemical plus electrical) are for a 3D case, while in this master thesis, a 2D problem was considered. On the other hand, a 2D problem for low-thrust trajectories using the exponential sinusoids was implemented in Galomusit by Stefano Corradini. The results were verified for 3 individuals in an Earth-Mars flight. The test scenario is shown in table 9.1.

	r _{Earth} (km)	r_{Mars} (km)	$k_{_2}$	$\gamma_{_1}$ (rad)	$\Delta\theta$ (rad)
Individual 1	151366683.169	206953872.627	0.7013	-0.03858	1.9532 (N=0)
Individual 2	150950940.668	207035807.816	0.3192	0.02342	1.7915 (N=1)
Individual 3	147943444.631	222257727.478	0.1524	0.01048	0.0419 (N=3)

Table 9.1: Test scenario (Earth-Mars mission) for verification of the excess velocities, TOF and fuel mass consumption computed in low2D

Given the heliocentric distance at the departure planet, at the arrival planet, the geometric parameter k_2 , the initial flight path angle γ_1 , the transfer angle $\Delta\theta$ and the number of revolutions N; the geometric parameters k_0 , k_1 and ϕ , the excess velocities at departure and arrival, the TOF and the fuel mass consumption during the low-thrust phase were computed using low2D and Galomusit. Table 9.2 shows the values achieved for the test scenario in table 9.1, using Galomusit and low2D. The initial mass used was 1000 kg and the specific impulse during the low-thrust phase was 3000 seconds.

	Individual 1		Individ	dual 2	Individual 3	
	Galomusit	Low2D	Galomusit	Low2D	Galomusit	Low2D
$V_{\infty,dep}(km/s)$	4.2057	4.2057	0.7339	0.7339	0.3218	0.3218
$V_{\infty,arr}(km/s)$	7.6969	7.6969	0.2569	0.2569	0.0818	0.0818
TOF (days)	123.4091	126.2335	624.0333	624.3738	1552.3217	1552.6437
M _{fuel} (kg)	27.5688	27.1462	132.3082	124.1012	183.4770	167.8474

Table 9.2: Results from Galomusit and low2D for the 3 individuals, Earth-Mars flight

In terms of excess velocities, values from low2D match the ones given by Galomusit. However, the values for the TOF and the fuel mass consumption are significantly different. In table 9.3, the errors between the excess velocity, the TOF and the fuel mass consumption values computed with Galomusit and the ones given in low2D (considering the values obtained with Galomusit the nominal ones) are given.

Error (%)	Individual 1	Individual 2	Individual 3
$V_{_{\infty,dep}}$	0	0	0
$V_{\scriptscriptstyle{\infty,arr}}$	0	0	0
TOF	2.29	0.06	0.02
$M_{_{fuel}}$	1.53	6.20	8.52

Table 9.3: Errors between the results given by Galomusit and low2D

Note that the error for the TOF decreases for higher values of number of complete revolutions N. In order to compute the TOF, an integrator is required: in Galomusit, a composite Cavalieri-Simpson formula was used, while in low2D the integrator used was a Runge-Kutta 4(5). A second verification was made using the integrator routines that Dario Izzo [Izzo, 2006] used to compute the TOF for the exponential sinusoid problem. Given the geometric parameters of the exponential sinusoid from Galomusit as an input, the TOF is calculated using a recursive adaptive Lobatto quadrature. The values for individual 1, individual 2 and individual 3 presented in the test scenario in table 9.1 are given in table 9.4.

	TOF Galomusit (days)	TOF Low2D (days)	TOF Izzo (days)	Error (%)
Individual 1	123.4091	126.2335	126.2338	2×10 ⁻⁴
Individual 2	624.0333	624.3738	624.3739	2×10 ⁻⁵
Individual 3	1552.3217	1552.6437	1552.6427	6×10 ⁻⁵

Table 9.4: TOF given by Galomusit, low2D and Izzo's integrator routines and the errors between the results given by Izzo and low2D

Considering the values obtained with Izzo's integrator the nominal ones, the errors between the TOF values calculated with Izzo's integrator and the Runge-Kutta 4(5) are shown in table 9.4 for individual 1, 2 and 3. Due to the significantly small error values between Izzo's integrator and low2D integrator, the Runge-Kutta 4(5) used in this master thesis can be considered well implemented in low2D. A test with a different integrator in Galomusit is recommended.

In terms of fuel mass consumption, the errors between Galomusit and low2D increase for higher values of complete number of revolutions. The number of iteration steps to compute this parameter was fixed and equal to 200 for Galomusit, while for low2D it depends on the number of steps and the tolerance used by the Runge-Kutta 4(5) integrator. In low2D, the number of steps was 633, 521 and 653 for individuals 1, 2 and 3, respectively. Note also that the integrator RK4 (5) uses a variable step-size. So, even if the number of steps was the same between the two programs, the results for the fuel mass consumption will still be different, since it depends on the instant of time that the thrust acceleration is being calculated. Although the comparison between STA and low2D is not fair, since both software were developed by me, the results for the TOF and fuel mass consumption during the low-thrust transfer are shown in table 9.5. Note that STA was verified using JAQAR (see appendix F).

	Iı	ndividual 1		Individual 2			Individual 3		
	STA	'Main'	Error	STA	'Main'	Error	STA	'Main'	Error
			(%)			(%)			(%)
TOF (days)	126.2335	126.2335	0	624.3738	624.3738	0	1552.6437	1552.6437	0
M _{fuel} (kg)	27.1278	27.1462	0.0678	124.0658	124.1012	0.0285	167.8411	167.8474	0.0038

Table 9.5: Results from STA and low2D for the 3 individuals, for Earth to Mars

Although STA and the low2D are programmed in different languages, C++ and MATLAB, respectively, the integrators implemented are Runge-Kutta 4(5). Therefore, the error for the TOF between the two software is zero. Regarding fuel mass consumption, STA uses a fix step size of 500 and the errors between STA and low2D are smaller than 0.07%, which is much smaller than the values of error achieved between Galomusit and low2D. This is probably due to a smaller value of integration steps used in Galomusit compared with the number used in STA and in low2D.

Considering the differences between these three software and that errors below 10% were achieved, the fuel mass consumption computation will be considered well implemented in low2D.

10. Results

During 2008, a master student Bram De Vogeleer developed a shape-based method: expansions of power series, which are expressions with linear combinations of many terms (coefficients) that allow an optimisation procedure [De Vogeleer, 2008]. His pseudo-spectral method is useable and it provides good results in many problems. He compared his results with the ones given by the exponential sinusoid and he concluded that this shape requires velocity increments at departure and arrival planets, also sometimes requires high acceleration levels that his shape-based analysis did not show.

In this chapter, like in Bram De Vogeleer's thesis, a comparison between the analytical representations mentioned in the previous chapters and the exponential sinusoid will be made. The Pareto fronts will be illustrated and analysed for the 6 shapes mentioned before: the Archimedean spiral, the logarithmic spiral, the Poinsot's spiral (sine hyperbolic), the Poinsot's spiral (cosine hyperbolic), the sinusoidal spiral and the exponential sinusoid. Only the Earth-to-Mars flight and the Earth-to-Mercury flight will be analysed in this section. Two cases of the thrust profile were studied: the acceleration inversely square and the tangential cases of the thrust profile described in chapter 6. However, for the acceleration inversely square case, due to lack of time, only the sinusoidal spiral and the exponential sinusoid were analysed, since they had the best performances in terms of the Pareto front in the tangential case (see sections 10.1 and 10.2). The results for the Earth-to-Jupiter mission using the tangential thrust profile are given in appendix H. The computation time required for the Earth-Jupiter mission using the acceleration inversely square case was extremely high and unfortunately it was not possible to obtain results. Therefore, the results for this mission will not be given in this master thesis.

10.1. Earth - Mars Flight: Tangential Thrust

Figure 10.1 illustrates the Pareto fronts using the tangential thrust profile in an Earth-Mars flight for all 6 shapes. As already mentioned in chapter 8, the population that is being used is 75000 individuals for each shape.

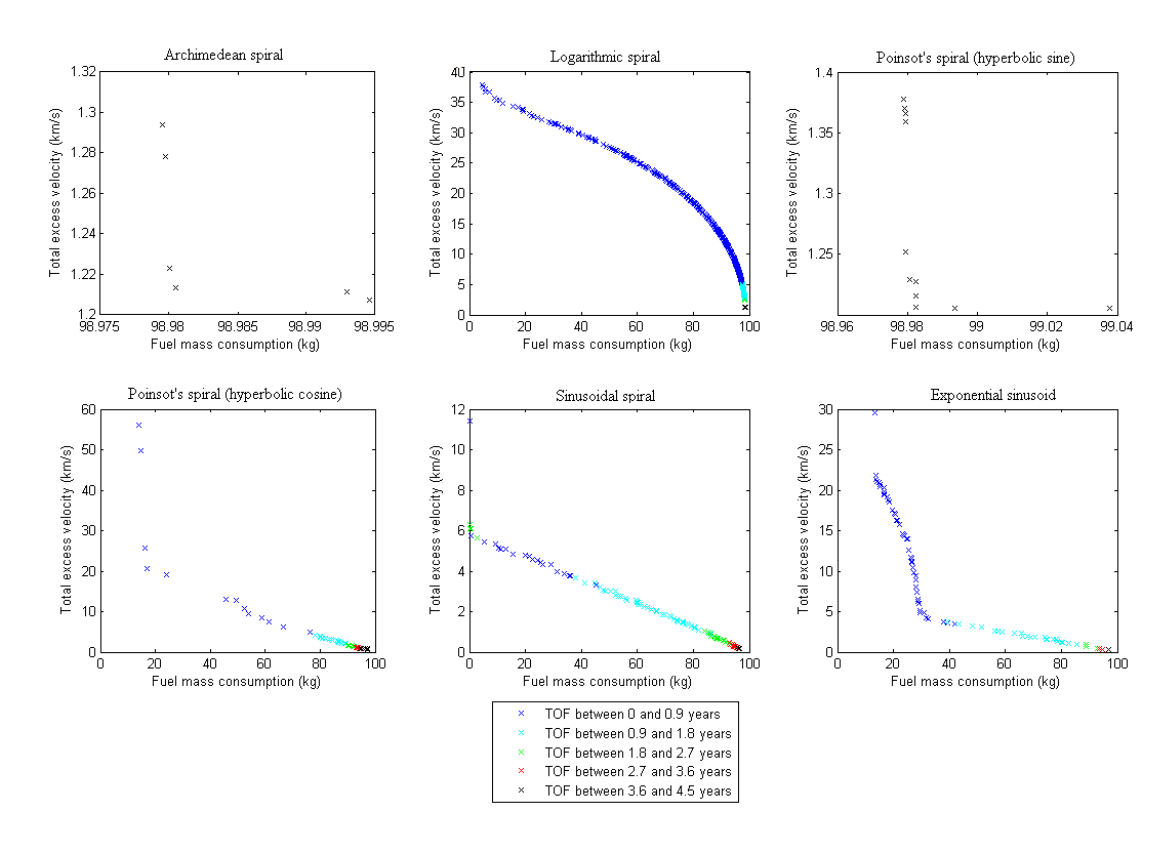


Figure 10.1: Pareto fronts for the Archimedean spiral, logarithmic spiral, Poinsot's spiral (hyperbolic sine), Poinsot's spiral (hyperbolic cosine), sinusoidal spiral and exponential sinusoid, tangential thrust profile, Earth-Mars flight

In figure 10.1, there are significantly high differences in scale in terms of total excess velocity between the 6 shapes illustrated. For the Archimedean spiral and the Poinsot's spiral (hyperbolic sine), only individuals with low values of total excess velocity and high values of fuel mass consumption were selected for the Pareto front. These two shapes show worse results compared with the other 4 shapes, because the number of individuals in the Pareto front is significantly low and individuals with lower values of total excess velocity and fuel mass consumption can be obtained using the other shapes.

Figure 10.2 summarizes the Pareto fronts for all 6 shapes. In the plot in the right-hand side, the same Pareto fronts are represented but only with individuals with values of total excess velocity lower than $3 \, km/s$ and values of fuel mass consumption between 80 and 100 kg.

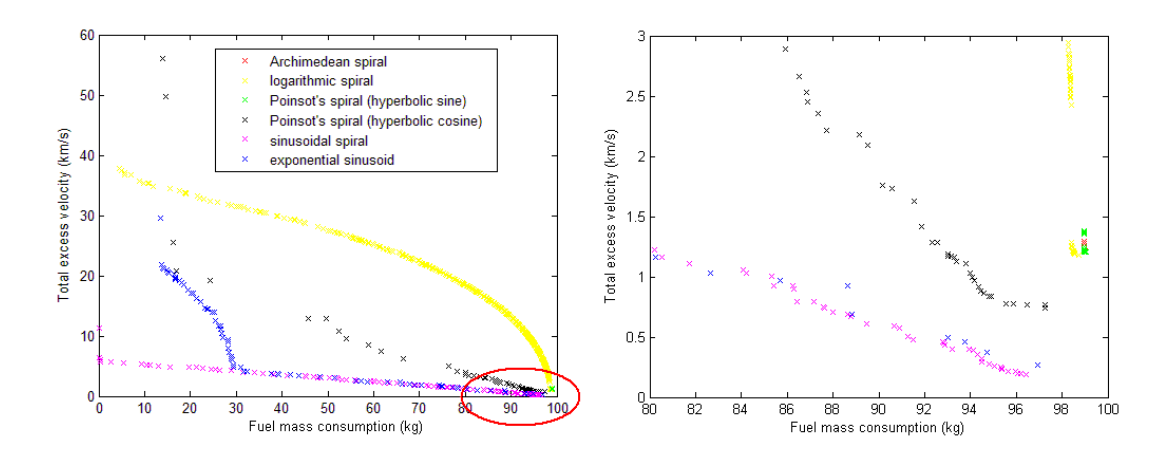


Figure 10.2: Pareto fronts for the Archimedean spiral, logarithmic spiral, Poinsot's spiral (hyperbolic sine), Poinsot's spiral (hyperbolic cosine), sinusoidal spiral and exponential sinusoid, tangential thrust profile, Earth-Mars flight. On the right, only individuals with values of total excess velocity lower than 3 km/s and values of fuel mass consumption between 80 and 100 kg are present

Table 10.1 shows the minimum values for the fuel mass consumption and the total excess velocity for the individuals represented in the Pareto fronts for all 6 shapes.

	Archimedean spiral	Logarithmic spiral	Poinsot's spiral (hyperbolic sine)	Poinsot's spiral (hyperbolic cosine)	Sinusoidal spiral	Exponential sinusoid
Minimum	98.98	4.4	98.98	13.9	0.09	13.5
$M_{_{fuel}}$ (kg)						
Minimum	1.2075	1.1817	1.2053	0.7444	0.1854	0.2645
$V_{\infty,T}(km/s)$						

Table 10.1: Minimum values for the fuel mass consumption during the low-thrust phase and for the total excess velocity for the individuals in the Pareto fronts for all 6 shapes, tangential case, Earth-Mars flight

The minimum value of fuel consumption is achieved with the sinusoid spiral (for $\theta_f = 109.1^{\circ}$) and it is 0.09 kg, i.e., negligibly small (close to the high-thrust Lambert problem). Note that the total excess velocity values for lower values of fuel mass consumption are significantly high. It is more important to choose individuals with lower values of total excess velocity than with lower values of fuel mass consumption during the heliocentric phase (chapter 8). This is because the fuel spent during the chemical burns (even for small values of excess velocity) is much higher than fuel spent during the low-thrust phase. Individuals with high values of total excess velocity cannot be taken into

account in a real mission. However, in order to understand the limits of each shape, they were not excluded from the Pareto front.

In table 10.1, the minimum value of the total excess velocity is achieved with the sinusoid spiral and it is $0.1854 \, km/s$. Individuals with TOF values higher than approximately 4.2 years were not selected for the Pareto fronts, since there was a limit for the maximum number of complete revolutions: 3 (chapter 8).

From figure 10.2, the Pareto fronts for the exponential sinusoid and the sinusoidal spiral provide lower values of fuel mass consumption for the same total excess velocity when comparing with the other shapes. The logarithmic spiral has the highest number of individuals in the Pareto front of all 6 shapes. The range of fuel mass consumption values for the sinusoidal spiral is the widest one. This shape and the exponential sinusoid have similar performances for fuel mass consumptions higher than ~30 kg. However, in general, the sinusoidal spiral has the best Pareto front of all 6 shapes.

10.1.1. Analysis of the Pareto Fronts

In this section, an analysis of the Pareto fronts shown in figure 10.1 will be given. In particular, the results achieved for the sinusoidal spiral and the exponential sinusoid will be discussed in the following paragraphs.

From figure 10.1, generally for higher TOF values (higher values of transfer angle $\Delta\theta$ and higher values of number of complete revolutions N), the total excess velocity decreases while the total fuel consumption increases. However, there are some individuals in the Pareto front of the sinusoidal spiral for which this situation does not happen and they seem to be misplaced (see figure 10.3).

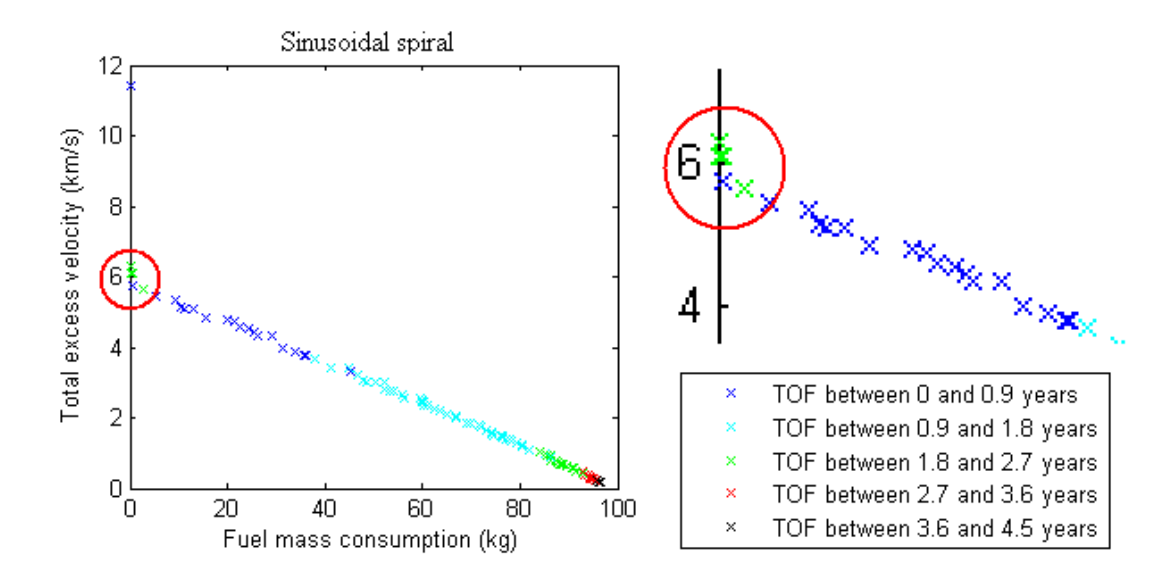


Figure 10.3: Pareto front for the sinusoidal spiral, Earth-Mars flight

For this shape, there are 3 individuals in the Pareto front that have TOF values between 1.8 and 2.7 years and fuel mass consumption values lower than 0.5 kg (see figure 10.3, individuals with green colour). The geometric parameter |m| is approximately 1 in all 3 cases. Figure 10.4 illustrates the trajectory of one of these shapes.

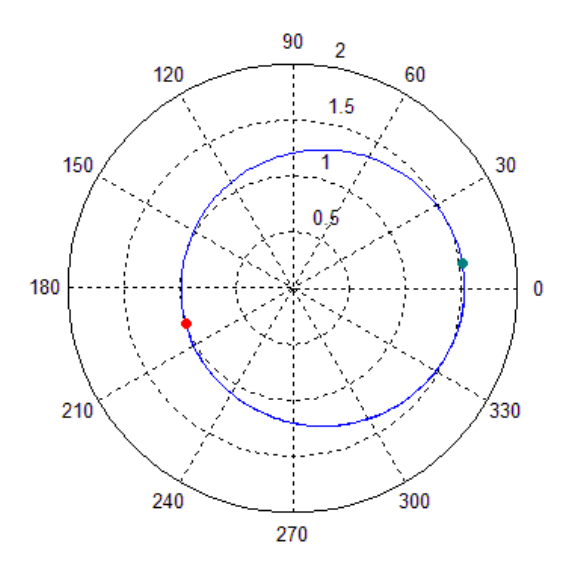


Figure 10.4: Polar plot for the sinusoidal spiral, Earth-to-Mars flight (m = -0.9996, $\Delta \theta = 175.8^{\circ}$ with N=1 and $\theta_i = 194.7^{\circ}$)

From figure 10.4, the spacecraft no longer performs a spiral type of trajectory, but almost a circular one. The spacecraft will depart from the Earth (red dot) and it encounters the target planets' orbital trajectory (green dot) twice: one with N=0 and the other after completing already one revolution. Note this trajectory is similar to a high-thrust trajectory and it will not be used in a real mission, since other individuals with lower values of excess velocity can be used instead (with similar values of TOF).

The Pareto front obtained for the exponential sinusoid will have to be discussed in detail. Note that this Pareto front (figure 10.1) has 2 different trends: after and before \sim 30 kg. The bent seen in figure 10.1 at \sim 30 kg was studied in order to understand why there are two different curves in the Pareto front. To help in understanding, figure 10.5 shows the corresponding geometric parameter k_2 as function of the fuel mass consumption.

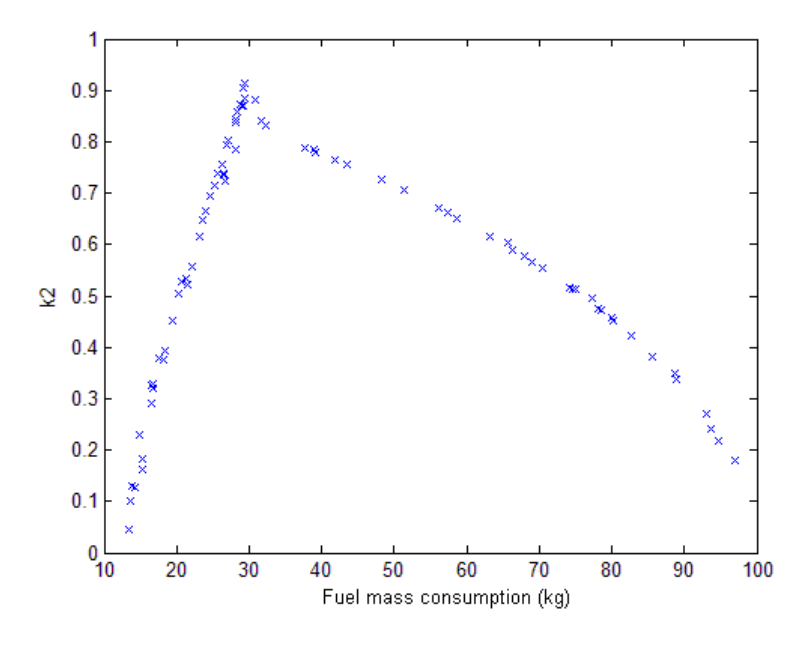


Figure 10.5: k_2 of the Pareto front individuals versus the fuel mass consumption during the low-thrust phase, exponential sinusoid, Earth-to-Mars flight

Note that for values of fuel mass consumption lower than ~30 kg, the parameter k_2 increases, while for higher values, it decreases. According to [Petropoulos and Longuski, 2004], for higher values of the transfer angle $\Delta\theta$ and higher number of complete revolutions N, the values for k_2 should decrease. As already discussed before, for the

exponential sinusoid, the fuel mass consumption is directly proportional to the TOF and consequently to the transfer angle and number of complete revolutions. In this way, the plot of k_2 should always decrease when increasing the values of the fuel mass consumption, which does not happen for values lower than ~30 kg. Note that at ~30 kg, k_2 reaches approximately the maximum value allowed by the optimisation program: 1. As already explained before in chapter 5, the maximum value for k_2 taken was 1, because according to Petropoulos and Longuski ([Petropoulos and Longuski, 2004]), the thrust levels can become unreasonably high when $(1-k_1k_2^2)$ approaches zero. This statement was proven to be correct, since if no constraints are given to this geometric parameter, the Pareto front will be the same as the one with the constraint $k_{2,\text{max}} = 1$. In this way, the difference between trends in the Pareto front of the exponential sinusoid is most likely due to the fact that the performance of this shape depends on the values chosen for the geometric parameters and their capability to describe the physical problem. An example can be given with the sinusoidal spiral in order to better understand the situation. In figure 10.6, two Pareto fronts of the sinusoidal spiral are represented: in blue is the one where the interval of values of m is (-1; 1); in red is the one where the interval of values of m is [-0.7; 0.7]. This means that in this last Pareto front, the interval for the optimisation variable mwas restricted.

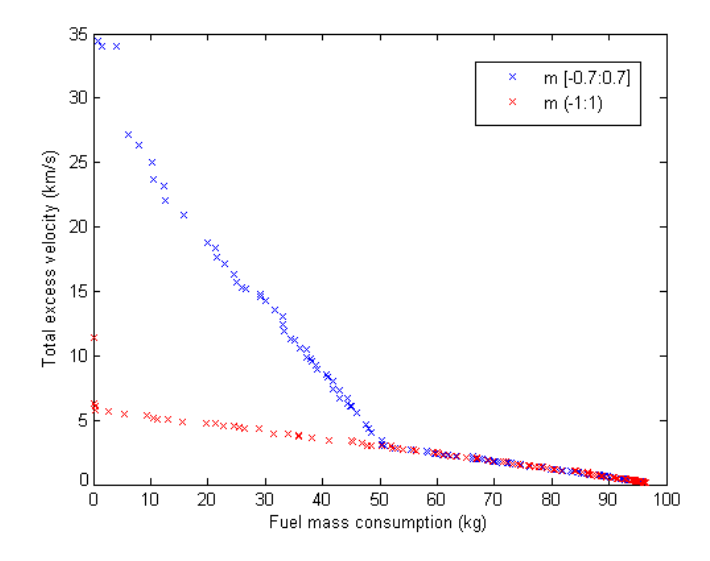


Figure 10.6: Pareto front of the sinusoidal spiral, using m=[-0.7;0.7] (blue) and m=(-1;1) (red)

In this case, a restriction in the geometric parameter m caused the bend, since values of $m \in (-0.7;1)$ that were being picked by the optimizer for fuel mass consumption values lower than ~50 kg in the Pareto front with a red colour can not be picked for the Pareto front in blue colour.

In the exponential sinusoid case, when increasing k_2 from higher fuel mass consumption to lower fuel mass consumption values (figure 10.1), after a certain value (~30 kg), the influence of this geometric parameter on the dynamics of the problem is different. Therefore, the bend occurs because the optimizer chooses smaller values of k_2 (see figure 10.5).

10.1.2. Thrust Acceleration Constraint

As already mentioned in section 8.3.4, the fuel mass spent during the flight is not sufficient to evaluate the performance of an individual during the transfer orbit. It is important that the maximum ratio between the thrust acceleration that is given as an output from a certain shape and the available thrust acceleration of each individual in the Pareto front is less or equal to 1.

Computation times were tracked for all 6 shapes and they are shown in table 10.2. Also, the percentage of the individuals in the Pareto front and in the population that respects the maximum ratio between the thrust acceleration that is given as an output from a certain shape and the available thrust acceleration (≤ 1) is presented for 3 different cases. The 3 cases are for the following available thrust acceleration trends: (1) $a_{available} = 0.032 \,\mu/r^2$ (the same as DS1), (2) $a_{available} = 0.048 \,\mu/r^2$ (1.5 times $a_{available}$ in DS1) and (3) $a_{available} = 0.064 \,\mu/r^2$ (twice $a_{available}$ in DS1) (see chapter 8).

Shapes	Computation time (hours)	N_{Pf}	G _{Pf} (%)	G _{Pop} (%)
Archimedean spiral	0.5	6	100/100/100	17.5/26.8/32.9
Logarithmic spiral	0.45	486	3.3/15/23.9	4.8/9.3/14.2
Poinsot's spiral (hyperbolic sine)	0.42	11	100/100/100	46.6/61.4/69.9
Poinsot's spiral (hyperbolic cosine)	0.47	54	53.7/68.5/77.8	62.1/73.6/79.5
Sinusoidal spiral	1.23	104	49/100/100	16.1/32.7/47.3
Exponential sinusoid	1.9	80	7.8/54.5/59.7	0.8/4.9/10

Table 10.2: Computation time, number of individuals in the Pareto front (N_{pf}) and the percentage of individuals in the Pareto front G_{pf} and in the population G_{pop} that respect the maximum value for the ratio between the required thrust acceleration of the spacecraft and the available one for the 6 shapes and for the 3 cases of $a_{0,available} = a_{0,DSL}(1;1.5;2)$, Earth-Mars flight (tangential case)

From table 10.2, the optimisation procedure when using the exponential sinusoid took more computation time than the other shapes. Also, the percentage of individuals in the population that do not respect the maximum value for the ratio between the required thrust acceleration of the spacecraft and the available one is the highest for the exponential sinusoid for all 3 cases. On the other hand, the logarithmic spiral has the lowest percentage of individuals in the Pareto front that respects the constraints for the thrust acceleration. Note that although 100% of the individuals in the Pareto front respect the thrust acceleration constraint for the Archimedean spiral and the Poinsot's spiral (hyperbolic sine), the fuel mass consumption for both shapes is higher when compared with the fuel mass consumption of the other 4 shapes.

Figures 10.8 and 10.9 illustrate the Pareto fronts for the sinusoidal spiral and for the exponential sinusoid when considering only the individuals in the population that respect the condition in (8.7). Only these two shapes are represented, since they have the best Pareto fronts (figure 10.2). Using the condition in (8.7) as a constraint, for the two shapes

named before a certain number of individuals in the population is discarded before the Pareto front is built. Figures 10.7 and 10.8 show the Pareto fronts for the sinusoidal spiral and exponential sinusoid, respectively when the available thrust acceleration $a_{available} = (0.032; 0.048; 0.064) \mu/r^2$ is given as a constraint.

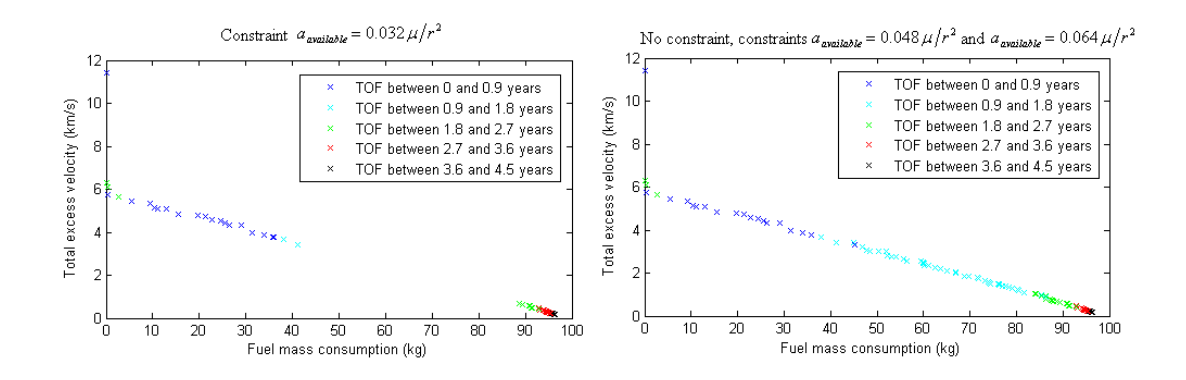


Figure 10.7: Pareto fronts for the sinusoidal spiral, for the entire population (on the right) and only for individuals in the population that respect the condition (8.7) (the 3 cases of available thrust acceleration), tangential thrust profile, Earth-Mars flight

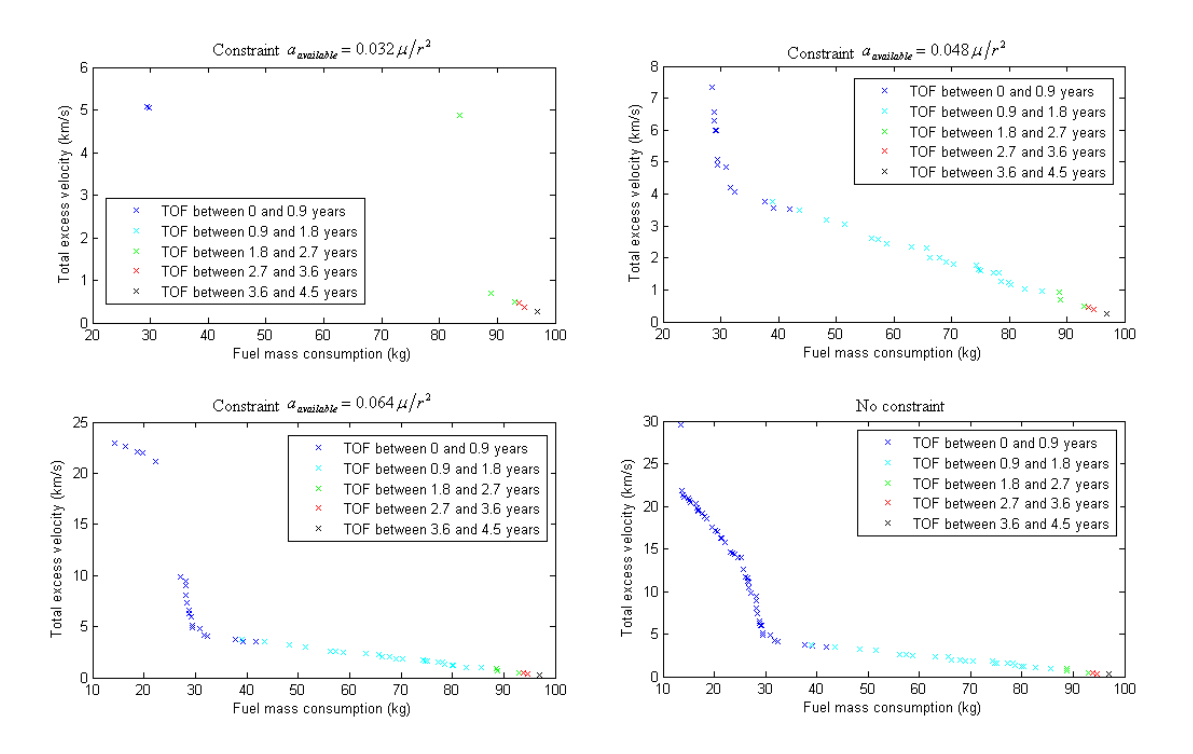


Figure 10.8: Pareto fronts for the exponential sinusoid, for the entire population (on bottom right) and only for individuals in the population that respect the condition (8.7) (the 3 cases of available thrust acceleration), tangential thrust profile, Earth-Mars flight

From figures 10.8 and 10.9, for both sinusoidal spiral and exponential sinusoid, there is a gap in the Pareto fronts, where there are no individuals for $a_{available} = 0.032 \,\mu/r^2$. For the sinusoidal spiral, Pareto fronts for the cases where $a_{available} = (0.048;0.064) \,\mu/r^2$ are the same as the Pareto front for the case without a constraint. It can be concluded that there is a higher percentage of individuals that respect the thrust acceleration constraint using the sinusoidal spiral than using the exponential sinusoid.

10.2. Earth - Mercury Flight: Tangential Thrust

Figure 10.9 gives the Pareto fronts using the tangential thrust profile for the Earth-Mercury flight for all 6 shapes. As already said before, the population that is being used for each shape contains 75000 individuals.

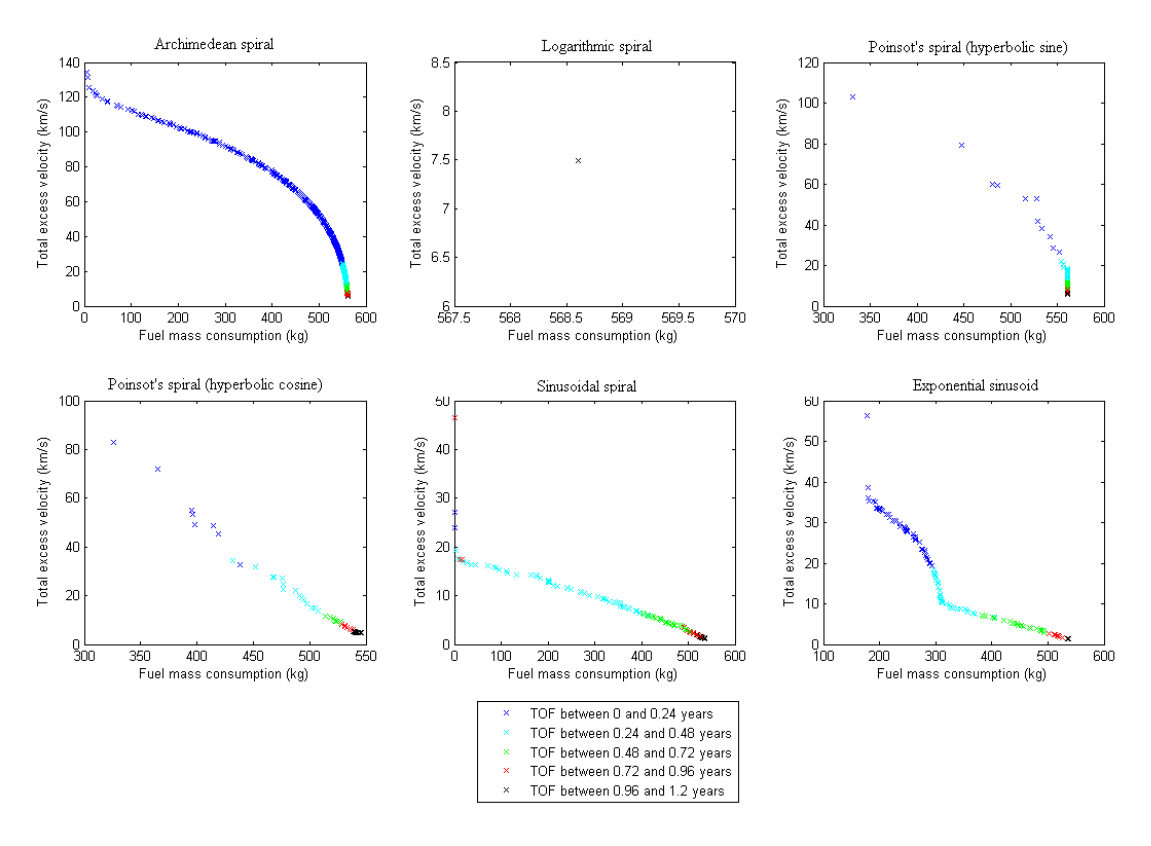


Figure 10.9: Pareto fronts for the Archimedean spiral, logarithmic spiral, Poinsot's spiral (hyperbolic sine), Poinsot's spiral (hyperbolic cosine), sinusoidal spiral and exponential sinusoid, tangential thrust profile, Earth-Mercury flight

In figure 10.9, the logarithmic spiral shows the worst results compared with the other 5 shapes, since there is only one individual in the Pareto front and it has the highest value of fuel mass consumption of all individuals in all Pareto fronts. A similar situation to the one for the Archimedean spiral and the Poinsot's spiral (hyperbolic sine) in an Earth-Mars flight occurs for this shape when the target planet is inner with respect to the departure planet.

Figure 10.10 shows the Pareto fronts for all 6 shapes. In the plot in the right-hand side, the same Pareto fronts are represented but only with individuals with values of total excess velocity lower than $10 \, km/s$ and values of fuel mass consumption between 500 and 570 kg.

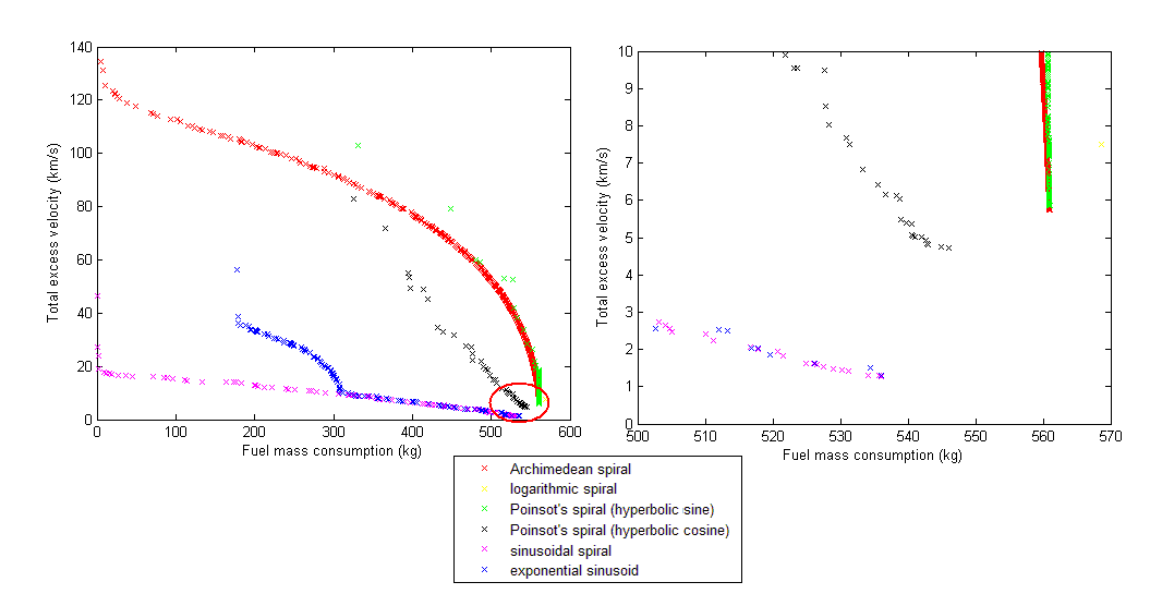


Figure 10.10: Pareto fronts for the Archimedean spiral, logarithmic spiral, Poinsot's spiral (hyperbolic sine), Poinsot's spiral (hyperbolic cosine), sinusoidal spiral and exponential sinusoid, tangential thrust profile, Earth-Mercury flight

Table 10.3 shows the minimum values for the fuel mass consumption and the total excess velocity for the individuals represented in the Pareto fronts for all 6 shapes.

	Archimedean	Logarithmic	Poinsot's	Poinsot's	Sinusoidal	Exponential
	spiral	spiral	spiral	spiral	spiral	sinusoid
			(hyperbolic	(hyperbolic		
			sine)	cosine)		
Minimum	5.2	568.6	331.8	325.8	0.28	178.3
M _{fuel} (kg)						
Minimum	5.7375	7.4889	5.8513	4.7214	1.2609	1.3082
$V_{\infty,T}(km/s)$						

Table 10.3: Minimum values for the fuel mass consumption during the low-thrust phase and for the total excess velocity for the individuals in the Pareto fronts for all 6 shapes, tangential case, Earth-Mercury flight

The minimum values of fuel mass consumption are achieved with the sinusoid spiral (for $\theta_f = 161.9^\circ$) and it is 0.28 kg, respectively (close to the high-thrust Lambert problem). Note that, in this case, the values achieved for the total excess velocity are significantly high and they are not used in a real mission. The minimum value of the total excess velocity is achieved with the sinusoid spiral and it is $1.2609 \, km/s$. Note that the total excess velocity values for this mission are higher than the values for the Earth-Mars flight. This was possibly due to the restriction made in the maximum value of N (complete number of revolutions) that was 2. Again, the sinusoidal spiral has the best Pareto front of all 6 shapes. Individuals with TOF higher than 1.2 years were not selected for the Pareto fronts, due to the limitation on N.

The range of fuel mass consumption values is the widest one for the sinusoidal spiral. This shape and the exponential sinusoid have similar performances for fuel mass consumptions higher than ~320 kg. Note that the Pareto front of the exponential sinusoid has 2 different trends: after and before ~320 kg. The situation for the Earth-Mars case that was already studied in section 10.1.1 and this one are similar (see explanation in this section).

10.2.1. Thrust Acceleration Constraint

Computation times were tracked for all 6 shapes and they are shown in table 10.4. Also, the percentage of the individuals in the Pareto front and in the population that respects the maximum ratio between the thrust acceleration that is given as an output from a certain shape and the available thrust acceleration (≤ 1) is presented for 3 different cases. The 3

cases are for the following available thrust acceleration: (1) $a_{available} = 0.048 \,\mu/r^2$ (1.5 times $a_{available}$ in DS1), (2) $a_{available} = 0.072 \,\mu/r^2$ (2.25 times $a_{available}$ in DS1) and (3) $a_{available} = 0.096 \,\mu/r^2$ (3 times $a_{available}$ in DS1) (see chapter 8).

Shapes	Computation time (hours)	N_{Pf}	G_{Pf} (%)	G _{Pop} (%)
Archimedean spiral	0.61	1430	9.7/35.1/47.7	2.2/13/23.3
Logarithmic spiral	0.46	1	0/100/100	0.03/0.46/0.5
Poinsot's spiral (hyperbolic sine)	0.64	224	23.2/54/78.6	13.5/35.3/49.5
Poinsot's spiral (hyperbolic cosine)	0.45	52	23.1/40.4/55.8	20.5/46.1/58.7
Sinusoidal spiral	1.28	105	19/46.7/97.1	3.62/11.9/23.5
Exponential sinusoid	1.37	111	0/7.2/26.1	0.05/0.9/3

Table 10.4: Computation time, number of individuals in the Pareto front (N_{pf}) and the percentage of individuals in the Pareto front G_{pf} and in the population G_{pop} that respect the maximum value for the ratio between the required thrust acceleration of the spacecraft and the available one for the 6 shapes and for the 3 cases of $a_{0,available} = a_{0,DSI} \left(1.5; 2.25; 3 \right)$, Earth-Mercury flight (tangential case)

From table 10.4, the optimisation procedure when using the exponential sinusoid took more computation time than the other shapes. Also, the percentage of individuals in the population and in the Pareto front that do not respect the maximum value for the ratio between the required thrust acceleration of the spacecraft and the available one is highest for the exponential sinusoid in all 3 cases (excluding the logarithmic spiral). Note that although 100% of the individuals in the Pareto front for the logarithmic spiral respect the constraint in the thrust acceleration, the fuel mass consumption for this shape is higher when compared with the other 5 shapes. Like for the Earth-Mars mission, the Poinsot's spiral (hyperbolic cosine) had the highest number of individuals in the population that respect the acceleration constraint cases. Note that, compared with the previous mission,

the percentage of individuals that respect the constraint is lower in the population and in the Pareto fronts.

Figures 10.11 and 10.12 illustrate the Pareto fronts for the sinusoidal spiral and for the exponential sinusoid when considering only the individuals in the population that respect the condition in (8.7). As for the Earth-Mars flight, these 2 shapes have the best performance in terms of the Pareto front (figure 10.11). Using the condition in (8.7) as a constraint, for the 2 shapes named before a certain number of individuals in the population is discarded before the Pareto front is built. Figures 10.11 and 10.12 illustrate the Pareto fronts for the sinusoidal spiral and exponential sinusoid, respectively when the available thrust acceleration $a_{available} = (0.048;0.072;0.096)\mu/r^2$ is given as a constraint.

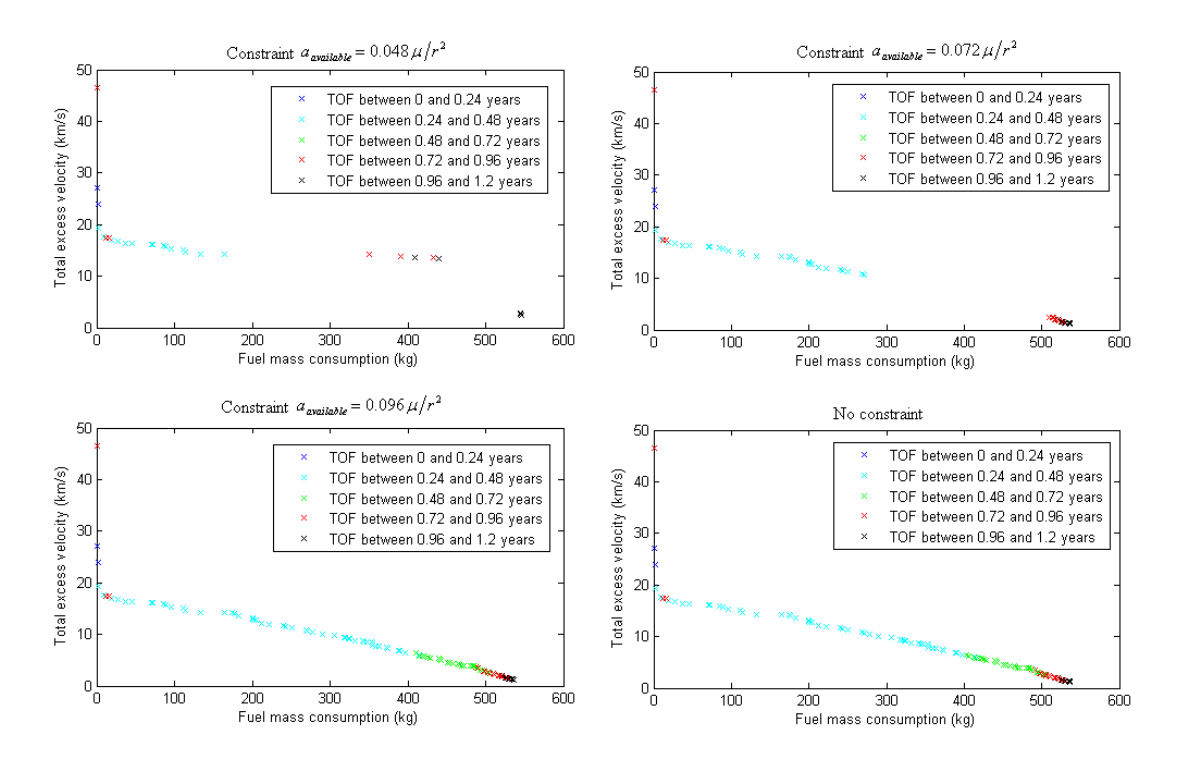


Figure 10.11: Pareto fronts for the sinusoidal spiral, for the entire population (on the right) and only for individuals in the population that respect the condition (8.7) (the 3 cases of the available thrust acceleration), tangential thrust profile, Earth-Mercury flight

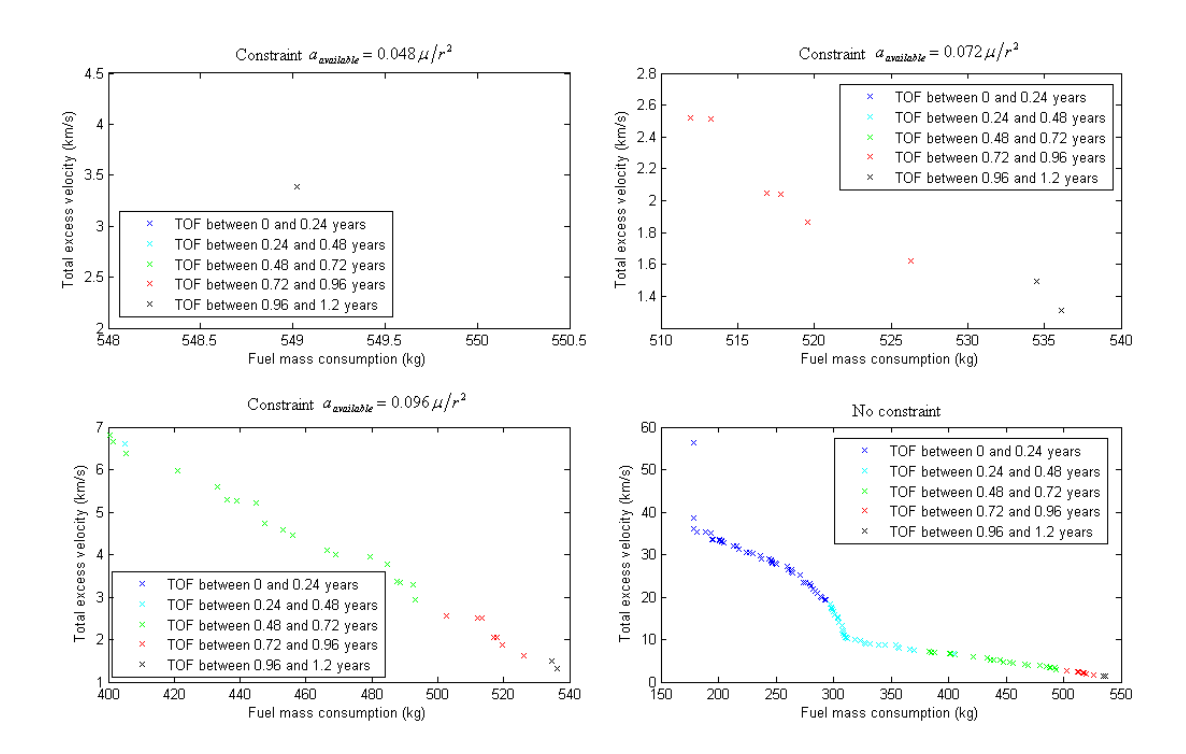


Figure 10.12: Pareto fronts for the exponential sinusoid, for the entire population (on the right) and only for individuals in the population that respect the condition (8.7) (the 3 cases of the available thrust acceleration), tangential thrust profile, Earth-Mercury flight

From figure 10.12, for the exponential sinusoid, only individuals with a fuel mass consumption higher than 400.5 kg for the case with the highest value of $a_{available}$ were selected for the Pareto front. For increasing values of $a_{available}$, the number of individuals in the Pareto front increases and lower values of fuel mass consumption are allowed. For the sinusoidal spiral (figure 10.11), there is a gap in the Pareto front for the cases $a_{available} = (0.072; 0.096) \mu/r^2$, where no individuals are presented, as it happened for the Earth-Mars mission. Again, the sinusoidal spiral shows a higher percentage of individuals in the Pareto front that respect the thrust acceleration constraints compared with the exponential sinusoid.

10.3. Earth-Mars Flight: Acceleration Inversely Square Case

Figure 10.13 gives the Pareto fronts using the acceleration inversely square case in an Earth-Mars flight only for the sinusoidal spiral and the exponential sinusoid. As already mentioned in chapter 8, the population that is being used is 75000 for each shape.

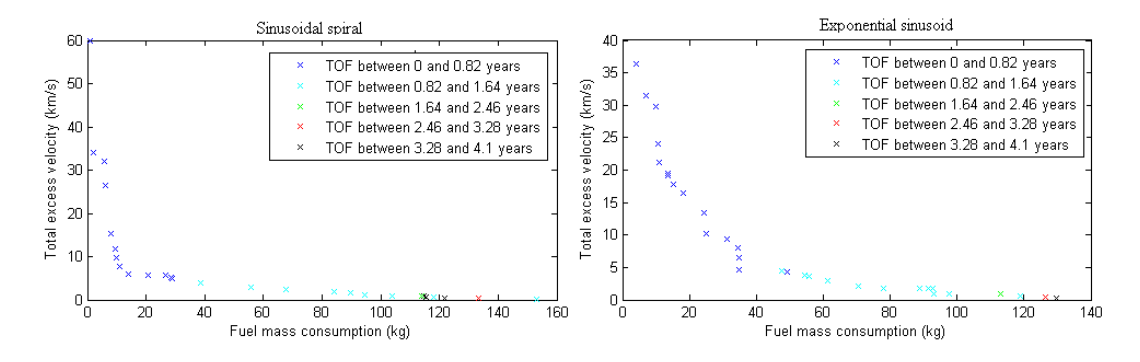


Figure 10.13: Pareto fronts for the sinusoidal spiral and the exponential sinusoid, acceleration inversely square case, Earth-Mars flight

In order to provide a clear representation in figure 10.13 of the Pareto fronts, an upper limit for the total excess velocity was given: $60 \, km/s$. Otherwise, since individuals with values of the order of $10^3 \, km/s$ were selected for the Pareto front (untenably high), the range of values for the total excess velocity represented would be large and it would have been more complicated to analyse the Pareto front. Obviously $60 \, km/s$ is still an unreasonably high value. Individuals with TOF values higher than ~4 and ~3.5 years were not selected for the Pareto fronts, for the sinusoidal spiral and the exponential sinusoid, respectively. Note that for both shapes, the maximum number of revolutions is 3 (see chapter 8), which restricts the maximum value for the TOF of the individuals selected for the Pareto fronts.

From figure 10.13, generally for higher TOF values (higher values of transfer angle $\Delta\theta$ and of number of complete revolutions N), the total excess velocity decreases while the total fuel consumption increases. Unlike for the tangential case, there are no individuals in the Pareto front that seem to be misplaced in terms of TOF for the sinusoidal spiral (section 10.1.1). Also, the presence of two curves in the Pareto front of the exponential sinusoid cannot be clearly seen in figure 10.13, since the number of individuals in the Pareto front is

significantly smaller for the acceleration inversely square case of the thrust profile than for the tangential case.

Figure 10.14 shows the Pareto fronts of both shapes. In the plot in the right-hand side, the same Pareto fronts are represented but only with individuals with values of total excess velocity lower than 2km/s and values of fuel mass consumption between 80 and 130 kg.

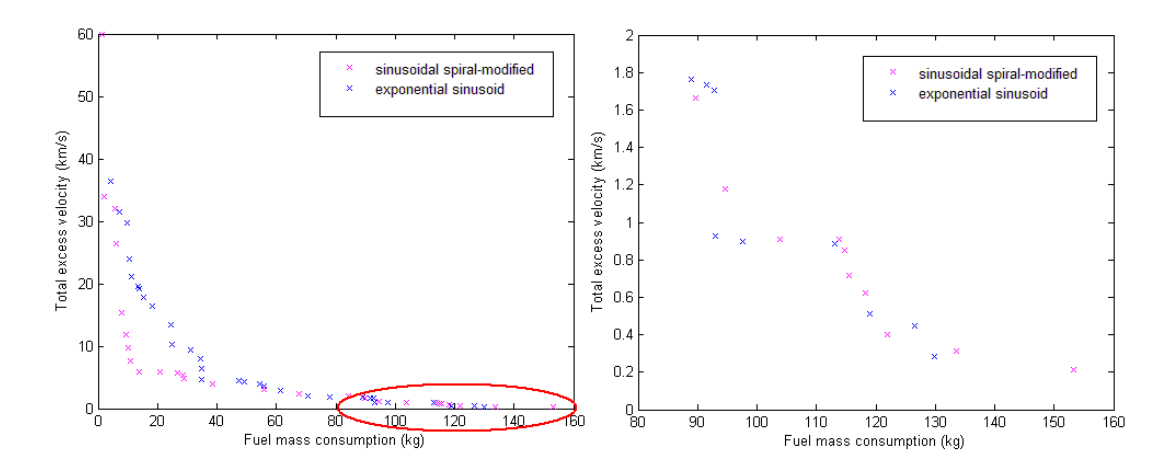


Figure 10.14: Pareto fronts for the sinusoidal spiral and the exponential sinusoid – acceleration inversely square case of the thrust profile, Earth-Mars flight

In figure 10.14, individuals with values lower than 1.1 kg and 4.1 kg are not present in the Pareto fronts for the sinusoidal spiral and for the exponential sinusoid, respectively. The minimum values of the total excess velocity in the Pareto fronts are $0.2145 \, km/s$ and $0.2835 \, km/s$ for the sinusoidal spiral and for the exponential sinusoid, respectively. The Pareto front for the sinusoidal spiral provides lower values of fuel mass consumption for the same total excess velocity when compared with the exponential sinusoid, for fuel mass consumption values lower than ~40 kg. Both shapes have similar performances for fuel mass consumption values higher than ~ 40 kg. The range of fuel mass consumption for the sinusoidal spiral is the widest one.

10.3.1. Thrust Acceleration Constraint

Computation times were tracked for both shapes and they are shown in table 10.5. Also, the percentage of the individuals in the Pareto front and in the population that respects the maximum ratio between the thrust acceleration that is given as an output from a certain shape and the available thrust acceleration (≤ 1) is presented for 3 different cases. The 3 cases are for the following nominal thrust values: (1) $a_{available} = 0.032 \,\mu/r^2$ (the same as DS1), (2) $a_{available} = 0.048 \,\mu/r^2$ (1.5 times $a_{available}$ in DS1) and (3) $a_{available} = 0.064 \,\mu/r^2$ (twice $a_{available}$ in DS1) (see chapter 8).

Shapes	Computation time (hours)	N_{Pf}	G _{Pf} (%)	G _{Pop} (%)
Sinusoidal spiral	57.6	26	77.8/94.4/100	1.3/4.3/8.6
Exponential sinusoid	94	31	80.6/100/100	0.1/0.7/2

Table 10.5: Computation time, number of individuals in the Pareto front (N_{pr}) and the percentage of individuals in the Pareto front G_{pr} and in the population G_{pop} that respect the maximum value for the ratio between the required thrust acceleration of the spacecraft and the available one, for the sinusoidal spiral and the exponential sinusoid, 3 cases of $a_{0,available} = a_{0,DS1} \left(1;1.5;2\right)$, Earth-Mars flight (acceleration inversely square case)

From table 10.5, the optimisation procedure when using the exponential sinusoid used more computation time than the sinusoidal spiral. Compared with the tangential case, the computation time is significantly higher. This is due to integrations errors (section 6.4) that occur for individuals using the acceleration inversely square case. Also, in table 10.5, the number of individuals in the population that respect the thrust acceleration constraint is lower for this case of the thrust profile compared with the tangential one. This percentage of individuals in the population is higher for the sinusoidal spiral. However, the exponential sinusoid presents a significantly higher number of individuals in the Pareto front that respect the thrust acceleration constraint, unlike for the tangential case where this shape was the one that had lower percentage of individuals in the Pareto front that respect this constraint.

Figures 10.15 and 10.16 illustrate the Pareto fronts for the sinusoidal spiral and for the exponential sinusoid when considering only individuals in the population that respect the condition in (8.7). Figures 10.15 and 10.16 show the Pareto fronts for the sinusoidal spiral and exponential sinusoid, respectively when the available thrust acceleration $a_{available} = (0.032; 0.048; 0.064) \mu/r^2$ is given as a constraint.

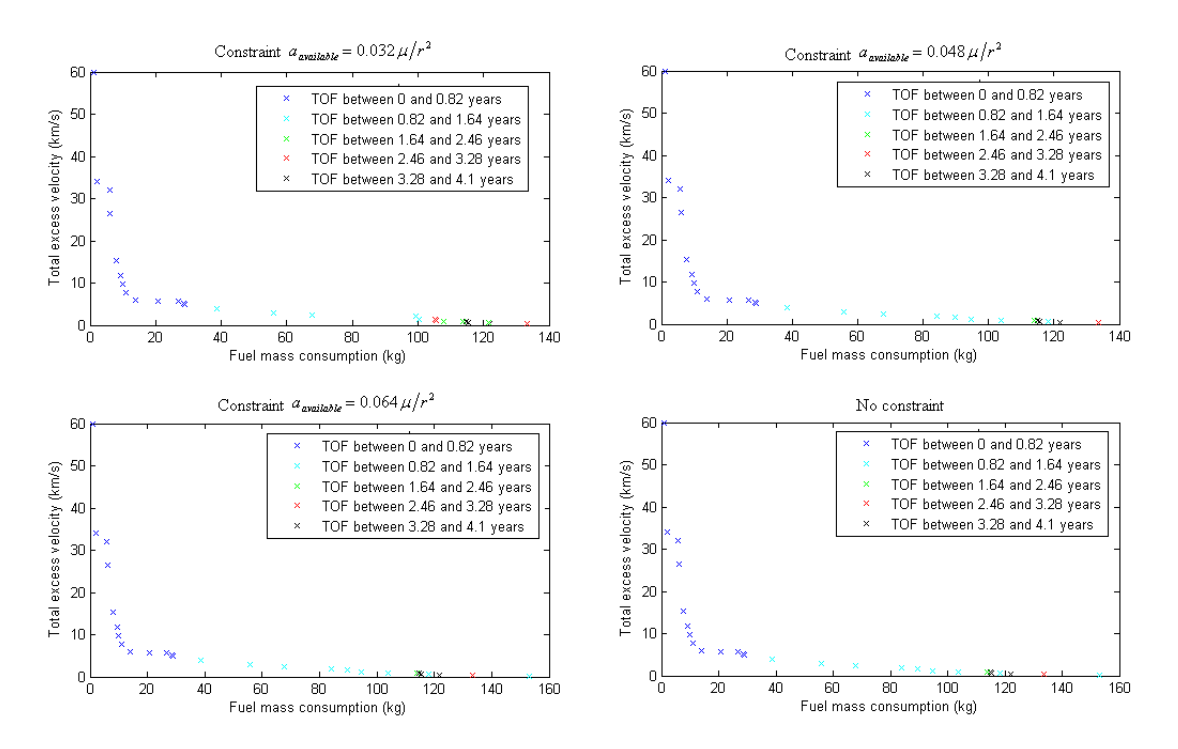


Figure 10.15: Pareto fronts for the sinusoidal spiral, for the entire population (on the bottom right) and only for individuals in the population that respect the condition (8.7) (the 3 cases of the available thrust acceleration), acceleration inversely square case, Earth-Mars flight

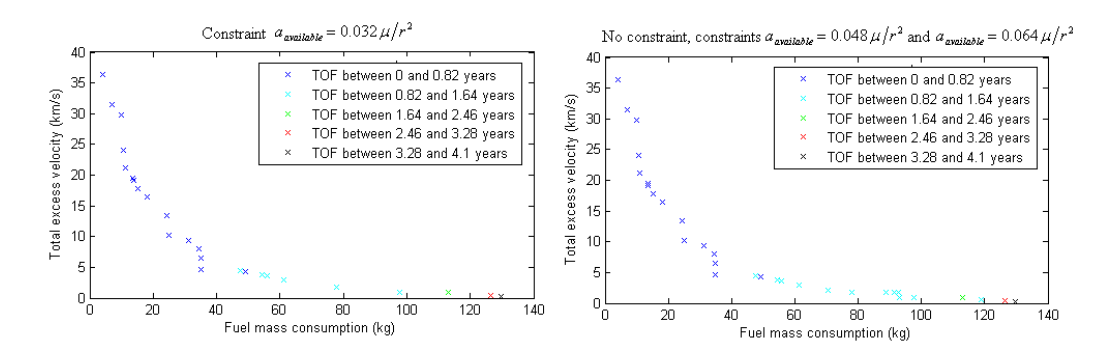


Figure 10.16: Pareto fronts for the exponential sinusoid, for the entire population (on the right) and only for individuals in the population that respect the condition (8.7) (the 3 cases of the available thrust acceleration), acceleration inversely square case, Earth-Mars flight

From figures 10.15 and 10.16, for both sinusoidal spiral and exponential sinusoid, there are no significant differences between the Pareto fronts for all 3 cases. From the first to the second cases of $a_{available}$, for both shapes, there is a lack of individuals between 80 kg and 100 kg.

10.4. Earth - Mercury Flight: Acceleration Inversely Square Case

Figure 10.17 illustrates the Pareto fronts using the acceleration inversely square case in the Earth-to-Mercury flight for the sinusoidal spiral and for the exponential sinusoid. As already said before, the population that is being used is 75000 individuals for each shape.

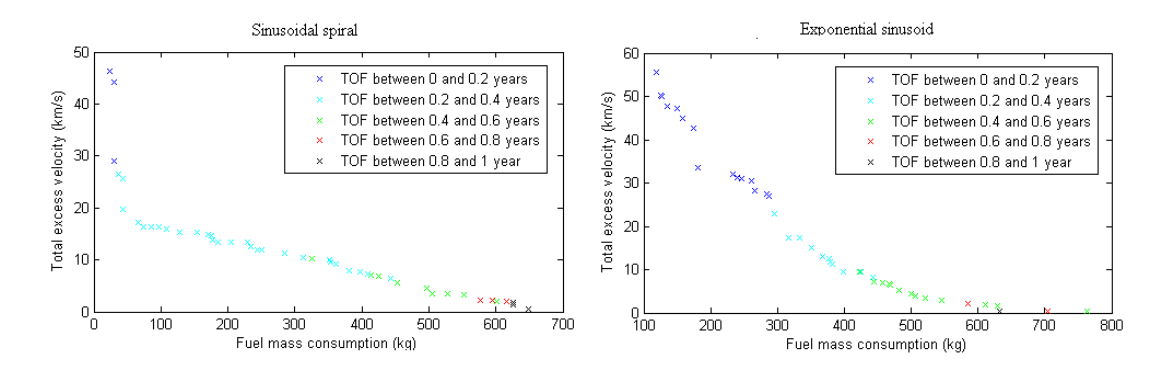


Figure 10.17: Pareto fronts for the sinusoidal spiral and the exponential sinusoid, acceleration inversely square case, Earth-Mercury flight

Note that the total excess velocity values for lower values of fuel mass consumption are significantly high. Individuals with these values of total excess velocity cannot be taken into account in a real mission. Again an upper limit for the total excess velocity was used: $60 \, km/s$ for the same reasons already mentioned in section 10.3.

Figure 10.18 illustrates the Pareto fronts for the sinusoidal spiral and for the exponential sinusoid. In the plot in the right-hand side, the same Pareto fronts are represented but only with individuals with values of total excess velocity lower than $4 \, km/s$ and values of fuel mass consumption between 550 and 800 kg.

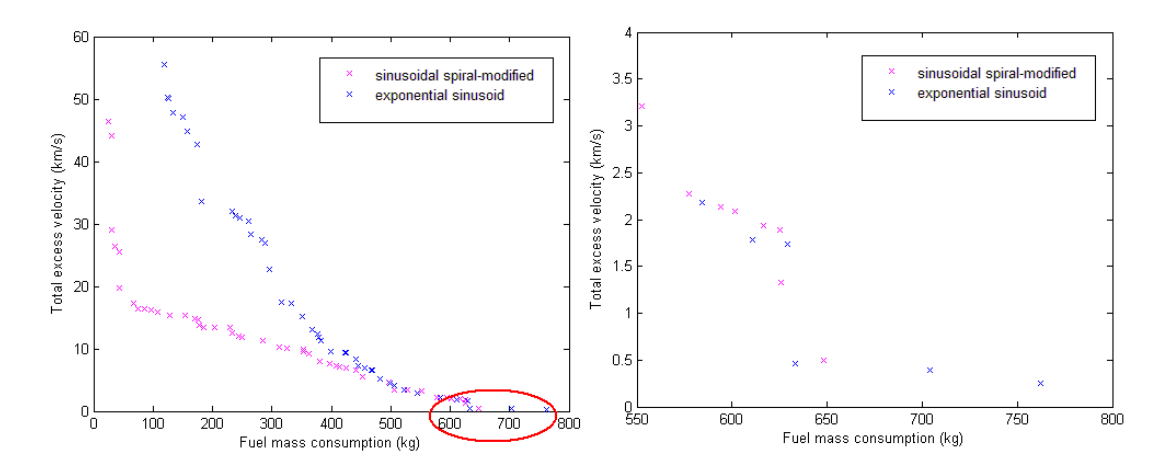


Figure 10.18: Pareto fronts for the sinusoidal spiral and for the exponential sinusoid, acceleration inversely square case, Earth-Mercury flight

Individuals with values lower than 24.4 kg and 118.3 kg are not present for the Pareto fronts for the sinusoidal spiral and for the exponential sinusoid, respectively. The minimum values of the total excess velocity in the Pareto fronts are $0.4967 \, km/s$ and 0.2551 km/s for the sinusoidal spiral and the exponential sinusoid, respectively. Unlike for the other 3 missions shown in this chapter, the minimum value of the total excess velocity is lower for the exponential sinusoid and not for the sinusoidal spiral. Individuals with TOF values higher than ~ 0.94 years were not selected for the Pareto fronts for a maximum number of complete revolutions of 2.

From figure 10.18, the Pareto fronts for the sinusoidal spiral provide lower values of fuel mass consumption (for values lower than $\sim 500~\rm kg$) for the same total excess velocity when comparing with the exponential sinusoid. The range of fuel mass consumption values for the sinusoidal spiral is the widest one. This shape and the exponential sinusoid have similar performances for fuel mass consumptions higher than $\sim 500~\rm kg$.

10.4.1. Thrust Acceleration Constraint

Computation times are given for both shapes in table 10.6. Also, the percentage of the individuals in the Pareto front and in the population that respects the maximum ratio between the thrust acceleration that is given as an output from a certain shape and the available thrust acceleration (≤ 1) is presented for 3 different cases of available thrust

acceleration: (1) $a_{available} = 0.048 \,\mu/r^2$ (1.5 times $a_{available}$ in DS1), (2) $a_{available} = 0.072 \,\mu/r^2$ (2.25 times $a_{available}$ in DS1) and (3) $a_{available} = 0.096 \,\mu/r^2$ (3 times $a_{available}$ in DS1) (see chapter 8).

Shapes	Computation time (hours)	N_{Pf}	G _{Pf} (%)	G _{Pop} (%)
Sinusoidal spiral	40.5	46	47.8/84.8/100	0.5/2/5.3
Exponential sinusoid	85.5	41	0/23.8/97.6	0.02/0.5/2.5

Table 10.6: Computation time, number of individuals in the Pareto front (N_{pf}) and the percentage of individuals in the Pareto front G_{pf} and in the population G_{pop} that respect the maximum value for the ratio between the required thrust acceleration of the spacecraft and the available one, for the sinusoidal spiral and the exponential sinusoid, 3 cases of $a_{0,available} = a_{0,DS1} \left(1.5; 2.25; 3 \right)$, Earth-Mercury flight (acceleration inversely square case)

From table 10.6, the optimisation procedure using the exponential sinusoid required more computation time than the sinusoidal spiral. Also, the percentage of individuals in the population and in the Pareto front that do not respect the maximum value for the ratio between the required thrust acceleration of the spacecraft and the available one is highest for the exponential sinusoid in all 3 cases. Compared with the Mars mission, there are more individuals in the Pareto front for the Earth-Mercury flight.

Figures 10.19 and 10.20 illustrate the Pareto fronts for the sinusoidal spiral and for the exponential sinusoid when considering only the individuals in the population that respect the condition in (8.7). Figures 10.19 and 10.20 illustrate the Pareto fronts for the sinusoidal spiral and exponential sinusoid, respectively when the available thrust acceleration $a_{available} = (0.048; 0.072; 0.096) \mu/r^2$ is given as a constraint.

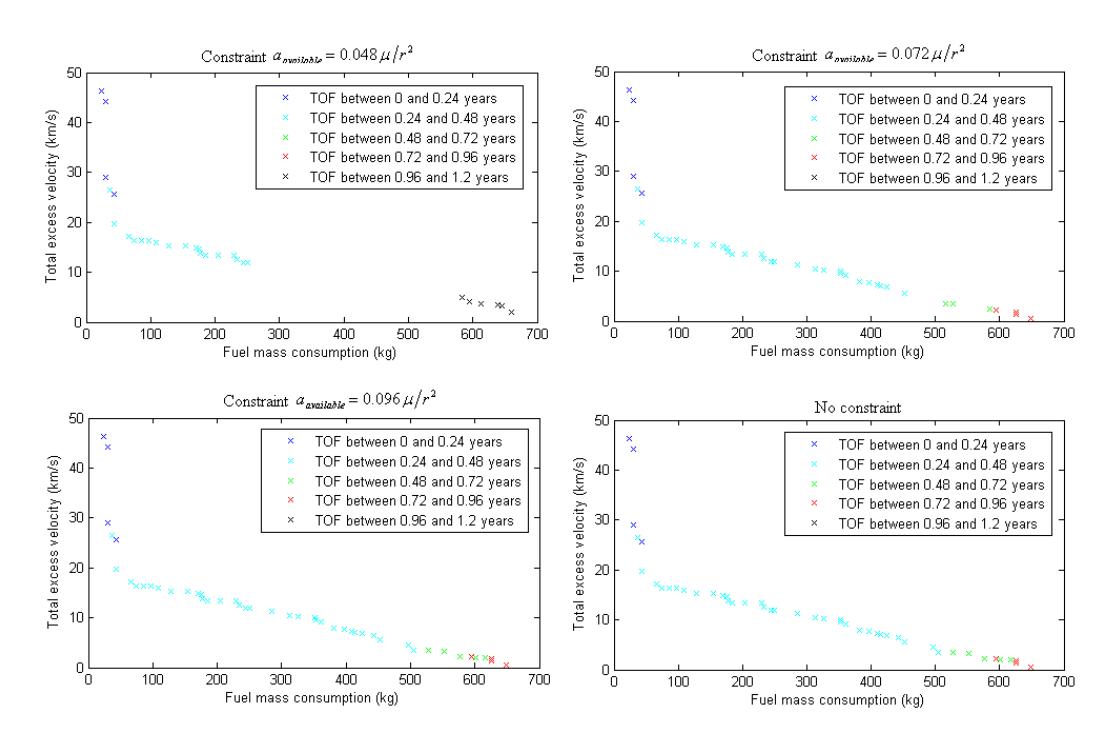


Figure 10.19: Pareto fronts for the sinusoidal spiral, for the entire population (on the right) and only for individuals in the population that respect the condition (8.7) (the 3 cases of the available thrust acceleration), acceleration inversely square case, Earth-Mercury flight

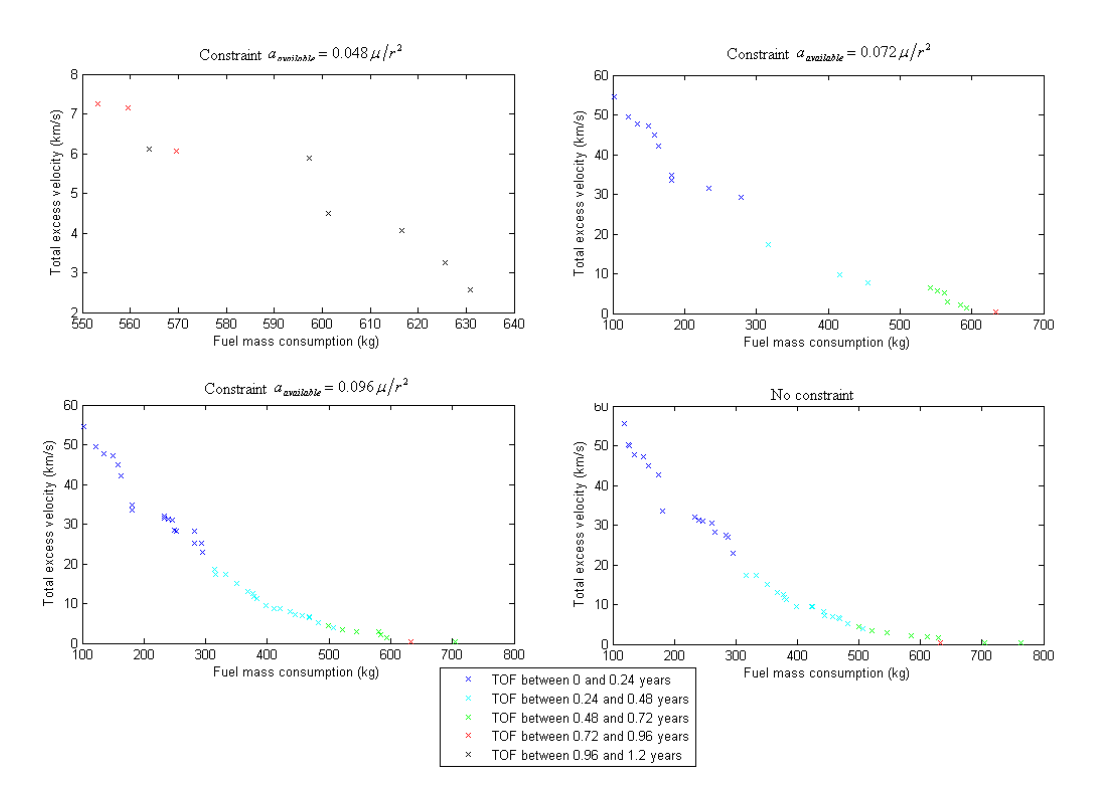


Figure 10.20: Pareto fronts for the exponential sinusoid, for the entire population (on the right) and only for individuals in the population that respect the condition (8.7) (the 3 cases of the available thrust acceleration), acceleration inversely square case, Earth-Mercury flight

From figure 10.19, for the sinusoidal spiral, there is a gap in the Pareto front for the case $a_{available}=0.048\,\mu/r^2$, where individuals with fuel mass consumption values between ~260 kg and ~560 kg are not present. From figure 10.20, the Pareto front for the exponential sinusoid only has individuals with fuel mass consumption values higher than 550 kg for the constraint $a_{available}=0.048\,\mu/r^2$. For the other cases and for both shapes, there no significant differences between the Pareto front without applying the constraint and with the constraint $a_{available}=(0.072;0.096)\,\mu/r^2$. Note that in some cases, the individuals chosen had TOF higher than 1 year (maximum TOF in the Pareto front in figure 10.17 was ~0.94 years).

10.5. Conclusions

Some important remarks can be made in this section about the optimisation results presented in this chapter.

For all example missions and for both thrust profiles presented, the sinusoidal spiral achieved the best results in terms of Pareto front. The exponential sinusoid was generally the second best in all analyse, but always the shape that required the highest computation time. The Archimidean spiral and the Poinsot's spiral (hyperbolic sine) had the worst performance in the Earth-to-Mars mission (tangential case), since the number of individuals in the Pareto front was significantly small and their fuel mass consumption values were higher compared with the values for the other shapes. The same situation occurred for the logarithmic spiral in the Earth-Mercury mission. In this way, after a more detailed study, conclusions can be drawn: the geometric properties of these shapes cannot satisfy the physical problem when the target planet is inner (logarithmic spiral) and outer (Archimedean spiral and the Poinsot's spiral (hyperbolic sine)) with respect to the departure planet. For this reason, these 3 shapes should not be used as analytical representations for low-thrust trajectories.

In terms of the thrust acceleration constraint, the sinusoidal spiral shows always a higher percentage of individuals in the Pareto front that respect this constraint than the exponential sinusoid, except for the Earth-Mars mission using the acceleration inversely square case. For higher values of transfer angle and number of complete revolutions N, generally there is a higher difference between the maximum values of thrust acceleration used and the maximum thrust available.

When comparing the results between the acceleration inversely square case and the tangential case, the computation time required for the first case is significantly higher than for the later one (at least 30 times higher for the sinusoidal spiral and 49 times for the exponential sinusoid). Also, the number of individuals in the Pareto front is at least twice higher for the tangential case. Figure 10.21 illustrates the Pareto fronts for the sinusoidal spiral and the exponential sinusoid for an Earth-Mars mission.

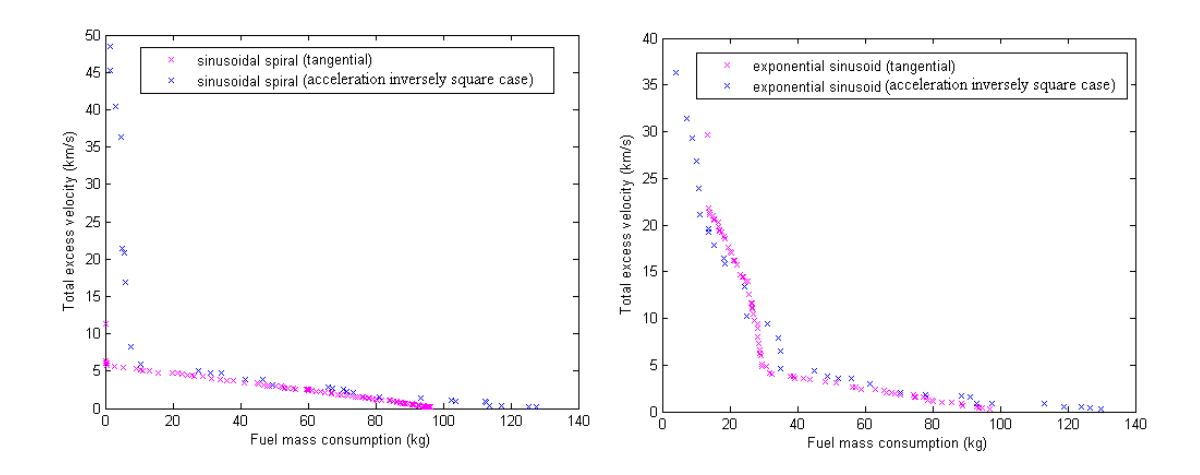


Figure 10.21: Pareto fronts for the sinusoidal spiral and the exponential sinusoid, acceleration inversely square case, tangential thrust, Earth-Mars flight

From figure 10.21, the sinusoidal spiral performs always better (for values of fuel mass consumption lower than 100 kg), using the tangential profile than the acceleration inversely square case. The exponential sinusoid performs better with the tangential profile for fuel mass consumption values higher than ~35 kg and lower than 100 kg. The minimum values of total excess velocity (Earth-Mars mission) for the sinusoidal spiral were $0.1854 \, km/s$ and $0.2145 \, km/s$ for the tangential and accelerations inversely square cases of the thrust profile, respectively. In terms of fuel mass consumption during the lowthrust phase, the sinusoid spiral, for the acceleration inversely square case uses 153.25 kg, while for the tangential case 96.43 kg are spent. This means that the fuel mass consumption spent during the heliocentric phase and the total excess velocity required were higher for the acceleration inversely square case compared with the tangential case. In terms of thrust acceleration constraint, the number of individuals in the Pareto front that respect the constraint is always higher for the acceleration inversely square case than for the tangential case. On the other hand, the number of individuals in the population that respect the thrust acceleration constraint is generally higher for the tangential case than for the acceleration inversely square case.

Figure 10.22 shows the Pareto fronts for the sinusoidal spiral and the exponential sinusoid for an Earth-Mercury mission. For this mission, the minimum values of total excess velocity for the sinusoidal spiral were $1.2609 \, km/s$ and $0.4967 \, km/s$ for the tangential and

accelerations inversely square cases, respectively. In terms of fuel mass consumption during the low-thrust phase, the sinusoid spiral, for the acceleration inversely square case uses 648.18 kg, while for the tangential case 536.04 kg are spent. This means that although the fuel mass consumption spent during the low-thrust phase was higher for the acceleration inversely square, the total excess velocity required is smaller compared with the tangential case.

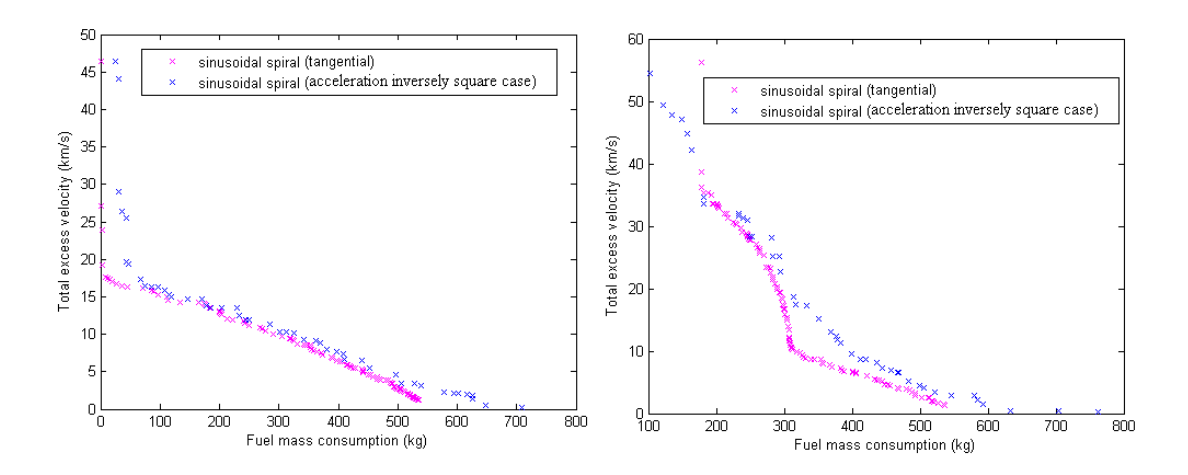


Figure 10.22: Pareto fronts for the sinusoidal spiral and the exponential sinusoid for the acceleration inversely square case of the thrust profile and the tangential thrust for an Earth-Mercury flight

Due to the significantly high computation time and the worse performances for most of the individuals in the Pareto fronts, the acceleration inversely square case of the thrust profile should not be considered for a mission generator for low-thrust trajectories.

From the excess velocity values achieved in the Pareto fronts in this chapter, the application of this shape-based technique is only meaningful if a multi-revolution case is considered (see figure 10.23). For smaller values of N (lower TOF), for the examples shown in this chapter, the total excess velocity values are, many times, too high to be considered in a mission and/or to have the advantage of using the low-thrust propulsion technology instead of the chemical one in a mission.

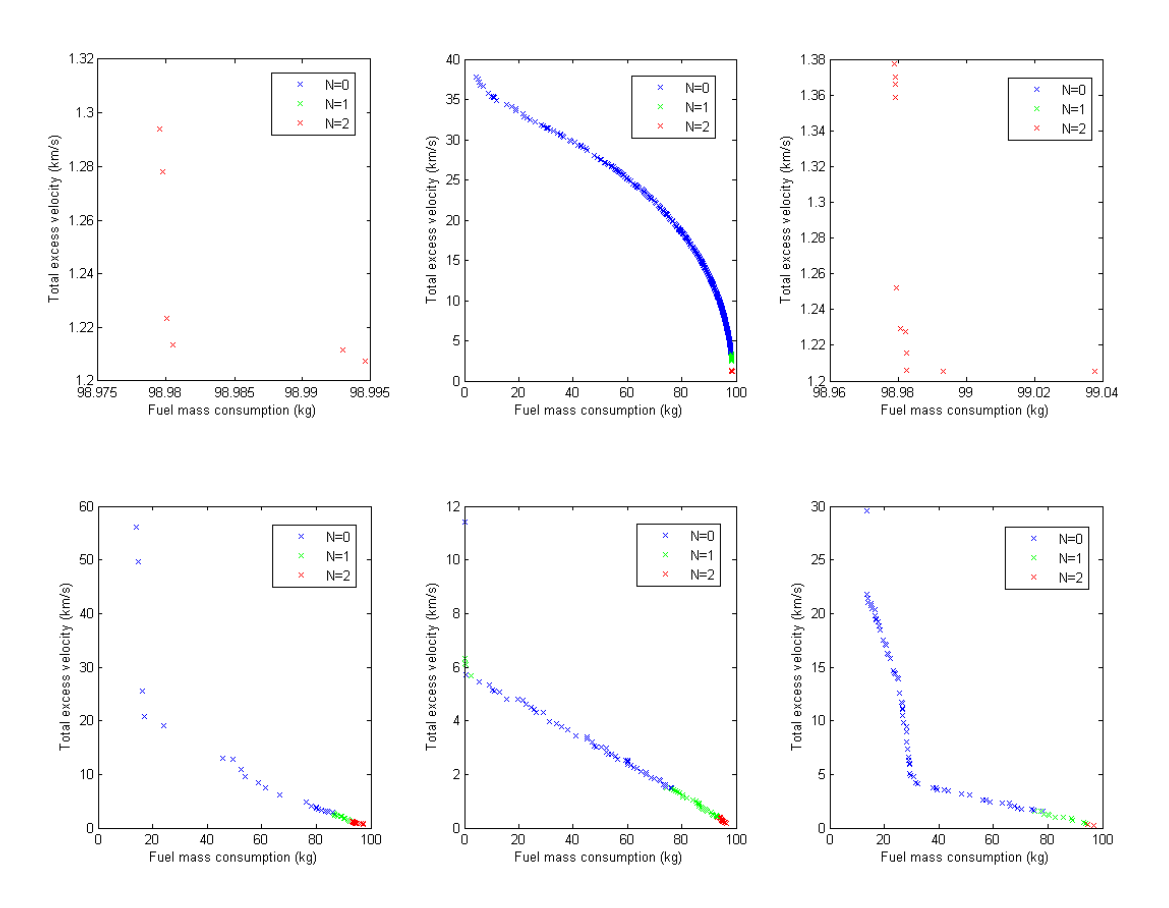


Figure 10.23: Pareto fronts for the Archimedean spiral, logarithmic spiral, Poinsot's spiral (hyperbolic sine), Poinsot's spiral (hyperbolic cosine), sinusoidal spiral and exponential sinusoid, tangential thrust, Earth-to-Mars flight, for different values of N

11. Final conclusions

The aim of this master thesis was to come up with alternative mathematical functions and thrust profiles to represent low-thrust interplanetary trajectories, different from the one presented in [Petropoulos et al., 1999] (exponential sinusoid using continuous tangential thrusting). Six shapes (including the exponential sinusoid), combined with three thrust profiles (the tangential profile included) were studied.

The constant acceleration case of the thrust profile, where the thrust acceleration is constant and equal to $a = a_0 \, \mu / r_1^2$, was discarded after the sensitivity analysis (chapter 7) and consequently it was not used in the optimisation (chapter 9). The results shown for this thrust profile case were not as satisfactory as for the other thrust profiles, in terms of total excess velocity and thrust acceleration. Therefore and also due to lack of time, the study of this thrust profile was not extended. An optimisation procedure was done for 6 shapes, with 2 different thrust profiles and for 3 different missions: Earth-Mars, Earth-Jupiter and Earth-Mercury (chapter 9).

Concerning the results from the sensitivity analysis, by using the acceleration inversely square and constant acceleration cases, integration errors can easily occur. Many times, for certain geometric parameters and normalised thrust acceleration values, feasible trajectories cannot be computed. When the integration is completed without errors, the shapes combined with these thrust profiles force the spacecraft to use negative (but higher than -90°) values of the thrust angle α . This means that the spacecraft most of its time is thrusting inwards in the radial direction, while its radial velocity is positive (like the engine is trying to slow down the spacecraft). Also, from the analysis done in chapter 7, the search space for the input variables required cannot be restricted in order to prevent integration errors. This led to significantly higher values of computation time in the optimisation procedure (chapter 10) using the acceleration inversely square case than with the tangential thrust profile. Any definite conclusions could not be made after the sensitivity analysis in chapter 7. Optimisation was necessary to analyse the performances of each shape and to compare them.

In chapter 10, Pareto fronts were built for the acceleration inversely square and the tangential cases and for 2 missions. Generally, the sinusoidal spiral had the best performance in terms of the Pareto front in all cases. Compared with the exponential sinusoid, the computation time was smaller.

The Pareto front trend of the exponential sinusoid was studied in chapter 10. Two types of curvatures were verified in the Pareto front for the tangential thrust profile for the 2 mission examples. For values of fuel mass consumption lower than a certain value $M_{\it fuel}$, the parameter k_2 increases, while for higher values, it decreases. According to Petropoulos and Longuski [Petropoulos and Longuski, 2004], for higher values of the transfer angle $\Delta\theta$ and higher number of complete revolutions N (higher values of fuel mass consumption), the values for k_2 should decrease. In this way, the plot of k_2 should always decrease when increasing the values of the fuel mass consumption, which does not happen for values lower than $M_{\it fuel}$. At $M_{\it fuel}$, k_2 approximately reaches the maximum value allowed by the optimisation program: 1. When increasing k_2 from higher fuel mass consumption to lower fuel mass consumption values, after $M_{\it fuel}$, the influence of this geometric parameter on the dynamics of the problem is different. Therefore, the bend occurs because the optimizer chooses smaller values of k_2 .

From the optimisation results obtained for the tangential case, the Archimedean spiral, the logarithmic spiral and the Poinsot's spiral (hyperbolic sine) were not considered suitable for the representation of low-thrust trajectories. Only the sinusoidal spiral and the exponential sinusoid were used in the optimisation procedure, using the acceleration inversely square case. Compared with the tangential case, the computation time is more than 30 times higher and the number of individuals in the Pareto front is more than twice less. The minimum values for the total excess velocity are higher for the acceleration inversely square case than for the tangential case in the Earth-Mars flight, while for the Earth-Mercury mission, the opposite occurs. For both missions, the fuel mass consumption values are much higher for the acceleration inversely square case than for the tangential one. The acceleration inversely square case is expected to have a better Pareto front than the tangential case, since it uses 2 more variables than the other one (there is more

flexibility). This does not happen, because the problem also becomes more complex. Again, the geometry combined with the demands on the thrust profile cause integration errors that narrow the search space of each input parameter (section 6.4) and it limits the number and the performance of the individuals in the Pareto front. Also, there is a restriction in the thrust acceleration trend. For these reasons, the tangential case should be the thrust profile chosen to be used in a mission generator.

Note that although the sinusoidal spiral had a better overall performance than the exponential sinusoid, it is worse than this last shape (chapter 6) in terms of constraint equations and singularities. It was not possible in chapter 6 to find a constraint equation to ensure that $\dot{\theta}^2$ is always positive. Individuals that do not respect $\dot{\theta}^2 > 0$ were discarded during the integration procedure, unlike the exponential sinusoid where only individuals that respect $\dot{\theta}^2 > 0$ a priori are picked. In spite of this, the computation time of the sinusoidal spiral was shorter than for the exponential sinusoid. Note that, as already explained before, a three-dimensional problem was not implemented in the optimisation procedure and consequently, the geometric parameter for a required TOF for a specific mission was not computed using the plot TOF as function of the free geometric parameter (in case of the sinusoidal spiral is m - see section 5.5). In the case of the sinusoidal spiral (unlike the exponential sinusoid), the interval of values for m would have been always (-1,1) and $m \neq 0$. However, there is no guarantee that there will be always a sinusoidal spiral for the TOF required.

In terms of the thrust acceleration constraint, the sinusoidal spiral showed always a higher percentage of individuals that respect this constraint than the exponential sinusoid, for the tangential case.

Finally, from chapter 10, the application of this shape-based technique is only meaningful if a multi-revolution case is considered. For a zero value of N, the total excess velocity values are many times too high to be considered in a mission and/or to have the advantage of using the low-thrust propulsion technology instead of the chemical one (constraints in the maximum thrust acceleration available are violated).

From this master thesis 6 shapes and 3 different thrust profiles were studied. Only the sinusoidal spiral performs better than the exponential sinusoid using continuous tangential thrust in terms of computation time, total excess velocity and thrust acceleration constraint.

12. Recommendations

Although much analysis has been done in this master thesis, there are some areas that still need to be investigated.

Even if the sinusoidal spiral was considered the shape that had the best performance after the optimisation procedure, a more detailed mathematical and physical analysis should be done, in order to find a constraint equation as Petropoulos did for the exponential sinusoid [Petropoulos and Longuski, 2004].

During the optimisation procedure, the fuel mass consumption during the high-thrust phase should be computed. Another combination of objective functions should be tested, like the total impulse shots ΔV (chemical) versus the fuel mass consumption during the interplanetary low-thrust phase.

Also, the optimisation procedure was done without giving the TOF as an input for the optimizer (three-dimensional case). The exponential sinusoid is already implemented in Galomusit [Corradini, 2008] together with a multi-objective optimizer (with the objective functions: total hyperbolic excess velocity versus fuel mass consumption during the interplanetary phase). The sinusoidal spiral can be also implemented in Galomusit and results between these two shapes can be compared using the JPL's Ephemeris model, instead of a two-dimensional one.

The results obtained from the exponential sinusoid and the sinusoidal spiral should serve as an input for a real mission generator, where perturbations are taken into account. The concept of using analytical representations for low-thrust trajectories should be analysed. If the variation in final position and velocity of the spacecraft using the full numerical integration of the transfer orbit with respect to the results given by the analytical representation technique is significantly small, then this shape technique using the sinusoidal spiral or the exponential sinusoid will be worthwhile taking into account for an initial guess to compute low-thrust trajectories. On the other hand, if the differences between the numerical integration results and the analytical representation results are not

acceptable, other methods different from the one developed by Dario Izzo [Izzo, 2006] should be taken into account. The method developed by [Biesbroek, 2006] that uses predescribed thruster models or the one done by De Vogeleer [De Vogeleer, 2008] already mentioned in this thesis are two examples of such techniques. In the following paragraphs, a comparison between the software implemented by De Vogeleer [De Vogeleer, 2008] and Izzo's technique will be done in order to understand their advantages and disadvantages.

As mentioned before, the purpose of the thesis developed by De Vogeleer was to find a method that serves as an initial guess to compute short low-thrust trajectories between two celestial bodies. The method works very well as long as the number of revolutions N is smaller than 2, while Izzo's method has no limitation on this parameter. Both methods are independent of the initial or final orbit parameters. De Vogeleer's method calculates feasible trajectories for fixed initial and final positions and velocities, while in Izzo's technique [Izzo, 2006] there is only a match in initial and final positions. As mentioned in the beginning of this chapter, De Vogeleer uses expansions of power series to represent the low-thrust trajectory of the spacecraft, i.e., expressions with linear combinations of many terms (coefficients). These coefficients act as degrees of freedom and are therefore some of the optimization variables. The amount of coefficients depends on the range of the mission, i.e., for an Earth-Mars flight the software will need fewer coefficients than for an Earth-Jupiter flight. Izzo's technique, on the other hand, uses only 3 optimization variables $(t_{departure}, TOF, k_2)$ for a direct flight (exponential sinusoid) independently of the initial and final orbit parameters. Also, a sensitivity analysis is required in order to choose the correct values for the order of the expansions and the density of the time grid to achieve consistent integrations. This kind of sensitivity analysis is not needed with Izzo's technique.

Advantages and disadvantages can be found in both methods with respect to each other. De Vogeleer's method is more desirable for orbit insertion missions, because a match in position and velocity is achievable. Izzo's technique is a much more straightforward method, but it requires significantly high initial and final excess velocities in order to perform orbit insertions. Note that the sinusoidal spiral and the exponential sinusoid have similar performances in terms of excess velocity for high values of number of revolutions. Therefore, De Vogeleer's method is still more suitable for orbit insertion missions than Izzo's technique using the sinusoidal spiral. On the other hand, the excess velocities

achieved by Izzo's method make it more attractive for thrust arcs where flybys are taken into account. In this situation De Volgeleer's method cannot perform efficiently, since the final velocity is already fixed. A combination of Izzo's technique and the Vogeleer's method will be advantageous for a mission generator of low-thrust trajectories.

Bibliography

Bate, R.R., Mueller, D.D., White, J.E. (1971); *Fundamentals of Astrodynamics*; Dover Publications, Inc. New York.

Biesbroek, G.J.R. (2006), A Simple Low-Thrust Lambert Solver Using Pre-Described Engine Models, JAQAR Internal Report, JAQ-SBC-PAP2006-LTT

Cornelisse, J.W., Schöyer, H.F.R., Wakker, K.F. (1979); *Rocket Propulsion and Spaceflight Dynamics*; London: Pitman Publishing Limited.

Corradini, Sefano (2008), *Interplanetary Transfer with Low-thrust Trajectories*, Delft University of Technology, Faculty of Aerospace Engineering.

De Vogeleer, Bram (2008); Automatic and Fast Generation of Sub-optimal and Feasible Low-Thrust Trajectories Using a Boundary-Value Paseudo-Spectral Method, Thesis Report, Delft University of Technology, Faculty of Aerospace Engineering and GMV Aerospace and Defense, S.A..

ESA/BepiColombo (2008), Science and Technology; http://sci.esa.int/science-e/www/area/index.cfm?fareaid=30, last accessed September, 21st 2008.

ESA/SMART-1 (2007I), Science and Technology; http://smart.esa.int; last accessed October, 30th 2007.

ESA/SMART-1 (2007II); http://www.esa.int/SPECIALS/SMART-1/; last accessed October, 30th 2007.

Izzo, Dario (2006); *Lambert's problem for exponential sinusoids*; Journal of Guidance, Control and Dynamics, Vol.29, No. 5.

JAQAR (2007), Swing-by Calculator - Software User Manual, JAQAR Space Engineering, Issue 8.

Komurasaki, K. (2003); An overview of electric propulsion activities in Japan; AIAA 2003-5272.

Kuninaka, H., Nishiyama, K., Shimizu, Y, Hosoda, S, Koizumi, H., Kawaguchi J. (2007); *Status of Microwave Discharge Ion Engines on Hayabusa Spacecraft*; AIAA 2007-5196.

Lawrence, J.D. (1972); A Catalog of Special Plane Curves; Dover Publications, Inc. New York.

Lockwood, E.H. (1961); A book of curves; The Syndics of the Cambridge University Press.

Melman, J.C.P. (2007), *Trajectory Optimisation for a Mission to Neptune and Triton*, Thesis Report, Delft University of Technology, Faculty of Aerospace Engineering.

Montenbruck, O., Eberhard, G (2005); *Satellite Orbits: Models, Methods and Applications*; Springer; corrected printing 1st edition 2000.

NASA/JPL (2002) Deep Space 1; http://nmp.jpl.nasa.gov/ds1; Last accessed: October, 30th 2007.

NASA/GSFC (2007), Lunar and Planetary Science; http://nssdc.gsfc.nasa.gov/planetary; last accessed: October, 30th 2007.

Noomen R., (2007), Space Mission Design: Optimisation, Delft University of Technology, Faculty of Aerospace Engineering, lecture notes ae4-878.

Paulino, T. (2007); Analytical Representation for Low-thrust Trajectories, Literature survey, Delft University of Technology, Faculty of Aerospace Engineering.

Paulino, T. (2008); Requirement Document of the Interplanetary Low-Thrust module, STA-ECM-SRD-0801 Iss.1.0 ILT

Petropoulos, E., Longuski, J.M. (2000); *Automated Design of Low-Thrust Gravity-Assist Trajectories*; AIAA-2000-4033.

Petropoulos, E., Longuski, J.M. (2004); *Shaped-based Algorithm for Automated Design of Low-Thrust, Gravity-Assist Trajectories*; Journal of Spacecraft and Rockets, Vol. 41, No. 5, September-October 2004.

Petropoulos, E., Longuski, J.M., Vinh, N.X. (1999); *Shape-based Analytic Representations of Low-Thrust Trajectories for Gravity-Assist Applications*; AAS 99-337, page 563-581.

Rayman M.D., Varghese P., Lehman D.H., Livesay L.L.; *Results from the Deep Space 1 technology validation mission*; AIAA 1999, JPL, California Institute of Technology.

Wakker, K.F. (2005I); *Astrodynamics I*; Delft University of Technology, Faculty of Aerospace Engineering, Lecture notes AE4-873, Part 1.

Wakker, K.F. (2005II); *Astrodynamics II*; Delft University of Technology, Faculty of Aerospace Engineering, Lecture notes AE4-873, Part 2.

Weisstein, E. (2007); http://mathworld.wolfram.com/; Wolfram Math world, Wolfram Research; last accessed November 5th 2007.

Wertz, J.R. (2001); *Mission Geometry; Orbit Constellation Design and Management*, Space Technology Library and Microcosm Press.

Wertz, J.R., Larson W.J. (1999); *Space Mission Analysis and Design*; 3rd edition Space Technology Library and Microcosm Press.

Zandbergen, B.T.C. (2004); *Thermal Rocket Propulsion*; Delft University of Technology, Faculty of Aerospace Engineering, Lecture notes AE4-S01.

Appendices

Table of Contents

List of Fig	gures	v
List of Tal	bles	xiii
Appendix	A: Derivation of Equations	2
Appendix	B: Equations of the Shapes	10
Appendix	C: Integration Error	20
Appendix	D: Analysis of the Shapes for the Constant Acceleration Case of	f the Thrust
Profile		24
1.	Archimedean spiral	24
2.	Logarithmic spiral	31
3.	Poinsot's spiral (hyperbolic sine)	37
4.	Poinsot's spiral (hyperbolic cosine)	44
5.	Sinusoidal spiral	50
6.	Exponential Sinusoid	56
Appendix	E: Analysis of the Exponential Sinusoid for an Earth-Jupiter Fli	ght and for an
Earth-Mer	reury Flight	64
Appendix	F: Verification	92
Appendix	G: Test of the Number of Individuals	98
Appendix	F: Optimization for an Earth-Jupiter Flight	100

List of Figures

Figure 1: $\dot{\alpha}$ as function of time from 1.416985×10' $s \approx 0.449323$ years
Figure 2: TOF for θ_i values of (0°, 120°, 240°, 360°) from left to right in the figure, α_0 values of (-60°, -50°,
-40°, -30°, -20°), $\Delta\theta$ values of (90°, 150°, 210°, 270°, 340°) (N=0), m =0.05, a_0 =0.07, constant acceleration
case of the thrust profile (Archimedean spiral), Earth-Mars flight
Figure 3: $V_{\infty,T}$ for θ_i values of (0°, 120°, 240°, 360°) from left to right in the figure, α_0 values of (-60°, -50°, -
40° , -30° , -20°), $\Delta\theta$ values of (90°, 150°, 210°, 270°, 340°) (N=0), m =0.05, $a_{_0}$ =0.07, constant acceleration
case of the thrust profile (Archimedean spiral), Earth-Mars flight
Figure 4: TOF for θ_i values of (0°, 120°, 240°, 360°) from left to right in the figure, α_0 values of (-60°, -50°,
-40°, -30°, -20°), $\Delta\theta$ values of (90°, 150°, 210°, 270°, 340°), m =0.05, constant acceleration case of the
thrust profile (Archimedean spiral), Earth-Mars flight, N=1 (a_0 =0.03) and N=2 (a_0 =0.02)26
Figure 5: $V_{\infty,T}$ for θ_i values of (0°, 120°, 240°, 360°) from left to right in the figure, α_0 values of (-60°, -50°, -
40° , -30° , -20°), $\Delta\theta$ values of (90°, 150°, 210°, 270°, 340°), m =0.05, constant acceleration case of the thrust
profile (Archimedean spiral), Earth-Mars flight, N=1 (a_0 =0.03) and N=2 (a_0 =0.02)27
Figure 6: Polar plot for N=1 (a_0 =0.04) and N=2 (a_0 =0.02), θ_i =0°, $\Delta\theta$ =90°, α_0 =-20°, m values of (0.02;
0.64; 1.26; 1.88; 2.5), constant acceleration case (Archimedean spiral), Earth-Mars flight29
Figure 7: α plot for N=1 (a_0 =0.04) and N=2 (a_0 =0.02), θ_i =0°, $\Delta\theta$ =90°, α_0 =-20°, m values of (0.02; 0.64;
1.26; 1.88; 2.5), constant acceleration case (Archimedean spiral), Earth-Mars flight30
Figure 8: $\dot{\theta}$ plot for N=1 ($a_0 = 0.04$) and N=2 ($a_0 = 0.02$), $\theta_i = 0^{\circ}$, $\Delta \theta = 90^{\circ}$, $\alpha_0 = -20^{\circ}$, m values of (0.02; 0.64;
1.26; 1.88; 2.5), constant acceleration case (Archimedean spiral), Earth-Mars flight30
Figure 9: γ plot for N=1 (a_0 =0.04) and N=2 (a_0 =0.02), θ_i =0°, $\Delta\theta$ =90°, α_0 =-20°, m values of (0.02; 0.64;
1.26; 1.88; 2.5), constant acceleration case (Archimedean spiral), Earth-Mars flight31
Figure 10: TOF for θ_i values of (0°, 120°, 240°, 360°) from left to right in the figure, α_0 values of (-60°, -50°,
-40°, -30°, -20°), $\Delta\theta$ values of (90°, 150°, 210°, 270°, 340°) (N=0), m =0.05, $a_{_0}$ =0.08, constant acceleration
case of the thrust profile (logarithmic spiral), Earth-Mars flight
Figure 11: $V_{\infty,T}$ for θ_i values of (0°, 120°, 240°, 360°) from left to right in the figure, α_0 values of (-60°, -50°,
-40°, -30°, -20°), $\Delta\theta$ values of (90°, 150°, 210°, 270°, 340°) (N=0), m =0.05, a_0 =0.08, constant acceleration
case of the thrust profile (logarithmic spiral). Earth-Mars flight 32

Figure 12: TOF for θ_i values of (0°, 120°, 240°, 360°) from left to right in the figure, α_0 values of (-60°, -50°)
-40°, -30°, -20°), $\Delta\theta$ values of (90°, 150°, 210°, 270°, 340°), m =0.05, constant acceleration case of the
thrust profile (logarithmic spiral), Earth-Mars flight, N=1 (a_0 =0.03) and N=2 (a_0 =0.02)3.
Figure 13: $V_{\infty,T}$ for θ_i values of (0°, 120°, 240°, 360°) from left to right in the figure, α_0 values of (-60°, -50°)
-40°, -30°, -20°), $\Delta\theta$ values of (90°, 150°, 210°, 270°, 340°), m =0.05, constant acceleration case of the
thrust profile (logarithmic spiral), Earth-Mars flight, N=1 (a_0 =0.03) and N=2 (a_0 =0.02)33
Figure 14: Polar plot for N=1 and N=2, $\theta_i = 0^{\circ}$, $\Delta \theta = 90^{\circ}$, $\alpha_0 = -20^{\circ}$, $\alpha_0 = 0.03$, m values of (0.05; 0.15; 0.25;
0.35; 0.45), constant acceleration case of the thrust profile (logarithmic spiral), Earth-Mars flight35
Figure 15: α plot for N=1 and N=2, θ_i =0°, $\Delta\theta$ =90°, α_0 =-20°, a_0 =0.03, m values of (0.05; 0.15; 0.25;
0.35; 0.45), constant acceleration case of the thrust profile (logarithmic spiral), Earth-Mars flight36
Figure 16: $\dot{\theta}$ plot for N=1 and N=2, θ_i =0°, $\Delta\theta$ =90°, α_0 =-20°, a_0 =0.03, m values of (0.05; 0.15; 0.25; 0.35)
0.45), constant acceleration case of the thrust profile (logarithmic spiral), Earth-Mars flight30
Figure 17: γ plot for N=1 and N=2, θ_i =0°, $\Delta\theta$ =90°, α_0 =-20°, a_0 =0.03, m values of (0.05; 0.15; 0.25; 0.35)
0.45), constant acceleration case of the thrust profile (logarithmic spiral), Earth-Mars flight
Figure 18: TOF for $\theta_i + \phi$ values of (120°, 200°, 280°, 360°) from left to right in the figure, α_0 values of (-
60°, -50°, -40°, -30°, -20°), $\Delta\theta$ values of (90°, 150°, 210°, 270°, 340°) (N=0), m =0.6, $a_{_0}$ =0.1, constant
acceleration case of the thrust profile (Poinsot's spiral (hyperbolic sine)), Earth-Mars flight33
Figure 19: $V_{\infty,T}$ for $\theta_i + \phi$ values of (120°, 200°, 280°, 360°) from left to right in the figure, α_0 values of (-
60°, -50°, -40°, -30°, -20°), $\Delta\theta$ values of (90°, 150°, 210°, 270°, 340°) (N=0), m =0.6, $a_{_0}$ =0.1, constant
acceleration case of the thrust profile (Poinsot's spiral (hyperbolic sine)), Earth-Mars flight33
Figure 20: TOF for $\theta_i + \phi$ values of (120°, 200°, 280°, 360°) from left to right in the figure, α_0 values of (-
60°, -50°, -40°, -30°, -20°), $\Delta\theta$ values of (90°, 150°, 210°, 270°, 340°), m =0.6, constant acceleration case
(Poinsot's spiral (hyperbolic sine), Earth-Mars flight, N=1 ($a_0 = 0.05$) and N=2 ($a_0 = 0.04$)39
Figure 21: $V_{_{\infty,T}}$ for $\theta_i + \phi$ values of (120°, 200°, 280°, 360°) from left to right in the figure, α_0 values of (-
60°, -50°, -40°, -30°, -20°), $\Delta\theta$ values of (90°, 150°, 210°, 270°, 340°), m =0.6, constant acceleration case
(Poinsot's spiral (hyperbolic sine), Earth-Mars flight, N=1 ($a_0 = 0.05$) and N=2 ($a_0 = 0.04$)40
Figure 22: Polar plot for N=1 (a_0 =0.05) and N=2 (a_0 =0.04), $\theta_i + \phi = 120^\circ$, $\Delta\theta = 90^\circ$, α_0 =-20°, α_0 =0.04, m
values of (0.01; 0.11; 0.21; 0.31; 0.41), constant acceleration case (Poinsot's spiral (hyperbolic sine)),
Earth-Mars flight

Figure 23: α plot for N=1 (a_0 =0.05) and N=2 (a_0 =0.04), θ_i + ϕ =120°, $\Delta\theta$ =90°, α_0 =-20°, a_0 =0.04, m values of (0.01; 0.11; 0.21; 0.31; 0.41), constant acceleration case (Poinsot's spiral (hyperbolic sine)), Earth-Mars flight	42
Figure 24: $\dot{\theta}$ plot for N=1 (a_0 =0.05) and N=2 (a_0 =0.04), θ_i + ϕ =120°, $\Delta\theta$ =90°, α_0 =-20°, a_0 =0.04, m values of (0.01; 0.11; 0.21; 0.31; 0.41), constant acceleration case (Poinsot's spiral (hyperbolic sine)), Earth-Mars flight	43
Figure 25: γ plot for N=1 (a_0 =0.05) and N=2 (a_0 =0.04), θ_i + ϕ =120°, $\Delta\theta$ =90°, α_0 =-20°, a_0 =0.04, m values of (0.01; 0.11; 0.21; 0.31; 0.41), constant acceleration case (Poinsot's spiral (hyperbolic sine)), Earth-Mars flight	43
Figure 26: TOF for θ_i values of (30°, 140°, 250°, 360°) from left to right in the figure, α_0 values of (-60°, -50°, -40°, -30°, -20°), $\Delta\theta$ values of (90°, 150°, 210°, 270°, 340°) (N=0), m=0.05, a_0 =0.07, constant acceleration case (Poinsot's spiral (hyperbolic cosine)), Earth-Mars flight	44
Figure 27: $V_{\infty,T}$ for θ_i values of (30°, 140°, 250°, 360°) from left to right in the figure, α_0 values of (-60°, -50°, -40°, -30°, -20°), $\Delta\theta$ values of (90°, 150°, 210°, 270°, 340°) (N=0), m=0.05, a_0 =0.07, constant acceleration case (Poinsot's spiral (hyperbolic cosine)), Earth-Mars flight	45
Figure 28: TOF for θ_i values of (30°, 140°, 250°, 360°) from left to right in the figure, α_0 values of (-60°, -50°, -40°, -30°, -20°), $\Delta\theta$ values of (90°, 150°, 210°, 270°, 340°), m =0.05, constant acceleration case (Poinsot's spiral (hyperbolic cosine)), Earth-Mars flight, N=1 (α_0 =0.03) and N=2 (α_0 =0.02)	4 <i>6</i>
Figure 29: $V_{\infty,T}$ for θ_i values of (30°, 140°, 250°, 360°) from left to right in the figure, α_0 values of (-60°, -50°, -40°, -30°, -20°), $\Delta\theta$ values of (90°, 150°, 210°, 270°, 340°), m =0.05, constant acceleration case (Poinsot's spiral (hyperbolic cosine)), Earth-Mars flight, N=1 (α_0 =0.03) and N=2 (α_0 =0.02)	46
Figure 30: Polar plot for N=1 (a_0 =0.03) and N=2 (a_0 =0.02), θ_i =30°, $\Delta\theta$ =90°, α_0 =-20°, m values of (0.01 0.11; 0.21; 0.31; 0.41), constant acceleration case (Poinsot's spiral (hyperbolic cosine)), Earth to Mars	
Figure 31: α plot for N=1 (a_0 =0.03) and N=2 (a_0 =0.02), θ_i =30°, $\Delta\theta$ =90°, α_0 =-20°, m values of (0.01; 0.11; 0.21; 0.31; 0.41), constant acceleration case (Poinsot's spiral (hyperbolic cosine)), Earth to Mars	49
Figure 32: $\dot{\theta}$ plot for N=1 (a_0 =0.03) and N=2 (a_0 =0.02), θ_i =30°, $\Delta\theta$ =90°, α_0 =-20°, m values of (0.01; 0.11; 0.21; 0.31; 0.41), constant acceleration case (Poinsot's spiral (hyperbolic cosine)), Earth to Mars	50
Figure 33: γ plot for N=1 (a_0 =0.03) and N=2 (a_0 =0.02), θ_i =30°, $\Delta\theta$ =90°, α_0 =-20°, m values of (0.01; 0.11; 0.21; 0.31; 0.41), constant acceleration case (Poinsot's spiral (hyperbolic cosine)), Earth to Mars	50

Figure 34: TOF for θ_i values of (120°, 200°, 280°, 360°) from left to right in the figure, α_0 values of (-60°, -
50°, -40°, -30°, -20°), $\Delta\theta$ values of (90°, 150°, 210°, 270°, 340°) (N=0), m =0.05, a_0 =0.07, constant
acceleration case (sinusoidal spiral), Earth-Mars flight
Figure 35: $V_{_{\infty,T}}$ for θ_i values of (120°, 200°, 280°, 360°) from left to right in the figure, α_0 values of (-60°, -
50°, -40°, -30°, -20°), $\Delta\theta$ values of (90°, 150°, 210°, 270°, 340°) (N=0), m =0.05, $a_{_0}$ =0.07, constant
acceleration case (sinusoidal spiral), Earth-Mars flight
Figure 36: TOF for θ_i values of (120°, 200°, 280°, 360°) from left to right in the figure, α_0 values of (-60°, -
50°, -40°, -30°, -20°), $\Delta\theta$ values of (90°, 150°, 210°, 270°, 340°), m =0.05, constant acceleration case
(sinusoidal spiral), Earth-Mars flight, N=1 (a_0 =0.02) and N=2 (a_0 =0.02)52
Figure 37: $V_{\infty,T}$ for θ_i values of (120°, 200°, 280°, 360°) from left to right in the figure, α_0 values of (-60°, -
50°, -40°, -30°, -20°), $\Delta\theta$ values of (90°, 150°, 210°, 270°, 340°), m =0.05, constant acceleration case
(sinusoidal spiral), Earth-Mars flight, N=1 (a_0 =0.02) and N=2 (a_0 =0.02)53
Figure 38: Polar plot for N=1 and N=2, $\theta_i = 120^{\circ}$, $\Delta \theta = 90^{\circ}$, $\alpha_0 = -20^{\circ}$, m values for (0.01; 0.055; 0.1; 0.145;
0.19), $a_0 = 0.02$, constant acceleration (sinusoidal spiral), Earth-Mars flight55
Figure 39: α plot for N=1 and N=2, θ_i =120°, $\Delta\theta$ =90°, α_0 =-20°, m values for (0.01; 0.055; 0.1; 0.145;
0.19), $a_0 = 0.02$, constant acceleration (sinusoidal spiral), Earth-Mars flight
Figure 40: $\dot{\theta}$ plot for N=1 and N=2, $\theta_i = 120^\circ$, $\Delta \theta = 90^\circ$, $\alpha_0 = -20^\circ$, m values for (0.01; 0.055; 0.1; 0.145;
0.19), $a_0 = 0.02$, constant acceleration (sinusoidal spiral), Earth-Mars flight
Figure 41: γ plot for N=1 and N=2, θ_i =120°, $\Delta\theta$ =90°, α_0 =-20°, m values for (0.01; 0.055; 0.1; 0.145;
0.19), $a_0 = 0.02$, constant acceleration (sinusoidal spiral), Earth-Mars flight
Figure 42: TOF for k_2 values of (0.1; 0.15; 0.2; 0.25) from left to right in the figure, α_0 values of (20°, 30°,
40°, 50°, 60°), $\Delta\theta$ values of (90°, 150°, 210°, 270°, 340°) (N=0), γ_1 =0°, a_0 =0.05, constant acceleration
case (exponential sinusoid), Earth-Mars flight
Figure 43: $V_{\omega,T}$ for k_2 values of (0.1; 0.15; 0.2; 0.25) from left to right in the figure, α_0 values of (20°, 30°,
40°, 50°, 60°), $\Delta\theta$ values of (90°, 150°, 210°, 270°, 340°) (N=0), γ_1 =0°, a_0 =0.05, constant acceleration
case (exponential sinusoid). Earth-Mars flight

Figure 44: TOF for k_2 values of (0.1; 0.15; 0.2; 0.25) from left to right in the figure, α_0 values of (20°, 30°,
40°, 50°, 60°), $\Delta\theta$ values of (90°, 150°, 210°, 270°, 340°), $\gamma_1 = 0$ °, constant acceleration case (exponential
sinusoid), Earth-Mars flight, N=1 ($a_0 = 0.03$) and N=2 ($a_0 = 0.03$)58
Figure 45: $V_{\infty,T}$ for k_2 values of (0.1; 0.15; 0.2; 0.25) from left to right in the figure, α_0 values of (20°, 30°,
40°, 50°, 60°), $\Delta\theta$ values of (90°, 150°, 210°, 270°, 340°), γ_1 =0°, constant acceleration case (exponential
sinusoid), Earth-Mars flight, N=1 ($a_0 = 0.03$) and N=2 ($a_0 = 0.03$)59
Figure 46: Polar plot for N=1 and N=2, k_2 =0.01, $\Delta\theta$ =90°, α_0 =20°, γ_1 values of (0°; 0.75°; 1.5°; 2.25°; 3°),
a_0 =0.03, constant acceleration case (exponential sinusoid), Earth-Mars flight
Figure 47: α plot for N=1 and N=2, k_2 =0.01, $\Delta\theta$ =90°, α_0 =20°, γ_1 values of (0°; 0.75°; 1.5°; 2.25°; 3°),
a_0 =0.03, constant acceleration case (exponential sinusoid), Earth-Mars flight
Figure 48: $\dot{\theta}$ plot for N=1 and N=2, k_2 =0.01, $\Delta\theta$ =90°, α_0 =20°, γ_1 values of (0°; 0.75°; 1.5°; 2.25°; 3°),
a_0 =0.03, constant acceleration case (exponential sinusoid), Earth-Mars flight
Figure 49: γ plot for N=1 and N=2, k_2 =0.01, $\Delta\theta$ =90°, α_0 =20°, γ_1 values of (0°; 0.75°; 1.5°; 2.25°; 3°),
$a_0 = 0.03$, constant acceleration case (exponential sinusoid), Earth-Mars flight
Figure 50: TOF for k_2 values of (0.05; 0.08; 0.11; 0.14) from left to right in the figure, α_0 values of (20°,
30°, 40°, 50°, 60°), $\Delta\theta$ were (90°, 150°, 210°, 270°, 340°) (N=1), γ_1 =0°, a_0 =0.13, acceleration inversely
square case (exponential sinusoid), Earth-Jupiter flight
Figure 51: $V_{_{\infty,T}}$ for $k_{_2}$ values of (0.05; 0.08; 0.11; 0.14) from left to right in the figure, $\alpha_{_0}$ values of (20°,
$30^{\circ}, 40^{\circ}, 50^{\circ}, 60^{\circ}), \ \Delta\theta \ \ \text{were (90^{\circ}, 150^{\circ}, 210^{\circ}, 270^{\circ}, 340^{\circ}) (N=1)}, \ \gamma_{_{1}}=0^{\circ}, \ a_{_{0}}=0.13, \ \text{acceleration inversely}$
square case (exponential sinusoid), Earth-Jupiter flight
Figure 52: TOF for k_2 values of (0.05; 0.08; 0.11; 0.14) from left to right in the figure, α_0 values of (20°,
30°, 40°, 50°, 60°), $\Delta\theta$ were (90°, 150°, 210°, 270°, 340°), $\gamma_1 = 0$ °, acceleration inversely square case
(exponential sinusoid), Earth-Jupiter flight, for N=2 (a_0 =0.09) and N=3 (a_0 =0.07)60
Figure 53: $V_{_{\!$
30°, 40°, 50°, 60°), $\Delta\theta$ were (90°, 150°, 210°, 270°, 340°), $\gamma_1 = 0$ °, acceleration inversely square case
(exponential sinusoid), Earth-Jupiter flight, for N=2 (a_0 =0.09) and N=3 (a_0 =0.07)60

Figure 54: Polar plot for N=2 (a_0 =0.09) and N=3 (a_0 =0.07), k_2 =0.01, $\Delta\theta$ =90°, α_0 =20°, γ_1 values of (0°;
0.75°; 1.5°; 2.25°; 3°), acceleration inversely square case (exponential sinusoid), Earth-Jupiter flight68
Figure 55: a plot for N=2 (a_0 =0.09) and N=3 (a_0 =0.07), k_2 =0.01, $\Delta\theta$ =90°, α_0 =20°, γ_1 values of (0°;
0.75°; 1.5°; 2.25°; 3°), acceleration inversely square case (exponential sinusoid), Earth-Jupiter flight69
Figure 56: α plot for N=2 (a_0 =0.09) and N=3 (a_0 =0.07), k_2 =0.01, $\Delta\theta$ =90°, α_0 =20°, γ_1 values of (0°;
0.75°; 1.5°; 2.25°; 3°), acceleration inversely square case (exponential sinusoid), Earth-Jupiter flight69
Figure 57: $\dot{\theta}$ plot for N=2 (a_0 =0.09) and N=3 (a_0 =0.07), k_2 =0.01, $\Delta\theta$ =90°, α_0 =20°, γ_1 values of (0°;
0.75°; 1.5°; 2.25°; 3°), acceleration inversely square case (exponential sinusoid), Earth-Jupiter flight70
Figure 58: γ plot for N=2 (a_0 =0.09) and N=3 (a_0 =0.07), k_2 =0.01, $\Delta\theta$ =90°, α_0 =20°, γ_1 values of (0°;
0.75°; 1.5°; 2.25°; 3°), acceleration inversely square case (exponential sinusoid), Earth-Jupiter flight70
Figure 59: TOF for k_2 values of (0.05; 0.08; 0.11; 0.14) from left to right in the figure, γ_1 values of (0°;
0.75° ; 1.5° ; 2.25° ; 3°), $\Delta\theta$ values of (90°, 150°, 210°, 270°, 340°) (N=1), tangential thrust (exponential sinusoid), Earth-Jupiter flight
Figure 60: $V_{_{\!$
0.75° ; 1.5° ; 2.25° ; 3°) and for $\Delta\theta$ values of (90°, 150°, 210°, 270°, 340°) (N=1) when the tangential thrust profile is being applied (exponential sinusoid), Earth-Jupiter flight72
Figure 61: TOF for k_2 values of (0.05; 0.08; 0.11; 0.14) from left to right in the figure, γ_1 values of (0°;
0.75° ; 1.5° ; 2.25° ; 3°), $\Delta\theta$ values of (90°, 150°, 210°, 270°, 340°), tangential thrust, (exponential sinusoid), Earth-Jupiter flight, N=2 and N=373
Figure 62: $V_{\infty,T}$ for k_2 values of (0.05; 0.08; 0.11; 0.14) from left to right in the figure, γ_1 values of (0°;
0.75° ; 1.5° ; 2.25° ; 3°), $\Delta\theta$ values of (90°, 150°, 210°, 270°, 340°), tangential thrust (exponential sinusoid), Earth-Jupiter flight, N=2 and N=373
Figure 63: Polar plot for N=2 and N=3, k_2 =0.01, $\Delta\theta$ =90°, γ_1 values of (0°; 0.75°; 1.5°; 2.25°; 3°), tangential thrust (exponential sinusoid), Earth-Jupiter flight
Figure 64: a plot for N=2 and N=3, k_2 =0.01, $\Delta\theta$ =90°, γ_1 values of (0°; 0.75°; 1.5°; 2.25°; 3°), tangential thrust (exponential sinusoid), Earth-Jupiter flight
Figure 65: α plot for N=2 and N=3, k_2 =0.01, $\Delta\theta$ =90°, γ_1 values of (0°; 0.75°; 1.5°; 2.25°; 3°), tangential thrust (exponential sinusoid), Earth-Jupiter flight
Figure 66: $\dot{\theta}$ plot for N=2 and N=3, k_2 =0.01, $\Delta\theta$ =90°, γ_1 values of (0°; 0.75°; 1.5°; 2.25°; 3°), tangential
thrust (exponential sinusoid). Farth-Juniter flight

Figure 67: TOF for k_2 values of (0.05; 0.08; 0.11; 0.14) from left to right in the figure, α_0 values of (20°,
30°, 40°, 50°, 60°), $\Delta\theta$ values of (90°, 150°, 210°, 270°, 340°) (N=0), γ_1 =0°, a_0 =-0.25, acceleration
inversely square case (exponential sinusoid), Earth-Mercury flight
Figure 68: $V_{\infty,T}$ for k_2 values of (0.05; 0.08; 0.11; 0.14) from left to right in the figure, α_0 values of (20°,
30°, 40°, 50°, 60°), $\Delta\theta$ values of (90°, 150°, 210°, 270°, 340°) (N=0), γ_1 =0°, a_0 =-0.25, acceleration
inversely square case (exponential sinusoid), Earth-Mercury flight
Figure 69: TOF for k_2 values of (0.05; 0.08; 0.11; 0.14) from left to right in the figure, α_0 values of (20°,
30°, 40°, 50°, 60°), $\Delta\theta$ values of (90°, 150°, 210°, 270°, 340°), γ_1 =0°, acceleration inversely square case
(exponential sinusoid), Earth-Mercury flight, N=1 (a_0 =-0.09) and N=2 (a_0 =-0.06)79
Figure 70: $V_{_{\infty,T}}$ for $k_{_2}$ values of (0.05; 0.08; 0.11; 0.14) from left to right in the figure, $\alpha_{_0}$ values of (20°,
30°, 40°, 50°, 60°), $\Delta\theta$ values of (90°, 150°, 210°, 270°, 340°), for γ_1 =0°, acceleration inversely square case
(exponential sinusoid), Earth-Mercury flight, N=1 (a_0 =-0.09) and N=2 (a_0 =-0.06)80
Figure 71: Polar plot for N=1 (a_0 =-0.09) and N=2 (a_0 =-0.06), k_2 =0.01, $\Delta\theta$ =90°, α_0 =20°, γ_1 values of (-
3°;-2.25°;-1.5°;0.75°;0°), acceleration inversely square case (exponential sinusoid), Earth to Mercury82
Figure 72: a plot for N=1 (a_0 =-0.09) and N=2 (a_0 =-0.06), k_2 =0.01, $\Delta\theta$ =90°, α_0 =20°, γ_1 values of (-3°;-
2.25°;-1.5°;0.75°;0°), acceleration inversely square case (exponential sinusoid), Earth to Mercury82
Figure 73: α plot for N=1 (a_0 =-0.09) and N=2 (a_0 =-0.06), k_2 =0.01, $\Delta\theta$ =90°, α_0 =20°, γ_1 values of (-3°;-
2.25°;-1.5°;0.75°;0°), acceleration inversely square case (exponential sinusoid), Earth to Mercury83
Figure 74: $\dot{\theta}$ plot for N=1 (a_0 =-0.09) and N=2 (a_0 =-0.06), k_2 =0.01, $\Delta\theta$ =90°, α_0 =20°, γ_1 values of (-3°;-
2.25°;-1.5°;0.75°;0°), acceleration inversely square case (exponential sinusoid), Earth to Mercury83
Figure 75: γ plot for N=1 (a_0 =-0.09) and N=2 (a_0 =-0.06), k_2 =0.01, $\Delta\theta$ =90°, α_0 =20°, γ_1 values of (-3°;-
2.25°;-1.5°;0.75°;0°), acceleration inversely square case (exponential sinusoid), Earth to Mercury84
Figure 76: TOF for k_2 values of (0.05; 0.08; 0.11; 0.14) from left to right in the figure, γ_1 values of (-3°; -
2.25° ; -1.5° ; -0.75° ; 0°), $\Delta\theta$ values of (90°, 150°, 210°, 270°, 340°) (N=0), tangential thrust (exponential
sinusoid), Earth-Mercury flight85
Figure 77: $V_{\infty,T}$ for k_2 values of (0.05; 0.08; 0.11; 0.14) from left to right in the figure, γ_1 values of (-3°; -
2.25°; -1.5°; -0.75°; 0°), $\Delta\theta$ values of (90°, 150°, 210°, 270°, 340°) (N=0), tangential thrust (exponential
sinusoid), Earth-Mercury flight

Figure 78: TOF for k_2 values of (0.05; 0.08; 0.11; 0.14) from left to right in the figure, γ_1 values of (-3°; -
2.25° ; -1.5° ; -0.75° ; 0°), $\Delta\theta$ values of (90°, 150°, 210°, 270°, 340°), tangential thrust (exponential sinusoid),
Earth-Mercury flight, N=1 and N=286
Figure 79: $V_{\infty,T}$ for k_2 values of (0.05; 0.08; 0.11; 0.14) from left to right in the figure, γ_1 values of (-3°; -
2.25° ; -1.5° ; -0.75° ; 0°), $\Delta\theta$ values of (90°, 150°, 210°, 270°, 340°), tangential thrust (exponential sinusoid),
Earth-Mercury flight, N=1 and N=287
Figure 80: Polar plot for N=1 and N=2, $k_2 = 0.01$, $\Delta \theta = 90^{\circ}$, γ_1 values of (-3°; -2.25°; -1.5°; -0.75°; 0°),
tangential thrust profile (exponential sinusoid), Earth-Mercury flight
Figure 81: <i>a</i> plot for N=1 and N=2, k_2 =0.01, $\Delta\theta$ =90°, γ_1 values of (-3°; -2.25°; -1.5°; -0.75°; 0°), tangential
thrust profile (exponential sinusoid), Earth-Mercury flight
Figure 82: α plot for N=1 and N=2, k_2 =0.01, $\Delta\theta$ =90°, γ_1 values of (-3°; -2.25°; -1.5°; -0.75°; 0°),
tangential thrust profile (exponential sinusoid), Earth-Mercury flight90
Figure 83: $\dot{\theta}$ plot for N=1 and N=2, k_2 =0.01, $\Delta\theta$ =90°, γ_1 values of (-3°; -2.25°; -1.5°; -0.75°; 0°), tangential
thrust profile (exponential sinusoid), Earth-Mercury flight
Figure 84: Pareto fronts for the number of individuals of the population: 25 000, 50 000, 75 000 and98
Figure 85: Pareto fronts for the number of individuals of the population: 25 000, 50 000, 75 000 and99
Figure 86: Pareto fronts for the Archimedean spiral, logarithmic spiral, Poinsot's spiral (hyperbolic sine),
Poinsot's spiral (hyperbolic cosine), sinusoidal spiral and exponential sinusoid, tangential thrust, Earth-
Jupiter flight
Figure 87: Pareto fronts for the Archimedean spiral, logarithmic spiral, Poinsot's spiral (hyperbolic sine),
Poinsot's spiral (hyperbolic cosine), sinusoidal spiral and exponential sinusoid, tangential thrust, Earth-
Jupiter flight
Figure 88: Pareto fronts for the sinusoidal spiral, for the entire population (on the right) and only for
individuals in the population that respect the condition (8.7) (the three cases), tangential thrust, Earth-
Jupiter flight
Figure 89: Pareto fronts for the exponential sinusoid, for the entire population (on the right) and only for
individuals in the population that respect the condition (8.7) (the three cases), tangential thrust, Earth-
Jupiter flight

List of Tables

Table 1: The excess velocities and the TOF values for N=1, θ_i =0°, $\Delta\theta$ =90°, α_0 =-20°, for α_0 =0.04, m values
of (0.02; 0.64; 1.26; 1.88; 2.5), constant acceleration case (Archimedean spiral), Earth to Mars28
Table 2: The excess velocities and the TOF values for N=2, $\theta_i = 0^{\circ}$, $\Delta\theta = 90^{\circ}$, $\alpha_0 = -20^{\circ}$, $a_0 = 0.03$, m values of
(0.02; 0.64; 1.26; 1.88; 2.5), constant acceleration case (Archimedean spiral), Earth to Mars29
Table 3: The excess velocities and the TOF values for N=1, θ_i =0°, $\Delta\theta$ =90°, α_0 =-20°, α_0 =0.03, m values of
(0.05; 0.15; 0.25; 0.35; 0.45), constant acceleration case (logarithmic spiral), Earth-Mars flight34
Table 4: The excess velocities and the TOF values for N=2, θ_i =0°, $\Delta\theta$ =90°, α_0 =-20°, α_0 =0.03, m values of
(0.05; 0.15; 0.25; 0.35; 0.45), constant acceleration case (logarithmic spiral), Earth-Mars flight35
Table 5: The excess velocities and the TOF values for N=1, $\theta_i + \phi = 120^\circ$, $\Delta\theta = 90^\circ$, $\alpha_0 = -20^\circ$, $\alpha_0 = 0.05$, m
values of (0.01; 0.11; 0.21; 0.31; 0.41), constant acceleration case (Poinsot's spiral (hyperbolic sine), Earth-Mars flight
Table 6: The excess velocities and the TOF values for N=2, $\theta_i + \phi = 120^\circ$, $\Delta\theta = 90^\circ$, $\alpha_0 = -20^\circ$, $\alpha_0 = 0.04$, m
values of (0.01; 0.11; 0.21; 0.31; 0.41), constant acceleration case (Poinsot's spiral (hyperbolic sine), Earth-
Mars flight41
Table 7: The excess velocities and the TOF values for N=1, θ_i =30°, $\Delta\theta$ =90°, α_0 =-20°, m values of (0.01;
0.11; 0.21; 0.31; 0.41), $a_0 = 0.03$, constant acceleration case of the thrust profile (Poinsot's spiral
(hyperbolic cosine)), Earth-Mars flight
Table 8: The excess velocities and the TOF values for N=2, θ_i =30°, $\Delta\theta$ =90°, α_0 =-20°, m values of (0.01;
0.11; 0.21; 0.31; 0.41), $a_0 = 0.02$, constant acceleration case of the thrust profile (Poinsot's spiral
(hyperbolic cosine)), Earth-Mars flight
Table 9: The excess velocities and the TOF values for N=1, θ_i =120°, $\Delta\theta$ =90°, α_0 =-20°, m values for (0.01;
0.055; 0.1; 0.145; 0.19), $a_0 = 0.02$, constant acceleration case (sinusoidal spiral), Earth-Mars flight54
Table 10: The excess velocities and the TOF values for N=2, θ_i =120°, $\Delta\theta$ =90°, α_0 =-20°, m values for
$(0.01; 0.055; 0.1; 0.145; 0.19), a_0 = 0.02$, constant acceleration case (sinusoidal spiral), Earth-Mars flight.54
Table 11: The excess velocities and the TOF values for N=1, k_2 =0.01, $\Delta\theta$ =90°, α_0 =20°, γ_1 values of (0°;
0.75° ; 1.5° ; 2.25° ; 3°), $a_{0} = 0.03$, constant acceleration case (exponential sinusoid), Earth-Mars flight60

Table 12: The excess velocities and the TOF values for N=2, k_2 =0.01, $\Delta\theta$ =90°, α_0 =20°, γ_1 values of (0°;
0.75° ; 1.5° ; 2.25° ; 3°), a_{0} =0.03, constant acceleration case (exponential sinusoid), Earth-Mars flight60
Table 13: The excess velocities and the TOF values for N=2, k_2 =0.01, $\Delta\theta$ =90°, α_0 =20°, γ_1 values of (0°;
0.75° ; 1.5° ; 2.25° ; 3°), $a_{_0}$ =0.09, acceleration inversely square case (exponential sinusoid), Earth-Jupiter
flight66
Table 14: The excess velocities and the TOF values for N=3, k_2 =0.01, $\Delta\theta$ =90°, α_0 =20°, γ_1 values of (0°;
0.75° ; 1.5° ; 2.25° ; 3°), a_{0} =0.07, acceleration inversely square case (exponential sinusoid), Earth-Jupiter
flight
Table 15: Excess velocities and TOF values for N=2, k_2 =0.01, $\Delta\theta$ =90°, γ_1 values of (0°; 0.75°; 1.5°; 2.25°;
3°), tangential thrust (exponential sinusoid), Earth-Jupiter flight
Table 16: Excess velocities and TOF values for N=3, k_2 =0.01, $\Delta\theta$ =90°, γ_1 values of (0°; 0.75°; 1.5°; 2.25°;
3°), tangential thrust (exponential sinusoid), Earth-Jupiter flight
Table 17: The excess velocities and the TOF values for N=1, k_2 =0.01, $\Delta\theta$ =90°, α_0 =20°, γ_1 values of (-3°;
2.25° ; -1.5° ; 0.75° ; 0°), $a_{\scriptscriptstyle 0}$ =-0.09, acceleration inversely square case (exponential sinusoid), Earth-Mercury
flight8
Table 18: The excess velocities and the TOF values for N=2, k_2 =0.01, $\Delta\theta$ =90°, α_0 =20°, γ_1 values of (-3°;
2.25° ; -1.5° ; 0.75° ; 0°), $a_{\scriptscriptstyle 0}$ =-0.06, acceleration inversely square case (exponential sinusoid), Earth-Mercury
flight8
Table 19: Excess velocities and TOF values for N=1, k_2 =0.01, $\Delta\theta$ =90°, γ_1 values of (-3°; -2.25°; -1.5°; -
0.75°; 0°), tangential thrust (exponential sinusoid), Earth-Mercury flight
Table 20: Excess velocities and TOF values for N=2, k_2 =0.01, $\Delta\theta$ =90°, γ_1 values of (-3°; -2.25°; -1.5°; -
0.75°; 0°), tangential thrust profile (exponential sinusoid), Earth-Mercury flight88
Table 21: Variation between the values given in Low2D and the 'test' program for the position and velocity
at the target planet, Earth-Mars flight, $\Delta\theta = 90^{\circ}$, N=1, acceleration inversely square case
Table 22: Variation between the values given in Low2D and the 'test' program for the position and velocity
at the target planet, Earth-Jupiter flight, $\Delta\theta$ =90°, N=1, acceleration inversely square case
Table 23: Variation between the values given in Low2D and the 'test' program for the position and velocity
at the target planet, Earth-Mercury flight, $\Delta\theta$ =90°, N=1, acceleration inversely square case
Table 24: Variation between the values given in Low2D and the 'test' program for the position and velocity at the target planet, Earth-Mars flight, $\Delta \theta = 90^{\circ}$, N=1, constant acceleration case
at the target pranet. Darm-Iviars ingul. $\Delta r = 70$. $N=1$. Constant acceleration case

Table 25: Variation between the values given in Low2D and the 'test' program for the position and velocity at the target planet, Earth to Jupiter, $\Delta\theta = 90^{\circ}$, N=1, constant acceleration case94
Table 26: Variation between the values given in Low2D and the 'test' program for the position and velocity at the target planet, Earth to Mercury, $\Delta\theta$ =90°, N=1, constant acceleration case94
Table 27: Variation between the values given in Low2D and the 'test' program for the position and velocity at the target planet, Earth-Mars flight, $\Delta\theta$ =90°, N=1, tangential case94
Table 28: Variation between the values given in Low2D and the 'test' program for the position and velocity at the target planet, Earth-Jupiter flight, $\Delta\theta$ =90°, N=1, tangential case94
Table 29: Variation between the values given in Low2D and the 'test' program for the position and velocity at the target planet, Earth-Mercury flight, $\Delta\theta$ =90°, N=1, tangential case
Table 30: Test scenario for STA
Table 31: Values for the excess velocities and the fuel mass consumption using STA and JAQAR, for the test scenario in table 30
Table 32: Computation time, number of individuals in the Pareto front ($N_{_{Pf}}$) and the percentage of
individuals in the Pareto front G_{pf} and in the population G_{pop} that respect the maximum value for the ratio
between the required thrust acceleration of the spacecraft and the available one for the 6 shapes and for the
3 cases of $a_1 = a_2 = \left[\frac{2}{3}\right]$ in an Earth-Jupiter flight (tangential case)

Appendix A: Derivation of Equations

1. Derivation of the equation:
$$\dot{\theta}^2 = \left(\frac{\mu}{r^3}\right) \frac{a_0 \cos \alpha \tan \gamma - a_0 \sin \alpha + 1}{\tan^2 \gamma + k_1 k_2^2 s + 1}$$

First the derivatives in equations (5.6) are substituted in the first equation of motion represented in (5.5):

$$r(\ddot{\theta}(q+k_1k_2c)+\dot{\theta}^2(q+k_1k_2c)^2-\dot{\theta}^2k_1k_2^2s)-r\dot{\theta}^2+\frac{\mu}{r^2}=a\sin\alpha$$
(A.1)

The second equation of motion in (5.5) is used to eliminate $\ddot{\theta}$ from equation (A.1) and $(q+k_1k_2c)$ is substitute by $\tan \gamma$ (equation (5.7)):

$$(a\cos\alpha - 2\dot{r}\dot{\theta})\tan\gamma + r(\dot{\theta}^2\tan^2\gamma - \dot{\theta}^2k_1k_2^2s) - r\dot{\theta}^2 + \frac{\mu}{r^2} = a\sin\alpha \Leftrightarrow$$

$$(a\cos\alpha - 2\dot{r}\dot{\theta}^2\tan\gamma)\tan\gamma + r(\dot{\theta}^2\tan^2\gamma - \dot{\theta}^2k_1k_2^2s) - r\dot{\theta}^2 + \frac{\mu}{r^2} = a\sin\alpha \Leftrightarrow$$

$$r\dot{\theta}^2(-2\tan^2\gamma + \tan^2\gamma - k_1k_2^2s - 1) = a\sin\alpha - a\cos\alpha\tan\gamma - \frac{\mu}{r^2} \Leftrightarrow$$

$$\frac{r^3}{\mu}\dot{\theta}^2(\tan^2\gamma + k_1k_2^2s + 1) = \frac{r^2}{\mu}(a\cos\alpha\tan\gamma - a\sin\alpha + 1)$$
(A.2)

In the following step, the thrust acceleration a is replaced by the parameter a_0 according to equation (5.9). Passing all the terms in left hand-side to the right hand-side except $\dot{\theta}^2$, equation (5.8) is obtained.

Note that for the tangential thrusting case: $\alpha = \gamma + n\pi$, with n = 0,1 and consequently $a\cos\alpha\tan\gamma = a\sin\alpha$.

2. Derivation of the equation:

$$\dot{\alpha} = \left[\left(\tan \gamma \dot{\theta}^2 r^3 / \mu - 2a_0 \cos \alpha \right) \left(\tan^2 \gamma + k_1 k_2^2 s + 1 \right)^2 - \right. \\
\left. - \left(a_0 \cos \alpha \tan \gamma - a_0 \sin \alpha + 1 \right) \left(k_1 k_2^3 c - 2 \tan \gamma k_1 k_2^2 s \right) \right. \\
\left. - a_0 k_1 k_2^2 s \cos \alpha \left(\tan^2 \gamma + k_1 k_2^2 s + 1 \right) \right] \dot{\theta} / \left[\left(a_0 \sin \alpha \tan \gamma + a_0 \cos \alpha \right) \left(\tan^2 \gamma + k_1 k_2^2 s + 1 \right) \right]$$

Equation (5.8) can be written as:

$$\dot{\theta}^2 \left(\tan^2 \gamma + k_1 k_2^2 s + 1 \right) = \frac{\mu}{r^3} \left(a_0 \cos \alpha \tan \gamma - a_0 \sin \alpha + 1 \right)$$

Taking the derivative of equation (5.8) in both right and left sides:

$$\frac{d}{dt} \left[\dot{\theta}^{2} \left(\tan^{2} \gamma + k_{1} k_{2}^{2} s + 1 \right) \right] = \frac{d}{dt} \left[\frac{\mu}{r^{3}} \left(a_{0} \cos \alpha \tan \gamma - a_{0} \sin \alpha + 1 \right) \right] \Leftrightarrow
2 \ddot{\theta} \dot{\theta} \left(\tan^{2} \gamma + k_{1} k_{2}^{2} s + 1 \right) + \dot{\theta}^{3} \left(-2k_{1} k_{2}^{2} s \tan \gamma + k_{1} k_{2}^{3} c \right) = -3 \frac{\mu \dot{r}}{r^{4}} \left(a_{0} \cos \alpha \tan \gamma - a_{0} \sin \alpha + 1 \right) +
+ \frac{a_{0} \mu}{r^{3}} \left(-\dot{\alpha} \sin \alpha \tan \gamma - \dot{\theta} k_{1} k_{2}^{2} s \cos \alpha - \dot{\alpha} \cos \alpha \right) \Leftrightarrow
\dot{\theta} \left(2 \ddot{\theta} \frac{r^{3}}{\mu} \left(\tan^{2} \gamma + k_{1} k_{2}^{2} s + 1 \right) + \dot{\theta}^{2} \frac{r^{3}}{\mu} \left(-2k_{1} k_{2}^{2} s \tan \gamma + k_{1} k_{2}^{3} c \right) +
+ 3 \tan \gamma \left(a_{0} \cos \alpha \tan \gamma - a_{0} \sin \alpha + 1 \right) + a_{0} k_{1} k_{2}^{2} s \cos \alpha \right) = -\dot{\alpha} a_{0} \left(\sin \alpha \tan \gamma + \cos \alpha \right)$$
(A.3)

Substituting the second equation of (5.5) in (A.3) in order to eliminate $\ddot{\theta}$:

$$\frac{\dot{\theta}\left(2\left(a\cos\alpha-2r\dot{\theta}^{2}\tan\gamma\right)\frac{r^{2}}{\mu}\left(\tan^{2}\gamma+k_{1}k_{2}^{2}s+1\right)+\dot{\theta}^{2}\frac{r^{3}}{\mu}\left(-2k_{1}k_{2}^{2}s\tan\gamma+k_{1}k_{2}^{3}c\right)+\right. \\
\left.+3\tan\gamma\left(a_{0}\cos\alpha\tan\gamma-a_{0}\sin\alpha+1\right)+a_{0}k_{1}k_{2}^{2}s\cos\alpha\right)=-\dot{\alpha}a_{0}\left(\sin\alpha\tan\gamma+\cos\alpha\right) \Leftrightarrow \\
\dot{\theta}\left(\left(2a_{0}\cos\alpha-4\tan\gamma\dot{\theta}^{2}\frac{r^{3}}{\mu}\right)\left(\tan^{2}\gamma+k_{1}k_{2}^{2}s+1\right)+\dot{\theta}^{2}\frac{r^{3}}{\mu}\left(-2k_{1}k_{2}^{2}s\tan\gamma+k_{1}k_{2}^{3}c\right)+\right. \\
\left.+3\tan\gamma\dot{\theta}^{2}\frac{r^{3}}{\mu}\left(\tan^{2}\gamma+k_{1}k_{2}^{2}s+1\right)+a_{0}k_{1}k_{2}^{2}s\cos\alpha\right)=-\dot{\alpha}a_{0}\left(\sin\alpha\tan\gamma+\cos\alpha\right) \Leftrightarrow \\
\dot{\theta}\left(\left(-2a_{0}\cos\alpha+\tan\gamma\dot{\theta}^{2}\frac{r^{3}}{\mu}\right)\left(\tan^{2}\gamma+k_{1}k_{2}^{2}s+1\right)+\dot{\theta}^{2}\frac{r^{3}}{\mu}\left(-2k_{1}k_{2}^{2}s\tan\gamma+k_{1}k_{2}^{3}c\right)-\right. \\
\left.-a_{0}k_{1}k_{2}^{2}s\cos\alpha\right)=\dot{\alpha}a_{0}\left(\sin\alpha\tan\gamma+\cos\alpha\right)$$

Finally, multiplying both right and left parts of equation (A.4) by $(\tan^2 \gamma + k_1 k_2^2 s + 1)$, the equation (5.11) is obtained.

3. Derivation of the equation:

$$a_0 = \frac{(-1)^n \tan \gamma}{2 \cos \gamma} \left[\frac{1}{\tan^2 \gamma + k_1 k_2^2 s + 1} - \frac{k_2^2 (1 - 2k_1 s)}{\left(\tan^2 \gamma + k_1 k_2^2 s + 1\right)^2} \right]$$

Equations of motion (5.5) are added, yielding:

$$\ddot{r} - r\dot{\theta}^{2} + \frac{\mu}{r^{2}} + 2\dot{r}\dot{\theta} + r\ddot{\theta} = a\left(\cos\alpha + \sin\alpha\right) \Leftrightarrow$$

$$r\left(\ddot{\theta}\tan\gamma + \dot{\theta}^{2}\tan^{2}\gamma - \dot{\theta}^{2}k_{1}k_{2}^{2}s - \dot{\theta}^{2} + 2\dot{\theta}^{2}\tan\gamma + \ddot{\theta}\right) + \frac{\mu}{r^{2}} = a\left(\cos\alpha + \sin\alpha\right) \Leftrightarrow$$

$$r\left(\ddot{\theta}\left(\tan\gamma + 1\right) + \dot{\theta}^{2}\left(2\tan^{2}\gamma + 2\tan\gamma - \tan^{2}\gamma - k_{1}k_{2}^{2}s - 1\right) - \dot{\theta}^{2}k_{1}k_{2}^{2}s\right) +$$

$$+ \frac{\mu}{r^{2}} = a\left(\cos\alpha + \sin\alpha\right) \Leftrightarrow$$

$$r\left(\ddot{\theta}\left(\tan\gamma + 1\right) + \dot{\theta}^{2}\left(2\tan^{2}\gamma + 2\tan\gamma\right) - \dot{\theta}^{2}\left(\tan^{2}\gamma + k_{1}k_{2}^{2}s + 1\right)\right) + \frac{\mu}{r^{2}} = a\left(\cos\alpha + \sin\alpha\right)$$

$$r\left(\ddot{\theta}\left(\tan\gamma + 1\right) + \dot{\theta}^{2}\left(2\tan^{2}\gamma + 2\tan\gamma\right) - \dot{\theta}^{2}\left(\tan^{2}\gamma + k_{1}k_{2}^{2}s + 1\right)\right) + \frac{\mu}{r^{2}} = a\left(\cos\alpha + \sin\alpha\right)$$

Substituting equation (5.13) in this last step and dividing it by $\cos \gamma$, the expression for the thrust acceleration magnitude is given by:

$$a = \frac{r}{\cos \gamma} \left(\ddot{\theta} + 2\dot{\theta}^2 \tan \gamma \right) \tag{A.6}$$

Now, an expression for $\ddot{\theta}$ must be computed differentiating equation (5.13) with respect to time:

$$\frac{d}{dt} \left(\dot{\theta}^2 \left(\tan^2 \gamma + k_1 k_2^2 s + 1 \right) \right) = \frac{d}{dt} \left(\frac{\mu}{r^3} \right) \Leftrightarrow
2 \ddot{\theta} \dot{\theta} \left(\tan^2 \gamma + k_1 k_2^2 s + 1 \right) + \dot{\theta}^3 \left(-2k_1 k_2^2 s \tan \gamma + k_1 k_2^3 c \right) = -\frac{3\dot{r}\mu}{r^4}$$
(A.7)

Isolating $\ddot{\theta}$ term, the equation (A.7) yields:

$$\ddot{\theta} = \frac{-3\tan\gamma\mu/r^3 - \dot{\theta}^2 \left(-2k_1k_2^2 s \tan\gamma + k_1k_2^3 c\right)}{2\left(\tan^2\gamma + k_1k_2^2 s + 1\right)}$$
(A.8)

Substituting this last equation (A.8) in equation (A.6), the thrust acceleration is given by:

$$a = \frac{r}{\cos \gamma} \left[\frac{\mu \tan \gamma}{2r^{3} \left(\tan^{2} \gamma + k_{1} k_{2}^{2} s + 1 \right)} \left(-3 + \frac{2k_{1} k_{2}^{2} s - k_{2}^{2}}{\left(\tan^{2} \gamma + k_{1} k_{2}^{2} s + 1 \right)} \right) + \frac{2\mu \tan \gamma}{r^{3} \left(\tan^{2} \gamma + k_{1} k_{2}^{2} s + 1 \right)} \right]$$

$$a = \frac{r\mu \tan \gamma}{\cos \gamma r^{3}} \left(\frac{-3/2 + 2}{\left(\tan^{2} \gamma + k_{1} k_{2}^{2} s + 1 \right)} + \frac{2k_{1} k_{2}^{2} s - k_{2}^{2}}{2\left(\tan^{2} \gamma + k_{1} k_{2}^{2} s + 1 \right)^{2}} \right) \Leftrightarrow$$

$$a = \frac{\mu \tan \gamma}{2 \cos \gamma r^{2}} \left(\frac{1}{\left(\tan^{2} \gamma + k_{1} k_{2}^{2} s + 1 \right)} - \frac{k_{2}^{2} \left(1 - 2k_{1} s \right)}{\left(\tan^{2} \gamma + k_{1} k_{2}^{2} s + 1 \right)^{2}} \right)$$

$$(A.9)$$

To obtain the normalised thrust acceleration a_0 , the left side of equation (A.9), a should be substituted by equation (5.9) to finally obtain equation (5.14). Note that only the situation where the thrust vector is along the velocity vector was considered in equation (A.9).

4. Derivation of the conditions:

$$k_2^2 \le \frac{\tan^2 \gamma - 2k_{12s} \ln(r_{\min}/r_B)}{\left(\ln(r_{\min}/r_B)\right)^2}$$
 and $k_2^2 \le \frac{\tan^2 \gamma + 2k_{12s} \ln(r_B/r_{\max})}{\left(\ln(r_B/r_{\max})\right)^2}$

Note that the quantity k_{12s} is given by:

$$k_{12s} = k_1 k_2^2 s (A.10)$$

Using the trigonometry identity: $\sin^2 \theta + \cos^2 \theta = 1$ and equation (5.7), equation (A.10) can be rewritten as:

$$k_1^2 k_2^4 - k_2^2 \tan^2 \gamma - k_{12s}^2 = 0 \iff k_2^2 = \frac{\tan^2 \gamma + k_1^2 k_2^2 s^2}{k_1^2}$$
(A.11)

The geometric parameter k_1 can be rewritten through the variables $r_{\min} = k_0 e^{-k_1}$ and $r_B = k_0 e^{k_1 s}$, that are given by equation (5.3):

$$k_{1} = -\left(k_{1}s + \ln\left(\frac{r_{\min}}{r_{B}}\right)\right) \tag{A.12}$$

To obtain the condition given in (5.17), equation (A.12) is substituted in the denominator of equation (A.11). A similar reasoning is applied to obtain the condition (5.18), using $r_{\text{max}} = k_0 e^{k_1}$, instead of r_{min} .

5. Derivation of the equation:
$$k_1^2 = \left(\frac{\ln\left(r_1/r_2\right) + \left(\tan\gamma_1/k_2\right)\sin\left(k_2\theta_f\right)}{1 - \cos\left(k_2\theta_f\right)}\right)^2 + \frac{\tan^2\gamma_1}{k_2^2}$$

Using the two equations of motion in (5.29) and considering $\theta_i = 0^{\circ}$, the following relation can be derived:

$$\frac{r_1}{r_2} = \exp\left(\frac{k_1 \sin \phi}{k_1 \sin(k_2 \theta_2 + \phi)}\right) \Leftrightarrow \ln(r_1/r_2) = k_1 \left(\sin \phi - \sin(k_2 \theta_f + \phi)\right) \tag{A.13}$$

Using the addition theorem: $\sin(\beta_1 + \beta_2) = \sin(\beta_1)\cos(\beta_2) + \cos(\beta_1)\sin(\beta_2)$, equation (A.13) can be rewritten as:

$$\ln(r_1/r_2) = k_1 \left(\sin \phi - \left(\sin \left(k_2 \theta_f \right) \cos \phi + \sin \phi \cos \left(k_2 \theta_f \right) \right) \right) \Leftrightarrow$$

$$\ln(r_1/r_2) = k_1 \sin \phi - \sin \left(k_2 \theta_f \right) \tan \gamma_1/k_2 - k_1 \sin \phi \cos \left(k_2 \theta_f \right) \Leftrightarrow$$

$$k_1 \sin \phi = \frac{\ln(r_1/r_2) + \sin(k_2 \theta_f) \tan \gamma_1/k_2}{1 - \cos(k_2 \theta_f)}$$
(A.14)

The left side of equation (A.14) can be rewritten as:

$$k_1 \sin \phi = k_1 \sqrt{1 - \cos^2 \phi} = k_1 \sqrt{1 - \tan^2 \gamma_1 / (k_1 k_2)^2} = \frac{k_1}{|k_1|} \sqrt{k_1^2 - \tan^2 \gamma_1 / k_2^2}$$
(A.15)

Substituting equation (A.15) in equation (A.14) and squaring both, right and left sides of the last equation in (A.14), the geometric parameter k_1 can be computed:

$$\left(\operatorname{sign}(k_{1})\sqrt{k_{1}^{2}-\tan^{2}\gamma_{1}/k_{2}^{2}}\right)^{2} = \left(\frac{\ln(r_{1}/r_{2})+\sin(k_{2}\theta_{f})\tan\gamma_{1}/k_{2}}{1-\cos(k_{2}\theta_{f})}\right)^{2} \Leftrightarrow k_{1}^{2}-\tan^{2}\gamma_{1}/k_{2}^{2} = \left(\frac{\ln(r_{1}/r_{2})+\sin(k_{2}\theta_{f})\tan\gamma_{1}/k_{2}}{1-\cos(k_{2}\theta_{f})}\right)^{2} \Leftrightarrow k_{1}^{2} = \left(\frac{\ln(r_{1}/r_{2})+(\tan\gamma_{1}/k_{2})\sin(k_{2}\theta_{f})}{1-\cos(k_{2}\theta_{f})}\right)^{2} + \frac{\tan^{2}\gamma_{1}}{k_{2}^{2}}$$
(A.16)

Note that the sign of the geometric parameter k_1 is the same as the right side of the last equation in (A.14).

6. Derivation of the condition: $\tan \gamma_1 \in (\tan \gamma_{1,m}, \tan \gamma_{1,m})$,

with
$$\tan \gamma_{l_{m,M}} = \frac{k_2}{2} \left[-\ln \left(\frac{r_1}{r_2} \right) \cot \frac{k_2 \theta_f}{2} \pm \sqrt{\Delta} \right]$$
 and $\Delta = \frac{2 \left(1 - \cos k_2 \theta_f \right)}{k_2^4} - \ln^2 \left(\frac{r_1}{r_2} \right)$

The constraint condition given in (5.34) can be rewritten as:

$$k_{1}^{2}k_{2}^{4} < 1 \Leftrightarrow \left(\frac{\ln\left(r_{1}/r_{2}\right) + \left(\tan\gamma_{1}/k_{2}\right)\sin\left(k_{2}\theta_{f}\right)}{1 - \cos\left(k_{2}\theta_{f}\right)} \right)^{2} + \frac{\tan^{2}\gamma_{1}}{k_{2}^{2}} k_{2}^{4} < 1 \Leftrightarrow \left(k_{2}^{2}\ln\left(r_{1}/r_{2}\right) + k_{2}\tan\gamma_{1}\sin\left(k_{2}\theta_{f}\right) \right)^{2} + k_{2}^{2}\tan^{2}\gamma_{1} - \left(1 - \cos\left(k_{2}\theta_{f}\right)\right)^{2} < 0$$
(A.17)

After some algebraic manipulation, the last condition introduced in (A.17) can be written as:

$$2k_{2}^{2}\left(1-\cos\left(k_{2}\theta_{f}\right)\right)\tan^{2}\gamma_{1}+2k_{2}^{3}\ln\left(\frac{r_{1}}{r_{2}}\right)\sin\left(k_{2}\theta_{f}\right)\tan\gamma_{1}+\\+k_{2}^{4}\ln^{2}\left(\frac{r_{1}}{r_{2}}\right)-\left(1-\cos\left(k_{2}\theta_{f}\right)\right)^{2}<0$$
(A.18)

Solving this quadratic equation in $\tan \gamma_1$ through the formula:

$$\tan \gamma_1 = \frac{-b \pm \sqrt{\Delta^*}}{2a}$$
 and $\Delta^* = c^2 - 4ac$, where:

$$a = 2k_2^2 \left(1 - \cos\left(k_2 \theta_f\right) \right)$$

$$b = 2k_2^3 \ln\left(\frac{r_1}{r_2}\right) \sin\left(k_2 \theta_f\right)$$

$$c = k_2^4 \ln^2\left(\frac{r_1}{r_2}\right) - \left(1 - \cos\left(k_2 \theta_f\right)\right)^2$$

In this way, Δ^* can be derived:

$$\Delta^{*} = 4k_{2}^{6} \ln^{2} \left(\frac{r_{1}}{r_{2}} \right) \left(1 - \cos^{2} \left(k_{2} \theta_{f} \right) \right) - 8k_{2}^{2} \left(1 - \cos \left(k_{2} \theta_{f} \right) \right) \left(k_{2}^{4} \ln^{2} \left(\frac{r_{1}}{r_{2}} \right) - \left(1 - \cos \left(k_{2} \theta_{f} \right) \right)^{2} \right) \Leftrightarrow$$

$$\Delta^{*} = 4k_{2}^{6} \left(1 - \cos \left(k_{2} \theta_{f} \right) \right) \left(\ln^{2} \left(\frac{r_{1}}{r_{2}} \right) \left(1 + \cos \left(k_{2} \theta_{f} \right) \right) - 2 \ln^{2} \left(\frac{r_{1}}{r_{2}} \right) + \frac{2}{k_{2}^{4}} \left(1 - \cos \left(k_{2} \theta_{f} \right) \right)^{2} \right) \Leftrightarrow$$

$$\Delta^{*} = 4k_{2}^{6} \left(1 - \cos \left(k_{2} \theta_{f} \right) \right)^{2} \left(\frac{2}{k_{2}^{4}} \left(1 - \cos \left(k_{2} \theta_{f} \right) \right) - \ln^{2} \left(\frac{r_{1}}{r_{2}} \right) \right)$$

$$\Delta^{*} = 4k_{2}^{6} \left(1 - \cos \left(k_{2} \theta_{f} \right) \right)^{2} \left(\frac{2}{k_{2}^{4}} \left(1 - \cos \left(k_{2} \theta_{f} \right) \right) - \ln^{2} \left(\frac{r_{1}}{r_{2}} \right) \right)$$

Note that $\Delta = \frac{2}{k_2^4} \left(1 - \cos\left(k_2 \theta_f\right) \right) - \ln^2\left(\frac{r_1}{r_2}\right)$ in equation (A.19). Finally, $\tan \gamma_1$ can be computed through:

$$\tan \gamma_{m,M} = -\frac{k_2}{2} \left(\frac{\ln(r_1/r_2)\sin(k_2\theta_f)}{1 - \cos(k_2\theta_f)} \mp \sqrt{\Delta} \right) \Leftrightarrow$$

$$\tan \gamma_{m,M} = -\frac{k_2}{2} \left(\frac{\ln(r_1/r_2)(1 + \cos(k_2\theta_f))}{\sin(k_2\theta_f)} \mp \sqrt{\Delta} \right) \Leftrightarrow$$

$$\tan \gamma_{m,M} = -\frac{k_2}{2} \left(\frac{\ln(r_1/r_2)(1 + \cos^2(k_2\theta_f/2) - \sin^2(k_2\theta_f/2))}{2\sin(k_2\theta_f/2)\cos(k_2\theta_f/2)} \mp \sqrt{\Delta} \right) \Leftrightarrow$$

$$\tan \gamma_{m,M} = -\frac{k_2}{2} \left(\ln(r_1/r_2)\cot(k_2\theta_f/2) \mp \sqrt{\Delta} \right)$$

$$\tan \gamma_{m,M} = -\frac{k_2}{2} \left(\ln(r_1/r_2)\cot(k_2\theta_f/2) \mp \sqrt{\Delta} \right)$$

Appendix B: Equations of the Shapes

In this appendix, the equations for the dynamic parameters for each one of the 6 shapes: Archimedean spiral, the logarithmic spiral, the Poinsot's spiral (hyperbolic sine and cosine expressions), the sinusoidal spiral and the exponential sinusoid will be presented. The equations for the dynamic parameters are given for the 3 cases of the thrust profile.

1. Archimedean spiral

The radius equation for the Archimedean spiral is given by equation (6.2):

$$r = \left(k_0 \theta + k_1\right)^{1/m}$$

The radial velocity and acceleration and the flight path angle for the Archimedean spiral are given by:

$$\dot{r} = (1/m)k_0\dot{\theta}r(k_0\theta + k_1)^{-1} \tag{B.1}$$

$$\tan \gamma = \frac{\dot{r}}{r\dot{\theta}} = (1/m)k_0 \left(k_0 \theta + k_1\right)^{-1} \tag{B.2}$$

$$\ddot{r} = (1/m)k_0(k_0\theta + k_1)^{-1}(\ddot{\theta}r + \dot{\theta}\dot{r} - \dot{\theta}^2rk_0(k_0\theta + k_1)^{-1})$$
(B.3)

For acceleration inversely square case of the thrust profile, $\dot{\theta}^2$ and $\dot{\alpha}$ are given by:

$$\dot{\theta}^2 = \frac{\mu}{r^3} \frac{a_0 \cos(\alpha) \tan \gamma - a_0 \sin(\alpha) + 1}{(m+1) \tan^2 \gamma + 1}$$
(B.4)

$$\dot{\alpha} = \left\{ -2\dot{\theta}\ddot{\theta} \left[(m+1)\tan^2 \gamma + 1 \right] + 2\dot{\theta}^3 \left[(m^2 + m)\tan^3 \gamma \right] - \frac{\mu}{r^3} m \tan^2 \gamma \dot{\theta} a_0 \cos(\alpha) + \frac{3\mu \dot{r}}{r^4} \left(a_0 \sin(\alpha) - a_0 \cos(\alpha) \tan \gamma - 1 \right) \right\} / \left[\frac{\mu}{r^3} \left(a_0 \cos(\alpha) + a_0 \sin(\alpha) \tan \gamma \right) \right]$$
(B.5)

For constant acceleration case of the thrust profile, $\dot{\theta}^2$ and $\dot{\alpha}$ are given by:

$$\dot{\theta}^2 = \frac{a_0 \cos(\alpha) \tan \gamma - a_0 \sin(\alpha) + \frac{\mu}{r^2}}{r((m+1) \tan^2 \gamma + 1)}$$
(B.6)

$$\dot{\alpha} = \left\{ \left(-2\dot{\theta}\ddot{\theta}r - \dot{\theta}^{2}\dot{r} \right) \left[(m+1)\tan^{2}\gamma + 1 \right] + 2\dot{\theta}^{3}r \left(m^{2} + m \right)\tan^{3}\gamma + 1 - a_{0}\cos(\alpha)\dot{\theta}m\tan^{2}\gamma + 1 - 2\frac{\mu\dot{r}}{r^{3}} \right\} / \left[a_{0}\cos(\alpha) + a_{0}\sin(\alpha)\tan\gamma \right]$$
(B.7)

For the tangential thrust profile, $\dot{\theta}^2$ is given by equation (B.4). Note that in the tangential case, $a_0 \cos(\alpha) \tan \gamma = a_0 \sin(\alpha)$. Parameter a_0 is given by:

$$a_0 = \frac{r^3 \left(\ddot{\theta} + 2\dot{\theta}^2 \tan \gamma\right)}{\mu \cos \gamma} \tag{B.8}$$

Parameter $\ddot{\theta}$ is given by:

$$\ddot{\theta} = \frac{-3\mu\dot{r}}{r^4} + 2\dot{\theta}^3 (m^2 + m)\tan^3 \gamma - \frac{1}{2\dot{\theta}((m+1)\tan^2 \gamma + 1)}$$
(B.9)

2. Logarithmic spiral

The radius equation for the logarithmic spiral is given by equation (6.4):

$$r = k_0 e^{m\theta} + k_1$$

The radial velocity and acceleration and the flight path angle for the logarithmic spiral are given by:

$$\dot{r} = m\dot{\theta}k_0 e^{m\theta} \tag{B.10}$$

$$\tan \gamma = \frac{\dot{r}}{r\dot{\theta}} = \frac{k_0 m e^{m\theta}}{k_0 e^{m\theta} + k_1} \tag{B.11}$$

$$\ddot{r} = k_0 m e^{m\theta} \left(\ddot{\theta} + m \dot{\theta}^2 \right) \tag{B.12}$$

For acceleration inversely square case of the thrust profile, $\dot{\theta}^2$ and $\dot{\alpha}$ are given by:

$$\dot{\theta}^2 = \frac{\mu}{r^3} \frac{a_0 \cos \alpha \tan \gamma - a_0 \sin \alpha + 1}{2 \tan^2 \gamma - m \tan \gamma + 1}$$
(B.13)

$$\dot{\alpha} = \left(2\dot{\theta}\ddot{\theta}\left(2\tan^2\gamma - m\tan\gamma + 1\right) + \dot{\theta}^3\left(5m\tan^2\gamma - 4\tan^3\gamma - m^2\tan\gamma\right) + 3\mu\dot{r}/r^4\left(a_0\cos\alpha\tan\gamma - a_0\sin\alpha + 1\right) - \mu/r^3\dot{\theta}a_0\cos\alpha\left(m\tan\gamma - \tan^2\gamma\right)\right)/$$

$$\left(-\mu/r^3\left(a_0\sin\alpha\tan\gamma + a_0\cos\alpha\right)\right)$$
(B.14)

For constant acceleration case of the thrust profile, $\dot{\theta}$ and $\dot{\alpha}$ are given by:

$$\dot{\theta}^2 = \frac{1}{r} \frac{a_0 \cos \alpha \tan \gamma - a_0 \sin \alpha + \mu/r^2}{2 \tan^2 \gamma - m \tan \gamma + 1}$$
(B.15)

$$\dot{\alpha} = \left(\left(2\dot{\theta}\ddot{\theta}r + \dot{\theta}^2\dot{r} \right) \left(2\tan^2\gamma - m\tan\gamma + 1 \right) + \dot{\theta}^3r \left(5m\tan^2\gamma - 4\tan^3\gamma - m^2\tan\gamma \right) + 2\mu\dot{r}/r^3 - a_0\cos\alpha\dot{\theta} \left(m\tan\gamma - \tan^2\gamma \right) \right) / \left(-\left(a_0\sin\alpha\tan\gamma + a_0\cos\alpha \right) \right)$$
(B.16)

For the tangential thrust profile, $\dot{\theta}^2$ is given by equation (B.13). Note that in the tangential case, $a_0 \cos(\alpha) \tan \gamma = a_0 \sin(\alpha)$. Parameter a_0 is given by:

$$a_0 = \frac{r^3 \left(\ddot{\theta} + 2\dot{\theta}^2 \tan \gamma \right)}{\mu \cos \gamma}$$

Parameter $\ddot{\theta}$ is given by:

$$\ddot{\theta} = \frac{-3\mu \tan \gamma / r^3 - 2\dot{\theta}^2 \left(5m \tan^2 \gamma - 4 \tan^3 \gamma - m^2 \tan \gamma\right)}{2\left(2 \tan^2 \gamma - m \tan \gamma + 1\right)}$$
(B.17)

3. Poinsot's spiral (hyperbolic sine)

The radius equation for the Poinsot's spiral (hyperbolic sine) is given by equation (6.7):

$$r = k_0 \left[\sinh \left(m \left(\theta + \varphi \right) \right) \right]^{-k_1}$$

The radial velocity and acceleration and the flight path angle for the Poinsot's spiral (hyperbolic sine) are given by:

$$\dot{r} = -k_1 m \dot{\theta} \coth(m(\theta + \varphi)) r \tag{B.18}$$

$$\tan \gamma = \frac{\dot{r}}{r\dot{\theta}} = -mk_1 \coth\left(m(\theta + \varphi)\right) \tag{B.19}$$

$$\ddot{r} = -k_1 m \left[\ddot{\theta} r \coth\left(m(\theta + \varphi)\right) + \dot{\theta} \dot{r} \coth\left(m(\theta + \varphi)\right) - \dot{\theta}^2 r m \left[\sinh\left(m(\theta + \varphi)\right)\right]^{-2} \right]$$
(B.20)

Parameter φ was added in equation (6.7) in order to warn the user that the term inside the $\sinh(\)$ should not be zero, otherwise r becomes ∞ .

For acceleration inversely square case of the thrust profile, $\dot{\theta}$ and $\dot{\alpha}$ are given by:

$$\dot{\theta}^2 = \frac{\mu}{r^3} \frac{a_0 \cos(\alpha) \tan \gamma - a_0 \sin(\alpha) + 1}{\tan^2 \gamma - k_1 m^2 \sinh(m(\theta + \varphi))^{-2} + 1}$$
(B.21)

$$\dot{\alpha} = \left\{ 2\dot{\theta}\ddot{\theta} \left(\tan^2 \gamma - k_1 m^2 \left(\sinh \left(m(\theta + \varphi) \right) \right)^{-2} + 1 \right) + \right. \\
+ 2\dot{\theta}^3 m^3 \coth \left(m(\theta + \varphi) \right) \left(\sinh \left(m(\theta + \varphi) \right) \right)^{-2} \left(k_1 - k_1^2 \right) + \right. \\
+ 3\mu \dot{r} / r^4 \left(a_0 \cos \left(\alpha \right) \tan \gamma - a_0 \sin \left(\alpha \right) + 1 \right) - \\
- \mu / r^3 k_1 m^2 a_0 \cos \left(\alpha \right) \dot{\theta} \left(\sinh \left(m(\theta + \varphi) \right) \right)^{-2} \right\} / \left[- \mu / r^3 \left(a_0 \cos \left(\alpha \right) + a_0 \sin \left(\alpha \right) \tan \gamma \right) \right]$$
(B.22)

For constant acceleration case of the thrust profile, $\dot{\theta}$ and $\dot{\alpha}$ are given by:

$$\dot{\theta}^2 = \frac{a_0 \cos(\alpha) \tan \gamma - a_0 \sin(\alpha) + \mu/r^2}{r \left(\tan^2 \gamma - k_1 m^2 \left(\sinh(m(\theta + \varphi)) \right)^{-2} + 1 \right)}$$
(B.23)

$$\dot{\alpha} = \left\{ \left(2\dot{\theta}\ddot{\theta}r + \dot{r}\dot{\theta}^{2} \right) \left(\tan^{2}\gamma - k_{1}m^{2} \left(\sinh\left(m(\theta + \varphi)\right) \right)^{-2} + 1 \right) + \right. \\
+ 2\dot{\theta}^{3}rm^{3} \coth\left(m(\theta + \varphi)\right) \left(\sinh\left(m(\theta + \varphi)\right) \right)^{-2} \left(k_{1} - k_{1}^{2} \right) - \\
- a_{0} \cos\left(\alpha\right) k_{1}m^{2}\dot{\theta} \left(\sinh\left(m(\theta + \varphi)\right) \right)^{-2} + 2\mu\dot{r}/r^{3} \right\} / \left(-a_{0} \cos\left(\alpha\right) - a_{0} \sin\left(\alpha\right) \tan\gamma \right)$$
(B.24)

For the tangential thrust profile, $\dot{\theta}^2$ is given by equation (B.21). Note that in the tangential case, $a_0 \cos(\alpha) \tan \gamma = a_0 \sin(\alpha)$. Parameter a_0 is given by:

$$a_0 = \frac{r^3 \left(\ddot{\theta} + 2\dot{\theta}^2 \tan \gamma \right)}{\mu \cos \gamma}$$

Parameter $\ddot{\theta}$ is given by:

$$\ddot{\theta} = \frac{-3\mu\dot{r}/r^4 + 2\dot{\theta}^3 m^3 \left(\sinh\left(m(\theta + \varphi)\right)\right)^{-2} \cosh\left(m(\theta + \varphi)\right) \left(k_1^2 - k_1\right)}{2\dot{\theta} \left(\tan^2 \gamma - k_1 \left(\sinh\left(m(\theta + \varphi)\right)\right)^{-2} m^2 + 1\right)}$$
(B.25)

4. Poinsot's spiral (hyperbolic cosine)

The radius equation for the Poinsot's spiral (hyperbolic cosine) is given by equation (6.8):

$$r = k_0 \left(\cosh \left(m\theta \right) \right)^{-k_1}$$

The radial velocity and acceleration and the flight path angle for the Poinsot's spiral (hyperbolic cosine) are given by:

$$\dot{r} = -k_1 m \dot{\theta} \tanh(m\theta) r \tag{B.26}$$

$$\tan \gamma = \frac{\dot{r}}{r\dot{\theta}} = -mk_1 \tanh(m\theta) \tag{B.27}$$

$$\ddot{r} = -k_1 m \left[\ddot{\theta} \tanh \left(m\theta \right) r + \dot{\theta} \dot{r} \tanh \left(m\theta \right) + \dot{\theta}^2 r m \cosh^{-2} \left(m\theta \right) \right]$$
(B.28)

For acceleration inversely square case of the thrust profile, $\dot{\theta}$ and $\dot{\alpha}$ are given by:

$$\dot{\theta}^2 = \frac{\mu}{r^3} \frac{a_0 \cos(\alpha) \tan \gamma - a_0 \sin(\alpha) + 1}{\tan^2 \gamma + k_1 m^2 \cosh^{-2}(m\theta) + 1}$$
(B.29)

$$\dot{\alpha} = \left\{ -2\dot{\theta}\ddot{\theta} \left(\tan^2 \gamma + k_1 m^2 \cosh^{-2} \left(m\theta \right) + 1 \right) - \right. \\
\left. - 2m^3 \dot{\theta}^3 \left(\cosh \left(m\theta \right) \right)^{-2} \tanh \left(m\theta \right) \left(k_1^2 - k_1 \right) + \right. \\
\left. 3\mu \dot{r} / r^4 \left(a_0 \sin \left(\alpha \right) - a_0 \cos \left(\alpha \right) \tan \gamma - 1 \right) - \right. \\
\left. - \mu / r^3 k_1 m^2 \dot{\theta} \left(\cosh \left(m\theta \right) \right)^{-2} a_0 \cos \left(\alpha \right) \right\} / \left(\mu / r^3 \left(a_0 \cos \left(\alpha \right) + a_0 \sin \left(\alpha \right) \tan \gamma \right) \right)$$
(B.30)

For constant acceleration case of the thrust profile, $\dot{\theta}$ and $\dot{\alpha}$ are given by:

$$\dot{\theta}^2 = \frac{1}{r} \frac{a_0 \cos(\alpha) \tan \gamma - a_0 \sin(\alpha) + \mu/r^2}{\tan^2 \gamma + k_1 m^2 \cosh^{-2}(m\theta) + 1}$$
(B.31)

$$\dot{\alpha} = \left\{ -\left(2\dot{\theta}\ddot{\theta}r + \dot{\theta}^{2}\dot{r}\right)\left(k_{1}^{2}m^{2}\tanh^{2}\left(m\theta\right) + k_{1}m^{2}\cosh^{-2}\left(m\theta\right) + 1\right) - \\
-2m^{3}\dot{\theta}^{3}r\left(\cosh\left(m\theta\right)\right)^{-2}\tanh\left(m\theta\right)\left(k_{1}^{2} - k_{1}\right) - \\
-k_{1}m^{2}\dot{\theta}\left(\cosh\left(m\theta\right)\right)^{-2}a_{0}\cos\left(\alpha\right) - \frac{2\mu\dot{r}}{r^{3}}\right\} / \left(a_{0}\cos\left(\alpha\right) - k_{1}m\tanh\left(m\theta\right)a_{0}\sin\left(\alpha\right)\right)$$
(B.32)

For the tangential thrust profile, $\dot{\theta}^2$ is given by equation (B.29). Note that in the tangential case, $a_0 \cos(\alpha) \tan \gamma = a_0 \sin(\alpha)$. Parameter a_0 is given by:

$$a_0 = \frac{r^3 \left(\ddot{\theta} + 2\dot{\theta}^2 \tan \gamma \right)}{\mu \cos \gamma}$$

Parameter $\ddot{\theta}$ is given by:

$$\ddot{\theta} = \frac{-3\mu\dot{r}/r^4 - 2\dot{\theta}^3 m^3 \left(\cosh(m\theta)\right)^{-2} \tanh(m\theta) \left(k_1^2 - k_1\right)}{2\dot{\theta} \left(\tan^2 \gamma + k_1 \left(\cosh(m\theta)\right)^{-2} m^2 + 1\right)}$$
(B.33)

5. Sinusoidal spiral

The radius equation for the sinusoidal spiral is given by equation (6.10):

$$r = \left(k_0 \cos\left(m\theta\right) + k_1\right)^{1/m}$$

The radial velocity and acceleration and the flight path angle for the sinusoidal spiral are given by:

$$\dot{r} = -\dot{\theta}rk_0\sin(m\theta)\left(k_0\cos(m\theta) + k_1\right)^{-1} \tag{B.34}$$

$$\tan \gamma = \frac{\dot{r}}{r\dot{\theta}} = -k_0 \sin(m\theta) \left(k_0 \cos(m\theta) + k_1\right)^{-1}$$
(B.35)

$$\ddot{r} = -k_0 \left[\dot{C} \sin(m\theta) \dot{\theta} r + Cm \dot{\theta}^2 \cos(m\theta) r + C \sin(m\theta) \dot{\theta} r + C \sin(m\theta) \dot{\theta} \dot{r} \right]$$
(B.36)

where
$$C = (k_0 \cos(m\theta) + k_1)^{-1}$$
 and $\dot{C} = k_0 m \dot{\theta} \sin(m\theta) C^2$

For acceleration inversely square case of the thrust profile, $\dot{\theta}$ and $\dot{\alpha}$ are given by:

$$\dot{\theta}^2 = \frac{\mu}{r^3} \frac{a_0 \cos \alpha \tan \gamma - a_0 \sin \alpha + 1}{\tan^2 \gamma (1+m) + k_0 C \cdot m \cos(m\theta) + 1}$$
(B.37)

$$\dot{\alpha} = \left[2\dot{\theta}\ddot{\theta} \left(-\tan^2 \gamma (1+m) - k_0 C m \cos(m\theta) - 1 \right) + \right. \\
\left. - \dot{\theta}^2 \left(2\dot{C} C k_0^2 \sin^2 \left(m\theta \right) (1+m) + k_0^2 C^2 m \dot{\theta} \sin(2m\theta) (1+m) + \right. \\
\left. + k_0 \dot{C} m \cos(m\theta) - \tan \gamma m^2 \dot{\theta} \right) + 3\mu \dot{r} / r^4 \left(a_0 \sin \alpha - a_0 \cos \alpha \tan \gamma - 1 \right) - \right. \\
\left. - \mu / r^3 a_0 \cos \alpha k_0 \left(\dot{C} \sin(m\theta) + C m \dot{\theta} \cos(m\theta) \right) \right] / \left(\mu / r^3 \left(a_0 \cos \alpha + a_0 \sin \alpha \tan \gamma \right) \right)$$
(B.38)

For constant acceleration case of the thrust profile, $\dot{\theta}$ and $\dot{\alpha}$ are given by:

$$\dot{\theta}^2 = \frac{a_0 \cos \alpha \tan \gamma - a_0 \sin \alpha + \mu/r^2}{r\left(\tan^2 \gamma (1+m) + k_0 C \cdot m \cos(m\theta) + 1\right)}$$
(B.39)

$$\dot{\alpha} = \left\{ -\left(2\dot{\theta}\ddot{\theta}r + \dot{\theta}^{2}\dot{r}\right)\left((1+m)\tan^{2}\gamma + k_{0}Cm\cos\left(m\theta\right) + 1\right) + \\
-\dot{\theta}^{2}r\left(2k_{0}^{2}\dot{C}C\sin^{2}\left(m\theta\right)(1+m) + k_{0}^{2}C^{2}m\dot{\theta}\sin\left(2m\theta\right)(1+m) + \\
+k_{0}\dot{C}m\cos\left(m\theta\right) + m^{2}\dot{\theta}\tan\gamma\right) - a_{0}\cos\alpha k_{0}\left(\dot{C}\sin\left(m\theta\right) + Cm\dot{\theta}\cos\left(m\theta\right)\right) - \\
-\frac{2\mu\dot{r}}{r^{3}}\right\} / (a_{0}\cos\alpha + a_{0}\sin\alpha\tan\gamma)$$
(B.40)

For the tangential thrust profile, $\dot{\theta}^2$ is given by equation (B.37). Note that in the tangential case, $a_0 \cos(\alpha) \tan \gamma = a_0 \sin(\alpha)$. Parameter a_0 is given by:

$$a_0 = \frac{r^3 \left(\ddot{\theta} + 2\dot{\theta}^2 \tan \gamma \right)}{\mu \cos \gamma}$$

Parameter $\ddot{\theta}$ is given by:

$$\ddot{\theta} = \left\{ \frac{-3\mu\dot{r}}{r^4} - \dot{\theta}^2 \left(-2\tan\gamma k_0^m \left(1 + m \right) \left(m\dot{\theta}C\cos\left(m\theta \right) + \dot{C}\sin\left(m\theta \right) \right) + \right. \\ \left. + k_0^m m \left(\dot{C}\cos\left(m\theta \right) - Cm\dot{\theta}\sin\left(m\theta \right) \right) \right) / \left\{ 2\dot{\theta} \left(\tan^2\gamma \left(1 + m \right) + k_0^m C \cdot m\cos\left(m\theta \right) + 1 \right) \right\}$$
(B.41)

6. Exponential sinusoid

The radius equation for the exponential sinusoid is given by equation (5.3):

$$r = k_0 e^{q\theta + k_1 \sin(k_2\theta + \phi)}$$

The radial velocity and acceleration and the flight path angle for the exponential sinusoid are given by equations (5.6) and (5.7), respectively:

$$\dot{r} = \dot{\theta} (q + k_1 k_2 c) r$$

$$\ddot{r} = (\ddot{\theta} (q + k_1 k_2 c) + \dot{\theta}^2 (q + k_1 k_2 c)^2 - \dot{\theta}^2 k_1 k_2^2 s) r$$

$$\tan \gamma = \frac{\dot{r}}{r\dot{\theta}} = q + k_1 k_2 c$$

For acceleration inversely square case of the thrust profile, $\dot{\theta}$ and $\dot{\alpha}$ are given by equations (5.8) and (5.11), respectively:

$$\dot{\theta}^2 = \frac{\mu}{r^3} \frac{a_0 \cos \alpha \tan \gamma - a_0 \sin \alpha + 1}{\tan^2 \gamma + k_1 k_2^2 s + 1}$$

$$\dot{\alpha} = \left\{ \left(\tan \gamma \dot{\theta}^2 r^3 / \mu - 2a_0 \cos \alpha \right) \left(\tan^2 \gamma + k_1 k_2^2 s + 1 \right)^2 - \right. \\
\left. - \left(a_0 \cos \alpha \tan \gamma - a_0 \sin \alpha + 1 \right) \left(k_1 k_2^3 c - 2 \tan \gamma k_1 k_2^2 s \right) \right. \\
\left. - a_0 k_1 k_2^2 s \cos \alpha \left(\tan^2 \gamma + k_1 k_2^2 s + 1 \right) \right\} \dot{\theta} / \left(\left(a_0 \sin \alpha \tan \gamma + a_0 \cos \alpha \right) \left(\tan^2 \gamma + k_1 k_2^2 s + 1 \right) \right)$$

For constant acceleration case of the thrust profile, $\dot{\theta}$ and $\dot{\alpha}$ are given by:

$$\dot{\theta}^2 = \frac{a_0 \cos \alpha \tan \gamma - a_0 \sin \alpha + \mu/r^2}{r(\tan^2 \gamma + k_1 k_2^2 s + 1)}$$
(B.42)

$$\dot{\alpha} = \left\{ \left(\tan^2 \gamma + k_1 k_2^2 s + 1 \right) \left(2\dot{\theta}\ddot{\theta}r + \dot{\theta}^2 r \right) + \dot{\theta}^3 r \left(-2k_1 k_2^2 s \tan \gamma + k_1 k_2^3 c \right) + a_0 \cos \alpha k_1 k_2^2 s \dot{\theta} + \frac{2\mu \dot{r}}{r^3} \right\} / \left(-\left(a_0 \sin \alpha \tan \gamma + a_0 \cos \alpha \right) \right)$$
(B.43)

For the tangential thrust profile, $\dot{\theta}^2$ is given by equation (5.13). Note that in the tangential case, $a_0 \cos(\alpha) \tan \gamma = a_0 \sin(\alpha)$. The equation for the parameter a_0 was already derived in appendix A.

Appendix C: Integration Error

The objective in this appendix is to study and show the behaviour of the thrust angle rate $(\dot{\alpha})$ during the integration procedure to obtain the thrust angle (α) , using the integration method Runge-Kutta 4(5).

The Archimedean spiral combined with the acceleration inversely square case will be used in this demonstration. The equations for the dynamic parameters $\dot{\theta}^2$ and $\dot{\alpha}$ are given in appendix B.

A mission example is presented: a flight from Earth to Mars, using one revolution (N = 1). The phase angle between one arbitrary point at Earth's orbit (P_1) and one arbitrary point at Mars' orbit (P_2) is 7.1427 $rad \approx 409.247^{\circ}$. The initial values for θ_0 and α_0 are assumed to be zero and the value for a_0 is assumed to be 0.04.

When m=2.2, there is an integration error, stating that the program was unable to meet integration tolerances without reducing the step size below the smallest value allowed $(2.980232\times10^{-8}\,\mathrm{s})$ at instant of time $1.416985\times10^7\,\mathrm{s}\approx0.449323\,\mathrm{years}$. Figure 24 illustrates $\dot{\alpha}$ values before and at the moment that the failure in the integration occurs.

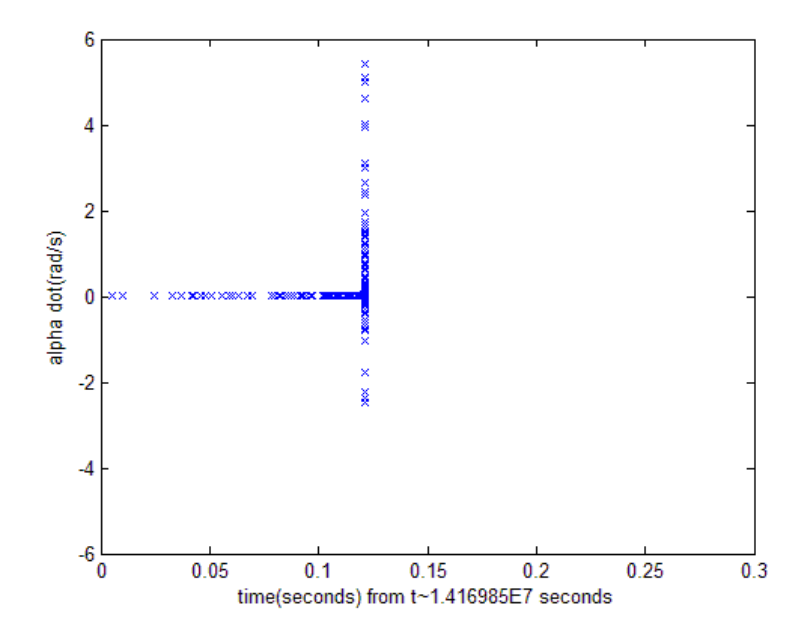


Figure 24: $\dot{\alpha}$ as function of time from $1.416985 \times 10^7 s \approx 0.449323$ years

In order to understand why the failure occurs, $\dot{\alpha}$ is computed at the two last instants of time before the error message, named t_{i-1} and t_i , where t_i is the last instant of time computed.

$$\dot{\alpha}(t_{i-1}) = -1.04364155689890 \ rad / s$$

 $\dot{\alpha}(t_i) = 4.9993525934841 \ rad / s$

The expression for $\dot{\alpha}$ is complex, so in order to find where the problem is, the equation was divided in two parts: the numerator (n_{α}) (upper part of the fraction) and the denominator (d_{α}) (the lower part of the fraction):

$$n_{\alpha}(t_{i-1}) = 2.470491936027266 \times 10^{-22}$$

 $n_{\alpha}(t_{i}) = 2.470491070356708 \times 10^{-22}$

$$d_{\alpha}(t_{i-1}) = -2.367184326549962 \times 10^{-22}$$

$$d_{\alpha}(t_{i}) = 4.941621988367792 \times 10^{-23}$$

Clearly, the denominator of equation $\dot{\alpha}$ is responsible for the large variations in $\dot{\alpha}$ results for small time step sizes. d_{α} is given by:

$$d_{\alpha} = \frac{\mu}{r^3} \left(a_0 \cos(\alpha) + \frac{1}{m} k_0^m \left(k_0^m \theta + k_1^m \right)^{-1} a_0 \sin(\alpha) \right) = \frac{\mu}{r^3} \left(a_0 \cos(\alpha) + \tan \gamma a_0 \sin(\alpha) \right)$$

Parameters μ and a_0 are constants and equal to $1.32712440018 \times 10^{20} m^3 / s^2$ and 0.04, respectively.

For m = 2.2, $k_0 = 7.315587756966051 \times 10^{10}$ and $k_1 = 1.471041108704898 \times 10^{11}$. Since the difference between t_{i-1} and t_i is very small, it is understandable that θ and r yielded the same values for both instants of time:

$$\theta$$
 = 2.42739686030349 rad
r = 1.780522308862669×10¹¹ m

Since θ is constant from t_{i-1} to t_i , $\tan \gamma$ is also constant between time instants. In this way, the only variable that changes between the two instants of time is α :

$$\alpha(t_{i-1}) = 1.63493601954405 \ rad$$

 $\alpha(t_i) = 1.63493571591232 \ rad$

The difference between the α values is significantly small, but it is sufficient to cause the integration error. Neglecting the term μ/r^3 :

$$a_0 \cos(\alpha) + \tan \gamma a_0 \sin(\alpha) = \begin{cases} t_{i-1} : -1.006845193199726 \times 10^{-8} \\ t_i : 2.10184238286572 \times 10^{-9} \end{cases}$$

By changing α value by $10^{-5} rad$ will make $a_0 \cos(\alpha) + \tan \gamma a_0 \sin(\alpha)$ vary between negative and positive values. At a certain instant of time, $a_0 \cos(\alpha) + \tan \gamma a_0 \sin(\alpha) \approx 0$.

According to [Petropoulos et al, 1999], when past the point in the trajectory where the denominator of $\dot{\alpha}$ is zero, there is no thrust direction which can maintain the selected shape and continuity of velocity, using the current thrust profile. In this way, the fact the integration procedure cannot be completed is due to geometric properties of the shape selected that cannot satisfy the physic problem.

If this situation happens during the optimization procedure, the individual is discarded. Unfortunately, this integration error cannot be predicted before the integration starts.

Appendix D: Analysis of the Shapes for the Constant Acceleration Case of the Thrust Profile

In this appendix, results and some remarks will be given for all 6 shapes using the constant acceleration case of the thrust profile, for an Earth-to-Mars mission. The conclusions about these results are presented in section 7.7.

1. Archimedean spiral

In this section, results for the TOF, for the excess velocities and for the thrust acceleration will be shown and discussed for the Archimedean spiral. The thrust profile used in this analysis is the second thrust profile mentioned in chapter 6, where the magnitude of the thrust acceleration is constant and equal to $a = a_0 \mu/r_1^2$, where r_1 is the heliocentric distance of the starting point of the thrust arc.

Figures 2 and 3 show the TOF and the total excess velocity when changing parameter θ_i and the transfer angle $\Delta\theta$ (N=0). Note that the polar angle at the target planet is given by: $\theta_f = \theta_i + \Delta\theta + 2\pi N$. The value used in figures 2 and 3 for the geometric parameter m was 0.05, the values used for the initial value of α were (-60°, -50°, -40°, -30°, -20°), for the initial polar angle θ_i were (0°, 120°, 240°, 360°) and for the transfer angle $\Delta\theta$ were (90°, 150°, 210°, 270°, 340°). The normalized thrust acceleration a_0 value used in figures 2 and 3 was 0.07.

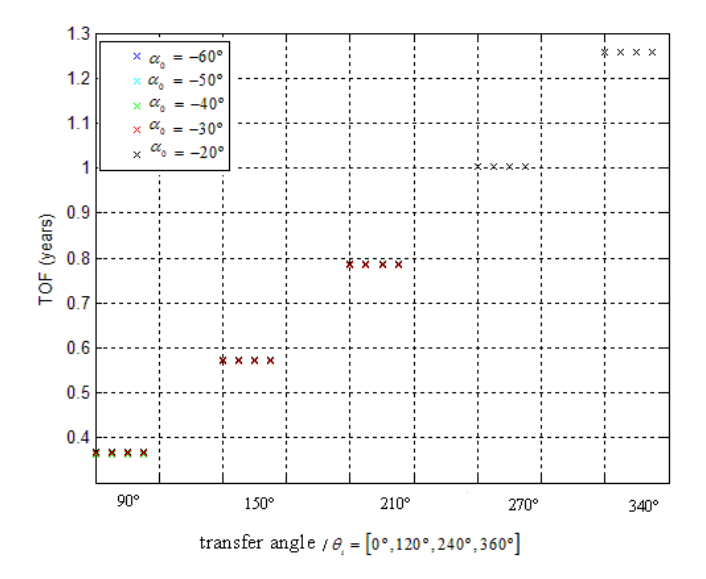


Figure 25: TOF for θ_i values of (0°, 120°, 240°, 360°) from left to right in the figure, α_0 values of (-60°, -50°, -40°, -30°, -20°), $\Delta\theta$ values of (90°, 150°, 210°, 270°, 340°) (N=0), m=0.05, a_0 =0.07, constant acceleration case of the thrust profile (Archimedean spiral), Earth-Mars flight

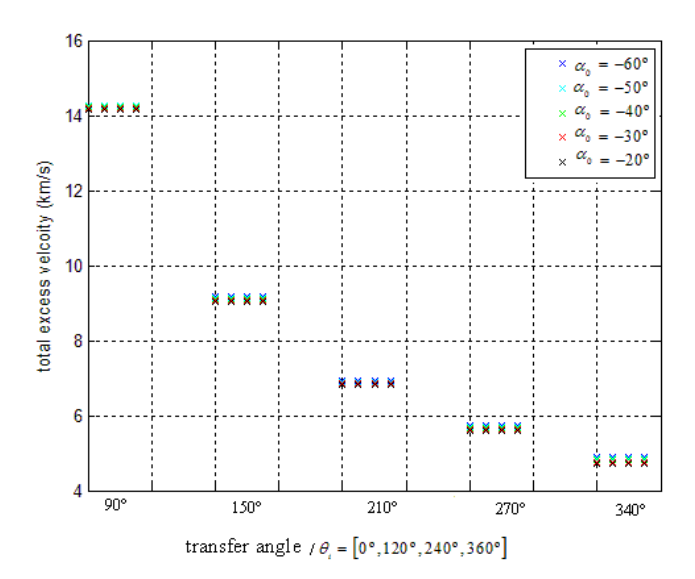


Figure 26: $V_{\omega,\tau}$ for θ_i values of (0°, 120°, 240°, 360°) from left to right in the figure, α_0 values of (-60°, -50°, -40°, -30°, -20°), $\Delta\theta$ values of (90°, 150°, 210°, 270°, 340°) (N=0), m=0.05, a_0 =0.07, constant acceleration case of the thrust profile (Archimedean spiral), Earth-Mars flight

Some remarks can be drawn from figures 2 and 3. As expected, the TOF increases when increasing the transfer angle, while the total excess velocity decreases. By changing the initial polar angle θ_i , the differences between values for the TOF and for the total excess

velocity are significantly small. The order of magnitude of the highest difference in the time of flight between different θ_i for the same phase angle and α_0 is 10^{-5} seconds, while for the highest difference in the total excess velocity is $10^{-8} \, m/s$. The TOF increases when increasing values of α_0 , while the total excess velocity decreases (figure 3).

Similar figures can be shown for 1 and 2 revolutions, using the same values for the geometric parameter m, for the transfer angle $\Delta\theta$ and for the initial values of α and θ . The values for the normalized thrust acceleration a_0 used in figures 4 and 5 were 0.03 and 0.02, respectively for N=1 and N=2.

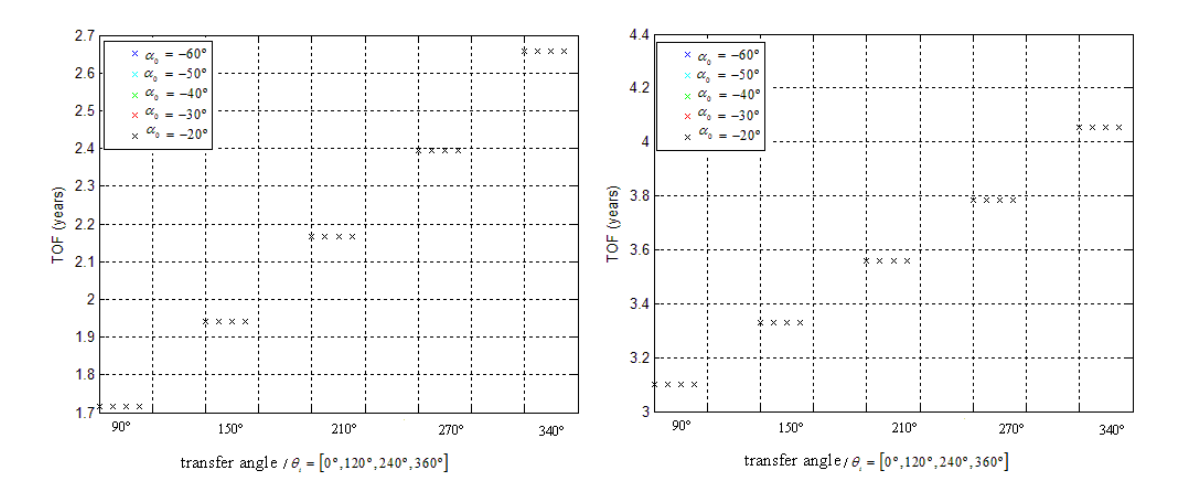


Figure 27: TOF for θ_i values of $(0^\circ, 120^\circ, 240^\circ, 360^\circ)$ from left to right in the figure, α_0 values of $(-60^\circ, -50^\circ, -40^\circ, -30^\circ, -20^\circ)$, $\Delta\theta$ values of $(90^\circ, 150^\circ, 210^\circ, 270^\circ, 340^\circ)$, m=0.05, constant acceleration case of the thrust profile (Archimedean spiral), Earth-Mars flight, N=1 (a_0 =0.03) and N=2 (a_0 =0.02)

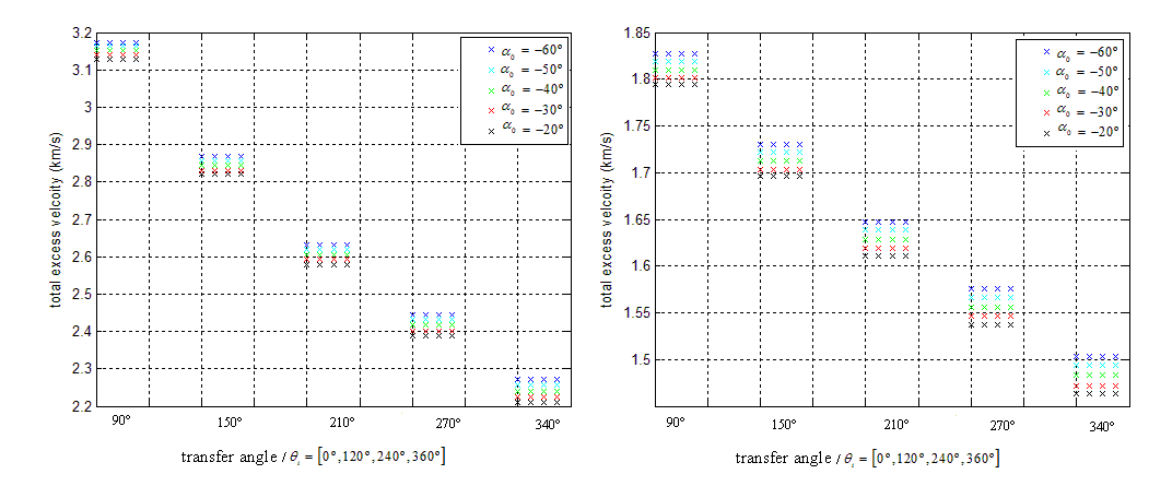


Figure 28: $V_{\omega,T}$ for θ_i values of (0°, 120°, 240°, 360°) from left to right in the figure, α_0 values of (-60°, -50°, -40°, -30°, -20°), $\Delta\theta$ values of (90°, 150°, 210°, 270°, 340°), m=0.05, constant acceleration case of the thrust profile (Archimedean spiral), Earth-Mars flight, N=1 (a_0 =0.03) and N=2 (a_0 =0.02)

Similar remarks to the ones given for N=0 can be drawn for figures 4 and 5. Note that when increasing the number of complete revolutions N (figures 3 and 5), the differences in total excess velocity between different values of α_0 increase. As for the N=0 case, the differences in the TOF and total excess velocity between different θ_i and for the same transfer angle and α_0 can be neglected for N=1 and N=2. In this way, due to the significantly small influence that the parameter θ_i has in the TOF, in the total excess velocity and also, although not shown in the previous figures, in the thrust acceleration, this parameter would not be considered a variable in the optimization procedure.

The TOF range for this Earth-Mars flight is from 0.3622 years to 4.0527 years. The total excess velocity has a minimum value of $1.4630 \, km/s$ and a maximum value of $14.2794 \, km/s$. As expected, the minimum value for the TOF and the maximum value for the total excess velocity occur for the smallest transfer angle -90° (N=0); while the maximum value for the TOF and minimum value for the total excess velocity occur for the highest transfer angle presented -340° (N=2).

The maximum differences in TOF between two consecutive values of the transfer angle $\Delta\theta$ are about 0.27 years. For a certain number of revolutions, these differences increase when increasing the transfer angle. The differences in terms of total excess velocity

between two consecutive transfer angles is always highest between $\Delta\theta = 90^{\circ}$ and $\Delta\theta = 150^{\circ}$. The maximum value for these differences is $5.1203 \, km/s$ for N=0 and the minimum value is about $71 \, m/s$ for 2 revolutions.

Tables 1 and 2 show the values of the TOF and the excess velocity for an Earth-Mars flight. Parameter θ_i was assumed 0°, parameter α_0 was assumed -20°, the transfer angle $\Delta\theta$ was assumed 90° and the number of revolutions was taken 1 for the first table and 2 for the second one. In table 1 the normalized thrust acceleration a_0 was 0.04, while in table 2, this parameter was 0.02. Note that these values for a_0 for N=1 and N=2 are the minimum values that can be used in both cases for this shape without facing integration problems for the interval of the input parameters considered.

N=1	m = 0.02	m = 0.64	m = 1.26	m = 1.88	m = 2.5
$V_{\infty,total}\left(km/s\right)$	3.3071	3.4080	3.5776	3.8203	4.1444
$V_{\infty,1}(km/s)$	1.6362	1.8581	2.1225	2.4394	2.8216
$V_{\infty,2}(km/s)$	1.6709	1.5500	1.4551	1.3809	1.3228
TOF (years)	1.7003	1.7241	1.7480	1.7722	1.7970

Table 7: The excess velocities and the TOF values for N=1, θ_i =0°, $\Delta\theta$ =90°, α_0 =-20°, for a_0 =0.04, m values of (0.02; 0.64; 1.26; 1.88; 2.5), constant acceleration case (Archimedean spiral), Earth to Mars

N=2	m = 0.02	m = 0.64	m = 1.26	m = 1.88	m = 2.5
$V_{\scriptscriptstyle{\infty,total}}\left(km/s ight)$	1.7942	1.8533	1.9501	2.0872	2.2691
$V_{\infty,1}(km/s)$	0.9054	1.0304	1.1796	1.3582	1.5730
$V_{\infty,2}(km/s)$	0.8888	0.8229	0.7705	0.7290	0.6961
TOF (years)	3.1004	3.1425	3.1847	3.2270	3.2701

Table 8: The excess velocities and the TOF values for N=2, θ_i =0°, $\Delta\theta$ =90°, α_0 =-20°, a_0 =0.03, m values of (0.02; 0.64; 1.26; 1.88; 2.5), constant acceleration case (Archimedean spiral), Earth to Mars

From tables 1 and 2, the order of magnitude of the total excess velocity values is $10^0 \ km/s$. For increasing values of m, the total excess velocity and the TOF increase. The values for the total excess velocity are higher when N=1 than when N=2. Note that the excess velocity $V_{\infty,1}$ increases faster than the excess velocity $V_{\infty,2}$ decreases and the value of $V_{\infty,2}$ when m=2.5 is more than twice smaller than the value of $V_{\infty,1}$ in both cases of N.

In figures 6 to 9, the polar plot, the thrust angle α , the polar angle rate $\dot{\theta}$ and the flight path angle as function of time are illustrated for N=1 and N=2 (tables 1 and 2).

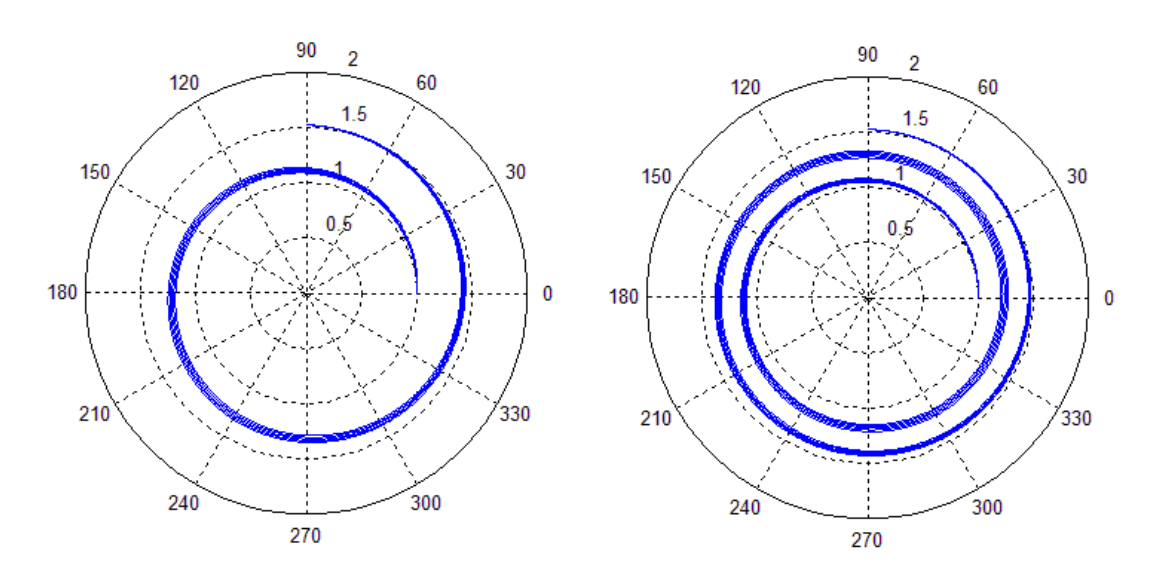


Figure 29: Polar plot for N=1 (a_0 =0.04) and N=2 (a_0 =0.02), θ_i =0°, $\Delta\theta$ =90°, α_0 =-20°, m values of (0.02; 0.64; 1.26; 1.88; 2.5), constant acceleration case (Archimedean spiral), Earth-Mars flight

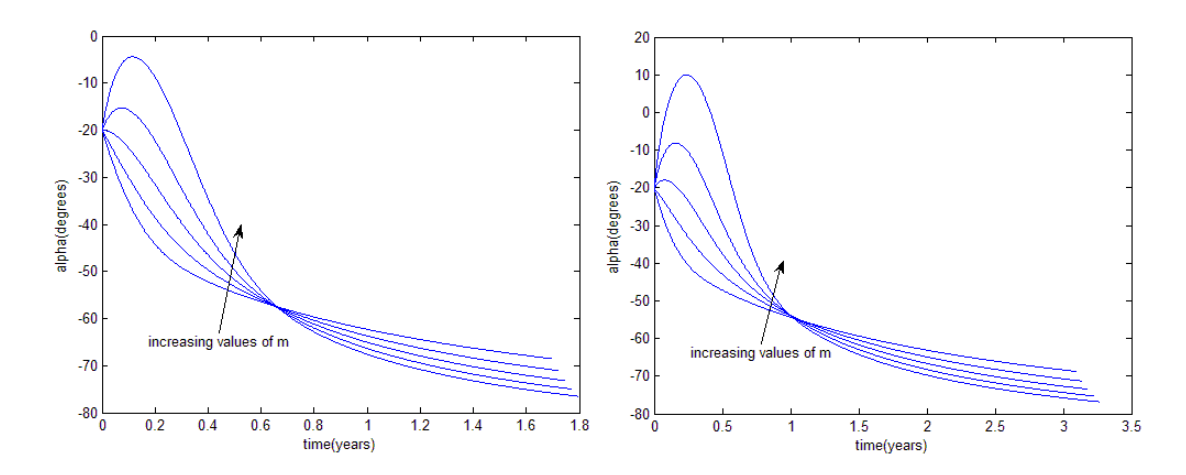


Figure 30: α plot for N=1 (a_0 =0.04) and N=2 (a_0 =0.02), θ_i =0°, $\Delta\theta$ =90°, α_0 =-20°, m values of (0.02; 0.64; 1.26; 1.88; 2.5), constant acceleration case (Archimedean spiral), Earth-Mars flight

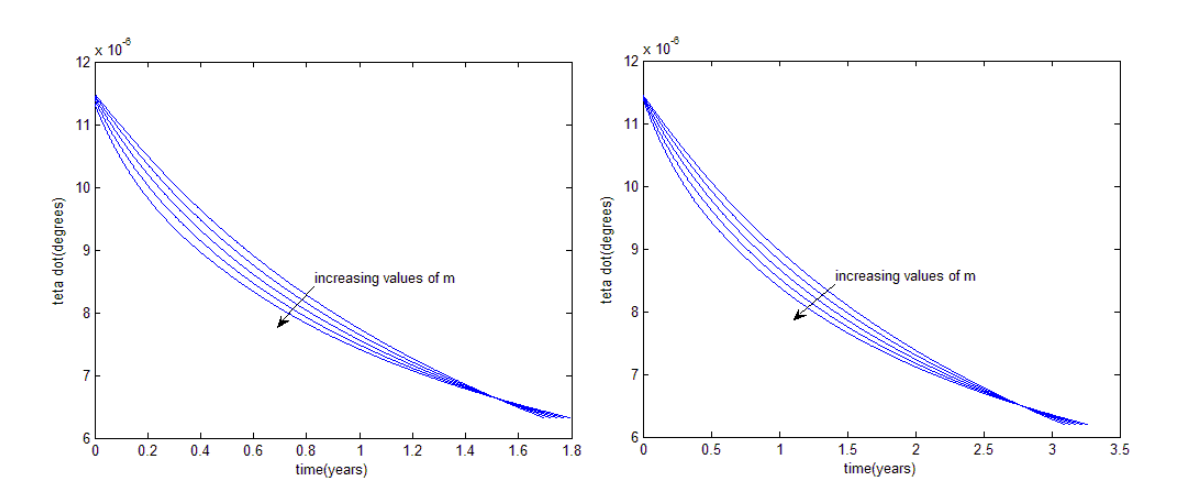


Figure 31: $\dot{\theta}$ plot for N=1 (a_0 =0.04) and N=2 (a_0 =0.02), θ_i =0°, $\Delta\theta$ =90°, α_0 =-20°, m values of (0.02; 0.64; 1.26; 1.88; 2.5), constant acceleration case (Archimedean spiral), Earth-Mars flight

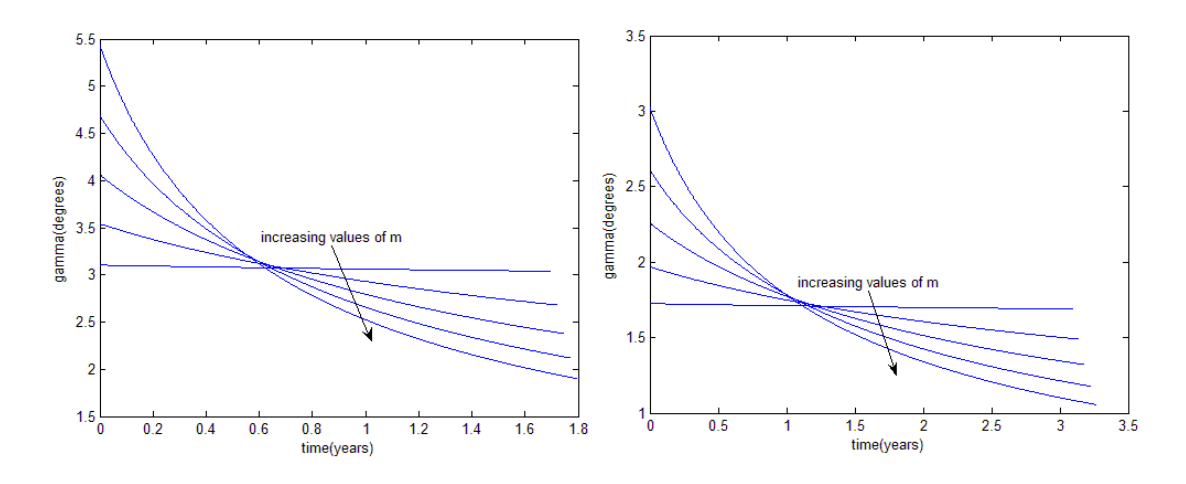


Figure 32: γ plot for N=1 (a_0 =0.04) and N=2 (a_0 =0.02), θ_i =0°, $\Delta\theta$ =90°, α_0 =-20°, m values of (0.02; 0.64; 1.26; 1.88; 2.5), constant acceleration case (Archimedean spiral), Earth-Mars flight

The values of the thrust angle α are higher for N=2 than for N=1. During the interplanetary flight for both cases in figure 7, the spacecraft is thrusting inwards in the radial direction, while in the tangential direction it thrusts in the positive direction (α is negative, higher than -90°). This means that the vehicle is thrusting in favour of the gravitational acceleration. This situation is explained in section 7.7. The magnitude values of the flight path angle γ are smaller for N=2 than for N=1.

2. Logarithmic spiral

In this section, results for the TOF, the excess velocities and the thrust acceleration will be shown and discussed for the Logarithmic spiral. Figures 10 and 11 show the TOF and the total excess velocity when changing parameter θ_i and the transfer angle $\Delta\theta$, when the number of revolutions N is 0. The value used in figures 10 and 11 for the geometric parameter m was 0.05; the values used for the initial value of α , for the initial polar angle θ_i and for the transfer angle $\Delta\theta$ were the same as for the Archimedean spiral. The normalized thrust acceleration a_0 value used in figures 10 and 11 was 0.08.

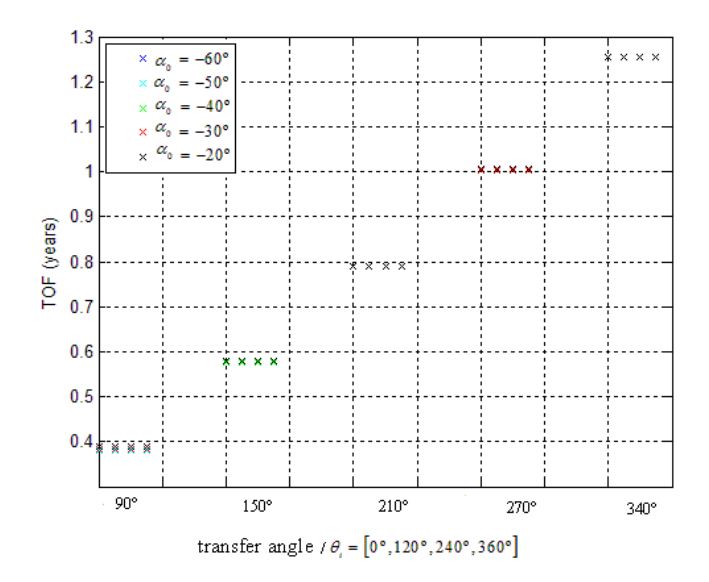
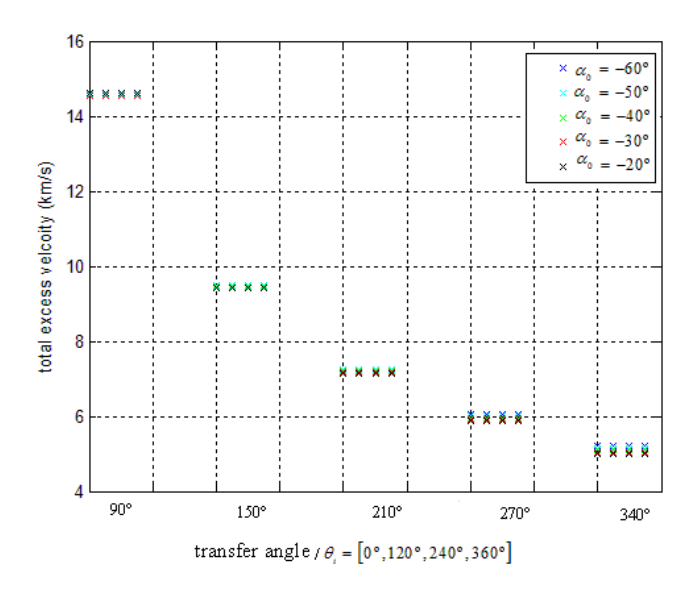


Figure 33: TOF for θ_i values of (0°, 120°, 240°, 360°) from left to right in the figure, α_0 values of (-60°, -50°, -40°, -30°, -20°), $\Delta\theta$ values of (90°, 150°, 210°, 270°, 340°) (N=0), m=0.05, a_0 =0.08, constant acceleration case of the thrust profile (logarithmic spiral), Earth-Mars flight



From figures 10 and 11, by changing the initial polar angle θ_i , the differences between values for the TOF and for the total excess velocity are significantly small. For increasing values of α_0 , the total excess velocity decreases, while the TOF increases. The total excess

velocity differences between different values of α_0 increase when increasing the transfer angle $\Delta\theta$.

Similar figures can be shown for 1 and 2 revolutions, using the same values for the geometric parameter m, for the transfer angle $\Delta\theta$ and for the initial values of α and θ . The normalized thrust acceleration a_0 values used in figures 12 and 13 were 0.03 and 0.02 for N=1 and N=2, respectively.

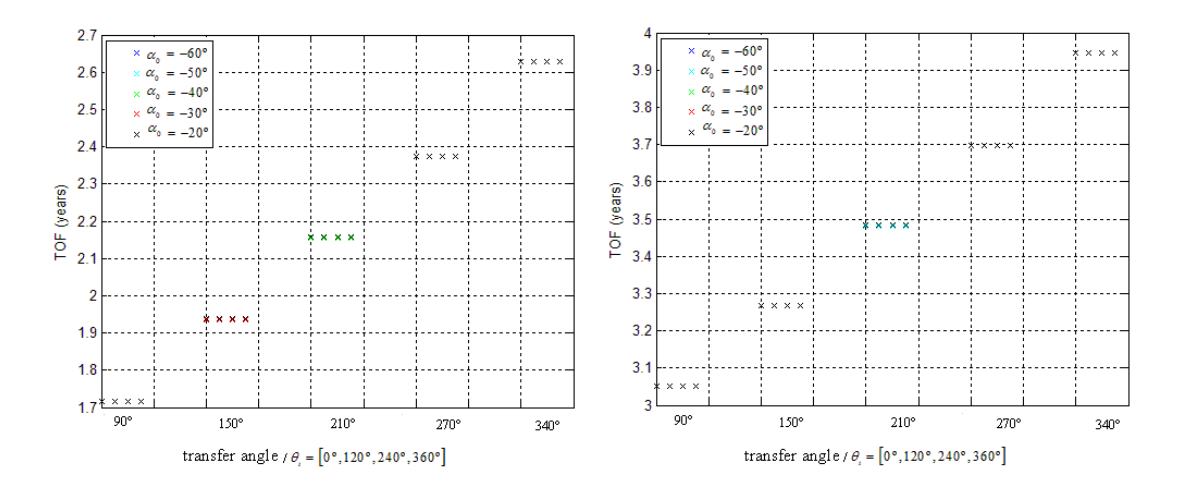


Figure 35: TOF for θ_i values of (0°, 120°, 240°, 360°) from left to right in the figure, α_0 values of (-60°, -50°, -40°, -30°, -20°), $\Delta\theta$ values of (90°, 150°, 210°, 270°, 340°), m=0.05, constant acceleration case of the thrust profile (logarithmic spiral), Earth-Mars flight, N=1 (a_0 =0.03) and N=2 (a_0 =0.02)

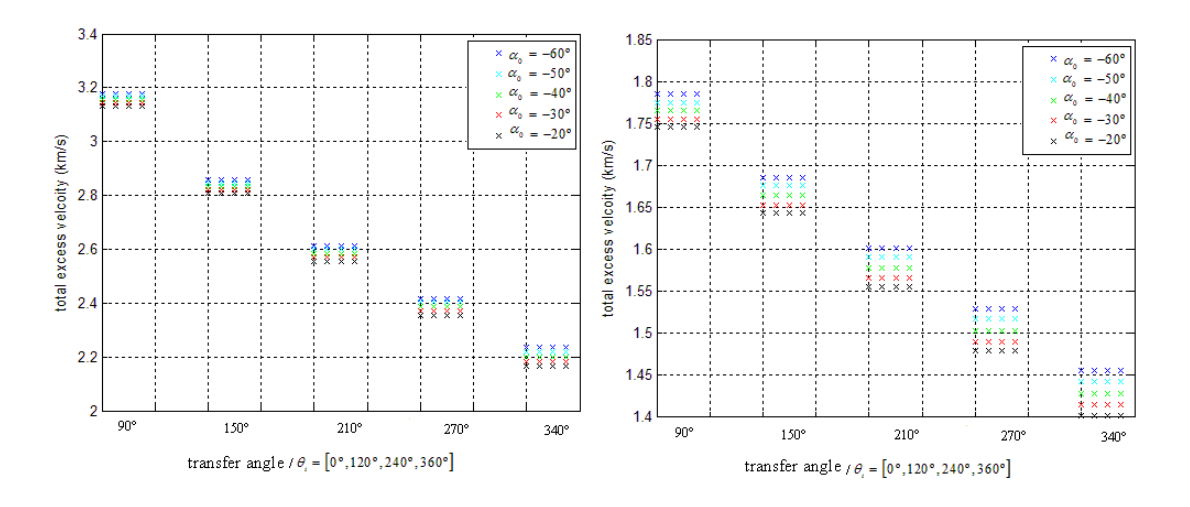


Figure 36: $V_{_{\circ,,T}}$ for $\theta_{_i}$ values of (0°, 120°, 240°, 360°) from left to right in the figure, $\alpha_{_0}$ values of (-60°, -50°, -40°, -30°, -20°), $\Delta\theta$ values of (90°, 150°, 210°, 270°, 340°), m=0.05, constant acceleration case of the thrust profile (logarithmic spiral), Earth-Mars flight, N=1 ($a_{_0}$ =0.03) and N=2 ($a_{_0}$ =0.02)

Similar remarks to the ones given for N=0 can be drawn for figures 12 and 13. As for N=0, the differences in the TOF and in total excess velocity between different θ_i for the same transfer angle and α_0 can be neglected. In this way, like for the Archimedean spiral, due to the significantly small influence that the parameter θ_i has in the TOF, in the total excess velocity and also, although not shown in the previous figures, in the thrust acceleration, this parameter would not be considered a variable in the optimization procedure.

The TOF range for this Earth-Mars flight is from 0.3798 years to 3.9452 years. The total excess velocity has a minimum value of 1.4021 km/s and a maximum value of 14.5984 km/s. The maximum differences in TOF between two consecutive values of the transfer angle $\Delta\theta$ are about 0.25 years. The differences in terms of total excess velocity between two consecutive transfer angles is always the highest one between $\Delta\theta = 90^{\circ}$ and $\Delta\theta = 150^{\circ}$. The maximum value for these differences is 5.5853 km/s for zero value of N and the minimum value is about 72.86 m/s for 2 revolutions.

Tables 3 and 4 show the values for the TOF and the excess velocities for an Earth-Mars flight. Parameter θ_i considered was 0°, parameter α_0 considered was -20°, the transfer angle $\Delta\theta$ considered was 90° and the number of revolutions taken was 1 for the first table and 2 for the second one. In tables 3 and 4, the normalized thrust acceleration a_0 was 0.03.

N=1	m = 0.05	m = 0.15	m = 0.25	m = 0.35	m = 0.45
$V_{\infty,total}\left(km/s\right)$	3.1337	3.0405	3.2302	3.6326	4.1674
$V_{\infty,1}(km/s)$	1.6349	1.0696	0.6815	0.4354	0.2931
$V_{\infty,2}(km/s)$	1.4987	1.9708	2.5487	3.1972	3.8743
TOF (years)	1.7166	1.6464	1.5841	1.5312	1.4883

Table 9: The excess velocities and the TOF values for N=1, θ_i =0°, $\Delta\theta$ =90°, α_0 =-20°, a_0 =0.03, m values of (0.05; 0.15; 0.25; 0.35; 0.45), constant acceleration case (logarithmic spiral), Earth-Mars flight

N=2	m = 0.05	m = 0.15	m = 0.25	m = 0.35	m = 0.45
$V_{\infty,total}\left(km/s\right)$	1.9389	2.0149	2.5141	3.2109	3.9482
$V_{\infty,1}(km/s)$	0.7810	0.3670	0.2056	0.1646	0.1558
$V_{\infty,2}(km/s)$	1.1580	1.6479	2.3085	3.0463	3.7923
TOF (years)	3.0260	2.8259	2.6739	2.5687	2.4984

Table 10: The excess velocities and the TOF values for N=2, θ_i =0°, $\Delta\theta$ =90°, α_0 =-20°, a_0 =0.03, m values of (0.05; 0.15; 0.25; 0.35; 0.45), constant acceleration case (logarithmic spiral), Earth-Mars flight

For increasing values of m, the total excess velocity increases (except for N=1, between m=0.05 and m=0.15), while the TOF decreases. The values for the total excess velocity are higher when N=1 than when N=2. Note that, the excess velocity $V_{\infty,1}$ decreases slower than the excess velocity $V_{\infty,2}$ increases (except for N=1, between m=0.05 and m=0.15). The value of $V_{\infty,2}$ when m=0.45 is more than 13 times higher than the value of $V_{\infty,1}$ for N=1 and more than 24 times higher for N=2.

In figures 14 to 17, the polar plot, the thrust angle α , the polar angle rate $\dot{\theta}$ and the flight path angle as function of time are illustrated for N=1 and N=2 cases (tables 3 and 4).

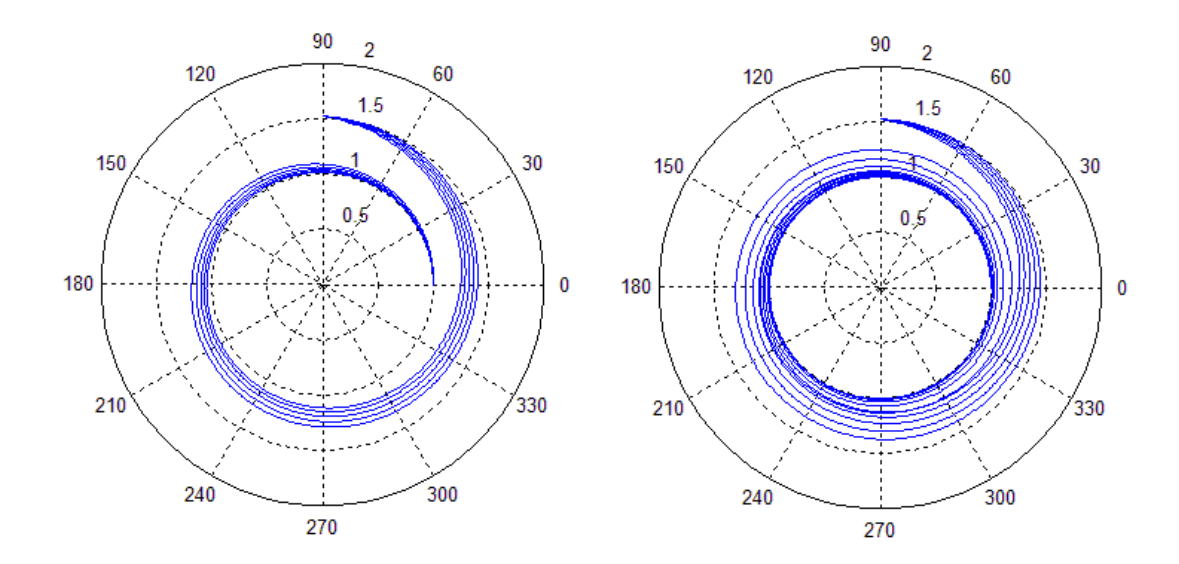


Figure 37: Polar plot for N=1 and N=2, θ_i =0°, $\Delta\theta$ =90°, α_0 =-20°, a_0 =0.03, m values of (0.05; 0.15; 0.25; 0.35; 0.45), constant acceleration case of the thrust profile (logarithmic spiral), Earth-Mars flight

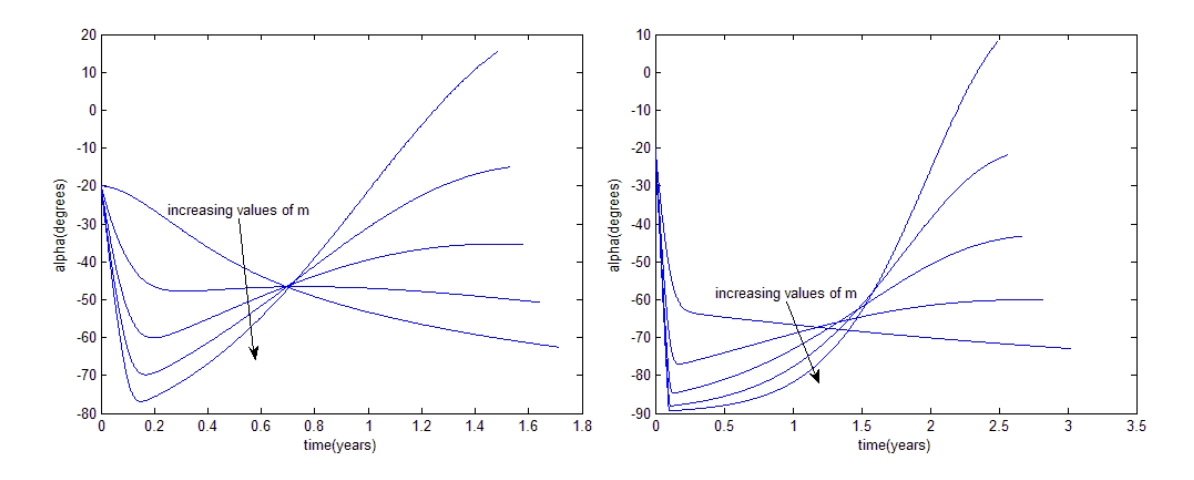


Figure 38: α plot for N=1 and N=2, θ_i =0°, $\Delta\theta$ =90°, α_0 =-20°, a_0 =0.03, m values of (0.05; 0.15; 0.25; 0.35; 0.45), constant acceleration case of the thrust profile (logarithmic spiral), Earth-Mars flight

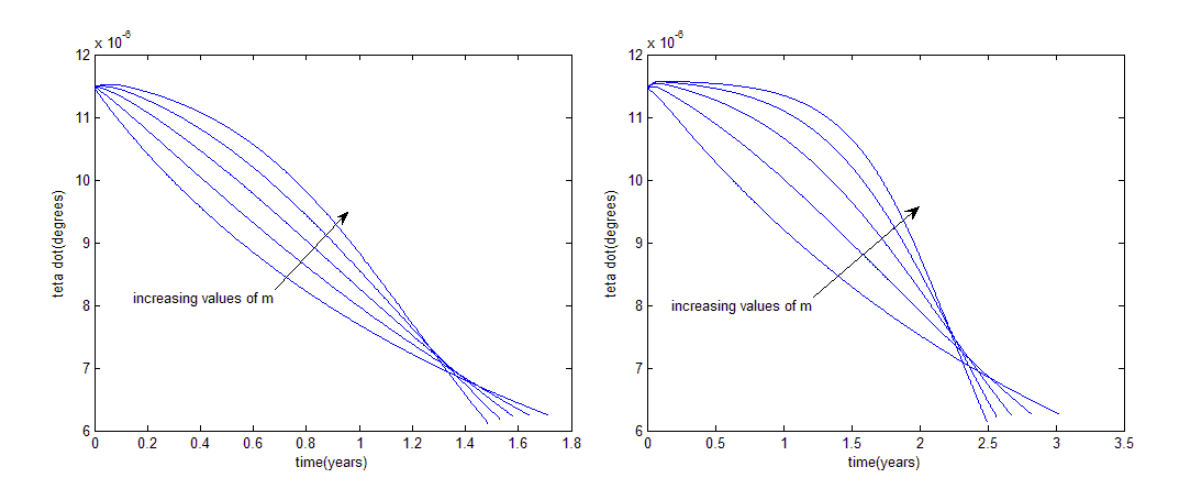


Figure 39: $\dot{\theta}$ plot for N=1 and N=2, θ_i =0°, $\Delta\theta$ =90°, α_0 =-20°, a_0 =0.03, m values of (0.05; 0.15; 0.25; 0.35; 0.45), constant acceleration case of the thrust profile (logarithmic spiral), Earth-Mars flight

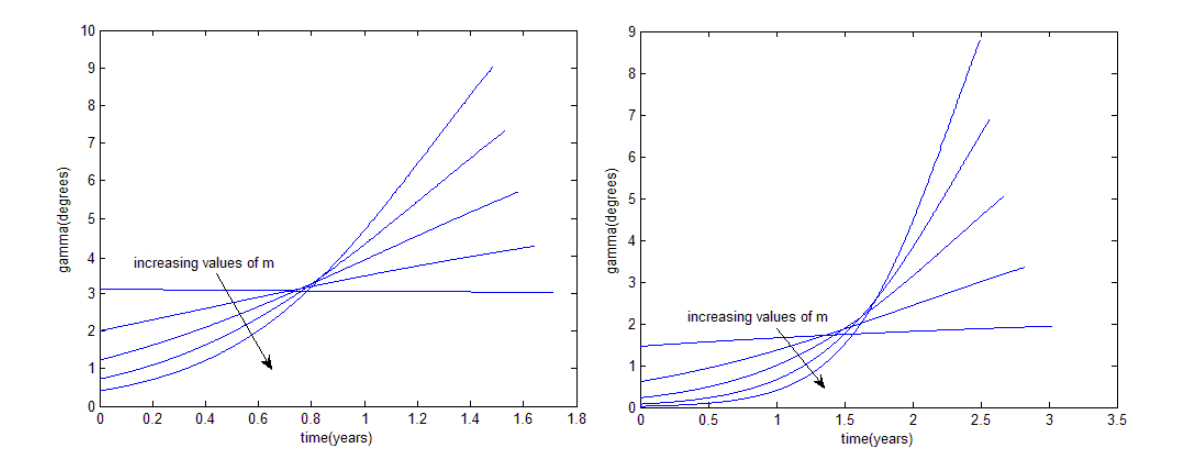


Figure 40: γ plot for N=1 and N=2, θ_i =0°, $\Delta\theta$ =90°, α_0 =-20°, a_0 =0.03, m values of (0.05; 0.15; 0.25; 0.35; 0.45), constant acceleration case of the thrust profile (logarithmic spiral), Earth-Mars flight

The values of the thrust angle α are higher for N=1 than for N=2. During the interplanetary flight for both cases in figure 15, the spacecraft is thrusting inwards in the radial direction, while in the tangential direction it thrusts in the positive direction (α is negative, higher than -90°), like for the Archimedean spiral. This situation was analysed in section 7.7. The magnitude values of the flight path angle γ are smaller for N=2 than for N=1.

3. Poinsot's spiral (hyperbolic sine)

In this section, results for the TOF, the excess velocities and the thrust acceleration will be shown and discussed for the Poinsot's spiral (hyperbolic sine). Figures 18 and 19 show the TOF and the total excess velocity when changing parameter $\theta_i + \phi$ and the transfer angle $\Delta\theta$, when the number of revolutions N is 0. The value used in figures 18 and 19 for the geometric parameter m was 0.6, the values used for the initial value of α were (-60°, -50°, -40°, -30°, -20°), for the angle $\theta_i + \phi$ were (120°, 200°, 280°, 360°) and for the transfer angle $\Delta\theta$ were (90°, 150°, 210°, 270°, 340°). Note that $\theta_i + \phi$ cannot be zero, otherwise $r = \infty$. The normalized thrust acceleration a_0 value used in figures 18 and 19 was 0.1.

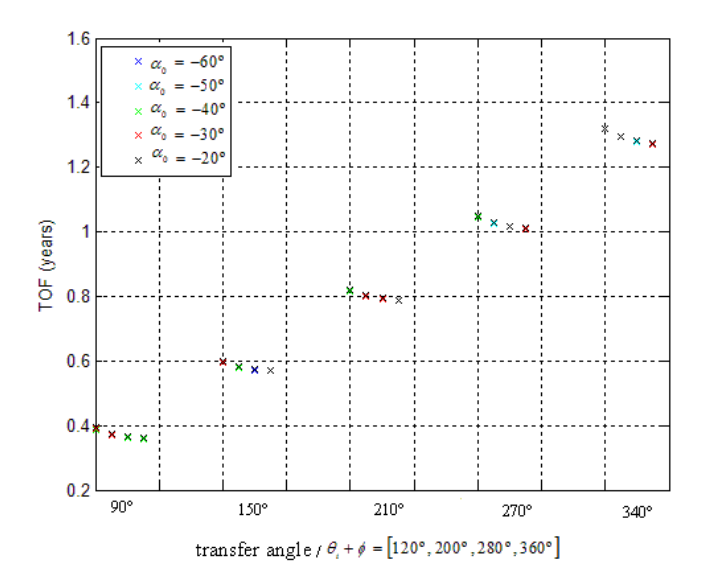


Figure 41: TOF for $\theta_i + \phi$ values of (120°, 200°, 280°, 360°) from left to right in the figure, α_0 values of (-60°, -50°, -40°, -30°, -20°), $\Delta\theta$ values of (90°, 150°, 210°, 270°, 340°) (N=0), m=0.6, a_0 =0.1, constant acceleration case of the thrust profile (Poinsot's spiral (hyperbolic sine)), Earth-Mars flight

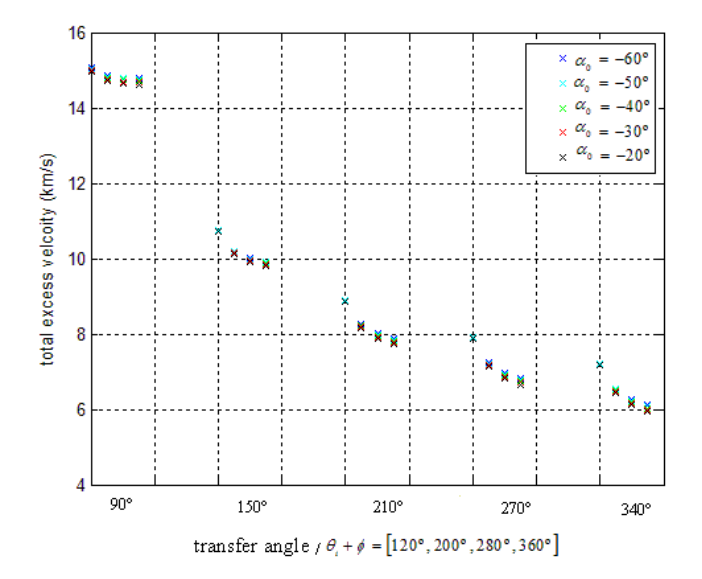


Figure 42: $V_{\infty,T}$ for $\theta_i + \phi$ values of (120°, 200°, 280°, 360°) from left to right in the figure, α_0 values of (-60°, -50°, -40°, -30°, -20°), $\Delta\theta$ values of (90°, 150°, 210°, 270°, 340°) (N=0), m=0.6, a_0 =0.1, constant acceleration case of the thrust profile (Poinsot's spiral (hyperbolic sine)), Earth-Mars flight

Some remarks can be drawn from figures 18 and 19. By increasing the combination of angles $\theta_i + \phi$, the TOF and the total excess velocity decrease. The highest difference in TOF and in total excess velocity between different $\theta_i + \phi$ occurs between $\theta_i + \phi = 120^\circ$ and $\theta_i + \phi = 200^\circ$. For higher values of $\theta_i + \phi$, the variations in TOF and in total excess velocity are significantly small. The highest difference in the TOF between different $\theta_i + \phi$ for the same phase angle and α_0 is about 0.0456 years, while the highest difference in the total excess velocity is about 1.2399 km/s. For increasing values of the initial thrust angle α_0 , the total excess velocity decreases, while the TOF increases.

Similar figures can be shown for 1 and 2 revolutions, using the same values for the geometric parameter m, for the transfer angle $\Delta\theta$ and for the initial values of α and $\theta_i + \phi$. The normalized thrust acceleration a_0 values used in figures 20 and 21 were 0.05 and 0.04 for N=1 and N=2, respectively.

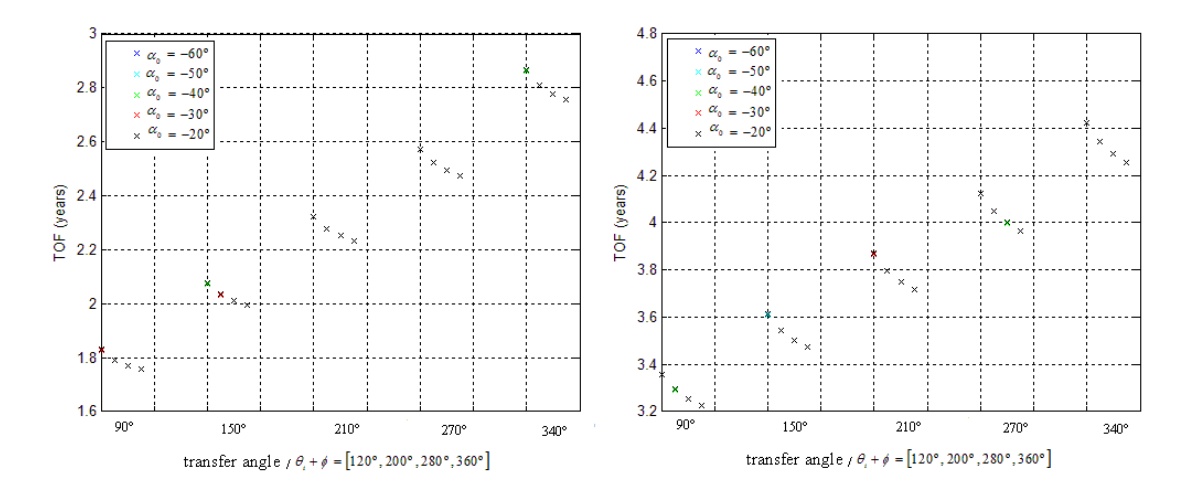


Figure 43: TOF for $\theta_i + \phi$ values of (120°, 200°, 280°, 360°) from left to right in the figure, α_0 values of (-60°, -50°, -40°, -30°, -20°), $\Delta\theta$ values of (90°, 150°, 210°, 270°, 340°), m=0.6, constant acceleration case (Poinsot's spiral (hyperbolic sine), Earth-Mars flight, N=1 (a_0 =0.05) and N=2 (a_0 =0.04)

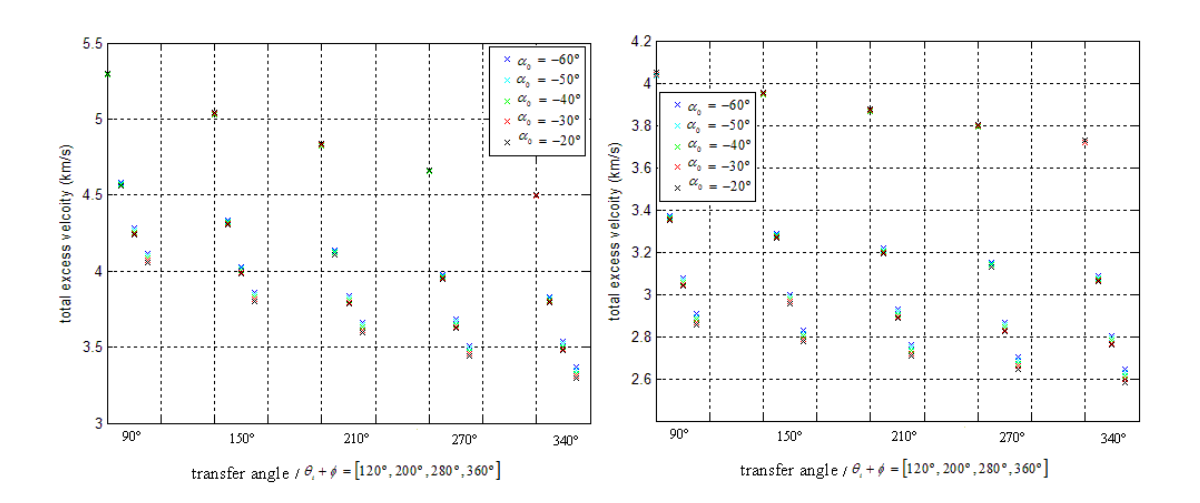


Figure 44: $V_{_{\circ,T}}$ for $\theta_{_{!}}+\phi$ values of (120°, 200°, 280°, 360°) from left to right in the figure, $\alpha_{_{0}}$ values of (-60°, -50°, -40°, -30°, -20°), $\Delta\theta$ values of (90°, 150°, 210°, 270°, 340°), m=0.6, constant acceleration case (Poinsot's spiral (hyperbolic sine), Earth-Mars flight, N=1 ($a_{_{0}}$ =0.05) and N=2 ($a_{_{0}}$ =0.04)

Similar remarks to ones given for N=0 can be drawn for figures 20 and 21. Note that the variation in total excess velocity between $\theta_i + \phi = 120^\circ$ and $\theta_i + \phi = 200^\circ$ is considerably higher for N=1 and N=2 than for N=0. For N=1, the highest difference in TOF between different $\theta_i + \phi$ and for the same transfer angle and α_0 is 0.1067 years, while the highest difference in the total excess velocity is 1.2456 km/s. For N=2, the highest difference in

TOF between different $\theta_i + \phi$ and for the same transfer angle and α_0 is 0.1655 years, while the highest difference in the total excess velocity is 1.1920 km/s.

The TOF range for this Earth-Mars flight is from 0.3582 years to 4.0485 years. The total excess velocity has a minimum value of $2.5842 \, km/s$ and a maximum value of $15.0523 \, km/s$. The maximum differences in TOF between two consecutive values of the transfer angle $\Delta\theta$ are about 0.3 years and for a certain number of revolutions, these differences increase when increasing the transfer angle. The differences in terms of total excess velocity between two consecutive transfer angles is always the highest one between $\Delta\theta = 90^{\circ}$ and $\Delta\theta = 150^{\circ}$. The maximum value for these differences is $4.8602 \, km/s$ for N=0 and the minimum value is about $59 \, m/s$ for 2 revolutions.

Tables 5 and 6 show the values for the TOF and the excess velocities for an Earth-Mars flight. Parameter $\theta_i + \phi$ was considered 120°, parameter α_0 was considered -20°, the transfer angle $\Delta\theta$ was considered 90° and the number of revolutions was taken 1 for the first table and 2 for the second one. In table 5 the normalized thrust acceleration a_0 was 0.05, while in table 6, this parameter was 0.04. Note that these values for a_0 , for N=1 and N=2 are the minimum values that can be used in both cases for this shape without facing integration problems for the interval of input parameters considered.

N=1	m = 0.01	m = 0.11	m = 0.21	m = 0.31	m = 0.41
$V_{\infty,total}\left(km/s\right)$	5.3020	5.0473	4.6156	4.2441	3.9823
$V_{\infty,1}(km/s)$	3.8225	3.4865	2.9270	2.4680	2.1601
$V_{\infty,2}(km/s)$	1.4795	1.5608	1.6885	1.7760	1.8222
TOF (years)	1.8297	1.8000	1.7559	1.7249	1.7071

Table 11: The excess velocities and the TOF values for N=1, $\theta_i + \phi = 120^\circ$, $\Delta\theta = 90^\circ$, $\alpha_0 = -20^\circ$, $a_0 = 0.05$, m values of (0.01; 0.11; 0.21; 0.31; 0.41), constant acceleration case (Poinsot's spiral (hyperbolic sine), Earth-Mars flight

N=2	m = 0.01	m = 0.11	m = 0.21	m = 0.31	m = 0.41
$V_{\infty,total}\left(km/s\right)$	4.0485	3.6050	3.0692	2.7283	2.5287
$V_{\infty,1}(km/s)$	2.9203	2.4177	1.8182	1.4476	1.2351
$V_{\infty,2}(km/s)$	1.1282	1.1873	1.2510	1.2807	1.2937
TOF (years)	3.3588	3.2524	3.1469	3.0953	3.0714

Table 12: The excess velocities and the TOF values for N=2, $\theta_i + \phi = 120^\circ$, $\Delta\theta = 90^\circ$, $\alpha_0 = -20^\circ$, $a_0 = 0.04$, m values of (0.01; 0.11; 0.21; 0.31; 0.41), constant acceleration case (Poinsot's spiral (hyperbolic sine), Earth-Mars flight

For increasing values of m, the total excess velocity and the TOF decrease. The values for the total excess velocity are higher when N=1 than when N=2. Note that the excess velocity $V_{\infty,1}$ decreases faster than the excess velocity $V_{\infty,2}$ increases.

In figures 22 to 25, the polar plot, the thrust angle α , the polar angle rate $\dot{\theta}$ and the flight path angle as function of time are illustrated for N=1 and N=2 cases that were presented in tables 5 and 6.

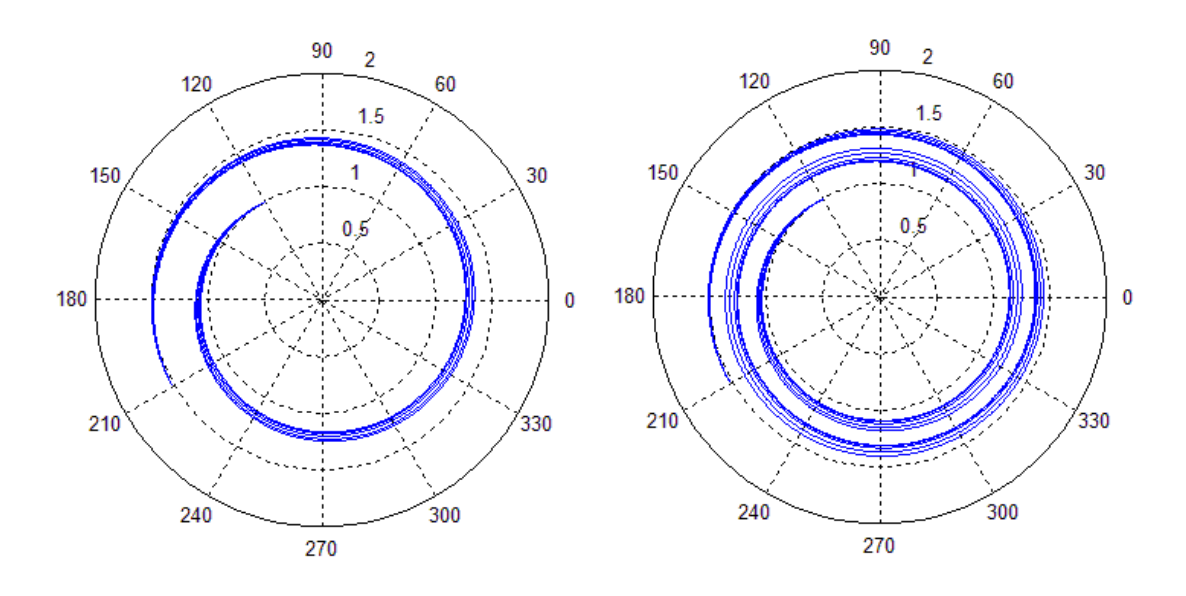


Figure 45: Polar plot for N=1 (a_0 =0.05) and N=2 (a_0 =0.04), θ_i + ϕ =120°, $\Delta\theta$ =90°, α_0 =-20°, a_0 =0.04, m values of (0.01; 0.11; 0.21; 0.31; 0.41), constant acceleration case (Poinsot's spiral (hyperbolic sine)), Earth-Mars flight

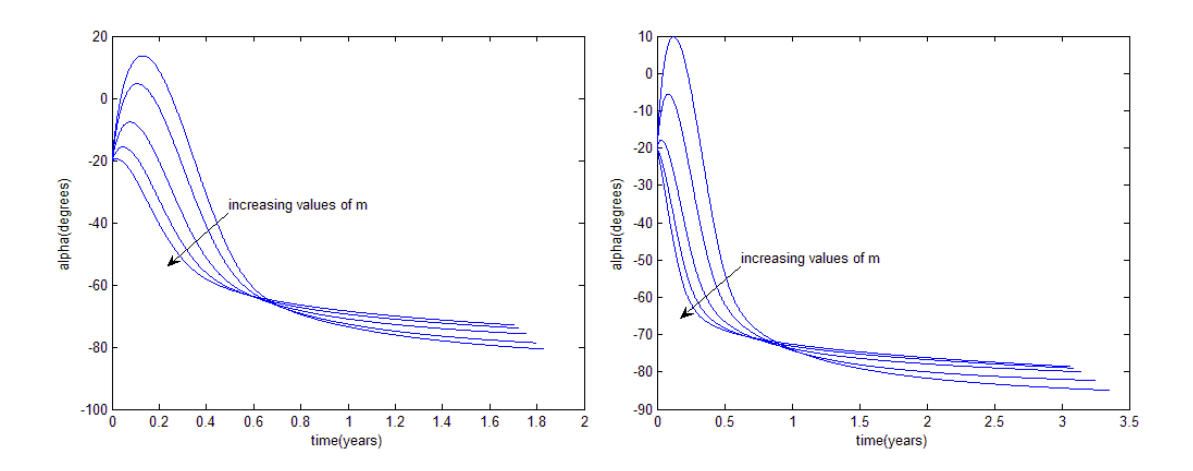


Figure 46: α plot for N=1 (a_0 =0.05) and N=2 (a_0 =0.04), θ_i + ϕ =120°, $\Delta\theta$ =90°, α_0 =-20°, a_0 =0.04, m values of (0.01; 0.11; 0.21; 0.31; 0.41), constant acceleration case (Poinsot's spiral (hyperbolic sine)), Earth-Mars flight

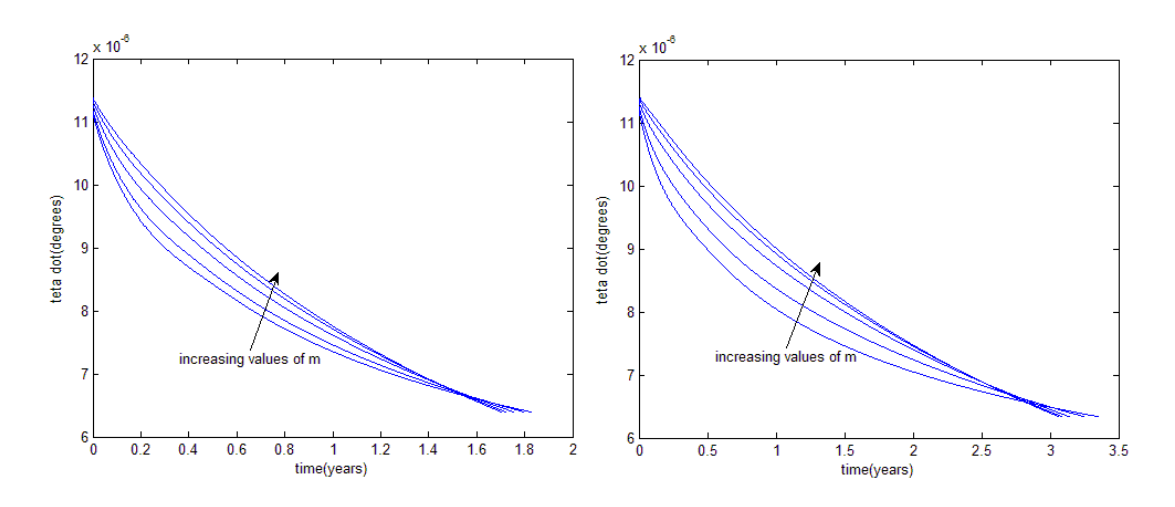


Figure 47: $\dot{\theta}$ plot for N=1 ($a_{_0}$ =0.05) and N=2 ($a_{_0}$ =0.04), $\theta_{_i}$ + ϕ =120°, $\Delta\theta$ =90°, $\alpha_{_0}$ =-20°, $a_{_0}$ =0.04, m values of (0.01; 0.11; 0.21; 0.31; 0.41), constant acceleration case (Poinsot's spiral (hyperbolic sine)), Earth-Mars flight

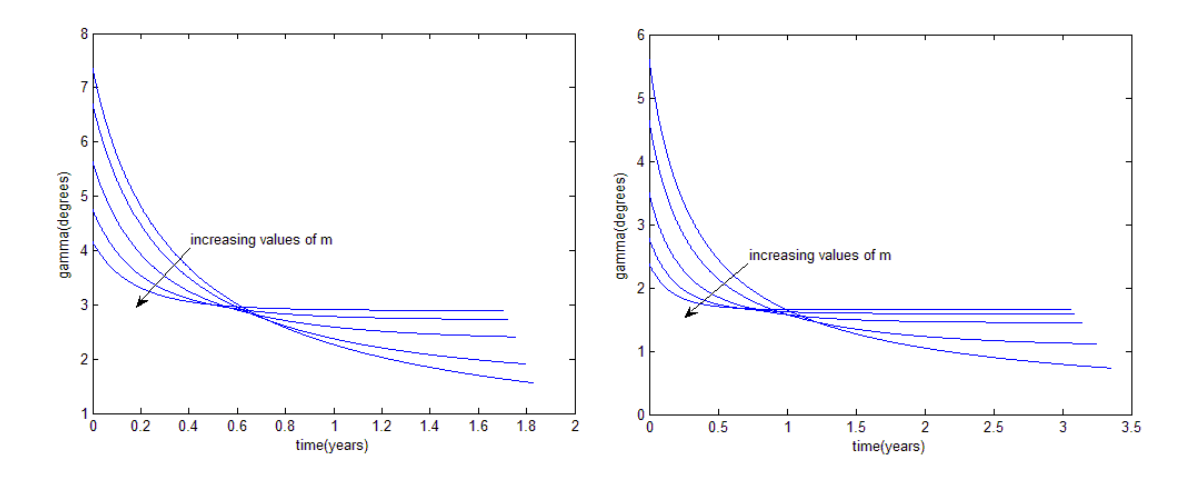


Figure 48: γ plot for N=1 (a_0 =0.05) and N=2 (a_0 =0.04), θ_i + ϕ =120°, $\Delta\theta$ =90°, α_0 =-20°, a_0 =0.04, m values of (0.01; 0.11; 0.21; 0.31; 0.41), constant acceleration case (Poinsot's spiral (hyperbolic sine)), Earth-Mars flight

The values of the thrust angle α are higher for N=1 than for N=2. For most of the interplanetary flight for both cases in figure 23, the spacecraft is thrusting inwards in the radial direction, while in the tangential direction it thrusts in the positive direction (α is negative, higher than -90°), like for the other 2 shapes. The magnitude values of the flight path angle γ are smaller for N=2 than for N=1.

4. Poinsot's spiral (hyperbolic cosine)

In this section, results for the TOF, the excess velocities and the thrust acceleration will be shown and discussed for the Poinsot's spiral (hyperbolic cosine). Figures 26 and 27 show the TOF and the total excess velocity when changing parameter θ_i and the transfer angle $\Delta\theta$ (N=0). The value used in figures 26 and 27 for m was 0.05; the values used for α_0 were (-60°, -50°, -40°, -30°, -20°), for θ_i were (30°, 140°, 250°, 360°) and for $\Delta\theta$ were (90°, 150°, 210°, 270°, 340°). The normalized thrust acceleration a_0 value used in figures 26 and 27 was 0.07.

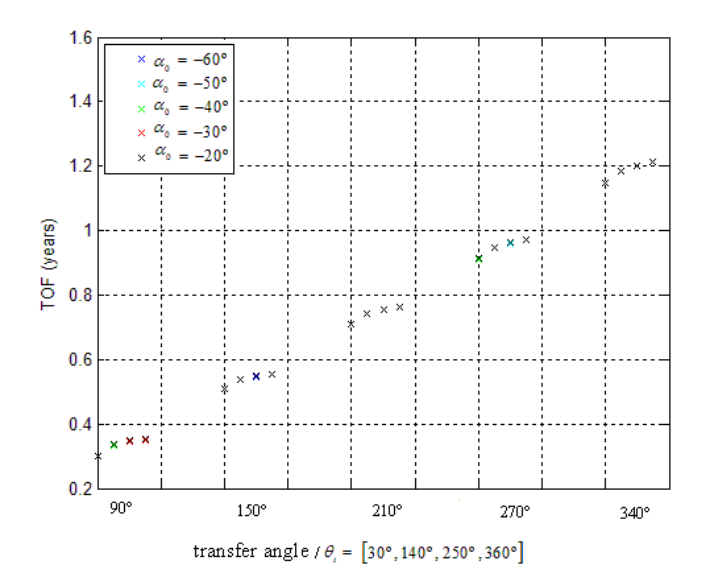


Figure 49: TOF for θ_i values of (30°, 140°, 250°, 360°) from left to right in the figure, α_0 values of (-60°, -50°, -40°, -30°, -20°), $\Delta\theta$ values of (90°, 150°, 210°, 270°, 340°) (N=0), m=0.05, a_0 =0.07, constant acceleration case (Poinsot's spiral (hyperbolic cosine)), Earth-Mars flight

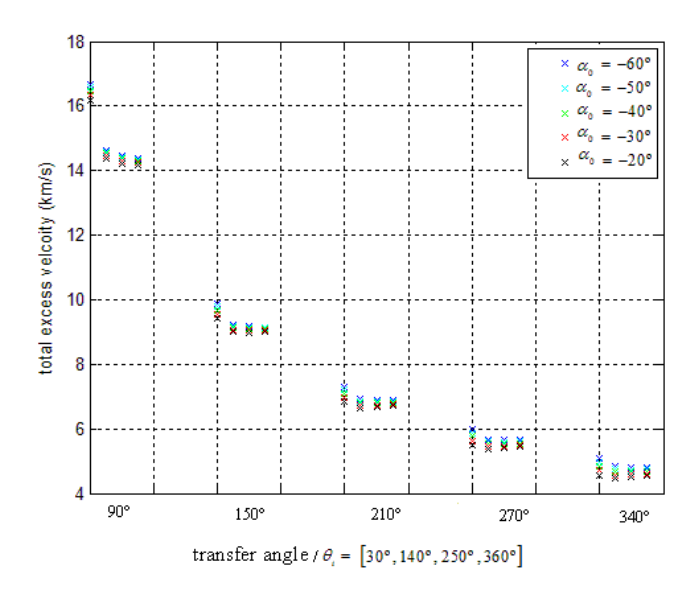


Figure 50: $V_{_{\circ,T}}$ for $\theta_{_{i}}$ values of (30°, 140°, 250°, 360°) from left to right in the figure, $\alpha_{_{0}}$ values of (-60°, -50°, -40°, -30°, -20°), $\Delta\theta$ values of (90°, 150°, 210°, 270°, 340°) (N=0), m=0.05, $a_{_{0}}$ =0.07, constant acceleration case (Poinsot's spiral (hyperbolic cosine)), Earth-Mars flight

Some remarks can be drawn from figures 26 and 27. By increasing the initial polar angle θ_i , the TOF increases while the total excess velocity decreases. The highest variation in TOF and in total excess velocity when changing θ_i is between $\theta_i = 30^{\circ}$ and $\theta_i = 140^{\circ}$.

This variation becomes smaller for higher values of the transfer angle $\Delta\theta$. The highest difference in TOF between different θ_i for the same phase angle and α_0 is 0.0649 years, while the highest difference in total excess velocity is $2.2820 \, km/s$. For increasing values of α_0 , the total excess velocity decreases and the TOF increases.

Similar figures can be shown for 1 and 2 revolutions, using the same values for the geometric parameter m, for the transfer angle $\Delta\theta$ and for the initial values of α and θ . The normalized thrust acceleration a_0 values used in figures 28 and 29 were 0.03 and 0.02 for N=1 and N=2, respectively.

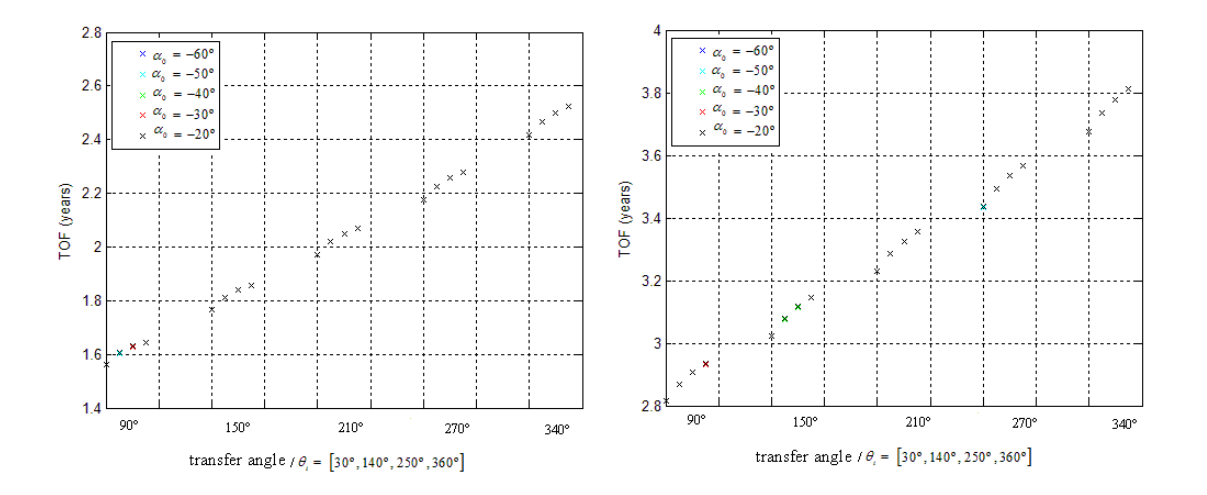


Figure 51: TOF for θ_i values of (30°, 140°, 250°, 360°) from left to right in the figure, α_0 values of (-60°, -50°, -40°, -30°, -20°), $\Delta\theta$ values of (90°, 150°, 210°, 270°, 340°), m=0.05, constant acceleration case (Poinsot's spiral (hyperbolic cosine)), Earth-Mars flight, N=1 (α_0 =0.03) and N=2 (α_0 =0.02)

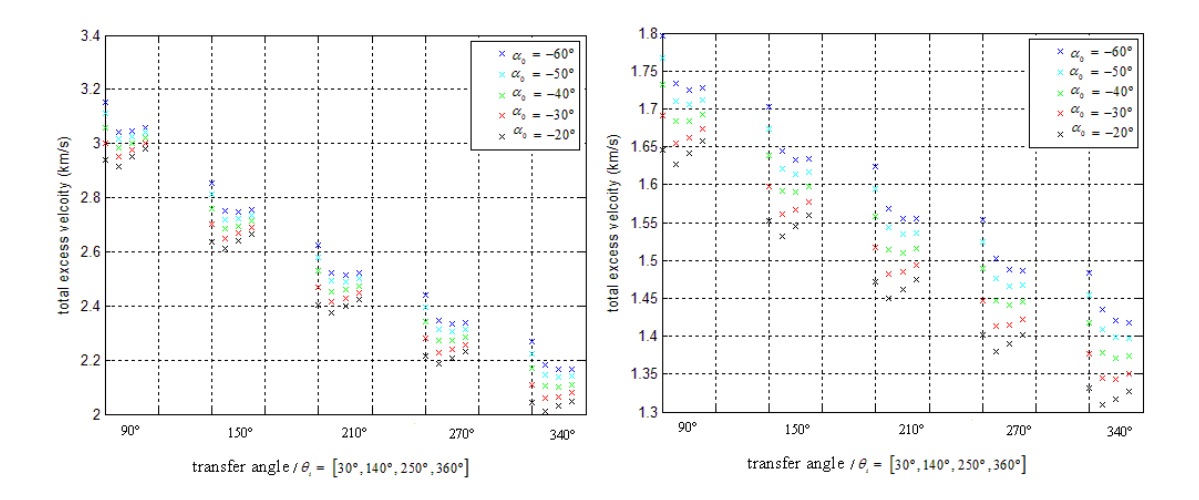


Figure 52: $V_{\omega,T}$ for θ_i values of (30°, 140°, 250°, 360°) from left to right in the figure, α_0 values of (-60°, -50°, -40°, -30°, -20°), $\Delta\theta$ values of (90°, 150°, 210°, 270°, 340°), m=0.05, constant acceleration case (Poinsot's spiral (hyperbolic cosine)), Earth-Mars flight, N=1 (α_0 =0.03) and N=2 (α_0 =0.02)

Note that for N=1 and N=2, the differences in the total excess velocity between different values of α_0 are higher than for N=0. Also, in figure 32, when increasing θ_i , the total excess velocity trend is not monotone, unlike for N=0. For N=1, the highest difference in TOF between different θ_i and for the same transfer angle and α_0 is 0.1083 years, while the highest difference in the total excess velocity is $0.1100 \, km/s$. For N=2, the highest difference in TOF between different θ_i and for the same transfer angle and α_0 is 0.1307 years, while the highest difference in total excess velocity is $71.4032 \, m/s$.

The TOF range for this Earth-Mars flight is from 0.2987 years to 3.8112 years. The total excess velocity has a minimum value of $1.3095\,km/s$ and a maximum value of $16.6611\,km/s$. The maximum differences in TOF between two consecutive values of the transfer angle $\Delta\theta$ are about 0.25 years and for a certain number of revolutions, these differences increase when increasing the transfer angle. The differences in terms of total excess velocity between two consecutive transfer angles is always highest between $\Delta\theta = 90^{\circ}$ and $\Delta\theta = 150^{\circ}$. The maximum value for these differences is $6.8028\,km/s$ for N=0 and the minimum value is about $66.0646\,m/s$ for two revolutions.

Tables 7 and 8 show the values for the TOF and the excess velocity for an Earth-Mars flight. Parameter θ_i was assumed 30°, parameter α_0 was assumed -20°, the transfer angle $\Delta\theta$ was assumed 90° and the number of revolutions was taken 1 for the first table and 2 for the second one. In table 7, the normalized thrust acceleration a_0 was 0.03, while in table 8, this parameter was 0.02. Note that these values for a_0 for N=1 and N=2 are the minimum values that can be used in both cases for this shape without facing integration problems for the interval of input parameters considered.

N=1	m = 0.01	m = 0.11	m = 0.21	m = 0.31	m = 0.41
$V_{\infty,total}\left(km/s\right)$	2.9391	2.7213	2.4838	2.3879	2.3819
$V_{\infty,1}(km/s)$	0.3869	0.4197	0.4907	0.5787	0.6723
$V_{\infty,2}(km/s)$	2.5522	2.3016	1.9932	1.8092	1.7096
TOF (years)	1.5615	1.5788	1.6074	1.6322	1.6504

Table 13: The excess velocities and the TOF values for N=1, θ_i =30°, $\Delta\theta$ =90°, α_0 =-20°, m values of (0.01; 0.11; 0.21; 0.31; 0.41), a_0 =0.03, constant acceleration case of the thrust profile (Poinsot's spiral (hyperbolic cosine)), Earth-Mars flight

N=2	m = 0.01	m = 0.11	m = 0.21	m = 0.31	m = 0.41
$V_{\infty,total}\left(km/s\right)$	1.6461	1.3943	1.2833	1.2801	1.3091
$V_{\infty,1}(km/s)$	0.1727	0.2003	0.2503	0.3056	0.3614
$V_{\infty,2}(km/s)$	1.4734	1.1940	1.0331	0.9745	0.9478
TOF (years)	2.8152	2.8865	2.9593	3.0021	3.0276

Table 14: The excess velocities and the TOF values for N=2, θ_i =30°, $\Delta\theta$ =90°, α_0 =-20°, m values of (0.01; 0.11; 0.21; 0.31; 0.41), a_0 =0.02, constant acceleration case of the thrust profile (Poinsot's spiral (hyperbolic cosine)), Earth-Mars flight

From tables 7 and 8, the order of magnitude of the total excess velocity values are $10^0 \, km/s$. For increasing values of m, the total excess velocity decreases, while the TOF increases for N=1. For N=2, the total excess velocity decreases until m = 0.31 and

increases between m = 0.31 and m = 0.41, while the TOF increases like for N=1. The values for the total excess velocity are higher when N=1 than when N=2. Note that the excess velocity $V_{\infty,2}$ decreases faster than the excess velocity $V_{\infty,1}$ increases, except for N=2 between m = 0.31 and m = 0.41.

In figures 30 to 33, the polar plot, the thrust angle α , the polar angle rate $\dot{\theta}$ and the flight path angle in function of time are illustrated for N=1 and N=2 cases that were presented in tables 7 and 8.

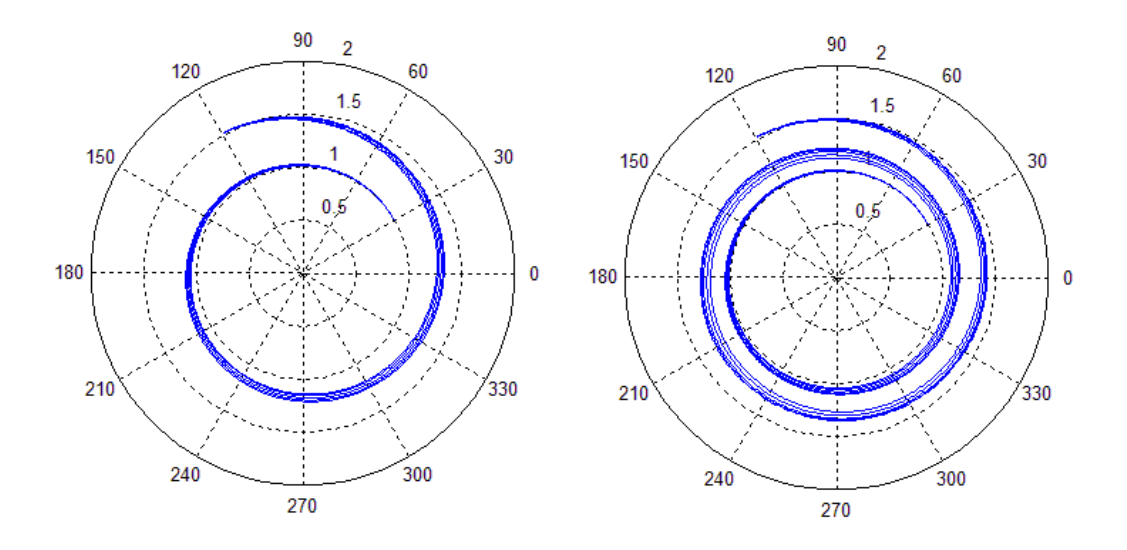


Figure 53: Polar plot for N=1 (a_0 =0.03) and N=2 (a_0 =0.02), θ_i =30°, $\Delta\theta$ =90°, α_0 =-20°, m values of (0.01; 0.11; 0.21; 0.31; 0.41), constant acceleration case (Poinsot's spiral (hyperbolic cosine)), Earth to Mars

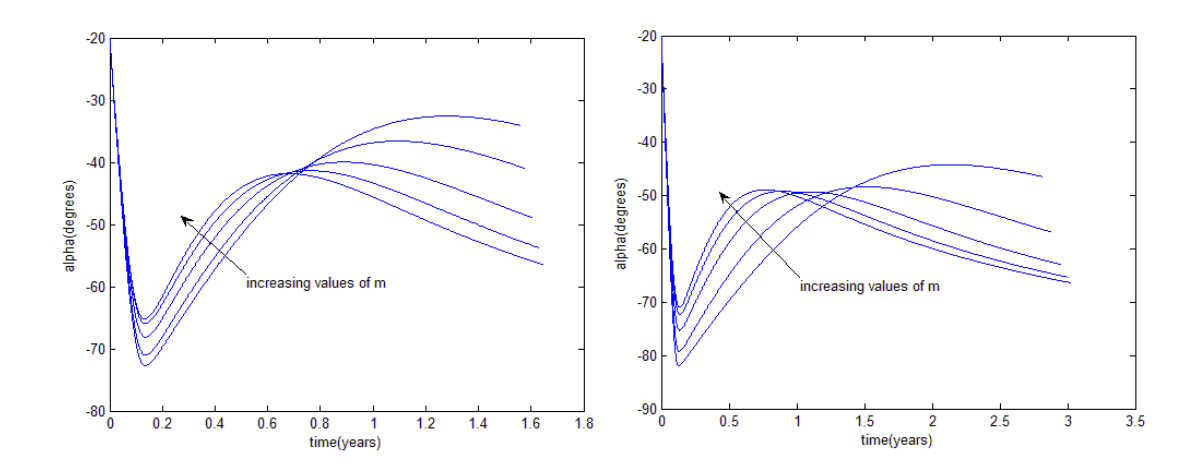


Figure 54: α plot for N=1 (a_0 =0.03) and N=2 (a_0 =0.02), θ_i =30°, $\Delta\theta$ =90°, α_0 =-20°, m values of (0.01; 0.11; 0.21; 0.31; 0.41), constant acceleration case (Poinsot's spiral (hyperbolic cosine)), Earth to Mars

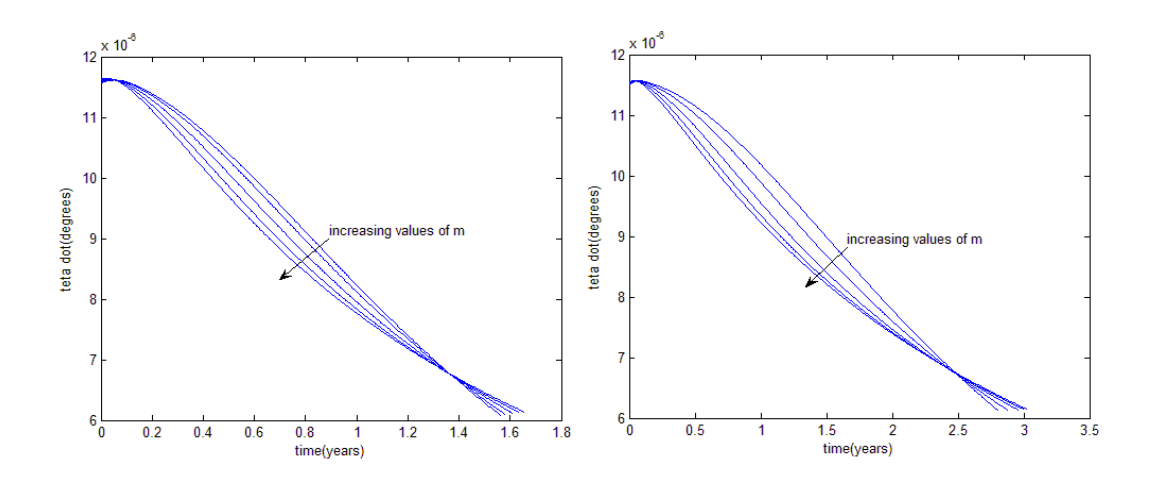


Figure 55: $\dot{\theta}$ plot for N=1 (a_0 =0.03) and N=2 (a_0 =0.02), θ_i =30°, $\Delta\theta$ =90°, α_0 =-20°, m values of (0.01; 0.11; 0.21; 0.31; 0.41), constant acceleration case (Poinsot's spiral (hyperbolic cosine)), Earth to Mars

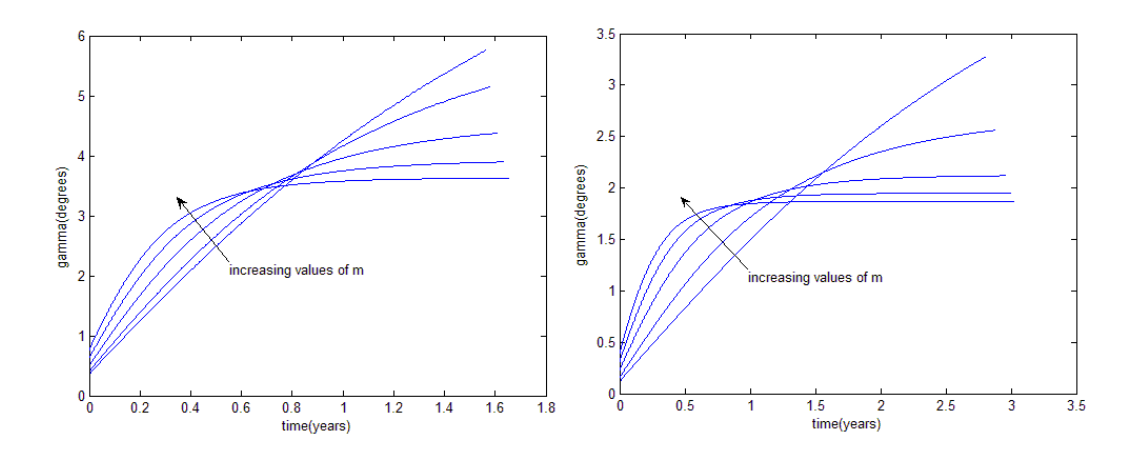


Figure 56: γ plot for N=1 (a_0 =0.03) and N=2 (a_0 =0.02), θ_i =30°, $\Delta\theta$ =90°, α_0 =-20°, m values of (0.01; 0.11; 0.21; 0.31; 0.41), constant acceleration case (Poinsot's spiral (hyperbolic cosine)), Earth to Mars

Similar remarks to the ones given for the previous shapes can be given.

5. Sinusoidal spiral

In this section, results for the TOF, the excess velocities and the thrust acceleration will be shown and discussed for the sinusoidal spiral. Figures 34 and 35 show the TOF and the total excess velocity when changing parameter θ_i and the transfer angle $\Delta\theta$, when the number of revolutions N is 0. The value used in figures 34 and 35 for the geometric parameter m was 0.05, the values used for the initial value of α were (-60°, -50°, -40°, -30°, -20°), for θ_i were (120°, 200°, 280°, 360°) and for $\Delta\theta$ were (90°, 150°, 210°, 270°, 340°). The normalized thrust acceleration a_0 value used in figures 34 and 35 was 0.07.

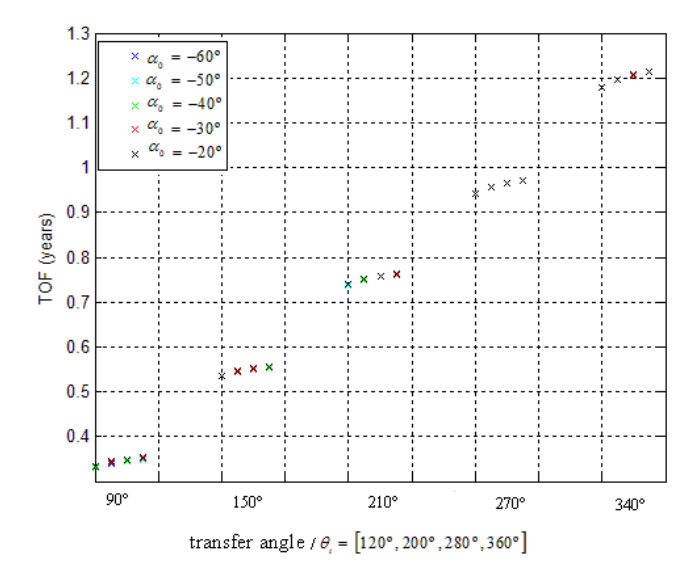


Figure 57: TOF for θ_i values of (120°, 200°, 280°, 360°) from left to right in the figure, α_0 values of (-60°, -50°, -40°, -30°, -20°), $\Delta\theta$ values of (90°, 150°, 210°, 270°, 340°) (N=0), m=0.05, a_0 =0.07, constant acceleration case (sinusoidal spiral), Earth-Mars flight

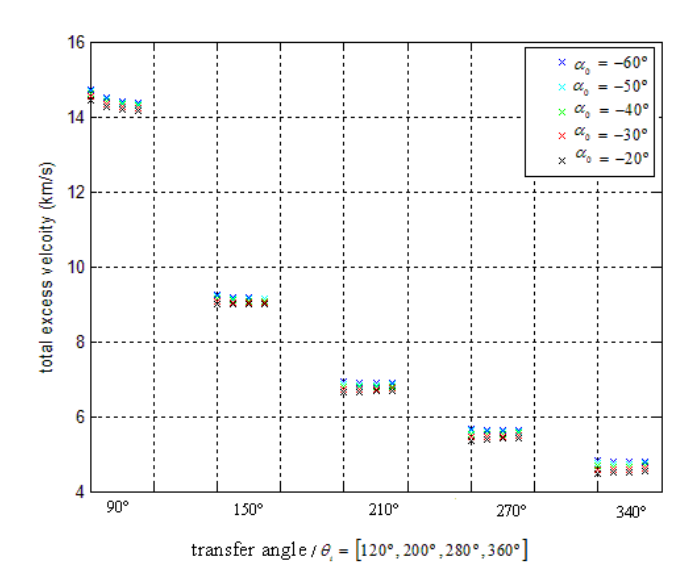


Figure 58: $V_{\omega,T}$ for θ_i values of (120°, 200°, 280°, 360°) from left to right in the figure, α_0 values of (-60°, -50°, -40°, -30°, -20°), $\Delta\theta$ values of (90°, 150°, 210°, 270°, 340°) (N=0), m=0.05, a_0 =0.07, constant acceleration case (sinusoidal spiral), Earth-Mars flight

Some remarks can be drawn from figures 34 and 35. As expected, the TOF increases when increasing the transfer angle, while the total excess velocity decreases. By increasing the initial polar angle θ_i , the TOF increases while the total excess velocity decreases. The

differences in TOF and in total excess velocity between different values of θ_i , decreases for higher values of the initial polar angle. The highest difference in TOF between different θ_i for the same phase angle and α_0 is 0.0332 years, while the highest difference in the total excess velocity is 0.3371km/s. For higher values of α_0 , the total excess velocity decreases, while the TOF increases.

Similar figures can be shown for 1 and 2 revolutions, using the same values for the geometric parameter m, for the transfer angle $\Delta\theta$ and for the initial values of α and θ . The normalized thrust acceleration a_0 value used in figures 36 and 37 was 0.02.

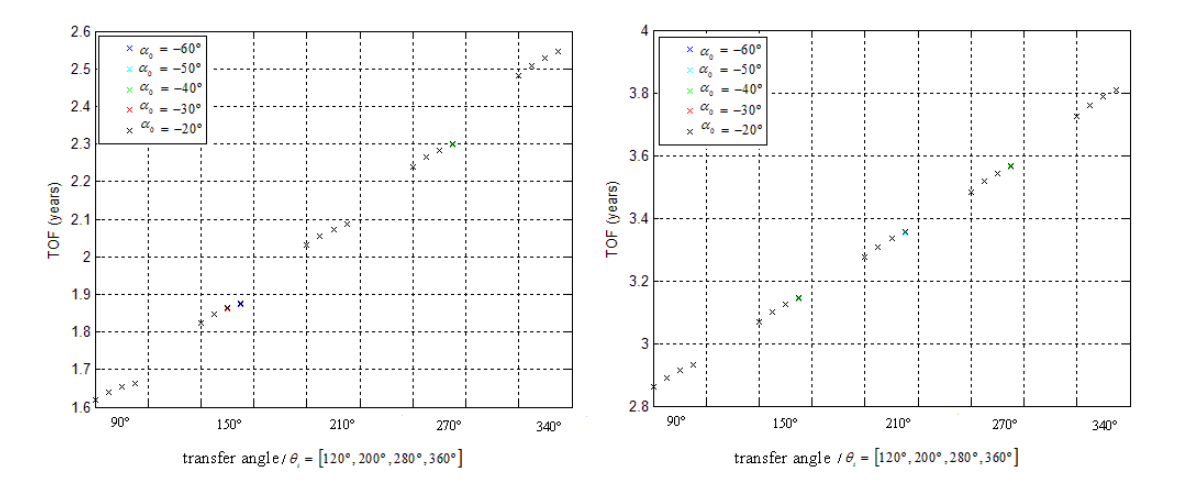


Figure 59: TOF for θ_i values of (120°, 200°, 280°, 360°) from left to right in the figure, α_0 values of (-60°, -50°, -40°, -30°, -20°), $\Delta\theta$ values of (90°, 150°, 210°, 270°, 340°), m=0.05, constant acceleration case (sinusoidal spiral), Earth-Mars flight, N=1 (a_0 =0.02) and N=2 (a_0 =0.02)

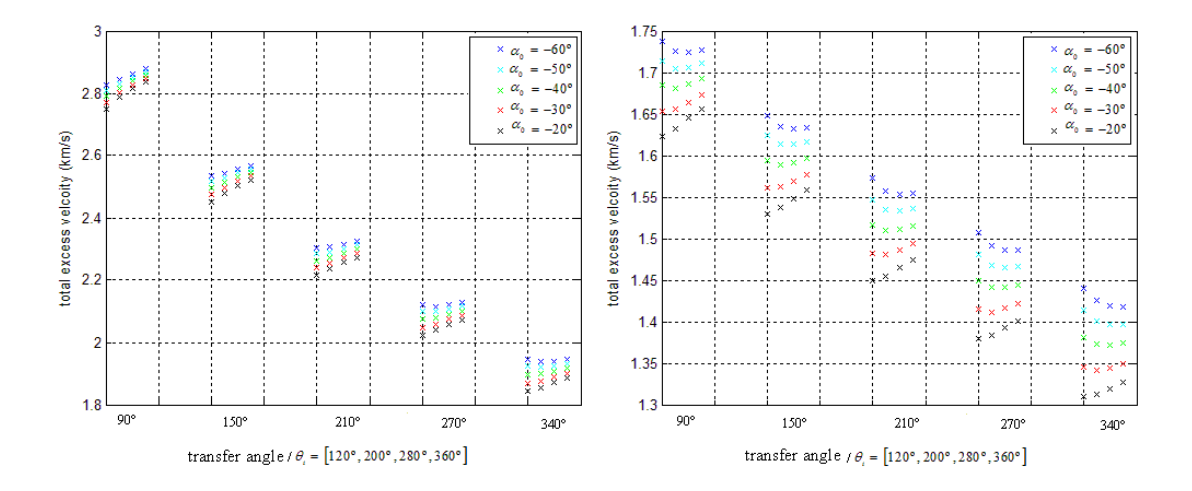


Figure 60: $V_{\omega,T}$ for θ_i values of (120°, 200°, 280°, 360°) from left to right in the figure, α_0 values of (-60°, -50°, -40°, -30°, -20°), $\Delta\theta$ values of (90°, 150°, 210°, 270°, 340°), m=0.05, constant acceleration case (sinusoidal spiral), Earth-Mars flight, N=1 (α_0 =0.02) and N=2 (α_0 =0.02)

From figures 36 and 37, the differences in the total excess velocity between different values of α_0 increase with the number of revolutions. For N=1, the highest difference in TOF between different θ_i for the same transfer angle and α_0 is about 0.0631 years, while the highest difference in total excess velocity is $87.6342 \, m/s$. For N=2, the highest difference in TOF between different θ_i for the same transfer angle is about 0.0823 years, while the highest difference in total excess velocity is $33.1082 \, m/s$.

The TOF range for this Earth-Mars flight is from 0.3311 years to 3.8103 years. The total excess velocity has a minimum value of $1.3107 \, km/s$ and a maximum value of $14.7125 \, km/s$. The maximum differences in TOF between two consecutive values of the transfer angle $\Delta \theta$ are about 0.25 years. For a certain number of revolutions, these differences increase when increasing the transfer angle. The differences in terms of total excess velocity between two consecutive transfer angles is always the highest one between $\Delta \theta = 90^{\circ}$ and $\Delta \theta = 150^{\circ}$. The maximum value for these differences is $6.8642 \, km/s$ for N=0 and the minimum value is about $71 \, m/s$ for N=2.

Tables 9 and 10 show the values for the TOF and the excess velocity for an Earth-Mars flight. Parameter θ_i was consider 30°, parameter α_0 was consider -20°, the transfer angle

 $\Delta\theta$ was consider 90° and the number of revolutions was taken 1 for the first table and 2 for the second one. In tables 9 and 10, the normalized thrust acceleration a_0 was 0.02.

N=1	m = 0.01	m = 0.055	m = 0.1	m = 0.145	m = 0.19
$V_{\infty,total}\left(km/s\right)$	2.7498	2.7044	2.6154	2.4829	2.3067
$V_{\infty,1}(km/s)$	0.6095	0.6281	0.6673	0.7322	0.8322
$V_{\infty,2}\left(km/s\right)$	2.1402	2.0762	1.9482	1.7507	1.4742
TOF (years)	1.6192	1.6243	1.6349	1.6522	1.6786

Table 15: The excess velocities and the TOF values for N=1, θ_i =120°, $\Delta\theta$ =90°, α_0 =-20°, m values for (0.01; 0.055; 0.1; 0.145; 0.19), a_0 =0.02, constant acceleration case (sinusoidal spiral), Earth-Mars flight

N=2	m = 0.01	m = 0.055	m = 0.1	m = 0.145	m = 0.19
$V_{\infty,total}\left(km/s\right)$	1.6247	1.5533	1.3982	1.1705	1.0130
$V_{\infty,1}(km/s)$	0.2550	0.2697	0.3076	0.3857	0.5489
$V_{\infty,2}(km/s)$	1.3697	1.2836	1.0906	0.7848	0.4641
TOF (years)	2.8613	2.8816	2.9317	3.0275	3.2122

Table 16: The excess velocities and the TOF values for N=2, θ_i =120°, $\Delta\theta$ =90°, α_0 =-20°, m values for (0.01; 0.055; 0.1; 0.145; 0.19), a_0 =0.02, constant acceleration case (sinusoidal spiral), Earth-Mars flight

From tables 9 and 10, the order of magnitude of the total excess velocity values is $10^0 \, km/s$. For increasing values of m, the total excess velocity decreases, while the TOF increases. The values for the total excess velocity are higher when N=1 than when N=2. Note that the excess velocity $V_{\infty,2}$ decreases faster than the excess velocity $V_{\infty,1}$ increases, for both cases N=1 and N=2.

In figures 38 to 41, the polar plot, the thrust angle α , the polar angle rate $\dot{\theta}$ and the flight path angle as function of time are illustrated for N=1 and N=2 (tables 9 and 10).

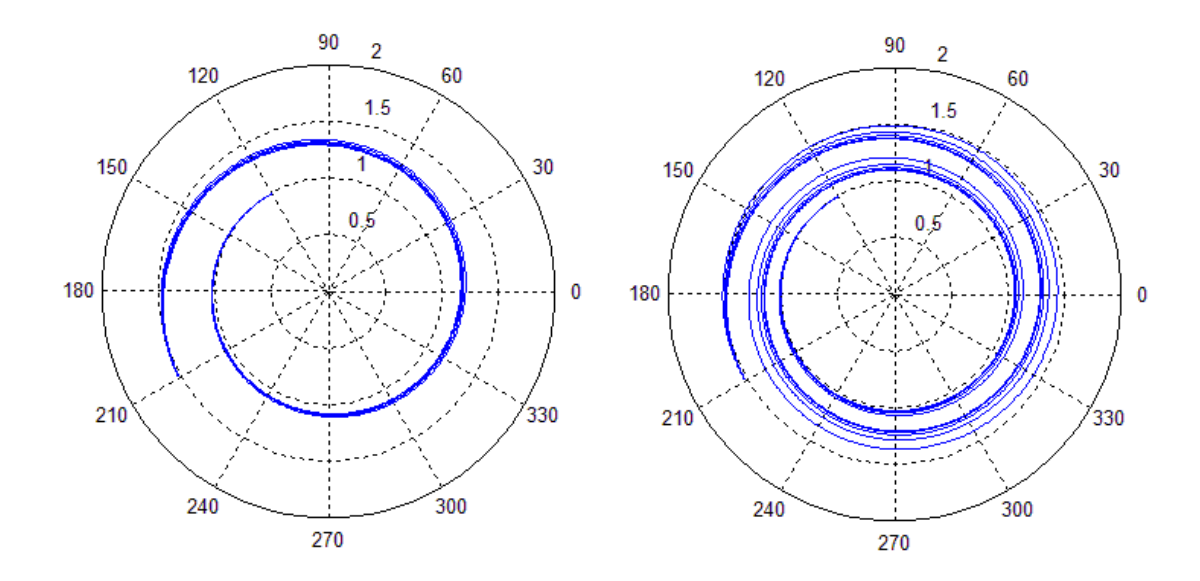


Figure 61: Polar plot for N=1 and N=2, θ_i =120°, $\Delta\theta$ =90°, α_0 =-20°, m values for (0.01; 0.055; 0.1; 0.145; 0.19), a_0 =0.02, constant acceleration (sinusoidal spiral), Earth-Mars flight

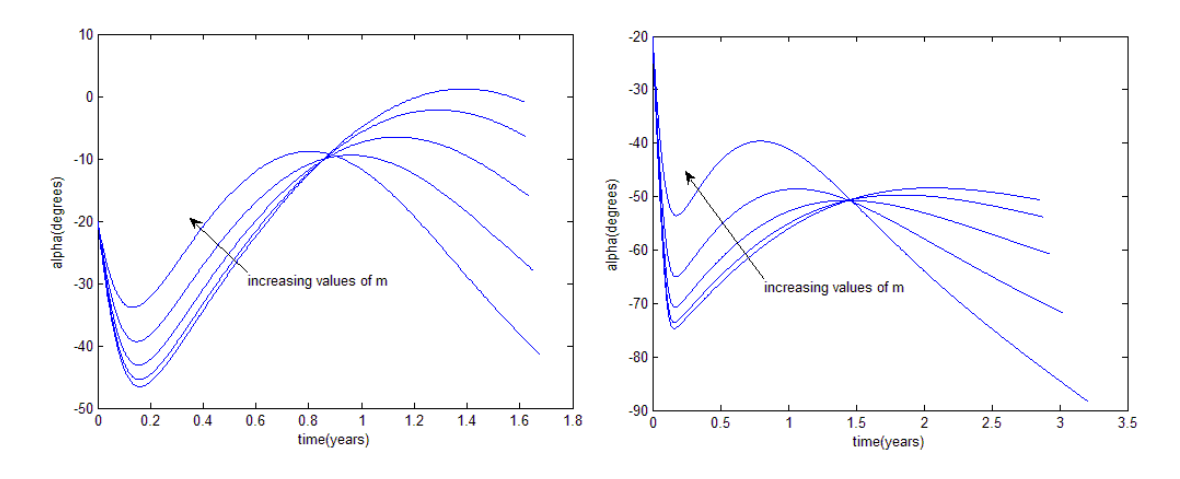


Figure 62: α plot for N=1 and N=2, θ_i =120°, $\Delta\theta$ =90°, α_o =-20°, m values for (0.01; 0.055; 0.1; 0.145; 0.19), a_o =0.02, constant acceleration (sinusoidal spiral), Earth-Mars flight

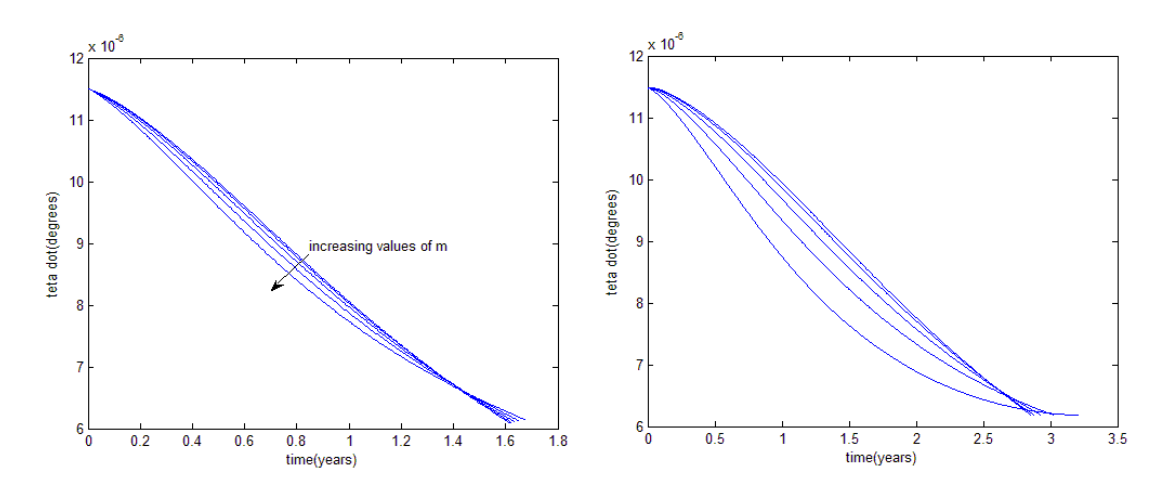


Figure 63: $\dot{\theta}$ plot for N=1 and N=2, θ_i =120°, $\Delta\theta$ =90°, α_0 =-20°, m values for (0.01; 0.055; 0.1; 0.145; 0.19), a_0 =0.02, constant acceleration (sinusoidal spiral), Earth-Mars flight

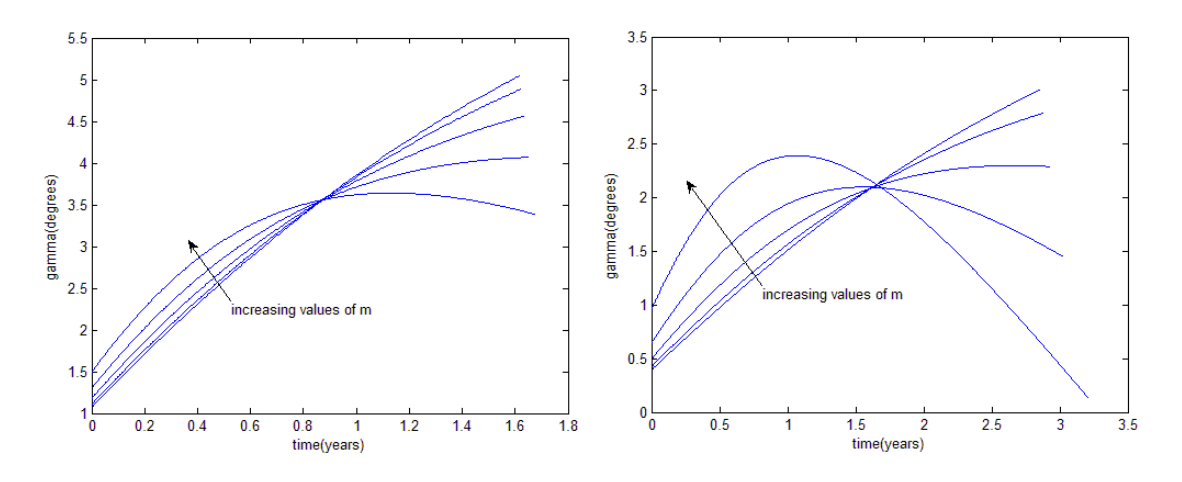


Figure 64: γ plot for N=1 and N=2, θ_i =120°, $\Delta\theta$ =90°, α_0 =-20°, m values for (0.01; 0.055; 0.1; 0.145; 0.19), a_0 =0.02, constant acceleration (sinusoidal spiral), Earth-Mars flight

Similar conclusions to the ones given for the previous shapes can be drawn.

6. Exponential Sinusoid

In this section, results for the TOF, the excess velocities and the thrust acceleration will be shown and discussed for the exponential sinusoid. Figures 42 and 43 show the TOF and the total excess velocity when changing parameter k_2 and the transfer angle $\Delta\theta$ (N=0). The values used in these figures for the geometric parameter k_2 , were (0.1; 0.15; 0.2; 0.25), for

 α_0 were (20°, 30°, 40°, 50°, 60°), for the initial flight path angle γ_1 was 0° and for $\Delta\theta$ were (90°, 150°, 210°, 270°, 340°). The value for α_0 used in figures 42 and 43 was 0.05.

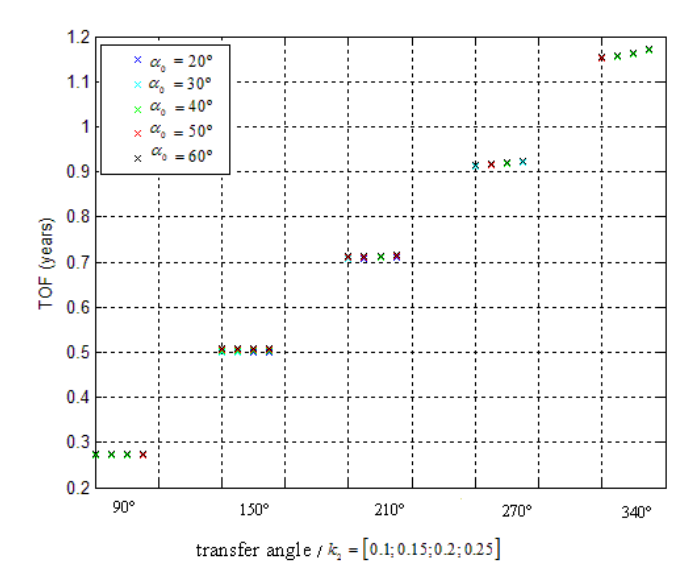
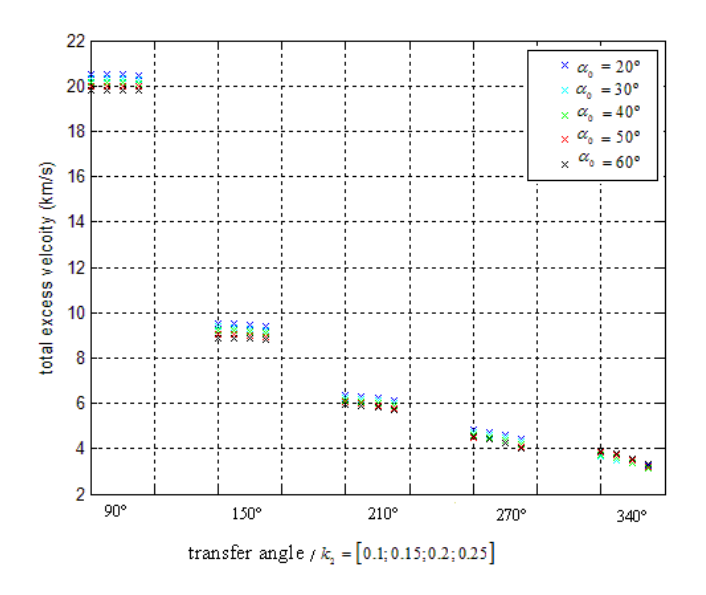


Figure 65: TOF for k_2 values of (0.1; 0.15; 0.2; 0.25) from left to right in the figure, α_0 values of (20°, 30°, 40°, 50°, 60°), $\Delta\theta$ values of (90°, 150°, 210°, 270°, 340°) (N=0), γ_1 =0°, a_0 =0.05, constant acceleration case (exponential sinusoid), Earth-Mars flight



Fom figures 42 and 43, by increasing the geometric parameter k_2 , the TOF increases, while the total excess velocity decreases. The differences in TOF and in total excess velocity between different values of k_2 increase for higher values of the transfer angle $\Delta\theta$. The highest difference in TOF between different θ_i for the same phase angle and α_0 is 0.0178 years, while the highest difference in total excess velocity is 0.6308 km/s. For increasing values of α_0 , the TOF increases while the total excess velocity decreases.

Similar figures can be shown for one and two revolutions, using the same values for the geometric parameter k_2 , for the transfer angle $\Delta\theta$ and for the initial values of α and γ_1 . The normalized thrust acceleration a_0 values used in figures 44 and 45 was 0.03.

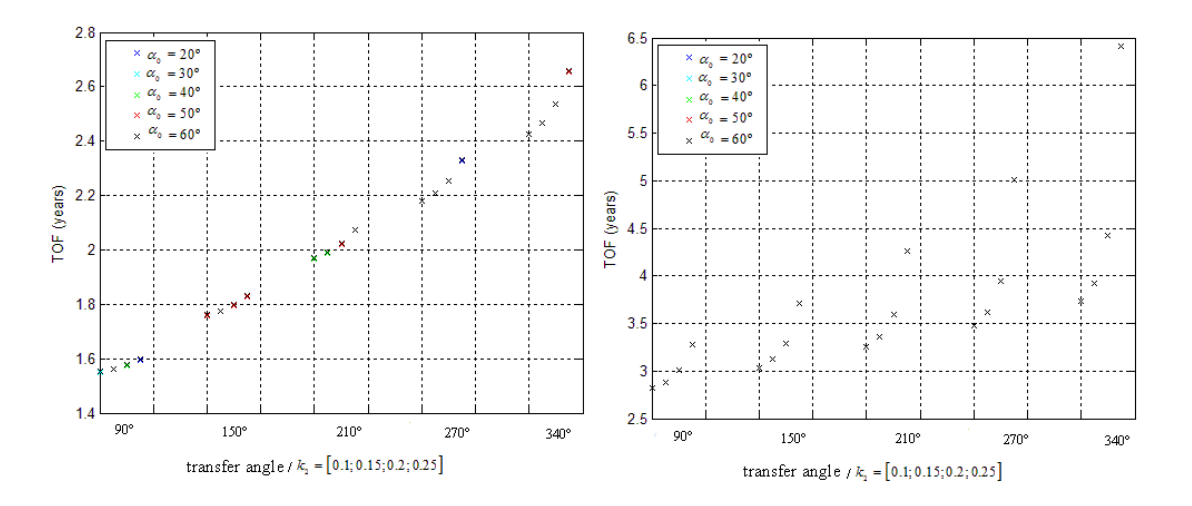


Figure 67: TOF for k_2 values of (0.1; 0.15; 0.2; 0.25) from left to right in the figure, α_0 values of (20°, 30°, 40°, 50°, 60°), $\Delta\theta$ values of (90°, 150°, 210°, 270°, 340°), γ_1 =0°, constant acceleration case (exponential sinusoid), Earth-Mars flight, N=1 (a_0 =0.03) and N=2 (a_0 =0.03)

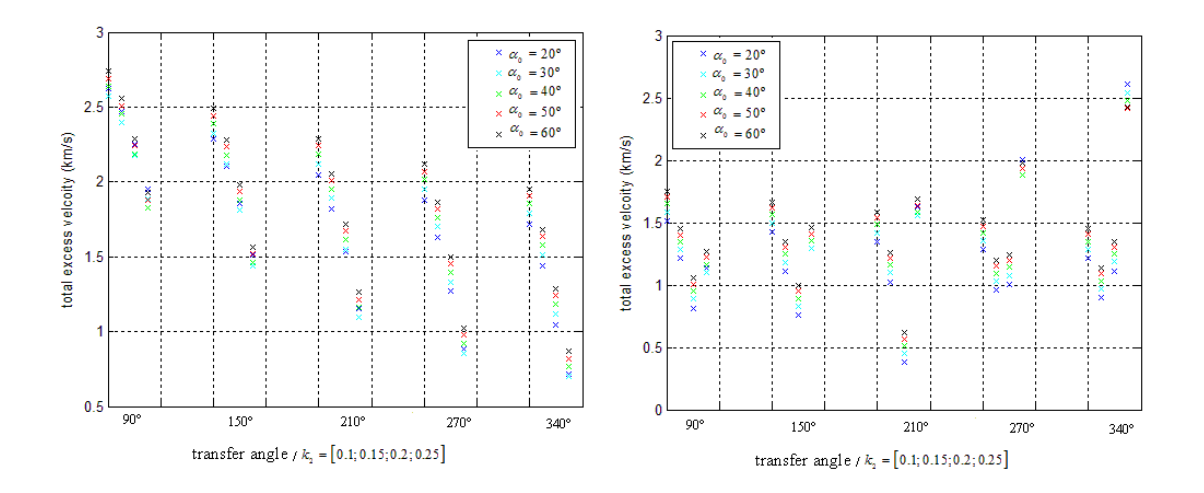


Figure 68: $V_{_{\circ,T}}$ for $k_{_2}$ values of (0.1; 0.15; 0.2; 0.25) from left to right in the figure, $\alpha_{_0}$ values of (20°, 30°, 40°, 50°, 60°), $\Delta\theta$ values of (90°, 150°, 210°, 270°, 340°), $\gamma_{_1}$ =0°, constant acceleration case (exponential sinusoid), Earth-Mars flight, N=1 ($a_{_0}$ =0.03) and N=2 ($a_{_0}$ =0.03)

Similar remarks to the ones given for N=0 can be drawn for figures 44 and 45. The differences in the total excess velocity between different values of α_0 are higher for N=1 and N=2 than N=0. Note that, unlike for N=0 and N=1, for N=2 and between $k_2 = 0.2$ and $k_2 = 0.25$, the total excess velocity increases. For N=1, the highest difference in TOF between different k_2 and for the same transfer angle and α_0 is about 0.2302 years, while the highest difference in total excess velocity is 1.0955 km/s. For N=2, the highest difference in TOF between different k_2 and for the same transfer angle is about 2.6039 years, while the highest difference in the total excess velocity is 1.3980 km/s.

The TOF range for this Earth-Mars flight is from 0.2702 years to 6.4163 years. The total excess velocity has a minimum value of $0.3772 \, km/s$ and a maximum value of $20.5265 \, km/s$. As expected, the minimum value for the TOF and the maximum value for the total excess velocity occur for the smallest transfer angle -90° (N=0). The minimum value for the total excess velocity occur for the transfer angle -210° (N=2).

The maximum differences in TOF between two consecutive values of the transfer angle $\Delta\theta$ are about 1.4080 years. The maximum value for these differences is 11.0787 km/s for N=0 and the minimum value is about 58.3969 m/s for 2 revolutions.

Tables 11 and 12 show the values for the TOF and the excess velocity for an Earth-Mars flight. Parameter k_2 assumed was 0.01, parameter α_0 assumed was 20°, the transfer angle $\Delta\theta$ assumed was 90° and the number of revolutions taken was one for the first table and two for the second one. In tables 11 and 12, the normalized thrust acceleration a_0 was 0.03.

N=1	$\gamma_1 = 0^{\circ}$	$\gamma_1 = 0.75^{\circ}$	$\gamma_1 = 1.5^{\circ}$	$\gamma_1 = 2.25^{\circ}$	$\gamma_1 = 3^{\circ}$
$V_{\infty,total}\left(km/s\right)$	2.7437	2.7940	2.8941	2.9954	3.1006
$V_{\infty,1}(km/s)$	0.0515	0.3900	0.7803	1.1710	1.5614
$V_{\infty,2}(km/s)$	2.6923	2.4040	2.1138	1.8244	1.5393
TOF (years)	1.5438	1.5829	1.6239	1.6670	1.7126

Table 17: The excess velocities and the TOF values for N=1, k_2 =0.01, $\Delta\theta$ =90°, α_0 =20°, γ_1 values of (0°; 0.75°; 1.5°; 2.25°; 3°), α_0 =0.03, constant acceleration case (exponential sinusoid), Earth-Mars flight

N=2	$\gamma_1 = 0^{\circ}$	$\gamma_1 = 0.75^{\circ}$	$\gamma_1 = 1.5^{\circ}$	$\gamma_1 = 2.25^{\circ}$	$\gamma_1 = 3^{\circ}$
$V_{\infty,total}\left(km/s\right)$	1.7485	1.7978	1.9373	2.1181	2.3695
$V_{\infty,1}(km/s)$	0.0904	0.4051	0.7896	1.1771	1.5650
$V_{\infty,2}(km/s)$	1.6581	1.3927	1.1477	0.9411	0.8044
TOF (years)	2.7739	2.9001	3.0341	3.1764	3.3277

Table 18: The excess velocities and the TOF values for N=2, k_2 =0.01, $\Delta\theta$ =90°, α_0 =20°, γ_1 values of (0°; 0.75°; 1.5°; 2.25°; 3°), α_0 =0.03, constant acceleration case (exponential sinusoid), Earth-Mars flight

For increasing values of m, the total excess velocity and the TOF increase. The values for the total excess velocity are higher when N=1 than when N=2. Note that the excess velocity $V_{\infty,2}$ decreases faster than the excess velocity $V_{\infty,1}$ increases, for both cases N=1 and N=2.

In figures 46 to 49, the polar plot, the thrust angle α , the polar angle rate $\dot{\theta}$ and the flight path angle as function of time are illustrated for N=1 and N=2 cases that were presented in tables 11 and 12.

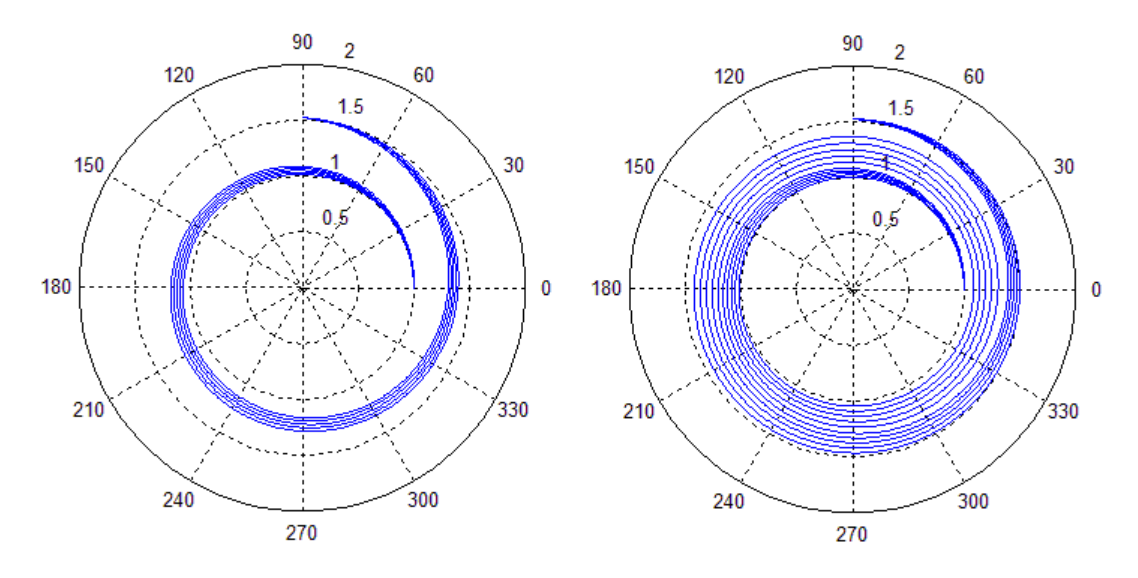


Figure 69: Polar plot for N=1 and N=2, k_2 =0.01, $\Delta\theta$ =90°, α_0 =20°, γ_1 values of (0°; 0.75°; 1.5°; 2.25°; 3°), α_0 =0.03, constant acceleration case (exponential sinusoid), Earth-Mars flight

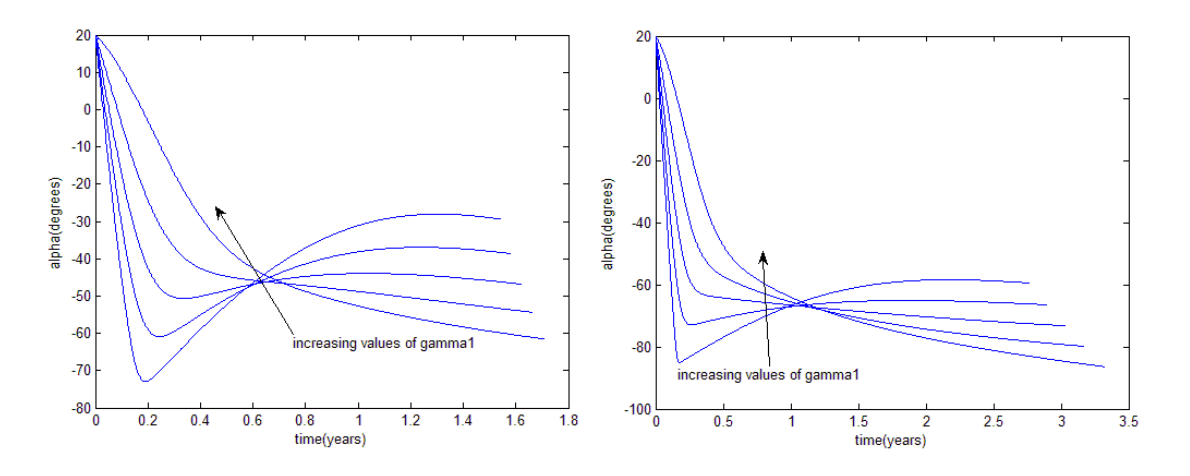


Figure 70: α plot for N=1 and N=2, k_2 =0.01, $\Delta\theta$ =90°, α_0 =20°, γ_1 values of (0°; 0.75°; 1.5°; 2.25°; 3°), α_0 =0.03, constant acceleration case (exponential sinusoid), Earth-Mars flight

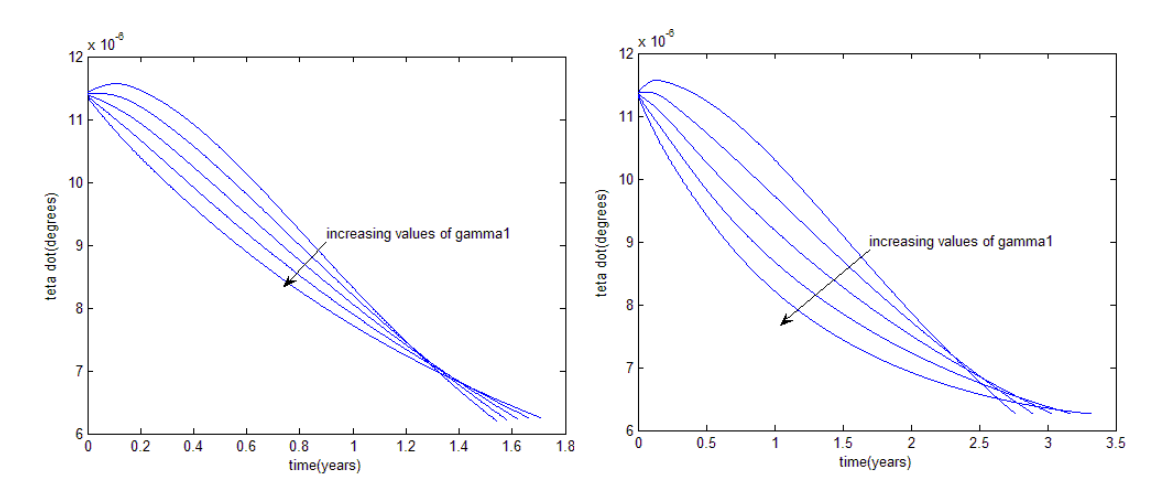


Figure 71: $\dot{\theta}$ plot for N=1 and N=2, k_2 =0.01, $\Delta\theta$ =90°, α_0 =20°, γ_1 values of (0°; 0.75°; 1.5°; 2.25°; 3°), α_0 =0.03, constant acceleration case (exponential sinusoid), Earth-Mars flight

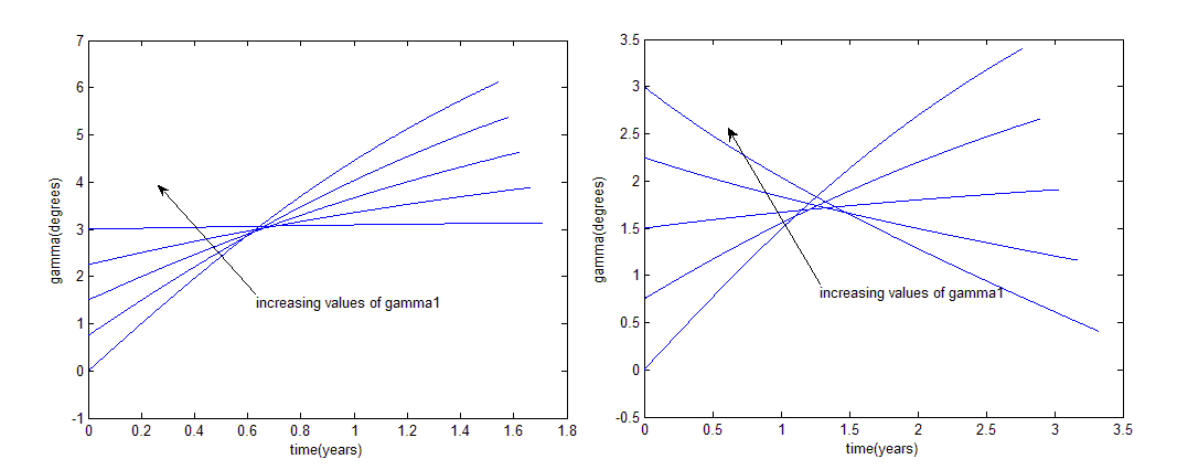


Figure 72: γ plot for N=1 and N=2, k_2 =0.01, $\Delta\theta$ =90°, α_0 =20°, γ_1 values of (0°; 0.75°; 1.5°; 2.25°; 3°), α_0 =0.03, constant acceleration case (exponential sinusoid), Earth-Mars flight

The values of the thrust angle α are higher for N=1 than for N=2. For most of the interplanetary flight for both cases in figure 47, the spacecraft is thrusting inwards in the radial direction, while in the tangential direction it thrusts in the positive direction (α is negative, higher than -90°). This means that the vehicle is thrusting in favour of the gravitational acceleration. This situation will be further analysed in section 7.7. The magnitude values of the flight path angle γ are smaller for N=2 than for N=1.

Appendix E: Analysis of the Exponential Sinusoid for an Earth-Jupiter Flight and for an Earth-Mercury Flight

In this appendix, a similar analysis to the one done in appendix D will be done one for the exponential sinusoid, for an Earth-to-Jupiter flight and an Earth-to-Mercury flight, using the acceleration inversely square and the tangential cases of the thrust profile. Results for the constant acceleration case of the thrust profile will not be shown (see chapter 7). Like in appendix D, the conclusions about these results are given in section 7.7.

1. Earth-Jupiter Flight, using the Acceleration Inversely Square Case of the Thrust Profile

Figures 50 and 51 show the TOF and the total excess velocity when changing parameter k_2 and the transfer angle $\Delta\theta$, when the number of revolutions N is 1. The values used in figures 50 and 51 for the geometric parameter k_2 were (0.05; 0.08; 0.11; 0.14), for the initial value of α were (20°, 30°, 40°, 50°, 60°), for the initial flight path angle γ_1 was 0° and for the transfer angle $\Delta\theta$ were (90°, 150°, 210°, 270°, 340°). The normalized thrust acceleration a_0 value used in figures 50 and 51 was 0.13.

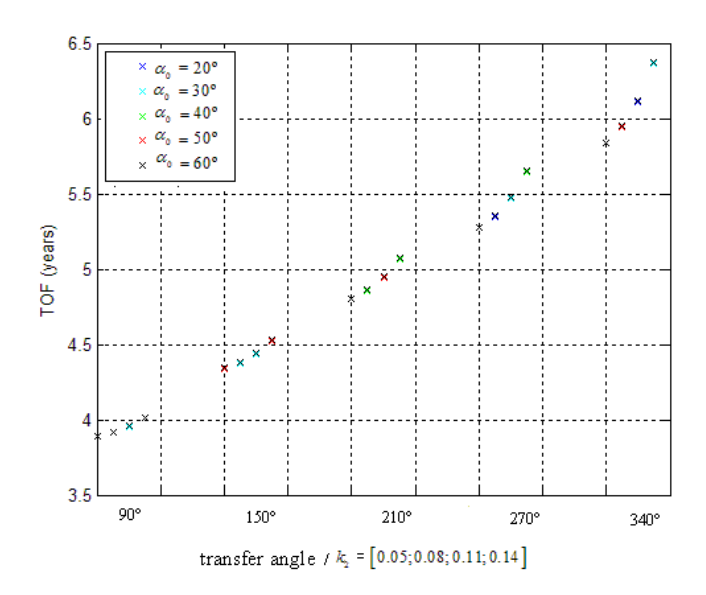


Figure 73: TOF for k_2 values of (0.05; 0.08; 0.11; 0.14) from left to right in the figure, α_0 values of (20°, 30°, 40°, 50°, 60°), $\Delta\theta$ were (90°, 150°, 210°, 270°, 340°) (N=1), γ_1 =0°, α_0 =0.13, acceleration inversely square case (exponential sinusoid), Earth-Jupiter flight

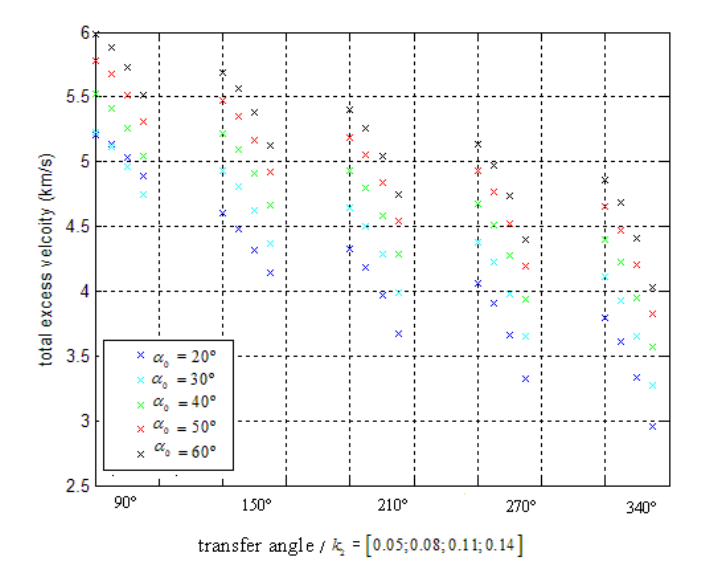


Figure 74: $V_{\omega,\tau}$ for k_2 values of (0.05; 0.08; 0.11; 0.14) from left to right in the figure, α_0 values of (20°, 30°, 40°, 50°, 60°), $\Delta\theta$ were (90°, 150°, 210°, 270°, 340°) (N=1), γ_1 =0°, a_0 =0.13, acceleration inversely square case (exponential sinusoid), Earth-Jupiter flight

Some remarks can be drawn from figures 50 and 51. As expected, the TOF increases when increasing the transfer angle, while the total excess velocity decreases. By increasing the geometric parameter k_2 , the TOF increases, while the total excess velocity decreases. The highest difference in TOF between different k_2 for the same phase angle and α_0 is 0.5154 years, while the highest difference in total excess velocity is 0.8344 km/s. For increasing values of α_0 , the TOF and the total excess velocity increases.

Similar figures can be shown for 2 and 3 revolutions, using the same values for the geometric parameter k_2 , for $\Delta\theta$ and the initial values of α and γ_1 . The normalized thrust acceleration a_0 values used in figures 52 and 53 were 0.09 and 0.07 for N=2 and N=3, respectively.

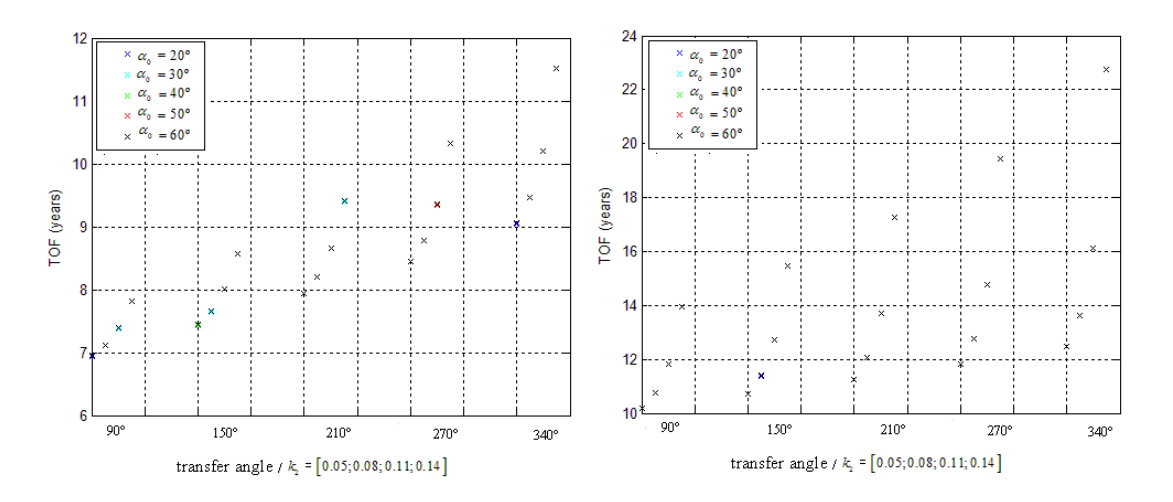


Figure 75: TOF for k_2 values of (0.05; 0.08; 0.11; 0.14) from left to right in the figure, α_0 values of (20°, 30°, 40°, 50°, 60°), $\Delta\theta$ were (90°, 150°, 210°, 270°, 340°), γ_1 =0°, acceleration inversely square case (exponential sinusoid), Earth-Jupiter flight, for N=2 (a_0 =0.09) and N=3 (a_0 =0.07)

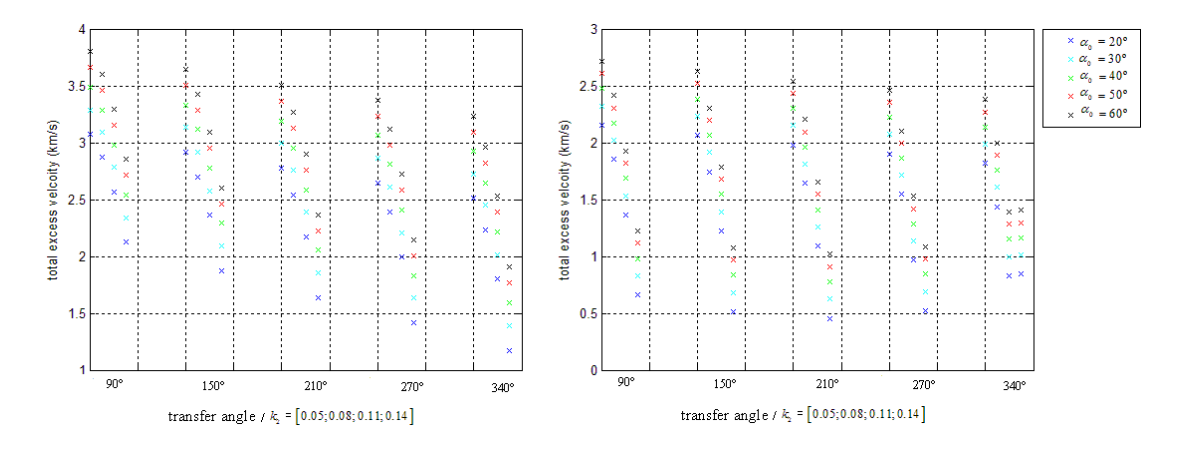


Figure 76: $V_{_{\circ,T}}$ for $k_{_2}$ values of (0.05; 0.08; 0.11; 0.14) from left to right in the figure, $\alpha_{_0}$ values of (20°, 30°, 40°, 50°, 60°), $\Delta\theta$ were (90°, 150°, 210°, 270°, 340°), $\gamma_{_1}$ =0°, acceleration inversely square case (exponential sinusoid), Earth-Jupiter flight, for N=2 ($a_{_0}$ =0.09) and N=3 ($a_{_0}$ =0.07)

Similar remarks to the ones given for N=1 can be drawn for figures 52 and 53. The differences in total excess velocity between different values of α_0 are higher for N=1 and N=2 than N=0. Note that, unlike for N=1 and N=2, for N=3 and between $k_2=0.11$ and $k_2=0.14$, the total excess velocity increases for a transfer angle of 340°. For N=2, the highest difference in TOF between different k_2 and for the same transfer angle is about 2.4626 years, while the highest difference in total excess velocity is 1.3337 km/s. For N=3,

the highest difference in TOF between different k_2 and for the same transfer angle is about 9.9958 years, while the highest difference in total excess velocity is $1.5506 \, km/s$.

The TOF range for this Earth-Jupiter flight is from 3.8876 years to 22.7594 years. The total excess velocity has a minimum value of $0.4552 \, km/s$ and a maximum value of $5.9872 \, km/s$. As expected, the minimum value for the TOF and the maximum value for the total excess velocity occur for the smallest transfer angle -90° (N=1); while the minimum value for the total excess velocity occur for the transfer angle 210° (N=3).

The maximum differences in TOF between two consecutive values of the transfer angle $\Delta\theta$ are about 1.52 years. The maximum value for these differences is $0.7543 \, km/s$ for N=1 and the minimum value is about $59.6903 \, m/s$ for 3 revolutions.

Tables 13 and 14 show the values for the TOF and the excess velocity for an Earth-Jupiter flight. Parameter k_2 was considered 0.01, parameter α_0 was considered 20°, $\Delta\theta$ was considered 90° and N was taken 1 for the first table and 2 for the second one. In tables 13 and 14, the normalized thrust acceleration values a_0 were 0.09 and 0.07, respectively. Note that these values for a_0 , for N=2 and N=3 are the minimum values that can be used in both cases for this shape without facing integration problems for the interval of the parameters considered.

N=2	$\gamma_1 = 0^{\circ}$	$\gamma_1 = 0.75^{\circ}$	$\gamma_1 = 1.5^{\circ}$	$\gamma_1 = 2.25^{\circ}$	$\gamma_1 = 3^{\circ}$
$V_{\infty,total}\left(km/s\right)$	3.1884	3.2792	3.4954	3.7244	3.9546
$V_{\infty,1}(km/s)$	0.2166	0.4501	0.8125	1.1912	1.5744
$V_{\infty,2}(km/s)$	2.9718	2.8291	2.6830	2.5332	2.3802
TOF (years)	6.8536	7.0891	7.3441	7.6177	7.9099

Table 19: The excess velocities and the TOF values for N=2, k_2 =0.01, $\Delta\theta$ =90°, α_0 =20°, γ_1 values of (0°; 0.75°; 1.5°; 2.25°; 3°), a_0 =0.09, acceleration inversely square case (exponential sinusoid), Earth–Jupiter flight

N=3	$\gamma_1 = 0^{\circ}$	$\gamma_1 = 0.75^{\circ}$	$\gamma_1 = 1.5^{\circ}$	$\gamma_1 = 2.25^{\circ}$	$\gamma_1 = 3^{\circ}$
$V_{\scriptscriptstyle{\infty,total}}\left(km/s ight)$	2.3289	2.3968	2.5988	2.8186	3.0426
$V_{\infty,1}(km/s)$	0.2412	0.4603	0.8168	1.1931	1.5751
$V_{\infty,2}(km/s)$	2.0877	1.9364	1.7821	1.6255	1.4651
TOF (years)	9.8651	10.3911	10.9668	11.5939	12.2757

Table 20: The excess velocities and the TOF values for N=3, k_2 =0.01, $\Delta\theta$ =90°, α_0 =20°, γ_1 values of (0°; 0.75°; 1.5°; 2.25°; 3°), a_0 =0.07, acceleration inversely square case (exponential sinusoid), Earth-Jupiter flight

For increasing values of m, the total excess velocity and the TOF increase. The values for the total excess velocity are higher when N=2 than when N=3. Note that the excess velocity $V_{\infty,2}$ decreases faster than the excess velocity $V_{\infty,1}$ increases, for both cases N=2 and N=3.

In figures 54 to 58, the polar plot, the thrust acceleration a, the thrust angle α , the polar angle rate $\dot{\theta}$ and the flight path angle as function of time are illustrated for N=2 and N=3 cases that were presented in tables 13 and 14.

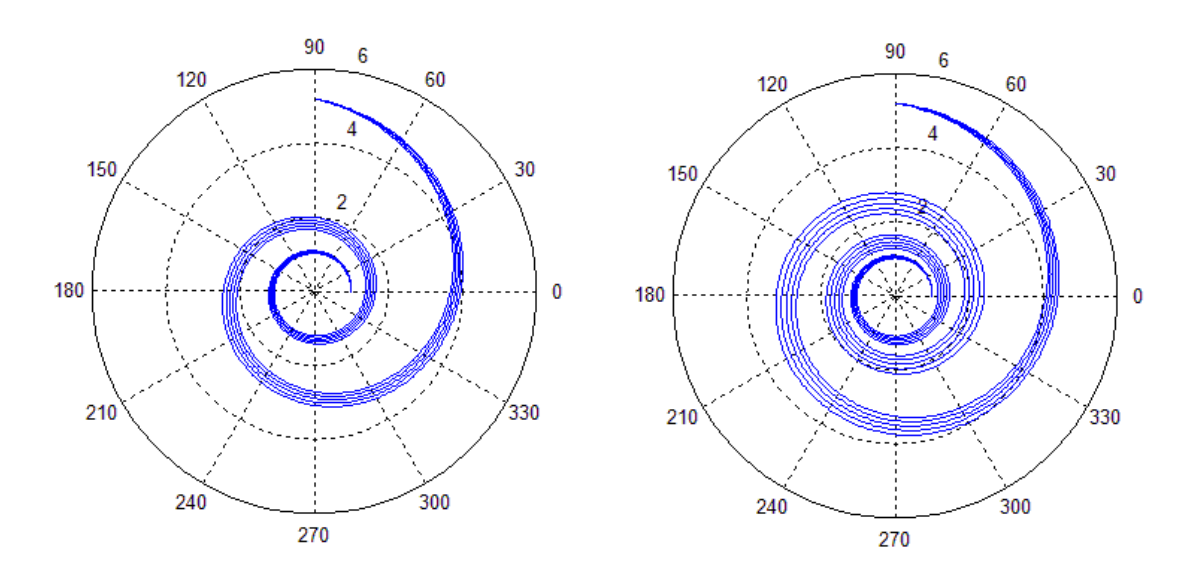


Figure 77: Polar plot for N=2 (a_0 =0.09) and N=3 (a_0 =0.07), k_2 =0.01, $\Delta\theta$ =90°, α_0 =20°, γ_1 values of (0°; 0.75°; 1.5°; 2.25°; 3°), acceleration inversely square case (exponential sinusoid), Earth-Jupiter flight

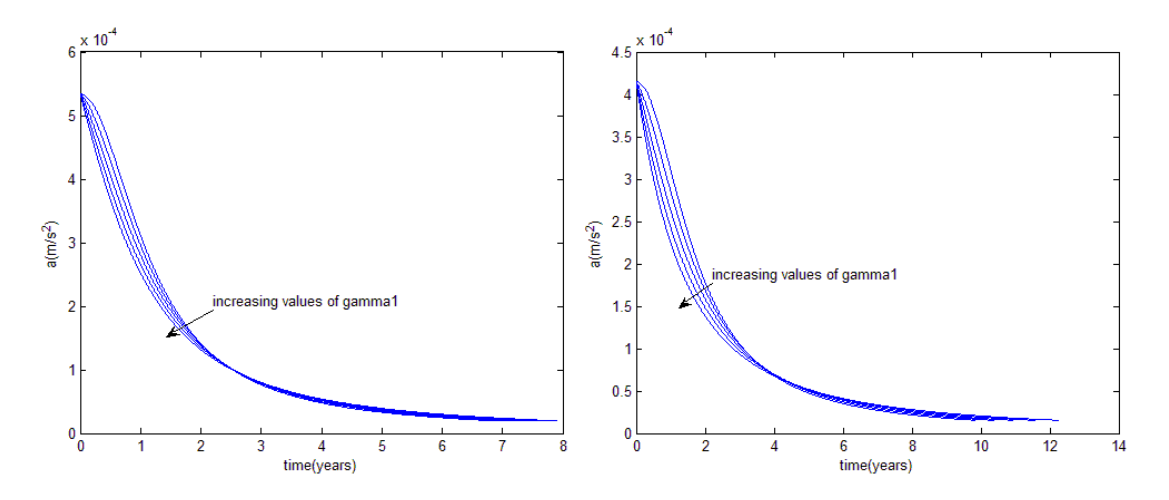


Figure 78: a plot for N=2 (a_0 =0.09) and N=3 (a_0 =0.07), k_2 =0.01, $\Delta\theta$ =90°, α_0 =20°, γ_1 values of (0°; 0.75°; 1.5°; 2.25°; 3°), acceleration inversely square case (exponential sinusoid), Earth-Jupiter flight

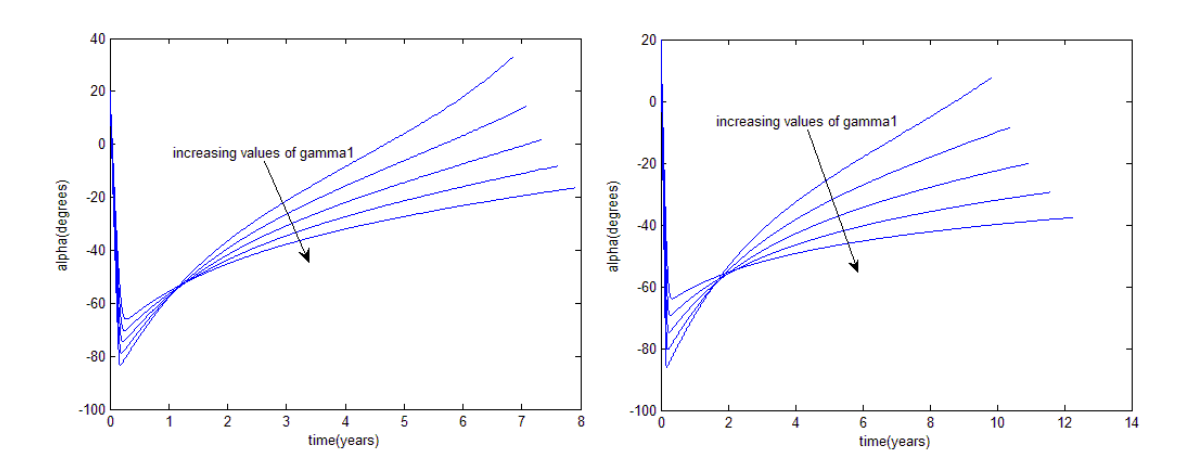


Figure 79: α plot for N=2 (a_0 =0.09) and N=3 (a_0 =0.07), k_2 =0.01, $\Delta\theta$ =90°, α_0 =20°, γ_1 values of (0°; 0.75°; 1.5°; 2.25°; 3°), acceleration inversely square case (exponential sinusoid), Earth-Jupiter flight

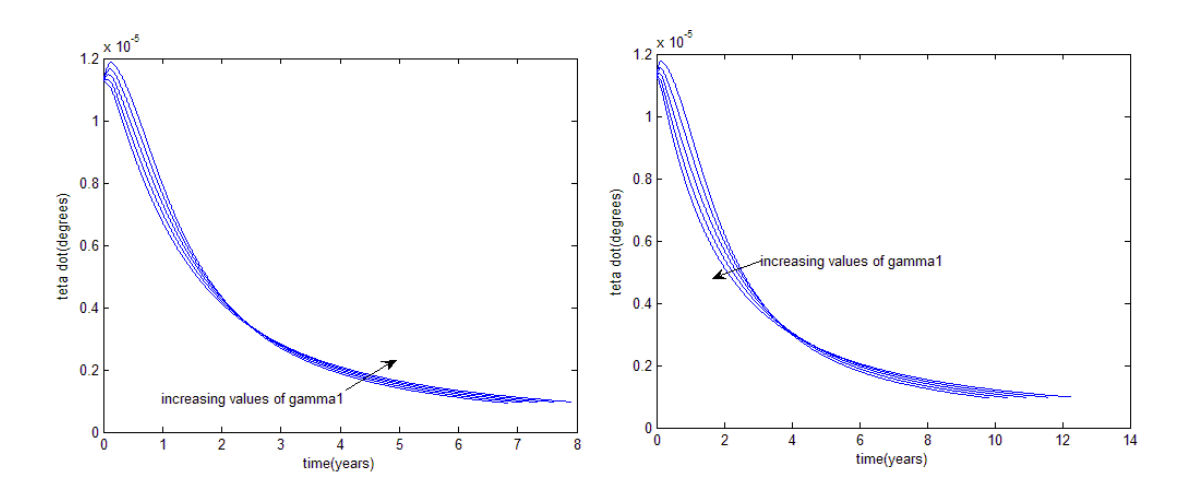


Figure 80: $\dot{\theta}$ plot for N=2 (a_0 =0.09) and N=3 (a_0 =0.07), k_2 =0.01, $\Delta\theta$ =90°, α_0 =20°, γ_1 values of (0°; 0.75°; 1.5°; 2.25°; 3°), acceleration inversely square case (exponential sinusoid), Earth-Jupiter flight

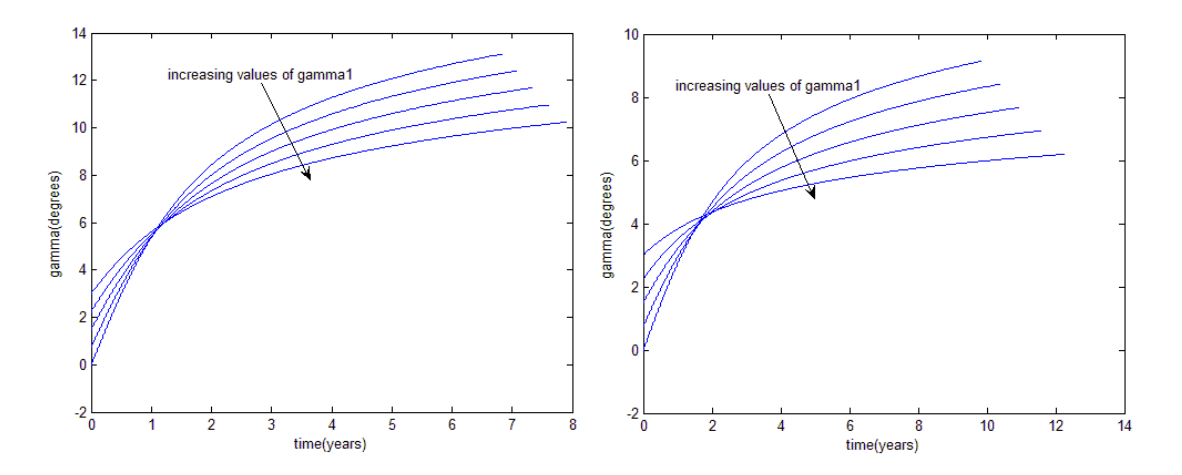


Figure 81: γ plot for N=2 (a_0 =0.09) and N=3 (a_0 =0.07), k_2 =0.01, $\Delta\theta$ =90°, α_0 =20°, γ_1 values of (0°; 0.75°; 1.5°; 2.25°; 3°), acceleration inversely square case (exponential sinusoid), Earth-Jupiter flight

The magnitude of the thrust acceleration is the smaller for N=2 than for N=3 because the assumed normalized thrust acceleration a_0 is also smaller for N=2 than for N=3. Note that the thrust acceleration trend is similar to the $\dot{\theta}$ trend. The values of the thrust angle α are higher for N=1 than for N=2. For most of the interplanetary flight for both cases in figure 56, the spacecraft is thrusting inwards in the radial direction, while in the tangential direction it thrusts in the positive direction (α is negative, higher than -90°), as already mentioned for the Earth-Mars flight. This situation will be further analysed in section 7.7. The magnitude values of the flight path angle γ are smaller for N=3 than for N=2.

2. Earth-Jupiter Flight, using the Tangential Thrust Profile

Figures 59 and 60 show the TOF and the total excess velocity when changing parameter k_2 and the transfer angle $\Delta\theta$ (N=1). The values used in these figures for the geometric parameter k_2 were (0.05; 0.08; 0.11; 0.14), for the initial flight path angle γ_1 were (0°; 0.75°; 1.5°; 2.25°; 3°) and the transfer angle $\Delta\theta$ were (90°, 150°, 210°, 270°, 340°).

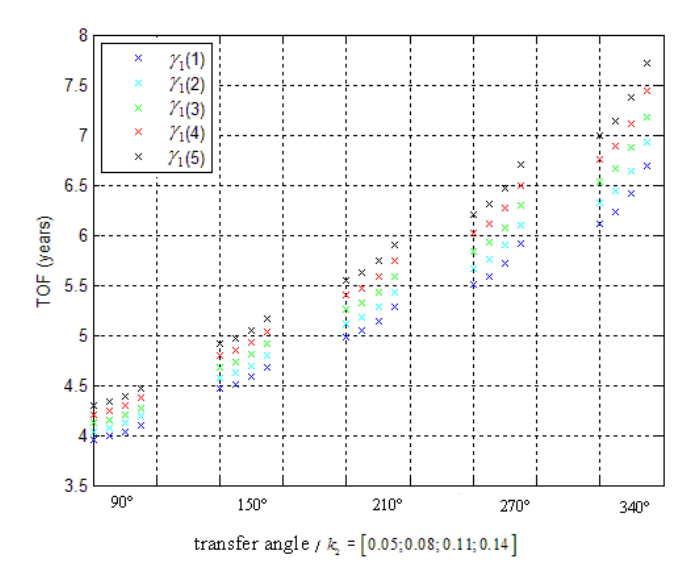


Figure 82: TOF for k_2 values of (0.05; 0.08; 0.11; 0.14) from left to right in the figure, γ_1 values of (0°; 0.75°; 1.5°; 2.25°; 3°), $\Delta\theta$ values of (90°, 150°, 210°, 270°, 340°) (N=1), tangential thrust (exponential sinusoid), Earth-Jupiter flight

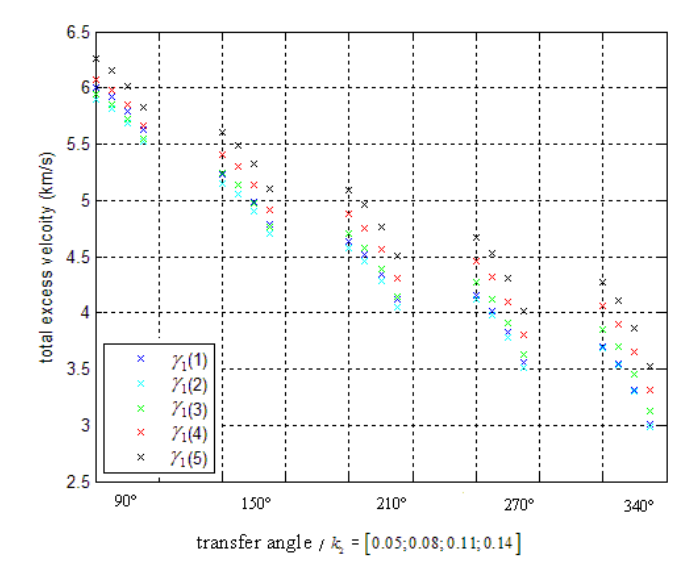


Figure 83: $V_{_{\circ,T}}$ for $k_{_2}$ values of (0.05; 0.08; 0.11; 0.14) from left to right in the figure, for $\gamma_{_1}$ values of (0°; 0.75°; 1.5°; 2.25°; 3°) and for $\Delta\theta$ values of (90°, 150°, 210°, 270°, 340°) (N=1) when the tangential thrust profile is being applied (exponential sinusoid), Earth-Jupiter flight

From figures 59 and 60, by increasing the geometric parameter k_2 , the TOF increases, while the total excess velocity decreases, while increasing the values of γ_1 , the TOF and the total excess velocity increases. The highest difference in TOF between different k_2 for the same phase angle and γ_1 is 0.7101 years, while the highest difference in total excess velocity is $0.7550 \, km/s$. The differences in TOF and in total excess velocity between different values of γ_1 increase for higher values of the transfer angle $\Delta\theta$.

Similar figures can be shown for 2 and 3 revolutions, using the same values for the geometric parameter k_2 , for the transfer angle $\Delta\theta$ and for the initial flight path angle γ_1 as the ones used for N=1.

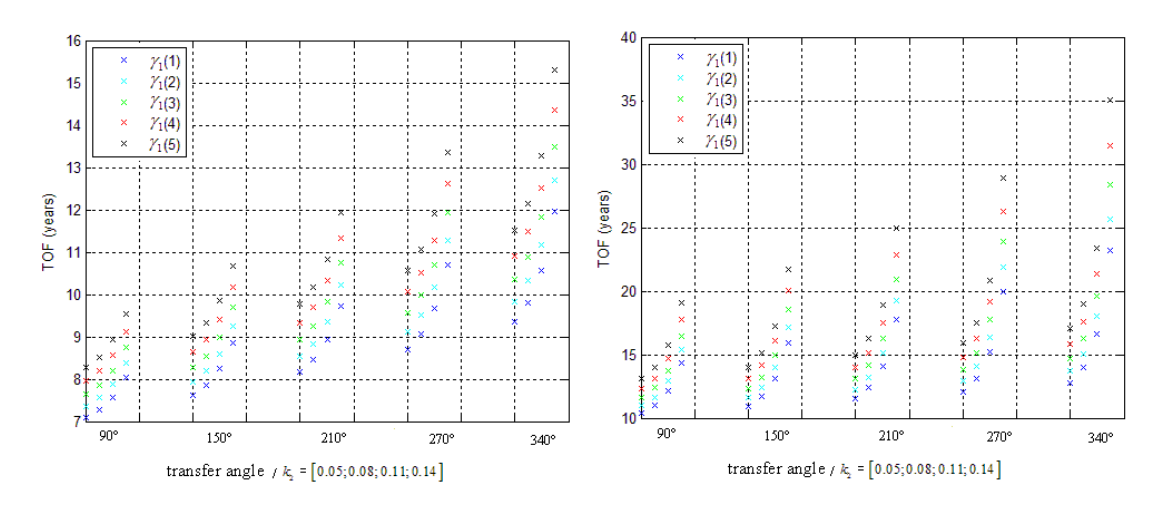


Figure 84: TOF for k_2 values of (0.05; 0.08; 0.11; 0.14) from left to right in the figure, γ_1 values of (0°; 0.75°; 1.5°; 2.25°; 3°), $\Delta\theta$ values of (90°, 150°, 210°, 270°, 340°), tangential thrust, (exponential sinusoid), Earth-Jupiter flight, N=2 and N=3

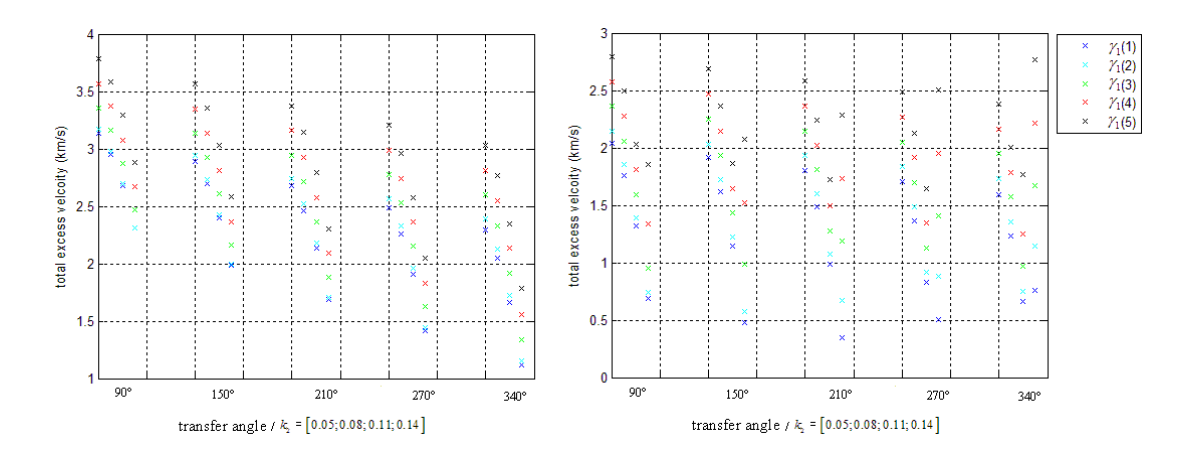


Figure 85: $V_{_{\circ,7}}$ for $k_{_2}$ values of (0.05; 0.08; 0.11; 0.14) from left to right in the figure, $\gamma_{_1}$ values of (0°; 0.75°; 1.5°; 2.25°; 3°), $\Delta\theta$ values of (90°, 150°, 210°, 270°, 340°), tangential thrust (exponential sinusoid), Earth-Jupiter flight, N=2 and N=3

Similar remarks to ones given for N=1 can be drawn for figures 61 and 62. The differences in TOF for different values of γ_1 are higher for N=2 and N=3 than N=1. For N=2, the total excess velocity decreases when increasing k_2 . However, for N=3, for transfer angles $\Delta\theta$ higher than 150°, the total excess velocity increases between k_2 = 0.11 and k_2 = 0.14 for higher values of γ_1 . For N=2, the highest difference in TOF between different k_2 for the same transfer angle and γ_1 is about 3.6608 years, while the highest difference in total excess velocity is 1.2603km/s. For N=3, the highest difference in TOF between different

 k_2 for the same transfer angle and γ_1 is about 17.4482 years, while the highest difference in total excess velocity is $1.4635 \, km/s$.

The TOF range for this Earth-Jupiter flight is from 3.9567 years to 35.0279 years. The total excess velocity has a minimum value of $0.3492 \, km/s$ and a maximum value of $6.2544 \, km/s$. As expected, the minimum value for the TOF and the maximum value for the total excess velocity occur for the smallest transfer angle -90° (N=1). Note that the minimum value for the total excess velocity occur for the transfer angle 210° (N=3).

The maximum differences in TOF between two consecutive values of the transfer angle $\Delta\theta$ are about six years. For a certain number of revolutions, these differences increase when increasing the transfer angle. The difference in terms of total excess velocity between two consecutive transfer angles is highest between $\Delta\theta = 90^{\circ}$ and $\Delta\theta = 150^{\circ}$ for N=1. The maximum value for these differences is $0.8419 \, km/s$ for N=1 and the minimum value is $35.2968 \, m/s$ for 3 revolutions.

Tables 15 and 16 show the values for the TOF and the excess velocity for an Earth-Jupiter flight. Parameter θ_i is zero and parameter k_2 was considered 0.01, the transfer angle $\Delta\theta$ was considered 90° and the number of revolutions was taken 2 for the first table and 3 for the second one.

N=2	$\gamma_1 = 0^{\circ}$	$\gamma_1 = 0.75^{\circ}$	$\gamma_1 = 1.5^{\circ}$	$\gamma_1 = 2.25^{\circ}$	$\gamma_1 = 3^{\circ}$
$V_{\infty,total}(km/s)$	3.2450	3.2815	3.4731	3.6862	3.9043
$V_{\infty,1}(km/s)$	0.2494	0.4495	0.8058	1.1845	1.5691
$V_{\infty,2}(km/s)$	2.9956	2.8319	2.6673	2.5018	2.3353
TOF (years)	6.9792	7.2470	7.5296	7.8281	8.1436

Table 21: Excess velocities and TOF values for N=2, k_2 =0.01, $\Delta\theta$ =90°, γ_1 values of (0°; 0.75°; 1.5°; 2.25°; 3°), tangential thrust (exponential sinusoid), Earth-Jupiter flight

N=3	$\gamma_1 = 0^{\circ}$	$\gamma_1 = 0.75^{\circ}$	$\gamma_1 = 1.5^{\circ}$	$\gamma_1 = 2.25^{\circ}$	$\gamma_1 = 3^{\circ}$
$V_{\infty,total}(km/s)$	2.2056	2.3223	2.5360	2.7547	2.9739
$V_{\infty,1}(km/s)$	0.1190	0.4031	0.7850	1.1725	1.5612
$V_{\infty,2}(km/s)$	2.0867	1.9192	1.7510	1.5822	1.4127
TOF (years)	10.0493	10.6167	11.2291	11.8906	12.6058

Table 22: Excess velocities and TOF values for N=3, k_2 =0.01, $\Delta\theta$ =90°, γ_1 values of (0°; 0.75°; 1.5°; 2.25°; 3°), tangential thrust (exponential sinusoid), Earth-Jupiter flight

For increasing values of γ_1 , the TOF and the total excess velocity increase. The values for the total excess velocity are higher when N=2 than when N=3. Note that the excess velocity $V_{\infty,1}$ has the same trend as the total excess velocity, while the excess velocity $V_{\infty,2}$ decreases.

In figures 63 to 66, the polar plot, the thrust acceleration a, the thrust angle α and the polar angle rate $\dot{\theta}$ as function of time are illustrated for N=2 and N=3 cases that were presented in tables 15 and 16.

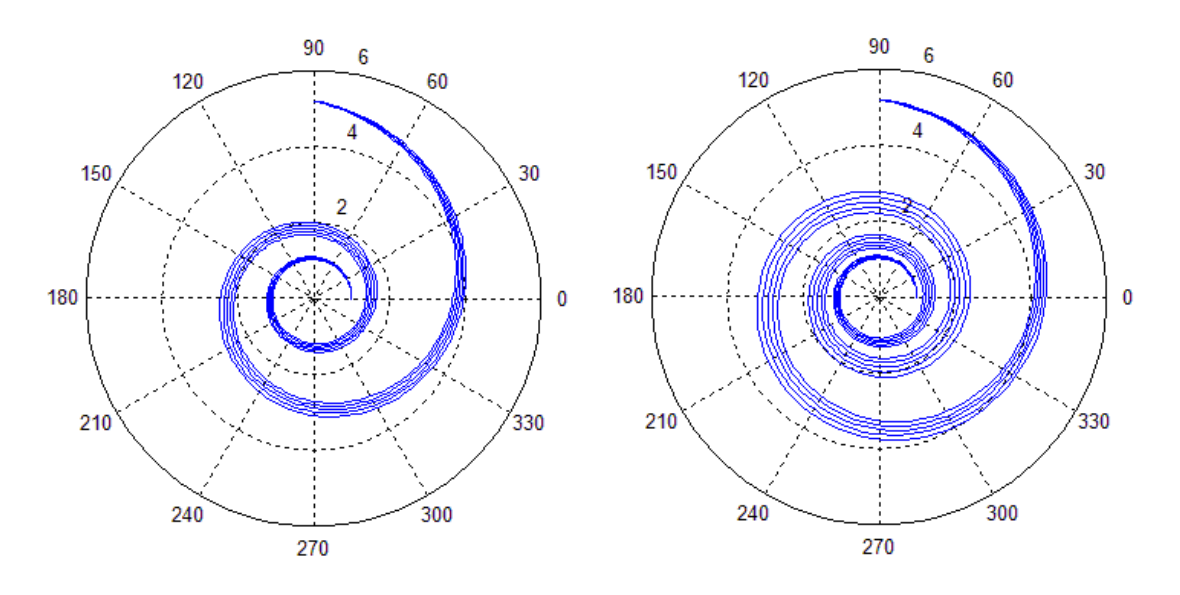


Figure 86: Polar plot for N=2 and N=3, k_2 =0.01, $\Delta\theta$ =90°, γ_1 values of (0°; 0.75°; 1.5°; 2.25°; 3°), tangential thrust (exponential sinusoid), Earth-Jupiter flight

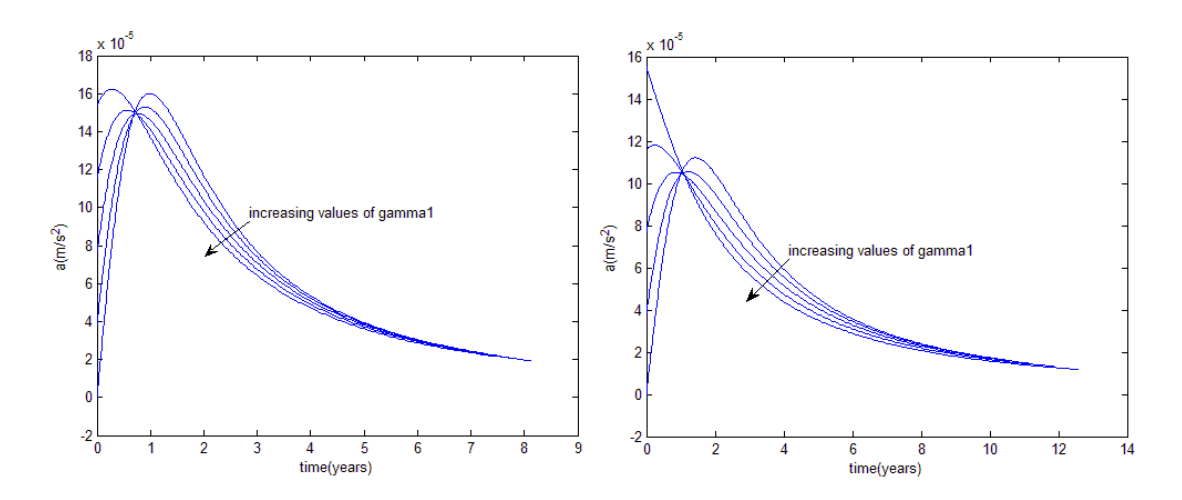


Figure 87: a plot for N=2 and N=3, k_2 =0.01, $\Delta\theta$ =90°, γ_1 values of (0°; 0.75°; 1.5°; 2.25°; 3°), tangential thrust (exponential sinusoid), Earth-Jupiter flight

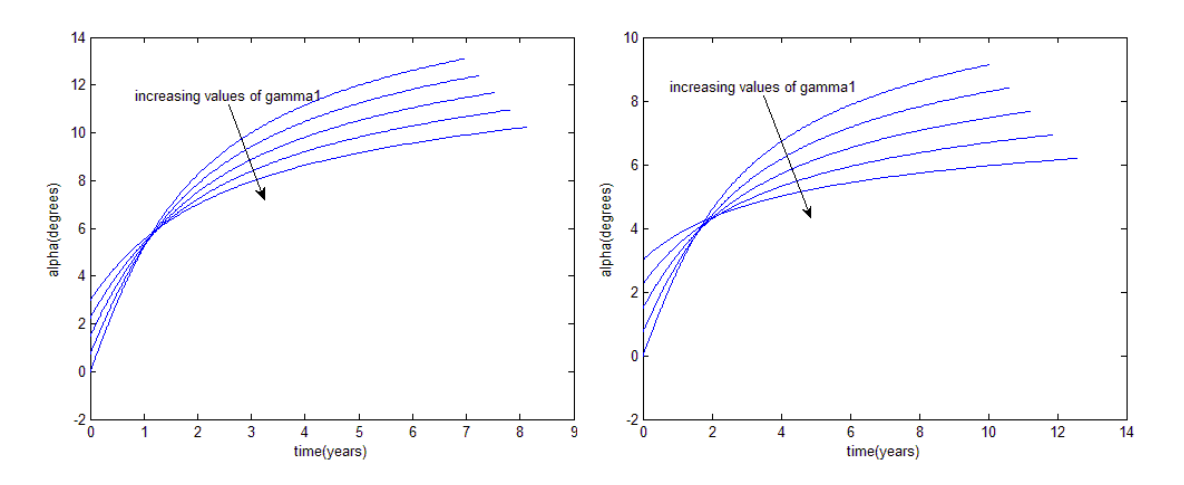


Figure 88: α plot for N=2 and N=3, k_2 =0.01, $\Delta\theta$ =90°, γ_1 values of (0°; 0.75°; 1.5°; 2.25°; 3°), tangential thrust (exponential sinusoid), Earth-Jupiter flight

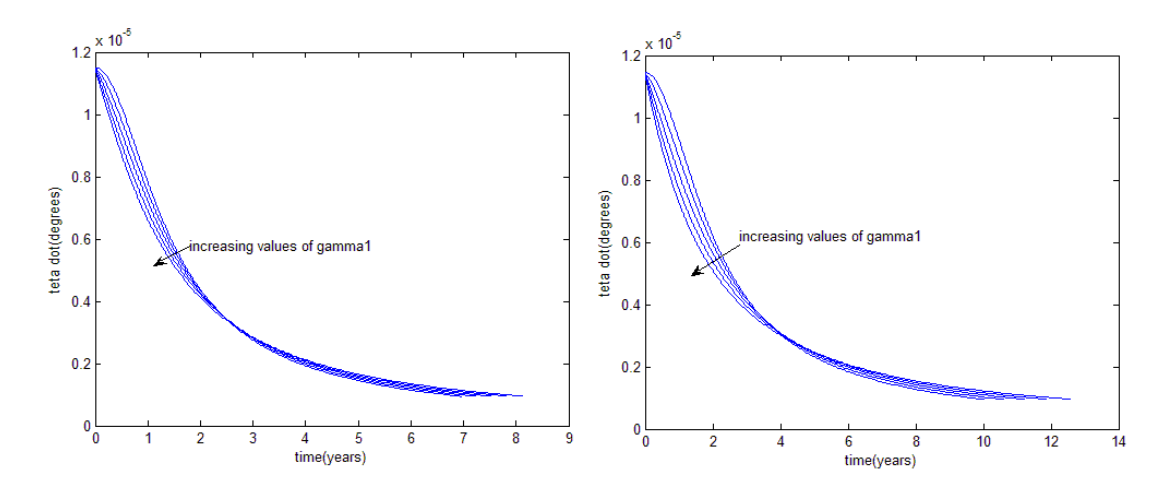


Figure 89: $\dot{\theta}$ plot for N=2 and N=3, k_2 =0.01, $\Delta\theta$ =90°, γ_1 values of (0°; 0.75°; 1.5°; 2.25°; 3°), tangential thrust (exponential sinusoid), Earth-Jupiter flight

The values for the thrust angle α are smaller for N=3 than for N=2. The plot of the flight path angle γ in function of time is not shown, since in the tangential case $\alpha = \gamma$. Finally, the thrust acceleration α values are smaller for N=3 than for N=2.

3. Earth-Mercury Flight, using the Acceleration Inversely Square Case of the Thrust Profile

Figures 67 and 68 show the TOF and the total excess velocity when changing parameter k_2 and the transfer angle $\Delta\theta$ (N=0). The values used in figures 67 and 68 for the geometric parameter k_2 were (0.05; 0.08; 0.11; 0.14), for α_0 were (20°, 30°, 40°, 50°, 60°), for γ_1 was 0° and for $\Delta\theta$ were (90°, 150°, 210°, 270°, 340°). The normalized thrust acceleration a_0 value used in figures 67 and 68 was -0.25.

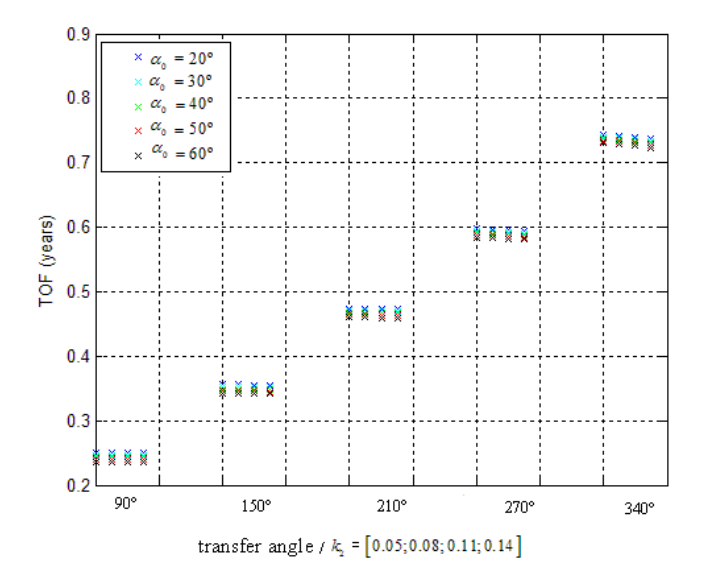


Figure 90: TOF for k_2 values of (0.05; 0.08; 0.11; 0.14) from left to right in the figure, α_0 values of (20°, 30°, 40°, 50°, 60°), $\Delta\theta$ values of (90°, 150°, 210°, 270°, 340°) (N=0), γ_1 =0°, a_0 =-0.25, acceleration inversely square case (exponential sinusoid), Earth-Mercury flight

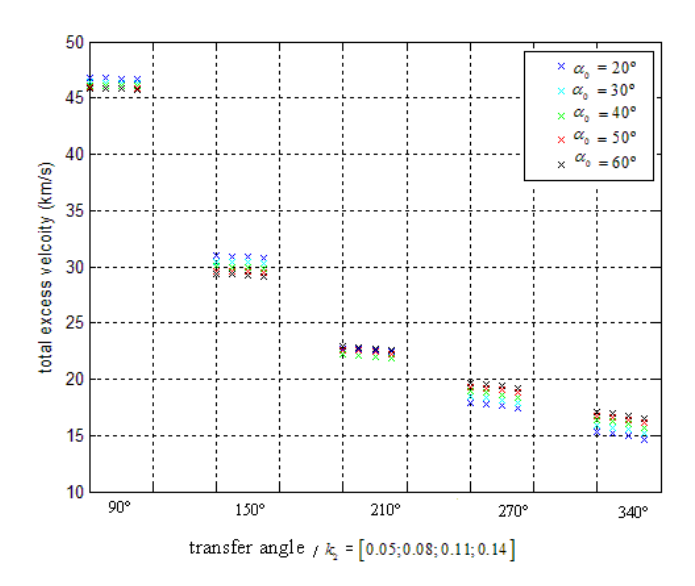


Figure 91: $V_{\infty,\tau}$ for k_2 values of (0.05; 0.08; 0.11; 0.14) from left to right in the figure, α_0 values of (20°, 30°, 40°, 50°, 60°), $\Delta\theta$ values of (90°, 150°, 210°, 270°, 340°) (N=0), γ_1 =0°, α_0 =-0.25, acceleration inversely square case (exponential sinusoid), Earth-Mercury flight

From figures 67 and 68, as expected, the TOF increases when increasing the transfer angle, while the total excess velocity decreases. By increasing the geometric parameter k_2 , the TOF and the total excess velocity decrease. The differences in TOF and in total excess

velocity between different values of k_2 increase for higher values of the transfer angle $\Delta\theta$. The highest difference in TOF between different θ_i for the same phase angle and α_0 is 0.0063 years, while the highest difference in total excess velocity is $0.6653 \, km/s$. For increasing values of α_0 , the TOF decreases while the total excess velocity increases for transfer angles higher than 210° and it decreases for transfer angles lower than 210°.

Similar figures can be shown for 1 and 2 revolutions, using the same values for the geometric parameter k_2 , for the transfer angle $\Delta\theta$ and for the initial values of α and γ_1 . The normalized thrust acceleration a_0 values used in figures 69 and 70 were -0.09 and -0.06 for N=1 and N=2, respectively.

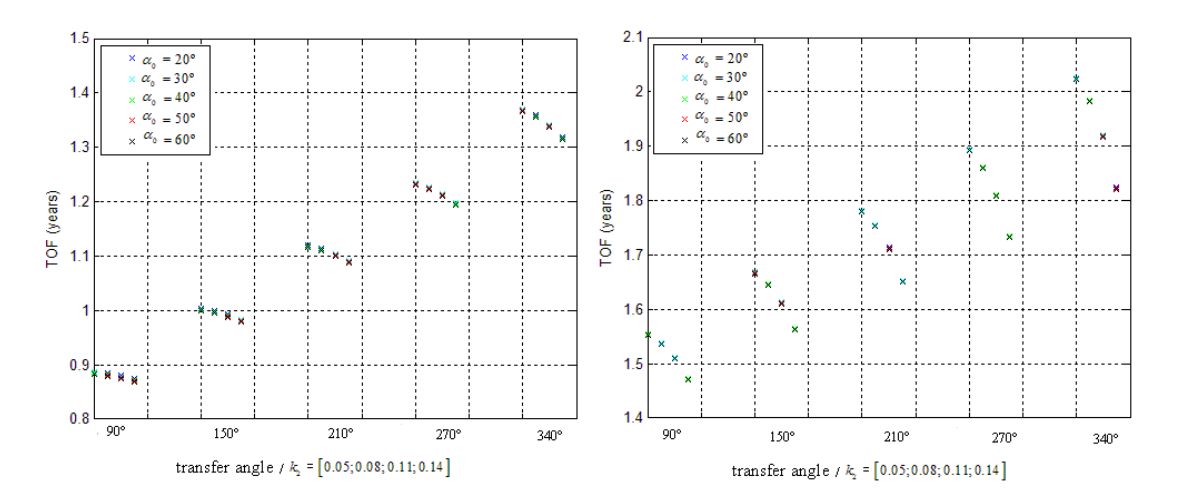


Figure 92: TOF for k_2 values of (0.05; 0.08; 0.11; 0.14) from left to right in the figure, α_0 values of (20°, 30°, 40°, 50°, 60°), $\Delta\theta$ values of (90°, 150°, 210°, 270°, 340°), γ_1 =0°, acceleration inversely square case (exponential sinusoid), Earth-Mercury flight, N=1 (a_0 =-0.09) and N=2 (a_0 =-0.06)

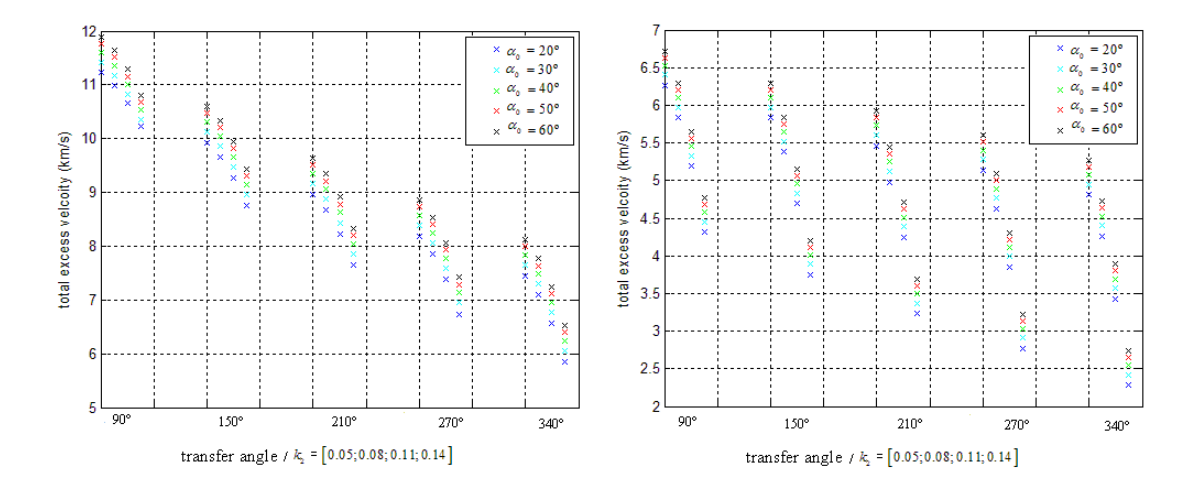


Figure 93: $V_{_{\circ,T}}$ for $k_{_2}$ values of (0.05; 0.08; 0.11; 0.14) from left to right in the figure, $\alpha_{_0}$ values of (20°, 30°, 40°, 50°, 60°), $\Delta\theta$ values of (90°, 150°, 210°, 270°, 340°), for $\gamma_{_1}$ =0°, acceleration inversely square case (exponential sinusoid), Earth-Mercury flight, N=1 ($a_{_0}$ =-0.09) and N=2 ($a_{_0}$ =-0.06)

Similar remarks to the ones given for N=0 can be drawn for figures 69 and 70. The differences in total excess velocity between different values of α_0 are higher for N=1 and N=2 than N=0. For N=1, the highest difference in TOF between different k_2 and for the same transfer angle and α_0 is about 0.0509 years, while the highest difference in total excess velocity is 1.5947 km/s. For N=2, the highest difference in TOF between different k_2 and for the same transfer angle is about 0.1954 years, while the highest difference in total excess velocity is 2.5275 km/s.

The TOF range for this Earth-Mercury flight is from 0.2358 years to 2.0252 years. The total excess velocity has a minimum value of 2.2831 km/s and a maximum value of 46.7494 km/s. The maximum differences in TOF between two consecutive values of the transfer angle $\Delta\theta$ are about 0.15 years. The maximum value for these differences is 16.5936 km/s for N=0 and the minimum value is about 0.3236 km/s for 2 revolutions.

Tables 17 and 18 show the values for the TOF and the excess velocity for an Earth-Mercury flight. Parameter k_2 was assumed 0.01, parameter α_0 was assumed 20°, the transfer angle $\Delta\theta$ was assumed 90° and N was taken 1 for the first table and 2 for the second one. In tables 17 and 18, the normalized thrust acceleration a_0 values were -0.09

and -0.06, respectively. Note that these values for a_0 , for N=1 and N=2 are the minimum values that can be used in both cases for this shape without facing integration problems for the interval of the input parameters considered.

N=1	$\gamma_1 = -3^{\circ}$	$\gamma_1 = -2.25^{\circ}$	$\gamma_1 = -1.5^{\circ}$	$\gamma_1 = -0.75^{\circ}$	$\gamma_1 = 0^{\circ}$
$V_{\infty,total}\left(km/s\right)$	10.4821	10.6811	10.8898	11.1134	11.3622
$V_{\infty,1}(km/s)$	1.5877	1.1895	0.7921	0.3956	3.97×10 ⁻⁵
$V_{\infty,2}(km/s)$	8.8944	9.4916	10.0976	10.7178	11.3621
TOF (years)	0.7947	0.8173	0.8405	0.8644	0.8890

Table 23: The excess velocities and the TOF values for N=1, k_2 =0.01, $\Delta\theta$ =90°, α_0 =20°, γ_1 values of (-3°; -2.25°; -1.5°; 0.75°; 0°), a_0 =-0.09, acceleration inversely square case (exponential sinusoid), Earth-Mercury flight

N=2	$\gamma_1 = -3^{\circ}$	$\gamma_1 = -2.25^{\circ}$	$\gamma_1 = -1.5^{\circ}$	$\gamma_1 = -0.75^{\circ}$	$\gamma_1 = 0^{\circ}$
$V_{\infty,total}\left(km/s\right)$	5.6018	5.7841	5.9779	6.1913	6.5220
$V_{\infty,1}(km/s)$	1.5993	1.2074	0.8186	0.4395	0.1620
$V_{\infty,2}(km/s)$	4.0025	4.5767	5.1593	5.7518	6.3598
TOF (years)	1.2949	1.3575	1.4233	1.4926	1.5657

Table 24: The excess velocities and the TOF values for N=2, k_2 =0.01, $\Delta\theta$ =90°, α_0 =20°, γ_1 values of (-3°; -2.25°; -1.5°; 0.75°; 0°), a_0 =-0.06, acceleration inversely square case (exponential sinusoid), Earth-Mercury flight

From tables 17 and 18, the order of magnitude of the excess velocity values is $10^0 \, km/s$ and $10^1 \, km/s$. For increasing values of m, the total excess velocity and the TOF increase. The values for the total excess velocity are higher when N=1 than when N=2. Note that the excess velocity $V_{\infty,2}$ increases faster than the excess velocity $V_{\infty,1}$ decreases, for both cases N=1 and N=2.

In figures 71 to 75 the polar plot, the thrust acceleration a, the thrust angle α , the polar angle rate $\dot{\theta}$ and the flight path angle as function of time are illustrated for N=1 and N=2 cases that were presented in tables 17 and 18.

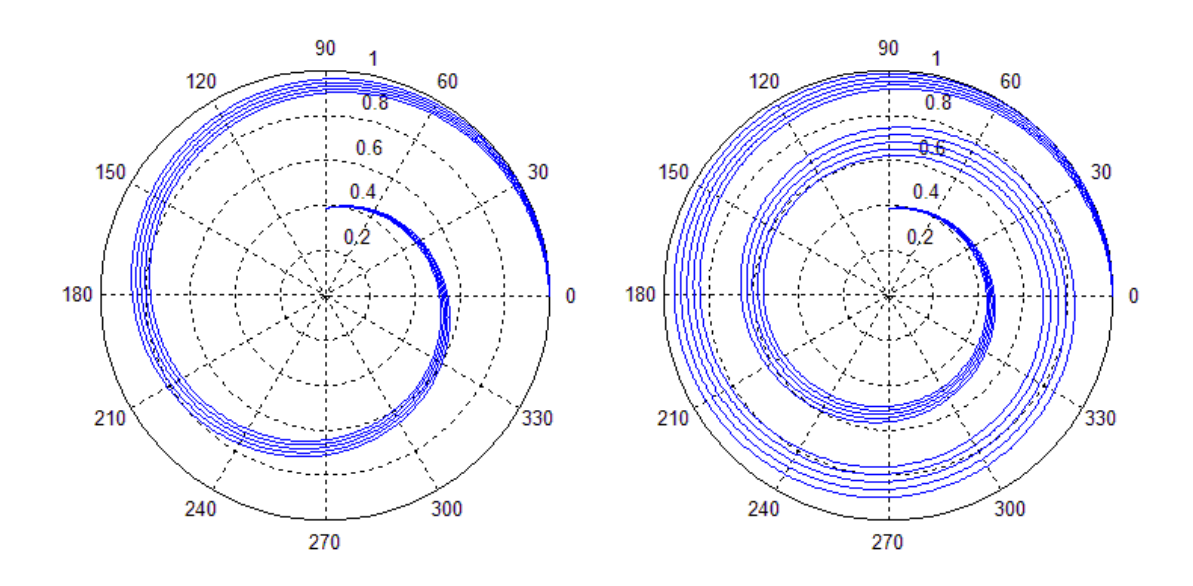


Figure 94: Polar plot for N=1 (a_0 =-0.09) and N=2 (a_0 =-0.06), k_2 =0.01, $\Delta\theta$ =90°, α_0 =20°, γ_1 values of (-3°;-2.25°;-1.5°;0.75°;0°), acceleration inversely square case (exponential sinusoid), Earth to Mercury

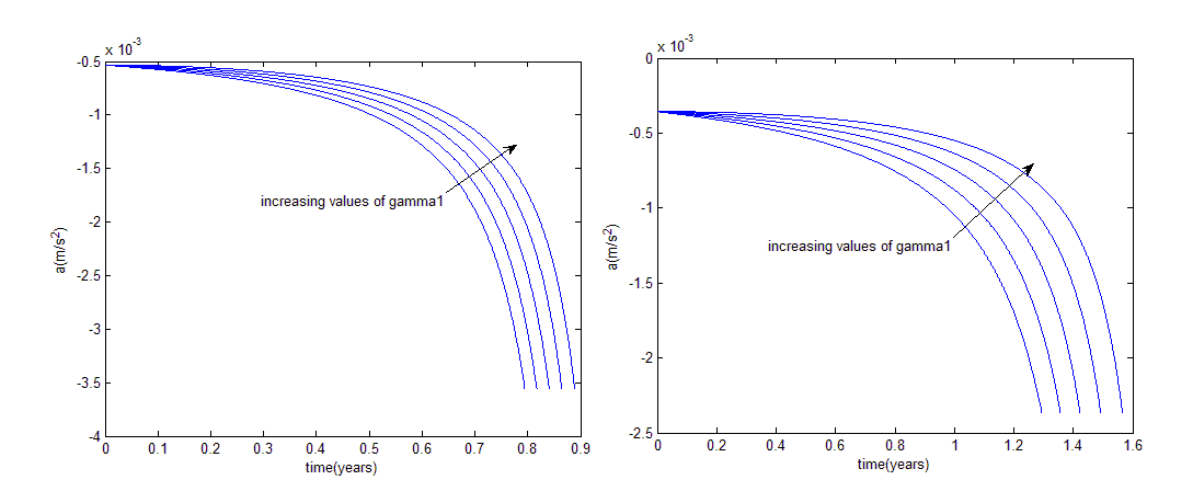


Figure 95: a plot for N=1 (a_0 =-0.09) and N=2 (a_0 =-0.06), k_2 =0.01, $\Delta\theta$ =90°, α_0 =20°, γ_1 values of (-3°; -2.25°; -1.5°; 0.75°; 0°), acceleration inversely square case (exponential sinusoid), Earth to Mercury

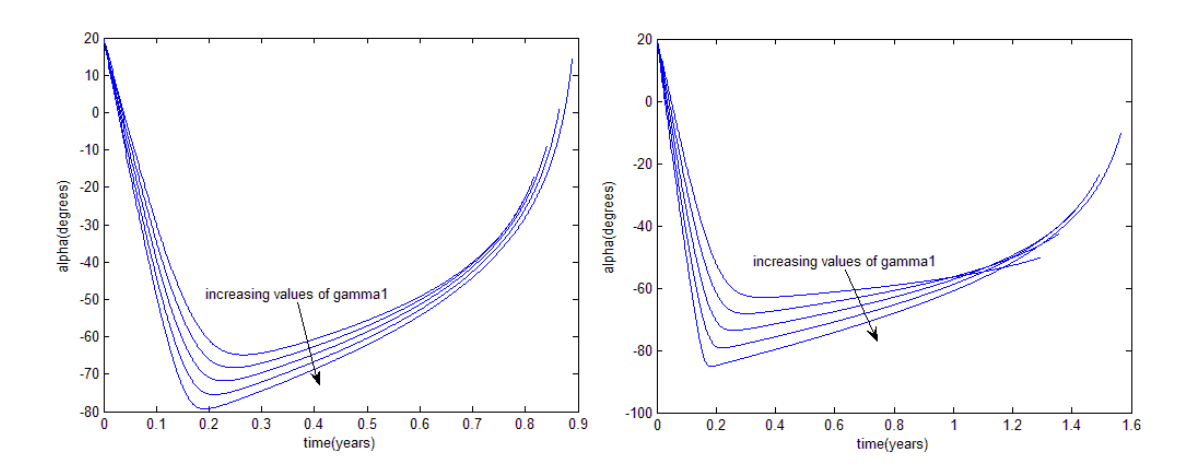


Figure 96: α plot for N=1 (a_0 =-0.09) and N=2 (a_0 =-0.06), k_2 =0.01, $\Delta\theta$ =90°, α_0 =20°, γ_1 values of (-3°;-2.25°;-1.5°;0.75°;0°), acceleration inversely square case (exponential sinusoid), Earth to Mercury

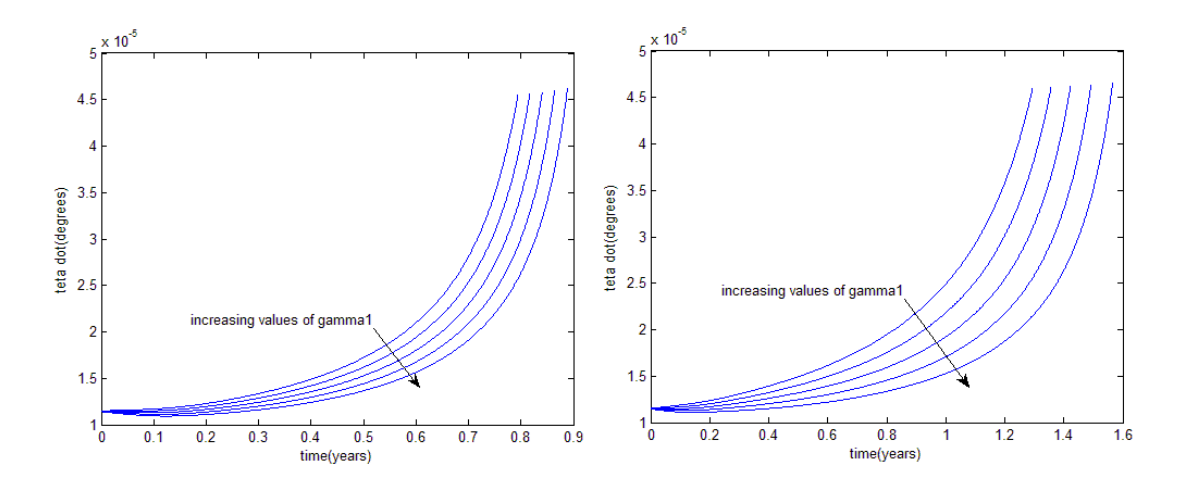


Figure 97: $\dot{\theta}$ plot for N=1 (a_0 =-0.09) and N=2 (a_0 =-0.06), k_2 =0.01, $\Delta\theta$ =90°, α_0 =20°, γ_1 values of (-3°;-2.25°;-1.5°;0.75°;0°), acceleration inversely square case (exponential sinusoid), Earth to Mercury

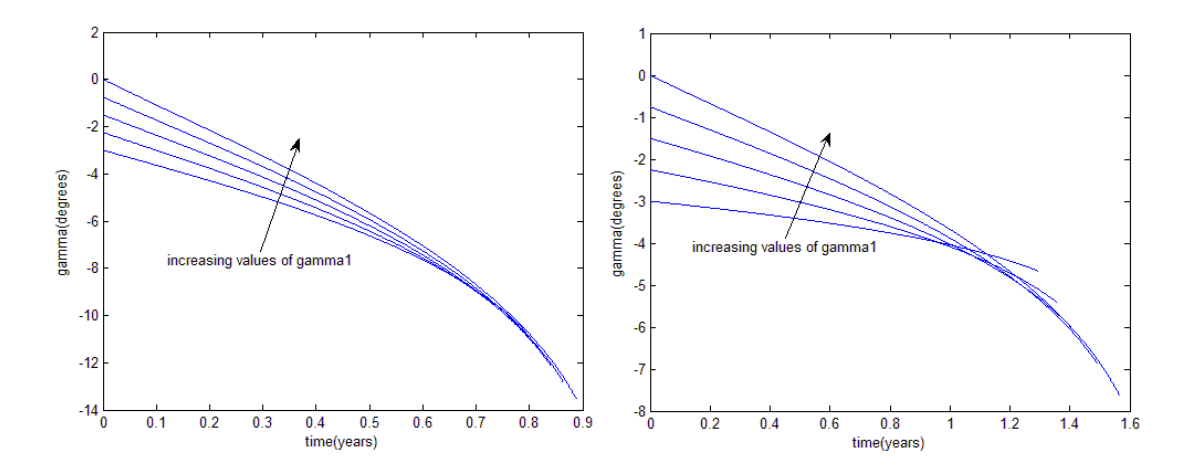


Figure 98: γ plot for N=1 (a_0 =-0.09) and N=2 (a_0 =-0.06), k_2 =0.01, $\Delta\theta$ =90°, α_0 =20°, γ_1 values of (-3°;-2.25°;-1.5°;0.75°;0°), acceleration inversely square case (exponential sinusoid), Earth to Mercury

The magnitude of the thrust acceleration is higher for N=1 and for N=2 because the assumed normalized thrust acceleration a_0 is also higher for N=1 than for N=2. For most of the interplanetary flight for both cases in figure 74, the spacecraft is thrusting inwards in the radial direction, while in the tangential direction it thrusts in the positive direction (α is negative, higher than -90°), like for the other two missions. This situation will be further analysed in section 7.7. The magnitude values of the flight path angle γ are smaller for N=2 than for N=1.

4. Earth-Mercury Flight, using the Tangential Thrust Profile

Figures 76 and 77 show the TOF and the total excess velocity when changing parameter k_2 and the transfer angle $\Delta\theta$ (N=0). The values used in these figures for k_2 were (0.05; 0.08; 0.11; 0.14), for γ_1 were (-3°; -2.25°; -1.5°; -0.75°; 0°) and for $\Delta\theta$ were (90°, 150°, 210°, 270°, 340°).

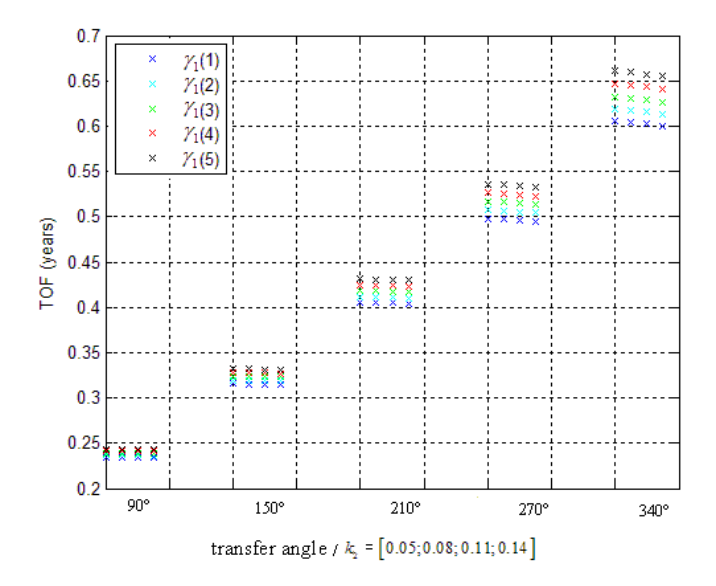


Figure 99: TOF for k_2 values of (0.05; 0.08; 0.11; 0.14) from left to right in the figure, γ_1 values of (-3°; -2.25°; -1.5°; -0.75°; 0°), $\Delta\theta$ values of (90°, 150°, 210°, 270°, 340°) (N=0), tangential thrust (exponential sinusoid), Earth-Mercury flight

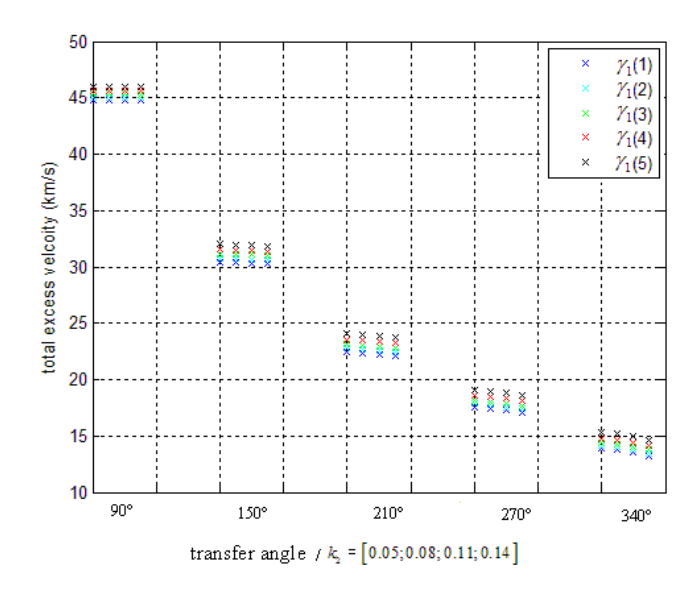


Figure 100: $V_{_{\infty,T}}$ for $k_{_2}$ values of (0.05; 0.08; 0.11; 0.14) from left to right in the figure, $\gamma_{_1}$ values of (-3°; -2.25°; -1.5°; -0.75°; 0°), $\Delta\theta$ values of (90°, 150°, 210°, 270°, 340°) (N=0), tangential thrust (exponential sinusoid), Earth-Mercury flight

From figures 76 and 77, as expected, the TOF increases when increasing the transfer angle, while the total excess velocity decreases. By increasing k_2 , the TOF and the total excess velocity decrease. For increasing values of γ_1 , the TOF and the total excess velocity

increase. The highest difference in the time of flight between different k_2 for the same phase angle and γ_1 is 0.0056 years, while the highest difference in the total excess velocity is $0.6826\,\text{km/s}$. The differences in TOF between different values of γ_1 increase for higher values of the transfer angle $\Delta\theta$.

Similar figures can be shown for one and two revolutions, using the same values for the geometric parameter k_2 , for the transfer angle $\Delta\theta$ and for the initial flight path angle γ_1 as the ones used for N=0.

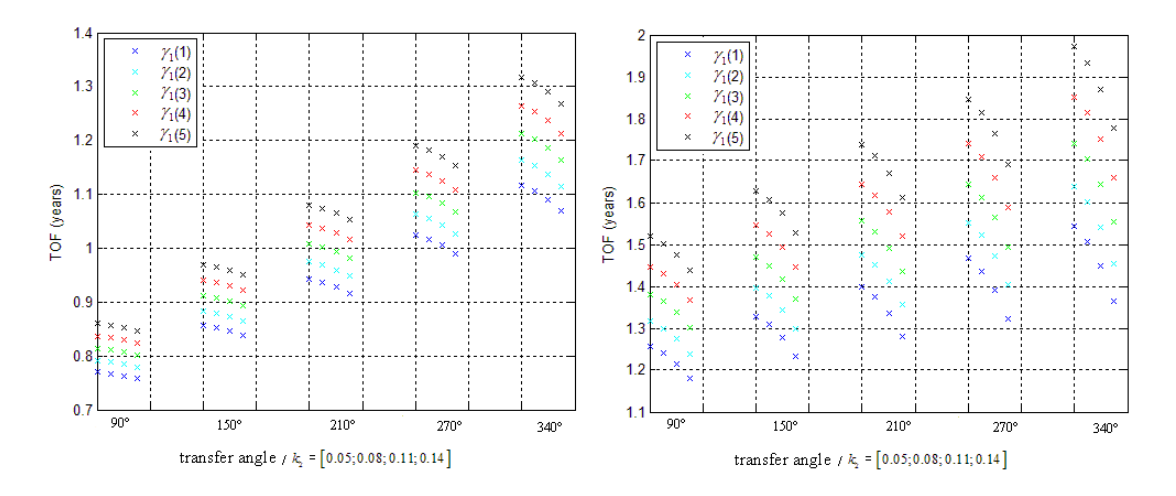


Figure 101: TOF for k_2 values of (0.05; 0.08; 0.11; 0.14) from left to right in the figure, γ_1 values of (-3°; -2.25°; -1.5°; -0.75°; 0°), $\Delta\theta$ values of (90°, 150°, 210°, 270°, 340°), tangential thrust (exponential sinusoid), Earth-Mercury flight, N=1 and N=2

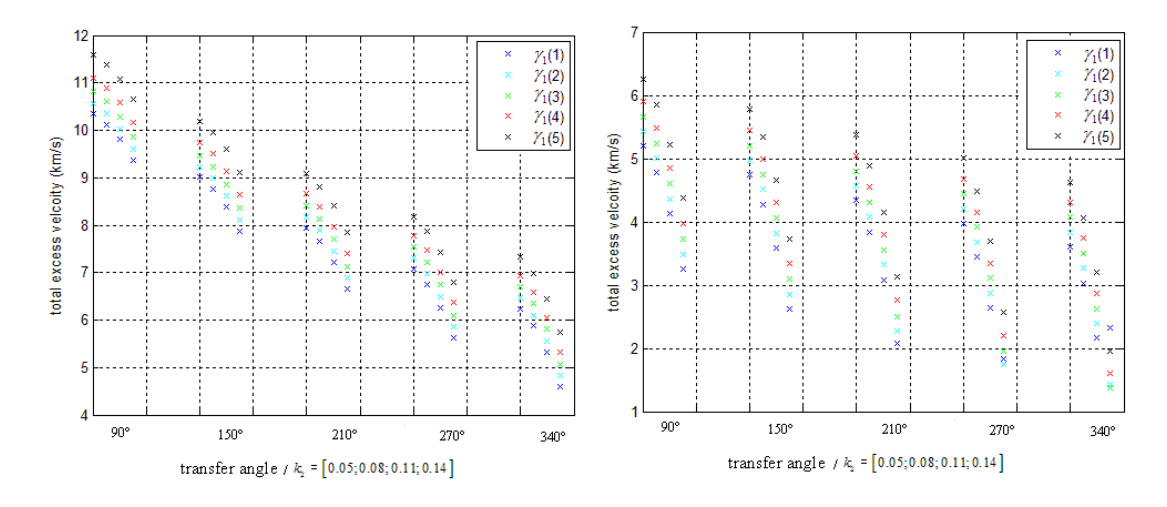


Figure 102: $V_{_{\circ,T}}$ for $k_{_2}$ values of (0.05; 0.08; 0.11; 0.14) from left to right in the figure, $\gamma_{_1}$ values of (-3°; -2.25°; -1.5°; -0.75°; 0°), $\Delta\theta$ values of (90°, 150°, 210°, 270°, 340°), tangential thrust (exponential sinusoid), Earth-Mercury flight, N=1 and N=2

Similar remarks to ones given for N=0 can be drawn for figures 78 and 79. The differences in TOF for different values of γ_1 are higher for N=1 and N=2 than N=0. For N=1, the highest difference in TOF between different k_2 for the same transfer angle and γ_1 is about 0.0489 years, while the highest difference in total excess velocity is 1.6434 km/s. For N=2, the highest difference in TOF between different k_2 for the same transfer angle and γ_1 is about 0.1897 years, while the highest difference in total excess velocity is 2.7032 km/s.

The TOF range for this Earth-Mercury flight is from 0.2343 years to 1.9719 years. The total excess velocity has a minimum value of $1.3834 \, km/s$ and a maximum value of $45.9447 \, km/s$. The maximum differences in TOF between two consecutive values of the transfer angle $\Delta\theta$ are about 0.13 years. For a certain number of revolutions, these differences increase when increasing the transfer angle. The difference in terms of total excess velocity between two consecutive transfer angles is the highest one between $\Delta\theta = 90^{\circ}$ and $\Delta\theta = 150^{\circ}$ for N=0. The maximum value for these differences is $14.4967 \, km/s$ for N=0 and the minimum value is $0.2335 \, km/s$ for N=2.

Tables 19 and 20 show the values for the TOF and the excess velocity for an Earth-Mercury flight. Parameter θ_i is zero and parameter k_2 assumed was 0.01, the transfer

angle $\Delta\theta$ assumed was 90° and the number of revolutions taken was 1 for the first table and 2 for the second one.

N=1	$\gamma_1 = -3^{\circ}$	$\gamma_1 = -2.25^{\circ}$	$\gamma_1 = -1.5^{\circ}$	$\gamma_1 = -0.75^{\circ}$	$\gamma_1 = 0^{\circ}$
$V_{\infty,total}(km/s)$	10.4787	10.7028	10.9418	11.2330	11.7050
$V_{\infty,1}(km/s)$	1.5738	1.2029	0.8516	0.5571	0.4481
$V_{\infty,2}(km/s)$	8.9049	9.4999	10.0902	10.6759	11.2569
TOF (years)	0.7721	0.7935	0.8156	0.8384	0.8621

Table 25: Excess velocities and TOF values for N=1, k_2 =0.01, $\Delta\theta$ =90°, γ_1 values of (-3°; -2.25°; -1.5°; -0.75°; 0°), tangential thrust (exponential sinusoid), Earth-Mercury flight

N=2	$\gamma_1 = -3^{\circ}$	$\gamma_1 = -2.25^{\circ}$	$\gamma_1 = -1.5^{\circ}$	$\gamma_1 = -0.75^{\circ}$	$\gamma_1 = 0^{\circ}$
$V_{\infty,total}\left(km/s\right)$	5.4540	5.6858	5.9173	6.1549	6.5023
$V_{\infty,1}(km/s)$	1.5590	1.1700	0.7835	0.4054	0.1407
$V_{\infty,2}(km/s)$	3.8949	4.5157	5.1338	5.7491	6.3616
TOF (years)	1.2661	1.3264	1.3900	1.4574	1.5287

Table 26: Excess velocities and TOF values for N=2, k_2 =0.01, $\Delta\theta$ =90°, γ_1 values of (-3°; -2.25°; -1.5°; -0.75°; 0°), tangential thrust profile (exponential sinusoid), Earth-Mercury flight

From tables 19 and 20, the order of magnitude of the total excess velocity values is $10^0 \, km/s$ and $10^1 \, km/s$. For increasing values of γ_1 , the TOF and the total excess velocity increase. The values for the total excess velocity are higher when N=1 than when N=2. Note that the excess velocity $V_{\infty,2}$ has the same trend as the total excess velocity, while the excess velocity $V_{\infty,1}$ decreases.

In figures 80 to 83, the polar plot, the thrust acceleration a, the thrust angle α and the polar angle rate $\dot{\theta}$ as function of time are illustrated for N=1 and N=2 cases that were presented in tables 19 and 20.

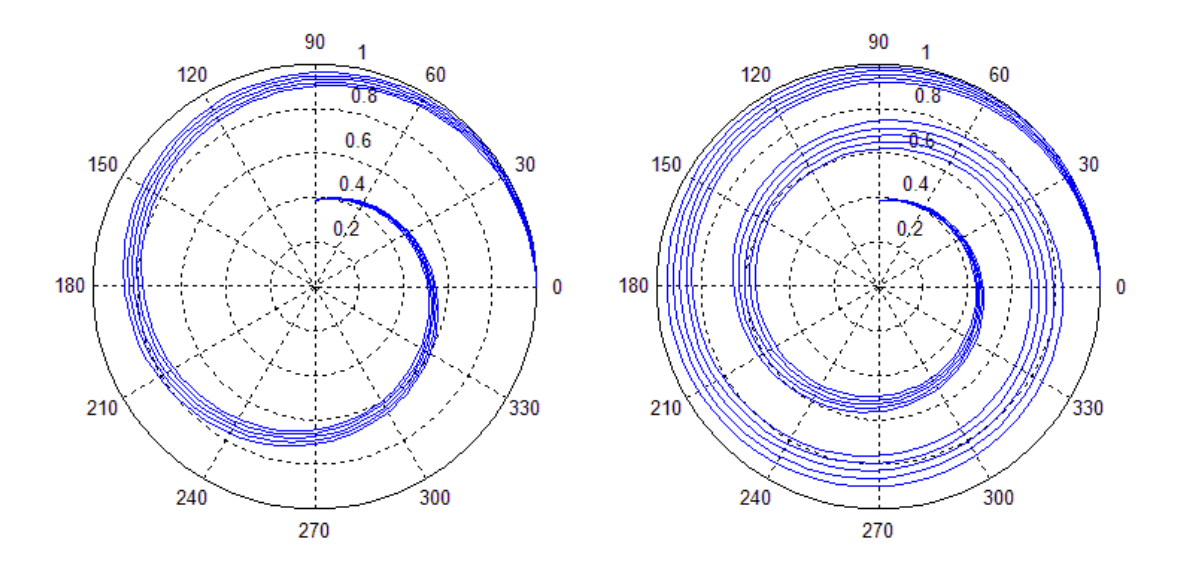


Figure 103: Polar plot for N=1 and N=2, k_2 =0.01, $\Delta\theta$ =90°, γ_1 values of (-3°; -2.25°; -1.5°; -0.75°; 0°), tangential thrust profile (exponential sinusoid), Earth-Mercury flight

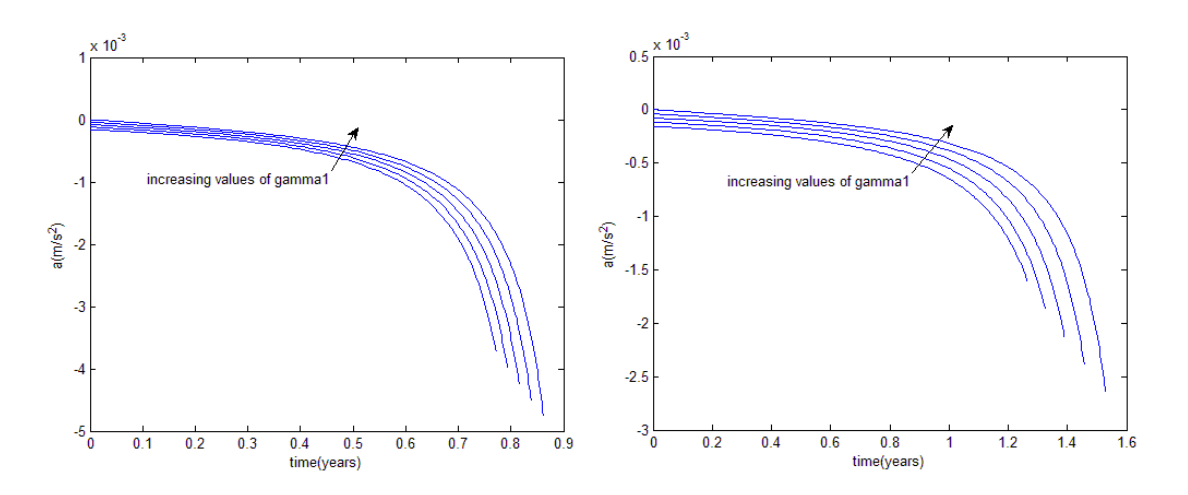


Figure 104: a plot for N=1 and N=2, k_2 =0.01, $\Delta\theta$ =90°, γ_1 values of (-3°; -2.25°; -1.5°; -0.75°; 0°), tangential thrust profile (exponential sinusoid), Earth-Mercury flight

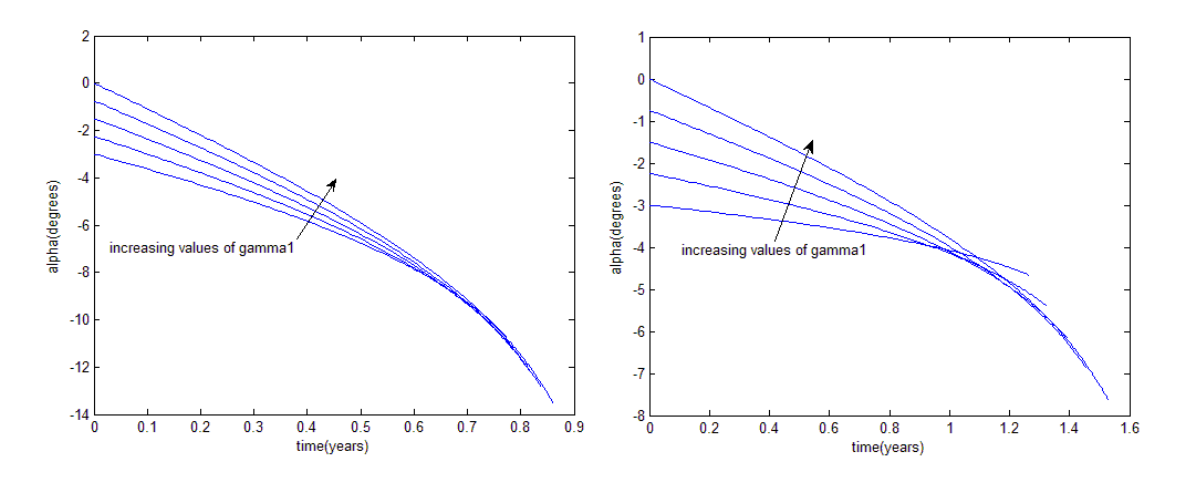


Figure 105: α plot for N=1 and N=2, k_2 =0.01, $\Delta\theta$ =90°, γ_1 values of (-3°; -2.25°; -1.5°; -0.75°; 0°), tangential thrust profile (exponential sinusoid), Earth-Mercury flight

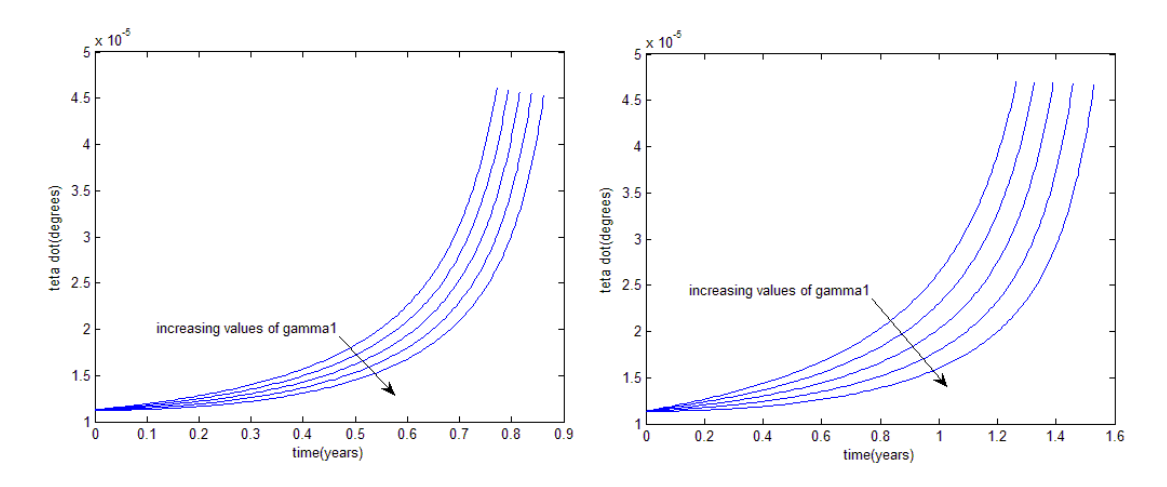


Figure 106: $\dot{\theta}$ plot for N=1 and N=2, k_2 =0.01, $\Delta\theta$ =90°, γ_1 values of (-3°; -2.25°; -1.5°; -0.75°; 0°), tangential thrust profile (exponential sinusoid), Earth-Mercury flight

The values for the thrust angle α are smaller in magnitude for N=2 than for N=1. The plot of the flight path angle γ in function of time is not shown, since in the tangential case $\alpha = \gamma$. Finally, the magnitude of the thrust acceleration α is higher for N=1 than for N=2.

Appendix F: Verification

As already mentioned in chapter 9, this master thesis deals with many mathematical expressions (appendix B). In this way, mistakes can be made when writing the equations in MATLAB code. The MATLAB program that was developed by giving the geometric parameters as an input in order to compute the thrust acceleration, the thrust angle, the TOF, the excess velocities and the fuel mass consumption for a certain mission is called *Low2D*. Since the results achieved for each shape need to be verified, a test program was developed: *Test2D*. This program uses the values of the thrust acceleration, thrust angle, the TOF and the initial position and velocity as inputs. Through a Runge-Kutta 4(5) integrator, it computes the trajectory of the spacecraft in the transfer plane. In the end, if the MATLAB code is correct, the values for the final position and velocity given by Test2D should match the ones used in Low2D.

Test2D was verified using the following inputs: the period of the Earth for the TOF, the circular velocity of the Earth and its distance to the Sun. In this test, the thrust acceleration and angle were considered zero. If Test2D is correct, the final position and velocity should be the same as the initial position and velocity, respectively. The trajectory was computed and the final position and velocity at the instance t = TOF differ from the initial position and velocity by $\sim 10^{-6} \, km$ and $\sim 10^{-10} \, km/s$, respectively. Since these differences are significantly small, the results given by Test2D can be considered verified.

Tables 21 to 23 present the differences in terms of position and velocity at the target planet between the values given by Low2D and Test2D. These tables were built for the acceleration inversely square case. In these tables, 'shape 1' is the Archimedean spiral, 'shape 2' is the logarithmic spiral, 'shape 3' is the Poinsot's spiral (hyperbolic sine), 'shape 4' is the Poinsot's spiral (hyperbolic cosine), 'shape 5' is the sinusoidal spiral and 'shape 6' is the exponential sinusoid.

	Shape 1	Shape 2	Shape 3	Shape 4	Shape 5	Shape 6
$\left \Delta r_{2}\right (km)$	0.5495	0.5471	1.7395	1.4766	1.066	1.4788
$ \Delta V_2 \ (mm/s)$	0.8985	0.9016	2.3288	1.1593	1.2178	1.1858

Table 27: Variation between the values given in Low2D and Test2D for the position and velocity at the target planet, Earth-Mars flight, $\Delta\theta$ =90°, N=1, acceleration inversely square case

	Shape 1	Shape 2	Shape 3	Shape 4	Shape 5	Shape 6
$\left \Delta r_2\right (km)$	3.5433	36.8599	49.2149	6.1633	6.5041	0.8981
$\left \Delta V_2\right (mm/s)$	0.6754	3.0193	3.5887	0.1	0.5996	0.4012

Table 28: Variation between the values given in Low2D and Test2D for the position and velocity at the target planet, Earth-Jupiter flight, $\Delta\theta$ =90°, N=1, acceleration inversely square case

	Shape 1	Shape 2	Shape 3	Shape 4	Shape 5	Shape 6
$\left \Delta r_{2}\right (km)$	0.8386	6.3592	2.5299	6.0732	5.7877	6.4705
$\left \Delta V_2\right (mm/s)$	3.3911	21.7885	5.1442	20.6900	21.5630	21.333

Table 29: Variation between the values given in Low2D and Test2D for the position and velocity at the target planet, Earth-Mercury flight, $\Delta\theta$ =90°, N=1, acceleration inversely square case

A similar test can be done for the constant acceleration case of the thrust profile case. The results are presented in tables 24 to 26.

	Shape 1	Shape 2	Shape 3	Shape 4	Shape 5	Shape 6
$\left \Delta r_{2}\right (km)$	0.2830	0.2635	2.4502	0.0585	0.4280	0.1912
$\left \Delta V_2\right (mm/s)$	0.1537	0.1342	0.8413	0.6048	0.8326	0.6327

Table 30: Variation between the values given in Low2D and Test2D for the position and velocity at the target planet, Earth-Mars flight, $\Delta\theta$ =90°, N=1, constant acceleration case

	Shape 1	Shape 2	Shape 3	Shape 4	Shape 5	Shape 6
$\left \Delta r_2\right (km)$	19.3649	48.7194	60.9231	27.4681	29.1238	39.6779
$ \Delta V_2 \ (mm/s)$	2.0560	1.082	0.8752	0.0227	0.326	0.6815

Table 31: Variation between the values given in Low2D and Test2D for the position and velocity at the target planet, Earth to Jupiter, $\Delta\theta$ =90°, N=1, constant acceleration case

	Shape 1	Shape 2	Shape 3	Shape 4	Shape 5	Shape 6
$\left \Delta r_{2}\right (km)$	1.8913	19.2616	1.088	25.5034	12.8667	56.1440
$\left \Delta V_2\right \ (\textit{mm/s})$	25.1917	108.82	2.316	127.4	64.67	297.9

Table 32: Variation between the values given in Low2D and Test2D for the position and velocity at the target planet, Earth to Mercury, $\Delta\theta$ =90°, N=1, constant acceleration case

A similar test can be done for the tangential case of the thrust profile case. The results are presented in tables 27 to 29.

	Shape 1	Shape 2	Shape 3	Shape 4	Shape 5	Shape 6
$\left \Delta r_{2}\right (km)$	0.3942	0.8078	118.0380	17.6294	14.8096	19.5991
$\left \Delta V_2\right \ (mm/s)$	0.2459	0.5656	238.9	13.71	14.5	13.07

Table 33: Variation between the values given in Low2D and Test2D for the position and velocity at the target planet, Earth-Mars flight, $\Delta\theta$ =90°, N=1, tangential case

	Shape 1	Shape 2	Shape 3	Shape 4	Shape 5	Shape 6
$\left \Delta r_{2}\right (km)$	4.1238	0.9518	125.6456	31.1107	33.8446	29.7854
$\left \Delta V_2\right (mm/s)$	0.6405	42	99.8	10.97	10.02	10.7

Table 34: Variation between the values given in Low2D and Test2D for the position and velocity at the target planet, Earth-Jupiter flight, $\Delta\theta$ =90°, N=1, tangential case

	Shape 1	Shape 2	Shape 3	Shape 4	Shape 5	Shape 6
$\left \Delta r_{2}\right (km)$	456.3820	121.6437	49.8625	41.9713	45.5778	41.8992
$\left \Delta V_2\right (mm/s)$	3193.5	243.7	288.9	89.34	112.7	82.14

Table 35: Variation between the values given in Low2D and Test2D for the position and velocity at the target planet, Earth-Mercury flight, $\Delta\theta$ =90°, N=1, tangential case

The variation values in terms of velocity of the spacecraft at the target are the highest one for the Earth-Mercury mission in all 3 cases of the thrust profile. In this case, a higher tolerance can be used. The variation values in terms of position are highest for the Earth-Jupiter mission except for the tangential case and for the exponential sinusoid. Generally, the errors increase for higher integration time. Since the order of magnitude of the travelling distance of the spacecraft is $10^{11}m$ and the order of magnitude of the velocity at the target is $10^4 m/s$, Low2D can be considered benchmarked in this test.

As already mentioned in chapter 9, Low2D was also verified with the MATLAB routines given by Dario Izzo [Izzo, 2006] for the exponential sinusoid using the tangential thrust.

Also, the computation of low-thrust trajectories using STA was verified with the software JAQAR. In table 30 the scenario for testing the STA module to compute low-thrust trajectories is shown. Note that this test scenario was performed with version 8 of the SBC [JAQAR, 2007].

Departure date (departure planet)	18/08/2009 (Earth)
Arrival date (arrival planet)	02/11/2010 (Mars)
Geometric parameter k_{3}	0.7071
Number of revolutions N	0

Table 36: Test scenario for STA

Departure	STA	JAQAR	Error			
planet	$V_{_{\infty}}(\mathrm{km/s})$	V_{∞} (km/s)	V _∞ (%)			
Earth	1.8528	1.8678	0.8031			
Arrival	STA	JAQAR	Error	STA: Mfuel (low-	JAQAR: Mfuel (low-	Error:
planet	V_{∞} (km/s)	V_{∞} (km/s)	V _∞ (%)	thrust+ ΔV_{Mars}) (kg)	thrust+ ΔV_{Mars}) (kg)	Mfuel (%)
Mars	1.7504	1.7522	0.1028	342.5350	342.3587	0.0515

Table 37: Values for the excess velocities and the fuel mass consumption using STA and JAQAR, for the test scenario in table 30

Since the ephemeris used in both software is different and that the values for the errors in table 31 are smaller than 1%, the computation of low-thrust trajectories in STA was considered well implemented.

Appendix G: Test of the Number of Individuals

In this appendix, a test will be made to verify if the number of individuals used for the population in the Monte Carlo optimization provide accurate results for the Pareto fronts. This test will only be made for one shape - the exponential sinusoid and for the tangential and the acceleration inversely square cases of the thrust profile. 4 Pareto fronts were built for: 25 000, 50 000, 75 000 and 100 000 individuals for the population, for the tangential case. Figure 107 shows these 4 Pareto fronts.

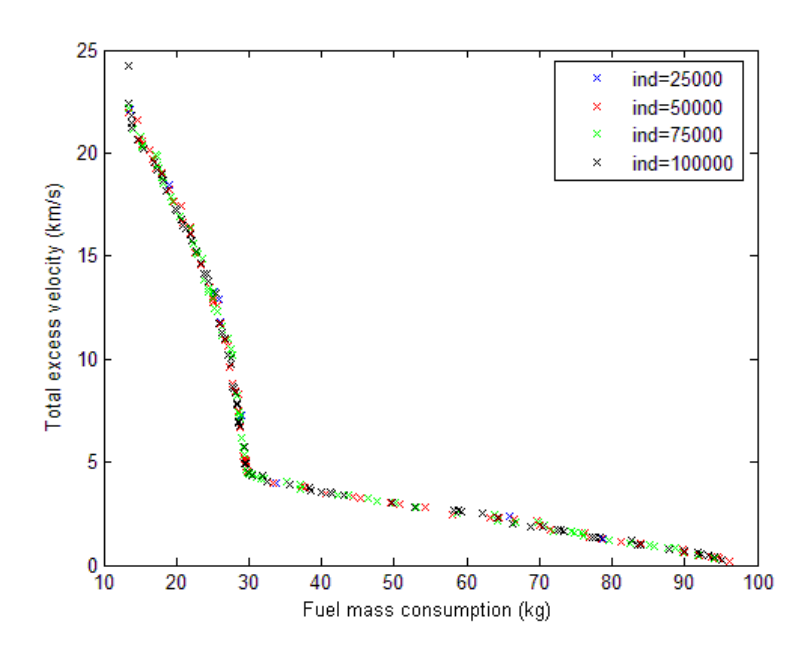


Figure 107: Pareto fronts for the number of individuals of the population: 25 000, 50 000, 75 000 and 100 000, tangential case

From figure 84, the differences between the Pareto fronts for different sizes of the population are significantly small. The number of individuals in the Pareto front is: 50 for 25 000 individuals, 75 for 50 000 individuals and 80 for 75 000 and 100 000 individuals. This means that, since the Pareto fronts are quite similar and there is no difference in terms of the number of individuals in the Pareto front for 75 000 and 100 000 individuals in the population, 75 000 will be the number of individuals chosen for the population.

For the acceleration inversely square case, 4 Pareto fronts were built for: 25 000, 50 000, 75 000 and 100 000 individuals for the population, as well.

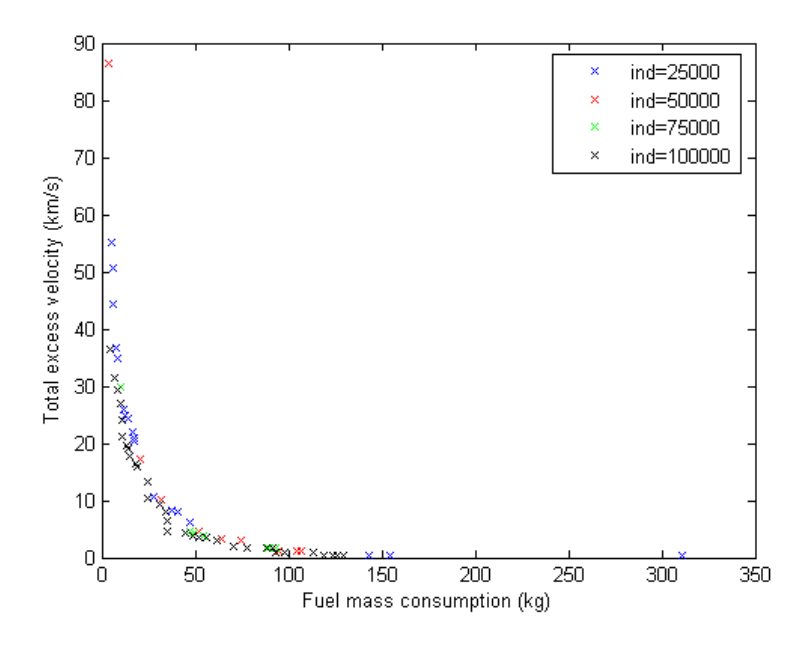


Figure 108: Pareto fronts for the number of individuals of the population: 25 000, 50 000, 75 000 and 100 000, acceleration inversely square case

From figure 85, the differences between the Pareto fronts for 75 000 and 100 000 individuals of the population are significantly small. Note that just a few green individuals can be seen in figure 85, because most of the individuals in the Pareto front for 75 000 individuals are also present in the Pareto front with 100 000 (black individuals). The number of individuals in the Pareto front is: 30 for 25 000 individuals, 29 for 50 000 individuals, 31 for 75 000 and 33 for 100 000 individuals. Note that these numbers are much lower than the ones given for the tangential case. This is due to the integration errors that occur for the acceleration inversely square case and consequently many individuals have to be discarded during the optimization procedure. Since the difference for the number of individuals between the 4 Pareto fronts is small and there is no much difference between the Pareto front for 75 000 and 100 000 individuals, the number of the population will be 75 000.

Appendix F: Optimization for an Earth-Jupiter Flight

In this appendix, the optimization results for the Earth-Jupiter flight using tangential thrust will be shown. Figure 109 illustrates the Pareto fronts using the tangential thrust profile in an Earth-Jupiter flight for all6 shapes. As already said in chapter 8, the population that is being used is 75000 individuals for each shape.

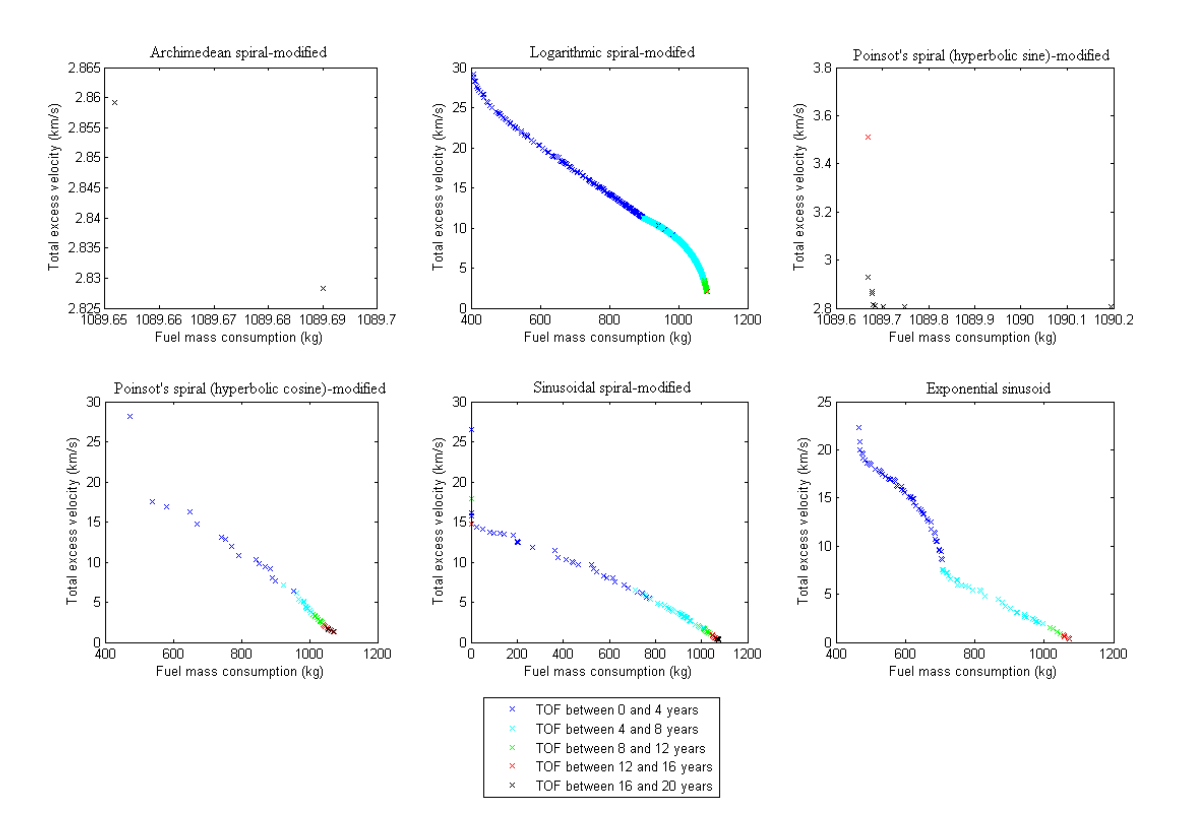


Figure 109: Pareto fronts for the Archimedean spiral, logarithmic spiral, Poinsot's spiral (hyperbolic sine), Poinsot's spiral (hyperbolic cosine), sinusoidal spiral and exponential sinusoid, tangential thrust, Earth-Jupiter flight

In figure 86, the Archimedean spiral and the Poinsot's spiral (hyperbolic sine) show worse results compared with the other 4 shapes: the fuel consumption values are higher and the number of individuals in the Pareto front is significantly low, as for the Earth-Mars flight.

Figure 110 summarizes the Pareto fronts for all 6 shapes. In the plot in the right-hand side, the same Pareto fronts are represented but only with individuals with values of total excess

velocity lower than $5 \, km/s$ and values of fuel mass consumption between 1000 and 1100 kg.

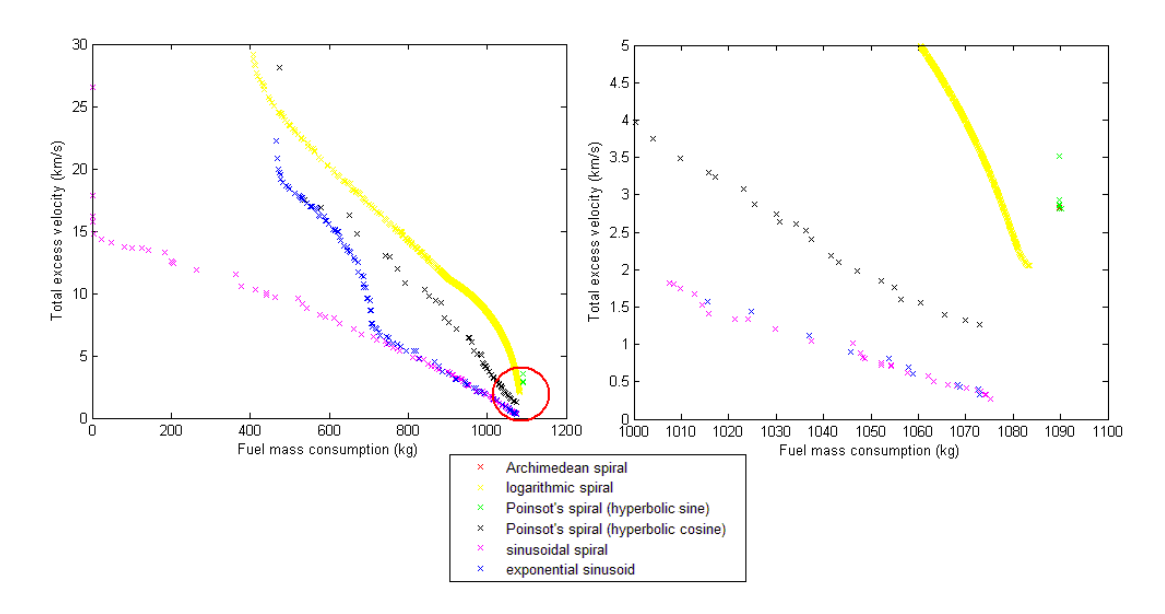


Figure 110: Pareto fronts for the Archimedean spiral, logarithmic spiral, Poinsot's spiral (hyperbolic sine), Poinsot's spiral (hyperbolic cosine), sinusoidal spiral and exponential sinusoid, tangential thrust, Earth-Jupiter flight

Individuals with values lower than 407.25 kg, 474.51 kg and 465.18 kg are not present for the Pareto fronts for the logarithmic spiral, for the Poinsot's spiral (hyperbolic cosine) and for the exponential sinusoid, respectively. The minimum value of fuel consumption is achieved with the sinusoidal spiral and it is 0.9439 kg (close to the targeting Lambert problem). The minimum values of the total excess velocity in the Pareto fronts are $2.0525 \, km/s$, $1.2693 \, km/s$ and $0.3270 \, km/s$ for the logarithmic spiral, for the Poinsot's spiral (hyperbolic cosine) and for the exponential sinusoid, respectively. The minimum value for the total excess velocity of all shapes is achieved with the sinusoidal spiral and it is $0.2711 \, km/s$. Individuals with TOF values higher than 20 years were not selected for the Pareto fronts, since the maximum number of complete revolutions was 3. The TOF range of most individuals in Pareto front for the 4 shapes mentioned above (logarithmic spiral, Poinsot's spiral (hyperbolic cosine), sinusoidal spiral and exponential sinusoid) is between 0 and 8 years.

Note that the total excess velocity values for lower values of fuel mass consumption are significantly high. Individuals with these values of total excess velocity cannot be taken into account in a real mission. However, in order to understand the limits of each shape, they were not excluded from the Pareto front.

From figure 87, the Pareto fronts for the exponential sinusoid and the sinusoidal spiral provide lower values of fuel mass consumption for the same total excess velocity when comparing with the Poinsot's spiral (hyperbolic cosine) or the logarithmic spiral. The logarithmic spiral has the highest number of individuals in the Pareto front of all 6 shapes.

The range of fuel mass and total excess velocity values for the sinusoidal spiral is the widest one. This shape and the exponential sinusoid have similar performances for fuel mass consumptions higher than $\sim 700~{\rm kg}$.

Note that the Pareto front of the exponential sinusoid has 2 different trends: after and before $\sim 700 \text{ kg}$. The bent seen in figure 86 at $\sim 700 \text{ kg}$ was already studied in section 10.1.1, in order to understand why there are two different curvatures in the Pareto front. The situation for the Earth-Mars case and this one are similar.

• Thrust Acceleration Constraint

Computation times were tracked for all 6 shapes and they are shown in table 32. Also, the percentage of the individuals in the Pareto front and in the population that respects the maximum ratio between the thrust acceleration that is given as an output from a certain shape and the available thrust acceleration (≤ 1) is presented for the three different cases. The three cases are for the following available thrust acceleration trends: (1) $a_{available} = 0.064 \,\mu/r^2$ (twice $a_{available}$ in DS1), (2) $a_{available} = 0.096 \,\mu/r^2$ (3 times $a_{available}$ in DS1) and (3) $a_{available} = 0.128 \,\mu/r^2$ (4 times $a_{available}$ in DS1) (see chapter 8).

Shapes	Computation time (hours)	N_{Pf}	G _{pf} (%)	G _{Pop} (%)
Archimedean spiral	1.41	2	100/100/100	2.7/5.8/8.2
Logarithmic spiral	0.69	6158	0.1/1.2/4.2	2.3/6.3/10.8
Poinsot's spiral (hyperbolic sine)	0.73	9	100/100/100	27.6/43.6/54.5
Poinsot's spiral (hyperbolic cosine)	0.72	49	34.7/53.1/63.3	47.4/63.8/72.5
Sinusoidal spiral	2.71	95	25.3/41/64.2	7.7/20/30.7
Exponential sinusoid	3.06	99	4/9.1/17.2	0.4/1.8/3.9

Table 38: Computation time, number of individuals in the Pareto front ($N_{\rm pf}$) and the percentage of individuals in the Pareto front $G_{\rm pf}$ and in the population $G_{\rm pop}$ that respect the maximum value for the ratio between the required thrust acceleration of the spacecraft and the available one for the 6 shapes and for the 3 cases of $a_{\rm 0,available} = a_{\rm 0,Deep space 1} \left[2/3/4 \right]$ in an Earth-Jupiter flight (tangential case)

The optimization procedure when using the exponential sinusoid used more computation time than the other shapes. Also, the percentage of individuals in the population that do not respect the maximum value for the ratio between the required thrust acceleration of the spacecraft and the available one is highest for the exponential sinusoid in all three cases. However, the logarithmic spiral has the lower percentage of individuals in the Pareto front that respects the constraints for the thrust acceleration available. Note that although 100% of the individuals in the Pareto front for the Archimedean spiral and the Poinsot's spiral (hyperbolic sine), the fuel consumption for both shapes are higher when compared with the other 4 shapes.

Figures 88 and 89 illustrate the Pareto fronts for the sinusoidal spiral and for the exponential sinusoid when only considering the individuals in the population that respect the condition in (8.7) in chapter 8. As for the Earth-Mars flight, these two shapes have the

best performance in terms of the Pareto front. Using the condition in (8.7) as a constraint, for the two shapes named before, a certain number of individuals in the population are discarded, respectively and a new Pareto front is built. Figures 88 and 89 show the Pareto fronts for the sinusoidal spiral and exponential sinusoid, respectively when the available thrust acceleration $a_{available} = (0.064;0.096;0.128)\mu/r^2$ is given as a constraint.

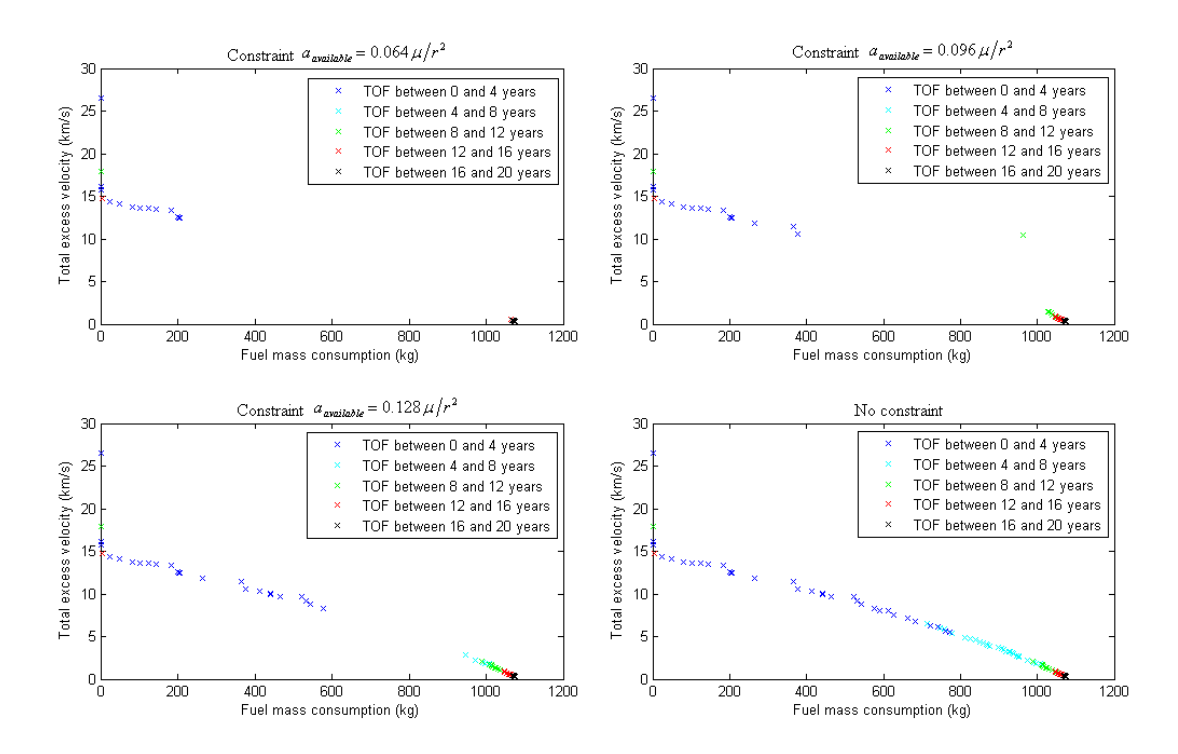


Figure 111: Pareto fronts for the sinusoidal spiral, for the entire population (on the right) and only for individuals in the population that respect the condition (8.7) (the three cases), tangential thrust, Earth-Jupiter flight

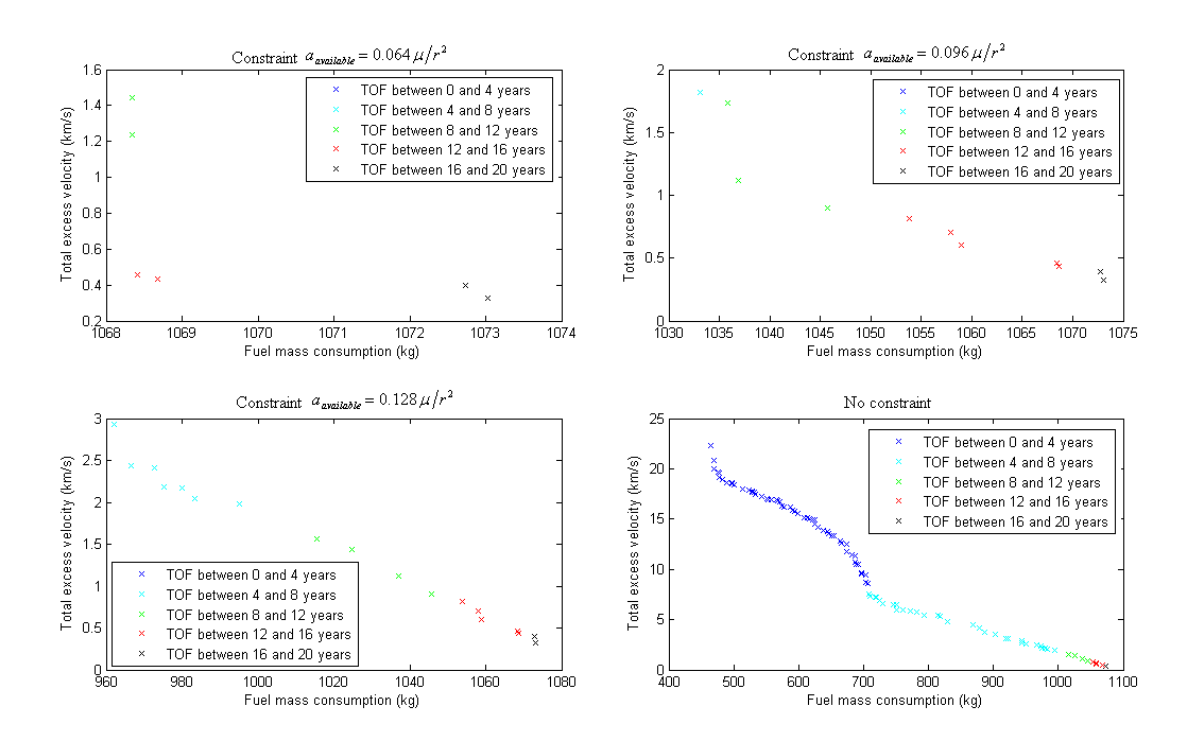


Figure 112: Pareto fronts for the exponential sinusoid, for the entire population (on the right) and only for individuals in the population that respect the condition (8.7) (the three cases), tangential thrust, Earth-Jupiter flight

From figures 88 and 89, for the exponential sinusoid, the individuals in the Pareto front have a mass fuel consumption values higher than 962 kg for the case with the highest value of $a_{0,available}$. For increasing values of $a_{0,available}$, the number of individuals in the Pareto front increases and lower values of fuel mass consumption are allowed. For the sinusoidal spiral, there is a gap in the Pareto front, where there are no individuals.

End of Document